DLES 13

13th ERCOFTAC Workshop on Direct & Large Eddy Simulation

26-28 October 2022

Udine, Italy

UNIVERSITÀ DEGLI STUDI DI UDINE

ERCOFTAC

European Research Community On Flow, Turbulence And Combustion

Session: Convection and heat/mass transfer

Wednesday, October 26, 2022

10:00 – 11:00

WORKSHOP
Direct and Large-Eddy Simulation 13
October 26th-29th 2022, Udine, Italy

A POSTERIORI LES OF FORCED CONVECTION ALONG HEATED AND COOLED WALLS WITH TEMPERATURE-DEPENDENT FLUID PROPERTIES

L. Sufrà[1] and **H. Steiner**[1]
[1]Institute of Fluid Mechanics and Heat Transfer
Graz University of Technology, Austria
helfried.steiner@tugraz.at

INTRODUCTION

The forced convective transfer of momentum and heat is frequently subject to a strong variation in local material properties, especially for working fluids with a high molecular Prandtl number, typically involving steep near wall gradients of temperature. The inherent disparity of smallest thermal and dynamic length scales does not only seriously challenge the spatial resolution, it also questions the commonly assumed Reynolds analogy, relating the turbulent heat flux directly to the turbulent flux of momentum. The present LES study particularly assesses three popular subgrid-scale models [1, 2, 3] in capturing adequately the feedback of the variation of the material properties on the turbulent motion near heated or cooled walls. Data from highly resolved Direct Numerical Simulations (DNS) [4] are used for validation. Fully developed turbulent pipe flow is considered as generic test configuration, assuming a real-life coolant, a $50/50 Vol\%$ mixture of ethylene glycol/water, with a molecular Prandtl number $Pr_w = 10$, based on wall conditions. The strongly varying dynamic viscosity significantly affects here the local molecular Prandtl number and Reynolds number inducing either a tendency to relaminarization or enhancement of turbulent mixing. Thus far, rather few DNS and LES studies addressed this issue, examining mainly the effect of a temperature-dependent viscosity on the turbulent flow field, while giving no or comparatively little attention to the turbulent heat transfer [5, 6].

FORMULATION AND TESTED SGS-MODELS

The present LES solved the Favre-filtered conservation equations of mass, momentum, and energy, generally written in non-dimensional representation as

$$\frac{\partial \widetilde{\varrho}^*}{\partial t} + \nabla \cdot \left(\widetilde{\varrho}^* \overline{\mathbf{U}}^+ \right) = 0 \tag{1}$$

$$\frac{\partial \widetilde{\varrho}^* \overline{\mathbf{U}}^+}{\partial t} + \nabla \cdot (\widetilde{\varrho}^* \overline{\mathbf{U}}^+ \, \overline{\mathbf{U}}^+) = -\nabla \widetilde{P}^+ + \nabla \cdot \left[\frac{\widetilde{\mu}^*}{Re_\tau} \left(2\,\underline{\widetilde{S}} - \frac{2}{3}\, tr(\underline{\widetilde{S}})\, \underline{\mathbf{I}} \right) \right] - \nabla \cdot \tau_{sgs} + \widetilde{\mathbf{f}}_w \tag{2}$$

$$\frac{\partial \overline{\chi}^+}{\partial t} + \nabla \cdot (\overline{\mathbf{U}}^+ \, \overline{\chi}^+) \; - \overline{\chi}^+ \nabla \cdot \overline{\mathbf{U}}^+ = \frac{1}{\widetilde{\varrho}^* Re_\tau Pr_w} \nabla \cdot \left(\frac{\widetilde{\lambda}^*}{\widetilde{c}_p^*} \nabla \widetilde{\chi}^+ \right) - \frac{1}{\widetilde{\varrho}^*} \nabla \cdot \mathbf{q}_{sgs} + \widetilde{f}_\chi, \tag{3}$$

respectively, using the pipe diameter D, the wall friction velocity $w_\tau = (\tau_w/\varrho_w)^{1/2}$, and friction enthalpy $h_\tau = \langle q_w \rangle / \varrho_w w_\tau$ as reference scales. $\langle q_w \rangle$ represents the imposed constant average wall heat flux, which is positive/negative in the heated/cooled case. $\overline{\mathbf{U}}^+ = \overline{\mathbf{U}}/w_\tau = (\bar{u}^+, \bar{v}^+, \bar{w}^+)^T$ and $\overline{\chi}^+ = (h_w - \bar{h})/h_\tau$ represent the filtered non-dimensional velocity vector in cylindrical coordinates and filtered enthalpy difference to the wall value, respectively. The asterisked material properties always refer to the corresponding wall values. $Re_\tau = \rho_w w_\tau D/\mu_w$ and $Pr_w = \mu_w c_{p,w}/\lambda_w$ denote the Reynolds and Prandtl number based on wall conditions, respectively. The terms $\widetilde{\mathbf{f}}_w = 4\,\mathbf{e}_z$ and $\widetilde{f}_\chi = \overline{w}^+/\dot{m}^*$ with $\dot{m}^* = \dot{m}/D^2 \pi \varrho_w w_\tau$ enforce axial periodicity.

The computational domain is sketched in Figure 1. At the wall, no-slip boundary conditions are assumed for the velocity, $\overline{\mathbf{U}}^+ = 0$, and isothermal boundary conditions are imposed for the instantaneous enthalpy difference, $\overline{\chi}^+ = 0$, The near wall resolution of the LES grid is $\Delta r^+ = 0.29$, $R^+ \Delta\varphi = 8.8$, and $\Delta z^+ = 28.1$ wall units in the radial, azimuthal, and axial direction, respectively.

The unresolved subgrid-scale fluxes are modelled based on the Boussinesq eddy viscosity/diffusivity concept

$$\tau_{sgs}^d = -2\,\widetilde{\rho}^* \frac{\nu_{sgs}^*}{Re_\tau} \underline{\widetilde{S}}^d, \quad \mathbf{q}_{sgs} = -\frac{1}{Re_\tau c_p^*} \frac{\nu_{sgs}^*}{Pr_{sgs}} \nabla \widetilde{\chi}^+ \tag{4}$$

with constant $Pr_{sgs} = 0.5$. Three popular models for the subgrid-scale eddy viscosity $\nu_{sgs}^* = \nu_{sgs}/\nu_w$ are tested: the Smagorinsky (SMAG) [1], the Wall-Adapting Local Eddy Viscosity (WALE) [2], and the Coherent Structure Model (CSM) [3]. The Smagorinsky model (SMAG) enforces vanishing eddy viscosity near the wall applying a Van Driest-type damping function. CSM and WALE inherently provide this important feature in their model formulation for ν_{sgs}^*.

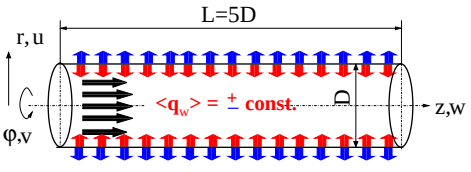

Figure 1: Computational domain

RESULTS

We considered fully developed pipe flow at Reynolds number $Re_\tau = 360$ and molecular Prandtl number $Pr_w = 10$,

based on wall conditions, specified by the average wall temperature being always $\langle T_w \rangle = 344.8K$. The wall is uniformly heated/cooled by a wall heat flux $\langle q_w \rangle = \pm 2 \cdot 10^4 W/m^2$, respectively. Figure 2 compares the predicted first order statistics against DNS, including also results from LES without a sgs-model. CSM and WALE produce evidently very good agreement with DNS over the whole y^+-range, while the LES with SMAG generally overestimates the velocity and underestimates the enthalpy difference. This discrepancy can be explained by the total turbulent shear stress/heat flux, $\tau^+_{turb} = -\langle \tilde{\rho}^* \overline{u}'^+ \overline{w}'^+ \rangle - \tau_{rz,sgs}$ and $q^+_{turb} = -\langle \tilde{\rho}^* \overline{u}'^+ \overline{\chi}'^+ \rangle - q_{r,sgs}$, which are consistently predicted too low/high, respectively, near the wall for LES with SMAG, as exemplarily shown in Figure 3 for the heated case. The accordingly higher/lower laminar components translate into a faster/slower increase in the axial mean velocity $\langle w^+ \rangle$ and mean enthalpy difference $\langle \overline{\chi}^+ \rangle$, respectively, seen for SMAG. CSM and WALE apparently provide a small, but still essential subgrid-scale model contribution, as indicated by the notable discrepancy of the LES without sgs-model in Figure 2. The SMAG predicted subgrid-scale eddy viscosity shown in Figure 4 appears as fairly insensitive to the decrease/increase of the local Reynolds number, as the molecular viscosity decreases/increases with distance to the heated/cooled wall, while CSM and WALE reasonably reflect this trend.

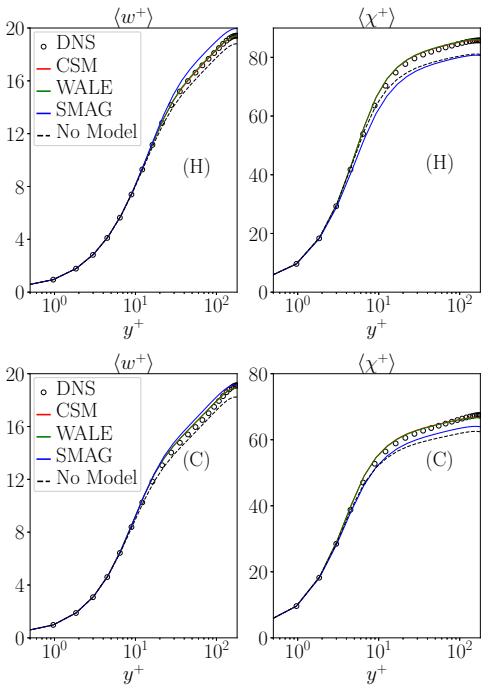

Figure 2: Mean axial velocity and enthalpy difference vs. wall distance y^+, (H) heated case, (C) cooled case

CONCLUSIONS

For the considered operating liquid and flow conditions, the approaches WALE and CSM are proven as well-suited subgrid-scale models for capturing adequately the dampened/enhanced turbulent convective transport near the heated/cooled pipe wall. The SMAG model overly dissipates the resolved small-scale motion instead. This deficit is not

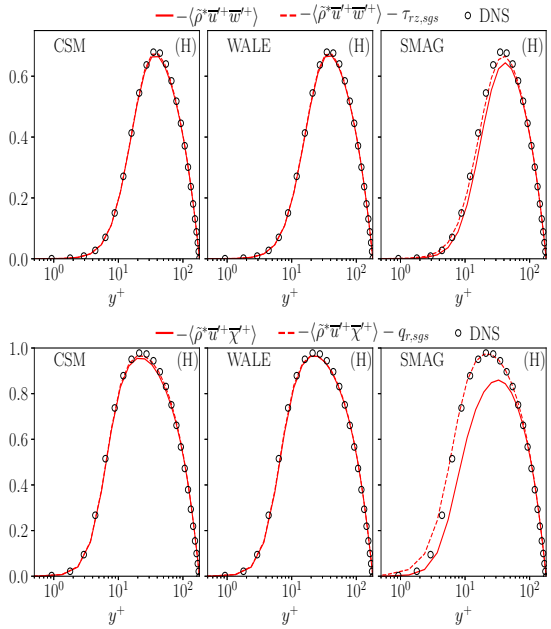

Figure 3: Turbulent fluxes of momentum and heat, heated case

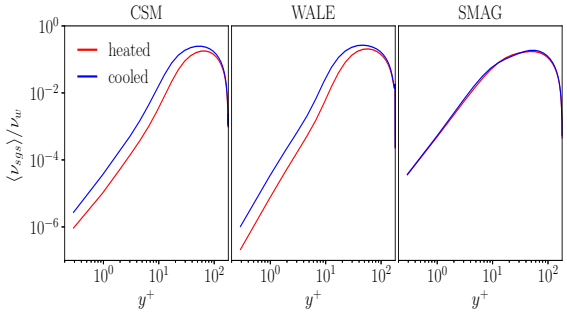

Figure 4: Subgrid-scale eddy viscosity $\nu^*_{sgs} = \nu_{sgs}/\nu_w$ vs. wall distance y^+

appropriately compensated by the modelled Van Driest-style dampened subgrid-scale contribution, as otherwise seen for WALE and CSM, which also need to model considerably less unresolved small-scale content.

REFERENCES

[1]Smagorinsky, J. : General circulation experiments with the primitive equations: I. The basic experiment, *Mon. Weather Rev.*, **91**,99–164 (1963).

[2]Nicoud, F. and Ducros, F. : Subgrid-scale stress modelling based on the square of the velocity gradient tensor, *Flow Turbul. Combust.*, **62**, 183–200 (1999).

[3]Kobayashi, H. : The subgrid-scale models based on coherent structures for rotating homogeneous turbulence and turbulent channel flow,*Phys. Fluids*, **17**, 45–104 (2005).

[4]Sufrà, L. and Steiner, H. : Forced turbulent convection along heated and cooled walls with variable fluid properties, *ASME. J. Fluids Eng.*, **144**, 011401 (2022).

[5]Lee, J., Jung, S.Y., Sung, H.J. and Zaki, T.A. : Effect of wall heating on turbulent boundary layers with temperature-dependent viscosity, *J. Fluid Mech.*, **726**,196–225 (2013).

[6]Zonta, F., Marchioli, C. and Soldati, A. : Modulation of turbulence in forced convection by temperature-dependent viscosity,*J. Fluid Mech.*, **697**,150–174 (2012).

WORKSHOP
Direct and Large-Eddy Simulation 13
October 26th-29th 2022, Udine, Italy

POOL BOILING SIMULATIONS USING A GEOMETRIC VOLUME OF FLUID METHOD

B.J. Boersma[1]
[1] Department of Maritime & Transport Technology
Delft University of Technology, The Netherlands
b.j.boersma@tudelft.nl

INTRODUCTION

Boiling and condensation play an important role in many applications. Only recently these phenomena have been incorporated in simulation model for two-phase flows, see for instance [1] and [3]. Popular methods to simulate two phase flows are levelset and volume of fluids methods. In these methods the moving, deformable interface is implicitly defined by a marker function on a fixed Eulerian grid. Levelset (LS) methods are easy to implement, mathematically well posed, but not strict mass conserving. Volume of Fluid (VOF) methods are mass conserving but require fairly complex interface reconstruction. Combination of both methods are possible, see for instance [7] and [8].

The main computational bottleneck in multi-phase simulation is the solution of the Poisson equation for the pressure (or pressure correction). Due to the density jump at the interface fast Poisson solvers, (see e.g. [2]), which are very common in single phase flow can not be implemented in a straightforward manner.

During the COVID period a new high performance model for boiling, condensation and cavitation has been developed that uses a geometric VOF method for the interface capturing. For the solution of the Poisson equation the method of [10] is used, which is orders of magnitude faster than commonly used iterative methods. With this new model computational time are drastically reduced and are comparable to times needed for single phase models.

GOVERNING EQUATIONS AND NUMERICAL METHOD

In the section we will describe the governing equations and the computational method. For simplicity we will only consider cubic cell, i.e. $\Delta x = \Delta y = \Delta z$, the number off cells per coordinate directions can be different. We will use a staggered arrangement of the variables with the scalars in the center of the cell and the velocity components at the faces. Furthermore, we will assume that thermodynamic properties are not a function of temperature and pressure and thus constant within the liquid and vapor phase.

For two-phase flows is convenient to introduce the mixture quality x which is defined as the vapor mass fraction in a computational cell divided by the total mass in the cell. The mixture quality can be used to related the specific volume and the enthalpy [4]

$$x = \frac{v - v_f}{v_g - v_f} = \frac{h - h_f}{h_g - h_f}. \tag{1}$$

Here the subscript f denotes the liquid phase and the subscript g the vapor phase. The specific volume of the saturated liquid v_f and saturated vapor v_g are only function of the thermodynamic pressure. The difference in the specific enthalpy of the vapor h_g and h_f is often denoted as the latent heat of evaporation $h_{fg} = h_g - h_f$.

The equations for conservation of momentum and energy read:

$$\frac{\partial \rho}{\partial t} + \frac{\partial \rho u_i}{\partial x_i} = 0, \tag{2}$$

$$\frac{\partial h}{\partial t} + u_i \frac{\partial h}{\partial x_i} = -\frac{1}{\rho}\frac{\partial q_i}{\partial x_i}, \quad \text{with} \quad q_i = -\kappa \frac{\partial T}{\partial x_i}, \tag{3}$$

where ρ is the density by definition equal to $1/v$, u_i the velocity vector, h the enthalpy, T the temperature, q_i the heat flux vector and κ the thermal conductivity. For computational cells that are complete filled with liquid ($x = 0$) or vapor ($x = 1$) the density ρ is assumed to be constant and the enthalpy change dh can be replaced by $c_p dT$ where c_p can have different values for the liquid and vapor phase . For cells with $x = 0$ or $x = 1$ the equations above reduce to:

$$\frac{\partial u_i}{\partial x_i} = 0, \tag{4}$$

$$\frac{\partial T}{\partial t} + u_i \frac{\partial T}{\partial x_i} = \frac{\kappa}{\rho c_p}\frac{\partial^2 T}{\partial x_i^2}. \tag{5}$$

For cells that contain a mixture, $0 < x < 1$, equation (2) can be reformulated in terms of the specific volume v as

$$\frac{\partial v}{\partial t} + u_i \frac{\partial v}{\partial x_i} = v \frac{\partial u_i}{\partial x_i}, \tag{6}$$

with help of the definition of the mixture quality x this can be rewritten as:

$$\frac{\partial x}{\partial t} + u_i \frac{\partial x}{\partial x_i} = \frac{v}{v_g - v_f}\frac{\partial u_i}{\partial x_i}. \tag{7}$$

In a similar way the equation for the enthalpy (3) can be written in terms of x as:

$$\frac{\partial x}{\partial t} + u_i \frac{\partial x}{\partial x_i} = -\frac{v}{h_g - h_f}\frac{\partial q_i}{\partial x_i}. \tag{8}$$

Thus it follows that

$$\frac{\partial u_i}{\partial x_i} = -\frac{v_g - v_f}{h_{fg}}\frac{\partial q_i}{\partial x_i}. \tag{9}$$

In an isothermal flow ($q_i =$) this relation reduce to the well known relation for incompressible flows.

COMPUTATIONAL PROCEDURE

The equations above are discretized on staggered mesh. The interface between the liquid is tracked by a geometric VOF method for the mixture quality x. A piece wise linear interface reconstruction is used[5]. The normal vector needed for the interface reconstruction are calculated with a least square method over a $3 \times 3 \times 3$ stencil. Surface tension effects are implemented by the continuous surface force method, where the curvature is calculated using the height function approach, [9].

Mass conservation is ensured by a pressure correction method. In this method the momentum equation (not given here) is integrated in time from time t, denoted by superscript n to time $t + \Delta t$, denoted by superscript $n + 1$. The velocity after integration at $t + \Delta t$ denoted by u_i^* does not satisfy equation (4) or (9) and a correction has to be made via the pressure p^{n+1}

$$u_i^{n+1} = u_i^* - \Delta t \frac{1}{\rho^n} \frac{\partial p^{n+1}}{\partial x_i} \rightarrow \frac{\partial}{\partial x_i} \left(\frac{1}{\rho^n} \frac{\partial p^{n+1}}{\partial x_i} \right) = \frac{1}{\Delta t} \frac{\partial u_i^*}{\partial x_i}.$$

Due to the jump in density at the interface the Poisson equation can not be solved with a fast Poisson solver. Dodd & Ferrante [10] propose the following approximation:

$$\frac{1}{\rho^n} \frac{\partial p^{n+1}}{\partial x_i} = \frac{1}{\rho_0} \frac{\partial p^{n+1}}{\partial x_i} + \left(\frac{1}{\rho^n} - \frac{1}{\rho_0} \right) \frac{\partial p^n}{\partial x_i},$$

where ρ_0 is a constant. The last term in the right hand side is now at time level n and can be lumped in the momentum equation. The resulting Poisson equation, (for more details see [6]):

$$\frac{\partial^2 p^{n+1}}{\partial x_i^2} = \frac{\rho_0}{\Delta t} \frac{\partial u_i^*}{\partial x_i},$$

can be solved by my means of a fast Poisson solver, see [2]

RESULTS

In Figure 1, we present four snapshots taken from a pool boiling simulation. The geometry used is a Cartesian box with 512×512 points in the horizontal directions and 256 points in the vertical direction. Initially the box is filled for 50% with saturated liquid. At time ($t = 0$) a ring at the bottom of the computational domain is heated and small vapor bubbles will form which will rise due to buoyancy.

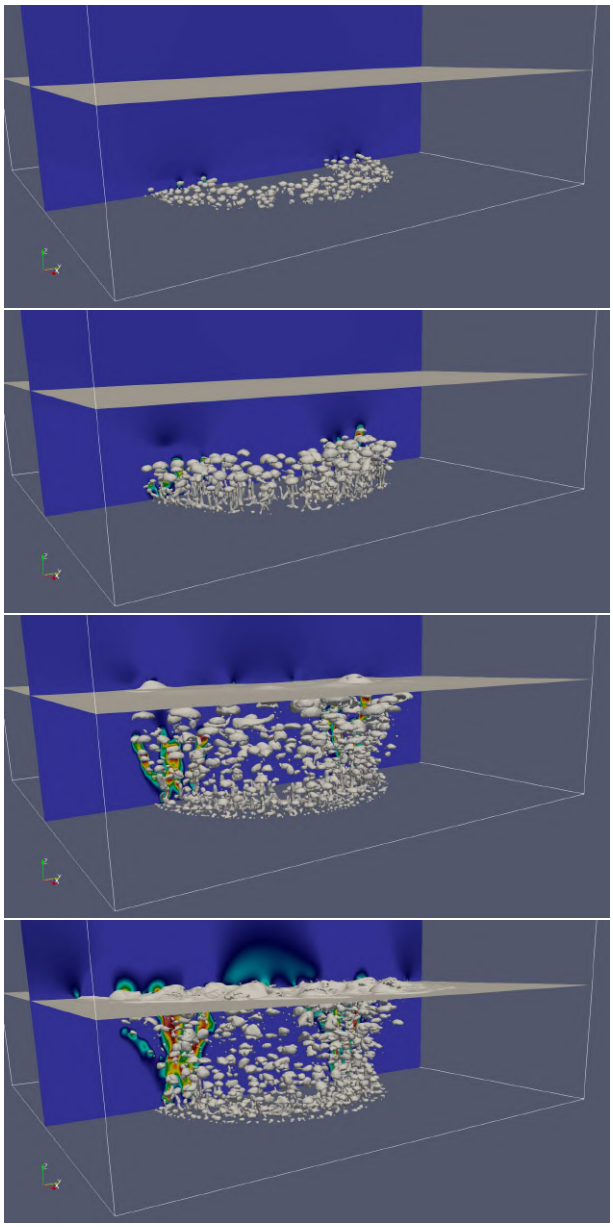

Figure 1: Pool boiling simulations, four snapshots equally space in time ($\rho_l/\rho_g = 400, \mu_l/\mu_g = 20, \kappa_l/\kappa_g = 10, c_{p,l}/c_{p,g} = 20$ and $h_{fg} = 25 c_{p,l}$). The flow is visualized with help of an isosurface of the mixture quality ($x = 0.5$) and the magnitude of the vertical velocity in the mid plane of the domain. For the simulations 32 Intel Xeon processors are used.

REFERENCES

[1]Sato, Y. & Niceno, B., 2013, A sharp-interface phase change model for a mass-conservative interface tracking method, *J. of Comp. Phys.*, **249**, 127-161.

[2]Schumann, U., & Sweet, R.A., 1988, Fast Fourier transforms for direct solution of Poisson's equation with staggered boundary conditions, **75**, 123-137.

[3]Malan, L.C., Malan, A.G., Zaleski, S. & Rousseau, 2021, A geometric VOF method for interface resolved phase change and conservative thermal energy advection, *J. of Comp. Phys.*, **426**, 109920.

[4]Moran, J.M., & Shapiro, H.N., 2006, Fundamentals of Engineering Thermodynamics, Wiley, New-York.

[5]Gueyffier, D., Li, J., Nadim, A., Scardovelli, R., & Zaleski, S., 1999, Volume-of-fluid interface tracking with smoothed surface stress methods for three dimensional flows, *J. of Comp. Phys.*, **153**, 423-456.

[6]Nemati, H., Breugem, W.P., Kwakkel, M., & Boersma, B.J., 2021, Direct numerical simulation of turbulent bubbly down flow using an efficient CLSVOF method, *Int. J. of Multiphase Flow*, **135**, 103500

[7]Van der Pijl, S.P., Segal, A., Vuik, C., & Wesseling, P., 2005, A mass-conserving Level-Set method for multiphase flows, *Int. J. for Num. Meth. in Fluids*, **47**, 339-361.

[8]Sussman, M, & Puckett, E.G., 2000, A Coupled Level Set and Volume-of-Fluid Method for Computing 3D Axisymmetric Incompressible Two-Phase Flows, *J. of Comp. Phys.*, **162**, 301-337.

[9]López, J. Zanzi, C., Gómes, P., Zamora, R., Faura, F., Hernández, J., An improved height function technique for computing interface curvature from volume fractions, *Comput. Methods Appl. Mech. Engrg*, **198**, 2555-2564.

[10]Dodd, M.S., Ferrante, A., A fast pressure-correction method for incompressible two-fluid flows, *J. of Comp. Phys.*, **273**, 416-434.

WORKSHOP
Direct and Large-Eddy Simulation 13
October 26th-29th 2022, Udine, Italy

EFFECT OF VARIABLE DENSITY ON SUBGRID SCALES

A. Abbà[1], M.H. Aliyoldashi[1], A. Cimarelli[2] and M. Germano[3]
[1] Dipartimento di Scienze e Tecnologie Aerospaziali
Politecnico di Milano, Italy
antonella.abba@polimi.it
[2] Department of Engineering 'Enzo Ferrari'
University of Modena and Reggio Emilia, Italy
[3] Department Civil and Environmental Engineering
Duke University, USA

INTRODUCTION

Variable density flows are very common in nature, in technology and in industry. The numerical simulation of complex flows of applicative interest and with relevant variable density flows requires the truncation of turbulent scales of the resolved velocity field, in order to reduce the required computational resources. By this way the averaged field is computed using the Reynolds averaged Navier-Stokes (RANS) equations, or the filtered in space equations if the Large Eddy Simulation (LES) approach is applied. Because of the non linearity of the governing Navier-Stokes equations, a closure model is required to represent the non resolved scales. The scales truncation applied to the mass conservation equation for compressible flows should require a closure model also for the mass flux. To avoid this, the Favre average [1] was introduced for the ensemble averaged quantities in RANS, and it has been estended to filter in space operator in LES [2]. The use of the Favre filter approach is prevalently preferred in LES of variable density flows. The works of Boersma and Lele [3] and Sun and Lu [4], where a subgrid scale (SGS) eddy viscosity model is added to the density equation, and the paper of Sidhart and Candler [5], where an equation for the unresolved density fluxes is solved, constitute exceptions.

The filtered velocity $\overline{\mathbf{u}}$ and the Favre filtered velocity $\widetilde{\mathbf{u}} = \overline{\rho\mathbf{u}}/\overline{\rho}$ represent two different physical variables with different dynamics and evolution. The relation between them is espressed by

$$\widetilde{\mathbf{u}} = \overline{\mathbf{u}} + \frac{1}{\overline{\rho}}\tau(\rho, \mathbf{u}) \tag{1}$$

where $\tau(\rho, \mathbf{u}) = \overline{\rho\mathbf{u}} - \overline{\rho}\,\overline{\mathbf{u}}$ represents the subgrid mass flux. The difference between the two velocities can be usually reasonably ignored also in compressible flows, but this is not justified in presence of strong density variation. Sidhart and Candler [5] observed, in decaying turbulence, that the effects of small-scale density gradient can affect the dynamics of large-scale velocity and vorticity. The difference between filtered and Favre filtered quantities have to be taken into account also comparing statistical quantities computed from LES with those one from DNS or experiments.

Particularly noteworthy is the influence of Favre fitering in the SGS modeling. Eddy viscosity type models are the most diffused models in LES and the eddy viscosity hypothesis is usually straightforward extended to model Favre filtered subgrid fluxes. This assumption is unjustified for compressible flows in presence of strong density gradient, as discussed in [8]. In [8] some additional terms are added to correctly compute the subgrid stress tensor in function of the Favre filtered velocity mantaining the eddy viscosity hypothesis.

The present research is finalised to analyse and to quantifie the effect of variable density flows in a multiscale approach to turbulence, focusing in particular the attention on the scale interaction and on the turbulence modeling.

ANALYSIS OF A MIXING LAYER FLOW

The fields obtained by a previous direct numerical simulation (DNS) of a turbulent compressible mixing layer of an ideal gas [6, 7] has been analysed in the present work. The sketch of the considered flow is represented in Figure 1. The computational domain has size $L_x \times L_y \times L_z = 344 \times 516 \times 172$. The non dimensional parameter of the simualtion are $Re = 160$, $Pr = 0.7$, $Ma = 0.7$, $s = 2$ where

$$Re = \frac{\rho_0 \Delta U \delta_\theta(0)}{\mu}, \qquad Ma = \sqrt{\frac{\Delta U \rho_0}{\gamma p_0}}, \qquad s = \frac{\rho_2}{\rho_1}. \tag{2}$$

$\rho_0 = (\rho_1 + \rho_2)/2$ is the mean initial density and $\delta_\theta(0)$ is the initial shear layer momentum thickness. The viscosity, the diffusion, the thermal conductivity and the specific heat ratio are assumed constants. Subgrid filtered and Favre filtered quantities are computed applying box filter in space to the fields obtained by the DNS. Three different filter size, as reported in Table 1, have been considered.

The analysis demonstrates that relevant differences are present between the filtered and the Favre filtered quantities, particularly accentuated in high density fluctations regions. As example, the root mean square of the SGS density fluctuation is shown in Figure 2. The Figures 3 and 4 represent the x, y component of the filtered strain rate $\overline{S}_{xy}$ and its the difference $(\overline{S}_{xy} - \widetilde{S}_{xy})$ respect to the Favre filtered one, respectively. These images show a difference between the filtered and Favre filtered strain rate with comparable magnitude of the corresponding component. Moreover it is evident that the more intense differences coincide with higher SGS density fluctuations. This observation confirms that the eddy viscosity hypothesis can not be straighforward extended to Favre filterd velocity fields.

REFERENCES

[1]Favre, A. :Turbulence: Space-time statistical properties and behavior in supersonic flows, *The Physics of Fluids* , **26**, 2851 (1983).

[2]Yoshizawa, A. : Statistical theory for compressible turbulent shear flows, with the application to subgrid modeling, *Phys. Fluids A*, **29**, 2152 (1986).

[3]Boersma, B.J., Lele, S.K. :Large eddy simulation of compressible turbulent jets, *Center for Turbulence Research: Annual Research Briefs (Center for Turbulence Research, Stanford, CA*, 365 (1999).

[4]Sun, B., Lu, X.Y. : A large eddy simulation approach of compressible turbulent flow without density weighting, *Phys. Fluids*, **18**, 118101 (2006).

[5]Sidhart GS, Candler, G.V. : Subgrid-scale effects in compressible variable-density decaying turbulence, *J. Fluid Mech.*, **846**, 428–459 (2018).

[6]Trane, D.: Study of the Mach and density ratio effects in mixing layers. Master thesis, University of Modena and Reggio Emilia (2021).

[7]Pantano, C., Sarkar, S. : A study of compressibility effects in the high-speed turbulent shear layer using direct simulation, *J. Fluid Mech.*, **451**, 329–371 (2002).

[8]Germano, M., Abbà , A., Arina , R. Bonaventura , L. : On the extension of the eddy viscosity model to compressible flows, *Phys. Fluids*, **26** (4), 041702 (2014).

	Δ_x	$\Delta_{y_{min}}$	$\Delta_{y_{max}}$	Δ_z
DNS	0.67	0.34	1.36	0.67
small filter	2.68	1.36	5.44	2.68
medium filter	5.36	2.72	10.88	5.36
large filter	10.72	5.44	21.76	10.72

Table 1: Grid resolution for the mixing layer DNS and for the filtered field.

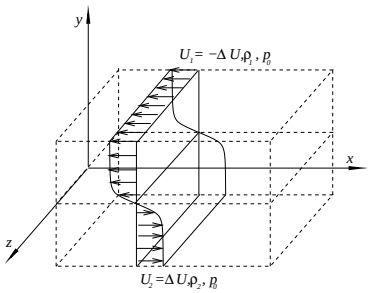

Figure 1: Geometry of the mixing layer previously simulated in the DNS by Trane [6].

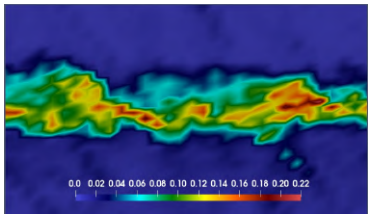

Figure 2: Root mean square of the sgs density fluctuations from filtered DNS of a mixing layer.

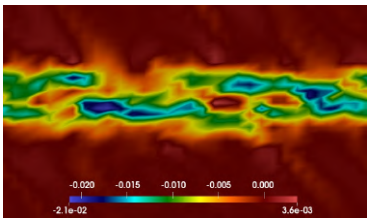

Figure 3: $\overline{S}_{xy}$ component of the filtered strain rate from filtered DNS of a mixing layer.

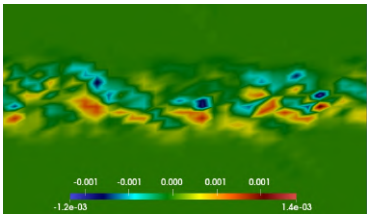

Figure 4: Difference $(\overline{S}_{xy} - \widetilde{S}_{xy})$ between the filtered strain rate and the Favre filtered strain rate xy component, from filtered DNS of the mixing layer.

WORKSHOP
Direct and Large-Eddy Simulation 13
October 26th-29th 2022, Udine, Italy

CONJUGATE HEAT TRANSFER SIMULATION OF TARGET STATION 2 OF THE ISIS MUON AND NEUTRON SOURCE

G. Cartland-Glover[1], S. Rolfo[1], D. R. Emerson[1], D. Wilcox[2], D. Blanco Lopez[2], L.G. Jones[2], D. M. Jenkins[2] AND S. Jago[2]
[1] Daresbury Laboratory
Science and Technology Facilities Council, UK Research and Innovation, United Kingdom
[2] Rutherford Appleton Laboratory
Science and Technology Facilities Council, UK Research and Innovation, United Kingdom
greg.glover@stfc.ac.uk, stefano.rolfo@stfc.ac.uk

INTRODUCTION

The ISIS Muon and Neutron source uses the spallation of protons accelerated to 84 % of the speed of light to generate neutrons at two tungsten targets clad in tantalum and cooled by recirculating water. The neutrons are then moderated and directed to a number of instruments that can measure the diffraction and scattering of the neutrons with applications in electronics and materials science.

The first target station has an operational lifetime of 5 years with spallation products remaining in the target geometry, while there is some egress of the spallation products after 18 months of use of target station 2. As the targets are encased in a radiologically shield zones, we rely on numerical simulations to understand the impact of various factors that could contribute to the shorter operational lifetime of the second target.

Studies have been performed that have examined residual and beam induced stresses in the target and shell [1], radiation damage [1], water hammer [1], flow induced erosion of tantalum [2], hydrogen generation and accumulation in the coolant via radiolysis, cavitation, and how they affect fatigue.

This work is part of the same effort in better understanding the complex multi-physics phenomena occurring the target geometry and try to extend its life span. Particularly, the focus is to understand the influence of the turbulent thermal fluctuations on the thermal fatigue of the different materials that compose the target.

TEST CASE DEFINITION

The second target station is a single piece of tungsten clad in several pieces of tantalum with an overall radius of 0.034 m and length 0.3m (see Figure 1). Two coolant channels situated in the cladding feed cooling water around the nose of the target. Each channel is 2 mm thick with an arched span of around 40 mm, and a flow length of about 600 mm with two long sections on either side of the target and a U-bend at the nose of the target. Note that the span of the channel closer to the head of the tungsten target tapers in the region of the head resulting in a narrower channel with sloping sides.

Water is fed to each channel at a temperature of 33.3 °C, a pressure of 6 bar and a flow rate of $45\,\mathrm{l\,min^{-1}}$, which results in a channel Reynolds number of around 23000, based on the channel and a Prandtl number of 5.4. Constant fluid properties (i.e. density, viscosity, etc) have been assumed despite the relatively large heat fluxes exchanged at the solid-liquid interface. This is a consequence of the very relatively large Reynolds number and quite low Richardson number that point towards a pure force convection regime.

The heat arising in the target by the spallation and transport of neutrons was obtained from a cylindrical model of the second target station modelled by FLUKA [4, 5]. Polynomial functions were used to approximate the heat distribution in the target and the shell that could approximate the steady state heat flux applied to the target by the pulsed beam.

MESH GENERATION AND NUMERICAL MODELS

The mesh comprised of about 22 million hybrid cells constructed from three parts with four regions modelled focussed on the 148.5 mm closest to the nose of the target, where most of the heat from spallation and neutron transport is released. Two hexahedral meshes were used to modelled both the inner and outer fluid channels plus about 0.5 mm of the cladding surrounding the channels (16 cells over the wall depth). The first node from either side of the solid-fluid interface at the wall was 2 µm with a resolution of 32 by 128 nodes in the cross-section of the fluid. There were 800 cells along the length of the inner channel and 864 cells along the length of the outer channel. The maximum values of $y^+ = 2.3$ and the $T^+ = 12.2$ with respective mean values of 0.2 and 1. The third part comprised two regions corresponding to the tungsten target (hexahedrally meshed) and the tantalum cladding (hybrid meshing due to the overlapping of the two channels) and contained 16 million cells. The meshes were the joined using the meshing procedures of *Code_Saturne* and conjugate heat transfer was modelled using an "internal coupling" procedure.

Two further meshes have also been generated using the meshing strategy to refine the near wall resolution. The meshes have 100 and 700 million cells with a maximum $y^+ \approx 1$ and $y^+ \approx 0.2$ respectively, bringing down the final $T^+ \approx 1$ for the finer mesh

Conjugate heat transfer in the target was modelled using version 7 of *Code_Saturne* [3]. The simulations were performed using the open-source finite volume software *Code_Saturne*, which is developed and maintained by EDF R&D. The code

is second order accurate in space and time and the velocity-pressure coupling is ensured through a prediction/correction method based on a SIMPLEC algorithm. The filtered, incompressible Navier-Stokes equations are resolved and the sub-grid terms are modelled using the a Smagorinky model. Reconstruction of the turbulent fluctuations at the inlet has been carried our using a Synthetic Eddy Method (SEM)

RESULTS

Profiles of the instantaneous heat flux and temperature are plotted in Figures 2 and 5. Two other turbulence models available in*Code_Saturne* were also selected for benchmarking purposes. These were the k-ω SST and the elliptic blending Reynolds stress model (EBRSM). The LES results are obtained on the coarser mesh. There are some noticeable differences between LES and RANS, with the LES showing large heat fluxes in the corner region of the channel whereas RANS identify the central part of the target as the most active zone Further refinement results, that will be presented at the conference, will be used to confirm the different trends between LES and RANS and particularly will be used to check the areas of larger temperature fluctuations that might have an impact on the thermal fatigue.

REFERENCES

[1]D. Wilcox, "ISIS Target modeling." `https://conference.sns.gov/event/267/contributions/485/`, 2021. Accessed: 2022-02-27.

[2]O. Caretta, T. Davenne, and C. Densham, "Water erosion tests on a tantalum sample: A short communication," *Journal of Nuclear Materials*, vol. 492, pp. 52–55, 2017.

[3]Y. Fournier, J. Bonelle, C. Moulinec, Z. Shang, A. Sunderland, and J. Uribe, "Optimizing Code Saturne computations on petascale systems," *Computers and Fluids*, vol. 45, pp. 103–108, 2011.

[4]A. Ferrari, P.R. Sala, A. Fassò, and J. Ranft, "FLUKA: a multi-particle transport code," Tech. Rep. CERN-2005-10, INFN/TC_05/11, SLAC-R-773, CERN, 2005.

[5]D. Wilcox, "Thermo-mechanical analysis of ISIS TS2 target," tech. rep., STFC, 2013.

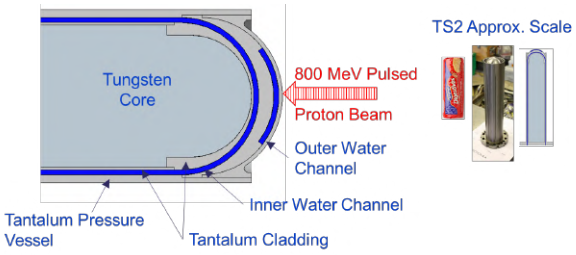

Figure 1: Configuration of target station two of the ISIS Muon and Neutron Source

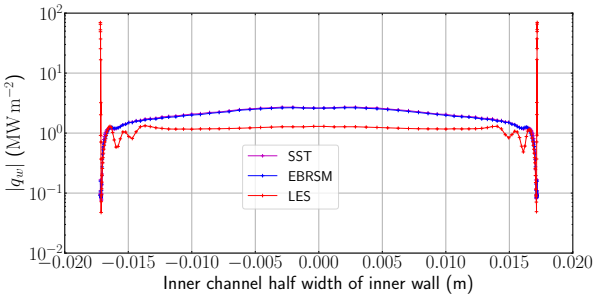

Figure 2: Profiles of the instantaneous heat flux on the solid side of the inner wall of the inner channel at the nose of the target

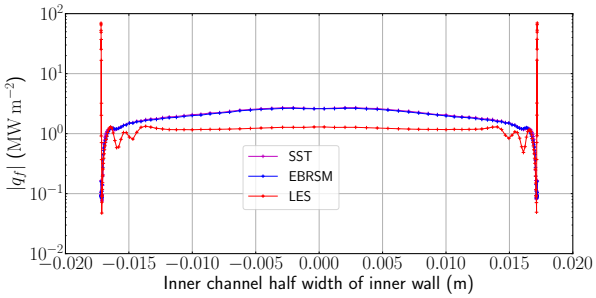

Figure 3: Profiles of the instantaneous heat flux on the fluid side of the inner wall of the inner channel at the nose of the target

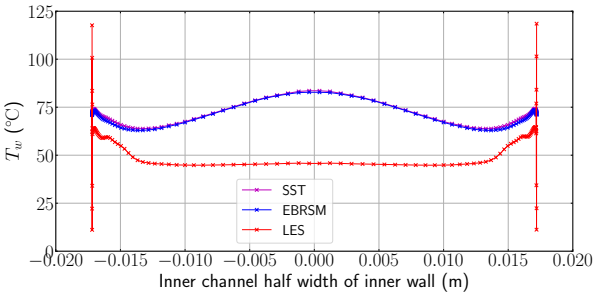

Figure 4: Profiles of the instantaneous temperature on the solid side of the inner wall of the inner channel at the nose of the target

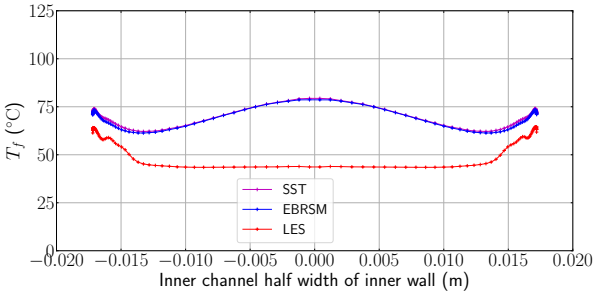

Figure 5: Profiles of the instantaneous temperature on the fluid side of the inner wall of the inner channel at the nose of the target

Session: Numerics and methodology

Wednesday, October 26, 2022

10:00 – 11:00

WORKSHOP
Direct and Large-Eddy Simulation 13
October 26th-29th 2022, Udine, Italy

APPROXIMATE DECONVOLUTION OF IMPLICIT FILTERS INDUCED BY NUMERICAL SCHEMES FOR IMPROVED SUBFILTER STRESSES EVALUATION

A. Boguslawski [1], **K. Wawrzak** [1], **B. J. Geurts** [2]
[1] Department of Thermal Machinery
Czestochowa University of Technology, Poland
[2] Multiscale Modeling and Simulation, Applied Mathematics
University of Twente, Netherlands
andrzej.boguslawski@pcz.pl

INTRODUCTION

Numerical schemes used for spatial discretization of differential equations introduce associated implied filtration. In Large Eddy Simulations (LES) such a filter implied by the numerical scheme represents an implicit LES filter. Knowing the explicit form of this numerical filter enables to partially recover by approximate deconvolution the numerically implied filter. The deconvolved velocity field can be used to evaluate subfilter stresses. As shown by Geurts and van der Bos [1] any finite difference scheme can be understood as an exact differentiation of the filtered function with a filter characterized by a filter kernel composed of top-hat filters. This reasoning can readily be extended to implicit compact differencing. Hence, for any explicit or implicit finite differencing scheme of arbitrary order we may apply a deconvolution procedure to recover part of the subfilter scales eliminated by the implicit filter induced by the numerical scheme. In this work, we show the results of such a deconvolution for second-order central finite differences and sixth-order compact differences. As a test case, two-dimensional decaying turbulence is studied. Special attention will be given to the importance of the filter kernel discretization in relation to the quality of the deconvolution procedure.

APPROXIMATE DECONVOLUTION OF INDUCED FILTERS

Consider a general finite difference method for numerically approximating the first-order partial derivative of a function u in one spatial dimension given by

$$\delta_x u(x_i) = \frac{1}{h} \sum_{j=-n}^{m} a_j u_{i+j} \tag{1}$$

where we denoted $u_{i+j} = u(x_{i+j})$, i.e., the solution in the point x_{i+j} of the grid $\{x_k\}$. For convenience we restrict to discretization on a uniform grid with grid spacing h, and adopt a general stencil of $m+n+1$ nodes, defining the stencil $[-n, m]$.

The implied filter L can be related to the discretization weights and expressed in terms of a series of explicit top-hat filters [1]. It can be expressed as a weighted average of skewed top-hat filters of width h

$$L(u(x_i)) = \sum_{j=-n+1}^{m} b_j \left(\frac{1}{h} \int_{x_i+(j-1)h}^{x_i+jh} u(\eta) d\eta \right) \tag{2}$$

where

$$b_j = \sum_{i=j}^{m} a_i, \quad j = -n+1, \ldots, m \tag{3}$$

To specify the implied filter (2) on a numerical mesh, the integral in (2) should be approximated. Several possible quadrature rules can be selected to approximate L - here we consider the trapezoidal rule, the Cavalieri-Simpson rule [2] and the Fourier series approximation [3], for periodic problems.

We start the analysis by selecting the trapezoidal rule for the numerical integration in (2), which implies

$$L(u(x_i)) = \sum_{j=-n+1}^{m} b_j \frac{u_{i+j-1} + u_{i+j}}{2} \tag{4}$$

Rearranging the sum one can arrive at the discrete form of the implied filter

$$\begin{aligned} &\sum_{j=-n+1}^{m} b_j \frac{u_{i+j-1} + u_{i+j}}{2} = \\ &= \frac{b_{-n+1}}{2} u_{i-n} + \sum_{j=-n+1}^{m-1} \frac{b_j + b_{j+1}}{2} u_{i+j} + \frac{b_m}{2} u_{i+m} \equiv \\ &\equiv \sum_{j=-n}^{m} G_j^{(-n,m),tr} u_{i+j} \end{aligned} \tag{5}$$

with the discrete filter kernel defined as

$$\begin{aligned} G_{-n}^{(-n,m),tr} &= \frac{b_{-n+1}}{2} \\ G_j^{(-n,m),tr} &= \frac{b_j + b_{j+1}}{2} \quad \text{for } j = -n+1, \ldots, m-1 \\ G_m^{(-n,m),tr} &= \frac{b_m}{2} \end{aligned} \tag{6}$$

Here, the superscript 'tr' is used to emphasize that the discrete filter adopts the trapezoidal rule for integration.

Knowing the discrete form of the implied filter kernel its approximate inverse can be found. First, Wiener [5] type inverse filtering will be considered, focussing attention to periodic problems in the domain $0 < x < 1$. Taking Fourier series of the discrete filter kernel over the computational domain

$$\hat{G}_k^{(-n,m),tr} = \frac{1}{N} \sum_{i=0}^{N-1} G_i^{(-n,m),tr} e^{-2\pi \underline{i} k x_i}; \quad k = -K, \ldots, K \tag{7}$$

where $\underline{i} = \sqrt{-1}$ and $N = 2K + 1$ is the odd number of mesh points, the inverse filter kernel in Fourier space is defined as

$$\hat{Q}_k^{(n,m),tr} = \frac{1}{\hat{G}_k^{(-n,m),tr} N^2} \tag{8}$$

and the inverse filter kernel in physical space is found by the inverse Fourier transform

$$Q_i^{(-n,m),tr} = \sum_{k-K}^{K} \hat{Q}_k^{(-n,m),tr} e^{2\pi \underline{i} k x_i}; \;\; i = 0, \ldots, N-1 \tag{9}$$

An analogous procedure to discretize the filter kernel can be applied using more precise methods of integration in Eq. (2). Examples include Simpson-Cavalieri [2] with parabolic interpolation, higher order Lagrange polynomials or, in the periodic test case under consideration, Fourier series. In the present paper trapezoidal, Simpson-Cavalieri and Fourier series methods are compared for the case of compact differences. The discrete form of the filter kernel induced by the numerical scheme and its inverse enables the subfilter stress tensor [4] to be expressed as

$$\tau_{ij} = G\left[Q\left(u_i\right) Q\left(u_j\right)\right] - u_i u_j \tag{10}$$

where u_i, u_j denote the resolved velocity components and G and Q general filtration in two dimensions with the filter corresponding to the numerical scheme and its inverse, respectively. We will investigate LES that employs Eq.(10) as sub-filter stress tensor model.

SAMPLE RESULTS

The initial field has been obtained following the method proposed by San and Staples [6]. Two-dimensional freely decaying incompressible flow on a square domain of length 2π and with periodic boundary conditions has been taken into consideration. The initial energy spectrum is assumed to be

$$E\left(k\right) = \frac{a_s}{2} \frac{1}{k_p} \left(\frac{k}{k_p}\right)^{2s+1} \exp\left[-\left(s + \frac{1}{2}\right)\left(\frac{k}{k_p}\right)^2\right] \tag{11}$$

where s is a shape parameter assumed to be equal 3 and where $a_s = \frac{(2s+1)^{s+1}}{2^s s!}$. The maximum value of initial energy spectrum is obtained for $k_p = 12$.

The LES calculations were performed on a mesh 257x257 using central finite differences of second-order and compact differences of 6^{th} order. Direct Numerical Simulations (DNS) were performed on the mesh 1025x1025 with a Fourier spectral method [3]. Pressure and velocity coupling was realised by the projection method. The time integration is conducted with fourth order Runge-Kutta method[4].

Figure 1 shows the energy spectra obtained by the use of the 6^{th} order compact differences for spatial discretization with the subfilter stress tensor evaluated on the basis of the deconvolved velocity field using different methods to discretize the combined top-hat filters induced by the numerical scheme. As a reference the DNS results are also presented as well as the results obtained on the LES mesh without subfilter model. It is seen that the mesh used for LES is not sufficiently fine to capture the smallest scales as energy accumulation is observed near the grid cut-off wave number. On the other hand it can be observed that the proposed models based on the deconvolved velocity fields perform well delivering an appropriate amount

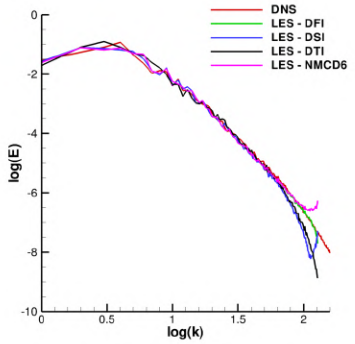

Figure 1: Energy spectra, DNS-direct numerical simulation, LES-DFI - Fourier series used for integration, LES-DSI - Simpson-Cavalieri method, LES-DTI - trapzoidal rule, LES-NMCD6 - simulations without any subfilter model, Re=4000

of energy dissipation. It is worth noting that accuracy of the induced filter discretization is crucial for the quality of the subfilter model as the best agreement with the DNS results is obtained by the use of Fourier series to form the filter kernel.

CONCLUSIONS

A new deconvolution method to recover the scales filtered by the spatial discretization scheme is proposed. It is shown that for each explicit and implicit finite difference method a dedicated filter kernel can be formed and its inverse can be applied to find an unfiltered velocity field to evaluate the subfilter stress tensor. An extension to non-periodic problems is subject of current research, as is extension to 3d.

ACKNOWLEDGMENTS

The research was supported by the Polish National Science Centre, Project No. 2018/29/B/ST8/00262, and by the National Agency for Academic Exchange (NAWA) within the International Academic Partnerships Programme No. PPI/APM/2019/1/00062.

REFERENCES

[1]Geurts B., J. van der Bos F.: Numerically induced high-pass dynamics in large-eddy simulation, *Phys. Fluids*, **17**, 125103-11 (2005).

[2]Quarteroni A., Sacco R., Saleri F.: Numerical Mathematics, *Springer*, (2007).

[3]Canuto C., Hussaini M.Y., Quarteroni A., Zang T.A.: Spectral methods in fluid dynamics, *Springer-Verlag*, (1988).

[4]Geurts B.J., Elements of direct and large-eddy simulation, *R.T. Edwards Inc.*, (2003).

[5]Wiener N.: Extrapolation, interpolation, and smoothing of stationary time series, *The MIT press, Cambridge, MA,* (1949).

[6]San O., Staples A.E.: High-order methods for decaying two-dimensional homogeneous isotropic turbulence,*Computers and Fluids*, **63**, 105-127, (2012).

WORKSHOP
Direct and Large-Eddy Simulation 13
October 26th-29th 2022, Udine, Italy

FINITE-DIFFERENCE VISCOUS FILTERING FOR NON-REGULAR MESHES

R. Perrin[1] **& E. Lamballais**[2]
[1] Department of Mechanical Engineering, Faculty of Engineering, Kasetsart University Sriracha, Thailand
rodolphe@eng.src.ku.ac.th
[2] Incompressible Turbulence and Control Group, Pprime Institute, CNRS - Univ-Poitiers - ENSMA, France
eric.lamballais@univ-poitiers.fr

INTRODUCTION

In a recent study [1], the authors have proposed a new solution filtering technique for direct and large-eddy simulation (DNS/LES). This method can represent both the molecular and artificial viscosity. It is particularly easy to code in a conventional finite-difference framework where only the scheme coefficients have to be designed to ensure the expected dissipation. The main strength of this "viscous filtering" technique lies in its numerical stability features. In this sense, it can be considered as a simple and computationally efficient alternative to implicit time integration of the viscous term.

The concept of viscous filtering and its advantages in the context of DNS/LES are presented in [1]. However, as a limitation of the technique, only the case of a regular mesh has been addressed. It was a way to design the coefficients for ensuring favourable spectral features defined in the Fourier space. In particular, the accuracy conditions are derived through Taylor's expansions expressed in wavenumbers.

The purpose of this contribution is to extend this viscous filtering technique to non-regular meshes. This generalization requires to express the expected features in the physical space in order to obtain the various relations to reach a given order of accuracy. The principles of these developments are first presented. Then, a preliminary validation is shown for the Burgers equation. Finally, to assess the method in a DNS/LES context, the case of a transitional boundary layer is considered with the use of a highly stretched mesh in the near-wall region.

METHODOLOGY

To present the general ideas of the approach, let us consider the simple one-dimensional equation

$$\frac{\partial u}{\partial t} = F(u) + \nu \frac{\partial^2 u}{\partial x^2} \tag{1}$$

where $u(x,t)$ is the solution and ν the constant molecular viscosity. The basic principle of the method is to split the time advancement into two steps with

$$u^* = u^n + \int_{t_n}^{t_n+\Delta t} F(u)\, dt \tag{2}$$

$$u^{n+1} = \widetilde{u^*} \tag{3}$$

with $u^n = u(x,t_n)$ and $u^{n+1} = u(x,t_n+\Delta t)$. Step (2) consists in the time advancement of the inviscid version of equation (1) where the integral can be evaluated for instance by an Adams-Bashforth scheme. Step (3) corresponds to the application of a spatial filter denoted $\widetilde{.}$ to restore the influence of viscosity. For simplicity, the splitting error is ignored here, but it has been shown in [1] that this error is negligible for typical DNS/LES while being removable if necessary.

The spatial discretization is based on a stretched mesh $x_i = h(s_i)$ where $s_i = (i-1)\Delta s$ corresponds to regularly distributed nodes on the computational coordinate s. This coordinate transformation enables to write successive derivatives as

$$\begin{aligned}
\frac{\partial u}{\partial x} &= g\frac{\partial u}{\partial s} \\
\frac{\partial^2 u}{\partial x^2} &= g^2\frac{\partial^2 u}{\partial s^2} + gg'\frac{\partial u}{\partial s} \\
\frac{\partial^3 u}{\partial x^3} &= g^3\frac{\partial^3 u}{\partial s^3} + 3g^2g'\frac{\partial^2 u}{\partial s^2} + \left(g^2g^{(2)} + gg'^2\right)\frac{\partial u}{\partial s} \\
\frac{\partial^n u}{\partial x^n} &= g^n\frac{\partial^n u}{\partial s^n} + ...
\end{aligned} \tag{4}$$

where $g = 1/h'$. To mimic the contribution of this viscous term in step (3), a finite-difference filter scheme of the form

$$\begin{aligned}
\alpha_p\tilde{u}_{i+1} + \tilde{u}_i + \alpha_m\tilde{u}_{i-1} = au_i &+ \frac{b_p}{2}u_{i+1} + \frac{b_m}{2}u_{i-1} \\
&+ \frac{c_p}{2}u_{i+2} + \frac{c_m}{2}u_{i-2}
\end{aligned} \tag{5}$$

is used where $u_i = u(x_i,t)$. As it is usual in a finite-difference framework, Taylor's expansion in space

$$\begin{aligned}
u_{i+k} &= u_i + \sum_{p=1}^{n}\frac{(k\Delta s)^p}{p!}\left.\frac{\partial^p u}{\partial s^p}\right|_i + O(\Delta s^{n+1}) \\
\left.\frac{\partial^q u}{\partial s^q}\right|_{i+k} &= \left.\frac{\partial^q u}{\partial s^q}\right|_i + \sum_{p=1}^{n}\frac{(k\Delta s)^p}{p!}\left.\frac{\partial^{p+q} u}{\partial s^{p+q}}\right|_i + O(\Delta s^{n+1})
\end{aligned} \tag{6}$$

provides relation orders in Δs^n between the coefficients $(\alpha_p, \alpha_m, a, b_p, b_m, c_p, c_m)$ in (5). Then, by Taylor's expansion in time

$$\tilde{u}_i = u_i + \Delta t\left.\frac{\partial u}{\partial t}\right|_i + \frac{\Delta t^2}{2}\left.\frac{\partial^2 u}{\partial t^2}\right|_i + \frac{\Delta t^3}{3!}\left.\frac{\partial^3 u}{\partial t^3}\right|_i + O(\Delta t^4) \tag{7}$$

while switching the time derivative by their spatial counterparts requiring that step (3) has to match a purely diffusive equation with

$$\frac{\partial u}{\partial t} = \nu\frac{\partial^2 u}{\partial x^2} \quad , \quad \frac{\partial^2 u}{\partial t^2} = \nu^2\frac{\partial^4 u}{\partial x^4} \quad , \quad \frac{\partial^3 u}{\partial t^3} = \nu^3\frac{\partial^6 u}{\partial x^6} \tag{8}$$

expansion (7) can also be written as

$$\tilde{u}_i = u_i + F\Delta s^2 \left.\frac{\partial^2 u}{\partial x^2}\right|_i + \frac{F^2\Delta s^4}{2}\left.\frac{\partial^4 u}{\partial x^4}\right|_i + \frac{F^3\Delta s^6}{3!}\left.\frac{\partial^6 u}{\partial x^6}\right|_i + O(F^4\Delta x^8) \quad (9)$$

where $F = \frac{\nu\Delta t}{\Delta s^2}$ is the Fourier number based on the constant cell Δs. To enable an identification between the relation orders given by (6) and (9) in the scheme (5), a conversion of the spatial derivatives from x to s is required. This can be done easily through relations (4) so that a 7×7 system $MX = N$ can be obtained where the component of $X = (\alpha_p, \alpha_m, a, b_p, b_m, c_p, c_m)^T$ are the unknown scheme coefficients of (5) which are function of F, g and its successive derivatives. This system can be solved analytically (using a symbolic calculation tool) leading to extremely long expressions for each coefficient. More conveniently, the same can be done numerically up to the machine accuracy before starting the simulation.

RESULTS

To assess this new type of filter scheme, Burgers' equation has been solved, namely $F(u) = u\partial u/\partial x$ in (1). As explained in the previous section, every time step, the inviscid Burger equation is solved and then, the viscous filter scheme (5) is applied on the discrete solution to restore the influence of the viscosity. A time interval after the shock formation is computed and the solution is compared to its exact counterpart. The mesh, composed of N nodes, is regular when using the initial scheme given in [1] whereas the mesh is stretched in the shock region when using the new scheme developed here. The sixth-order version is assessed, namely the highest-order enabled by scheme (5) because of its compact stencil.

As expected, at low resolution using a regular mesh, the solution is subjected to Gibbs' phenomenon, leading to unphysical grid-to-grid oscillations in the near-shock region as exhibited in figure 1-top. This problem can be fixed through the increase of the resolution everywhere in the domain, which is computationally inefficient. Alternatively, the use of a stretched grid enables us to remove the unphysical oscillations without any increase of the computational cost (see figure 1-top for $N = 64$).

The numerical convergence analysis is based on the computation of L_∞ to estimate the numerical error defined by reference to the exact solution. Figure 1-bottom shows that the expected sixth-order is correctly recovered for both the regular and non-regular meshes, but only at high resolution for the former as the signature of the Gibbs phenomenon at low resolution. The spectacular increase of the accuracy provided by the use of a stretched mesh can be observed, with for the two largest stretching parameters $\beta = (0.05, 0.025)$, a reduction by more than 2 orders of magnitude of the maximum error located near the shock. For a constant error, the computational saving corresponds to a factor of about 8 by comparison to a regular mesh. These preliminary results suggest that the concept of viscous filtering has been successfully generalized for non-regular meshes.

In the final paper, the use of the sixth-order version of this new scheme will be presented for performing LES of a spatially-evolving boundary layer subjected to bypass transition. For this demanding flow configuration, the mesh is highly stretched at the wall requiring to use an implicit time integration of the viscous term. Here, because this terms is removed and replaced by viscous filtering, which is essentially explicit, its benefit will be discussed in terms of code simplification, numerical stability and computational saving.

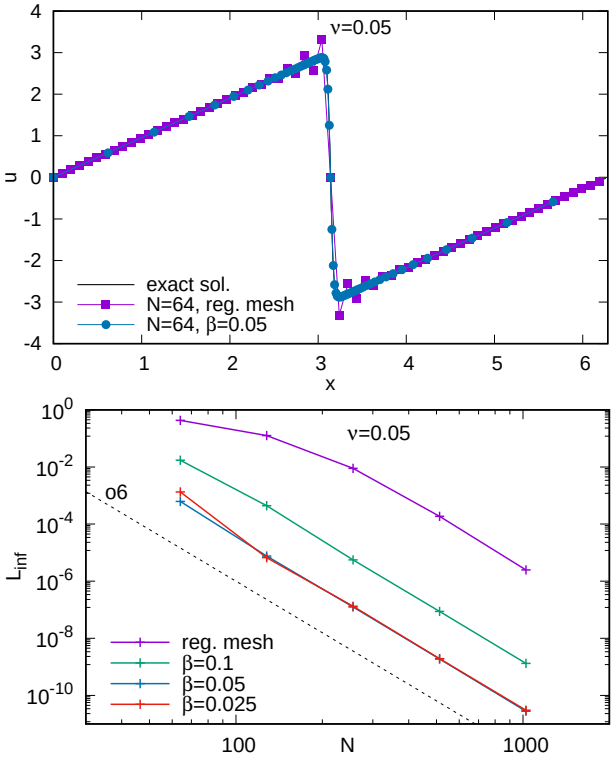

Figure 1: Computation of a shocked Burgers' solution. Top: solution at $t = 0.05$. Bottom: evolution of L_∞ with the number N of mesh nodes.

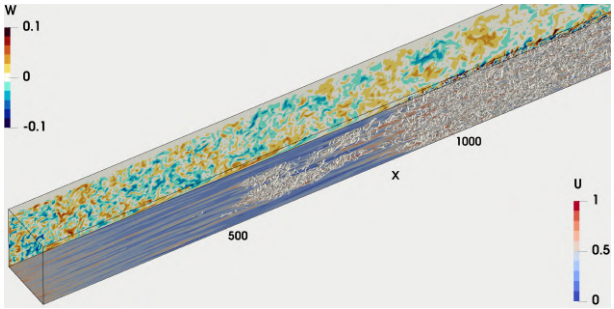

Figure 2: LES of bypass transition of a boundary layer [2]. Maps of longitudinal and spanwise velocities at $y = 1$ and $z = 1$ respectively. Q-criterion isosurface $Q = 0.005$ in grey.

ACKNOWLEDGEMENTS

This work was granted access to the HPC resources of IDRIS under the allocation A0072A07624 made by GENCI.

REFERENCES

[1] E. Lamballais, R. Vicente Cruz and R. Perrin, "Viscous and hyperviscous filtering for direct and large-eddy simulation", *J. Comp. Phys.*, vol. 431, p. 110115, 2021.

[2] R. Perrin and E. Lamballais, "Assessment of implicit LES modelling for bypass transition of a boundary layer", submitted to *Computers and Fluids*.

WORKSHOP
Direct and Large-Eddy Simulation 13
October 26th-29th 2022, Udine, Italy

THE BRINKMAN PENALIZATION TECHNIQUE FOR POROUS-FLUID MEDIA: A LATTICE BOLTZMANN AND SEMI-LAGRANGIAN VORTEX METHOD COMPARISON.

C. Mimeau[1], S. Marié[2] and I. Mortazavi[3]
[1,3] M2N Laboratory, Conservatoire National des Arts et Métiers, 2 rue Conté Paris 75003, France, chloe.mimeau@cnam.fr
[2] DynFluid Laboratory, Conservatoire National des Arts et Métiers, 2 rue Conté Paris 75003, France,

INTRODUCTION

Keywords: *Lattice Boltzmann method, incompressible flows in porous media, Brinkman penalization, numerical comparison with semi-Lagrangian vortex method*

The presence of porous layers around solid bodies modifies the flow behavior at the solid-porous-fluid interface. In nature, porous media are known for their flow regularization properties (e.g. forest canopy, velvet-like feathers under bird wings, ...) and the use of porous coatings at the surface of solid obstacles immersed in a fluid flow has been employed across several areas to change the flow dynamics. Modeling flows in porous media therefore appears as a real issue to design and simulate passive flow control strategies. In lattice Boltzmann methods, the treatment of fluid flows in porous media can be carried out with different types of boundary conditions. In the present work, the Brinkman penalization method [1] is used. This approach models the porous medium by adding a forcing term including the porosity and the permeability of the medium. The Brinkman penalization holds for the whole domain, it is local and has a negligible computational cost. This strategy, recently used with LBM to model complex diffusion in porous media [2], has also been successively applied in the context of semi-Lagrangian vortex methods [5] for the discretization of incompressible Brinkman-Navier-Stokes equations. The present work therefore proposes a numerical comparison between two alternative and non-traditional methods, namely a mesoscopic approach (the lattice Boltzmann method, denoted LBM in the following) and a hybrid Eulerian-Lagrangian macroscopic one (the semi-Lagrangian vortex method, denoted VM in the following), in their ability and efficiency to simulate the flow around a porous body with the Brinkman penalization technique. As enhanced by the authors in [4], the LBM and VM methods belong to families of methods where the flow is discretized in a non-macroscopic way and where the notion of particles is a common aspect. They therefore show structural similarities and have been also shown in this study to present their own advantages, like the low-dissipative and low-dispersive properties of the VM and the high accuracy at fine grid resolutions and the convergence order of LBM. Further comparisons of these two approaches are here proposed in the context of porous flow simulations.

THE BRINKMAN PENALIZATION

The Brinkman penalization technique has been introduced to model the presence of a porous body [7]. The idea is to add a body force in the macroscopical equation set. This body force takes into account the Reynolds number and the Darcy number and writes. The adimensionalized formulation of the forcing term is given by:

$$\mathbf{F_p} = -\frac{\phi}{ReDa}\mathbf{u} \tag{1}$$

where, ϕ, the porosity of the immersed body, has to be close to 1 [8]. This macroscopic formulation takes different implementation strategies for Vortex method and Lattice Boltzmann Methods.

Implementation in the VM framework

In the VM context, we solve the incompressible Navier-Stokes equations in their adimensionalized velocity($\mathbf{u}$) - vorticity($\boldsymbol{\omega}$) formulation. Adding the Brinkman penalization forcing term in these equations gives the so-called penalized Vorticity-Transport-Equation:

$$\partial_t\boldsymbol{\omega} + (\mathbf{u}\cdot\nabla)\boldsymbol{\omega} - (\boldsymbol{\omega}\cdot\nabla)\mathbf{u} = \frac{1}{Re}\Delta\boldsymbol{\omega} + \nabla\times\mathbf{F_p} \tag{2}$$

$$\Delta\mathbf{u} = -\nabla\times\boldsymbol{\omega}, \tag{3}$$

Such equations allow to model the flow in the whole domain thanks to the dimensionless penalization coefficient $-\phi/ReDa$. Indeed, at a given Re number, varying the value of Da thus directly defines the different media: in the fluid, the permeability goes to infinity, thus the fluid can be considered as a porous media with infinite permeability meaning that the penalization term vanishes. For regions with finite values of Da, one models a porous medium in which the flow has a Darcy velocity.

In the present VM framework, the system of equations (2)-(3) is solved with a fractional step technique (where the diffusive, convective and stretching effects are handled successively within one time step) and by using a semi-Lagrangian approach where the convection of the vorticity field is performed in a Lagrangian way and all the other substeps are resolved on a grid using classical Eulerian schemes (FD, spectral) thanks to the regular remeshing of the Lagrangian particles on the grid. The resolution of the penalization equation $\partial_t\boldsymbol{\omega} = \nabla\times F_p$

is one of the fractional step of the global algorithm, and such equation is solved on the grid with an implicit Euler scheme for time integration and FD scheme for the discretization of the curl operator :

$$\boldsymbol{\omega}^{n+1} = \boldsymbol{\omega}^{n} + \nabla \times \left(\frac{-\lambda\chi\Delta t\ \mathbf{u}^{n}}{1+\lambda\chi\Delta t} \right) \tag{4}$$

Implementation in the LBM framework

The LBM model used for this comparison is based on the D3Q19 incompressible formulation of the Multiple Relaxation time [3]. The implementation of the MRT model is based on a collision step done in the momentum space:

$$\begin{cases} \mathbf{m}^{coll} &= \mathbf{m} - \mathcal{S}(\mathbf{m} - \mathbf{m}^{eq}) + (1 - \dfrac{dt}{2})\mathcal{S}\mathcal{M}\mathbf{S} \\ \mathbf{g}(\mathbf{x}, t) &= \mathcal{M}^{-1}\mathbf{m}^{coll}(\mathbf{x} - \mathbf{c}_\alpha dt, t - dt) \end{cases} \tag{5}$$

where the matrix $\mathcal{M}$, transforms the distribution functions $\mathbf{g}$ into moments $\mathbf{m}$ and $\mathbf{m}^{eq}$ is computed from the standard second order equilibrium distribution function. The diagonal matrix $\mathcal{S}$ contains the relaxation rates associated to each moments to optimize numerical stability [3]. The source term $\mathbf{S}$ is computed according to the standard Guo formulation [6] and include the body force (1):

$$S_\alpha = \omega_\alpha \left[\frac{\mathbf{c}_\alpha - \mathbf{u}}{c_0^2} + \frac{(\mathbf{c}_\alpha \cdot \mathbf{u})\mathbf{c}_\alpha}{c_0^4} \right] \cdot \mathbf{F_p} \tag{6}$$

Then the source term is included in the mesh concerned by a porous body and are removed in the main flow mesh.

APPLICATION TO FLOW OVER A POROUS SPHERE

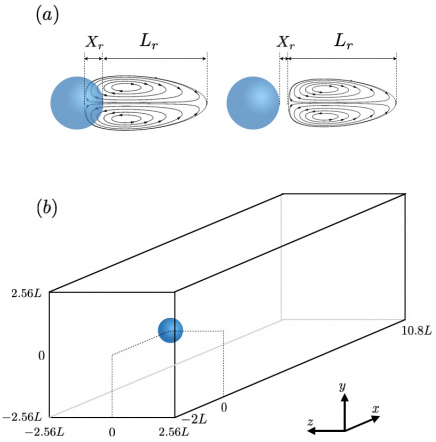

Figure 1: (a) Sketch of the flow configuration depending on the permeability (Da). X_r denotes the penetration or detachment length of the recirculation region and L_r denotes the recirculation length (notation and sketch inspired from [9]). (b) Computational domain.

The test case of the steady and axisymmetric flow past a permeable sphere at $Re = 200$ is here chosen to validate the Brinkman penalization implementation in the LBM and VM frameworks and to compare the two approaches in terms of numerical convergence, precision and ability to capture the correct physics of such flow.

Concerning the expected physics, previous studies (e.g. [9]) demonstrated that, increasing the permeability (i.e. the Da number) of the immersed body, the recirculation region first penetrates inside the body (at the rear) and is then shifted downstream and shrinked until it finally disappears for high permeability values (see Fig. 1(a)).

Based on the very recent work of Ledda [9], used here as a reference, we will validate our methods on the particular case of flow past a permeable sphere at $Re = 200$ with $Da = 10^{-3}$ and $Da = 10^{-2}$, for which we expect to observe the recirculation region entering the rear back of the sphere with $Da = 10^{-3}$ and its disappearing for $Da = 10^{-2}$. The direct numerical simulations will be performed in the physical domain represented in Fig. 1(b) and a grid convergence study will be carried out based on the following meshes:

G1	$80 \times 32 \times 32$
G2	$160 \times 64 \times 64$
G3	$320 \times 128 \times 128$
G4	$640 \times 256 \times 256$
G5	$1024 \times 512 \times 512$

Further simulations at higher Re numbers ($Re \sim \mathcal{O}(10^3)$) for the sphere case will also be proposed for G5 resolution through the two methods in order study more complex physics and to envision the effects of permeability on chaotic wakes.

REFERENCES

[1]P. Angot, C.-H. Bruneau and P. Fabrie, A penalization method to take into account obstacles in incompressible viscous flows. *Numer. Math.*, Vol. **81**, pp. 497–520, 1999.

[2]L. Vienne, S. Marié, A Lattice Boltzmann study of miscible viscous fingering for binary and ternary mixtures. *Pys. Rev. F*, Vol. **6**, pp. 053904, 2021.

[3]R. Du and B. Shi, Incompressible Multi-Relaxation-Time Lattice Boltzmann Model in 3-D Space *Journ. of Hydrodynamics*, Vol. **22**, pp. 782–787 2010.

[4]C. Mimeau, S. Marié , I. Mortazavi. A comparison of semi-Lagrangian Vortex method and Lattice Boltzmann method for incompressible flows. *Comp Fluids*, **224**, 104946, 2021.

[5]C. Mimeau and I. Mortazavi, A review of Vortex Methods and their applications: from creation to recent advances. *Fluids*, Vol. **6, 68**, 2021.

[6]Z.Guo, C.Zheng, and B.Shi, Discrete lattice effects on the forcing term in the lattice Boltzmann method, *Phys. Rev. E* , Vol.**65, 4** ,2002.

[7]H. C. Brinkman, A calculation of the viscous force exerted by a flowing fluid on a dense swarm of particles, *Appl. Sci. Res.* , Vol.**1, 27** ,1949.

[8]D.A. Nield and A. Bejan, Convection in Porous Media. *Springer: Berlin*, 1999.

[9]M. Ciuti, G. A. Zampogna, F. Gallaire, S. Camarri, P. G. Ledda, *Phys. Fluids*, **33**, 124103, 2021.

WORKSHOP
Direct and Large-Eddy Simulation 13
October 26th-29th 2022, Udine, Italy

DNS AND LES OF BUOYANCY-DRIVEN TURBULENCE AT HIGH RAYLEIGH NUMBERS: NUMERICAL METHODS AND SUBGRID-SCALE MODELS

F.X.Trias[1], X.Álvarez-Farré[1], D.Santos[1], A.Gorobets[2], A.Oliva[1]
[1] Heat and Mass Transfer Technological Center, Technical University of Catalonia
C/Colom 11, 08222 Terrassa (Barcelona) E-mail: francesc.xavier.trias@upc.edu
[2] Keldysh Institute of Applied Mathematics, 4A, Miusskaya Sq., Moscow 125047, Russia

INTRODUCTION

Buoyancy-driven flows have always been an important subject of scientific studies with numerous applications in environment and technology. The most famous example thereof is the thermally driven flow developed in a fluid layer heated from below and cooled from above, *i.e.* the Rayleigh-Bénard convection (RBC). It constitutes a canonical flow configuration that resembles many natural and industrial processes, such as solar thermal power plants, indoor space heating and cooling, flows in nuclear reactors, electronic devices, and convection in the atmosphere, oceans and the deep mantle.

In the last decades significant efforts, both numerically and experimentally, have been directed at investigating the mechanisms and the detailed scaling behavior of the Nusselt number as a function of Rayleigh and Prandtl numbers in the general form $Nu \propto Ra^{\gamma} Pr^{\beta}$. In this regard, Figure 1 shows the predictions of the Nu-number based on the classical Grossmann-Lohse (GL) theory [1] and its subsequent corrections [2, 3] where different scaling regimes, characterized by their corresponding exponents γ and β, are identified. Assuming this power-law scalings and following the same reasonings as in Ref. [4] leads to the estimations for the number of grid points shown in Figure 2 (top). This corresponds to mesh resolution requirements for DNS and clearly explain why nowadays DNS of RBC is still limited to relatively low Ra-numbers. However, many of the above-mentioned applications are governed by much higher Ra numbers, located in the region of the $\{Ra, Pr\}$ phase space where the thermal boundary layer becomes turbulent (see the black dash-dotted line in Figure 2). This region corresponds to the so-called asymptotic Kraichnan or ultimate regime of turbulence, with $\gamma = 1/2$. On the other hand, reaching such Ra-numbers experimentally while keeping the basic assumptions (Boussinesq approximation, adibaticity of the closing walls, isothermal horizontal walls, perfectly smooth surfaces...) is a very hard task; therefore, the observation of the Kraichnan regime also remains elusive [2, 3].

LES OF BUOYANCY-DRIVEN TURBULENCE

In this context, we may turn to LES to predict the large-scale behavior of incompressible turbulent flows driven by buoyancy at very high Ra-numbers. In LES, the large-scale motions are explicitly computed, whereas the effects of small-scale motions are modeled. Since the advent of CFD, many subgrid-scale (SGS) models have been proposed and successfully applied to a wide range of flows. However, there still exits inherent difficulties in the proper modelization of the SGS heat flux. This was analyzed in detail in the PRACE project entitled "Exploring new frontiers in Rayleigh-Bénard convection" (33.1 millions of CPU hours on MareNostrum4 in 2018-2019), where DNS simulations of air-filled ($Pr = 0.7$) RBC up to $Ra = 10^{11}$ were carried out using meshes up to 5600M grid points (see dots displayed in Figure 2, top). These results shed light into the flow topology and the small-scale dynamics which are crucial in constructing the turbulent wind and energy budgets [5]. Moreover, it also provided new insights into the preferential alignments of the SGS and its dependence with the Ra-numbers [6], highlighting that the modelization of the SGS heat flux is the main difficulty that (still) precludes reliable LES of buoyancy-driven flows at (very) high Ra-numbers. This inherent difficulty can be by-passed by carrying out simulations at low-Prandtl numbers. In this case, the ratio between the Kolmogorov length scale and the Obukhov-Corrsin length scale (the smallest scale for the temperature field) is given by $Pr^{3/4}$; therefore, for instance, at $Pr = 0.005$ (liquid sodium) we have a separation of more than one decade. Hence, it is possible to combine an LES simulation for the velocity field (momentum equation) with the numerical resolution of all the

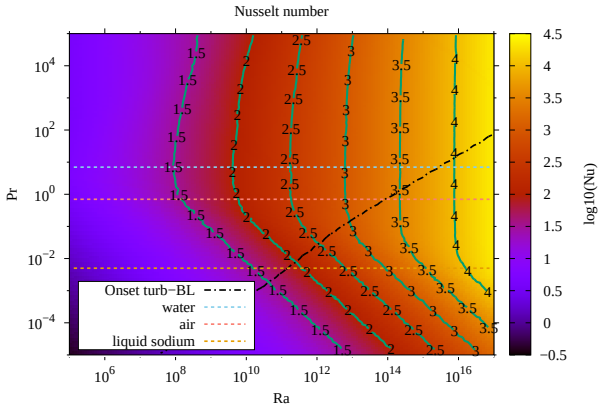

Figure 1: Estimation of the Nusselt number of a RBC in the $\{Ra, Pr\}$ phase space given by the classical GL theory [1] and its subsequent corrections [2]. Green solid isolines represent the $log10$ of the Nusselt. Three dashed horizontal lines correspond to three different working fluids: water ($Pr = 7$), air ($Pr = 0.7$) and liquid sodium ($Pr = 0.005$). Black dash-dotted line is an estimation for the onset of turbulence in the thermal boundary layer.

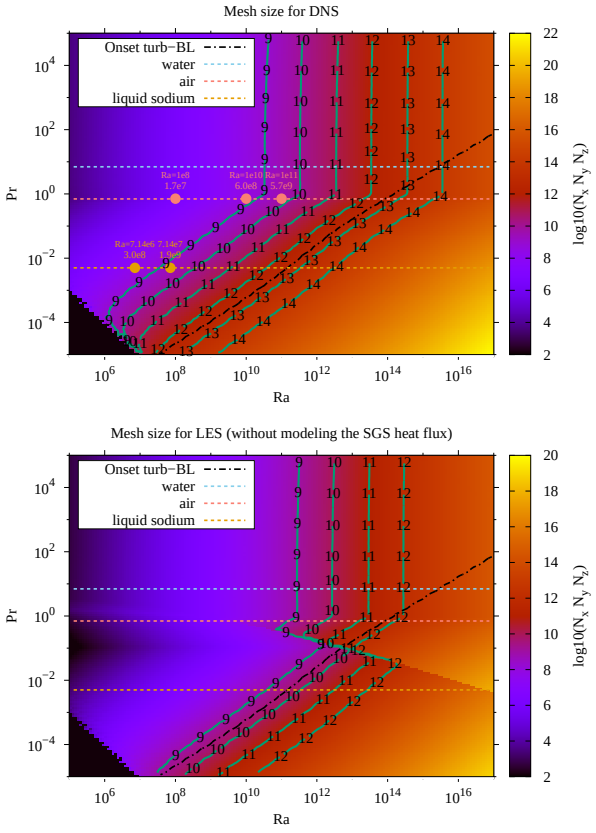

Figure 2: Estimation of the mesh sizes for DNS (top) and LES (bottom) simulations of RBC in the $\{Ra, Pr\}$ phase space. LES estimations assume that thermal scales are fully resolved, *i.e.* no SGS heat flux model is needed. Green solid isolines represent the $log10$ of the total number of grid points. Three dashed horizontal lines correspond to three different working fluids: water ($Pr = 7$), air ($Pr = 0.7$) and liquid sodium ($Pr = 0.005$). Dots displayed on top of these lines correspond to the DNS simulations carried out in previous studies [4, 5, 6]. Black dash-dotted line is an estimation for the onset of turbulence in the thermal boundary layer.

thermal scales. Results obtained in Ref. [6] suggest that accurate predictions of the overall Nu can be obtained with meshes significantly coarser than for DNS (*e.g.* in practice for $Pr = 0.005$ we can expect mesh reductions in the range 10^2-10^3 for the total number of grid points). This can be clearly observed in Figure 2 (bottom), where estimations of the mesh size for LES are given with the assumption that thermal scales are fully resolved. This opens the possibility to reach the ultimate regime carrying out LES at low-Pr using meshes of 10^{10}-10^{11} grid points. Nevertheless, to do so, we firstly need to combine proper numerical techniques for LES (also DNS) with an efficient use of modern supercomputers.

NUMERICAL METHODS AND ALGORITHMS FOR LARGE-SCALE SIMULATIONS ON MODERN SUPERCOMPUTERS

The essence of turbulence are the smallest scales of motion. They result from a subtle balance between convective transport and diffusive dissipation. Mathematically, these terms are governed by two differential operators differing in symmetry: the convective operator is skew-symmetric, whereas the diffusive is symmetric and negative-definite. At discrete level, operator symmetries must be retained to preserve the analogous (invariant) properties of the continuous equations: namely, the convective operator is represented by a skew-symmetric matrix, the diffusive operator by a symmetric, negative-definite matrix and the divergence is minus the transpose of the gradient operator. In our opinion, this is the first requirement for reliable DNS and LES simulations. Furthermore, these (large-scale) simulations should run efficiently on the variety of modern HPC systems (CPUs, GPUs, ARM,...) while keeping the code easy to port and maintain.

In this regard, a fully-conservative discretization for collocated unstructured grids was proposed [7]. It exactly preserves the symmetries of the underlying differential operators and is based on only five discrete operators (*i.e.* matrices): the cell-centered and staggered control volumes (diagonal matrices), Ω_c and Ω_s, the face normal vectors, N_s, the cell-to-face interpolation, $\Pi_{c\to s}$ and the cell-to-face divergence operator, M. Therefore, it constitutes a robust approach that can be easily implemented in existing codes such as OpenFOAM® [8]. Then, for the sake of cross-platform portability and optimization, CFD algorithms must rely on a very reduced set of (algebraic) kernels [9] (*e.g.* sparse-matrix vector product, SpMV; dot product; linear combination of vectors). Results showing the benefits of symmetry-preserving discretizations will be presented together with novel methods aiming to keep a good balance between code portability and performance. In particular, results of DNS and LES results of RBC at different Ra will be presented focusing of the feasibility of the developed LES technology to give accurate predictions of the above-explained Nu-vs-Ra scalings. Comparison with DNS results and with the classical GL theory will be conducted.

REFERENCES

[1] Siegfried Grossmann and Detlef Lohse. Scaling in thermal convection: a unifying theory. *Journal of Fluid Mechanics*, 407:27–56, 2000.

[2] R. J. A. M. Stevens, E. P. van der Poel, S. Grossmann, and D. Lohse. The unifying theory of scaling in thermal convection: the updated prefactors. *Journal of Fluid Mechanics*, 730:295–308, 2013.

[3] S. Bhattacharya, M. K. Verma, and R. Samtaney. Revisiting Reynolds and Nusselt numbers in turbulent thermal convection. *Physics of Fluids*, 33:015113, 2021.

[4] F. Dabbagh, F. X. Trias, A. Gorobets, and A. Oliva. On the evolution of flow topology in turbulent Rayleigh-Bénard convection. *Physics of Fluids*, 28:115105, 2016.

[5] F. Dabbagh, F. X. Trias, A. Gorobets, and A. Oliva. Flow topology dynamics in a three-dimensional phase space for turbulent Rayleigh-Bénard convection. *Physical Review Fluids*, 5:024603, 2020.

[6] F.X. Trias, F.Dabbagh, A.Gorobets, and C.Oliet. On a proper tensor-diffusivity model for large-eddy simulation of buoyancy-driven turbulence. *Flow, Turbulence and Combustion*, 105:393–414, 2020.

[7] F. X. Trias, O. Lehmkuhl, A. Oliva, C.D. Pérez-Segarra, and R.W.C.P. Verstappen. Symmetry-preserving discretization of Navier-Stokes equations on collocated unstructured meshes. *Journal of Computational Physics*, 258:246–267, 2014.

[8] E. Komen, J. A. Hopman, E. M. A. Frederix, F. X. Trias, and R. W. C. P. Verstappen. A symmetry-preserving second-order time-accurate PISO-based method. *Computers & Fluids*, 225:104979, 2021.

[9] X. Álvarez, A. Gorobets, and F. X. Trias. A hierarchical parallel implementation for heterogeneous computing. Application to algebra-based CFD simulations on hybrid supercomputers. *Computers & Fluids*, 214:104768, 2021.

Session: Combustion and reactive flows

Wednesday, October 26, 2022

11:30 – 12:45

WORKSHOP
Direct and Large-Eddy Simulation 13
October 26th-29th 2022, Udine, Italy

A FOUR MIXTURE FRACTION FPV-LES FOR THE CO-FIRING OF COAL AND AMMONIA

D. Meller[1] L. Engelmann[1] P. Wollny[1] A. M. Kempf[1]
[1] Fluid Dynamics, Institute of Combustion and Gasdynamics
University of Duisburg-Essen, Germany
dominikmeller@uni-due.de

INTRODUCTION

The rising energy demand of emerging countries will continue to cause coal to play an essential role in the supply of electricity in the coming years. However, coal is considered an environmentally harmful fuel that releases large amounts of greenhouse gases and pollutants during firing. Measures must therefore be taken to improve Pulverized Coal Combustion (PCC) and reduce emissions. Numerical simulations have become increasingly important for the detailed understanding of PCC in recent years. Combustion models for gaseous combustion were extended to describe PCC. Among these models, the flamelet model [1] has proven to be a precise model that can represent detailed chemical mechanisms with low computational effort. The flamelet/progress variable (FPV) model by Pierce and Moin [2] is an extension of this model, in which a progress variable is used as trajectory variable. This model has been widely applied to PCC simulations. In order to describe the important processes in coal gasification, devolatilisation and char burn-up, flamelet models with two mixture fractions Z were developed. However, it is difficult to stabilise the pulverized coal flame itself, which is why an additional pilot gas stream is usually used. This additional fuel stream makes strong assumptions necessary, i.e. assuming that char reactions do not take place or assuming the pilot gas to be modelled as volatile gas. A complex extension of the 2Z-flamelet model was the 3Z-flamelet model by Wen et al. [3], which offers the possibility to describe all three fuel streams with moderate computational effort. New measures to reduce i.e. CO_2 emissions, require the admixture of additional fuels. A promising measure of continuing to operate coal-fired power plants in the future and drastically reducing CO_2 emissions is the co-firing of coal and ammonia. This relatively new method has not yet been widely investigated, and there are hardly any numerical studies on it. Difficulties that arise in the numerical simulation of co-firing are caused by the additional fuel stream ammonia. Four mixture fractions would now have to be considered as fuel streams (volatiles, char-off gases, pilot gas, ammonia) in order to describe the co-firing with a stabilizing pilot stream in detail. In a previous study [4], the co-firing was already investigated numerically and the first LES with a detailed chemical description was delivered. In this study, char-off gases were neglected and a 3Z-flamelet model was used. In the present study, a flamelet model based on a flamelet/progress variable (FPV) approach will be presented, which represents four mixture fractions and thus considers all necessary fuel streams for an accurate description of co-firing of coal and ammonia with stabilizing pilot stream - volatiles, char-off gases, pilot gas, and ammonia.

FLAMELET MODELING

For piloted pulverized coal and ammonia co-firing, four fuel streams exist, resulting from 1) the pilot stream, 2) the NH_3 and air stream, and 3) and 4) the volatile matter and the char, from the coal particles. To characterize the mixing between the four fuel sources and oxidizer (ox) (ambient air), four mixture fractions $Z_j = Y_j/(Y_{ox} + Y_{vol} + Y_{char} + Y_{ammo} + Y_{pil})$ are needed, indicated by $j \in \{\text{pil, ammo, vol, char}\}$ for the pilot stream, the ammonia stream, the volatile stream, and the char gases. Following the approach of Wen et al. [3], a coordinate transformation is used to avoid numerical problems. The newly introduced parameters (Z, A, B, C) are as follows:

$$Z = Z_{pil} + Z_{vol} + Z_{ammo} + Z_{char} \tag{1}$$

$$A = \frac{Z_{pil}}{Z_{pil} + Z_{vol} + \epsilon} \tag{2}$$

$$B = \frac{Z_{pil} + Z_{vol}}{Z_{pil} + Z_{vol} + Z_{ammo} + \epsilon} \tag{3}$$

$$C = \frac{Z_{pil} + Z_{vol} + Z_{ammo}}{Z_{pil} + Z_{vol} + Z_{ammo} + Z_{char} + \epsilon}, \tag{4}$$

where ϵ denotes a small positive number. The new parameters (ranging from 0 to 1) describe all states of mixing. To represent these states in the flamelet table, one-dimensional steady non-premixed flamelet equations are solved using FlameMaster [5] based on the assumption of unity Lewis number for varying values of Z, A, B and C. To represent the interphase heat transfer between the particle and gas phase, different input stream temperatures (300 K, 600 K, 800 K) are set to vary the enthalpy levels. Scalar dissipation rates χ are varied when solving the non-premixed flamelet equations in mixture fraction space to account for different strain rates. Finally, the thermochemical quantities from the flamelet solutions are parameterized by the control variables. In addition to the four mixture fraction parameters Z, A, B and C, a progress variable is used, which results from the linear combination of different key species in the exhaust gas, following $Y_{PV} = Y_{CO_2} + Y_{CO} + Y_{H_2O} + 10\, Y_{NO}$, and the total enthalpy. The final parameterization follows $\Psi = F(A, B, C, Z, Y_{PV,norm}, H_{norm})$ for the thermochemical quantities Ψ, where $Y_{PV,norm}$ and H_{norm} are

the normalized quantities for the progress variable and the enthalpy. The table dimensions are $6 \times 6 \times 6 \times 132 \times 51 \times 6$ in $A \times B \times C \times Z \times Y_{PV,norm} \times H_{norm}$. A reduced CRECK mechanism consisting of 129 species and 1644 elementary reactions is used, which was previously designed to model co-firing of coal and ammonia [4].

FLAME SETUP

Figure 1 shows the geometry of the investigated burner. It consists of an inner tube and a coaxial pilot channel, using hydrogen to stabilize the flame. The burner has three operation modes which are to be investigated using highly-resolved FPV-LES, 1) a pure coal combustion mode, where only coal particles and air are injected in the main tube 2) a pure ammonia combustion mode, where ammonia and air are injected, and 3), a co-firing mode, where ammonia, air, and coal particles are injected. Experimental data is taken from [6, 7, 8].

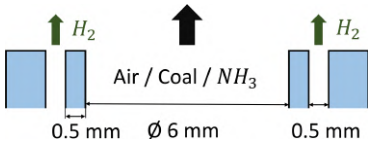

Figure 1: Setup of the investigated coaxial burner.

NUMERICAL SETUP

The massively parallel LES tool PsiPhi is used in this study. A low-Mach Finite Volume Method (FVM) with conjugated gradient solver and Jacobi preconditioner is applied. The solver uses an equidistant, orthogonal Cartesian grid. For diffusive fluxes and the convective flux of momentum, a second-order accurate Central Differencing Scheme (CDS) is applied. Convective scalar fluxes are discretized through a Total Variation Diminishing (TVD) scheme with a CHARM limiter. Time integration is done through an explicit third-order low-storage Runge-Kutta scheme. Radiation effects are neglected in this study, as previous studies showed neglectable influence. An Euler-Lagrange framework is used to couple particle-gas phases. Settings have been taken from our previous work on this burner and are applied here [9].

RESULTS

The following results show simulations that only take into account the hydrogen pilot, volatiles and ammonia as mixture fractions. Figure 2 shows the instantaneous and mean temperature, as well as the mixture fractions for volatiles, the hydrogen pilot and ammonia for the co-firing case of coal and ammonia. It can be clearly distinguished, where the respective mixture fractions come into play. Hydrogen is burned after entering the domain, this in turn ignites the ammonia. The heat forces the coal particles to release volatiles. Volatiles accumulate in the inner, lower temperature region, while they are burned in the edge regions. The outer hot temperature region refers to the combustion of hydrogen (immediately after the inflow), the combustion of ammonia and volatile gases. For the extension to include the important char-off gases, flamelet calculations are currently being made to generate the tables. The many flamelet calculations are particularly time-consuming. The extension by one dimension in the flow solver is relatively straightforward. The aim of this study is to first, develop a model to classifiy all significant fuel sources during co-firing of coal and ammonia with a pilot fuel and second, to clarify the influence of char reactions during co-firing.

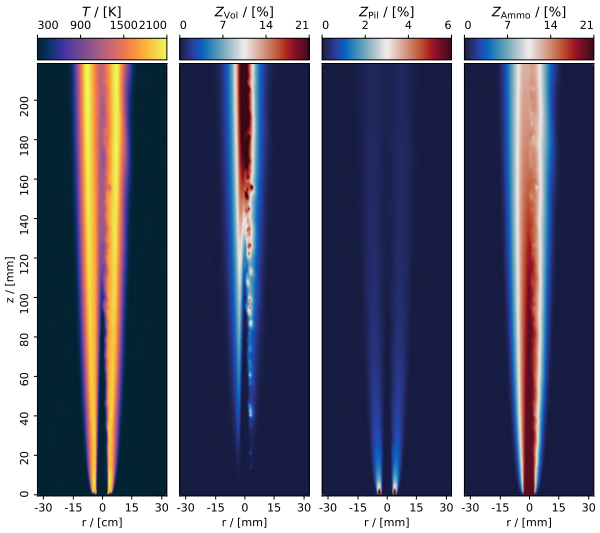

Figure 2: Instantaneous (left) and mean (right) temperature T and mixture fractions for volatiles (Z_{Vol}), hydrogen pilot Z_{Pil} and ammonia Z_{Ammo}. The co-firing case of coal and ammonia is shown.

REFERENCES

[1]Peters, N.: Laminar diffusion flamelet models in non-premixed turbulent combustion, *Prog. Energy Combust. Sci.*, **10**, 319–339 (1984).

[2]Pierce, C. D. and Moin, P.: Progress-variable approach for large-eddy simulation of non-premixed turbulent combustion, *J. Fluid Mech.*, **504**, 73–97 (2004).

[3]Wen, X., Luo, Y., Wang, H.,Luo, K., Jin, H., Fan, J.: A three mixture fraction flamelet model for multi-stream laminar pulverized coal combustion, *Proc. Combust. Inst.*, **37**, 2901–2910 (2019).

[4]Meller, D., Engelmann, L., Wollny, P., Tainaka, K., Watanabe, H., Debiagi, P., Stein, O. T., Kempf, A. M.: Evaluation of ammonia co-firing in the CRIEPI coal jet flame using a three mixture fraction FPV-LES, *Proc. Combust. Inst.*, **39**, accepted for oral presentation (2022).

[5]Pitsch, H.: FlameMaster, a computer code for homogeneous combustion and one-dimensional laminar flame calculations, Institute for Technical Mechanic, RWTH Aachen, *available from https://www.itv.rwth–aachen.de/downloads/flamemaster/* (1998).

[6]Tainaka, K., Yamamoto, A., Kimoto, M., Ozawa, Y., Hara, S.: Investigation of co-combustion characteristics of pulverized coal and ammonia in a jet flame, *Symposium (Japanese) on Combustion*, **56** (2018).

[7]Tainaka, K., Sawada, S., Okada, D., Akamatsu, F., Run, L.: Effects of co-firing ammonia on structure of a pulverized coal jet flame, *Symposium (Japanese) on Combustion*, **57** (2019).

[8]Stein, O. T. and Watanabe, H.: CRIEPI coal jet flame, *Proc. CBC Workshop*, **3**, 69-110 (2019).

[9]Meller, D., Lipkowicz, T., Rieth, M., Stein, O. T., Kronenburg, A., Hasse, C., Kempf, A. M.: Numerical analysis of a turbulent pulverized coal flame using a flamelet/progress variable approach and modeling experimental artifacts, *Energy Fuels*, **35**, 7133–7143 (2021).

WORKSHOP
Direct and Large-Eddy Simulation 13
October 26th -29th 2022, Udine, Italy

EFFECTS OF THE STRAIN RATES ON THE FORMATION AND GROWTH OF NANO-PARTICLES IN TURBULENT FLAMES

L. Cifuentes*, I. Wlokas, A. Kempf
Chair for Fluid Dynamics, Institute for Combustion and Gas Dynamics (IVG), University of Duisburg-Essen
Carl-Benz Strasse 199, 47057 Duisburg, Germany
*luis.cifuentes@uni-due.de

INTRODUCTION

In a real flame reactor forming nanoparticles, where turbulence can hardly be avoided, the smallest length scales - the Batchelor scales - of the nanoparticle field will be far smaller than the Kolmogorov length micro-scale of the turbulent flow. This makes the nanoparticle modelling very challenging since most practical computer simulations do not resolve these small nanoparticle structures. Under-resolution would lead to very significant errors, for example, orders of magnitude in simulated coagulation rates [1]. Therefore, it is crucial to perform direct numerical simulations (DNS) in the context of nanoparticle formation, solving the smallest scales of the nanoparticle field, to clarify the turbulence-particle-dynamics interaction and to guide the necessary modelling efforts.

In this work, the effect of turbulence on premixed and non-premixed particle forming flames are investigated via 2D and 3D direct numerical simulations. The change in particle concentrations due to diffusion, coagulation and nucleation are defined and characterized by the particle number concentration layers. Several regions of the computational domain with different turbulent intensities are analyzed, and the influence of the complex normal and tangential strain rates that control the thickness between particle number concentration fronts are evaluated. This information is subsequently used to discuss the physics of how the turbulent process affects premixed and non-premixed particle forming flames with the aim of developing transferable models for the simulations of nano-particle synthesis.

DIRECT NUMERICAL SIMULATIONS

The simulations were performed with the in-house DNS/LES code PsiPhi in a low-Mach number finite-volume formulation. These simulations resolve the smallest scales of the nanoparticle field. In all cases, the numerical simulations have been performed with a finite rate chemistry approach for evaluating the chemical kinetics and the sectional model [2] has been used to solve the population balance equation for the particle dynamics. In the sectional model, the particle size distribution is given for the particle volume v_k by the corresponding number concentration Q_k (in this study, v_k is a spherical volume of the nanoparticle of section k with a known diameter d_k). For the particle number concentration Q_k in every section k, the following transport equation is solved:

$$\frac{\partial Q_k}{\partial t} + \frac{\partial Q_k u_j}{\partial x_j} = \frac{\partial}{\partial x_j}\left(D_k \frac{\partial Q_k}{\partial x_j}\right) + \dot{W}_k + I_k \qquad (1)$$

In Eq. (1), D_k is the particle diffusivity, $\dot{W}_k$ is the coagulation source term, and I_k is the nucleation source term.

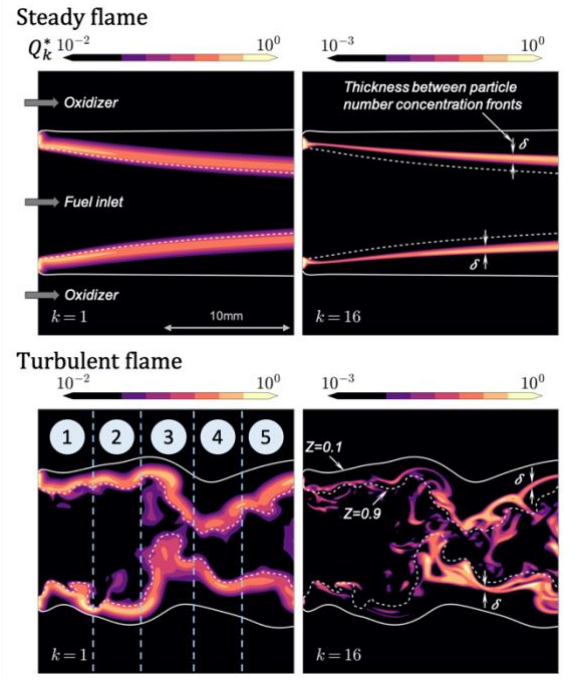

Figure 1: Instantaneous particle number concentration fields Q_k^* from the 3D non-premixed turbulent flame DNS data. Iso-lines represent the values of the mixture fraction $Z = 0.1$ and $Z = 0.9$. Vertical dotted lines mark the limits of the five regions of the computational domain where the results have been analyzed.

The 2D cases are DNS of premixed and non-premixed hydrogen flames (H_2/O_2/Ar), both doped with 200 ppm of iron pentacarbonyl $Fe(CO)_5$ for forming iron oxide nanoparticles and wrapped-up by a vortex. Interested readers are referred to Ref. [1] for further details about this DNS data. The three-dimensional DNS are premixed and non-premixed turbulent planar jet flames, both doped with 200 ppm of TTIP for forming titanium dioxide nanoparticles. For the premixed case, a methane-air mixture with an equivalence ratio $\emptyset = 0.7$ is injected through a turbulent central jet and surrounded by a co-flow of burned products. For the non-premixed flame, the fuel is injected through the turbulent central jet, surrounded by two air oxidizer streams (see Fig. 1).

NORMAL AND TANGENTIAL STRAIN RATES

The particle number concentration field Q in a turbulent flow can be viewed as a group of iso-Q surfaces, which are under compressive/expansive effects, stretching and Q-gradient growth induced by the flow field. Figure 2 depicts some non-material iso-Q surfaces on which act the normal and tangential strain rates. The unit normal vector is: $\mathbf{n} = -\nabla Q/|\nabla Q|$.

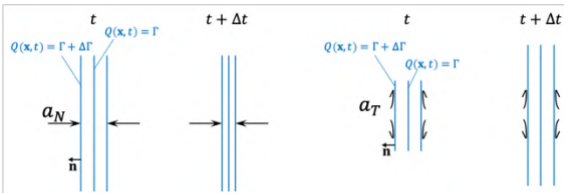

Figure 2: Schematic representation of the normal and tangential strain rates.

The flow strain rate normal to $Q(\mathbf{x}, t) = \Gamma$ is:

$$a_N = n_i S_{ij} n_i \quad (2)$$

The flow strain rate tangential to $Q(\mathbf{x}, t) = \Gamma$ is:

$$a_T = (\delta_{ij} - n_i n_j) S_{ij} \quad (3)$$

In Eqs. (2) and (3), δ_{ij} is the identity Kronecker delta tensor, and S_{ij} is the strain rate tensor.

The thickness of the particle number concentration field increases (decreases) with time if $a_N < 0$ ($a_N > 0$). On the other hand, the Q-surface stretching occurs if $a_T > 0$, which will increase the area affecting the structures of the nanoparticle field.

ANALYSIS AND DISCUSSION

Figure 1 shows instantaneous contours of particle number concentrations (sections 1 and 16, with particle diameters 0.4nm and 13nm, respectively) for the three-dimensional steady and turbulent non-premixed flames. It can be noticed that the particle number concentration fields have two fronts and that the thickness δ between particle number concentration fronts significantly decreases for high sections (or decreases with increasing Schmidt number), which confirms that in simulations of nanoparticle-forming turbulent reacting flows the grid resolution has to be very fine to resolve the characteristic scale for high sections.

Figure 3 shows the normal strain rate $a_{N20} = n_i^{20} S_{ij} n_j^{20}$, tangential strain rate $a_{T20} = (\delta_{ij} - n_i^{20} n_j^{20}) S_{ij}$ and normalized particle number concentration Q_{20}^* conditional upon the mixture fraction at different regions of the computational domain. For this section 20 predominantly $a_{N20} < 0$ and $a_{T20} > 0$. The local flow approaches iso-Q_{20}^* surfaces (compressive effects) from region 1 to regions 5 and, simultaneously, stretches them, which affect the thickness of Q_{20}^*. Further details about the flow fine-structure, the coagulation, nucleation and diffusion rates, and the particle number concentration layers will be discussed in the presentation.

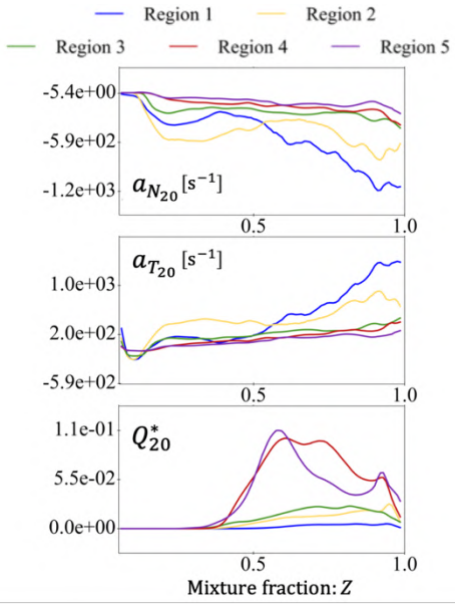

Figure 3: Normal strain rate a_{N20}, tangential strain rate a_{T20} and normalized particle number concentration Q_{20}^* conditional upon the mixture fraction at different regions of the computational domain. Results have been obtained from the 3D non-premixed turbulent flame.

ACKNOWLEDGMENTS

The authors gratefully acknowledge the Gauss Centre for Supercomputing e.V. (www.gauss-centre.eu) for providing computing time on the GCS Supercomputer SuperMUC-NG at Leibniz Supercomputing Centre (www.lrz.de), and the German Research Foundation (DFG project 262219004 - FOR2284 with grant KE 1751/7-2) for funding.

REFERENCES

[1] Cifuentes L., Sellmann J., Wlokas I., Kempf A.: Direct numerical simulations of nanoparticle formation in premixed and non-premixed flame-vortex interactions, *Phys. Fluids* 32, 093605 (2020).

[2] Jeong J., Choi M.: A sectional method for the analysis of growth of polydisperse non-spherical particles undergoing coagulation and coalescence, *J. Aerosol Sci.* 32, 565–582 (2001).

WORKSHOP
Direct and Large-Eddy Simulation 13
October 26th-29th 2022, Udine, Italy

HYDROGEN JET FLAME CONTROL BY GLOBAL MODE

A. Wawrzak[1], K. Wawrzak[1], A. Boguslawski[1], A. Tyliszczak[1], B.J. Geurts[2]
[1] Faculty of Mechanical Engineering and Computer Science
Czestochowa University of Technology, Poland
[2] Mathematics of Multiscale Modeling and Simulation
Faculty of Electrical Engineering, Mathematics and Computer Science
University of Twente, The Netherlands
agnieszka.wawrzak@pcz.pl

INTRODUCTION

Flame control has been in the centre of interest for decades and constitutes a subject of intensive research as it may lead to considerable improvement in efficiency and safety of various technical devices. Numerous industrial applications, such as aeroplane engines, involve jet-type flames with fuel issuing from a nozzle into an oxidizer stream. An interesting phenomenon emerging in round jets, which could be considered as a flow control technique, is self-excited global instability triggered by absolutely unstable local flow regions [1]. The theoretical predictions of Monkewitz and Sohn [2] and Jendoubi and Strykowski [3] showed that absolute instability can be triggered in variable density and counter-current jet configurations. Two absolutely unstable modes called Mode I and Mode II have been analytically identified [3] and additionally confirmed by experimental and numerical works [4, 5, 6, 8]. However, there are no investigations devoted to global instability in jet flames, despite their significance for practical solutions. In the present paper the effect of counter-current co-axial flow on the emergence of the global instability in the hydrogen jet flame is studied with the help of large-eddy simulations (LES).

COMPUTATIONS

The test case configuration is presented schematically in Fig. 1(a). It corresponds to the experimental set-up of Markides and Mastorakos [7] used for hydrogen autoignition in a turbulent co-flow of heated air. Mixture of hydrogen and nitrogen with the mass fractions Y_{H_2}=0.13 and Y_{N_2}=0.87 is injected into a heated air through a 2.25 mm (D) internal diameter pipe. Table 1 shows details of the temperature and velocity of the fuel jet as well as the co-flow stream. The density ratio $S = \rho_j/\rho_{cf}$, where ρ_j and ρ_{cf} denote density of the jet and co-flow, is slightly above the critical density ratio for which global oscillations emerge in a jet without counterflow for a given shear layer thickness characterized by the parameter $D/\theta = 40$ (θ - momentum thickness) [8]. The suction is applied through the annular nozzle which is placed around the main nozzle. It produces a counter-current region in the direct vicinity of the main jet. The strength of the counterflow is controlled by the velocity ratio $I = -U_{suc}/U_j$ (U_j - velocity of the jet, U_{suc} - velocity of the counter-current). The effect of the counterflows characterised by I= 0.1 and 0.2 is assessed in relation to the flame without suction ($I = 0$).

In the present work we do not consider the inner geometry of the nozzles and the computational domain is a rectangular box with dimensions $L_y = 30D, L_x = L_z = 15D$, where '$y$' is the axial direction. The applied mesh counts N_y=288, $N_x = N_z$=192 nodes in the axial and radial directions, respectively. The inlet boundary conditions are specified in terms of the instantaneous velocity profile. The velocity fluctuations are computed according to method proposed by Klein et al. [9] whereas the inlet mean velocity is described by the Blasius profile. Sample profiles of the mean axial velocity at the inlet plane of the computational domain are displayed in Fig. 1(b).

The LES solver used in this study is an in-house high-order solver based on the low Mach number approximation. The Navier-Stokes and continuity equations are discretised using the sixth order compact difference method on half-staggered meshes [10]. A sub-grid model of Vreman [11] is used to compute the sub-grid viscosity for SGS-stress tensor. The chemical reactions are computed using the CHEMKIN interpreter with the help of a detailed mechanism of hydrogen oxidation [12] involving 9 species and 21 reactions. The calculations are conducted without any closure for turbulence/combustion interactions at the sub-grid level. Correspondingly, the filtered reaction rates of species were obtained directly from the Arrhenius formula.

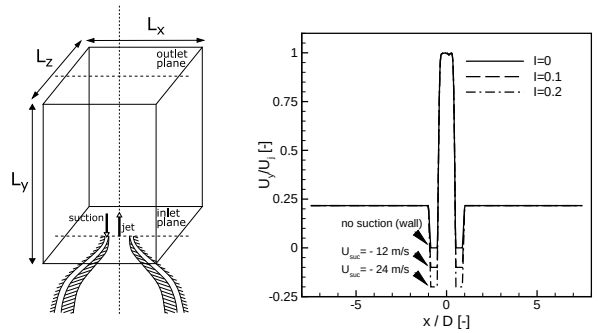

(a) (b)

Figure 1: Computational configuration (a) and the inlet velocity profiles (b) for the cases considered.

Fuel (jet)	Oxidiser (co-flow)	T_j [K]	T_{cf} [K]	S [-]	U_j [m/s]	I [-]	U_{cf} [m/s]
0.13 H_2/0.87 N_2	0.23 O_2/0.77 N_2	691	1010	0.53	120	0, 0.1, 0.2	26

Table 1: Summary of test cases considered.

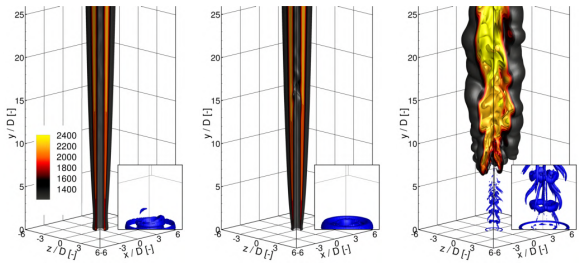

(a) I-00 (b) I-01 (c) I-02

Figure 2: Instantaneous iso-surfaces of the Q-parameter ($Q = 0.05$ s^{-2}, blue) and temperature inside the flames.

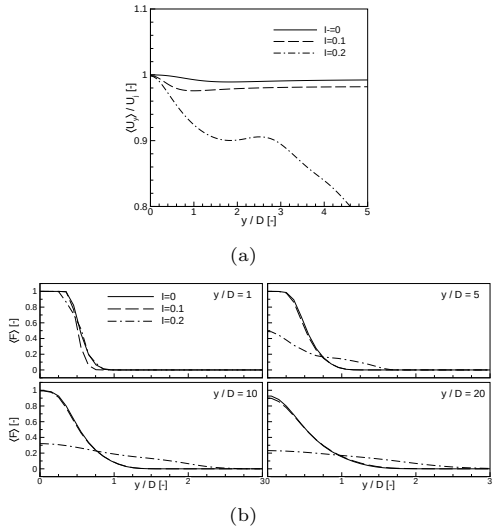

(a)

(b)

Figure 3: Profiles of the time averaged mean axial velocity along the jet axis (a) and the radial distributions of the time averaged mixture fraction at different axial locations (b).

RESULTS

Figure 2 displays fully developed flames visualised by the instantaneous iso-surfaces of the temperature inside the flame and the Q-parameter close to the inlet plane. It appears that the flow pattern is similar for I=0 and I=0.1 while significant differences emerge when the strongest suction is applied, i.e., for the case with $I = 0.2$. As can be seen in Fig. 2, the flame in the original configuration ($I = 0$) is attached to the nozzle, whereas strong counterflow stabilizes the lifted flame. Increasing the suction triggers global instability before autoignition occurs. In fact, at strong suction the velocity field drastically changes revealing the formation of strong coherent structures close to the nozzle. These structures pair and subsequently break up further downstream (see the blue iso-surfaces in Fig. 2). As can be seen in Fig. 3 showing velocity profiles along the jet axis the velocity decay appears close to the nozzle exit. In this case, mixing is drastically intensified directly behind the inlet plane as the mixture fraction is reduced. A large amount of fluid taken from the surroundings becomes mixed with the fuel to make the mixture leaner. This even prevents an upstream flame propagation and the flame lifts off. The lift-off height as well as the radial size of the flame can be deduced from the results presented in Figs. 2-3. One can see that the flame is nearly two times wider and stabilises at a distance of $6D$ from the nozzle. Moreover, in the case with $I = 0.2$ the temperature inside the flame is 120 K higher compared to the cases with $I = 0.0$ and $I = 0.1$ where the global mode does not appear.

CONCLUSIONS

The present study showed that the critical velocity ratio for which global instability is triggered in the considered jet flame is between 0.1 and 0.2. The global mode observed at sufficiently strong counter-current flow (I=0.2) causes qualitative changes of the flame characteristics. It was demonstrated that the position, global size and temperature of the flame can be effectively modified by the application of suction around the fuel jet. This may be desirable from a practical point of view since a suitable alteration of the flame would lead to considerable improvement of efficiency, safety or pollution reduction. Further calculations for a wider range of velocity ratios as well as different density ratios are planned to investigate whether the flame can be effectively controlled by the global mode.

REFERENCES

[1]Huerre P. and Monkewitz P.: Local and global instabilities in spatially developing flows, *Annu. Rev. Fluid Mech.*, **22**, 473–537 (1990).

[2]Monkewitz P. and Sohn K.: Absolute instability in hot jets, *AIAA J.*, **26**, 911–916 (1988).

[3]Jendoubi S. and Strykowski P.: Absolute and convective instability of axisymmetric jets with external flow, *Phys. Fluids*, **6**, 3000–3009 (1994).

[4]Strykowski P. and Niccum D.: The stability of countercurrent mixing layers in circular jets, *J. Fluid Mech.*, **227**, 309–343 (1991).

[5]Lesshafft L., Huerre P. and Sagaut P.: Frequency selection in globally unstable round jets, *Phys. Fluids*, **19**, 054108 (2007).

[6]Wawrzak K., Boguslawski A. and Tyliszczak A.: A numerical study of the global instability in counter-current homogeneous density incompressible round jets, *Flow Turbul. Combust.*, **107**, 901–935 (2021).

[7]Markides C. and Mastorakos E.: An experimental study of hydrogen autoignition in a turbulent co-flow of heated air, *Proc. Combust. Inst.*, **30**, 883–891 (2005).

[8]Boguslawski A., Tyliszczak A. and Wawrzak K.: Large eddy simulation predictions of absolutely unstable round hot jet, *Phys. Fluids*, **28**, 025108 (2016).

[9]Klein M., Sadiki A. and Janicka J.: A digital filter based generation of inflow data for spatially developing direct numerical or large eddy simulations, *J. Comput. Phys.*, **186**, 652–665 (2003).

[10]Tyliszczak A.: High-order compact difference algorithm on half-staggered meshes for low Mach number flows, *Comput. Fluids*, **127**, 131–145 (2016).

[11]Vreman A.: An eddy-viscosity subgrid-scale model for turbulent shear flow: Algebraic theory and applications, *Phys. Fluids*, **16**, 3670–3681 (2004).

[12]Mueller M., Kim T., Yetter R. and Dryer F.: Flow reactor studies and kinetic modeling of the H_2/O_2 reaction, *International Journal of Chemical Kinetics*, **31**, 113–125 (1999).

WORKSHOP
Direct and Large-Eddy Simulation 13
October 26th-29th 2022, Udine, Italy

LARGE-EDDY SIMULATION OF THE STRATIFIED SWIRL FLAMES SERIES USING AN ASSUMED OR HYBRID ASSUMED / TRANSPORTED FILTERED DENSITY FUNCTION APPROACH

S.-J. Baik[1], **E. Inanc**[1,2], **A.M. Kempf**[1]
[1] Chair for Fluid Dynamics, Institute for Combustion and Gas Dynamics (IVG),
University of Duisburg-Essen, Germany
[2] Current address: Jülich Supercomputing Centre, Forschungszentrum Jülich GmbH, Germany
seung.baik@uni-due.de

INTRODUCTION

The modern development of combustion systems is moving towards lean premixed combustion to reduce NOx and CO emissions, and consideration of stratification is a viable strategy to achieve lean combustion [1]. In many practical applications, swirl flows are commonly used in premixed and stratified combustion to improve mixing and stabilize the flames. Sweeney et al. [2] constructed a stratified burner to investigate the effect of stratification under swirling conditions (so-called Cambridge stratified flames). This present work conducts a large-eddy simulation (LES) of the Cambridge stratified flames under swirling conditions with the Eulerian-Lagrangian hybrid filtered density function (HDF) approach introduced by Rieth et al. [3]. Additionally, the conventional assumed filtered density function (ADF) approach is performed to compare the HDF model.

NUMERICAL METHOD

In the LES concept, the large scales of eddy are solved directly and the small scales have to be modelled by proper subgrid models of flow field and combustion. In the present work, two different combustion subgrid modeling strategies are tested. In the first approach, the subgrid distribution of composition fields of reacting flows can be reconstructed from commonly assumed filtered density function (FDF) shapes. Contrary to the ADF approach, in the second method, the Monte-Carlo particles are used to solve the transport of the filtered mass density function (FMDF) [4] which can be derived as,

$$\frac{\partial}{\partial t}F + \frac{\partial}{\partial x_i}\widetilde{u}_i F = -\frac{\partial}{\partial x_i}([\overline{u_i|\Psi} - \widetilde{u}_i]F) + \frac{\partial}{\partial \psi_\alpha}\left[\overline{\frac{1}{\rho}\partial J_i^\alpha/\partial x_i \middle| \Psi}\, F\right] - \frac{\partial}{\partial \psi_\alpha}S_\alpha F. \quad (1)$$

The latter method ensures that the reaction rate term is in the closed-form. In both approaches, the chemical and thermal quantities are determined from a pre-calculated chemistry table lookup depending only on parameters mixture fraction and progress variable.

To reduce the cost of the conventional Monte Carlo particles method to solve the transport equation of FMDF, a hybrid model combining ADF with Lagrangian transported FDF approach has been suggested by Rieth et al. [3]. In the HDF approach, apart from the conventional LES-FDF approach, which needs numerically expensive notional particles in the entire domain, in the hybrid method, the ADF is used throughout the entire computational domain, augmented by Lagrangian transported FDF in reacting regions (mixture fraction bounds of 0.02 and 0.06 for this work). The previous work by Rieth et al. [3] should be consulted for a further discussion of the hybrid modelling.

TEST CASES

The Cambridge stratified swirl flames are reproduced by the in-house LES solver PsiPhi [3, 5] with the artificially thickened flame model, which implies an assumed filtered density function (LES-ADF), or the hybrid modelling with a filtered density function (LES-HDF). In this work, the highly swirling condition with three different levels of stratification has been selected as summarized in Table 1. In all cases, the simulations were performed in a domain 168x168x168 mm^3 (336x336x336 grid nodes) on an equidistant Cartesian grid with Δ =0.5 mm spacing and 38 million cells at a temporal resolution of 0.7 μs (CFL criterion of 0.7). A 12 mm nozzle is included in the computational domain. The costs of simulations for LES-ADF and LES-HDF are 20,000 and 630,000 core hours respectively.

RESULTS

Figure 1 exemplary shows contour plot (SwB3) of an equivalence ratio with superimposed the three-dimensional isosurface for a progress variable of 0.5 to understand an overall flame structure. Figure 2 shows instantaneous and mean simulation contour plots of axial velocity in a burner cross section to show the flame structures and qualitatively compare the simulations from LES-ADF and LES-HDF model. The flames calculated by LES-HDF model generally spread wider after 60 mm downstream from nozzle and simulated recirculation zones for all three cases by LES-HDF model are formed in slightly father downstream, but stronger than LES-ADF model.

Comparisons of means radial profiles of temperature and mass fraction of CO from both simulations and experiments at three axial distances above the burner for the premixed case

SwB3, moderately stratified case SwB7 and highly stratified case SwB11 are shown in Fig. 3 and 4. Overall simulation results of two different combustion models are in good agreement with the measurements [2] for temperature and mass fraction of CO. Especially, CO mass fractions are overpredicted near the bluff body close to the inlet for the moderately and highly stratified case.

ACKNOWLEDGEMENTS

The authors gratefully acknowledge the financial support by the state North-Rhine-Westphalia. We thank the University of Duisburg-Essen and Center for Computational Sciences and Simulation (CCSS) for providing time on the HPC system magnitUDE (DFG grant INST 20876/209-1 FUGG) at the Zentrum für Informations- und Mediendienste (ZIM).

REFERENCES

[1]Lipatnikov, A.N., *Prog. Energy Comb. Sci.*, **62**, 87–132 (2017).
[2]Sweeney, M.S., Hochgreb, S., Dunn, M., Barlow, R.S.J., *Combust. Flame*, **159,9**, 2912–2929 (2012).
[3]Rieth, M., Chen, J.-Y., Menon, S., Kempf, A.M., *Phys. Fluids*, **23**, 85–106 (2019).
[4]Jaberi, F.A., Colucci, P.J., James, S., Givi, P., Pope, S.B., *J. Fluid Mech.*, **401**, 85–121 (1999).
[5]Proch, F., Kempf, A.M., *Comb. Flame*, **161**, 2627–2646 (2014).

Case	U_i m/s	U_o m/s	U_{co} m/s	Φ_i -	Φ_o -	SFR %
SwB 3	8.3	18.7	0.4	0.75	0.75	33
SwB 7	8.3	18.7	0.4	1.0	0.5	33
SwB 11	8.3	18.7	0.4	1.125	0.375	33

Table 1: Operating conditions for tested cases. SFR denotes the swirl-flow-ratios and is defined as the ratio of outer flow rate through the swirl plenum to the total outer flow.

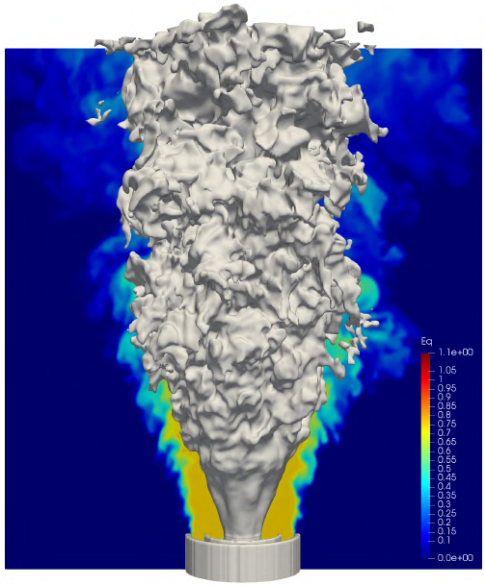

Figure 1: Contour plot of equivalence ratio in the burner mid-section, superimposed by an iso-surface for a progress variable value of $C = 0.5$.

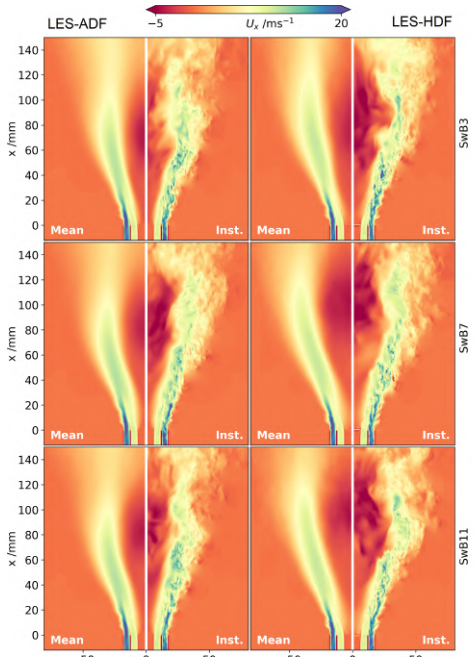

Figure 2: Contour plots in the burner mid-session of axial velocity.

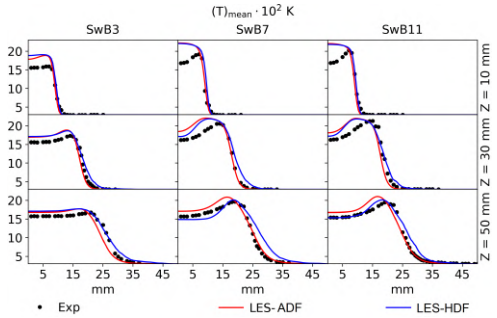

Figure 3: Radial profiles of the mean of temperature at different downstream locations.

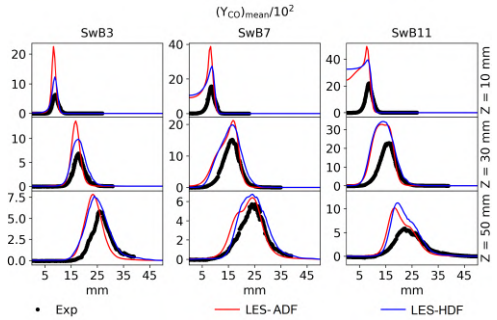

Figure 4: Radial profiles of the mean of CO mass fraction at different downstream locations.

WORKSHOP
Direct and Large-Eddy Simulation 13
October 26th -29th 2022, Udine, Italy

Reduced order combustion modelling with the Flamelet Generated Manifold method for turbulent ammonia/hydrogen flames

Nithin Mukundakumar[1]
n.nediyathu.mukundakumar@tue.nl
Rob Bastiaans[1]
[1] Mechanical Engineering, Power and Flow
Eindhoven University of Technology

INTRODUCTION

Ammonia as a fuel has gathered recent interest due to the absence of carbon atoms and as an efficient chemical storage method for Hydrogen. Within the flexible fuel concept, there is interest in utilizing methane and hydrogen blends of ammonia to be used in gas turbine power generators. As an additive hydrogen is especially attractive due to its lack of carbon based pollutants and the higher enhancement of flammability limits as compared to methane. Fundamental studies of these blends using DNS are needed to design highly efficient combustors, while also ensuring that NOx levels remain low, as with NH3, fuel borne NOx becomes especially challenging. DNS with detailed chemistry however leads to very expensive computations. To this end this paper showcases the tabulated chemistry method, Flamelet Generated Manifold (FGM) [1], applied to a spherically expanding turbulent flame kernel.

SETUP

For this study a 2-dimensional FGM was used. The control variables were a progress variable and mixture fraction. The mixture fraction dimension accounts for variation in local fuel-oxidizer composition due to preferential diffusion effects. The progress variable is any combination of the reacting species which is either monotonously increasing or decreasing along a flame path. The transport equations for these 2 variables are then solved during runtime. The table was generated using 1D adiabatic flames. The FGM method was studied for 50% ammonia and 50% hydrogen at an equivalence ratio of 1 with Karlovitz number of 10 and validated with corresponding detailed chemistry DNS results. The simulation was run up to 1 eddy turnover time. The in-house DNS code used, utilizes a compact-storage 6th order compact implicit differencing scheme from Lele [2] and 5th order implicit upwind scheme from De Lange [3] for the convective terms. The time discretization was done using a 3rd order compact Runge-Kutta scheme [4]. The boundary conditions were modelled using the Navier Stokes Characteristic Boundary Conditions [5].

RESULTS

The validation with the DNS results showed good qualitative agreement, with the method being able to reproduce the flame shape as observed from detailed DNS cases as seen in Figure 1.

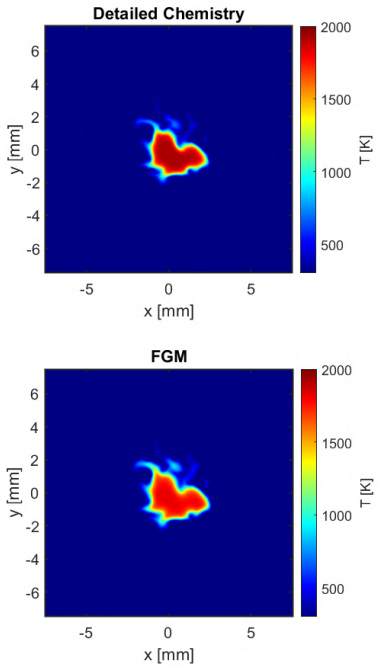

Figure 1: Comparison of temperature fields between detailed chemistry and the FGM method.

Although the method was able to account for preferential diffusion effects to a large extent, evaluation of the mass fractions of some species such as H2 however showed significant deviation from the detailed chemistry case. The temperature at the core of the flame, where the burnt products accumulate also showed underprediction.

CONCLUSIONS

The FGM method was studied and validated to show that although flame shape was predicted well, certain species were not predicted accurately. Further improvements to the method will be needed for a robust and accurate implementation. As a start, enthalpy will be added as a 3rd dimension in order to capture enthalpy variation due to preferential diffusion, with the assumption that the discrepancies are because of insufficient capture of stretch effects.

REFERENCES

[1] J. van Oijen, "Flamelet-generated manifolds : development and application to premixed laminar flames," Eindhoven University of Technology, 2002.

[2] S. K. Lele, "Compact finite difference schemes with spectral-like resolution," *J. Comput. Phys.*, vol. 103, no. 1, pp. 16–42, Nov. 1992, doi: 10.1016/0021-9991(92)90324-R.

[3] H. C. de Lange, "Inviscid flow modelling using asymmetric implicit finite difference schemes," *Int. J. Numer. Methods Fluids*, vol. 49, no. 9, pp. 1033–1051, Nov. 2005, doi: 10.1002/FLD.1044.

[4] C. A. Kennedy, M. H. Carpenter, and R. M. Lewis, "Low-storage, explicit Runge–Kutta schemes for the compressible Navier–Stokes equations," *Appl. Numer. Math.*, vol. 35, no. 3, pp. 177–219, Nov. 2000, doi: 10.1016/S0168-9274(99)00141-5.

[5] T. J. Poinsot and S. K. Lele, "Boundary conditions for direct simulations of compressible viscous flows," *J. Comput. Phys.*, vol. 101, no. 1, pp. 104–129, Jul. 1992, doi: 10.1016/0021-9991(92)90046-2.

Session: Bluff bodies

Wednesday, October 26, 2022

11:30 – 12:45

WORKSHOP
Direct and Large-Eddy Simulation 13
October 26^{th}-29^{th} 2022, Udine, Italy

LARGE-EDDY SIMULATION OF THE FLOW AROUND RECTANGULAR CYLINDERS OF DIFFERENT CHORD-TO-DEPTH RATIOS: IMPACT OF UPSTREAM-EDGE SHARPNESS

M.V. Salvetti, G. Lunghi, M. Morello and A. Mariotti
Department of Civil and Industrial Engineering
University of Pisa, Italy
maria.vittoria.salvetti@unipi.it

INTRODUCTION

Square and rectangular cylinders can be considered simplified models of structures of interest in civil engineering, such as, e.g., tall buildings or bridge sections. The chord-to-depth ratio has a strong influence on the dynamics of the flow around the cylinder. In all cases, the flow is characterized by flow separation at the upstream edges. The separated shear layers roll up forming vortical structures (Kelvin-Helmholtz instability), which are convected downstream and eventually interact by pairing with other vortical structures forming from the separated shear layers. For large chord-to-depth ratios, the flow reattaches in mean on the lateral side of the cylinder, and, thus, the mean flow is characterized by a closed separated-flow region. Further downstream, shear layers separate again from the trailing edge and in the near wake the flow is characterized by the classical Von-Karman vortex shedding. The mean flow reattachment does not occur for low cord-to-depth ratios, as, e.g., for the square cylinder.

The flow around a rectangular cylinder having 5:1 chord-to-depth ratio is the object of the international Benchmark on the Aerodynamics of a Rectangular 5:1 Cylinder (BARC). BARC was a double-blind benchmark, i.e. without a-priori selected reference measurements. The different contributions to the benchmark were characterized by significant differences in the mean flow topology on the cylinder side; this, in turn, resulted in large discrepancies in some quantities of interest, such as, for instance, the distribution of mean and fluctuating pressure on the cylinder side (see [1]). As for LES simulations, it was observed that the characteristics of the flow on the cylinder side, and hence the pressure distribution, are highly sensitive to grid resolution and subgrid-scale modeling [2].

Furthermore, Rocchio et al. [3] recently studied the effects of a small roundings of the upstream edges for the BARC case. It was shown that even small values of the curvature radius significantly impact on the results by increasing the length of the mean recirculation region. This is because sharp edges introduce significant velocity fluctuations in the shear-layer at separation that, when not artificially damped by numerical or SGS dissipation, cause an upstream roll up of the shear layers and, hence, a short mean recirculation region. This effect seems to be a numerical issue related to the flow resolution typical of LES simulations, since the impact of upstream-edge rounding was found to be much smaller in DNS simulations in [4] at lower Reynolds number.

We want to investigate herein whether the impact of the upstream edge sharpness on the LES results is peculiar of elongated rectangular cylinders characterized by mean flow reattachment. To this aim, we carry out the same analysis as in [3] also for a square cross-section and for a rectangular one having an aspect ratio of 3:1, which are characterized by different flow topologies. Indeed, for the square cylinder the mean flow does not reattach on the cylinder side, while for the 3:1 case it is about to reattach along the lateral side of the cylinder. Sharp upstream edges and different values of the upstream corner roundings are considered.

METHODOLOGY AND PROBLEM DEFINITION

We consider the incompressible flow around rectangular cylinders, having 1:1, 3:1, and 5:1 chord-to-depth ratios, at zero angle of attack. The upstream edges are sharp or rounded with curvature radii $r/D = 0.0037, 0.036, 0.0781, 0.1104$, D being the depth of the cylinder. The cylinder center is located at $x/D = y/D = 0$ and the computational domain span the following dimensions $-15.5 \leq x/D \leq 25.5$, $-15.1 \leq y/D \leq 15.1$ and $0 \leq z/D \leq 5$. A uniform velocity profile with no turbulence is imposed at the inlet, no slip is imposed at the body surface and traction-free boundary conditions are used for the outflow and for the upper and lower boundaries of the domain. Finally, periodicity is imposed in the spanwise direction. The Reynolds number, Re, based on the free-stream velocity and on the cylinder depth is $4 \cdot 10^4$.

The numerical simulations are performed by employing Nek5000, an open-source code based on a high-order spectral element method. Each spectral element is rectangular or a suitable coordinate mapping of a rectangle. The basis functions inside the elements are Legendre polynomials of order N for velocity and $N-2$ for pressure in each direction; $N = 6$ has been used in this work, as in [3]. A third-order backward finite-difference scheme based on the high-order splitting method is employed for time advancing.

The spectral element size and distribution are the same used in [3]. In particular, the element size in the streamwise and lateral directions is $\Delta x/D = \Delta y/D = 0.125$ near the cylinder, while in the spanwise direction the element size is uniform $\Delta z/D = 0.558$ as done in [3]. For rounded edges, the computational grid is the same as in the sharp-edge case except that the rounded part is handled by curvilinear elements.

Because the grid resolution is not fine enough to resolve all turbulent scales at the considered Reynolds number, a low-pass filter is applied to the velocity field in the modal space as in [3]. Since the filter introduces dissipation of the highest resolved modes only, this can be considered as a subgrid-scale dissipation.

SOME RESULTS AND DISCUSSION

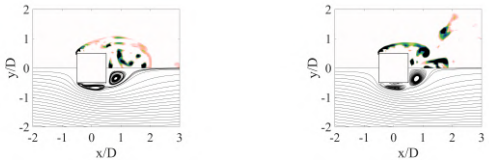

(a) (b)

Figure 1: Mean flow streamlines (top) and instantaneous vortex-indicator λ_2 (bottom) for the square cylinder: (a) $r/D = 0$ and (b) and $r/D = 0.037$.

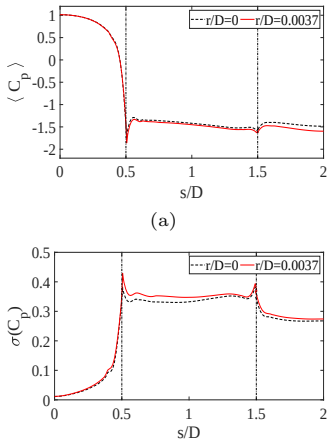

(a)

(b)

Figure 2: Mean pressure coefficient distribution (a) and standard deviation of the pressure coefficient (b) for the square cylinder.

Mean flow streamlines and isocontours of the instantaneous vortex-indicator λ_2 for $r/D = 0$ and $r/D = 0.037$ are shown in Fig. 1 and 3 for the square cylinder. In this case, which is characterized by a fully separated mean flow, a negligible effect of the upstream-corner sharpness on the mean flow topology is found. Consequently, the mean and fluctuating pressure distributions obtained in the two cases are also very similar.

The same quantities as in Fig. 1 are shown in Fig. 3 for the 3:1 rectangle. In this case, even a very small value of the curvature radius, i.e. $r/D = 0.037$, significantly changes the mean flow topology. Indeed, for sharp edges the mean flow reattaches near the end of the lateral side (Fig. 3a), while the mean flow does not reattach for rounded upstream edges (Fig. 3c). The mean and fluctuating pressure distributions on the cylinder side obtained for all the considered values of r/D are reported in Figs. 4a,b. Note that the distributions for the sharp-edge case are significantly different, while those obtained for the different values of r/D, which are changed of two orders of magnitude, are quite similar each other. This is consistent with the results of [3] for the 5:1 case. Physical discussion on these effects, in terms of the growth of the TKE along the shear layers and of the location of the Kelvin Helmholtz instability, will be given in the final presentation.

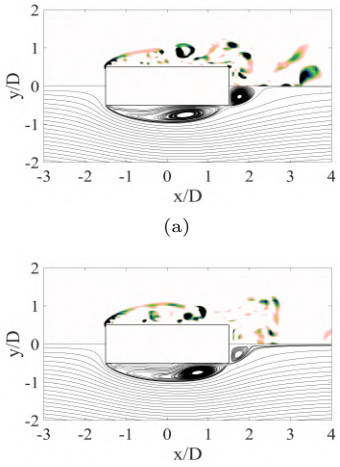

(a)

(b)

Figure 3: Mean flow streamlines (top) and instantaneous vortex-indicator λ_2 (bottom) for the 3:1 cylinder: (a) $r/D = 0$ and (b) and $r/D = 0.037$.

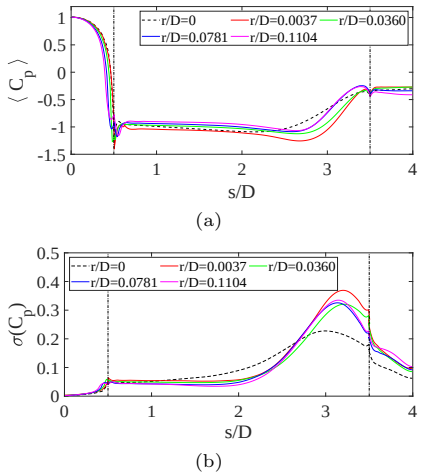

(a)

(b)

Figure 4: Mean pressure coefficient distribution (a) and standard deviation of the pressure coefficient (b) for the 3:1 cylinder.

REFERENCES

[1]Bruno, L., Salvetti, M.V. and Ricciardelli, F. : Benchmark on the aerodynamics of a rectangular 5:1 cylinder: and overview after the first four years of activity, *J. Wind Eng. Ind. Aerod.*, **126**, 87–106 (2014).

[2]Mariotti, A., Siconolfi, L., Salvetti, M.V. Stochastic sensitivity analysis of large-eddy simulation predictions of the flow around a 5:1 rectangular cylinder *Eur. J. Mech., B/Fluids* (2017) **62**:149-165.

[3]Rocchio, B., Mariotti, A., Salvetti, M.V. Flow around a 5:1 rectangular cylinder: Effects of upstream-edge rounding. *J. Wind Eng. Ind. Aerod.* (2020) **204**:104237.

[4]Chiarini, A., Quadrio, M. The importance of corner sharpness in the BARC test case: A numerical study *Wind and Structures, An International Journal* (2022) **34**(1):43-58.

WORKSHOP
Direct and Large-Eddy Simulation 13
October 26th-29th 2022, Udine, Italy

DIRECT NUMERICAL SIMULATIONS OF THE FLOW AROUND A 5:1 RECTANGULAR BODY WITH SHARP CORNERS

R. Corsini, A. Cimarelli and E. Stalio
Dipartimento di Ingegneria "Enzo Ferrari"
Universit degli studi di Modena e Reggio Emilia
enrico.stalio@unimore.it

INTRODUCTION

The turbulent flow about blunt, rectangular bodies is often encountered in civil and wind engineering applications as well as in land transport aerodynamics. Relevant examples include deck slabs of long-span bridges and high-rise buildings of rectangular section and the problem of the aerodynamics of vehicles of simple shape like trucks. The flow about an elongated rectangular cylinder with sharp corners involves several critical aerodynamics features like fixed-position separation in laminar conditions, reattachment and vortex shedding in the wake. In the applications, this gives place to vortex-induced vibration effects, promotes convective heat transfer between the atmospheric air and simple shaped, high-rise buildings and affects pollutant dispersion in the urban environment.

A considerable research effort has been expended since the past 20 years in the investigation of the aerodynamics of a two-dimensional rectangular cylinder with aspect ratio 5:1, especially by research groups based in Europe [1, 2, 3, 4, 5] and this in turn has made this aerodynamics case a canonical case, of acronym BARC, which stands for "Benchmark on the Aerodynamics of a two-dimensional Rectangular Cylinder".

Despite the context of abundance of research and publications, both numerical predictions and experimental data are characterized by a strong dependency upon the details of the setup and the quest for the "correct solution" at different Reynolds numbers is still underway. This is true also for Direct Numerical Simulations [6], where the difficulty in the numerical representation of the physical phenomenon does not include the modeling of turbulence.

In this work we present results from three Direct Numerical Simulation around the BARC body. The Reynolds numbers of the simulations are 3000, 8000 and 14000 respectively. Simulations are carried out using NEK5000 [7], which combines the geometric flexibility of finite element method with the high-order typical of spectral methods. The discussion includes a description of the flow configuration, macroscopic quantities, turbulence features and the time-scales of the flow. The Reynolds number effect on the above characteristics is investigated.

NUMERICAL METHODOLOGY

The numerical code used for this study is NEK5000 , which implements the spectral element method. In each hexahedral element, velocity and passive scalar interpolants are polynomials of order N, pressure is treated with order $N-2$. In the simulations we use $N = 7$.

Re	3000	8000	14000
$\Delta x^+_{\max}, \overline{\Delta x^+}$	$4.3, 1.7$	$3.2, 1.7$	$4.1, 2.3$
$\Delta y^+_{w\,\max}, \overline{\Delta y^+_w}$	$0.47, 0.23$	$0.60, 0.36$	$0.66, 0.41$
$\Delta z^+_{\max}, \overline{\Delta z^+}$	$3.9, 1.9$	$3.4, 2.0$	$5.1, 3.1$
$(\Delta x/\eta)_{\max}$	3.9	3.5	4.2
$(\Delta y/\eta)_{\max}$	3.3	3.8	4.6
$(\Delta z/\eta)_{\max}$	3.4	3.7	6.3

Table 1: Details of the spatial discretization employedat the three Reynolds numbers considered. The minimum spacings are located at the leading-edge corner. The overbar indicates a streamwise average over the rectangle length.

Time integration is performed treating implicitly the viscous terms by a third-order backward differentiation scheme while for the advective term, third-order extrapolation scheme is used. Dirichlet boundary conditions are set for the uniform velocity field at the inlet. The open boundary condition is imposed at outflow and along the crossflow directions. The rectangular cylinder of aspect ratio 5:1 and height D is represented in a computational domain of extension $L_x \times L_y \times L_z = 80Dx31Dx5D$, where x, y and z directions are the streamwise, cross-flow and spanwise directions.

The grid is designed in order to fully resolve turbulence, .

RESULTS

The full DNS datasets at three different Reynolds numbers provide a wealth of quantitative detail on the case.

The flow configuration consists in the laminar flow separation at the upstream corner, a transition process occurring in the separated shear-layer and the reattachment of the turbulent flow. Two boundary layers are formed starting from the reattachment position: one which leads to the final separation at the downstream corner and the shedding of vortices in the wake, and a second boundary layer developing upstream which finally generates a smaller, counter-rotating spanwise vortex of the mean flow. The flow configuration described above is well represented by the isocontours of the time-averaged streamfunction in figures 1, 2 and 3 for the three Reynolds numbers considered: Re = 3000, Re = 8000 and Re = 14000. In the Reynolds number range investigated, the reattachment position progressively moves downstream while the secondary vortex migrates upstream because of the larger energy content of the counter-flow boundary layer and its increased capability

of overcoming an adverse pressure gradient.

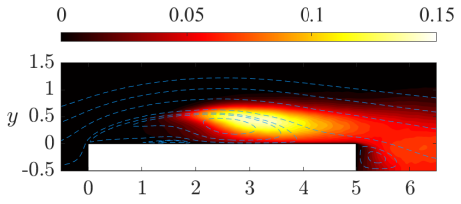

Figure 1: Isocountours of the time-averaged streamfunction at Re = 3000 with color map of the turbulent kinetic energy distribution.

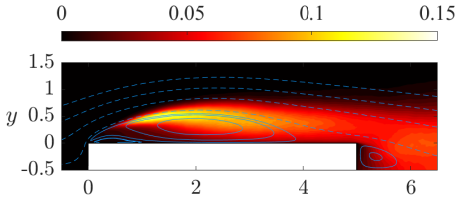

Figure 2: Isocountours of the time-averaged streamfunction at Re = 8000 with color map of the turbulent kinetic energy distribution.

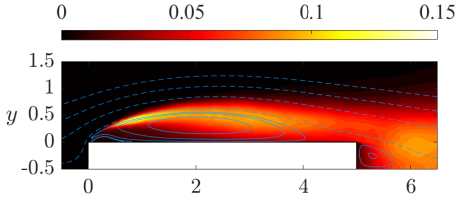

Figure 3: Isocountours of the time-averaged streamfunction at Re = 14000 with color map of the turbulent kinetic energy distribution.

The same figures 1, 2 and 3 report also the distribution of the time-averaged turbulent kinetic energy $\langle k \rangle$. The regions of peak $\langle k \rangle$ are due to the shear layer instability. For increasing Reynolds numbers, when the flow is more prone to transition, the regions of peak turbulent kinetic energy are located more upstream. The same tendency is also observed on the same geometry by Moore et al. [5], for higher Reynolds numbers. Accordingly, also transition to turbulence is shifted upstream for increasing Reynolds numbers.

Spectra of the lift coefficient and the cross-flow velocity fluctuations are investigated in order to extract the main physical time-scales of the flow and their dependency upon the Reynolds number within the investigated range. Two are the main time-scales obtained. One is related to the comparatively slow vortex shedding in the wake, and the other is associated with the faster Kelvin-Helmholtz instability at the interface between separated flow and outer flow. The frequency of vortex shedding is observed to decrease with the Reynolds number within the range of flow regimes investigated. Instead the higher frequency measured displays an increase with the Reynolds number, close to the $St \sim Re^{0.5}$ reported in the literature [5]. This smaller time scale is also a function of the position of the probe in the shear layer where it is calculated.

CONCLUSIONS

This numerical study of the BARC case does not make use of turbulence models and is characterized by a high-resolution representation both in space and time. The simulations carried out span the low to moderate Reynolds number range (Re = 3000, 8000, 14000), where the Strouhal number of the vortex shedding is not yet constant. In this work we discuss the macroscopic characteristics of the flow and the effect of the Reynolds number within the investigated range. Besides clarifying the macroscopic features of the flow and the Reynolds number effect on these global characteristics, results presented have the potential to be employed as reference data for the comparison of different numerical methods and models of turbulence applied to this benchmark case.

*

References

[1] L. Bruno, D. Fransos, N. Coste, and A. Bosco, "3d flow around a rectangular cylinder: A computational study," *Journal of Wind Engineering and Industrial Aerodynamics*, vol. 98, no. 6-7, pp. 263–276, 2010.

[2] F. Brusiani, S. De Miranda, L. Patruno, F. Ubertini, and P. Vaona, "On the evaluation of bridge deck flutter derivatives using rans turbulence models," *Journal of Wind Engineering and Industrial Aerodynamics*, vol. 119, pp. 39–47, 2013.

[3] D. Nguyen, D. Hargreaves, and J. Owen, "Vortex-induced vibration of a 5:1 rectangular cylinder: A comparison of wind tunnel sectional model tests and computational simulations," *Journal of Wind Engineering and Industrial Aerodynamics*, vol. 175, pp. 1–16, 2018.

[4] A. Cimarelli, A. Leonforte, and D. Angeli, "On the structure of the self-sustaining cycle in separating and reattaching flows," *J. Fluid Mech.*, vol. 857, pp. 907–936, 2018.

[5] D. Moore, C. Letchford, and M. Amitay, "Energetic scales in a bluff body shear layer," *J. Fluid Mech.*, vol. 875, pp. 543–575, 2019.

[6] R. Corsini, D. Angeli, E. Stalio, S. Chibbaro, and A. Cimarelli, "Flow solutions around rectangular cylinders: The question of spatial discretization," *Wind and Structures, An International Journal*, 2022.

[7] P. F. Fischer, J. W. Lottes, and S. G. Kerkemeier, "nek5000 web page." `http://nek5000.mcs.anl.gov`, 2008.

WORKSHOP
Direct and Large-Eddy Simulation 13
October 26th-29th 2022, Udine, Italy

LARGE-EDDY SIMULATION OF THE ACCELERATING FLOW AROUND SQUARE AND RECTANGULAR CYLINDERS

A. Mariotti[1], S. Brusco[2], G. Lunghi[1], G. Piccardo[2] and M.V. Salvetti[1]
[1] Department of Civil and Industrial Engineering
University of Pisa, Italy
[2] Department of Civil, Chemical and Environmental Engineering, Polytechnic School
University of Genova, Italy
alessandro.mariotti@unipi.it

INTRODUCTION

The present work is aimed at investigating the high-Reynolds unsteady flow around a square and a rectangular cylinder of aspect ratio 5:1, defined as the ratio between the streamwise length over the crossflow one. The two cases are paradigmatic flows of interest in the Wind Engineering field, such as, e.g., tall buildings and bridge sections. The chord-to-depth ratio influences the dynamics of the flow around the cylinder. For both geometries, the flow is characterized by shear-layers separation at the upstream edges. The shear layers roll up forming vortical structures (Kelvin-Helmholtz instability), which are convected downstream and eventually interact by pairing with other vortical structures forming from the separated shear layers. For the 5:1 rectangular cylinder, the flow reattaches in mean on the lateral side of the cylinder, and, thus, the mean flow is characterized by a closed separated-flow region. Further downstream, shear layers separate again from the trailing edge and in the near wake the flow is characterized by the Von-Karman vortex shedding. The mean flow reattachment does not occur for the square cylinder, where the vortex shedding occurs directly from the upstream separated shear layers. The mean flow streamlines and a snapshot of the instantaneous vortex-indicator λ_2 from LES simulations carried out for constant velocity at $Re = 40000$ (based on the cylinder depth, D, and on the freestream velocity, u_∞) for the square and rectangular [1] cylinders are shown in Figs. 1(a) and 1(b), respectively.

Square and rectangular cylinders with constant-velocity flows have been widely investigated in the literature and, in addition, the flow around the 5:1 rectangular cylinder is the object of the international benchmark BARC (see, e.g., [2]). The main experimental and numerical results are representative of the synoptic wind (constant wind), which is the most common type of event affecting civil buildings. On the other hand, in the last twenty years, the Wind Engineering community showed great interest in thunderstorm outflows (not constant wind). The consequences of thunderstorm outflows on buildings can be catastrophic, possibly causing serious damages and economical losses. Thunderstorm winds present high accelerations, making the steady-wind hypothesis questionable (see, e.g., [3]). In particular, accelerations play a crucial role in the dynamics of the flow around the body and in the consequent mean forces and fluctuations. Shear-layer dynamics and vortex shedding are sensitive to the variation of the inflow velocity, with changes in the dominating frequencies. The still open question is to identify which is the limit value of the incoming-flow acceleration for which the loads and frequencies evaluated under steady-wind conditions are still valid. To this aim, we numerically evaluate the effect of flow accelerations, typical of the thunderstorm outflows, on the square and on the 5:1 rectangular cylinders. Large-Eddy Simulations have been carried out starting from constant inflow conditions and then accelerating the flow. The Large-Eddy Simulations have been carried out by using the open-source spectral-element code Nek5000. The simulation set-up already validated in [1] has been used. The results of these simulations are validated by numerically performing the same inflow velocity and acceleration of the experiments carried out in the multiple-fan wind tunnel of the Tamkang University, Taipei, by [4],[5]. Despite the simple geometries, these simulations may be considered a first step towards the characterization of the dynamic loads on civil buildings due to the thunderstorm outflows and in the understanding of the limits of the steady-wind predictions for structure design.

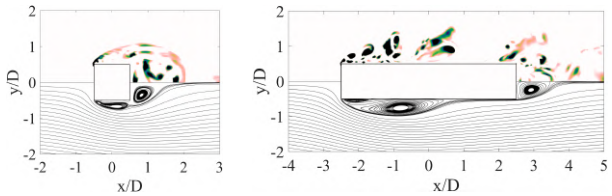

Figure 1: Instantaneous vortex-indicator λ_2 (top) and mean flow streamlines (bottom) at $Re = 40000$ for (a) the 1:1 and (b) the 5:1 rectangular cylinder.

PROBLEM DEFINITION, NUMERICAL METHODOLOGY AND RESULTS

We consider the incompressible flows around a square and a 5:1 rectangular cylinders at zero angles of attack. Large Eddy Simulations are performed by using the open-source code Nek5000, based on a high-order spectral element method. Each spectral element is rectangular or a suitable coordinate

mapping of a rectangle. The basis functions inside the elements are Legendre polynomials of order N for velocity and $N-2$ for pressure in each direction; $N=6$ has been used in this work, as in [1]. A third-order backward finite-difference scheme based on the high-order splitting method is used for time advancing.

The computational domains are sketched in Fig. 2. The cylinder center is located at $x/D = y/D = 0$, being D the width of the square or rectangular cylinder, and the computational domain spans the following dimensions $-75 \leq x/D \leq 125$, $-75 \leq y/D \leq 75$ and $0 \leq z/D \leq 5$. A uniform non-steady velocity profile with no turbulence is imposed at the inlet, no-slip is imposed at the body surface and traction-free boundary conditions are used for the outflow and for the upper and lower boundaries of the domain. Finally, periodicity is imposed in the spanwise direction. The spectral element size and distribution are the same used in [1]. In particular, the element size in the streamwise and lateral directions is $\Delta x/D = \Delta y/D = 0.125$ near the cylinder, while in the spanwise direction the element size is uniform $\Delta z/D = 0.558$ as done in [1]. Because the grid resolution is not fine enough to resolve all turbulent scales at the considered Reynolds number, a low-pass filter is applied to the velocity field in the modal space as in [1]. Since the filter introduces dissipation of the highest resolved modes only, this can be considered as a subgrid-scale dissipation.

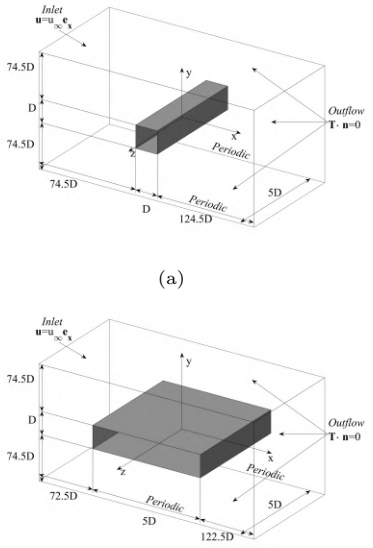

Figure 2: Sketch of the computational domain (not in scale) for (a) the 1:1 and (b) the 5:1 rectangular cylinder.

A first LES has been carried out in the same non-steady flow conditions of the experiments on the square cylinder carried out in the multiple-fan wind tunnel of the Tamkang University, Taipei, by [4],[5], for the validation of the simulation set-up. The time behavior on the Reynolds number, Re, and of the non-dimensional acceleration, aD/u_∞^2 are reported in Fig. 3. In particular, the inflow Reynolds number varies from $Re = 17200$ to $Re = 65300$ and the maximum non-dimensional acceleration is equal to 0.0076. Then, we considered different values of constant accelerations from $Re = 40000$ to $Re = 60000$ for the square and rectangular geometries to single out the effect of the acceleration values of the flow dynamics (as shown, e.g., in Fig. 4). Non-dimensional acceleration values of the same order or above the one in the experiments are considered to identify which is the limit value of the incoming-flow acceleration for which the loads and frequencies evaluated under steady-wind conditions are still valid.

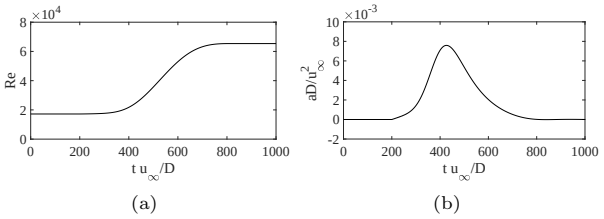

Figure 3: (a) Inflow Reynolds number, Re, and (b) non-dimensional acceleration, aD/u_∞^2, of the experiments carried out in the wind tunnel of the Tamkang University ([4],[5]).

In the final presentation, the numerical values will be compared with the experimental ones ([4],[5]), although some differences in the two set-ups are present, such as the different turbulence levels of the incoming flows in simulations and experiments, and taking into account all the limits of a non-standard experiment such as the one analyzed. Moreover, we will discuss the range of accelerations for which no variation of the flow topology is found compared with the steady-inflow conditions and the effect of accelerations above the critical values on the flow dynamics around the square and the 5:1 rectangular cylinders. Mean and the fluctuating force coefficients and wake frequencies will be also discussed to highlight the cases when steady-velocity predictions are still reliable.

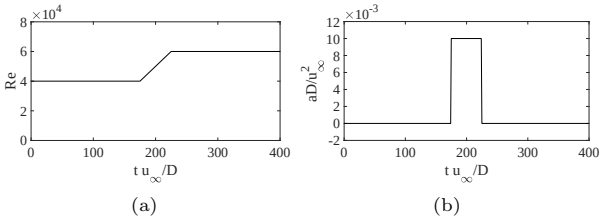

Figure 4: (a) Inflow Reynolds number, Re, and (b) non-dimensional acceleration, aD/u_∞^2, for the LES simulations with constant acceleration.

REFERENCES

[1]Mariotti, A., Siconolfi, L., Salvetti, M.V. : Stochastic sensitivity analysis of large-eddy simulation predictions of the flow around a 5:1 rectangular cylinder, *European Journal of Mechanics, B/Fluids* (2017) **62**, 149–165.

[2]Bruno, L., Salvetti, M.V. and Ricciardelli, F. : Benchmark on the aerodynamics of a rectangular 5:1 cylinder: and overview after the first four years of activity, *J. Wind Eng. Ind. Aerod.*, (2014) **126**, 87–106.

[3]Brusco, S. and Solari, G. : Transient aeroelasticity of structures subjected to thunderstorm outflows, *Eng Struct* (2021) **245**, 112801.

[4]Brusco, S., Buresti, G., Lo, Y., Piccardo, G. : Vortex-shedding from a square cylinder in accelerating flows, *under review.*

[5]Brusco, S. : Transient phenomena induced by thunderstorm outflows on slender structures, *PhD Thesis, University of Genoa* (2021).

WORKSHOP
Direct and Large-Eddy Simulation 13
October 26th -29th 2022, Udine, Italy

DATA-DRIVEN LARGE EDDY SIMULATION OF THE FLOW AROUND A 5:1 RECTANGULAR CYLINDER

G. MOLDOVAN[1], A. MARIOTTI[2], G. LEHNASCH[1], L. CORDIER[1], M.-V. SALVETTI[2] and M. MELDI[3]
[1]Institut Pprime, CNRS - ISAE-ENSMA - Université de Poitiers, 11 Bd. Marie et Pierre Curie, 86073 Poitiers, France. gabriel-ionut.moldovan@ensma.fr, guillaume.lehnasch@ensma.fr and Laurent.Cordier@univ-poitiers.fr
[2]Dipartimento di Ingegneria Civile e Industriale, Università di Pisa, Via G. Caruso 8, 56122, Pisa, Italy. alessandro.mariotti@unipi.it and maria.vittoria.salvetti@unipi.it
[3]Univ. Lille, CNRS, ONERA, Arts et Métiers ParisTech, Centrale Lille, UMR 9014 - LMFL- Laboratoire de Mécanique des fluides de Lille - Kampé de Feriet, F-59000 Lille, France. marcello.meldi@ensam.eu

INTRODUCTION

The analysis and control of complex high-Reynolds-number flows of industrial and practical interest is one of the most distinctive open challenges that the scientific community has to face for fluid mechanics applications in the coming decades. Modelling bias and uncertainty may strongly affect the predictive capabilities of both numerical simulations and experimental measurements. Under this perspective, data-driven tools from Data Assimilation, and, in particular, sequential tools such as the ensemble Kalman filter (EnKF), have been recently used to obtain a precise estimation of the physical flow state accounting for bias or uncertainty coming from real conditions. These strategies usually rely on a *model*, which provides a continuous or quasi-continuous description of the physical phenomenon at play, and on sparse, high-fidelity *observation*.

A newly developed sequential Data Assimilation algorithm, combining multi-grid aspects and the ensemble Kalman Filter, has recently been presented in Moldovan et al. [1]. The so-called MGEnKF algorithm (Multi-Grid Ensemble Kalman Filter) exploits physical states obtained on multiple grids of different resolution to perform the state estimation and parametric optimization procedures which can be performed using the EnKF. More precisely, an ensemble of low-fidelity simulations of the flow are run on a coarse grid level together with a single higher-resolution simulation on the finest mesh level. The state estimation obtained at the coarse level and the associated ensemble statistics are used to filter the finest mesh solution and optimise a set of parameters describing the model (boundary conditions, model parameters…). This procedure allows to i) reduce the computational costs of the EnKF and ii) ensure the conservativity and the smoothness of the final solution.

TEST CASE

The strategy is tested and validated against the international benchmark referred to as BARC (Benchmark of the Aerodynamics of a Rectangular 5:1 Cylinder) [2]. This configuration is a simplified model of problems of interest in civil engineering. Despite the simple geometry, the flow shows complex features characterized by shear-layer separation from the upstream edges, unsteady reattachment on the cylinder side and vortex shedding in the wake. A representation of the test case of interest is shown in Figure 1.

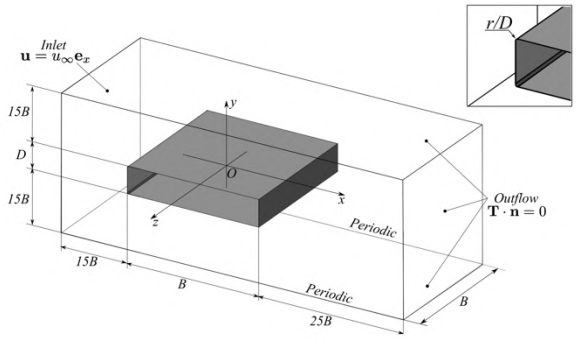

Figure 1: BARC model and domain geometry for the computational study.

A Data Assimilation experiment is performed where the MGEnKF algorithm is used to improve the predictive capabilities of an intermediate-fidelity LES (model) on a rather coarse grid, by integrating reference data (*observation*) from a high-fidelity LES, run on highly refined grid. The obtained state estimation is significantly improved when compared with the coarse LES model prediction. This increased efficiency is observed for numerous physical quantities characterizing the flow, such as the mean pressure coefficient on the surface of the immersed body (see Figure 2).

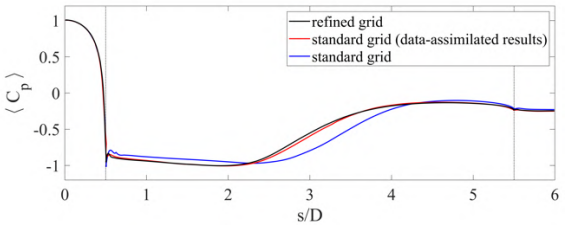

Figure 2: Mean pressure coefficient on the surface of the BARC test case. Results obtained via MGEnKF are compared with classical LES calculation and the high-fidelity reference simulation.

The state estimation was further used to optimize the parametric description of the model. More precisely, the value of the parameter calibrating the introduced subgrid scale dissipation was determined using a dual filtering approach, in which state estimation and parametric inference are sequentially performed. The optimized value exhibits a large difference when compared with the initially prescribed value (prior), as shown in Figure 3. A posteriori test showed that LES ran with the optimized parameter performs significantly better than the baseline LES simulations.

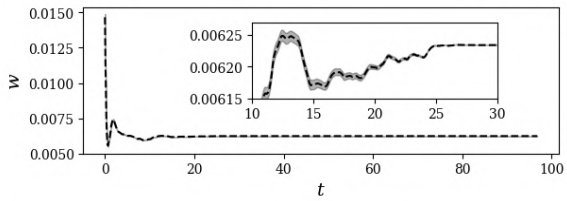

Figure 3: Convergence of the MGEnKF optimization of the explicit LES coefficient filter applied to the resolved equations. The coefficient is initialized with the baseline value.

REFERENCES

[1] Moldovan, G., Lehnasch, G., Cordier, L. and Meldi, M. : A multigrid/ensemble strategy for assimilation of unsteady flows, J. Comp. Phys. 443, 110481 (2021).

[2] Bruno, L., Salvetti, M.V. and Ricciardelli, F. : Benchmark on the aerodynamics of a rectangular 5:1 cylinder and overview after the first four years of activity, J. Wind Eng. Ind. Aerod., 126, 87-106 (2014).

WORKSHOP
Direct and Large-Eddy Simulation 13
October 26th -29th 2022, Udine, Italy

LARGE EDDY SIMULATION OF FLOW AROUND THE 25° AHMED CAR BODY AT DIFFERENT REYNOLDS NUMBERS

F. Menter[1*], D. Kolmogorov[2], A. Matushenko[2], A. Hüppe[1] and A. Garbaruk[2]
[1] ANSYS Germany GmbH
[2] St. Petersburg Polytechnic University, 29, Polytechnicheskaya Str., 195251, St.-Petersburg, Russia
[1*] florian.menter@ansys.com

INTRODUCTION

The Ahmed car body is a widely used test case for evaluation of CFD codes for automotive simulations. Especially the 25° slant angle configuration [1] at a Reynolds number of $Re_H = 0.768 \cdot 10^6$ (H – is the height of the body) has proven elusive both for RANS and LES methods. A publication of French-German authors [2] using a number of different LES codes and meshes has shown a disturbing variation of results. Even the best results in this study are far from the experimental data. No mesh independence has ever been demonstrated for this case. In contrast, the simulations presented at a reduced $Re_H = 0.2 \cdot 10^6$ shown a high level of consistency even on relatively coarse grids [3].

In this work a numerical study of the flow around the Ahmed body with slant angle of 25^o is carried out, using different LES approaches: Wall-Resolved LES (WRLES) and three cost-reduced approaches, such as Wall Modeled LES (WMLES), LES with Wall Functions (WFLES) and LES on Coarse Grids (CGLES). The simulations are carried out at low and high Reynolds numbers, $0.2 \cdot 10^6$ and $0.768 \cdot 10^6$, respectively. The prediction of high Re WRLES would require grids with much higher grid resolution (5-6 bill. cells for WRLES), therefore, this flow is predicted only using cost-reduced LES approaches (up to 0.6 bill cells). The final presentation will show a detailed comparison of different LES approaches for the two different Reynolds numbers.

NUMERICAL SETUP AND GRIDS

Hexahedral structured grids are used for all considered approaches, except for WFLES, which is carried out on series of Octree grids, see Tables 1 for grid specifications. ANSYS Fluent R21.1 using the WALE turbulence model for WRLES, CGLES and WFLES is applied. For the WMLES computations, an algebraic WMLES-SW with a mixing-length RANS model near the wall is used.

LES approach	Grid	$\max(\Delta_x^+)$	δ/Δ_x	Size, mil. cells
WRLES (low Re)	M1	35	100	560
	M2	50	80	180
CGLES (high re)	M1	140	80	560
CGLES (low Re)	M3	110	60	35
WFLES (low Re/high Re)	C1	35/140	20	100
	C2	70/280	10	35
	C3	140/560	5	7
WMLES (low Re/high Re)	C4	35/140	20	80
	C5	70/280	10	40
	C6	140/560	5	20

Table 1: Used grids and resolutions of the boundary layer in the middle part of the top side of the body.

COMPUTATIONAL RESULTS

The critical aspect of this test case is the flow over the slant, where the experiment shows separation and reattachment at about half of the slant.

First, the results at low Re are considered. In the most accurate and expensive LES approach, namely WRLES, the boundary layer (BL) on the top and side walls of the body starts from a laminar bubble separation, leading to transition. Velocity profiles across the BL obtained on the largest grid M1 agree with the logarithmic law. Mean friction and pressure distribution are grid converged with minor changes in bubble separation at the front. Velocity profiles above the slant are grid converged and in close agreement with high Re experimental data of Lienhart et. al [1], see Fig. 1 at bottom

The cost-reduced LES approaches at low Re show a fair accuracy, except for WFLES, which predicts a smaller size and strength of the separation zone, see Fig. 1. One should note that CGLES on the relatively coarse grid, M3, still shows close agreement with WRLES and experimental data.

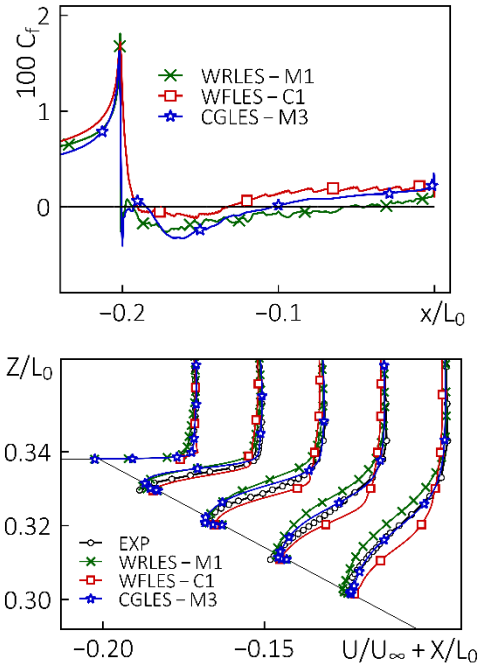

Figure 1: Friction distribution and velocity profiles for separation zone at middle XZ section at low Re number.

Second, we consider the results of cost-reduced LES approaches at high Re. The results are significantly deteriorated relative to the ones obtained at low Re. WFLES and WMLES predict flow acceleration prior to the upper slant corner and no flow separation above the slant, see Fig. 2. CGLES predicts no flow acceleration, however the predicted separation zone downstream is smaller compared to experimental data. The reason why the high Re results are worse can be twofold. Firstly, the grid resolution of the grids used for the high Re computations is insufficient. Secondly, at high Re, the flow might approach a bifurcation point. An indirect confirmation of the last statement is that CGLES at high Re fails to predict flow separation, while CGLES at low Re predicts the flow separation above the slant on a grid with similar Δ^+ resolution (see Table 1.).

CONCLUSIONS

All the tested approaches predict the overall flow configuration with fair accuracy. At low Re, high quality WRLES results were obtained, in close agreement with the high Re exp. data [1]. The results of cost reduced LES approaches at low Re show fairly good agreement with both WRLES and exp. data, compared to the high Re results, where flow separation above the slant is not predicted.

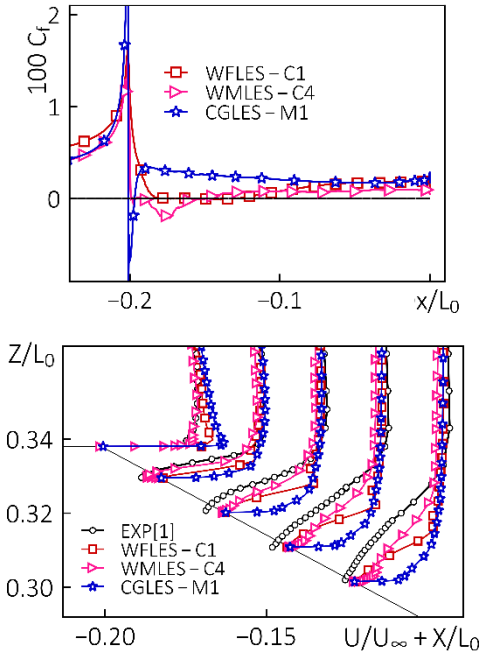

Figure 2: Friction distribution and velocity profiles for separation zone at middle XZ section at high Re number

Surprisingly, the results of CGLES at high Re number on grid with resolution similar to the one used at low Re are in strong disagreement with experimental data. This may be an indication that the flow configuration at the high Re reaches a bifurcation point which is extremely hard to predict with under-resolved LES approaches.

Computations were conducted with the use of SPbPU Computer Center "Polytechnichesky". Russian authors' research was funded by the Ministry of Science and Higher Education of the RF as part of World-class Research Center program (contract No. 075-15-2022-311 of Apr.20, 2022).

REFERENCES

[1] H. Lienhart, C. Stoots, and S. Becker, "Flow and Turbulence Structures in the Wake of a Simplified Car Model (Ahmed Modell)," in *New Results in Numerical and Experimental Fluid Mechanics III*, S. Wagner, U. Rist, H.-J. Heinemann, and R. Hilbig, Eds. Berlin, Heidelberg: Springer Berlin Heidelberg, 2002, pp. 323–330. doi: 10.1007/978-3-540-45466-3_39.

[2] E. Serre *et al.*, "On simulating the turbulent flow around the Ahmed body: A French–German collaborative evaluation of LES and DES," *Computers & Fluids*, vol. 78, pp. 10–23, Apr. 2013, doi: 10.1016/j.compfluid.2011.05.017.

[3] S. Krajnović and L. Davidson, "Flow Around a Simplified Car, Part 1: Large Eddy Simulation," *Journal of Fluids Engineering*, vol. 127, no. 5, pp. 907–918, Sep. 2005, doi: 10.1115/1.1989371.

Session: Hybrid LES/RANS

Wednesday, October 26, 2022

15:20 – 16:05

WORKSHOP
Direct and Large-Eddy Simulation 13
October 26th-29th 2022, Udine, Italy

AN ACTIVE HYBRID RANS/LES APPROACH FOR GREY AREA MITIGATION

M. Mehta[1], R. Manceau[1], Vladimir Duffal[2], B. de Laage de Meux[2]
[1] Universite de Pau et des Pays de l'Adour, E2S UPPA, CNRS, Inria, CAGIRE project-team, LMAP, Pau, France
[2] EDF R&D, MFEE Dept., 6 quai Watier, 78400 Chatou, France
mahitosh-ajaykumar.mehta@univ-pau.fr

INTRODUCTION

In continuous hybrid RANS/LES modelling, when the fluid flows from a RANS to a LES zone, the modelled stresses decrease drastically but the resolved stresses do not grow fast enough (*modelled-stress depletion*). This problem can be alleviated by decreasing to zero the subgrid viscosity in the initial region of a sheared detached layer, but this type of solution is not sufficiently general and will not work in flows without an inflection point [1]. This work aims at developing a more general, *active* approach, able to compensate the loss of turbulent energy in the modelled part by an injection of energy in the resolved part.

PROPOSAL FOR AN ACTIVE MODEL

In filtered approaches, it is easy to demonstrate [3] that when the filter size is varied (by refining the mesh), the equations display a term of energy transfer from the modelled part to the resolved part. But a simpler way to address this issue consists in noting that the resolved energy k_r and the modelled energy k_m are sensitive to the grid step Δ, but, in theory, not $k = k_r + k_m$. Thus, considering any variable ϕ as dependent on t, $\mathbf{x}$ and Δ, we have

$$\frac{\mathrm{d}\phi}{\mathrm{d}t} = \frac{\partial\phi}{\partial t} + \frac{\partial\phi}{\partial X_i}\frac{\mathrm{d}X_i}{\mathrm{d}t} + \frac{\partial\phi}{\partial\Delta}\frac{\mathrm{d}\Delta}{\mathrm{d}t} = \frac{\partial\phi}{\partial t} + \boldsymbol{\nabla}\phi\cdot\mathbf{U} + \frac{\partial\phi}{\partial\Delta}\frac{\mathrm{d}\Delta}{\mathrm{d}t}. \quad (1)$$

Since we want to have k independent of Δ, we must have

$$\frac{\partial k_r}{\partial\Delta}\frac{\mathrm{d}\Delta}{\mathrm{d}t} = -\frac{\partial k_m}{\partial\Delta}\frac{\mathrm{d}\Delta}{\mathrm{d}t} \quad (2)$$

The decrease of k_m due to mesh variations is thus compensated by an increase of k_r of the same amount. However, this mechanism does not exist in the models and must therefore be introduced.

In the context of zonal methods, [4] proposed the ALF approach to generate fluctuations in the resolved motion by introducing a volume force of the form

$$f_i = A_{ij}\widetilde{u}_j + B_i \quad (3)$$

in the momentum equation, where $\widetilde{u}_i$ represents the resolved velocity. In this approach, there is an overlap region between the RANS domain and the LES domain, and the tensor A_{ij} is determined by

$$A_{ik} < u_k u_j > + A_{jk} < u_k u_i > = C_{ij} \quad (4)$$

where u_i stands for the fluctuating part of the resolved velocity. The limitation of this approach is that the rhs $C_{ij} = (< u_i u_j >^{\mathrm{RANS}} - < u_i u_j >)/(C_r k/\varepsilon)$ depends on the target tensor $< u_i u_j >^{\mathrm{RANS}}$ given by the RANS model, which is only available because there is an overlap region between RANS and LES. In the framework of continuous hybrid RANS/LES, this target is not available, but Eq. (2) indicates at which rate the energy must be injected into the resolved motion, such that

$$C_{ij} = -C < u_i u_j > \frac{1}{\Delta}\frac{\mathrm{d}\Delta}{\mathrm{d}t} \quad ; \quad B_i = -A_{ij} < \widetilde{u}_j > \quad (5)$$

RESULTS AND DISCUSSION

The new active approach is applied to the periodic hill case with the HTLES model [5] based on the underlying k-ω-SST RANS model, using Code_Saturne. A periodic RANS solution is applied at the inlet and the transition from RANS to LES is performed between $x/h = 0$ and $x/h = 2$. Fig. 1 shows that, when no forcing term is introduced, the resolved structures take a long time to develop, and Fig. 2 that the turbulent energy remains too low until the fourth hill. Fig. 3 shows that the solution is then severely deteriorated until $x/h = 22$.

The introduction of the ALF forcing in the region $x/h \in [0; 2]$ solves this problem very efficiently, with a rapid development of the resolved content, which leads to a very good prediction of C_f. It can be seen that the active method also generates resolved structures rapidly, although it can be seen in Fig. 2 that it is not quite as efficient as the ALF method to reach the fully developed turbulent energy. Here, the forcing term is also only active up to $x/h = 2$. From $x/h = 4$, the solution of the active method is almost identical to that given by the ALF and very close to the periodic solution. Fig. 3 shows that the application of the forcing term makes it possible to avoid a completely false solution after the beginning of the transition from RANS to LES and to tend very quickly towards the periodic solution.

CONCLUSION

In this work, an active hybrid RANS/LES method is proposed, i.e., a method that injects energy into the resolved motion when the solution transitions from RANS to LES. This method is applicable to any hybrid model and only requires the introduction of a volume force into the resolved momentum equation. This forcing allows for the rapid development of realistic resolved structures, corrects much of the modelled-stress depletion problem and thus makes it possible to rapidly reach a fully developed LES solution.

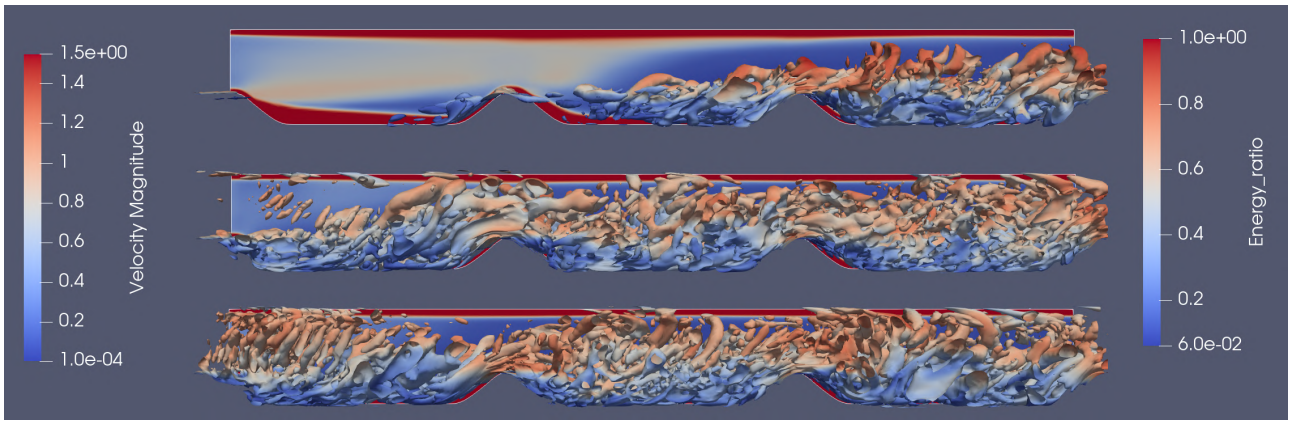

Figure 1: Isocontours $Q = 0.2U_b^2/h^2$ colored with the velocity magnitude and, in the background, modelled-to-total turbulent energy ratio r, indicating the regions solved in RANS ($r = 1$) and in LES ($r < 1$). Top: HTLES without forcing term; middle: HTLES with the ALF volume forcing; bottom: Active HTLES.

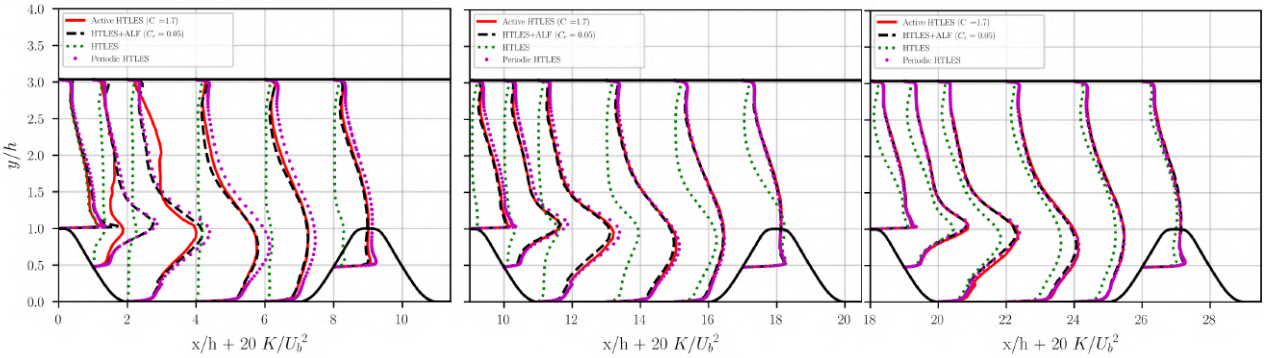

(a) Between hill #1 and hill #2 (b) Between hill #2 and hill #3 (c) Between hill #3 and hill #4

Figure 2: Profiles of turbulent energy (resolved+modelled).

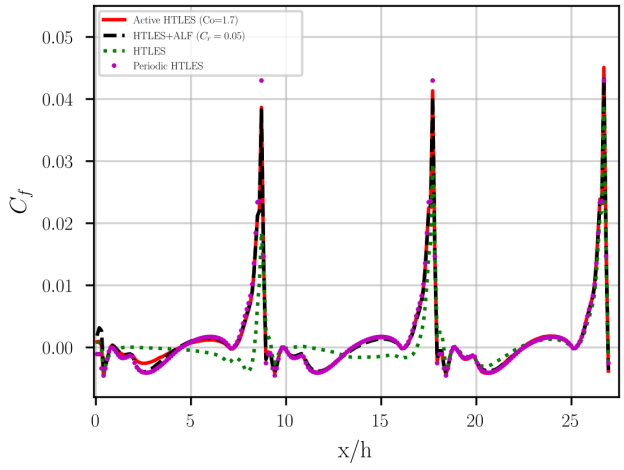

Figure 3: Friction coefficient.

REFERENCES

[1]C. Mockett, W. Haase, and D. Schwamborn, eds., *Go4Hybrid: Grey Area Mitigation for Hybrid RANS-LES Methods*, vol. 134 of *Notes on Numerical Fluid Mechanics and Multidisciplinary Design*. Springer-Verlag Berlin Heidelberg, 2017.

[2]R. Manceau, "Progress in Hybrid Temporal LES (invited keynote paper)," in *Papers contributed to the 6th Symp. Hybrid RANS-LES Methods, 26–28 September 2016, Strasbourg, France* (Y. Hoarau, S.-H. Peng, D. Schwamborn, and A. Revell, eds.), vol. 137 of *Notes on Numerical Fluid Mechanics and Multidisciplinary Design*, pp. 9–25, Springer, 2018.

[3]A. Fadai-Ghotbi, C. Friess, R. Manceau, T. Gatski, and J. Borée, "Temporal filtering: a consistent formalism for seamless hybrid RANS-LES modeling in inhomogeneous turbulence," *Int. J. Heat Fluid Fl.*, vol. 31, no. 3, pp. 378–389, 2010.

[4]B. de Laage de Meux, B. Audebert, R. Manceau, and R. Perrin, "Anisotropic Linear Forcing for synthetic turbulence generation in LES and hybrid RANS/LES modeling," *Phys. Fluids*, vol. 27, no. 035115, 2015.

[5]V. Duffal, B. de Laage de Meux, and R. Manceau, "Development and Validation of a new formulation of Hybrid Temporal Large Eddy Simulation," *Flow Turbul. Combust.*, 2022.

WORKSHOP
Direct and Large-Eddy Simulation 13
October 26th-29th 2022, Udine, Italy

SEAMLESS INTERFACE METHOD FOR GREY- AREA MITIGATION IN SCALE-RESOLVING HYBRID RANS-LES

M. Carlsson[1], S. Wallin[2], L. Davidson[1], S. Peng[3,1], S. Arvidson[4,1]
[1] Department of Mechanics and Maritime Sciences
Chalmers University of Technology, Gothenburg, Sweden
[2] Department of Engineering Mechanics
KTH Royal Institute of Technology, Stockholm, Sweden
[3] Division of Defense Technology, FOI
Swedish Defence Research Agency, Stockholm, Sweden
[4] Propulsion Department
Saab Aeronautics, Linköping, Sweden
magnus.carlsson@chalmers.se

INTRODUCTION

A new Grey-Area Mitigation (GAM) method for hybrid RANS-LES is presented. In regions of variable resolution, the transfer of energy between modelled (RANS) and resolved (LES) turbulence is quantified by a commutation residue term, originally formulated by Girimaji and Wallin [1]. They proposed a model for this term related to PANS and indicated extensions to length scale based models such as DES. In this work, we seek to exploit and extend this formulation for DES-based models aiming for a more rapid transition between unresolved and resolved turbulent scales in the vicinity of a RANS-LES interface. A zonal hybrid RANS-LES approach using a similar commutation residue term was investigated by Arvidson et al. [2], where they defined an explicit interface where the commutation residue term is active between the RANS and LES regions.

MATHEMATICAL FORMULATION

The energy balance in the spectral space is illustrated in Fig. 1 with $\kappa_c \propto 1/L_{ref}$ as the spectral cut-off wave number dividing the turbulence energy into the resolved and unresolved parts. For constant resolution, where κ_c is constant in space/time, the energy cascade σ is responsible for the energy exchange between the resolved and unresolved scales. With variable L_{ref}, κ_c can vary in time or space and correspondingly the position of the interface between K_r and K_u will change. This leads to an additional mechanism of energy exchange between K_r and K_u. Following Girimaji and Wallin [1], this energy exchange can be described by a commutation residue term, P_{Tr}, in terms of the variation of the hybrid length scale L_{ref}:

$$P_{Tr} = \frac{2}{3}\frac{K_u}{L_{ref}}\frac{DL_{ref}}{Dt}. \tag{1}$$

In this paper, we compute the hybrid length scale according to the hybrid $k-\omega$ SST DDES model [3, 4]

$$L_{ref} = L_{RANS} - f_d \max(0, L_{RANS} - L_{LES}), \tag{2}$$

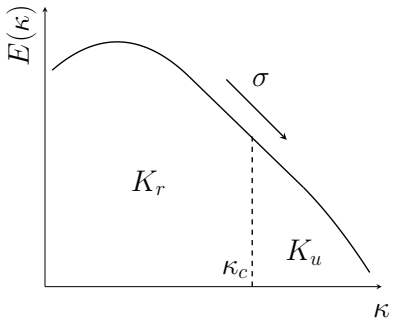

Figure 1: Illustration of energy spectrum with cut-off wave number.

where $L_{RANS} = \beta^* K_u \omega$ and $L_{LES} = C_{DES}\Delta$ are the RANS and LES length scales, respectively. In addition to $\Delta = \Delta_{max}$ used in the original formulation, we use $\tilde{\Delta}_\omega$ [5], which adapts the subgrid-scale based on the local vorticity direction of the flow. The commutation residue term P_{Tr} in Eq. (1) acts as a source/sink term in the equations for K_u and ω. In the case of decreasing L_{ref}, energy is transferred from the unresolved (RANS) to the resolved (LES) scales and $P_{Tr} < 0$. Energy conservation dictates that the energy transfer rate, P_{Tr}, removed from the unresolved scales must be added to the resolved scales. The energy transfer to/from the resolved scales is modelled as a diffusion term in the momentum equation [1]

$$\nu_{Tr} = \frac{P_{Tr}}{2S^2}, \tag{3}$$

where $S^2 = S_{ij}S_{ij}$. It must be emphasized that ν_{Tr} and ν_t represent different physics and should not be mixed up. For numerical solution they can be added through:

$$\nu^* = \nu_t + \nu_{Tr}. \tag{4}$$

When resolution improves in space/time, energy is transferred from unresolved to resolved turbulence. This is brought by a negative ν_{Tr}. We limit $\nu_{Tr} \geq -\nu_t$ to ensure positive total turbulent diffusion. Note that Eqs. (1) and (3) are computed and added everywhere in the computational domain.

RESULTS

The free shear layer flow, investigated experimentally by Delville [6], has been simulated using hybrid RANS-LES. The computational domain includes an infinitely thin flat plate, with boundary layers on each side, and the region downstream of the flat plate trailing edge where the two boundary layers mix. The experimental boundary layer properties at the trailing edge are presented in Table 1. The focus region of the

Measure	Notation	High vel. BL	Low vel. BL
Velocity	U_∞	41.54 m/s	22.40 m/s
Thickness	δ	9.6 mm	6.3 mm
Displ. thick.	δ_1	1.4 mm	1.0 mm
Mom. thick.	θ	1.0 mm	0.73 mm
Shape factor	H	1.35	1.37
Re based on θ	Re_θ	2900	1200
Turbulence level	u'/U_∞	~ 0.3 %	~ 0.3 %

Table 1: Summary of computational case considered. Data from experiment [6].

grid, i.e. the region from the flat plate trailing edge at $x = 0$ to $x = 1$ m, consists of $(n_x, n_y, n_z) = (640, 96, 96)$ cells. The total number of hexahedral grid cells are 13.7 million. The boundary layers are treated in RANS mode and the DDES automatically switches to LES after the trainling edge.

In Figs 2 - 4 resolved turbulent structures are visualized using iso-surfaces of Q-criterion. The grey area given with Δ_{max} (Fig. 2) is clearly recognized since there is a large part of the shear layer which does not show any resolved turbulent structures. This effect is somewhat mitigated by using the vorticity based length scale $\tilde{\Delta}_\omega$ (Fig. 3). By introducing the commutation residue terms given by Eqs. (1) and (3), a rapid development of resolved turbulent structures close to the trailing edge is observed in Fig. 4. It is also recognized that the two dimensional Kelvin-Helmholtz type of structures present in the results with Δ_{max} and $\tilde{\Delta}_\omega$ without the commutation term are diminished. The effect of the different formulations on the vorticity thickness is given in Fig. 5. In the legend of the figure, the commutation term is denoted $C2$, and $C2$ LIM corresponds to $P_{Tr} = 2\nu_{Tr}S^2$ whenever Eq. (4) is limited to remain positive. The commutation term with $\tilde{\Delta}_\omega$ captures reasonably well the growth of the vorticity thickness. If no commutation term is applied, there is a strong delay in the mixing of the two boundary layers, giving too slow growth of the vorticity thickness. This applies to both Δ_{max} and $\tilde{\Delta}_\omega$.

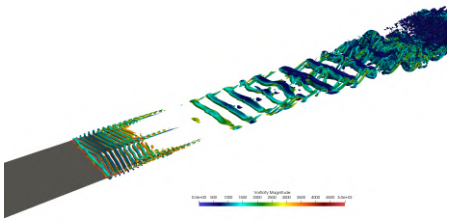

Figure 2: Resolved turbulent structures visualized using iso-surfaces of Q-criterion $Q(L/U_{low})^2 = 100$. $\Delta = \Delta_{max}$.

ACKNOWLEDGEMENT

The 2nd author would like to acknowledge all the early discussions with Prof. Sharath Girimaji on this and related topcis.

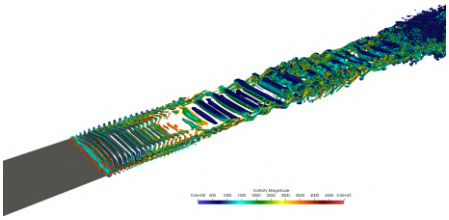

Figure 3: Resolved turbulent structures visualized using iso-surfaces of Q-criterion $Q(L/U_{low})^2 = 100$. $\Delta = \tilde{\Delta}_\omega$.

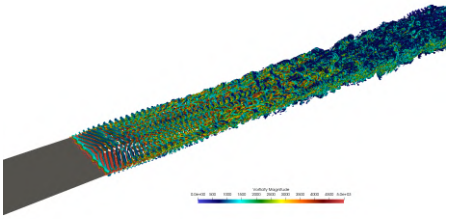

Figure 4: Resolved turbulent structures visualized using iso-surfaces of Q-criterion $Q(L/U_{low})^2 = 100$. $\Delta = \tilde{\Delta}_\omega$ + commutation term.

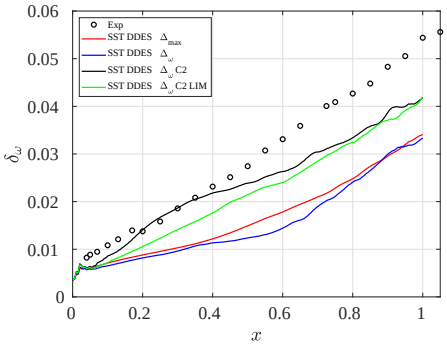

Figure 5: Vorticity thickness.

REFERENCES

[1]Girimaji S., Wallin S.: Closure modeling in bridging regions of variable-resolution (VR) turbulence computations, *Journal of Turbulence.*, **14:1**, 72–98 (2014).

[2]Arvidson S., Davidson L., Peng S.: Interface methods for grey-area mitigation in turbulence-resolving hybrid RANS-LES, *International Journal of Heat and Fluid Flow.*, **73**, 236–257 (2018).

[3]Spalart, P.R., Deck, S., Shur, M.L. et al. :A New Version of Detached-eddy Simulation, Resistant to Ambiguous Grid Densities, *Theoret. Comput. Fluid Dynamics.*, **20**, 181 (2006).

[4]Gritskevich, M., Garbaruk, A., Schütze, J., Menter, F. : Development of DDES and IDDES Formulations for the k-ω Shear Stress Transport Model. *Flow, Turbulence and Combustion.* **88**,(2012).

[5]Shur, M.L., Spalart, P.R., Strelets, M.K. et al.: An Enhanced Version of DES with Rapid Transition from RANS to LES in Separated Flows, *Flow Turbulence Combust.*, **95**, 709–737 (2015).

[6]Delville J.: *La décomposition orthogonale aux valeurs propres et l'analyse de l'organisation tridimensionnelle des écoulements turbulents ci saillés libre.* PhD Thesis, Université de Poitier (1995).

WORKSHOP
Direct and Large-Eddy Simulation 13
October 26th -29th 2022, Udine, Italy

A HYBRID RANS-LES APPROACH FOR THE NUMERICAL SIMULATION OF COMPACT INLINE GAS-LIQUID SEPARATORS

F. Maluta, A. Paglianti, G. Montante
Department of Industrial Chemistry "Toso Montanari"
University of Bologna, Italy
francesco.maluta@unibo.it

INTRODUCTION

Separation based on swirling flows is commonly adopted in a large variety of engineering applications, such as centrifuges, cyclones, and inline separators[1]. Being able to perform such separation operation without the need of dedicated units and directly inside the pipes would represent a significant advantage in the path towards process intensification[2].

In this work, the fluid dynamics of an innovative compact inline swirler specifically designed to perform gas-liquid separation in pipes is investigated from a numerical perspective, with a combination of LES and RANS approaches[3].

THE SYSTEM AND THE MODELLING APPROACH

A 0.09 m pipe with a compact swirler consisting of six flat blades pitched at 45° is investigated. The swirler has an axial length of 13 mm and the blades extend to the pipe walls. The system is shown in Figure 1.

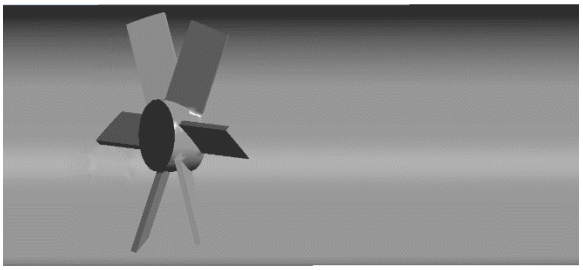

Figure 1: Cutaway drawing of the pipe with the compact inline swirler separator

The continuous phase consists of water and the dispersed gas phase is air. Different operative conditions are considered in terms of water and gas flow rates.

A hybrid Large eddy Simulation –Reynolds Averaged Navier-Stokes (LES-RANS) approach is adopted to predict the liquid flow field[3], with the unsteady RANS equations solved in the near wall region and the LES for the modelling of the free swirling flow.

The gas-liquid flow is described with a simplified algebraic slip model[4], in which one set of momentum equations for the mass averaged velocity is solved and the volume fraction of each fluid is tracked throughout the domain, assuming an empirically derived relation for the relative velocity of the phases. .

The calculation of the local mean age of the fluid parcels in the domain is also obtained by the solution of an additional transport equation, giving useful information on the flow circulation. The mean age distribution theory is described in the following.

After the attainment of the gas-liquid flow field, the bubble size distribution is calculated by the decoupled solution of a Population Balance Equation (PBM).

Based on the computational results, the capability of the compact swirler to provide efficient inline gas-liquid separation is finally assessed.

MEAN AGE DISTRIBUTION

Assuming to inject a passive tracer in a continuous system by means of a pulse input, mean age is defined as the average age of all the tracer molecules of a sample withdrawn at the general location **x** and for steady flows it is a function of space only[5]. Mean Age, a(x), is defined as[6]:

$$a(\boldsymbol{x}) = \frac{\int_0^\infty tC(\boldsymbol{x},t)dt}{\int_0^\infty C(\boldsymbol{x},t)dt} \quad (1)$$

Where C(**x**,t) is the concentration of a passive tracer injected in the system through a pulse input at a given location **x** and time t. The mean age governing equation can be derived, and it reads as:

$$\nabla\big(\boldsymbol{u}\, a(\boldsymbol{x})\big) = \nabla \cdot D_e \nabla\big(a(\boldsymbol{x})\big) + 1 \quad (2)$$

With D_e being the effective viscosity given by the sum of the laminar and turbulent viscosity and $\boldsymbol{u}$ being the mean velocity field. The spatial distribution of mean age gives information on the spatial nonuniformities of mixing and can highlight mean flow structures, such as recirculation loops.

RESULTS

In this work, the single-phase flow field predicted by the simulations is validated through direct comparison with Particle Image Velocimetry (PIV) measurements, Figure 2, and the pressure losses in the system are also compared with experimental results.

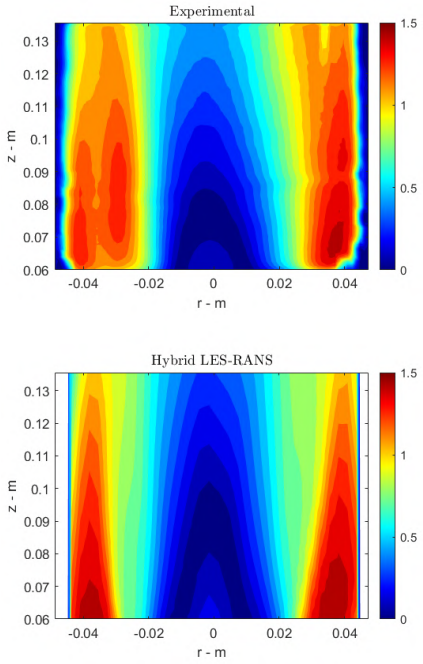

Figure 2: Comparison between experimental and numerical mean axial velocity.

The periodic velocity fluctuations observed downstream of the compact swirler are analyzed to establish a correlation industrially exploitable for measuring the volumetric flow rate inside the pipe. The Mean Age Distribution of an inert tracer is obtained from a simplified transport equation to quantitatively assess the state of mixing of the single-phase flow, Figure 3.

Lastly, the gas-liquid flow field obtained with the present approach will be compared against RANS simulations obtained with the k-ε turbulence model, and the differences in the bubble size distributions obtained from the two different modelling approaches will be assessed.

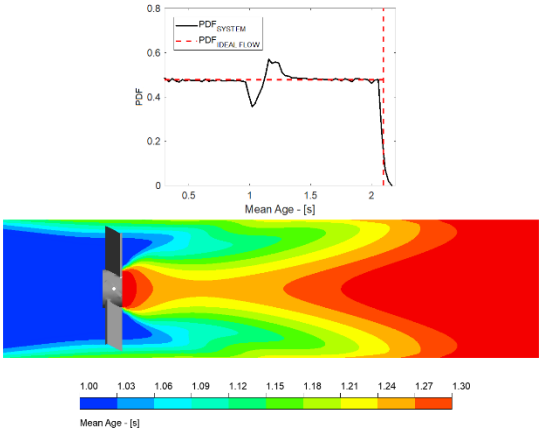

Figure 3: Mean age distribution on a plane close to the inline swirler and Probability Density Function (PDF) of the Mean Age, showing the flow deviations from ideality.

REFERENCES

[1] H.J. Noorman, W. van Winden, J.J. Heijnen, R.G.J.M. van der Lans, CHAPTER 1. Intensified Fermentation Processes and Equipment, in: RSC Green Chem., Royal Society of Chemistry, 2018: pp. 1–41. https://doi.org/10.1039/9781788010320-00001.

[2] R.A. Putra, T. Schäfer, M. Neumann, D. Lucas, CFD studies on the gas-liquid flow in the swirl generating device, Nucl. Eng. Des. 332 (2018) 213–225. https://doi.org/10.1016/j.nucengdes.2018.03.034.

[3] P.R. Spalart, S. Deck, M.L. Shur, K.D. Squires, M.K. Strelets, A. Travin, A New Version of Detached-eddy Simulation, Resistant to Ambiguous Grid Densities, Theor. Comput. Fluid Dyn. 20 (2006) 181–195. https://doi.org/10.1007/s00162-006-0015-0.

[4] M. Icardi, G. Ronco, D.L. Marchisio, M. Labois, Efficient simulation of gas–liquid pipe flows using a generalized population balance equation coupled with the algebraic slip model, Appl. Math. Model. 38 (2014) 4277–4290. https://doi.org/10.1016/j.apm.2014.04.052.

[5] M. Liu, Mean Age Theory for Quantitative Mixing Analysis, in: S.M. Kresta, A.W. Etchells, D.S. Dickey, V.A. Atiemo-Obeng (Eds.), Adv. Ind. Mix. a Companion to Handb. Ind. Mix., John Wiley & Sons Inc., Hoboken, New Jersey, USA, 2015: pp. 15–42.

[6] M. Liu, J.N. Tilton, Spatial distributions of mean age and higher moments in steady continuous flows, AIChE J. 56 (2010) 2561–2572. https://doi.org/10.1002/aic.12151.

Session: Moving bodies and fluid-structure interactions

Wednesday, October 26, 2022

15:20 – 16:05

WORKSHOP
Direct and Large-Eddy Simulation 13
October 26th-29th 2022, Udine, Italy

WIND GUST-INDUCED FLUTTER OF AN ELASTICALLY MOUNTED AIRFOIL: A FLUID-STRUCTURE INTERACTION STUDY BASED ON LES

K. Boulbrachene[1], **M. Breuer**[1]
[1]Professur für Strömungsmechanik, Helmut-Schmidt-Universität Hamburg, Hamburg, Germany
breuer@hsu-hh.de

INTRODUCTION

Classical investigations on the aeroelasticity of wings used for the analysis of flutter stability are often carried out based on simplifying model configurations given by elastically mounted rigid wings. For this purpose, either one degree of freedom (1-DOF) considering solely the pitch motion or two degrees of freedom (2-DOF: pitch and heave) are taken into account, see, e.g., Poirel et al. [4, 5]. Concerning the Reynolds number, flows in the transitional regime are of specific interest due to two reasons. First, unmanned air vehicles including Micro Air Vehicles (MAV) operate in this range. Second, specific flow phenomena such as laminar separation bubbles and transition render this an interesting and challenging case. Aeroelastic effects like laminar separation flutter (LSF) that are different compared to high-Re investigations typically carried out for airplanes are expected. In a precursor study by Wood et al. [8] experimental investigations on the fluid-structure interaction (FSI) of a 2-DOF elastically mounted wing were carried out in a wind tunnel. Complementary numerical predictions of the identical coupled FSI setup were performed by De Nayer et al. [3] relying on eddy-resolving simulations (LES). The results show that coupled high-fidelity solvers allow to predict the FSI problem with an acceptable accuracy leading to either small/large-amplitude oscillations or flutter depending on the case and Re number considered. Note that no wind gusts were taken into account in this preceding studies and thus the airfoil has to be initially excited by mechanical perturbations.

The objective of the present contribution is to study the aeroelastic response of the same 2-DOF NACA 0012 airfoil in the transitional Reynolds number regime subjected to vertical wind gusts. The effect of different gust parameters (wavelengths and amplitudes) on the dynamics of the airfoil is examined. Especially the question of interest is whether certain gusts can induce limit-cycle oscillations or even flutter.

APPLIED METHODOLOGY

The numerical methodology applied consists of a partitioned coupled solver combining large-eddy simulations on the fluid side with a solver for the governing equations of the translation and rotation of the rigid wing. The finite-volume Navier-Stokes solver works with curvilinear, block-structured body-fitted grids in the ALE formulation and is second-order accurate in space and time [1]. The standard Smagorinsky model with van-Driest damping near solid walls ($c_s = 0.1$) is applied. The rigid-body solver receives the fluid forces and moments, and predicts the translational and rotational motions based on Newton's second law using the standard Newmark method of second-order accuracy. The predicted structural displacements of the surface of the airfoil are the input parameters for the adaption of the inner grid. The hybrid grid adaption algorithm (IDW-TFI) developed by Sen et al. [6] is applied. Since in the present application the added-mass effect is negligible, a loose coupling algorithm is preferred.

To inject vertical wind gusts into the computational domain, the split velocity method proposed by Wales et al. [7] was found to be superior [2] since it is capable of capturing the full interaction between the gust and the structure. Furthermore, the gust can be injected directly in front of the structure, which avoids strong damping effects by numerical dissipation in region of coarse grids.

TEST CASE AND SETUP

As mentioned before, the FSI setup is inspired by precursor investigations [3, 8]. The airfoil exposed to a constant free-stream velocity u_∞ and vertical gravity undergoes heave and pitch motions modeled by a mass-spring-damper system for both DOF. These are described by six structural parameters: the mass and the mass moment of inertia of the airfoil as well as one material stiffness and one material damping coefficient for each direction of movement [3]. In the configuration considered the center of gravity nearly coincides with the center of rotation. In [3, 8] this setup was investigated for a wide range of transitional Re numbers. The most interesting case was found to be Re = 33,900, which is employed in the present study. Initiated by external perturbations, a series of sustained large bounded amplitude oscillations was detected in [3, 8]. Here, the effect of gust-induced perturbations and their effect on the airfoil's stability will be examined. For this purpose, vertical gusts which vary solely in the streamwise direction are introduced upstream of the airfoil (chord length c) and convected downstream with u_∞. Gusts of different wavelengths ($L_g^{x1}/c = 2$, 4 and 6) and amplitudes ($A_g/u_\infty = 1$, 2 and 3) are investigated. Note that a deterministic gust model is applied using an Extreme Coherent Gust (ECG) often denoted "1-cosine" shape defined in the IEC-Standard [9].

A C-type grid with about 1.9 million control volumes (CVs) is used and 60 CVs are distributed in the spanwise direction assuming periodic boundary conditions. The grid points are clustered near the surface such that the viscous sublayer can be resolved and no-slip conditions can be applied. At the inlet and the bottom boundary the constant free-stream velocity is

assumed. At the outlet and the top boundary a convective outflow boundary condition is prescribed to assure that the generated vortical structure can leave the computational domain without perceptible disturbances.

EXCERPT FROM THE RESULTS

First results compare the aerodynamic forces exerted on the airfoil between two cases, namely, a fixed airfoil (CFD) and free to move airfoil (FSI). Figure 1 depicts the instantaneous lift force and pitching moment of the airfoil encountering a 1-cosine vertical gust of length $L_g^{x1}/c = 2$ and strength $A_g/u_\infty = 2$. Although identical curves are obtained during the airfoil-gust interaction (i.e., until $t^* = t\,u_\infty/c = 3$), the curves of the FSI case continue to oscillate around zero while their CFD counterparts recover to the steady-state values. Oscillating aerodynamic forces contribute to both dampening and amplifying the motion as found in later investigations.

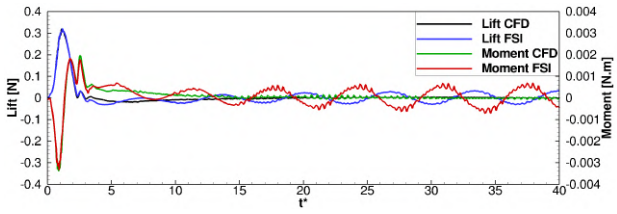

Figure 1: Instantaneous lift force and pitching moment of a fixed and an elastically mounted airfoil subjected to a vertical gust of length $L_g^{x1}/c = 2$ and amplitude $A_g/u_\infty = 2$.

Further insight into the physics involved is provided in Fig. 2, where four instants in time are chosen to depict the development and transport of flow structures during the free airfoil-gust encounter. Leading-edge vortices are formed and convected downstream as the airfoil undergoes heave and pitch motions as a result of the imposed aerodynamic loads.

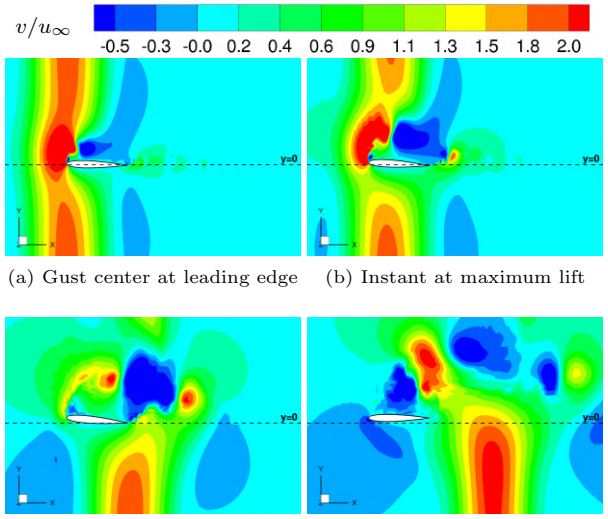

(a) Gust center at leading edge (b) Instant at maximum lift

(c) Gust center at trailing edge (d) Gust completely left airfoil

Figure 2: Four snapshots of the total vertical velocity of the gust encounter on the elastically mounted airfoil.

FSI simulations are carried out to investigate different gust lengths and strengths. The aeroelastic response is found to be strongly depending on the parameters of the gusts chosen. Figure 3 shows the instantaneous heave and pitch motion of the airfoil experiencing interaction with a vertical gust of length $L_g^{x1}/c = 4$. For low gust strength of $A_g/c = 1$ or 2, the amplitudes of both DOFs are found to show an initial increase upon the gust encounter followed by a steady decrease related to an overall positive damping effect of the aerodynamic forces. Obviously, both DOFs eventually settle after several oscillation cycles at a stage in which their amplitudes are sustained and bounded (i.e., limit cycle oscillation). In contrast, for a strong gust with $A_g/c = 3$ the gust induces high instabilities which triggers a pitch governed diverging motion also known as stall flutter. These and other results including the effect of the gust length on the airfoil behavior and an energy analysis will be discussed in more detail in the final paper.

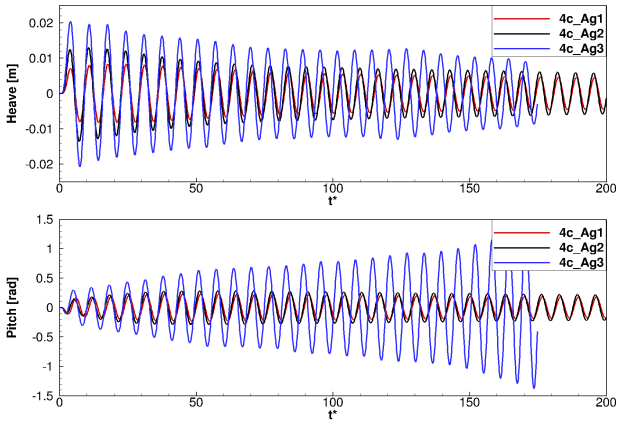

Figure 3: Instantaneous heave and pitch DOFs of the airfoil subjected to vertical gusts of varying strength A_g/u_∞ at a fixed gust length of $L_g^{x1}/c = 4$.

REFERENCES

[1] Breuer, M., De Nayer, G., Münsch, M., Gallinger, T., Wüchner, R.: Fluid-structure interaction using a partitioned semi-implicit predictor-corrector coupling scheme for the application of large-eddy simulation. J. Fluids Structures **29**, 107–130 (2012).

[2] Boulbrachene, K., De Nayer, G., Breuer, M.: Assessment of two wind gust injection methods: Field velocity vs. split velocity method. J. Wind Eng. Indus. Aerodyn. **218**, 104790 (2021).

[3] De Nayer, G., Breuer, M., Wood, J. N.: Numerical investigations on the dynamic behavior of a 2-DOF airfoil in the transitional Re number regime based on fully coupled simulations relying on an eddy-resolving technique. Int. J. Heat Fluid Flow **85**, 108631 (2020).

[4] Poirel, D., Harris, Y., Benaissa, A.: Self-sustained aeroelastic oscillations of a NACA 0012 airfoil at low-to-moderate Reynolds numbers. J. Fluids Structures **24**, 700–719 (2008).

[5] Poirel, D., Métivier, V., Dumas, G.: Computational aeroelastic simulations of self-sustained pitch oscillations of a NACA 0012 at transitional Reynolds numbers. J. Fluids Structures **27**, 1262–1277 (2011).

[6] Sen, S., De Nayer, G., Breuer, M.: A fast and robust hybrid method for block-structured mesh deformation with emphasis on FSI-LES applications. Int. J. Numer. Meth. Eng. **111**(3), 273–300 (2017).

[7] Wales, C., Jones, D., Gaitonde, A.: Prescribed velocity method for simulation of aerofoil gust responses. J. Aircraft **52**(1), 64–76 (2014).

[8] Wood, J. N., Breuer, M., De Nayer, G.: Experimental investigations on the dynamic behavior of a 2-DOF airfoil in the transitional Re number regime based on digital-image correlation measurements. J. Fluids Structures **96**, 103052 (2020).

[9] DIN EN 61400-1:2019, Wind energy generation systems - Part 1: Design requirements. Technical report, IEC (2019).

WORKSHOP
Direct and Large-Eddy Simulation 13
October 26th-29th 2022, Udine, Italy

DIRECT NUMERICAL SIMULATION OF FLOW AROUND SPANWISE-FLEXIBLE, FLAPPING WINGS IN HORIZONTAL TANDEM CONFIGURATION

C. Martínez-Muriel[1], G. Arranz[2], M. García-Villalba[1], O. Flores[1]
[1] Aerospace Engineering Department
Universidad Carlos III de Madrid, Madrid, Spain
[2] Department of Aeronautics and Astronautics
Massachusetts Institute of Technology, Cambridge, USA
cayetano.martinez@uc3m.es

INTRODUCTION

Dragonflies are fascinating insects. Opposed to most other species, they have two pairs of flexible wings arranged in horizontal tandem configuration, and they can move each wing independently. As a consequence, they are among the most agile and quickest flying insects in the world [1]. They are able to perform rapid manoeuvres, hover, flight in any direction, glide and cruise efficiently. Indeed, previous studies in idealized geometries suggest that the arrangement of rigid wings in tandem can be beneficial in terms of force generation and efficiency, if the wing kinematics are properly selected [2, 3].

On the other hand, previous works have shown that an enhancement on the aerodynamic performance of flapping wings may be obtained by tuning the wing's flexibility [4]. However, flexibility effects have been analyzed mostly on isolated wings, and little attention has been paid to flexibility effects on flapping wings in horizontal tandem configuration. It should be noted that the resulting fluid-structure interaction (FSI) problem for flexible flapping wings in tandem is very challenging, both from the point of view of experiments and simulations. Moreover, since the associated parametric space is very large, it is difficult to obtain information that can have a direct impact on the design of dragonfly-like micro air vehicles with flexible wings [5].

As a follow-up to our previous computational work on the aerodynamic performance of rigid wings in horizontal tandem configuration [3, 6], we analyze here the effect of the wing's flexibility on the aerodynamic performance and on the flow structures surrounding the wings.

METHODOLOGY

Two finite spanwise-flexible wings are immersed in a free stream of constant speed, U_∞. Wings are modelled as rectangular flat plates of chord c, thickness $h_s/c = 0.02$ and aspect ratio $AR = 4$. The Reynolds number based on the free-stream velocity and the chord of the wing is $Re = U_\infty c/\nu = 1000$. A heaving and pitching motion is prescribed at the mid section of the wings, following the laws

$$h_i(t) = h_0 \cos(\omega t + \phi_{fh,i}), \quad (1)$$

$$\theta_i(t) = \theta_0 \cos(\omega t + \phi_{hp} + \phi_{fh,i}), \quad (2)$$

where the subscript i refers to the forewing ($i = f$) or the hindwing ($i = h$). Both wings have the same heaving amplitude (h_0), pitching amplitude (θ_0), angular frequency (ω), and phase lag between heaving and pitching (ϕ_{hp}). The phase lag between the forewing and hindwing is controlled by $\phi_{fh,i}$. The frequency of the motion is given in terms of the Strouhal number based on the chord of the wing, $St_c = \omega c/(2\pi U_\infty)$. The values defining the kinematics are presented in table 1, and are based on a 2D optimal kinematics that maximizes the propulsive efficiency of a pair of airfoils. The wings are arranged in horizontal tandem with a separation $s = 0.5c$.

i	h_0	θ_0	St_c	ϕ_{hp}	$\phi_{fh,i}$
f	0.388	26.19°	0.496	90°	0
h					347.1°

Table 1: Kinematic parameters of the midsection of the forewing ($i = f$) and the hindwing ($i = h$)

The flexibility of the wings is modeled using a multi-body system (MBS) of connected rigid segments interacting with the surrounding fluid [7]. Hence, the wing is divided in $N = 21$ plates along the spanwise direction, connected with torsion springs to model the spanwise flexibility of the wing. The Young's modulus of the wings (i.e., the stiffness of the torsional springs) is specified in terms of the ratio of natural frequency of the wing immersed in fluid [8] over the angular frequency of the wing's motion, $\omega_{n,f}/\omega$. A density ratio of $\rho_s/\rho_f = 20$ is chosen, yielding values of the effective inertia typical of dragonfly wings.

To provide a baseline for the the horizontal tandem flexible wings, we also consider a case with horizontal tandem rigid wings (i.e., $\omega_{n,f}/\omega \to \infty$), and several flexible isolated wings with the same kinematics as the forewing.

Direct numerical simulations of the flow are performed using the in-house code TUCAN, a constant-density fluid solver that models the presence of the bodies using the Immersed Boundary Method (IBM) proposed by Uhlmann [9]. More details on the flow solver and its validation can be found elsewhere [7]. The time step is selected such that the CFL number is maintained under 0.3. Simulations are performed in a domain of $14c \times 11c \times 7c$ in the streamwise, spanwise and vertical directions, respectively. A refined zone is defined roughly at the middle of the domain with a uniform grid size of $\Delta r = c/96$.

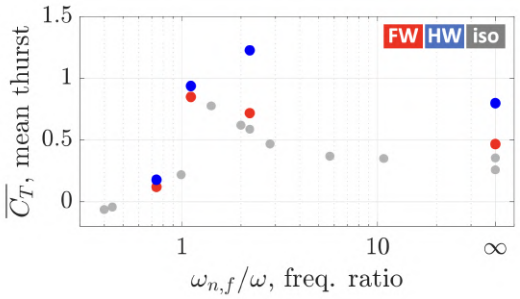

Figure 1: Averaged thrust coefficient $\overline{C_T}$ as a function of flexibility. $\omega_{n,f}/\omega \to \infty$ means rigid. Grey, red and blue dots refer to isolated wings, forewings and hindwings respectively.

RESULTS

Figure 1 shows the evolution of the time-averaged thrust coefficient of each wing, $\overline{C_T}$, as a function of the ratio of the natural frequency in the fluid over the angular frequency of the motion, $\omega_{n,f}/\omega$. The baseline is provided by the flexible isolated wings (grey bullets), which show that decreasing $\omega_{n,f}/\omega$ (i.e. increasing the flexibility) leads to increased thrust generation. The increase is not monotonic, and an optimal aerodynamic performance is achieved when $\omega_{n,f}/\omega \approx 1$. This suggests that the optimal performance of isolated flexible wings may be linked to a resonance phenomenon. As shown in Figure 1, the thrust coefficient near the resonance is increased by a factor of 2.4 with respect to the rigid case. For values of $\omega_{n,f}/\omega < 1$, a sudden drop of performance suddenly occurs, leading to lower thrust generation compared to the rigid case.

When comparing the isolated wing with the pair of wings in horizontal tandem, two main results can be highlighted. First, the behavior of the forewing is very similar to the behaviour of the isolated wings, with an optimal performance at $\omega_{n,f}/\omega \approx 1$. Interestingly, rigid and flexible forewings have slightly better aerodynamic performance than their isolated counterparts (compare red and grey dots on Figure 1), although this might be related to the selected kinematics (i.e., forewing and hindwing flapping almost in phase). Second, Figure 1 shows the optimal frequency ratio for the hindwing is $\omega_{n,f}/\omega \approx 2$, roughly twice larger than the optimal values for forewing and isolated wings. This discrepancy is not completely surprising, since the aerodynamic performance of the hindwing is dictated by the interaction of the hindwing with the vortices shed by the forewing. These interactions are depicted in Figure 2, which shows iso-Q contours to represent the vortical structures over the tandem wings. The figure shows that the evolution of the leading edge vortices and tip vortices shed by the forewing varies with the flexibility, as does their interaction with the hindwing.

In the presentation we will further discuss how flexibility impacts on the aerodynamic performance of isolated and tandem wings, trying to identify the optimal flexibilities for the tandem configuration.

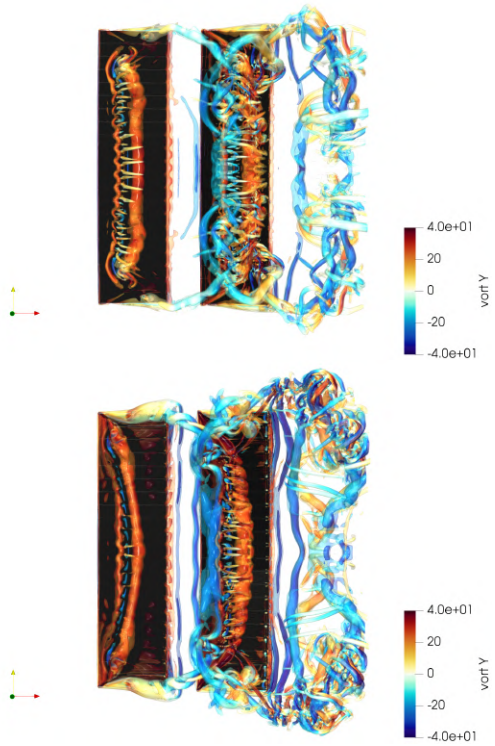

Figure 2: Top view of the iso-Q contours representing vortical structures for cases with (top) $\omega_{n,f}/\omega \approx 2$ and (bottom) $\omega_{n,f}/\omega \approx 1^+$. Free stream comes from the left. Iso-Q contours are coloured with the spanwise vorticity.

ACKNOWLEDGEMENTS

This work was supported by grant DPI2016-76151-C2-2-R (AEI/FEDER, UE). The authors thankfully acknowledge the computer resources at MareNostrum and the technical support provided by Barcelona Supercomputing Center (RES-IM-2020-2-0006), as well as at LUSITANIA III and the technical support provided by Centro Extremeño de Investigación, Innovación Tecnológica y Supercomputación (CénitS) (RES-IM-2020-3-0024).

REFERENCES

[1]Salami, Ward, Montazer, and Ghazali : A review of aerodynamic studies on dragonfly flight, *Proc IMechE Part C: J Mechanical Engineering Science*, **233**(18), 6519–6537 (2019).

[2]Boschitsch, Dewey and Smits : Propulsive performance of unsteady tandem hydrofoils in an in-line configuration, *Phys. Fluids*, **26**(5), 051901 (2014).

[3]Arranz, Flores and García-Villalba : Three-dimensional effects on the aerodynamic performance of flapping wings in tandem configuration, *J. Fluids Struct.*, **94**, 102893 (2020).

[4]Heathcote, Wang and Gursul : Effect of spanwise flexibility on flapping wing propulsion, *J. Fluids Struct.*, **24**(2), 183–199 (2008).

[5]Haider, Shahzad, Mumtaz Qadri and Ali Shah : Recent progress in flapping wings for micro aerial vehicle applications, *Proc. Inst. Mech. Eng. C J. Mech. Eng. Sci.*, **235**(2), 245–264 (2021).

[6]Jurado, Arranz, Flores and García-Villalba : Numerical simulation of flow over flapping wings in tandem: Wingspan effects, *Phys. Fluids*, **34**(1), 017114 (2022).

[7]Arranz, Martínez-Muriel, Flores and García-Villalba : Fluid-structure interaction of multi-body systems: Methodology and applications, *J. Fluids Struct.*, **110**, 103519 (2022).

[8]Arora, Kang, Shyy and Gupta : Analysis of passive flexion in propelling a plunging plate using a torsion spring model, *J. Fluid Mech.*, **857**, 562–604, (2018).

[9]Uhlmann : An immersed boundary method with direct forcing for the simulation of particulate flows, *J. Comput. Phys.*, **209**(2), 448–476 (2005).

WORKSHOP
Direct and Large-Eddy Simulation 13
October 26th-29th 2022, Udine, Italy

NUMERICAL SIMULATION OF SELF-PROPELLED FLEXIBLE PLATES IN TANDEM

G. Arranz[1], O. Flores[2], M. García-Villalba[2]
[1] Department of Aeronautics and Astronautics
Massachusetts Institute of Technology, Cambridge, USA
[2] Aerospace Engineering Department
Universidad Carlos III de Madrid, Madrid, Spain
garranz@mit.edu

INTRODUCTION

Fisch schooling is an example provided by Nature of interacting bodies through a fluid with surprising behaviours [1, 2]. Due to the presence of more than one fish, each individual has to interact with an ambient fluid which is disturbed by the surrounding individuals. These interactions can be exploited by the individual to extract energy from the fluid and move in a more efficient manner than if it were in isolation. Although the main reason why animals form schools or flocks may not be entirely clear yet, it is well known that animals benefit from collective motion in terms of flow interaction [3, 4].

In the present study, we focus on the minimal example of fish schooling, namely the coordinated, self-propelled swim of two individuals in tandem configuration. This example has been extensively studied in two-dimensions (2D) [5, 6, 7, 8]. However, it is known that the wake pattern of a self-propelled body significantly differs from 2D to 3D [9]: from a reverse von Kármán vortex street in 2D to a diverging wake of vortex rings in 3D. This could lead to significant differences of 3D stable positions of the collective and on their associated performance when compared to its 2D counterparts. In particular, the stable *quantized positions* observed by Ramananarivo *et. al* [6] and Newbolt *et. al* [8] on a von Kármán vortex street may no longer emerge on a 3D bifurcating wake. Hence, different vortical interactions might be expected in 3D with respect to 2D, which could alter the performance of the bodies. In order to address these questions, we perform direct numerical simulations of two, idealized, self-propelled swimmers in tandem configuration in 3D.

METHODOLOGY

Two rectangular self-propelling plates immersed in an otherwise quiescent fluid are considered. The plates have a chord C, span b; thickness, e; uniform density, ρ_s; and they are flexible along the chordwise direction. Under the arrangement of the plates considered in this study, one of the flappers *swims* downstream of the other. We denote the flapper swimming downstream as follower, and the upstream flapper as leader.

The flappers are free to move along the horizontal direction (X), whereas the vertical motion of their leading edge is prescribed as,

$$Z_l(t) = A\cos(2\pi f t), \quad Z_f(t) = H + A\cos(2\pi f t - \phi), \quad (1)$$

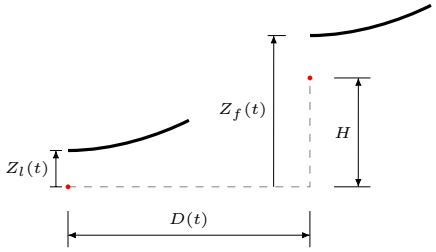

Figure 1: Side view of the schooling configuration.

b	e	A	Re	ρ_s/ρ	ω_n
$0.5C$	$0.02C$	$0.5C$	200	10	$0.35f$

Table 1: List of parameters that define the problem.

where A is the heaving amplitude, f is the frequency of oscillation, ϕ is the phase offset, and H is the mean vertical offset between the flappers, These magnitudes are sketched in Figure 1, alongside the instantaneous horizontal distance, $D(t) = X_f(t) - X_l(t)$. The subscripts l and f denote the leader and the follower flappers, respectively.

Three heaving offsets $H = [0, 0.3, 0.6]C$, and different phase offsets in the range $\phi = [0° - 360°]$ are considered to find stable equilibrium positions of the flapper in the $H - \phi$ plane. The rest of parameters that define the problem are kept fixed and gathered in Table 1. The Reynolds number is defined as, $Re = 2\pi f C/\nu$, where ν is the kinematic viscosity; ρ is the fluid density; and ω_n is the first natural frequency of the flapper's elastic response in vacuum.

A lumped-torsional flexibility model is used to simulate the chordwise flexibility of the flappers. Under this approach, each flapper is a multi-body system (MBS) of rigid bodies connected by torsional springs [11].

The flow surrounding the flappers is determined by solving the Navier-Stokes equations of the incompressible flow. The presence of the flappers is modelled using the immersed boundary method proposed by Uhlmann [10]. The flow equations and the dynamic equations of the MBS are weakly coupled. More details about the flow solver and its validation can be found in Arranz *et al.* [11].

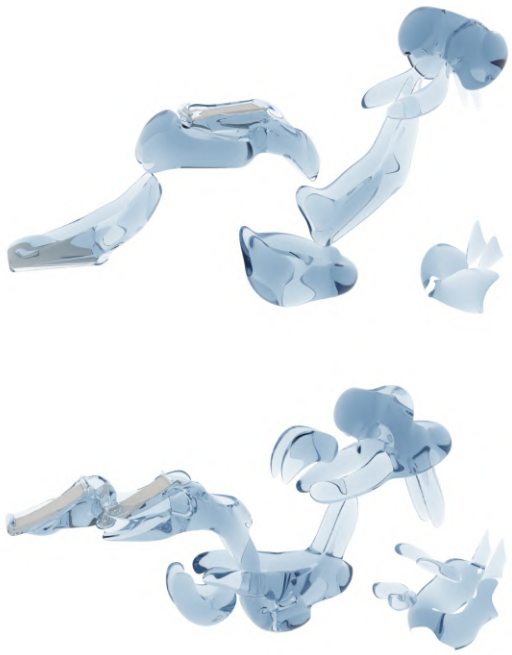

Figure 2: Flow visualization of (top) a regular ($H/C = 0.6$, $\phi = 180°$) and (bottom) a compact case ($H/C = 0$, $\phi = 0°$). Vortical structures correspond to iso-surfaces of the second invariant of the velocity gradient tensor, Q.

RESULTS

A total of 24 simulations, varying H and ϕ have been performed. Stable tandem configurations emerge in all cases, where both flappers swim at a constant average propulsive speed, maintaining an average horizontal distance, $\overline{D}$. Three schooling modes are observed: first, a *regular* mode ($\overline{D}/c > 1$), in which the performance of the leader is virtually equivalent to that of an isolated flapper, whereas the performance of the follower depends on the interaction with the leader's wake; second, a *compact* mode, characterized by $\overline{D}/c \approx 1$, in which the leader's performance is also affected by the presence of the leader; and third, an *aligned* mode, only observed for $H = 0.6C$, in which $\overline{D}/c < 1$ and the performance of both flappers, in terms of efficiency and propulsive speed, is less than that of the isolated flapper. For the sake of ilustration, Figure 2 depicts the flow for a regular and a compact configuration.

Results show that $\overline{D}$ linearly depends on ϕ as for 2D self-propelling tandem foils [8], and it is little influenced by H (see Figure 3). On the other hand, the performance of the follower's strongly depends on ϕ and H (not shown). In particular, depending on the interaction with the leader's wake, the propulsive efficiency of the follower can increase up to 10% as compared to that of the isolated flapper, or decrease by an 8%.

In the presentation, we will discuss in more detail the linear dependence between $\overline{D}$ and ϕ. In addition, we will show that the follower's performance can be linked to the vertical velocity induced by the vortex rings shed by the leader. Thus, a reduced order model can be built to qualitatively predict the performance of the follower based solely on the wake shed by an isolated flapper. The interested reader can find more details of the present study in Arranz *et al.* [12].

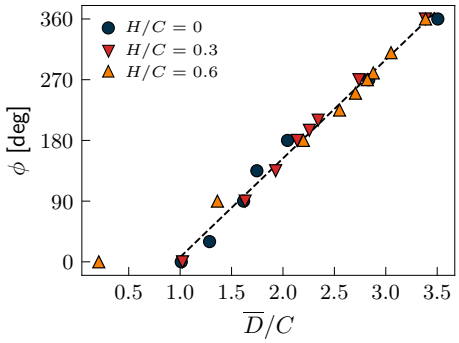

Figure 3: Relationship between ϕ and $\overline{D}$ for all cases. Each symbol stands for a different vertical offset, H.

ACKNOWLEDGEMENTS

This work was supported by the State Research Agency of Spain (AEI) under grant DPI2016-76151-C2-2-R including funding from the European Regional Development Fund (ERDF). The computations were partially performed at the supercomputer Caesaraugusta from the Red Española de Supercomputación in activity IM-2020-2-0005.

REFERENCES

[1]D. Weihs, "Hydromechanics of fish schooling," *Nature*, vol. 241, no. 5387, pp. 290–291, 1973.

[2]T. Mora, A. M. Walczak, L. Del Castello, F. Ginelli, S. Melillo, L. Parisi, M. Viale, A. Cavagna, and I. Giardina, "Local equilibrium in bird flocks," *Nature Phys.*, vol. 12, no. 12, pp. 1153–1157, 2016.

[3]H. Weimerskirch, J. Martin, Y. Clerquin, P. Alexandre, and S. Jiraskova, "Energy saving in flight formation," *Nature*, vol. 413, no. 6857, pp. 697–698, 2001.

[4]A. D. Becker, H. Masoud, J. W. Newbolt, M. Shelley, and L. Ristroph, "Hydrodynamic schooling of flapping swimmers," *Nature Comm.*, vol. 6, no. 1, p. 8514, 2015.

[5]X. Zhu, G. He, and X. Zhang, "Flow-mediated interactions between two self-propelled flapping filaments in tandem configuration," *Phys. Rev. Lett.*, vol. 113, p. 238105, 2014.

[6]S. Ramananarivo, F. Fang, A. Oza, J. Zhang, and L. Ristroph, "Flow interactions lead to orderly formations of flapping wings in forward flight," *Phys. Rev. Fluids*, vol. 1, p. 071201, 2016.

[7]Z.-R. Peng, H. Huang, and X.-Y. Lu, "Collective locomotion of two closely spaced self-propelled flapping plates," *J. Fluid Mech.*, vol. 849, pp. 1068–1095, 2018.

[8]J. W. Newbolt, J. Zhang, and L. Ristroph, "Flow interactions between uncoordinated flapping swimmers give rise to group cohesion," *Proc. Natl. Acad. Sci. USA*, vol. 116, no. 7, pp. 2419–2424, 2019.

[9]M. Gazzola, P. Chatelain, W. M. van Rees, and P. Koumoutsakos, "Simulations of single and multiple swimmers with non-divergence free deforming geometries," *J. Comput. Phys.*, vol. 230, no. 19, pp. 7093–7114, 2011.

[10]M. Uhlmann, "An immersed boundary method with direct forcing for the simulation of particulate flows," *J. Comput. Phys.*, vol. 209, no. 2, pp. 448–476, 2005.

[11]G. Arranz, C. Martínez-Muriel, O. Flores, and M. García-Villalba, "Fluid–structure interaction of multi-body systems: Methodology and applications," *J. Fluids Struct.*, vol. 110, p. 103519, 2022.

[12]G. Arranz, O. Flores, and M. García-Villalba, "Flow interaction of three-dimensional self-propelled flexible plates in tandem," *J. Fluid Mech.*, vol. 931, p. A5, 2022.

Session: Data assimilation and uncertainty quantification

Wednesday, October 26, 2022

16:30 – 17:45

WORKSHOP
Direct and Large-Eddy Simulation 13
October 26th-29th 2022, Udine, Italy

MACHINE LEARNING MODELS FOR SUBGRID SCALE TENSORS OF 2D RAYLEIGH-BÉNARD CONVECTION

L. Biferale[1], M. Buzzicotti[1], P. Cifani[2,3], B.J. Geurts[2,4], J-M. Leahy[2,5]
[1] Dept. of Physics and INFN, University of Rome "Tor Vergata," Rome, IT [2] Dept. of Applied Mathematics, University of Twente, Enschede, NL [3] Gran Sasso Science Institute, L'Aquila, IT [4] Dept. of Applied Physics, Eindhoven University of Technology, Eindhoven, NL [5] Dept. of Mathematics, Imperial College London, London, UK

RAYLEIGH-BÉNARD CONVECTION (RBC)

We consider Rayleigh-Bénard convection (RBC) in two-dimensions using the Oberbeck-Boussinesq approximation of the Navier-Stokes equations with constant kinematic viscosity $\nu > 0$, thermal diffusivity $\kappa > 0$, coefficient of thermal expansion α, gravitational magnitude g in the negative $\hat{\mathbf{z}}$-direction, periodic boundary conditions in the horizontal direction with length L, no-slip boundary conditions in the vertical direction with length H, and isothermal temperature $T_{\rm top}$ at the top and $T_{\rm bot}$ at the bottom. The system models a buoyancy-driven flow in a fluid layer heated from below and cooled from above. Denoting the aspect ratio of the domain by $\Lambda := L/H$, the equations governing the nondimensionalized velocity $\mathbf{u}$, temperature T, and pressure p are

$$\begin{cases} \partial_t \mathbf{u} + \nabla \cdot (\mathbf{u} \otimes \mathbf{u}) - \nabla p = \sqrt{\frac{\rm Pr}{\rm Ra}} \Delta \mathbf{u} + T \hat{\mathbf{z}} \,, \\ \partial_t T + \nabla \cdot (\mathbf{u} T) = \frac{1}{\sqrt{\rm Pr\, Ra}} \Delta T \,, \\ \nabla \cdot \mathbf{u} = 0 \,, \end{cases} \tag{1}$$

where the Rayleigh and Prandtl numbers are denoted $\mathrm{Ra} := \frac{\alpha \Delta T g H^2}{\nu \kappa}$ and $\mathrm{Pr} := \frac{\nu}{\kappa}$. The boundary conditions are:

$$\begin{cases} \mathbf{u}(t,x,z) = \mathbf{0} \quad (t,x,z) \in \mathbb{R}_+ \times [0,\Lambda] \times \{0,1\} \,, \\ T(t,x,z) = 1 \quad (t,x,z) \in \mathbb{R}_+ \times [0,\Lambda] \times \{0\} \,, \\ T(t,x,z) = 0 \quad (t,x,z) \in \mathbb{R}_+ \times [0,\Lambda] \times \{1\} \,, \end{cases}$$

and $\mathbf{u}, T, p$ are periodic with period Λ in the x-variable. The RBC initial-value problem is well-posed in the standard L^2-Sobolev classes with phase space denoted X, and the solution semigroup $\{S_t\}_{t \geq 0} : X \to X$ has a compact connected finite-dimensional maximal attractor $\mathcal{A} \subset X$ [1]. While the existence of an inertial manifold (i.e., $\exists$ a finite dimensional restriction) is unknown, it has recently been shown that there exists a finite-dimensional determining form involving only the velocity field [2]. The LES and a priori learning problem that we describe below can be understood as a learning problem for an approximate inertial map, with the filter replacing the 'slow' dissipation operator eigenspace.

A key diagnostic of RBC is the Nusselt number Nu, which is defined to be the ratio of bulk-averaged vertical heat flux Q from both conduction and convection to flux $\kappa \Delta T / H$ from conduction alone. In terms of nondimesional quantities,

$$\mathrm{Nu} := \langle (\sqrt{\mathrm{Pr\, Ra}}\, \mathbf{u} T - \nabla T) \cdot \hat{\mathbf{z}} \rangle = 1 + \sqrt{\mathrm{Pr\, Ra}} \langle u_z T \rangle \,,$$

where $\langle \cdot \rangle$ denotes the time and spatial average operator and $u_z = \mathbf{u} \cdot \hat{\mathbf{z}}$ denotes the vertical component of the velocity. The asymptotic behavior of Nu as $\mathrm{Ra} \to \infty$ is a long standing open problem [3]. Experiments and analysis have yet to confirm the 'classical' scaling $\mathrm{Nu} \sim \mathrm{Ra}^{1/3}$ or 'ultimate' scaling $\mathrm{Ra}^{1/2}$, which has been proved to be the upper limit [4]

SUBGRID-SCALE (SGS) TENSORS

We define a filtering operator acting on fields defined on the spatial domain via a product Gaussian filter with constant horizontal width Δ_x and non-uniform vertical width $\Delta_y(y)$ that is smaller near the vertical boundary. Applying the filter to (1) and using the notation $\overline{\cdot}$ for filtered fields, we find

$$\begin{cases} \partial_t \overline{\mathbf{u}} + \nabla \cdot (\overline{\mathbf{u}} \otimes \overline{\mathbf{u}}) - \nabla \overline{p} = \sqrt{\frac{\rm Pr}{\rm Ra}} \Delta \overline{\mathbf{u}} + \overline{T} \hat{\mathbf{z}} - \nabla \cdot \boldsymbol{\tau} + \mathbf{e}_{\mathbf{u}} \,, \\ \partial_t \overline{T} + \nabla \cdot (\overline{\mathbf{u}} \overline{T}) = \frac{1}{\sqrt{\rm Pr\, Ra}} \Delta \overline{T} - \nabla \cdot \mathbf{q} + \mathbf{e}_T \,, \\ \nabla \cdot \overline{\mathbf{u}} = 0 \,, \end{cases} \tag{2}$$

where the SGS stress and heat flux tensors are denoted

$$\boldsymbol{\tau} = \tau(\mathbf{u}) = \overline{\mathbf{u} \otimes \mathbf{u}} - \overline{\mathbf{u}} \otimes \overline{\mathbf{u}} \quad \text{and} \quad \mathbf{q} = \mathbf{q}(\mathbf{u}, T) = \overline{\mathbf{u} T} - \overline{\mathbf{u}} \overline{T} \,,$$

and the fields $\mathbf{e}_{\mathbf{u}}, \mathbf{e}_T$ are errors that arise due to non-uniformity. We define the total SGS by $\boldsymbol{\mathcal{T}} : X \times [0,\Lambda] \times [0,1] \to \mathbb{R}^6$ by $\boldsymbol{\mathcal{T}}(\mathbf{u}, T) = [\boldsymbol{\tau}(\mathbf{u}), \mathbf{q}(\mathbf{u}, T)]^\top$. It follows that

$$\mathrm{Nu} = 1 + \sqrt{\mathrm{Pr\, Ra}} \, \langle \overline{u_z} \overline{T} + q_z \rangle + e_{\rm Nu} \,, \tag{3}$$

where $e_{\rm Nu} = \langle u_z T - \overline{u_z T} \rangle$ is the commutator error.

CONTINUUM A PRIORI LEARNING

Denote by $F_\theta : [0,\Lambda] \times [0,1] \times \mathbb{R}^2 \times \mathbb{R} \times \mathbb{R}^{2\times 2} \times \mathbb{R}^2 \to \mathbb{R}^6$, $\theta \in \mathbb{R}^{d_\theta}$, a fully connected five hidden-layer neural network (NN) with tanh activation functions and hidden layer depth 512. The NN induces an SGS $\boldsymbol{\mathcal{T}}_\theta : X \times [0,\Lambda] \times [0,1] \to \mathbb{R}^6$:

$$\boldsymbol{\mathcal{T}}_\theta(\mathbf{u}, T)(x,z) = F_\theta(x, z, \mathbf{u}(x,z), T(x,z), \nabla \mathbf{u}(x,z), \nabla T(x,z)) \,,$$

with components denoted $[\tau_\theta, \mathbf{q}_\theta]^\top := \boldsymbol{\mathcal{T}}_\theta(\mathbf{u}, T)$.[1] The parametric family $\{\boldsymbol{\mathcal{T}}_\theta\}_{\theta \in \mathbb{R}^{d_\theta}}$ induces a closure model

$$\begin{cases} \partial_t \overline{\mathbf{u}}_\theta + \nabla \cdot (\overline{\mathbf{u}}_\theta \otimes \overline{\mathbf{u}}_\theta) - \nabla \overline{p}_\theta = \sqrt{\frac{\rm Pr}{\rm Ra}} \Delta \overline{\mathbf{u}}_\theta + \overline{T}_\theta \hat{\mathbf{z}} - \nabla \cdot \boldsymbol{\tau}_\theta(\overline{\mathbf{u}}_\theta, \overline{\mathbf{q}}_\theta) \,, \\ \partial_t \overline{T}_\theta + \nabla \cdot (\overline{\mathbf{u}}_\theta \overline{T}_\theta) = \frac{1}{\sqrt{\rm Pr\, Ra}} \Delta \overline{T}_\theta - \nabla \cdot \mathbf{q}_\theta(\overline{\mathbf{u}}_\theta, \overline{T}_\theta) \,, \\ \nabla \cdot \overline{\mathbf{u}}_\theta = 0 \,. \end{cases} \tag{4}$$

[1] It suffices to define a parametrization of, e.g., the upper triangular part of $\overline{\mathbf{u} \otimes \mathbf{u}} - \overline{\mathbf{u}} \otimes \overline{\mathbf{u}}$ and take the range of F_θ to be $\mathbb{R}^5$, but we avoid this in the presentation for simplicity.

We assume (4) is well-posed and induces a solution semigroup $\{\bar{S}_{\theta,t}\}_{t\geq 0} : X \to X$ with global attractor $\overline{\mathcal{A}}_\theta$. We would like to choose $\theta^* \in \mathbb{R}^{d_\theta}$ such that the closure dynamics $\{\overline{S}_{\theta,t}\}$ approximates the filtered true dynamics $\{\overline{S_t}\}$. Perhaps more modestly, we would like their first and second order statistics to agree approximately, and in particular (see Figure 1),

$$\mathrm{Nu} \approx \mathrm{Nu}_{\theta^*} := 1 + \sqrt{\mathrm{Pr}\,\mathrm{Ra}}\,\langle \overline{u}_{\theta^*,z}\overline{T}_{\theta^*} + q_{\theta^*,z}\rangle. \qquad (5)$$

Letting $\mu \in \mathcal{P}(X)$ denote an ergodic invariant measure of $\{S_t\}$, we define the a priori generalization error by

$$\begin{aligned} L(\theta) &= \frac{1}{2}\int_X |\boldsymbol{\mathcal{T}}(\mathbf{u},T) - \boldsymbol{\mathcal{T}}_\theta(\overline{\mathbf{u}},\overline{T})|^2_{L^2}\, d\mu(\mathbf{u},T) \\ &= \frac{1}{2}\lim_{T'\to\infty}\frac{1}{T'}\int_0^{T'} |\boldsymbol{\mathcal{T}}(\mathbf{u}_t,T_t) - \boldsymbol{\mathcal{T}}_\theta\left(\overline{\mathbf{u}_t},\overline{T_t}\right)|^2_{L^2} dt\,, \end{aligned}$$

and aim to find $\theta^* \in \arg\min_{\theta\in\mathbb{R}^{d_\theta}} L(\theta)$. The convenient property of the a priori loss is that it translates to a supervised learning problem. Indeed, one creates the data set

$$\mathcal{D} := \{(X_t := (\overline{u}_{t+T_0}, \overline{T}_{t+T_0}),\ \ Y_t := \boldsymbol{\mathcal{T}}(u_{t+T_0}, T_{t+T_0})\}_{t\leq T'}$$

for a burn-in time T_0 and total length T', and then minimizes

$$\hat{L}(\theta) = \frac{1}{2}\frac{1}{T'}\int_0^{T'} |Y_t - \boldsymbol{\mathcal{T}}_\theta(X_t)|^2_{L^2} dt\,.$$

Recent work on invariant measures of Itô diffusions in finite-dimensions [5], suggests that the error between the one and two point statistics of $\{\overline{S_t}\}$ and $\{\overline{S}_{\theta,t}\}$ can be bound in terms of the a priori generalization error, with a bias term depending on the non-uniformity 'errors' $\mathbf{e_u}, e_T$ in (2). There is additional error in the computation of unfiltered semigroup $\{S_t\}$ statistics. However, for the Nusselt number, the parameteric SGS heat flux $\mathbf{q}_\theta$ can be used in the recovery of Nu, with the only additional error being due to $\mathbf{e}_{\mathrm{Nu}}$ (cf. (3) and (5)). The non-uniformity errors, which we observe to be small in our numerical experiments, serve as placeholders for the, potentially, larger errors that appear in the discrete a priori learning problem due to the discrepancy between the discretization errors between fine and coarse grid (cf. (2) and (6)).

DISCRETE A PRIORI LEARNING

In our simulations, we set $\mathrm{Pr} = 1$ and $\Lambda = 2$ and investigate $\mathrm{Ra} \in \{10^k\}_{k=8}^{13}$. We integrate (1) in time using an explicit low-storage third-order Runge-Kutta scheme and in space using an energy-conserving second-order finite difference method on a staggered grid. The CFL condition determines the time step size δt as a function of Ra and the spatial step sizes $\delta x = 2^{-n}$ and δz. Since resolving the boundary layer improves the fidelity of the simulations, we use a non-uniform grid in the wall-normal direction with the $n_z = 2^n + 1$ grid points distributed according to a tanh profile, and the level of refinement chosen according to the Prandtl-Blasius (PB) theory developed in [7]. A hybrid MPI-openMP decomposition is used for parallelisation. We refer to [6] for more details.

We define a filtering operation on the 'fine' spatial-grid, denoted by G_δ, using a numerical implementation of the non-uniform product Gaussian filter described above. The total discrete filtering operation is the composition of the Gaussian filter with a 'projection' onto the coarse gird, denoted by G_Δ, with horizontal step size $\Delta x = 2^c \delta x$ and number of vertical grid points $N_z = 2^{-c} n_z$. The coarse time step size $\Delta t = M\delta t$, $M \in \mathbb{N}$, is chosen according to the CFL condition.

Denote by $\Phi_\delta : X_\delta \to X_\delta$ and $\Phi_\Delta : X_\Delta \to X_\Delta$ the fine grid and uncorrected coarse grid one-step solution maps, respectively. The fine grid solution $\mathbf{x}^\delta : \mathbb{N} \to X_\delta$ satisfies $\mathbf{x}^\delta_{n+1} = \Phi_\delta(\mathbf{x}^\delta_n)$. Noting that the M-times composition Φ^M_δ and Φ_Δ have comparable time scales, we find

$$\overline{\mathbf{x}^\delta_{n+M}} = \Phi_\Delta\left(\overline{\mathbf{x}^\delta_n}\right) + \nabla^\Delta\cdot\boldsymbol{\mathcal{T}}\left(\mathbf{x}^\delta_n\right) + \mathbf{e}^{\delta,\Delta}_n\,, \qquad (6)$$

where $\nabla^\Delta\cdot$ denotes the coarse grid divergence operator and $\mathbf{e}^{\delta,\Delta}$ arises due to the i) non-uniformity of the filter and ii) discrepancy between the fine and coarse time and space-grid discrete differential operators. The parametric coarse grid one-step solution map $\Phi_{\theta,\Delta} : X_\Delta \to X_\Delta$ is defined using $\boldsymbol{\mathcal{T}}_\theta$, so that the coarse grid solution $\overline{\mathbf{x}}^\Delta_\theta : \mathbb{N} \to X_\Delta$ satisfies

$$\overline{\mathbf{x}}^\Delta_{\theta,m+1} = \Phi_{\theta,\Delta}(\overline{\mathbf{x}}^\Delta_{\theta,m+1}) := \Phi_\Delta(\overline{\mathbf{x}}^\Delta_{\theta,m+1}) + \nabla^\Delta\cdot\boldsymbol{\mathcal{T}}_\theta(\overline{\mathbf{x}}^\Delta_{\theta,m+1})\,.$$

We then define the supervised learning problem as above.

NUMERICAL EXPERIMENTS

We will perform a priori and a posteriori tests of the NN closure model and compare it with the null, Clark, inverse-filtering, and dynamic Smagorinsky SGS models. Furthermore, we will investigate whether the NN SGS model can extrapolate to different Ra and c. In Figure 1, we provide an a posteriori test of Nu for $c = 4$ at $\mathrm{Ra} = 10^{12}$. This result shows favorable comparison of the NN closure with DNS reference computed on the fine grid with $2^{13} \times 2^{12}$ points.

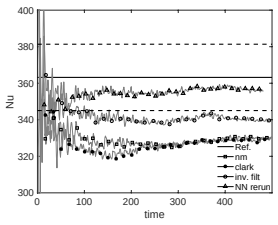

Figure 1: Running time average of Nu for $c = 4$ at $\mathrm{Ra} = 10^{12}$.

Acknowledgments. This research has received funding from the European Research Council (ERC) under the European Union's Horizon 2020 research and innovation programme (grant agreement No 882340).

REFERENCES

[1] Foias, C., Manley, O. and Temam, R. Attractors for the Bénard problem: existence and physical bounds on their fractal dimension. Nonlinear Anal. Theory Methods Appl.. **11**, 939-967 (1987)

[2] Cao, Y., Jolly, M. and Titi, E. A Determining Form for the 2D Rayleigh-Bénard Problem. ArXiv Preprint 1907.00387. (2019)

[3] Charles R. Doering Turning up the heat in turbulent thermal convection. PNAS. **117**, 9671-9673 (2020)

[4] Otto, F., Pottel, S. amd Nobili, C. Rigorous Bounds on Scaling Laws in Fluid Dynamics. Mathematical Thermodynamics Of Complex Fluids: Cetraro, Italy 2015. pp. 101-145 (2017)

[5] Zhang, H., Harlim, J. and Li, X. Error bounds of the invariant statistics in machine learning of ergodic Itô diffusions. Phys. D: Nonlinear Phenom.. **427** pp. 133022 (2021)

[6] Hasslberger, J., Cifani, P., Chakraborty, N. and Klein, M. A direct numerical simulation analysis of coherent structures in bubble-laden channel flows. J. Fluid Mech.. **905** pp. A37 (2020)

[7] Shishkina, O., Stevens, R., Grossmann, S. and Lohse, D. Boundary layer structure in turbulent thermal convection and its consequences for the required numerical resolution. New J. Phys.. **12**, 075022 (2010)

WORKSHOP
Direct and Large-Eddy Simulation 13
October 26th-29th 2022, Udine, Italy

MACHINE-ASSISTED SUBGRID-SCALE MODELLING FOR LARGE EDDY SIMULATION-PROBABILITY DENSITY FUNCTION APPROACHES

Tin-Hang Un[1], **Salvador Navarro-Martinez**[1]
[1] Department of Mechanical Engineering
Imperial College London, United Kingdom
tin.un17@imperial.ac.uk, s.navarro@imperial.ac.uk

INTRODUCTION

The application of Large Eddy Simulations (LES) to multi-physics problems, such as reactive, multi-phase flows and magneto-hydrodynamics (MHD), requires models for the non-linear sub-grid terms, including chemical reaction, phase change, non-ideal equation of state, etc. These models become less and less general and are very case-specific (e.g. finite-rate chemistry, dilute sprays). Some of these phenomena violate the assumption of isotropy of small scales (e.g. MHD).

The sub-grid probability density function (PDF) approach provides a unified model for complex multi-physics flows as non-linear terms are closed directly by a sub-grid PDF. It has proven successful in modelling reactive flows with LES [1]. The only model needed is the Langevin model [2] which transports the PDF and accounts for the sub-grid pressure gradient and molecular diffusion.

The most commonly used Langevin model is the Simplified Langevin Model (SLM) [2]. However, this assumes isotropy of the small scales and uses 40-year-old RANS-based closures and parameters. The Generalised Langevin Model (GLM) [2] is theoretically more complete, but no general closures have been proposed in the literature. *Can we do better?*

This paper proposes the use of deep neural network (DNN) to model the closures of the GLM. DNN has been used to model sub-grid stresses in LES (e.g. [3, 4]) with good degree of generality. The present work extends this to predicting the Langevin tensor and dissipation rate. The final model is a parameter-free sub-grid model that can be implemented in multi-physics LES-PDF simulations.

FORMULATION

In LES-PDF method, a sub-grid PDF $f_{\boldsymbol{\phi}}$ gives the likelihood of finding a point which has the flow state of $\boldsymbol{\phi} = \boldsymbol{\psi}$ within a filter width Δ at a particular position and time $(\mathbf{x}, t)$. It is formally defined as the convolution of Dirac delta function with a spatial filter $\mathcal{G}$:

$$f_{\boldsymbol{\phi}}(\mathbf{x}, t; \boldsymbol{\psi}) = \int \left(\prod_i \delta(\phi_i(\mathbf{x}', t) - \psi_i) \right) \mathcal{G}(\mathbf{x} - \mathbf{x}', \Delta) \, \mathrm{d}\mathbf{x}' \ . \quad (1)$$

When ϕ contains the reactive scalars, f_ϕ is a joint-scalar PDF, when ϕ contains both velocities and scalars, it is a joint-velocity-scalar PDF, and so on. By definition, the filtered quantity $\bar{\phi}$ corresponds to the mean of the PDF, and the $\overline{\phi_i \phi_j}$ are the second moments. The filtered value of any arbitrary quantities is closed exactly as long as it only depends on the variables that are in the sample space of the PDF.

$$\overline{Q(\boldsymbol{\phi})} = \int Q(\boldsymbol{\psi}) f_{\boldsymbol{\phi}}(\boldsymbol{\psi}) \, \mathrm{d}\boldsymbol{\psi} \ . \quad (2)$$

This is advantageous as the Reynolds stresses are in closed form if the PDF contains velocities, and the chemical reactive term can be closed with a PDF containing all reactive scalars and a thermodynamic quantity. Therefore, if the appropriate variables are selected in the PDF, we only need a model for the PDF equation. No case-specific model is needed.

For brevity in illustration of concept, this work will focus on a joint-velocity PDF, i.e. $\boldsymbol{\phi} = \mathbf{u}$. Since the sub-grid PDF is a high-dimensional system, it is usually solved using Monte Carlo methods, with an ensemble of either N Lagrangian particles [5] or N Eulerian fields [6, 7]:

$$f_{\mathbf{u}}(\mathbf{x}, t; \mathbf{v}) \approx \frac{1}{N} \sum_{n=1}^{N} \prod_{i=1}^{3} \delta(\mathcal{U}_i^n(\mathbf{x}, t) - v_i) \ . \quad (3)$$

For a Lagrangian particle $(\boldsymbol{\mathcal{X}}^n(t), \boldsymbol{\mathcal{U}}^n(t))$, the SDEs are

$$\begin{aligned} \mathrm{d}\mathcal{X}_i^n &= \mathcal{U}_i^n \mathrm{d}t \ , \\ \mathrm{d}\mathcal{U}_i^n &= \left(-\frac{1}{\rho} \frac{\partial \bar{p}}{\partial x_i} + \nu \frac{\partial^2 \bar{u}_i}{\partial x_j x_j} + G_{ij}(\mathcal{U}_j^n - \bar{u}_j) \right) \mathrm{d}t + \sqrt{C_0 \epsilon} \, \mathrm{d}W_i \ . \end{aligned} \quad (4)$$

For a stochastic field $\boldsymbol{\mathcal{U}}^n(\mathbf{x}, t)$, the SPDE is

$$\frac{\mathrm{d}\mathcal{U}_i^n}{\mathrm{d}t} + \frac{\partial \mathcal{U}_i^n \mathcal{U}_j^n}{\partial x_j} = -\frac{1}{\rho} \frac{\partial \bar{p}}{\partial x_i} + \nu \frac{\partial^2 \bar{u}_i}{\partial x_j x_j} + G_{ij}(\mathcal{U}_j^n - \bar{u}_j) + \sqrt{C_0 \epsilon} \, \frac{\mathrm{d}W_i}{\mathrm{d}t} \ . \quad (5)$$

W_i is a Wiener process (white noise), which has the properties of $\overline{W_i} = 0$, $\overline{W_i}^2 = \mathrm{d}t$, and $\overline{W_i W_j} = 0$ if $i \neq j$. G_{ij} and C_0 are the Langevin model coefficients. The G_{ij} term acts to shrink the PDF towards its mean and represents the effect of mixing. Conversely, the stochastic term widens the PDF and morphs it towards a joint normal distribution. The SLM reads

$$G_{ij} = -2.075 \, \frac{\epsilon_{sgs}}{k_{sgs}} \delta_{ij}, \quad C_0 = 2.1, \quad \epsilon_{sgs} = 1.05 \, \frac{{k_{sgs}}^{1.5}}{\Delta} \ , \quad (6)$$

and $k_{sgs} = \overline{u_i' u_i'}/2$ can be obtained from the PDF using (2). This implies that G is a time scale of which the fluctuating velocities return to their mean. Notice that the model constants -2.075 and 2.1 were calibrated in RANS context.

We further study the Langevin model by comparing the Reynolds stress equation to the second moment equation. Note that this work is restricted to incompressible flows, but the methodology can be extended to compressible case.

Exact Reynolds stress equation:

$$\frac{\bar{D}\overline{u_i'u_j'}}{Dt} = -\overline{u_i'u_k'}\frac{\partial \overline{u_j}}{\partial x_k} - \overline{u_j'u_k'}\frac{\partial \overline{u_i}}{\partial x_k} - \frac{\partial \overline{u_i'u_j'u_k'}}{\partial x_k} - \frac{1}{\rho}\overline{u_i'\frac{\partial p'}{\partial x_j}} + \overline{u_j'\frac{\partial p'}{\partial x_i}} + \nu\overline{u_i'\frac{\partial^2 u_j'}{\partial x_k x_k}} + \overline{u_j'\frac{\partial^2 u_i'}{\partial x_k x_k}} \,. \quad (7)$$

Second moment of the LES-PDF system:

$$\frac{\bar{D}\overline{u_i'u_j'}}{Dt} = -\overline{u_i'u_k'}\frac{\partial \overline{u_j}}{\partial x_k} - \overline{u_j'u_k'}\frac{\partial \overline{u_i}}{\partial x_k} - \frac{\partial \overline{u_i'u_j'u_k'}}{\partial x_k} + G_{ik}\overline{u_j'u_k'} + G_{jk}\overline{u_i'u_k'} + C_0\epsilon\delta_{ij} \,, \quad (8)$$

where $\bar{D}/Dt$ is the total derivative with mean velocity, δ_{ij} is the identity tensor, and ϵ is the turbulent dissipation rate,

$$\epsilon = \frac{1}{2}\epsilon_{ii} = \nu\overline{\frac{\partial u_i'}{\partial x_k}\frac{\partial u_i'}{\partial x_k}} \,. \quad (9)$$

It is clear that G_{ij} and C_0 are modelling the pressure transport and molecular diffusion terms as they cannot be closed by the PDF formulation. Since we are using a joint-velocity PDF, the Reynolds stress production and transport terms are closed automatically.

DEEP NEURAL NETWORK

Equating (7) and (8), and with the definition of ϵ (9), there are seven equations to solve six G_{ij} (assume G_{ij} is symmetric) and ϵ, while C_0 is obtained using the realisibility constraint given by [2] below. Hence, the problem is well defined.

$$G_{ij}\overline{u_i'u_j'} + \frac{3}{2}C_0\epsilon = -\epsilon \,. \quad (10)$$

We constructed three Multilayer-Perceptrons DNNs to perform regression on $\epsilon(\overline{u_i'u_j'}, \partial\bar{u}_i/\partial x_j, \Delta)$, $G_{ij}(\overline{u_i'u_j'}, \partial\bar{u}_i/\partial x_j, \epsilon)$, and jointly on ϵ and G_{ij}, respectively. All inputs to the DNNs can be obtained from the particle or field system using (2) and hence are known in a LES-PDF simulation.

For good performance and universality, the DNN should have a sufficient number of units in a layer to allow feature extraction and have multiple layers for capturing non-linearity of the target function. However, it must remain small for computational cost and to prevent the model from overfitting the data due to too many degrees of freedom.

Data used in this study are obtained from the JHTDB Turbulence Database [8]. A set of forced isotropic turbulence DNS of domain size $2\pi\times2\pi\times2\pi$ with different Re_λ are chopped into boxes corresponding to LES grids with different Δ. Table 1 confirms that the DNS is well resolved, and that the chosen filter width lies between the integral and Kolmogorov length scales. The last two terms on the RHS of (7) are computed and filtered using a box filter.

In order to yield physical results, ϵ must be positive. This is enforced by the `softplus` activation function at the output node. Also, the model must be rotational invariant. We examined 2 methods of enforcing this condition, the first being rotating all training data by 90 in all directions (a total of 24 combinations), while the second method is to convert all input tensors into their invariants, such as trace and determinant.

Re_λ	η/h	Δ/h	ℓ/Δ
418	0.456	9	24.7
418	0.456	31	7.17
611	0.902	31	29.3
1250	0.650	65	24.9

Table 1: Summary of DNS data used. h, ℓ, λ, and η refers to the DNS grid size, integral length scale, Taylor microscale, and the Kolmogorov length scale, respectively.

RESULTS

Figure 1 shows two example results of the DNN prediction on ϵ with $Re_\lambda = 433$. Both data were not seen by the DNN before. The DNN shows good agreement with the DNS data and outperforms the SLM in both filter widths. This result is important because ϵ is the variable that controls the strength of the Wiener process. Further training will be conducted with anisotropic data (e.g. boundary-layer flow and MHD) and be extended to higher Re.

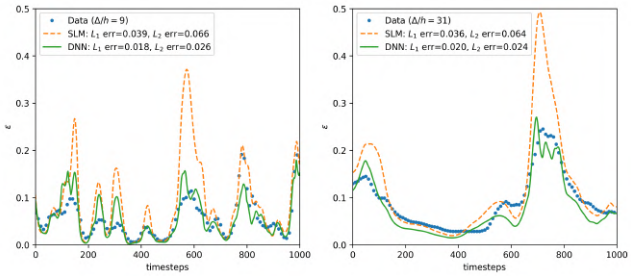

Figure 1: Comparison of DNN and SLM predicted dissipation rate for 1000 DNS timesteps.

In conclusion, the *a priori* result indicates that the present model yields good prediction of the Langevin model with various filter widths. It is parameter-free, general, and can be applied to both particle-based and field-based LES-PDF implementations for complex multi-physics problems.

REFERENCES

[1]Haworth, D.C. : Progress in probability density function methods for turbulent reacting flows, *Prog. Energy Combust. Sci.*, **36**(2), 168-259 (2010).

[2]Haworth, D.C. & Pope, S.B. : A generalized Langevin model for turbulent flows, *Phys. Fluids*, **29**, 387 (1986).

[3]Prat, A., Sautory, T., & Navarro-Martinez, S. : A Priori Subgrid Modelling Using Artificial Neural Networks, *Int. J. Comut. Fluid Dyn.*, **34**(6), 397–417 (2020).

[4]Beck, A., Flad, D., & Munz, C.D. : Deep neural networks for data driven LES closure models, *J. Comput. Phys.*, **398**, 108910 (2019).

[5]Pope, S.B. : PDF methods for turbulent reactive flows, *Prog. Energy Combust. Sci.*, **11**(2), 119-192 (1985).

[6]Valiño, L. : A field Monte Carlo formulation for calculating the probability density function of a single scalar in a turbulent flow. *Flow Turbul. Combust.*, **60**, 157–172 (1998).

[7]Soulard, O. and Sabel'nikov, V. : Eulerian Monte Carlo method for the joint velocity and mass-fraction probability density function in turbulent reactive gas flows. *Combust. Explos. Shock Waves*, **42**(6), 753–762 (2006).

[8]Perlman, E., Burns, R., Li, Y. and Meneveau, C. : Data Exploration of Turbulence Simulations using a Database Cluster. *Supercomputing SC07, ACM, IEEE* (2007).

WORKSHOP
Direct and Large-Eddy Simulation 13
October 26th-29th 2022, Udine, Italy

NUMERICAL SIMULATION OF LEFT ATRIUM HEMODYNAMICS: UNCERTAINTY QUANTIFICATION WITH RESPECT TO INFLOW CONDITIONS

E. Durán[1], M. García-Villalba[1], P. Martínez-Legazpi[2], A. Gonzalo[3], E. McVeigh[4], A.M. Kahn[5], O. Flores[1], J. Bermejo[6], J. C. del Álamo[3]
[1] Bioengineering and Aerospace Eng. Dept., Universidad Carlos III de Madrid, Spain
[2] Mathematical Physics and Fluids Dept., UNED, Spain
[3] Dept. of Mechanical Engineering & Center for Cardiovascular Biology, University of Washington, US
[4] Bioengineering Dept., University of California San Diego, US
[5] Dept. of Cardiology, University of California San Diego, US
[6] Hospital General Universitario Gregorio Marañón, Spain
edduranv@ing.uc3m.es

INTRODUCTION

Cardiovascular diseases are the leading cause of mortality worldwide. In particular, ischemic stroke affects over 18 million people each year. It is estimated that 30% of these strokes are caused by thrombi generated in the left atrium (LA) of patients with atrial fibrillation (AF), the most common arrhythmia. Furthermore, up to an additional 30% of all ischemic strokes are suspected to be atriogenic in patients with subclinical AF or normal cardiac rhythm. Most of these thrombi are formed inside the left atrial appendage (LAA), a small saccular protuberance whose anatomy and hemodynamics vary significantly among patients. However, current medical procedures to estimate ischemic stroke risk are based on population demographics and do not consider patient-specific information about LA haemodynamics, a crucial causal thrombosis factor.

Computational fluid dynamics (CFD) analysis based on patient-specific medical images is a powerful tool for investigating LA thrombosis. This approach is used to explore different aspects of LA hemodynamics, e.g., LAA blood stasis (LAA) [1], non-Newtonian effects inside the LAA [2], or the influence of pulmonary vein (PV) flow rates and orientation [3], [4]. Recent studies have provided useful guidance for setting up models and boundary conditions that precisely reproduce each patient's hemodynamics representative of a specific time or physiological state. However, these circumstances can vary significantly during a patient's daily life, making it necessary to consider uncertainty when computing risk scores. Notably, a patient's body position significantly affects how much flow comes into the LA from left and right pulmonary veins (PV) [5]. Here, we analyze how this uncertainty in the PV flow split affects LA hemodynamics and, in particular, LAA stasis.

METHODOLOGY

We perform CFD simulations of LA hemodynamics using an in-house immersed boundary solver (TUCAN) on patient-specific anatomies obtained from 4D CT scans [1]. We study N=9 patients with different atrial volumes and functions (see table 1), including normal rhythm and AF, and patients with and without histories of LAA thrombus and transient ischemic attacks.

Case	$\bar{V}_{LA}$	EF_{LA}	$\bar{V}_{LAA}$	EF_{LAA}	SR	T/TIAs
1	86ml	45%	6.9ml	52%	Yes	No
2	70ml	46%	4.85ml	50%	Yes	No
3	115ml	40%	14.3ml	43%	Yes	No
4	84ml	44%	3.1ml	66%	Yes	No
5	96ml	43%	3.6ml	52%	Yes	No
6	51ml	54%	4ml	68%	Yes	No
7	145ml	23%	10.7ml	22%	No	TIAs
8	157ml	10%	15.5ml	21%	No	T
9	180ml	23%	22ml	20%	No	T

Table 1: Cases and main physiological parameters, including mean LA and LAA volumes ($\bar{V}$) and ejection fractions (EF) and information about cases in sinus rythm (SR) and cases with thrombus or history of TIAs (T/TIAs).

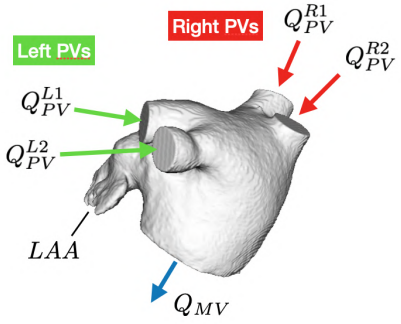

Figure 1: Flow balance in the LA. All the flow coming through left (Q_{PV}^{Li}) and right (Q_{PV}^{Ri}) pulmonary veins exits through the mitral valve (Q_{MV}).

The moving LA geometry is obtained after segmenting and meshing the 4D anatomical images. The outflow through the mitral valve (MV) is computed from the variation of the left ventricle volume, also obtained from the 4D CT scans. The total inflow through the PVs is obtained by applying mass conservation in the LA (see figure 1), considering the variation

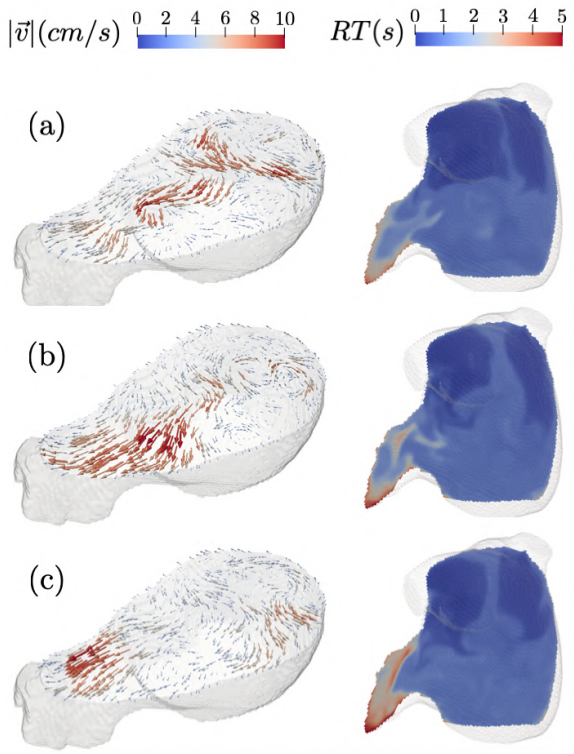

Figure 2: Flow velocity field contained in a cross plane parallel to the mitral valve (left) and residence time in a plane perpendicular to the mitral valve (right) for even (a), 45-55% (b) and 40-60% (c) splits. All the figures correspond to case 3 and represent the same instant, during the atrial diastole.

of the LA volume and the MV outflow:

$$Q_{PV} = \frac{\partial V_{LA}}{\partial t} + Q_{MV}. \tag{1}$$

The specific flow rates through each PV inlet depend on the impedances of the different branches of the pulmonary tree, introducing uncertainty. We perform simulations with different flow split between the pulmonary veins to investigate how this uncertainty affects CFD predictions of LAA blood stasis. In particular, we consider 50-50% left-right flow split and 45-55% and 40-60% splits.

We use blood residence time (RT) to quantify blood stasis. The RT is computed solving the transport equation

$$\frac{\partial RT}{\partial t} + \vec{v} \cdot \nabla RT = 1, \tag{2}$$

where $\vec{v}$ is the flow velocity, with homogeneous initial and inflow conditions. Thus, RT indicates the time that each fluid particle spends in the LA. The discretization of the RT equation is performed using a WENO scheme to minimize numerical diffusivity while avoiding spurious oscillations near sharp fronts.

RESULTS AND DISCUSSION

The flow split through the PVs modifies the flow patterns in the LA body and the LAA (figure 2), affecting blood stasis as measured by RT in the LA and, in particular, in the LAA . The RT averaged inside the LAA volume, RT_{LAA}, varies appreciably for different flow split conditions, and this variability

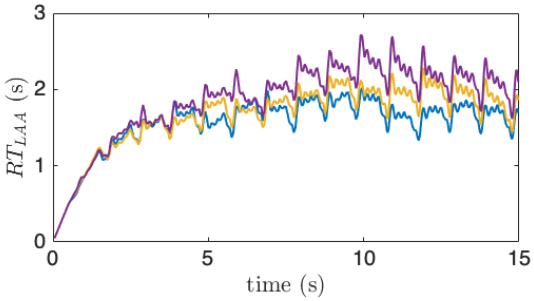

Figure 3: Mean LAA residence time dynamics from case 3 for even (blue), 45-55% (yellow) and 40-60% (purple) PV flow splits.

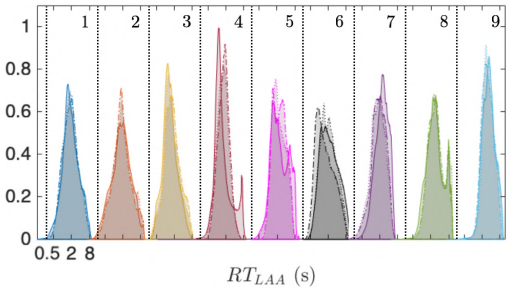

Figure 4: Probability distributions of LAA residence time along three cardiac cycles (13^{th} to 15^{th}) for cases 1 to 9 with even (−), 45-55% (−·) and 40-60% (−−) splits.

can be larger than the beat-to-beat variability (see example in figure 3). Besides, the effect of the flow split on LAA stasis differs from patient to patient (figure 4). Overall, these results suggest that PV flow split uncertainty should be considered when estimating the patient-specific risk of LAA thrombosis based on CFD simulations of LA hemodynamics. A detailed evaluation of these results and their implications will be discussed in the presentation.

ACKNOWLEDGMENTS

This work was supported by grants from the Regional Government of Madrid (Spain), MECD (Spain), the NHLBI, and the American Heart Association. Computational time provided by RES (Calendula) is gratefully acknowledged.

REFERENCES

[1]García-Villalba, M. et al. : Demonstration of patient-specific simulations to assess left atrial appendage thrombogenesis risk. *Frontiers in Physiology*, **12**, 596596 (2020).

[2]Gonzalo, A. et al. : Non-Newtonian blood rheology impacts left atrial stasis in patient-specific simulations, *Int. J. Meth. Biomed. Engng.*, e3597 (2022).

[3]Lantz, J. et al. : Impact of pulmonary venous inflow on cardiac flow simulations: comparison with in vivo 4D flow MRI. *Ann. Biomed. Eng.*, **47**, 413-424 (2019).

[4]Mill, J. et al. : In-Silico Analysis of the Influence of Pulmonary Vein Configuration on Left Atrial Haemodynamics and Thrombus Formation in a Large Cohort. *International Conference on Functional Imaging and Modeling of the Heart*, Springer, 605-616 (2021).

[5]Wieslander, B. et al. : Supine, prone right and left gravitational effects on human pulmonary circulation. *Journal of Cardiovascular Magnetic Resonance*, **21**, 29 (2019).

WORKSHOP
Direct and Large-Eddy Simulation 13
October 26th-29th 2022, Udine, Italy

UNCERTAINTY QUANTIFICATION OF LES FOR THE BUOYANCY-DRIVEN MIXING PROCESS BETWEEN TWO MISCIBLE FLUIDS USING STAGGERED PCE AND KLE – DIFFERENTIALLY HEATED CAVITY OF ASPECT RATIO 4

Philipp J. Wenig[1], **Stephan Kelm**[2] **and Markus Klein**[1],
[1] Institute of Applied Mathematics and Scientific Computing, University of the Bundeswehr Munich, Werner-Heisenberg-Weg 39, 85577 Neubiberg, Germany
[2] Institute for Energy and Climate Research, Forschungszentrum Jülich GmbH, 52425 Jülich, Germany
philipp.wenig@unibw.de

INTRODUCTION

The investigation of uncertainties in large-scale CFD-applications requires methods that efficiently provide reliable stochastic results with a justifiable number of calculation runs. Therefore, Staggered Polynomial Chaos Expansions (SPCE) along with Staggered Karhunen-Loève Expansions (SKLE) are proposed in this paper as new Uncertainty Quantification (UQ) methods, which can provide high result accuracy with efficient resource utilization and bring great flexibility in stochastic model construction. The presented UQ-methods are developed based on the investigation of a buoyancy-driven mixing process between two miscible fluids within the Differentially Heated Cavity (DHC). Models for stochastic processes at hand are derived from Large Eddy Simulations (LES) by means of SPCE and SKLE. Current results include the description of the random temporal evolution of Quantities of Interest (QoI). The work will be extended to the comparison with reference results and the calculation of error estimates in order to accentuate the proposed method.

CFD-METHODS

Low-Mach number flow of two Newtonian viscous fluids within the DHC of aspect ratio 4 is investigated by means of 3D-LES. The DHC is filled with air and 40vol% of helium in the upper third, as shown in a schematic sketch for the case setup in Figure 1. Calculations are performed by using the finite volume code OpenFOAM. The Prandtl numbers are $Pr_{Air} = 0.71$ and $Pr_{He} = 0.66$. The Rayleigh number Ra , which is derived from material values for air, is equal to 2×10^9. Temporal advancement is achieved by the Crank-Nicolson scheme. The CFL number is always below the value of 0.5. For modeling of the sub-grid scale effects in the LES the WALE-model and the gradient flux approach with a turbulent Prandtl- and Schmidt-number $Pr_t = Sc_t = 0.85$ is applied. The spatial grid resolution is chosen according to [1]. The uncertain input parameters $\boldsymbol{\mathcal{Q}}$ comprise the temperature difference between the left and right wall ΔT, the top and bottom wall temperatures $T_{b/t}$, the vertical temperature gradient at the left and right wall $T_y|_{l,r}$, the initial helium stratification via ΔX and the molecular diffusion coefficient D.

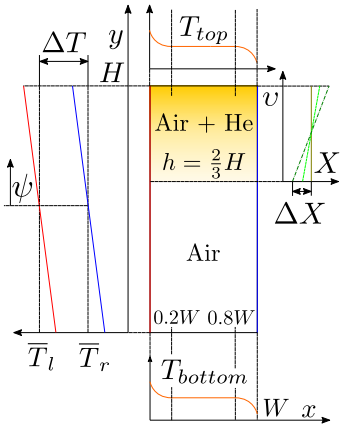

Figure 1: Schematic sketch of the DHC with uncertain parameters.

UQ-METHODS

Non-intrusive PCE's together with KLE's [2, 3] were applied for the approximation of stochastic processes $\mathcal{R}(t,\omega) = R(t,\boldsymbol{\mathcal{Q}})$ through the discrete KLE-method with K terms and numerically generated orthogonal polynomials $\Psi_p(\boldsymbol{\mathcal{Q}})$ with corresponding time-dependent expansion coefficients $\alpha_p^K(t)$:

$$\mathcal{R}^{P,K}(t,\omega) = \mu_{\mathcal{R}}(t) + \sum_{p=1}^{P} \left[\alpha_p^K(t)\right] \Psi_p(\boldsymbol{\mathcal{Q}}) \ . \qquad (1)$$

The PCE's are truncated after P terms. The expansion coefficients are estimated by using discrete projection by means of Gauss quadrature with quadrature order of 5. The approach is extended to the new method, which proposes the utilization of Stochastic Spectral Methods in a staggered manner. When individual parameters or parameter sets exhibit and are proven to have low mutual interaction behavior, these can be combined into N_c parameter clusters and independent stochastic response models $\mathcal{R}_{i_c}^{P,K}$ for each cluster are constructed. Finally, the individual models can be merged by summation of the overall staggered expectation $\left[\mu^{P,K}\right]^s$ and the overall staggered centered stochastic process $\left[\mathcal{R}_0^{P,K}\right]^s$ to the final

stochastic model $\left[\mathcal{R}^{P,K}\right]^s$:

$$\left[\mathcal{R}^{P,K}\right]^s = \left[\mu^{P,K}\right]^s + \left[\mathcal{R}_0^{P,K}\right]^s \quad , \quad (2)$$

$$\left[\mu^{P,K}\right]^s = R\left(t, \mathbb{E}\left[\boldsymbol{\mathcal{Q}}\right]\right) + \sum_{i_c}^{N_c} \left(\mathbb{E}\left[\mathcal{R}_{i_c}^{P,K}\right] - R\left(\mathbb{E}\left[t, \boldsymbol{\mathcal{Q}}\right]\right)\right) \quad , \quad (3)$$

$$\left[\mathcal{R}_0^{P,K}\right]^s = \sum_{i_c}^{N_c} \left(\mathcal{R}_{i_c}^{P,K} - \mathbb{E}\left[\mathcal{R}_{i_c}^{P,K}\right]\right) \quad . \quad (4)$$

$\left[\mu^{P,K}\right]^s$ is calculated through the sum of the response for the common expectation of input variables $R\left(t, \mathbb{E}\left[\boldsymbol{\mathcal{Q}}\right]\right)$ with the expectation shifts $\Delta_{i_c}^{P,K} = \mathbb{E}\left[\mathcal{R}_{i_c}^{P,K}\right] - R\left(\mathbb{E}\left[t, \boldsymbol{\mathcal{Q}}\right]\right)$, which are caused by individual parameter clusters. The model for the variance representation is built through the sum of the respective centered stochastic processes.

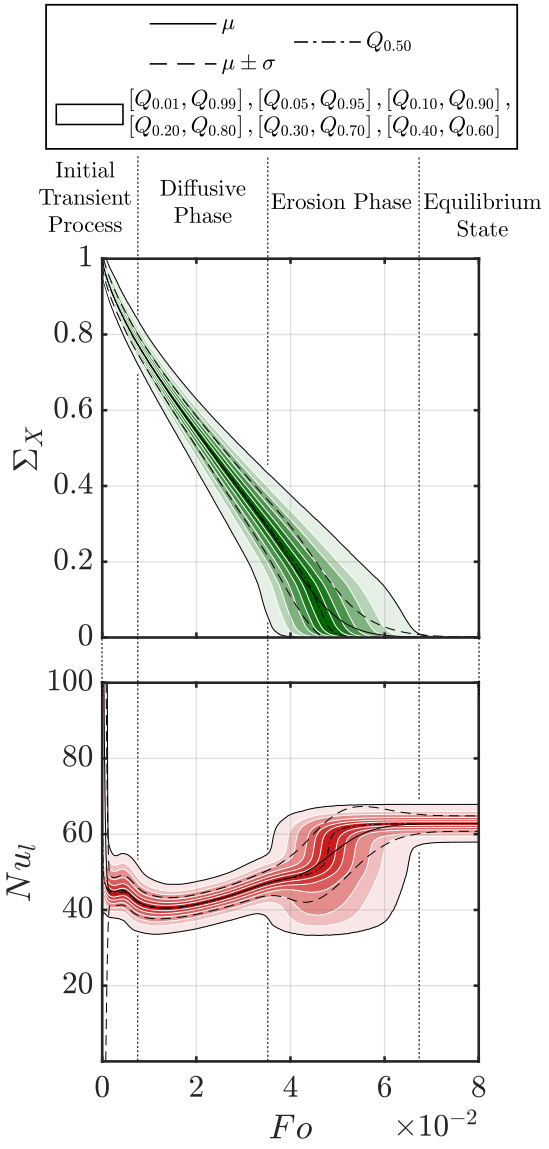

Figure 2: Stochastic process representations of the normalized mixture uniformity Σ_X and the left-wall Nusselt number Nu_l.

RESULTS

The proposed method is applied for the stochastic process representation of QoI, that characterize the underlying buoyancy-driven mixing process. Since the random input variables lead to mostly mutually independent variance contributions, stochastic models are calculated for every single random variable in a univariate manner. After the construction of the five single models, their combination according to Equation 2–4 yields the staggered stochastic models. Results are visualized by the expectation μ, the standard deviation σ along with quantiles Q or quantile intervals $[Q_i, Q_j]$ and plotted against the Fourier number Fo, which allows for the dimensionless description of time. In Figure 2 the stochastic processes of the normalized mixture uniformity Σ_X and the left-wall Nusselt number Nu_l are depicted and corresponding quantile intervals are highlighted in green and red, respectively. Σ_X indicates the progress of the mixing process. The inhomogeneous state of the mixture is characterized by $\Sigma_X = 1$ and the homogeneous state is achieved, if Σ_X is equal to 0. Convective heat transfer in the cavity is analyzed by Nu_l. The evolution of the mixture uniformity in Figure 2 reveals that the mixing process consists of the initial diffusive dissolution and the subsequent convective erosion of the helium layer. The transition to the convective erosion phase is evident from larger gradients of the mixture uniformity towards the end of the mixing process. Moreover, it is evident, that the duration of the mixing process is subject to considerable uncertainty. Through the consideration of the stochastic process of Nu_l, one can see, that a dynamic transient process takes place at the beginning. This is followed by the aforementioned diffusive dissolution phase with a narrow uncertainty band. Finally, the convective erosion occurs, which involves a larger uncertainty band due to the dynamic transition to the new equilibrium state.

CONCLUSIONS

If small interaction effects with respect to random responses occur between individual random variable sets, SPCE or SKLE are proven a promising UQ-method for large-scale CFD applications, since they allow for the investigation of a large number of random inputs and further model extensions at will. In addition, the proposed methodology for the stochastic model construction is distinguished through its efficiency by taking advantage of the high convergence rate of numerical integration methods like Gauss quadrature for individual low-dimensional random input spaces. This reduced the number of 105 simulation runs for the reference results to 21 simulation runs with consistent accuracy. Hence, staggered stochastic modeling facilitates tremendous savings of computing resources with simultaneous preservation of high accuracy.

REFERENCES

[1]Wenig, P.J.; Ji, R.; Kelm, S. and Klein, M., Towards Uncertainty Quantification of LES and URANS for the Buoyancy-Driven Mixing Process between Two Miscible Fluids - Differentially Heated Cavity of Aspect Ratio 4. *Fluids* 2021, 6, 161 (2021).

[2]Jivani et al.: Uncertainty quantification for a turbulent round jet using Multifidelity Karhunen-Loeve Expansions, *AIAA Scitech 2021 Forum*, 1–16 (2021).

[3]Huan et al.: Uncertainty propagation using conditional random fields in large-eddy simulations of scramjet computations , *AIAA Scitech 2019 Forum*, 1–17 (2019).

WORKSHOP
Direct and Large-Eddy Simulation 13
October 26th-29th 2022, Udine, Italy

DATA-DRIVEN POD-BASED MODELING FOR HIGH-FIDELITY COARSENING OF TWO-DIMENSIONAL RAYLEIGH-BENARD TURBULENCE

S.R. Ephrati[1], **P. Cifani**[1,2], **J. Leahy**[3], **E. Luesink**[1], **A.D. Franken**[1], **B.J. Geurts**[1,4]
[1] Department of Applied Mathematics, University of Twente, The Netherlands
[2] Gran Sasso Science Institute, Italy
[3] Department of Mathematics, Imperial College London, United Kingdom
[4] Faculty of Applied Physics, Eindhoven University of Technology, The Netherlands
s.r.ephrati@utwente.nl

INTRODUCTION

The transport of momentum in fluid dynamics induces interaction between small scale and large scale flow features. In geophysical fluid dynamics, characteristic length scales range from hundreds of kilometres down to the Kolmogorov scale. This implies that a good fluid-mechanical model requires in principle that all these scales are fully resolved, demanding very large computational grids. It is therefore a challenge to make simplifications to the fluid description in order to obtain a computationally feasible model. Such simplifications may be introduced by neglecting or averaging physical processes in the fluid model and subsequently employing coarse spatial or temporal computational settings. Due to the simplifications, the dynamics of either of these approaches contain inaccuracies when compared to that of the original, complete fluid model. A promising way to compensate for these discrepancies is by means of data-driven forcing, which we pursue in this study. One possible approach to facilitate data-driven forcing is by processing snapshots of high-resolution numerical results into an empirical basis of the solution space via proper orthogonal decomposition (POD).

In the presentation at the workshop, we anticipate to apply high-fidelity coarsening using data-driven POD-based reduced-order modeling to two-dimensional Rayleigh-Bénard turbulence. Subsequent uncertainty quantification will be carried out by means stochastic reduced-order modeling.

HIGH-FIDELITY COARSENING USING SUB-GRID DATA

An offline/online approach is used to obtain a reduced-order data-driven forcing term. Explicit knowledge of small-scale dynamics is acquired through offline high-resolution numerical simulations and is subsequently compared to coarse numerical results. This procedure yields spatio-temporal data that contain features *lacking* from a coarse numerical solution. These data are decomposed into spatial modes and corresponding time series via POD, accounting for the intended coarsening. The POD algorithm ensures that the spatial profiles are orthonormal and that the time series are mutually uncorrelated. These POD modes are added as a forcing term to a coarse discretization of the fluid model to arrive at a reduced-order model.

This data-driven POD-based approach was applied to the one-dimensional shallow water equations [1]. It was shown that zero-error pointwise agreement of the coarse numerical solution and the high-resolution simulation result is possible when all available POD modes are used in constructing the reduced-order model. In addition, the level of approximation of the original data set when applying different numbers of POD modes was investigated. It was shown that the inclusion of POD modes significantly reduces the error on coarse computational grids. An example, reconstructing the fine-grid numerical solution (512 grid points) by a forced coarse numerical simulation (32 grid points) is shown in Figure 1. By perturbing the initial conditions of the coarse numerical simulation, it was shown that applying the POD modes to a different data set still yielded significant error reduction. This implies that the time series corresponding to the POD modes are robust to some level of approximation and may be modeled to obtain accurate forcing terms.

UNCERTAINTY QUANTIFICATION THROUGH STOCHASTIC REDUCED-ORDER MODELING

Uncertainty is introduced in the coarsening since small-scale processes cannot be resolved well on coarse numerical grids. Due to the complex behaviour of these small scales, stochastic processes appear a natural tool to model these dynamics. In the key work [2], a stochastic reduced order model for fluid dynamics is derived by means of a variational principle. As a consequence, transport in ideal fluids can be perturbed stochastically, whilst retaining conserved quantities. This concept finds meaningful applications in geophysical fluid dynamics, since many geophysical fluid models can be derived from a variational viewpoint. Stochastic reduced-order modeling following this methodology has already been used for uncertainty quantification [3], where the two-dimensional Euler equations were studied. In a follow-up study [4], a decreased uncertainty was achieved by tailoring the stochastic processes that are coupled to the POD modes. Here, the stochastic processes were defined specifically to match certain statistical quantities of the measured POD time series. An example of uncertainty quantification using this method is given in Figure 2.

The approaches used in these studies motivate further use of stochastic reduced-order modeling of fluid flows with the purpose of quantifying uncertainty in simulations on coarse computational grids. We will show first results for Rayleigh-

Bénard convection in 2D at the workshop.

REFERENCES

[1]Ephrati, S.R., Luesink, E., Wimmer, G., Cifani, P. and Geurts, B.J.: Computational modeling for high-fidelity coarsening of shallow water equations based on subgrid data, *arXiv preprint, 10.48550/ARXIV.2110.07966*.

[2]D.D. Holm, Variational principles for stochastic fluid dynamics. *Proceedings of the Royal Society A: Mathematical, Physical and Engineering Sciences*, 471(2176):20140963.

[3]C. Cotter, D. Crisan, D.D. Holm, W. Pan and I. Shevchenko, Numerically Modeling Stochastic Lie Transport in Fluid Dynamics. *Multiscale Modeling & Simulation*, 17(1):192–232.

[4]Ephrati, S.R., Cifani, P., Luesink, E., and Geurts, B.J.: Data-driven stochastic Lie transport modelling of the 2D Euler equations, *arXiv preprint, 10.48550/ARXIV.2204.02193*

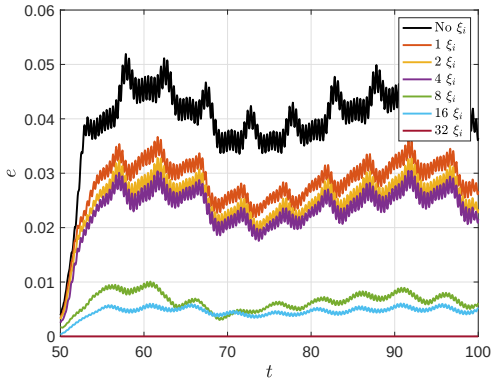

Figure 1: Pointwise L_2 error over time when reconstructing the high-resolution solution (512 grid points) of the one-dimensional shallow water equations on a coarse grid (32 grid points), using an increasing number of POD modes (denoted by ξ_i).

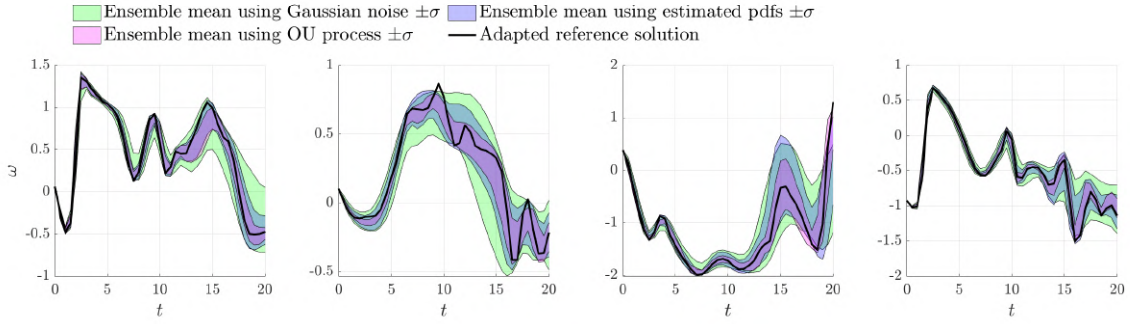

Figure 2: Vorticity of the two-dimensional Euler equations on a bounded unit square, measured on four points in the domain. The black lines show the development of the deterministically forced coarse solution, which provides the reference. The POD modes are coupled to stochastic processes to yield stochastic forcing. The green band is generated using Gaussian noise. The blue band uses the estimated distributions such that moments of the POD time series match. The purple band uses Ornstein-Uhlenbeck processes such that the temporal correlation of the time series match. The results for each method are generated from an ensemble of 200 realizations.

Session: Bubbly flow

Wednesday, October 26, 2022

16:30 – 17:45

WORKSHOP
Direct and Large-Eddy Simulation 13
October 26th-29th 2022, Udine, Italy

VOLUME CONSERVATION METHODS FOR VOF-BASED LONG-TERM SIMULATIONS OF TURBULENT BUBBLE-LADEN FLOWS ON COARSE GRIDS

E. Trautner[1,*], J. Hasslberger[1], P. Cifani[2,3] and M. Klein[1]
[1] Department of Aerospace Engineering, University of the Bundeswehr Munich, Germany
[2] Faculty EEMCS, University of Twente, The Netherlands [3] Gran Sasso Science Institute, L'Aquila, Italy
*elias.trautner@unibw.de

INTRODUCTION

Turbulent bubble-laden flows are an integral part of numerous technical applications. The recent increase in computational power has allowed first large-scale Direct Numerical Simulations (DNS) of reduced-complexity bubbly flows at limited Reynolds numbers. However, bubbly flows in technical applications are usually characterized by high Reynolds numbers. Therefore, Large Eddy Simulation (LES) comes into focus for the design of technical devices. However, multiphase flow LES is still in an early development stage.

One of the most severe challenges for this field is the significant under-resolution of the interface dynamics, which leads to a variety of issues with numerical algorithms designed for two-phase flows, e.g. imprecise curvature computation or violation of the volume conservation. This work discusses the latter in the context of Volume-of-Fluid (VOF)-based simulations of turbulent bubble-laden channel flows. In general, the VOF method is known to exhibit significantly better volume conservation properties than, e.g., the Level-set or Front-tracking methods. Still, as will be demonstrated, minimal volume errors on a time-step level can add up to severe errors when bubbly flows are simulated in periodic domains and on coarse grids. The problem is reinforced for long simulation intervals, which are indispensable to compute converged statistics, in particular for quantities involving the gas volume fraction.

This work firstly demonstrates the problem by investigating the volume errors for a number of coarse-grid test cases. Subsequently, two volume conservation strategies for eliminating the problem are presented. Finally, the resulting flow and bubble statistics for the methods are compared.

NUMERICAL METHOD AND FLOW CONFIGURATION

The study is performed using the state-of-the-art code "TBFsolver" [1], which is based on the one-fluid formulation of the incompressible Navier-Stokes equations and the Continuous-Surface-Force approach for computing surface tension. The variables are arranged on a staggered grid and a height function method is used to compute the interface curvature. To avoid numerical coalescence of the bubbles, a multiple-marker formulation [2] is used, i.e., an individual VOF marker function f_b is advected for each bubble b:

$$\frac{\partial f_b}{\partial t} + u_i \frac{\partial f_b}{\partial x_i} = 0. \tag{1}$$

Equation 1 is solved using a geometrical reconstruction and advection algorithm retaining a sharp interface [3]. A split-direction advection is used.

The investigated configuration (see Fig. 1a) is a vertical downflow channel of size $L_x = 8H$, $L_y = 2H$ and $L_z = 4H$, where H is the half width and x, y and z denote the stream-wise, the wall-normal and the span-wise direction. The x and z directions are periodic, whereas no-slip walls are prescribed in y-direction. The flow is controlled by a constant pressure gradient corresponding to a friction Reynolds number of $Re_\tau = 590$. A total of 780 freely deformable bubbles with an initial diameter of $d_b = 0.25H$ are considered, leading to a gas volume fraction of 10%. The domain is discretized using an equidistant cubic mesh. The grid resolution is intentionally coarse (LES-like), such that it corresponds to either $d_b/\Delta = 10$ or $d_b/\Delta = 12.5$. Both the density and dynamic viscosity ratio are set to 20, and the Eötvös number is varied between $Eo = 0.67$ and $Eo = 3.75$. For this setup, the former leads to nearly spherical bubbles, while the bubbles are wobbling and deformed to an ellipsoidal shape for the latter.

VOLUME CONSERVATION METHODS

The introduced method combines a multiple-marker formulation with a split advection algorithm. In this context, there are three root causes for the violation of volume conservation for the tracked gas phase:

1. Over- ($f_b > 1$) and undershoots ($f_b < 0$) of VOF values in single cells that are clipped to one or zero, respectively.

2. Resetting of cell VOF values to zero in cells with $0 < f_b < 1$, when no cell with $f_b = 1$ is detected within a region of $5 \times 5 \times 5$ cells around the respective cell.

3. Removal of small gas structures that can separate from the respective main bubble when high shear forces overcome the restoring surface tension force.

The first scenario can lead to both an increase and a decrease of gas volume, while the latter two can only lead to volume losses. The procedure explained in the second point is also used in comparable two-phase flow solvers. Under less challenging conditions (DNS-like resolution, lower Re_τ), the observed volume errors are negligible [1].

Figure 1b illustrates the global amount of gas volume loss for $Eo = 0.67$ and the two investigated resolutions. As the figure shows, several percent of the gas volume is lost during the

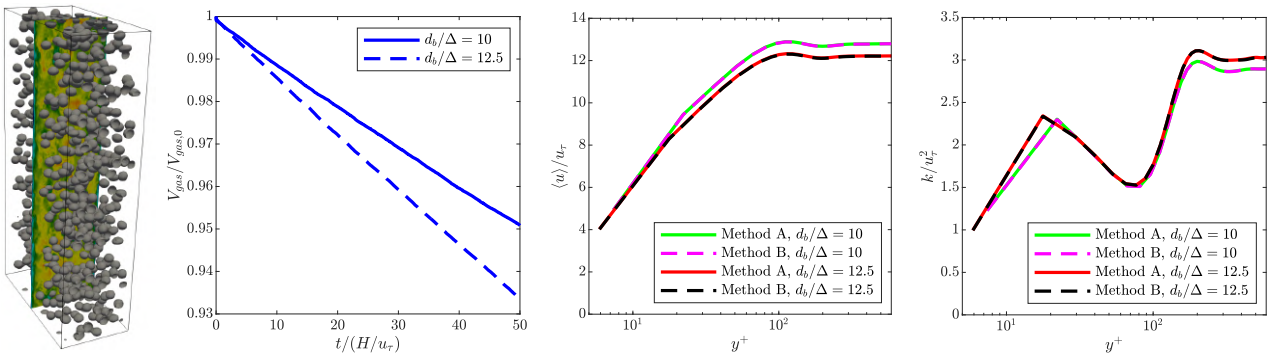

Figure 1: Investigated configuration (a); Relative error of the global gas volume over the normalized time (b); Average normalized stream-wise velocity profiles $\langle u \rangle / u_\tau$ (c); Average normalized turbulent kinetic energy profiles k/u_τ^2 (d). u_τ is the friction velocity.

investigated time interval. The global volume error depends on the error per cell, the number of cells and the number of time steps ($CFL = 0.2 = \text{const.}$), which interact in a non-linear manner. For the investigated setup, this gives rise to a slightly larger error for $d_b/\Delta = 12.5$.

On an individual basis, VOF over- and undershoots (1) could be treated by locally redistributing volume to neighbor cells instead of clipping the values to one or zero. However, this does not resolve the issues related to points 2 and 3. Since it is undesirable to perform two different volume correction steps, the methods introduced in the following compensate the total volume error originating from all three issues in each time step. The multiple marker formulation forms the basis for the methods, i.e., the correction is performed for each bubble individually. Both methods rely on the given circumstance that the volume conservation error is minimal for a single time step and only has an impact over a large number of time steps.

Method A uses a straightforward approach to correct the volume error ΔV_b^t for bubble b in time step t. All N cells with $\text{tol} < f_b < (1 - \text{tol})$ are identified. Then, the volume error is corrected by adding or subtracting $\Delta V_b^t / (N \cdot V_{cell})$ to the VOF values of these cells. For the investigated setup, $\text{tol} = 1 \times 10^{-4}$ has been used. This avoids additional over- and undershoots in the correction step.

Method B applies a more sophisticated, parameter-free technique. The evolution of a single bubble's volume can be expressed as

$$\frac{\mathrm{d}V_b}{\mathrm{d}t} = \int_{V_b} (\nabla \cdot \boldsymbol{u}) \, \mathrm{d}V. \tag{2}$$

Consequently, imposing a fictitious velocity field with $\nabla \cdot \boldsymbol{u} \neq 0$ allows to correct the volume error for the bubble. Assuming $\alpha = \nabla \cdot \boldsymbol{u}$, where α is a constant valid for one time step and a single bubble, Eq. 2 can be approximated as

$$\frac{V_b^{\text{corr.}} - V_b^t}{\Delta t} = \alpha V_b^t, \tag{3}$$

where $V_b^{\text{corr.}}$ is the correct bubble volume to be conserved. Since the volume error in Eq. 3 can be measured, α can be computed. Now, a velocity field with $\nabla \cdot \boldsymbol{u} = \alpha$ can be determined as

$$\boldsymbol{u} = \frac{\alpha}{3} \left(x - x_0, \quad y - y_0, \quad z - z_0 \right)^T, \tag{4}$$

where (x_0, y_0, z_0) denotes the center of the bubble. This velocity field is now used to perform an additional reconstruction and advection step for the bubble's VOF field. This can be interpreted as a slight dilatation (contraction) of the bubble for $V_b^t < V_b^{\text{corr.}}$ ($V_b^t > V_b^{\text{corr.}}$). It can be shown that this procedure preserves the bubble volumes to machine precision.

RESULTS

It is desirable that the volume conservation methods do not exhibit a notable influence on the flow and bubble behavior. One way to evaluate this is to compare the flow statistics resulting for the two different methods. Figure 1c shows the average stream-wise velocity profiles for the setups / methods at $Eo = 0.67$, while the respective average turbulent kinetic energy profiles are given in Fig. 1d. Unlike the grid resolution, which affects both these statistics, the two different volume conservation methods yield quasi-identical profiles at the same resolution. This indicates that, while both techniques successfully conserve the gas volume, their influence on the flow behavior is negligible.

Performing the simulations without applying one of the volume conservation strategies will negatively affect the statistics for long simulation intervals. Due to the continuous loss of gas volume (see Fig. 1b), the flow statistics will slowly deviate from the ones shown in Figs. 1c, 1d.

OUTLOOK

In the current work, four different setups will be investigated. In addition to varying the bubble resolution d_b/Δ, a variation between $Eo = 0.67$ and $Eo = 3.75$ will be performed to additionally evaluate the two proposed methods for deformed, wobbling bubbles. The methods will be assessed based on the flow and bubble statistics. Besides the global flow statistics, the oscillations of individual bubbles will be evaluated on the basis of their surface area fluctuations.

REFERENCES

[1] Cifani, P., Kuerten, J.G.M. and Geurts, B.J.: Highly scalable DNS solver for turbulent bubble-laden channel flow, *Comput. Fluids*, **172**, 67–83 (2018).

[2] Coyajee, E. and Boersma, B.J.: Numerical simulation of drop impact on a liquid-liquid interface with a multiple marker front-capturing method, *J. Comput. Phys.*, **228**, 4444–4467 (2009).

[3] Cifani, P., Michalek, W.R., Priems, G., Kuerten, J.G.M., van der Geld, C.W.M. and Geurts, B.J.: A comparison between the surface compression method and an interface reconstruction method for the VOF approach, *Comput. Fluids*, **136**, 421–435 (2016).

WORKSHOP
Direct and Large-Eddy Simulation 13
October 26th-29th 2022, Udine, Italy

DNS OF DISPERSED BUBBLY TAYLOR-COUETTE TURBULENCE

A.D. Franken[1], **S. R. Ephrati**[1], **P. Cifani**[1,2], **B.J. Geurts**[1,3]
[1] Mathematics of Multiscale Modeling and Simulation University of Twente, The Netherlands
[2] Gran Sasso Science Institute, Viale F. Crispi 7, 67100 L'Aquila, Italy
[3] Multiscale Physics, Center for Computational Energy Research, Department of Applied Physics, Eindhoven University of Technology, PO Box 513, 5600 MB Eindhoven, The Netherlands
a.d.franken@utwente.nl

INTRODUCTION

Direct numerical simulation (DNS) of the Navier-Stokes equations describing a gas-liquid flow of dispersed deformable bubbles in water enables quantitative characterization of the modulation of turbulence arising from an immersed phase. This paper adopts the volume-of-fluid method as implemented in the TBFSolver (https://github.com/cifanip/TBFsolver) to simulate dispersed bubbly turbulence, at considerably higher global gas volume fractions compared to literature, using high-performance computing. Attention is given to (i) the fundamental resolution of bubble-bubble and bubble-wall interactions and (ii) to the clustering of bubbles in Taylor-Couette turbulence.

The numerical technique used in the TBFsolver is based on the volume-of-fluid (VOF) method in which the one-fluid formulation is adopted, i.e., a single set of equations is solved on the entire domain. To describe the dispersed embedded flow discontinuous material properties and interfacial terms associated with the bubbles are accounted for using a marker function f_i for each bubble i. Each bubble is given a marker which equals 1 in cells where the bubble fully occupies the cell, 0 where the fluid occupies the cell, and a value between 0 and 1 indicates that the cell contains a bubble interface. The value of the marker function is also referred to as the volume fraction. Given N bubbles, the marker functions are advected via

$$\frac{\partial f_i}{\partial t} + \mathbf{u} \cdot \nabla f_i = 0 \qquad \text{for } i = 1, \ldots, N. \tag{1}$$

The nondimensionalized incompressible Navier-Stokes equations and continuity equation are used to describe the flow:

$$\rho \frac{D\mathbf{u}}{Dt} = -\nabla p + \frac{1}{\mathrm{Fr}^2}\rho\hat{\mathbf{g}} + \frac{1}{\mathrm{Re}}\nabla \cdot (2\mu\mathbf{S}) + \frac{1}{\mathrm{We}} k\mathbf{n}\delta(n) \tag{2}$$

$$\nabla \cdot \mathbf{u} = 0 \tag{3}$$

Here $D\mathbf{u}/Dt$ is the material derivative of the velocity $\mathbf{u}$ with t the time. Moreover, p is the pressure, ρ the mass density, μ the viscosity, k is the curvature, $\hat{\mathbf{g}}$ is the normalized gravity vector, $\mathbf{S}$ the deformation tensor, and $\mathbf{n}$ is the normal vector to the interface. The dimensionless numbers are the Froude number $\mathrm{Fr} = U/\sqrt{gL}$, the Reynolds number $\mathrm{Re} = UL\rho_1/\mu_1$, and the Weber number $\mathrm{We} = LU^2\rho_1/\sigma$. Here L and U denote a characteristic length and a characteristic velocity, respectively. The subscript 1 denotes the continuous phase mass density.

The mass density and viscosity at a certain point follow from the marker functions and the properties of the continuous and dispersed phases. For instance, a cell with volume fraction c would have a density and a viscosity of

$$\rho = \rho_1\ (1 - c) + \rho_2\ c, \tag{4}$$

$$\mu = \mu_1\ (1 - c) + \mu_2\ c. \tag{5}$$

were $c = \max_i f_i$. The continuous surface force (CSF) method is used to model the surface tension term. This method replaces the delta function $\delta(n)\mathbf{n}$ by a smooth term, which is computationally easier but may induce spurious currents. Reducing such spurious currents can effectively be done by accurately computing the curvature of the interface for which a height function method is adopted.

A three-dimensional uniform Cartesian grid is used to discretize the domain and a staggered arrangement of the variables was selected. The spatial discretization of the convective term is based on the finite volume approach. Additionally, the QUICK interpolation scheme is implemented to avoid unphysical oscillations that may occur as the spatial resolution is too low. A second-order finite difference scheme is employed for the diffusive term. Finally, a third-order Runge-Kutta scheme is used to discretize the convection and diffusion terms of the Navier-Stokes equations, while a Crank-Nicolson scheme is employed for the surface tension term.

RESOLVED BUBBLE COLLISIONS

The motion of a bubble impacting a solid wall was simulated in detail. In Figure 1 the energy dissipation in the vicinity of the bubble is plotted at various instances as the bubble rises under an angle of 45 degrees toward the wall and subsequently bounces back. Although the main features are well represented on a grid of 128^3 the findings at 256^3 convey a more precise capturing of the dynamics. This is also expressed by the centre of mass trajectory of the bubbly in Figure 2(a) and the evolution of the y-component of the centre of mass in Figure 2(b). The vertical line in the latter figure corresponds to the moment at which the distance between the bubble centre and the wall is reduced to four grid cells of the finest grid. Despite the modest spatial resolutions of these brief encounters, the overall capturing of the motion appears highly accurate.

BUBBLY TAYLOR-COUETTE TURBULENCE

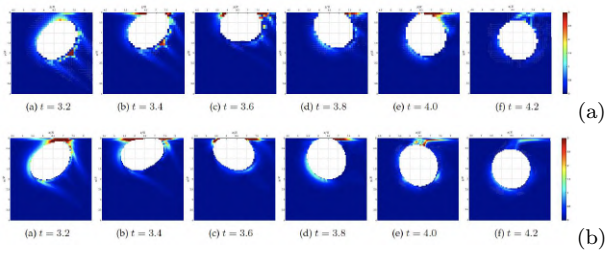

Figure 1: Energy dissipation in the vicinity of the bubble at different times using a grid with 128^3 (a) and 256^3 (b) grid cells.

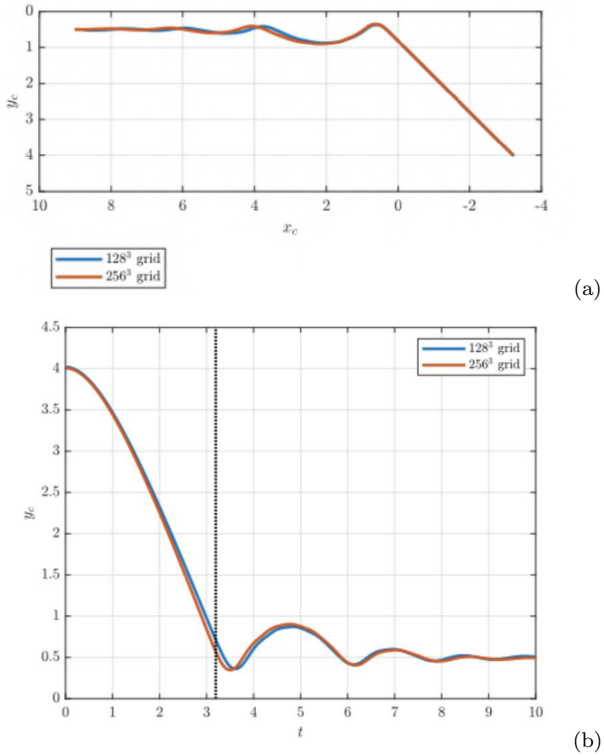

Figure 2: Bubble trajectory (a) and y-component of the center of mass motion (b) at 128^3 and 256^3.

The numerical method in the TBFSolver can also be used to simulate a large number of bubbles. We concentrate on turbulence in Taylor-Couette flow as this presents a finite domain in which all conditions can be controlled with high fidelity. To simulate the turbulent flow in this configuration the TBFSolver was extended to cylindrical coordinates. In Figure 3 the domain is shown and a snapshot of the flow with 120 bubbles simulated on a grid with $[N_\theta, N_r, N_z] = [768, 192, 384]$ cells in the circumferential, radial and vertical directions respectively is presented in Figure 4. We observe some degree of clustering in the bubble concentration, which is further quantified in Figure 5. The simulations allow us to study the effects of buoyancy and deformability of large bubbles in turbulent TC flow, which appear to be crucial ingredients for drag reduction.

In the final presentation at the workshop, we expect to have completed further simulations of the Taylor-Couette flow and analysed the drag reduction phenomenon in more detail.

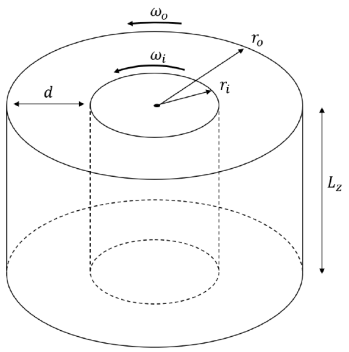

Figure 3: Domain for the Taylor-Couette flow.

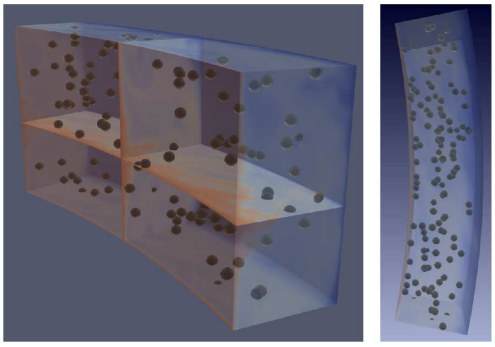

Figure 4: Snapshot of the velocity magnitude in two-phase TC flow - red/blue indicates high/low velocity. Bubbles are seen to cluster near the inner wall as seen clearly in the top-view (right figure).

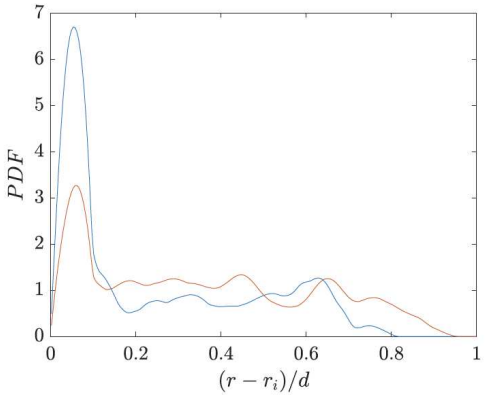

Figure 5: Probability distribution function of the radial coordinates of the gas phase. PDFs are based on averages over 2 flow-through times, taken after 18 (blue) and 48 (red) flow-through times.

WORKSHOP
Direct and Large-Eddy Simulation 13
October 26th-29th 2022, Udine, Italy

ANALYSIS OF TURBULENT KINETIC ENERGY BUDGETS IN CO-CURRENT TAYLOR BUBBLE FLOW

E.M.A. Frederix[1], **S. Tajfirooz**[1] and **E.M.J. Komen**[1]
[1] Nuclear Research and Consultancy Group, the Netherlands
frederix@nrg.eu

INTRODUCTION

Boiling in a nuclear reactor core may occur at normal operation or only in accident scenarios, depending on the reactor type. After a planned or emergency shutdown, residual heat removal is crucial to prevent irreparable damage to the reactor. The rate of heat removal reduces dramatically when too much steam is generated. Thus, accurate two-phase models describing the complex turbulent flow dynamics inside reactor core sub-channels are needed in order to determine operational safety limits.

Whereas in the past, such models have mainly relied on spatial averaging (system codes) or full temporal averaging (two-fluid model), current research is dedicated to a new hybrid approach for the description of two-phase structures. The idea is to rely on unsteady Reynolds-Averaged Navier-Stokes (RANS) models for the description of the Reynolds stress tensor, but to apply a separation of two-phase scales treating small bubbles sub-grid while resolving large structures. Such an approach is called *multiple flow regime* modeling, and carries an obvious similarity with the treatment of eddies in LES.

However, predictions of Turbulent Kinetic Energy (TKE) by traditional single phase RANS models applied to two-phase scenarios are known to be much too high as a result of the presence of resolved two-phase interfaces [1]. Improved RANS models are therefore needed, tailored to two-phase flows incorporating surface tension effects and applying asymmetric TKE damping at the interface. In support of such model development, high-fidelity simulation of relevant turbulent two-phase flow plays a pivotal role.

In this work, we analyze two-phase TKE budgets using high fidelity simulation of turbulent co-current Taylor bubble flow. We use the simulation setup developed in [2], which leverages a Moving Frame of Reference (MFR) attached to the Taylor bubble, allowing to compute two-phase TKE budgets as given in [3].

MODEL & SIMULATION SETUP

The two-phase flow is modeled by the one-fluid Volume Of Fluid (VOF) method, in which the liquid volume fraction f adheres to

$$\partial_t f + u_j \partial_j f = 0 \tag{1}$$

with mixture velocity u_j. The momentum equation is given by

$$\partial_t u_i + \partial_j (u_i u_j) = \frac{1}{\rho}\left[-\partial_i p + \frac{\partial_j (2\mu S_{ij})}{\mathrm{Re}} + \frac{\kappa \partial_i f}{\mathrm{We}}\right] + \frac{g_i}{\mathrm{Fr}^2} \tag{2}$$

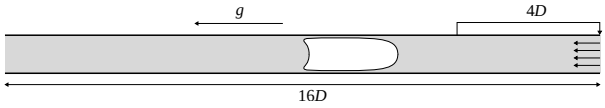

Figure 1: Co-current Taylor bubble flow simulation setup.

with mixture density ρ, mixture viscosity μ, pressure p, interface curvature κ, strain rate tensor S_{ij}, gravity $g_i = (-1, 0, 0)$, Reynolds number Re, Weber number We and Froude number Fr. All quantities in Eq. (1–2), including density and viscosity, are non-dimensional. The scaling of density and viscosity introduces two additional non-dimensional parameters, i.e., the viscosity ratio Γ_μ and density ratio Γ_ρ, see [2]. The momentum equation is supplemented by the continuity equation which, as a result of assumed incompressibility, is given by $\partial_i u_i = 0$.

Fig. 1 shows the simulation setup of the considered co-current Taylor bubble flow problem. The domain consists of a pipe with a diameter D and length $16D$. Gravity points from right to left, and both liquid and gas flow from left to right. However, an MFR is adopted that is attached to the bubble so that in this frame the bubble is idle, conveniently allowing for statistical averaging of data. Because the bubble rises faster than the liquid due to buoyancy, in the MFR, liquid moves from right to left meaning that the inlet is above the bubble. In order to have developed single phase turbulent flow ahead of the bubble, the velocity field is recycled over a distance of $4D$ as indicated in Fig. 1. Simulations are initialized from a fully developed single phase flow into which a cylindrical bubble with diameter $0.85D$ and length $2D$ with an attached hemispherical head is imposed, in such a way that its nose is at $6D$ from the inlet. After some initial development phase, data is averaged in time and space (circumferentially), and across four different realizations of the same flow. This ensemble averaging is needed, because the bubble slowly loses void by break-up, thus limiting the temporal averaging window beyond which the flow topology has changed too much.

Preliminary simulations have identified suitable values for the five non-dimensional parameters. First, the Reynolds number (based on the liquid bulk velocity) is set to 5300, allowing for comparison with single phase DNS databases of the flow ahead of the bubble. The Weber number is set to 40 and the Froude number to 1.5, allowing for significant relative velocity (about 32% of the liquid bulk velocity) without too much break-up. The density ratio does not affect the Taylor bubble flow much, and is moderately set to 10 which improves

numerical convergence. Likewise, the viscosity ratio is also set to 10 so that the liquid-based and gas-based Reynolds numbers are comparable.

The problem is simulated using the second order collocated finite volume code *Basilisk*, in which a uniform Cartesian mesh is employed with cubic cells. The wall of the pipe is modeled using 'embedded boundaries'. Simulations are performed on 'Mesh 11', having $2^{11} = 2048$ cells along the pipe length, and 'Mesh 12', having $2^{12} = 4096$ cells along the pipe length. Mesh 11 and 12 have 31M and 247M cells, respectively. More details can be found in [2].

RESULTS & DISCUSSION

Fig. 2 shows two-phase TKE budgets (per unit mass) in the gas phase (top) and liquid phase (bottom), across a radial line through the bubble at a distance of roughly D below its nose. The position where the average void fraction $\overline{f}$ is 0.5 is indicated by the black dot. Shown are the production, dissipation, convection, viscous diffusion and surface tension budgets. All other budgets, including pressure diffusion, transport and two interfacial terms (see [3]), are combined and calculated as the negative sum of the others, leveraging the fact that the budget sum should be zero. This indirect computation is preferred because a direct calculation is troubled by the interfacial void fraction gradient $\partial_i f \to \infty$ for decreasing mesh size. Moreover, in RANS models these contributions are virtually always lumped into a single term too, and approximated using a gradient-diffusion model. Thus, their indirect lumped representation may offer a validation base for RANS models.

Three important conclusions that can be drawn from Fig. 2 are the following. First, it is observed that the TKE budgets are still quite sensitive to the mesh, suggesting that these results cannot be regarded as true DNS. However, the mesh is such that Δy^+ values for the considered Re are uniform and close to unity, indeed providing excellent agreement with reference data for the single phase TKE budgets ahead of the bubble (not shown here). Thus, the two-phase nature of the problem induces additional requirements on the mesh that are not yet met, or may never be met due to $\partial_i f \to \infty$. This is signified by the relatively large surface tension gas budget inside the bubble for the finer Mesh 12, revealing the presence of tiny droplets that cannot be resolved on the coarser mesh.

Second, it is observed that surface tension plays a significant role in the production and destruction of TKE. In the liquid phase, surface tension is seen to damp turbulence while in the gas phase it is seen to produce turbulence. This is an effect that has not been considered in any conventional RANS models and gives rise to further research in this direction, e.g., by study of the influence of We on the surface tension TKE budget.

Third, it can be observed that production and dissipation in the gas phase close to the interface behave much like they would in single phase wall-bounded flow, while in the liquid phase there is negligible TKE production close to the interface. This suggests that two-phase RANS model improvement using wall functions in the gas phase may have merit. Moreover, as for example presented in [4], suitable two-phase RANS models should posses an asymmetric damping term.

In summary, this work explores the behavior of two-phase TKE budgets near large scale resolved interfaces using high fidelity simulation, allowing for better understanding of the behavior of separate terms affecting TKE. In turn, RANS models may be improved from the insight generated by this data, to be potentially harvested by modern machine learning tools. The results establish the relevance of surface tension in the modeling of mean TKE, and suggest an asymmetry in the modeling of production and dissipation on either side of the interface.

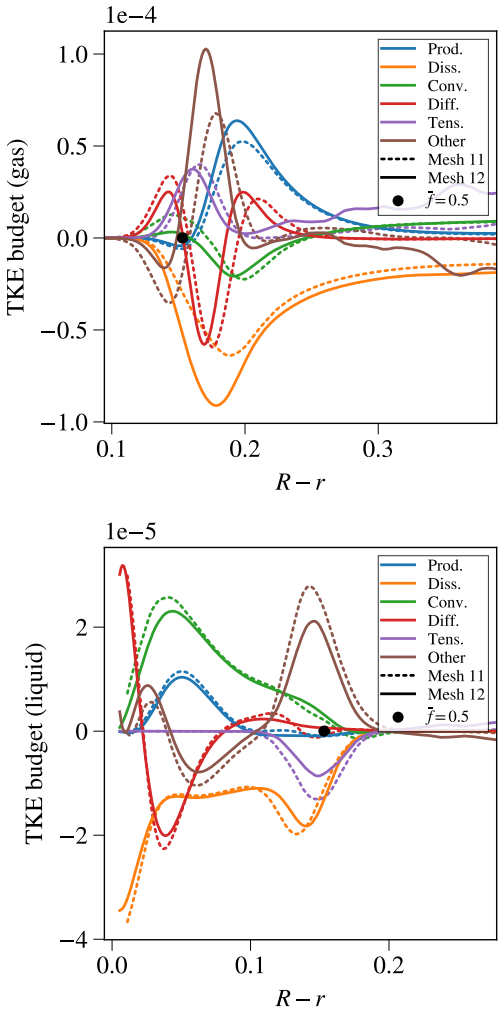

Figure 2: Gas (top) and liquid (bottom) TKE budgets calculated across the Taylor bubble on Mesh 11 and 12. Data is in simulated units, with $D = 1$, radius $R = D/2$ and liquid bulk velocity $U_\ell = 1$. The variable r is the radial coordinate.

REFERENCES

[1]Frederix, E.M.A., Mathur, A., Dovizio, D., Geurts, B.J. and Komen, E.M.J.: Reynolds-averaged modeling of turbulence damping near a large-scale interface in two-phase flow, *Nuclear Engineering and Design*, **333**, 22–130 (2018).

[2]Frederix, E.M.A., Tajfirooz, S., Komen, E.M.J. and Hopman, J.A.: Two-phase turbulent kinetic energy budget computation in co-current Taylor bubble flow, *NURETH-19 proceedings* (2022).

[3]Vreman, A.W. and Kuerten, J.G.M.: Turbulent channel flow past a moving array of spheres, *Journal of Fluid Mechanics*, **856**, 580–632 (2018).

[4]Dong, Z., Bürgler, M., Hohermuth, B. and Vetsch, D.F.: Density-based turbulence damping at large-scale interface for Reynolds-averaged two-fluid models, *Chemical Engineering Science*, **247**, 116975 (2022).

WORKSHOP
Direct and Large-Eddy Simulation 13
October 26th-29th 2022, Udine, Italy

DNS OF MASS TRANSFER IN BI-DISPERSED BUBBLY FLOWS IN A VERTICAL PIPE

Néstor Balcázar-Arciniega[1,*], Joaquim Rigola[1], Assensi Oliva[1]
[1,*] Heat and Mass Transfer Technological Center (CTTC),
Universitat Politècnica de Catalunya (UPC) - BarcelonaTech,
ESEIAAT, Colom 11, E-08222 Terrassa, Barcelona, Spain.
nestor.balcazar@upc.edu, nestorbalcazar@yahoo.es

Mass transfer in bubble swarms is frequent in nature and industry. Chemical reactors and unit operations of chemical engineering use bubbly flows to produce chemical products or to promote separation processes. Although empirical correlations have been reported to estimate mass transfer rates in bubbles and droplets, the interplay between fluid mechanics and mass transfer in turbulent bubbly flows is not well understood yet. The present work investigates the mass transfer in bi-dispersed gravity-driven turbulent bubbly flows, employing Direct Numerical Simulation (DNS) of the Navier-Stokes equations and the multiple-marker unstructured level-set method [2, 5, 6, 7, 8].

MATHEMATICAL FORMULATION

The Navier-Stokes equations for the dispersed phase (Ω_d) and continuous phase (Ω_c) follow the one-fluid formulation,

$$\frac{\partial}{\partial t}(\rho\mathbf{v}) + \nabla\cdot(\rho\mathbf{v}\mathbf{v}) = -\nabla p + \nabla\cdot\mu\left(\nabla\mathbf{v} + (\nabla\mathbf{v})^T\right) + (\rho-\rho_0)\mathbf{g} + \mathbf{f}_\sigma, \quad (1)$$

$$\nabla\cdot\mathbf{v} = 0, \quad (2)$$

where $\mathbf{v}$ is the fluid velocity, p is the pressure field, ρ is the fluid density, μ is the dynamic viscosity, $\mathbf{g}$ is the gravitational acceleration, $\mathbf{f}_\sigma$ is the surface tension force concentrated at the interface (Γ), subscripts d and c denote the dispersed phase and continuous phase, respectively. Physical properties are constant at each fluid-phase with a jump discontinuity at Γ:

$$\rho = \rho_d H_d + \rho_c(1-H_d),\ \mu = \mu_d H_d + \mu_c(1-H_d), \quad (3)$$

where H_d is the Heaviside step function that is one at fluid d and zero elsewhere. Since periodic boundary conditions are used, a force $-\rho_0\mathbf{g}$ ($\rho_0 = V_\Omega^{-1}\int_\Omega(\rho_d H_d + \rho_c(1-H_d))\,dV$), is included in Eq. (1) to prevent the acceleration of the entire flow field in the downward vertical direction [2, 6, 7, 8].

This research employs the unstructured conservative level-set method (UCLS), as introduced by [1, 7, 9] for interface capturing on unstructured meshes. A multiple marker strategy [2, 5, 6, 7, 8, 11] avoids the numerical coalescence of bubbles. In this framework [2, 5, 6, 7, 8], the ith interface transport equation for each bubble can be written as follows:

$$\frac{\partial\phi_i}{\partial t} + \nabla\cdot\phi_i\mathbf{v} = 0,\ i = 1,2,...,n_d. \quad (4)$$

where n_d is the number of bubbles.

Furthermore, a re-initialization equation is solved up to steady-state to keep a sharp and constant interface profile:

$$\frac{\partial\phi_i}{\partial\tau} + \nabla\cdot\phi_i(1-\phi_i)\mathbf{n}_i = \nabla\cdot\varepsilon\nabla\phi_i,\ i = 1,2,...,n_d. \quad (5)$$

where $\varepsilon_P = 0.5h_P^{0.9}$ in the cell Ω_P, h_P is the local grid size [1, 5, 7]. Normal vectors $\mathbf{n}_i$ and curvatures κ_i are computed as: $\mathbf{n}_i = \nabla\phi_i\|\nabla\phi_i\|^{-1}$ and $\kappa_i = -\nabla\cdot\mathbf{n}_i$. Surface tension force is calculated by the Continuous Surface Force model [10], extended to the multiple marker UCLS method in [2, 5, 6, 7, 8]: $\mathbf{f}_\sigma = \sum_{i=1}^{n_d}\sigma\kappa_i\mathbf{n}_i\delta^s_{\Gamma,i} = \sum_{i=1}^{n_d}\sigma\kappa_i\nabla\phi_i$, where $\delta^s_{\Gamma,i} = ||\nabla\phi_i||$ is the regularized Dirac delta function concentrated at Γ [1, 6, 7]. Fluid properties in Eq. (3) are regularized by a global level-set function $H^s_d = \phi_d$, e.g., $\phi_d = \max\{\phi_1,\phi_2,...,\phi_{n_d}\}$ [2, 5, 7, 8].

This research focuses on external mass transfer. As a consequence, the concentration of chemical species (C) is computed in Ω_c:

$$\frac{\partial C}{\partial t} + \nabla\cdot(\mathbf{v}C) = \nabla\cdot(\mathcal{D}\nabla C) + \dot{r}(C), \quad (6)$$

where $\mathcal{D} = \mathcal{D}_c$ is the diffusivity in Ω_c, $\dot{r}_j = -k_1 C$ is the chemical reaction rate, and k_1 is the reaction rate constant. Thermodynamic equilibrium is assumed, with $C_{\Gamma,c} = HC_{\Gamma,d}$, where H is the Henry constant. The discontinuity introduced by $H \neq 1$, can be treated by rescaling the concentration and diffusion coefficient to obtain a continuous solution. As a consequence, it is considered that the value of C on the bubble interface ($C_{\Gamma,c}$) is to be given. The concentration at the interface-cells is linearly interpolated [7, 8], whereas a constant concentration is assumed inside the bubbles [7, 8, 12, 13].

NUMERICAL EXPERIMENTS AND DISCUSSION

Validations and verifications of the UCLS method [1, 2, 5, 6, 7, 8] include: gravity-driven motion of single bubbles [1, 3, 4], binary droplet collision [2], collision of a droplet against a fluid interface [2], mono-dispersed bubbly flow in a vertical channel [6, 7, 8], thermocapillary migration of droplets [5], and liquid-vapor phase change [9]. This research is a further step in mass transfer in bi-dispersed bubbly flows.

Bi-dispersed bubbly flow in a vertical pipe is characterized by: Morton number $Mo = g\mu_c^4(\rho_c-\rho_d)\rho_c^{-2}\sigma^{-3}$, Eötvös number $Eo = gd^2(\rho_c-\rho_d)\sigma^{-1}$, density ratio $\eta_\rho = \rho_c/\rho_d$, viscosity ratio $\eta_\mu = \mu_c/\mu_d$, $\alpha = V_{\Omega_d}/V_\Omega$, confinement ratio CR $= d/D_\Omega$, volume ratio VR $= V_{\Omega_{d,d^*}}/V_{\Omega_{d,d}}$, Reynolds

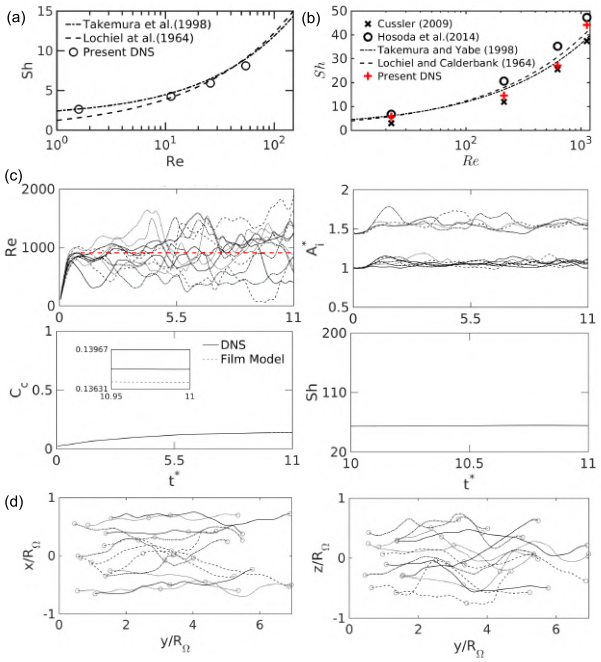

Figure 1: (a) Mass transfer from single bubble in unconfined domain [7, 8], $Eo = 3.125$, $10^{-3} \leq Mo \leq 10^{-7}$, $\eta_\rho = 100, \eta_\mu = 100$, $Sc = 1$, $Da = 0$. (b) Mass transfer from single bubble in a vertical pipe, $Eo = 3.125$, $10^{-6} \leq Mo \leq 10^{-11}$, $\eta_\rho = 100$, $\eta_\mu = 100$, $Sc = 1$, $Da = 0$, CR $= d/D_\Omega = 0.33$. (c) Mass transfer in bi-dispersed bubble swarm in a vertical pipe: $Re(t)$, normalized surface $A_i(t)$, concentration in Ω_c ($C_c(t)$), $Sh(t)$, and (d) bubble trajectories, for $Eo = 3.125$, $Mo = 10^{-11}$, $\eta_\rho = 100, \eta_\mu = 100$, $Sc = 1$, $Da = 400$, $\alpha_d = V_{\Omega_{d,d}}/V_\Omega = 8.3\%$, $\alpha_{d^*} = V_{\Omega_{d,d^*}}/V_\Omega = 7.2\%$, $\alpha = (V_{\Omega_{d,d}} + V_{\Omega_{d,d^*}})/V_\Omega = 15.5\%$, DR $= d^*/d = 1.2$, CR $= d/D_\Omega = 0.25$, VR $= V_{\Omega_{d,d^*}}/V_{\Omega_{d,d}} = 0.864$.

number Re $= \rho_c U_T d/\mu_c$, diameter ratio DR $= d^*/d$. Here d is the smaller bubble diameter, d^* denotes bigger bubble diameter, $V_{\Omega_{d,d^*}}$ is the volume of bubbles with diameter d^*, and $V_{\Omega_{d,d}}$ is the volume of bubbles with diameter d. Reactive mass transfer is characterized by the Damköler (Da) number $Da = k_1 d^2/\mathcal{D}_c$, Schmidt number ($Sc = \mu_c/(\rho_c \mathcal{D}_c)$) or Péclet number ($Pe = ReSc$), and Sherwood number ($Sh = k_c d/\mathcal{D}_c$), where k_c is the mass transfer coefficient at Ω_c. This research aims to predict the Sherwood number Sh $=$ Sh$(Re, Sc, Da, \alpha, \text{CR}, \text{VR}, \text{DR})$ in bi-dispersed bubbly flow in a vertical pipe. Figure 1-2 show validations and some of the present numerical results for $Re \sim O(1000)$. In the full paper a wider range of flow regimes will be reported.

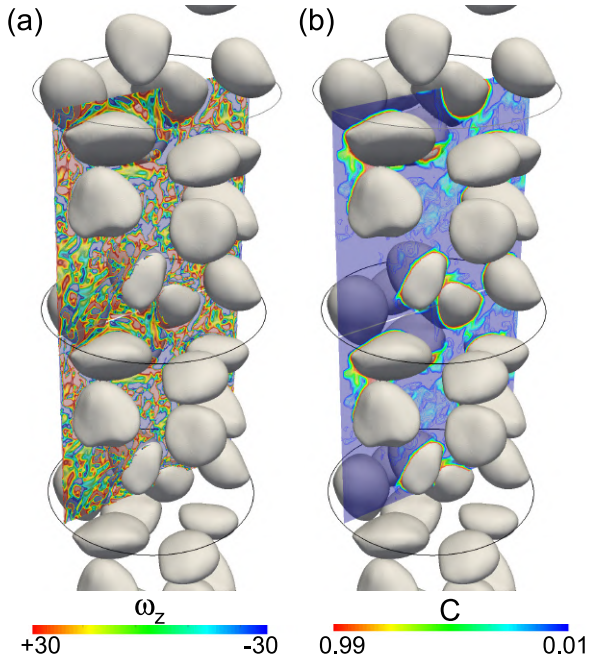

Figure 2: Mass transfer in bi-dispersed bubbly flow in a vertical pipe. Instantaneous vorticity ($\omega_z = \mathbf{e}_z \cdot (\nabla \times \mathbf{v})$) and concentration ($C$) on the plane $x - z$. Domain discretized by 10.44×10^6 triangular-prism cells, on 960 CPU-cores. $Eo = 3.125$, $Mo = 10^{-11}$, $\eta_\rho = 100, \eta_\mu = 100$, $Sc = 1$, $Da = 400$, $\alpha_d = V_{\Omega_{d,d}}/V_\Omega = 8.3\%$, $\alpha_{d^*} = V_{\Omega_{d,d^*}}/V_\Omega = 7.2\%$, $\alpha = (V_{\Omega_{d,d}} + V_{\Omega_{d,d^*}})/V_\Omega = 15.5\%$, DR $= d^*/d = 1.2$, CR $= d/D_\Omega = 0.25$, VR $= V_{\Omega_{d,d^*}}/V_{\Omega_{d,d}} = 0.864$.

REFERENCES

[1]Balcázar, N., Jofre, L., Lehmkhul, O., Castro, J., Rigola, J. : A finite-volume/level-set method for simulating two-phase flows on unstructured grids. *International Journal of Multiphase Flow* **64**, 55-72 (2014).

[2]Balcázar, N., Lehmkhul, O., Rigola, J., Oliva, A. : A multiple marker level-set method for simulation of deformable fluid particles. *International Journal of Multiphase Flow* **74**, 125-142 (2015).

[3]Balcázar, N., Lemhkuhl, O., Jofre, L., Oliva, A. : Level-set simulations of buoyancy-driven motion of single and multiple bubbles. *International Journal of Heat and Fluid Flow* **56**, 91-107 (2015).

[4]Balcázar, N., Lehmkhul, O., Jofre, L., Rigola, J., Oliva, A. : A coupled volume-of-fluid/level-set method for simulation of two-phase flows on unstructured meshes. *Computers and Fluids* **124**, 12-29 (2016).

[5]Balcázar, N., Rigola, J., Castro, J., Oliva, A. : A level-set model for thermocapillary motion of deformable fluid particles. *International Journal of Heat and Fluid Flow* **62**, Part B, 324-343 (2016).

[6]Balcázar, N., Castro, J., Rigola, J., Oliva, A. : DNS of the wall effect on the motion of bubble swarms. *Procedia Computer Science* **108**, 2008-2017 (2017).

[7]Balcázar, N., Antepara, O., Rigola, J., Oliva, A. (2019) A level-set model for mass transfer in bubbly flows. *International Journal of Heat and Mass Transfer* 138. 335-356.

[8]Balcázar N., Antepara O., Rigola J., Oliva A. (2020). DNS of Drag-Force and Reactive Mass Transfer in Gravity-Driven Bubbly Flows. In: Garca-Villalba M., Kuerten H., Salvetti M. (eds) *Direct and Large Eddy Simulation XII. DLES 2019. ERCOFTAC Series*, vol 27. Springer, Cham.

[9]N. Balcazar, J. Rigola and A. Oliva, (2021). Unstructured Level-Set Method For Saturated Liquid-Vapor Phase Change, in: WCCM-ECCOMAS2020. URL `https://www.scipedia.com/public/Balcazar_et_al_2021a`, doi: 10.23967/wccm-eccomas.2020.352

[10]Brackbill, J.U., Kothe, D.B., Zemach, C. : A Continuum Method for Modeling Surface Tension, *J. Comput. Phys.* **100**, 335-354 (1992).

[11]Coyajee, E., Boersma, B.J. : Numerical simulation of drop impact on a liquidliquid interface with a multiple marker front-capturing method. *J. Comput. Phys.* **228**, 4444-4467 (2009).

[12]Roghair, I., Van Sint Annaland, M., Kuipers, J.A.M. : An improved Front-Tracking technique for the simulation of mass transfer in dense bubbly flows. *Chem. Eng. Sci.* **152**, 351-369 (2016).

[13]Aboulhasanzadeh, B., Thomas, S., Taeibi-Rahni, M., Tryggvason, G., Multiscale computations of mass transfer from buoyant bubbles. *Chem. Eng. Sci.* **75**, 456-467 (2012).

WORKSHOP
Direct and Large-Eddy Simulation 13
October 26th-29th 2022, Udine, Italy

TAYLOR BUBBLE BREAKUP IN COUNTER-CURRENT TURBULENT FLOW USING ALGEBRAIC AND GEOMETRIC VOLUME OF FLUID METHOD

J. Kren[1,2], E.M.A. Frederix[3], B. Mikuž[1]
[1] Reactor Engineering Division
Jožef Stefan Institute, Slovenia
[2] Faculty of Mathematics and Physics
University of Ljubljana, Slovenia
[3] Nuclear Research and Consultancy Group (NRG)
The Netherlands
jan.kren@ijs.si

INTRODUCTION

Turbulent flow of two-phase fluids occurs in many industrial systems. One of the manifestations of the two-phase flow in a pipe is slug flow, which consist of large gas bubbles (i.e. Taylor bubbles) separated from each other by liquid slugs. We are particularly interested in the phenomena of coalescence and breakup in the slug flow regime and the development of the numerical models for the Large Eddy Simulation (LES) method as they are still in early stages of development for two-phase flows.

Counter-current Taylor bubble flow regime is subjected to bubble breakup due to several effects, such as breakup due to turbulent fluctuations, shearing-off process or due to viscous shear forces. Comparison between LES simulations and experimental measurements [1] show that the simulations overpredict the bubble breakup. Rate of artificial numerical breakup is the result of the used numerical method for interface capturing and in this work we present the results obtained with improved geometric Piecewise Linear Interface Capturing (PLIC) method in the OpenFOAM computer code.

SIMULATION OF TAYLOR BUBBLE IN TURBULENT COUNTER-CURRENT FLOW

A two-phase mixture of gas and liquid is modeled using the one-fluid formulation of the Navier-Stokes equations with the Volume Of Fluid (VOF) approach for interface capturing. In this method a void fraction α is introduced and the advection equation for this quantity is the following:

$$\partial_t \alpha + \mathbf{u} \cdot \nabla \alpha = 0, \tag{1}$$

with partial time derivative ∂_t, velocity vector $\mathbf{u}$ and gradient operator ∇. The fluid mixture is described by the incompressible Navier-Stokes equations, i.e.,

$$\nabla \cdot \mathbf{u} = 0 \tag{2}$$

and

$$\partial_t(\rho\mathbf{u}\mathbf{u}) + \nabla\cdot(\rho\mathbf{u}\mathbf{u}) = -\nabla p + \rho\mathbf{g} + \nabla\cdot(2\mu_{eff}\mathbf{D}) + \sigma\kappa\delta(n)\mathbf{n} \tag{3}$$

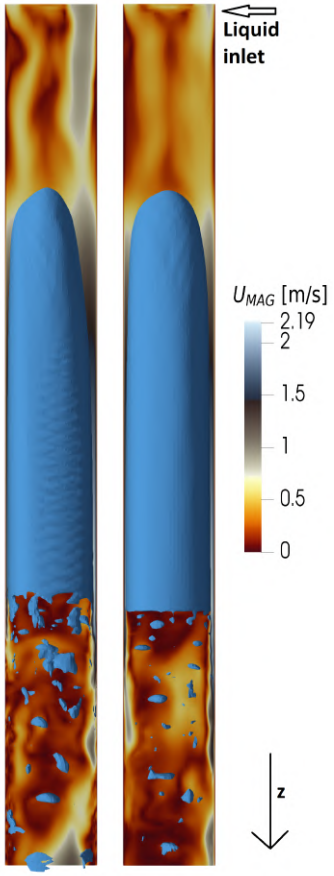

Figure 1: Isosurfaces of the instantaneous gas void fraction at 2.2 seconds after the initial state obtained with standard algebraic interface capturing (left) and PLIC reconstruction (right). The color scheme in the liquid phase represents the velocity magnitude.

with mass density ρ, pressure p, gravitational acceleration $\mathbf{g}$, deformation tensor $\mathbf{D}$, effective mixture viscosity μ_{eff}, with the harmonic expression of viscosity, interface curvature κ, interface normal unit vector $\mathbf{n}$ and interface Dirac delta function $\delta(n)$.

The described equations were solved in OpenFOAM v9 [2]. We have used a modified interFoam solver, which enables the usage of the Diagonally Implicit Runge-Kutta (DIRK) time integration schemes integrated with PLIC geometric reconstruction. This solver was based on a solver developed before in OpenFOAM v4 by Frederix et al [3]. Turbulence at the sub-grid scales was modeled by Vreman model [4]. In the current case, the fluid properties were selected to mimic water-air mixture. The pipe diameter was 26 mm and pipe length 52 cm.

A recycling boundary condition was used at the inlet, which in this case is ahead of the Taylor bubble, in order to achieve a fully developed turbulent flow. The flowrate was also adjusted at every timestep so that the net force on the bubble is zero and the bubble stays at approximately constant position throughout the simulation, such that its buoyancy is balanced by hydrodynamic drag.

The key to an algebraic VOF method is to correctly compute the numerical fluxes to update the function of fluid fraction. Originally, a donor-acceptor formulation was used with flux limiters to ensure the boundendness of the α function. Algebraic capturing is in the OpenFOAM v9 performed through Multidimensional universal limiter for explicit solution (MULES) framework, that uses Flux Corrected Transport (FCT) with interface compression scheme.

As opposed to the algebraic VOF method, a geometric VOF method can be divided into reconstruction and the advection of the interface [5]. Firstly, the approximation of the interface is built from the information on the volume fraction. This can be done in various manners such as PLIC interface reconstruction methods. Second, the reconstructed interface is advected by the given velocity field. For PLIC methods the reconstruction is a two-step procedure. In any given cell the normal is first determined from the knowledge of the α function in this cell and in the neighboring ones. Geometrically, the line is then moved in the normal direction so that the interface position in each cell corresponds to the local void fraction value.

RESULTS

Figure 1 shows isosurfaces for the instantenous gas void fraction for the two different interface capturing methods at time $t = 2.2s$ after the initial state. Clearly at the skirt of the bubble the velocities are the largest which essentialy slowly breaks the bubble. For the algebraic capturing the breakup is much more significant and faster as signified by the many smaller bubbles in the wake of the Taylor bubble.

Figure 2 shows the surface averaged α at the outlet of the domain. It is shown that breakup as predicted by the geometric method is much more moderate than that by the algebraic method, giving better agreement with experimental values. For the PLIC method the bubble was still present in the simulation after 15 seconds, but with the algebraic capturing the bubble completely broke down in less than 6 seconds. This shows that accurate determination of the bubble shape is extremely important and has high impact on the breakup and coalescence rate. Additional models for the breakup and coalescence should be developed after the usage of more accurate interface capturing schemes.

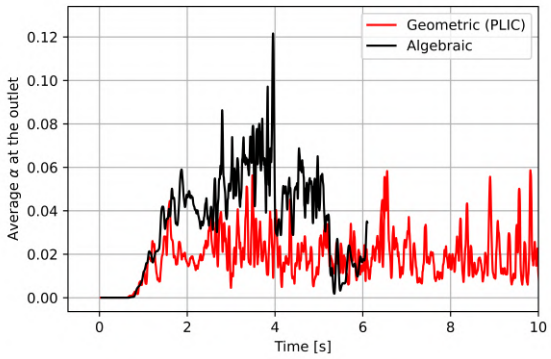

Figure 2: Comparison of the surface averaged α at the pipe outlet between PLIC and algebraic interface capturing method.

SUMMARY

In this work we presented a comparison between the performance of algebraic and geometric interface capturing methods for the VOF solver with Runge-Kutta time-integration. The methods were tested and validated in the OpenFOAM v9 and were based on the solver developed. Current results of the Taylor bubble in the counter-current turbulent flow case show that the usage of the geometric interface reconstruction scheme PLIC significantly reduces artificial numerical breakup of the bubble and makes it closer to the experimental results. This confirms that the PLIC method is superior to algebraic capturing. It also suggests that bubble breakup depends significantly on the shape of the bubble interface.

REFERENCES

[1]Mikuž, B.; Frederix, E. M. A.; Komen, E. M. J.; Tiselj, I. : Taylor Bubble Behaviour in Turbulent Flow Regime, *Proceedings of the conference Computational Fluid Dynamics for Nuclear Reactor Safety (CFD4NRS-8)*, (2020).

[2]The OpenFOAM Foundation : OpenFOAM | Free CFD Software , *https://openfoam.org/*, (2022).

[3]Frederix, E. M. A. and Komen, E. M. J. and Tiselj, I. and Mikuž, B. : LES of Turbulent Co-current Taylor Bubble Flow, *Flow, Turbulence and Combustion*, **2**, 471–495 (2020).

[4]Vreman, A. W. : An eddy-viscosity subgrid-scale model for turbulent shear flow: Algebraic theory and applications , *Physics of Fluids*, 3670–3681 (2004).

[5]Dai, D. and Tong, A. Y. : Analytical interface reconstruction algorithms in the PLIC-VOF method for 3D polyhedral unstructured meshes, *International Journal for Numerical Methods in Fluids*, **5**, 213–227 (2019).

[6]Mikuž, B. and Kamnikar, J. and Prošek, J. and Tiselj, I. : Experimental Observation of Taylor Bubble Disintegration in Turbulent Flow, *Proceedings of the 28th International Conference Nuclear Energy for New Europe*, 87–106 (2019).

[7]Klein, M. and Ketterl, S. and Hasslberger, J. : Large eddy simulation of multiphase flows using the volume of fluid method: Part 1—Governing equations and a priori analysis , *Experimental and Computational Multiphase Flow*, 130–144 (2019).

[8]Tryggvason, G. and Scardovelli, R. and Zaleski, S. : Direct numerical simulations of gas-liquid multiphase flows, *Cambridge University Press*, 324, (2011).

Session: Flow separation 1

Thursday, October 27, 2022

09:50 – 10:50

WORKSHOP
Direct and Large-Eddy Simulation 13
October 26th-29th 2022, Udine, Italy

DATA-DRIVEN WALL SHEAR STRESS MODEL FOR LARGE EDDY SIMULATIONS APPLIED TO FLOW SEPARATION

M. Boxho*[,1,4], M. Rasquin[1], T. Toulorge[1], G. Dergham[2], G. Winckelmans[3] and K. Hillewaert[1,4]
[1] Cenaero, 29, Rue des Frères Wright, 6041 Gosselies, Belgium
[2] Safran Tech, Rue des jeunes bois, Châteaufort, 78114 Magny-les-Hameaux, France
[3] Institute of Mechanics, Materials and Civil Engineering, UCLouvain, 1348 Louvain-la-Neuve, Belgium
[4] Aerospace and Mechanics dept., Université de Liège, 4000 Liège, Belgium
margaux.boxho@cenaero.be

INTRODUCTION

RANS simulations are the reference in the industry for turbomachinery design due to their low computational cost. Even if progress has been made towards more accurate closure models for RANS, they still fail at off-design conditions due to their inherent assumptions. At those conditions, different flow regimes occur in blade passages where complex flow features coexist, including secondary flows and flow separation.

Direct Numerical Simulations (DNS) provide a reliable prediction of such a flow physics. However, they require a considerable amount of computational resources that overcome the current capabilities of modern clusters and hence they cannot be used for the actual complex geometries and high Reynolds number flows tackled by industry. Even wall-resolved Large Eddy Simulations (wrLES), which aims to resolve at least 80% of the turbulent energy spectrum while modeling the effect on the small unresolved scales on the resolved ones, remains too expensive at high Reynolds numbers.

Since the inner part of the boundary layer is the most demanding in terms of resolution, the LES community came up with the idea of modeling this part rather than resolving it. Such wall-modeled LES (wmLES) require much less computational resources, yet the modeling errors are larger and may become unacceptable. Indeed, most wall models assume that the flow is attached, fully turbulent, aligned, and at equilibrium. Hence, they fail at predicting complex flow features. In the case of flow separation, treated in this work, these assumptions do not hold, and the wall model must be reformulated.

Since DNS and LES perform well on academic configurations and several industrial configurations, coupled with the recent improvement in the Machine Learning community, we have the opportunity to construct databases to train deep neural networks afterwards. Our work is based on the universal approximation capabilities of deep neural networks. A wall model can be seen as a high-dimensional regression problem that takes as inputs (a) instantaneous volume fields (e.g., velocity, pressure gradients) and (b) geometry notions, and that outputs the two components of the wall shear stress, $\boldsymbol{\tau}_w$. Three databases, obtained using a high-order Discontinuous Galerkin (DG) flow solver, are composed of a channel flow at a friction Reynolds number of 950 and the two walls (i.e., the flat upper surface and the curved lower one) of the two dimensional periodic hill at a bulk Reynolds number of 10595.

The next sections present: (i) which stencil is taken as input for the data-driven wall model, (ii) how are the three databases normalized to train the network on a unified and consistent database and (iii) which neural networks are picked.

TEST CASES

Two test cases are considered for the present study. One of them is a channel flow at $Re_\tau = 950$ [1]. The walls are separated by a distance 2δ and the channel is periodic and homogeneous in the streamwise and spanwise direction, respectively of size $L_x/\delta = 2\pi$ and $L_z/\delta = \pi$. A uniform pressure gradient drives the flow. A compressible wrLES using a DG flow solver is performed at Mach number of 0.1 to ensure a fair comparison with the incompressible flow reference. The second test case is the periodic hill flow [8], a geometry used for the development of wall models, and that consists of a channel with a hill (of height h). There is a massive flow separation from the hill top, followed by a reattachment and flow recovery on the flat part. The flow is then strongly re-accelerated on the ascending part of the next hill. The bulk Reynolds number Re_b is $10,959$ and is controlled using a uniform pressure gradient. The control procedure is inspired by the work of Benocci and Pinelli [2], and further modified by Carton de Wiart et al. [3] to take into account compressibility. Note that the flat top wall is subjected to a non-uniform pressure gradient generated by the flow contraction and the separation on the hill top but the flow on that wall does not separate.

INPUTS STENCIL

The input of the wall model is a mix between flow field and geometry data. For the flow fields, the velocity and the pressure gradients are considered. These fields are interpolated from a high-order solution to a probe grid and then projected on the local frame of reference following the wall; the data are therefore expressed in curvilinear coordinates (ξ, η, z). A crucial information for the wall model is the wall normal distance at which the flow fields are extracted, defined as h_{wm}. The curvature K of the wall is also added and has drastically improved the prediction of the $\boldsymbol{\tau}_w$ on the curved wall.

To answer the question (i), the choice of stencil is based on a deep analysis of space-time correlations between instantaneous flow fields and the two components of $\boldsymbol{\tau}_w$ [9]. In Machine Learning, this step is called feature selection. Our work has

shown that, near the separation, the high correlation domain is shifted downstream ($\delta\xi/h \simeq 0.5$), indicating that, at a given time, the information should be sought downstream to better characterize the relationship with $\boldsymbol{\tau}_w$. Finally, a stencil going from $-0.5\,\delta\xi/h$ to $0.5\,\delta\xi/h$ relatively to the location where $\boldsymbol{\tau}_w$ is predicted is adopted. As multiple spatial positions are considered, the relative positions are introduced as input.

NORMALIZATION

This section answers the question (ii). The inputs described in the previous section need to be normalized to train the neural network on a unified database. The inputs and outputs of the wall model are summarized in Table 1. Recall that h_{wm} is the wall-normal distance at which the fields are measured and fed to the model. We also define $u_{\parallel} = \sqrt{(u_\xi^2 + u_z^2)}$, the norm of the wall-parallel velocity. The normalization of h_{wm} is based on the near wall scaling proposed by Duprat et *al.* [4] combined to the work of Zhou et *al.* [5]. The near-wall scaling compatible with separation uses $y_{\nu,p} = \nu/u_{\nu,p}$ with $u_{\nu,p} = \sqrt{(u_\nu^2 + u_p^2)}$ where $u_\nu = \sqrt{(\nu\, u_{\parallel}/h_{wm})}$ and $u_p = \left|(\nu/\rho)\partial_\xi p\right|^{1/3}$. A natural normalization of the velocity field would be based on the friction velocity u_τ; however, the friction velocity is undefined near separation. An alternative is to use its extended definition $u_{\nu,p}$ defined above. Regarding the pressure gradient, It is non-dimensionalised in an analogous way as the Clauser parameter, using the adapted velocity scale $u_{\nu,p}$, see Table 1. Finally, the outputs are normalized following the definition of the friction coefficient where the friction velocity is replaced by the spatial averaging of $u_{\nu,p}$. No normalization of the curvature is used as it is already dimensionless.

Field		*Normalized*
Velocity	$\boldsymbol{u}$	$\boldsymbol{u}^\star = \boldsymbol{u}/u_{\nu,p}$
Pressure Gradients	∇p	$(\nabla p)^\star = \left(h_{wm}/\left(\rho u_{\nu,p}^2\right)\right)\nabla p$
Length scale	h_{wm}	$h_{wm}^\star = \ln\left(h_{wm}/y_{\nu,p}\right)$
Curvature	K	
Relative pos.	$\delta\xi$	$(\delta\xi)^* = \delta\xi/h$
Wall shear stress	$\boldsymbol{\tau}_w$	$\boldsymbol{\tau}_w^\star = \dfrac{\boldsymbol{\tau}_w}{\frac{1}{2}\rho\langle u_{\nu,p}^2\rangle_{\xi,z}}$

Table 1: Inputs and output of the data-driven wall model.

NEURAL NETWORK ARCHITECTURE

This section aims to answer the question (iii). Since the stencil includes multiple locations, convolutional neural networks (CNNs [7]) are preferred over multi-layer perceptrons. Indeed, the translation-invariance (i.e., convolution) is encapsulated in the obtained model, which is a desirable property. For attached flows, the space-time correlations study has revealed that local and instantaneous data are sufficient to describe the relationship with $\boldsymbol{\tau}_w$. The input stencil for such flows is too big and should be reduced. Such a reduction can be seen as re-weighting of the input data through a self-attention layer [6]. The hyperparameters (e.g., kernel size, padding, stride, dilation, ...) of the model were adjusted to obtain the optimal receptive field. The most successful model (CNN-1D-SAL) contains two consecutive self-attention layers, seven one-dimensional convolutional layers, and one max-pooling layer. The model has been trained through the Mean Square Error (MSE) loss. Such a model performs well on average, but the variance of the outputs is not correctly predicted. One way to retrieve the first and second moment of the output distribution is to use Gaussian Mixture Heads (GMHs). These heads are connected at the end of the CNN (CNN-1D-SAL-GMH) and aim to predict N means, standard deviations, and mixture coefficients (μ_n, σ_n, π_n). The loss function was adapted accordingly. A third model (CNN-2D) composed of two-dimensional convolutional layers was also tested, based on an extended stencil in the spanwise direction.

DISCUSSION

The three models trained on various combinations of databases are validated *a priori*. The obtained results were very promising in the three cases. CNN-1D-SAL behaves well on averaged while CNN-1D-SAL-GMH better predicts the first and second moment of the output distribution. However, it is not able to capture the skewness of the $\tau_{w,\xi}$ distribution. CNN-2D retrieves better two-dimensional structures in the instantaneous wall shear stress field, compared to its two 1D counterparts. The second validation step, the *a posteriori* one, aims to test the model into the flow solver. This validation is first performed on the same test cases as used for the training. Then, the validation will be extended to other Reynolds numbers to evaluate the capabilities of the model to generalize. Those steps are on going work.

ACKNOWLEDGMENTS

The present research benefited from computational resources made available on the Tier-1 supercomputer of the Fédération Wallonie-Bruxelles, infrastructure funded by the Walloon Region under the grant agreement n°1117545. The SafranTech funding is gratefully acknowledged.

REFERENCES

[1]S. Hoyas and J. Jimenez. : Reynolds number effects on the Reynolds-stress budgets in turbulent channels. *Physics of Fluids*, 20:101511 (2008).

[2]Benocci, C., & Pinelli, A. : The role of the forcing term in the large-eddy simulation of equilibrium channel flow. *Engineering turbulence modeling and experiments*, pp. 287–96 (1990).

[3]Carton de Wiart, C., Hillewaert, K., Bricteux, L., & Winckelmans, G. : LES using a Discontinuous Galerkin method: Isotropic turbulence, channel flow and periodic hill flow. In J. Fröhlich, H. Kuerten, B. J.Geurts, & V. Armenio (Eds.), Direct and large-eddy simulation IX, *Springer*, (Vol.20), pp. 97–102 (2015).

[4]C. Duprat, G. Balarac, O. Métais, P. M. Congedo, and O. Brugière. : A wall-layer model for large-eddy simulations of turbulent flows with/out pressure gradient. *Physics of Fluids*, 23(1):015101, (2011-01). ISSN 1070-6631, 1089-7666.

[5]Zhideng Zhou, Guowei He, and Xiaolei Yang. : Wall model based on neural networks for LES of turbulent flows over periodic hills. *Phys. Rev. Fluids*, 6(5): 054610, (2021).

[6]Vaswani et al. : Attention Is All You Need, 31st Conference on Neural Information, Processing Systems, NIPS, USA (2017).

[7]Sakshi Indolia, Anil Kumar Goswami, S.P. Mishra, Pooja Asopa : Conceptual Understanding of Convolutional Neural Network- A Deep Learning Approach, Procedia Computer Science (Vol.132), pp.679-688 (2018).

[8]X. Gloerfelt and P. Cinnella : Investigation of the flow dynamics in a channel constricted by periodic hills, In 45th AIAA Fluid Dynamics Conference, AIAA (2015).

[9]Boxho et *al.* : Analysis of space-time correlations for the two-dimensional periodic hill problem to support the development of wall models, ETMM13 (2021).

WORKSHOP
Direct and Large-Eddy Simulation 13
October 26th-29th 2022, Udine, Italy

IN-SITU ANALYSIS OF BACKFLOW EVENTS AND THEIR RELATION TO SEPARATION IN TURBULENT WING FLOWS THROUGH WELL-RESOLVED LES

F. Mallor[1], J. Liu[2], M. Atzori[3], A. Peplinski[1], R. Vinuesa[1], R. Örlü[1], T. Weinkauf[2], P. Schlatter[1]
[1] FLOW, Engineering Mechanics, KTH Royal Institute of Technology
[2] Division of Computational Science and Technology, KTH Royal Institute of Technology
[3]Department of Particulate Flow Modelling, Johannes Kepler University, Linz, Austria
mallor@kth.se

INTRODUCTION

Wall-bounded turbulent flows occurring in transportation (*e.g.* aviation) and industrial applications (*e.g* turbomachinery), are usually subjected to pressure gradients (PGs). The presence of such PGs affects greatly the development and physics of the turbulent boundary layer (TBL), making it an open research area. An important phenomena associated with the presence of strong adverse PGs (APGs) as appearing in wings, is the separation of the boundary layer, which can lead to stall. Moreover, recent and upcoming environmental restrictions have made drag reduction crucial in aviation. With a high proportion of the drag associated to the TBLs developing over the wet surfaces of the aircraft, their study and understanding is of paramount importance.

Initial research on TBLs in wings was conducted experimentally in wind tunnels, such as the nominal study of the turbulent flow past a NACA 4412 wing profile [4]. In recent years, developments in high-performance computing (HPC) architectures and numerical methods have enabled the study of these complex flows through accurate numerical simulations. Some examples of these are the large-eddy simulations (LES) of the turbulent flow around wing profiles [6, 8, 12]. However, the chord-based Reynolds numbers (Re_c) and angles of attach (AoA) achieved so far are still moderate, and the computational domains small (particularly in the spanwise direction, a fact that can affect separation physics greatly).

The current project leverages both the increase in availability of HPC resources, as well as the improvements in simulation methods (such as the introduction of adaptive mesh refinement and non-conformal meshing into the spectral-element method code Nek5000), in order to increase the achievable Reynolds number and angle of attack, while using a sufficiently large computational domain. Moreover, Nek5000 is coupled to the visualization software Catalyst, allowing for the in-situ analysis of backflow events and the turbulent structures associated with them. The high-fidelity simulation data is then used to study the characteristics of such events, and their relation with APGs and flow separation.

METHODOLOGY

Well-resolved (quasi-DNS) large-eddy simulations (using a relaxation-term filtering, analogous to the one described in Ref. [9]) are carried out using the massively-parallel spectral-element method code Nek5000 [5]. The case considered in this work is the turbulent flow past a NACA 4412 wing profile, as in Refs. [4, 6, 12]. Combinations of four different angles of attack (5°, 8°, 11° and 14°, ranging from fully attached flow to stalled conditions) and three chord-based Reynolds numbers ($Re_c = U_\infty c/\nu = 2\times10^5$, 4×10^5 and 1×10^6) are studied. The introduction of adaptive mesh refinement (AMR) and non-conformal meshing allows to overcome some of the limitations faced in previous computational studies (such as in Ref. [12]). Firstly, the domain size (L_x; L_y; L_z) is considerably larger: (50c; 40c; 0.4c for 5°, and 0.6c 11°) in the AMR case and (6c; 4c; 0.2c) in previous conformal cases. Secondly, the boundary conditions in conformal cases have to be obtained from a precursor RANS simulation due to the proximity of the domain boundaries to the wing. As this is not an issue in the AMR case, a uniform Dirichlet boundary condition is imposed in the inlet, top and bottom boundaries. Moreover, the elements are concentrated in areas in which a higher resolution is needed (based on a spectral error indicator as described in Ref. [10]), allowing to reduce the overall computational cost of the simulation. In-situ tracking of backflow events is carried out using the Catalyst adaptor for Nek5000 [1]. The use of in-situ data analysis is paramount in this work: the high level of refinement around the wing surface and the TBL, together with the time resolution needed to track backflow events makes the traditional offline post-processing methods unfeasible.

The introduction of AMR into Nek5000, its performance, and its use in turbulent wing flow simulations is covered thoroughly in Ref. [10]. Excellent agreement was found with previous conformal simulations of the same wing profile at an AoA of 5 degrees and $Re_c = 2\times10^5$. In this work, the AMR setup is further validated against new experimental data obtained in the Minimum Turbulence Level (MTL) wind tunnel at KTH (the details of the experimental campaign can be found in Ref. [7]). The results reported in Fig. 1 show a high level of agreement between the numerical (AMR) and experimental data for the mean velocity profile in the TBL at two different angles of attack (5 and 11 degrees). It should be noted that at this station (60% of the chord), the APG is already strong, with a Clauser parameter ($\beta = \mathrm{d}P\mathrm{d}x(\delta^*/\tau_w)$) of 1.14 and 3.9, respectively. Moreover, through the use of of two-point-synchronized hot-wire measurements, the computational domain is show to be appropriately sized in order to capture correctly the largest turbulent structures, which is particularly important in the study of separated flow.

ANALYSIS OF THE RESULTS

As discussed above, the main focus of this work is the study of backflow events occurring in TBLs subjected to strong APGs and Reynolds numbers. Previous work has characterised backflow events for a variety of flow cases [3] and pressure gradient conditions (up to moderate pressure-gradient conditions) and found that both the length ($20l^+$) and life time ($2t^+$) of these events scales in inner units. Instead, merely the frequency of these events was found to increase with increasing pressure-gradient conditions. With diminishing mean wall-shear stress, when approaching mean separation, it is, however, known that inner scaling is destined to break. Hence, a structural change in the size and life time of these events is anticipated when going to strong pressure-gradient conditions and to mean flow separation. Such a structural change can be anticipated from the iso-contours of negative velocity in Fig. 2, where the region populated with back-flow events has substantially grown. This also explains the larger sizes and life times observed in stronger APG TBLs as those by [2]. Similarly to the work in Ref. [11], conditional analysis of these extreme events will be used in order to shed light on their characteristics, as well as on the flow phenomena that leads to their formation. The present study extends greatly the APG strengths previously considered, and thus the backflow levels, as evidenced in Fig. 2. Moreover, the 11° and 14° cases exhibit mean-flow separation in the region close to the trailing edge, allowing to study the relation between backflow events and mean-flow separation, therefore, shedding some light on the physics behind the initial stages of stall.

ACKNOWLEDGEMENTS

The simulations were performed on resources provided by the Swedish National Infrastructure for Computing (SNIC) at the PDC Center for High Performance Computing, in KTH, Stockholm. This research is funded by the Knut and Alice Wallenberg Foundation.

REFERENCES

[1]Atzori, M., Köpp, W., Chien, S. W., Massaro, D., Mallor, F., Peplinski, A., Rezaei, M., Jansson, N., Markidis, S., Vinuesa, R., Schlatter, P., Weinkauf, T.: In situ visualization of large-scale turbulence simulations in Nek5000 with ParaView Catalyst, *The J. of Super Comp.*, **78 (3)**, 3605–3620 (2022).

[2]Bross, M., Fuchs, T., and Kähler, Christian J. : Interaction of coherent flow structures in adverse pressure gradient turbulent boundary layers, *J. of Fluid Mech.*, **873**, 287-–321 (2019).

[3]Chin, R.C. and Vinuesa, R. and Örlü, R. and Cardesa, J.I. and Noorani, A. and Chong, M.S. and Schlatter, P. : Backflow events under the effect of secondary flow of Prandtl's first kind, *Phys. Rev. Fluids*, **5 (7)**, 074606 (2020).

[4]Coles, D., and Wadcock, A.J.: Flying-hot-wire study of flow past an NACA 4412 airfoil at maximum lift, *AIAA Journal*, **17 (4)**, 321–329 (1979).

[5]Fischer, P., Kruse, J., Mullen, J., Tufo, H., Lottes, J., and Kerkemeier, S.: Nek5000: Open source spectral element CFD solver, *Argonne National Laboratory, Mathematics and Computer Science Division, Argonne, IL*, (2008).

[6]Frère, A., Hillewaert, K., Chatelain, P., and Winckelmans, G.: High Reynolds number airfoil: From wall-resolved to wall-modeled LES, *Flow, Turb. and Comb.*, **101 (2)**, 457–476 (2018).

[7]Mallor, F., Parikh, A., Dogan, E., Atzori, M., Hajipour, M., Tabatabaei, N., Örlü, R., Vinuesa, R., and Schlatter, P.: Design and setup of a wing model in the Minimum-Turbulence-Level wind tunnel, *Tech. Report, KTH Royal Inst. of Technology* (2021).

[8]Sato, M., Asada, K., Nonomura, T., Kawai, S., and Fujii, K.: High Reynolds number airfoil: Large-eddy simulation of NACA 0015 airfoil flow at Reynolds number of 1.6×10^6, *AIAA Journal*, **55 (2)**, 673–679 (2017).

[9]Schlatter, P., Stolz, S., and Kleiser, L.: LES of transitional flows using the approximate deconvolution model, *Int. J. of Heat and Fluid Flow*, **25 (3)**, 549–558 (2004).

[10]Tanarro, A., Mallor, F., Offermans, N., Peplinski, A., Vinuesa, R., and Schlatter, P.: Enabling adaptive mesh refinement for spectral-element simulations of turbulence around wing sections, *Flow, Turb. and Comb.*, **105**, 415–436 (2020).

[11]Vinuesa, R., Örlü, R., and Schlatter, P.: Characterisation of backflow events over a wing section, *J. of Turbulence*, **18**, 170–185 (2017).

[12]Vinuesa, R., Negi, P.S., Atzori, M., Hanifi, A., Henningson, D.S., and Schlatter, P.: Turbulent boundary layers around wing sections up to Re_c= 1,000,000, *Int. J. of Heat and Fluid Flow*, **72**, 86–99 (2018).

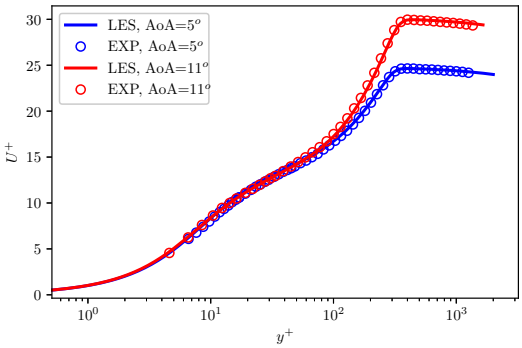

Figure 1: Mean velocity profiles in the suction side of the NACA 4412 wing at 60% of the chord. Data for 5 and 11 degrees AoA is shown, both at a Re_c=400,000.

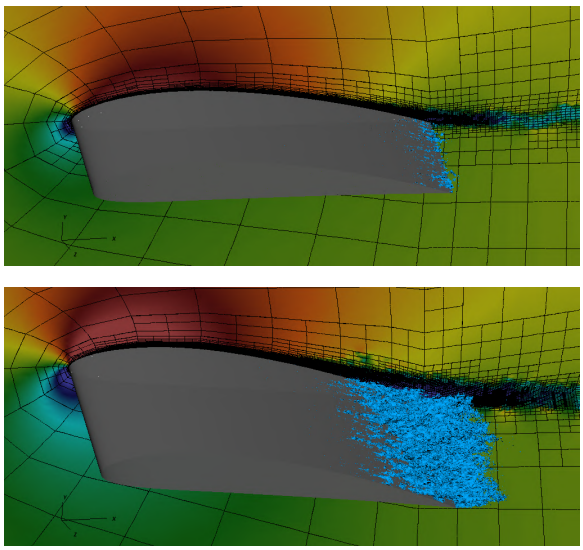

Figure 2: Instantaneous flow visualization, showing (in blue) regions with backflow ($U_x < 0$). A 2D plane of the spectral element mesh, as well as the instantaneous streamwise velocity field are shown in the background. The top and bottom images correspond to an angle of attack of 5 and 11 degrees, respectively, both at a Re_c=400,000.

WORKSHOP
Direct and Large-Eddy Simulation 13
October 26th-29th 2022, Udine, Italy

DNS AND POD/DMD ANALYSIS OF SEPARATED FLOW IN A THREE-DIMENSIONAL DIFFUSER

A. Miró [1], B. Eiximeno[1,2], I. Rodríguez[2], O. Lehmkuhl [1],
[1] Large Scale Computational Fluid Dynamics group, Barcelona Supercomputing Center
[2] TUAREG - Turbulence and Aerodynamics Research Group, Universitat Politècnica de Catalunya
arnau.mirojane@bsc.es

INTRODUCTION

The three-dimensional (Stanford) diffuser is a well documented case with complex internal corner flow and 3D separation while having a relatively simple geometry. It has an inlet section, an expansion section and an outlet section (see Figure 1).

This diffuser configuration has already been investigated in the framework of two ERCOFTAC-SIG15 Workshops and in the European ATAAC project. They studied two 3D diffuser geometries, one of which is the present geometry presented in this work. The workshop reports were published in the ERCOFTAC Bulletin Issues, see Steiner et al. [1], Jakirlić et al. [2]. Although there has been many studies on this geometry, the only high-fidelity data available is the direct numerical simulation (DNS) performed by Ohlsson et al. [3]. This DNS had a Re=10,000 and was computed using a spectral element code with 11th order polynomials. The flow was computed for 13 flow-through-times (based on the bulk inlet velocity and diffuser length) before gathering statistics, which were computed over an additional 21 flowthrough-times.

However, results presented were limited to comparison with experimental results. In the current work, we go a step further in the analysis of the physics and complexity of the flow in a 3D geometry by presenting turbulent kinetic energy (TKE) and Reynolds stress budgets, as well as a POD/DMD analysis of the relevant sections of the flow.

MATHEMATICAL AND NUMERICAL MODEL

For this DNS, the data has been obtained by solving the incompressible Navier-Stokes equations since the flow is not subject to compressibility effects. For the computations, the code Alya, developed at Alya the Barcelona Supercomputing Centre is used. Alya is a parallel multi-physics/multi-scale finite-element simulation code developed to run efficiently on high-performance computing environments. The general code is described in Vazquez et al. [4]. Details about the numerical schemes for the incompressible flow solver are described in Lehmkuhl et al. [5].

For the current diffuser, the upper-wall expansion angle is 11.3◦ and the side-wall expansion angle is 2.56◦. The flow in the inlet duct (height $h = 1$, width $B = 3.33$) corresponds to fully-developed turbulent rectangular duct flow. The origin of coordinates is set at the entrance of the diffuser. The $L = 15h$ long diffuser section is followed by a straight outlet part ($12.5h$ long). Downstream of this the flow goes through a $10h$ long contraction followed by a $5h$ straight duct in order to minimize the effect of the outlet to the diffuser.

The flow at the inlet is assumed to be a fully developed rectangular channel flow. At the outlet ($x = 47.5h$), standard Dirichlet condition for the pressure is prescribed. An inflow Reynolds number (Re) of 10,000 is considered

$$Re = \frac{uh}{\nu}, \tag{1}$$

where u is the inflow velocity ($u, v, w = 1, 0, 0$) and h is the duct height. The flow is considered to be incompressible. Turbulence is triggered by creating a small discontinuity in the form of a small chevron in the duct. This method is preferred over using a precursor calculation of rectangular duct flow with streamwise periodicity conditions. As Nikitin [6] argued, such conditions might not be suitable since they cause a spatial periodicity, which is not physical for turbulent flows. The walls of the duct and the diffuser are set to no slip.

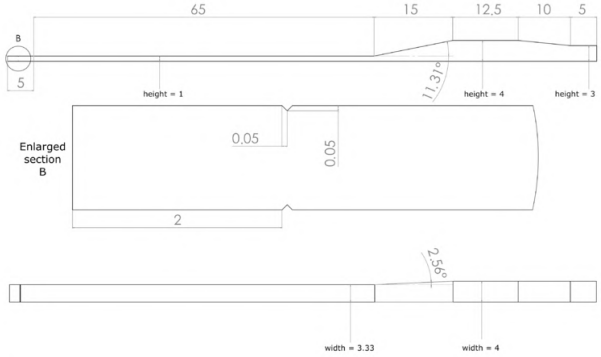

Figure 1: Domain geometry for the computational study.

The computational grid resulted in about 250 million elements. With a stretched grid, the maximum grid resolution in the duct centre is $\Delta z^+ = 11.6$, $\Delta y^+ = 13.2$, $\Delta x^+ = 19.5$. At the wall, the resolution is $z^+ = 0.074$, $y^+ = 0.37$ in the spanwise and normal directions, respectively. This resolution was deemed sufficient to compute the flow in the diffuser and is based on the previous work of Ohlsson et al. [3]. For the temporal resolution, a third order explicit Runge Kutta was used with a dynamic time stepping that ensured a CFL below 0.9.

RESULTS AND VALIDATION

The mesh resolution is quantified by obtaining the ratio between the mesh characteristic length (Δ) and characteristic lengths of the turbulence, i.e., the Taylor microscale (η_T) and Kolmogorov length scale (η_K). The latter is shown in Figure 2. As can be seen, this ratio indicates that the resolution achieved by the present grid is at DNS level.

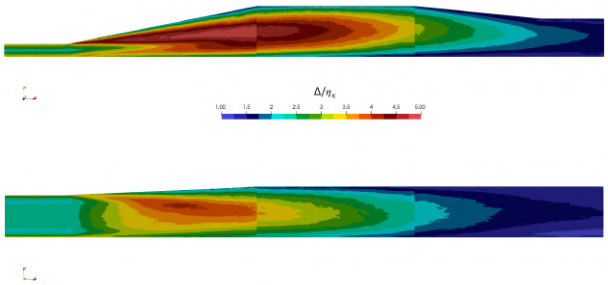

Figure 2: Stanford double diffuser, Alya DNS-250M DoF, ratio between the mesh size and the Kolmogorov lengthscale.

For verification of the quality of the results obtained in the present simulations, these are compared with those of the DNS of Ohlsson et al. [3] and the experimental data of Cherry et al. [7]. Figures 3 and 4 show, respectively, the mean streamwise velocity and its RMS values along characteristic lines of the diffuser for the experimental data and both DNS.

When compared to reference results, good agreement between present DNS and the results by Ohlsson et al. is observed. Deviations from experiments by Cherry et al. are observed in some locations, but in general, present data matches better experimental results. It should be noted that the inclusion of a roughness element in the long inlet duct in order to trigger turbulence has a negligible effect on the quality of the results.

The turbulent kinetic energy budget equation terms have also been computed. Plots have been represented for each of the budget terms of the TKE equation and the Reynolds stress equations. The magnitudes of the residuals for both equations are deemed sufficiently small for the present case. In the final version of the manuscript, turbulent kinetic energy budget will be presented and discussed in detail.

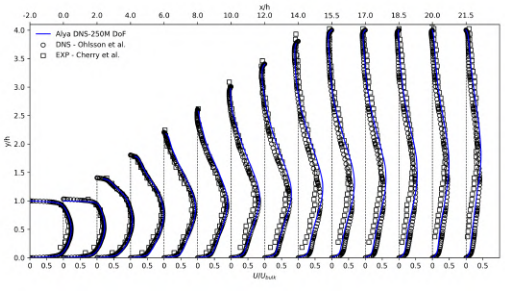

Figure 3: Stanford double diffuser, Re=10000, validation. Average velocities, Cherry et al. [7] and Ohlsson et al. [3] vs data obtained with Alya.

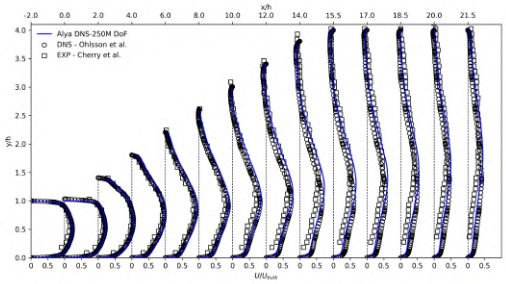

Figure 4: Stanford double diffuser, Re=10000, validation. Average streamwise velocity fluctuations, Cherry et al. [7] and Ohlsson et al. [3] vs data obtained with Alya.

Moreover, a POD/DMD analysis of the flow will also be presented. The results will be useful to understand the effect of separation in the wall-shear stress and will be useful for wall modeling purposes. Moreover, a general understanding of the flow is expected to be gained so that, for example, the Reynolds stress equation budgets can be understood.

REFERENCES

[1] H. Steiner, S. Jakirlic, G. Kadavelil, R. Manceau, S. Saric, and G. Brenn, "13th ERCOFTAC workshop on refined turbulence modelling," (Graz University of Technology, Austria), p. 7.

[2] S. Jakirlić, G. Kadavelil, M. Kornhaas, M. Schäfer, D. Sternel, and C. Tropea, "Numerical and physical aspects in LES and hybrid LES/RANS of turbulent flow separation in a 3-D diffuser," *International Journal of Heat and Fluid Flow*, vol. 31, pp. 820–832, Oct. 2010.

[3] J. Ohlsson, P. Schlatter, P. F. Fischer, and D. S. Henningson, "Direct numerical simulation of separated flow in a three-dimensional diffuser," *Journal of Fluid Mechanics*, vol. 650, pp. 307–318, May 2010.

[4] A. M. Vazquez, G. Houzeaux, S. Koric, A. Artigues, J. Aguado-Sierra, R. Aris, D. Mira, H. Calmet, F. Cucchietti, H. Owen, E. Casoni, A. Taha, E. D. Burness, J. M. Cela, and M. Valero, "Alya: Multiphysics engineering simulation towards exascale," *J. Comput. Sci.*, vol. 14, pp. 15–27, 2016.

[5] O. Lehmkuhl, G. Houzeaux, H. Owen, G. Chrysokentis, and I. Rodriguez, "A low-dissipation finite element scheme for scale resolving simulations of turbulent flows," *Journal of Computational Physics*, vol. 390, pp. 51 – 65, 2019.

[6] N. Nikitin, "On the rate of spatial predictability in near-wall turbulence," *Journal of Fluid Mechanics*, vol. 614, pp. 495–507, Nov. 2008.

[7] E. M. Cherry, C. J. Elkins, and J. K. Eaton, "Geometric sensitivity of three-dimensional separated flows," *International Journal of Heat and Fluid Flow*, vol. 29, pp. 803–811, June 2008.

WORKSHOP
Direct and Large-Eddy Simulation 13
October 26th-29th 2022, Udine, Italy

REYNOLDS-NUMBER DEPENDENCE OF SEPARATING FLOW OVER A BUMP IN SPANWISE ROTATING CHANNEL FLOWS

W. Wu[1,*], D. Patel[1], B. Savino[1]
[1] Fundamental & Applied Science of Turbulence Laboratory
Department of Mechanical Engineering, University of Mississippi, USA
wu@olemiss.edu

INTRODUCTION

Rotation characterizes many turbulent flows, both in nature (*e.g.*, geophysical flows) and in engineering applications (for instance, turbines, pumps, cyclone separators, the flow in cooling systems in radars, and so on). The literature on the subject of rotating flow is quite large. For a channel that is rotating about its spanwise axis (z), the Coriolis force appears as terms $2\Omega v$ and $-2\Omega u$ in the streamwise-(x) and wall-normal (y)-momentum equations, respectively. It destabilizes the flow when the rotation has the same sign as the mean shear vorticity and stabilizes the turbulence when the two have opposite signs (figure 1). A flow phenomenon that frequently occurs

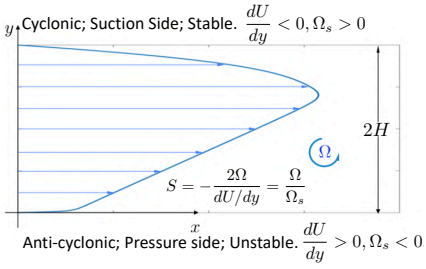

Figure 1: Schamatic of a spanwise rotating channel flow.

and has a dramatic effect on the performance of a rotating device is massive flow separation. It is often induced by either an abrupt expansion or an adverse pressure gradient in the flow. The stabilization/destabilization influence of the Coriolis force may promote or delay flow separation and reattachment. The effects of spanwise rotation on separation have been investigated in backward-facing steps [1, 2], sudden expansion channel [3], rib-roughened channel [4] and diffuser [5]. A common finding is that the separation bubble decreases with increasing anti-cyclonic rotation and increases with increasing rate of cyclonic rotation. Since separation is enforced by the geometrical singularities in these studies, the recirculation region can be reduced but not completely eliminated. Compared with the geometry-induced separation, limited information is available on the dynamics of the adverse pressure gradient(APG)-induced flow separation in which the onset of separation may constantly change with the upstream condition.

In this study, we study the flow separation produced by a lower curved bump in a turbulent channel. The bump has a smooth geometry variation that allows the separation point to move freely in the aft part of the bump. The flow is examined at three rotation numbers including the non-rotating condition and two Reynolds numbers. Both the cyclonic and anti-cyclonic rotations are examined.

PROBLEM FORMULATION

Turbulent channel flows rotating in the spanwise direction at Reynolds number $Re_b = U_b H/\nu = 2500$ and 5000 (H is the channel half-height and U_b the bulk velocity) are simulated by DNS. The friction Reynolds number, Re_τ, is 162 and 296 when the channel is not rotating respectively. A two-dimensional bump defined by $y = -a(x-4)^2 + h$ is placed on the bottom wall of the channel. Depending on the sign of the rotation rate, this side is either anti-cyclonic (*i.e.*, positive Ro) or cyclonic (negative Ro). The height of the bump is $h = 0.25H$. The bump is $2.58H$ long on the wall with a=0.15. Six simulations are performed at three rotation numbers $Ro = 0$ and $\pm$ 0.42 at the two Reynolds numbers. The parameters of the cases are listed in Table 1. 'P', 'N', and 'H' in the names of the cases denote positive Ro, negative Ro, and high Reynolds number cases, respectively. The friction Reynolds number at the bump crest ranges from 174 to 210 (276 to 347) at the lower (higher) Reynolds number. A calculation domain of $39H \times 2H \times 6H$ in the streamwise (x), wall-normal (y), and spanwise (z) directions is employed. The long streamwise domain size is used to ensure the flow is fully recovered by the outlet and recycled back to the inlet by the periodic boundary condition.

Cases	Ro	x_{sep}	y_{sep}	L_{sep}
Ro0	0	4.55 (0)	0.203	1.79 (0)
P42	0.42	4.74 (+0.19)	0.166	0.90 (-50%)
N42	-0.42	4.48 (-0.07)	0.214	3.77 (+110%)
Ro0H	0	4.47 (-0.08)	0.216	1.42 (-21%)
P42H	0.42	4.66 (+0.11)	0.185	0.85 (-53%)
N42H	-0.42	4.38 (-0.17)	0.228	2.96 (+66%)

Table 1: Simulation parameters and separation region measurements. The bulk Reynolds numbers are 2,500 (Ro0, P42, N42) and 5,000 (Ro0H, P42H, N42H). Values in the brackets are changes with respect to Case Ro0.

The equations of motion are solved using a well-validated finite difference code that solves the incompressible Navier-Stokes equations on a staggered grid. The solver has been successfully applied to many fluid flow problems with embed-

ded structures [6, 7]. Snapshots are collected over $400H/U_b$ for statistical averaging. Grid independent results are obtained by $1196 \times 192 \times 184$ and $2496 \times 386 \times 384$ grid points at the two Reynolds numbers respectively. The maximum Δx^+, Δz^+, and Δy^+ at the walls are 9.3, 6.5, and 0.5. Away from the wall, the grid spacing is less than six times the local Kolmogorov length scale in all the cases. In the following, we will refer to the two sides as *anti-cyclonic* or *cyclonic* with respect to the mean shear near the bottom wall.

RESULTS AND DISCUSSIONS

Contours of mean streamwise velocity and the separating streamlines are shown in figure 2. The separation region is reduced when flow over the bump is under anti-cyclonic rotation, and enlarged under cyclonic rotation (also refer to Table 1), in line with the existing literature. Surprisingly, as Re increases, separation occurs about $0.08H$ $\sim 0.1H$ earlier in the aft part of the bump compared with the corresponding lower Re cases at each rotation number. The flow reattaches earlier as well, leading to the shorter recirculation zones. The reduction of the mean separation bubble due to increasing Re is most significant when the bump is on the stable/suction/cyclonic side of the channel.

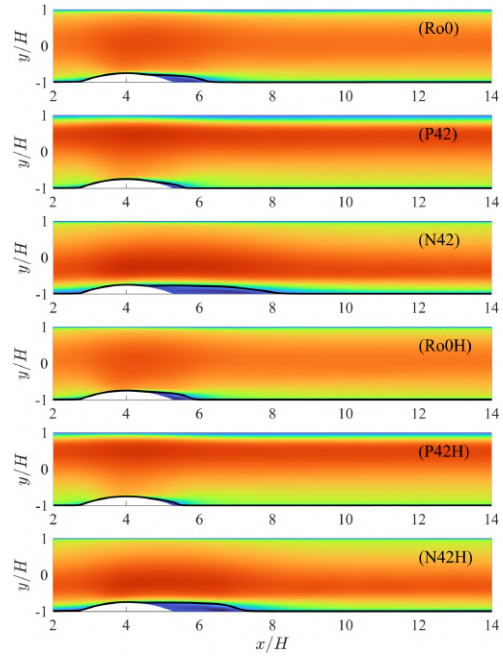

Figure 2: Contours of the mean streamwise velocity. Solid line are mean separation streamlines.

Figure 3 shows the profiles of the total drag accumulated from the inflow boundary of the calculation domain. Since the flow over the bump and the separation also affect the flow on the other wall of the channel, the skin friction drag and form drag on all the surfaces are taken into consideration. For the region around the bump ($x \leq 5.3H$), anti-cyclonic rotation reduces the drag by the end of the bump by 20% at the lower Re. The reduction, however, is not as remarkable as it is for the mean separation region (*i.e.*, -50%). The cyclonic rotation shows a total drag that is comparable to the non-rotating case (-3%) over the bump region, in spite of the more than doubled separation region. Comparing the cases at the same Ro but different Re, the total drag decreases as Re increases as expected. Unlike its counterpart at the lower Re, cyclonic rotation at higher Re shows a significant drag reduction (-25%) compared with the non-rotating case at the same Re. The anti-cyclonic rotation reduces the total drag by 17% at the higher Re. Note that the separation region in case P42H is so small that one may intuitively think that the form drag is close to zero. The current data indicates that the size of the separation bubble is a poor indicator of the drag created by the bump. Even if there is no massive separation, the form drag may still be quite large.

When considering the overall drag up to the streamwise location where the flow in all the cases is recovered from the wake of the bump ($x = 32H$), the bump contributes to 27%$\pm$ 1% of the total drag at both Reynolds numbers when $Ro =$ 0 and -0.42. For the anti-cyclonic rotation, its contribution increases from 24% to 32% as the Reynolds number increases. The friction drag after the flow reattachment is significant. The profiles in figure 3 show that Case P42H has a higher total drag up to $x/H \sim 12$ compared with case N42H. But after that, the friction drag produced by the former is less than it is in the latter. By $x = 32H$, the drag is lower by $0.017\ U_b^2/H$ in case P42H than in N42H.

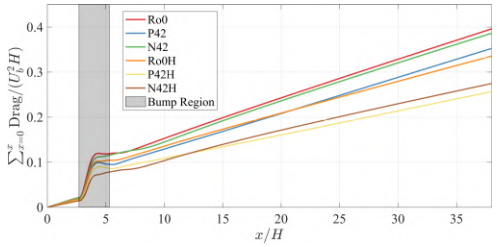

Figure 3: Profiles of the total drag accumulated from the inflow boundary.

In conclusion, separation is almost completed eliminated at $Ro = 0.42$. As the Reynolds number increases, the separation occurs earlier over the bump in the current configuration. The separation region reduces with the increasing Re at all three rotation rates especially when the rotation is cyclonic. The size of the recirculation zone is a poor indicator of the total drag.

REFERENCES

[1]Barri M. and H.I. Andersson: Turbulent flow over a backward-facing step. Part 1. Effects of anti-cyclonic system rotation. *J. Fluid Mech.*, **665**, 382–417 (2010).

[2]Visscher J. and H.I. Andersson: Particle image velocimetry measurements of massively separated turbulent flows with rotation. *Phys. Fluids*, **23**, 075108 (2011).

[3]Lamballais, E.: Direct numerical simulation of a turbulent flow in a rotating channel with a sudden expansion. *J. Fluid Mech.*, **745**, 92–131 (2014).

[4]Coletti F., Lo Jacono D., Cresci I. and Arts T.: Turbulent flow in rib-roughened channel under the effect of Coriolis and rotational buoyancy forces. *Phys. Fluids*, **26**, 045111 (2014).

[5]Rothe P. H. and Johnston J. P.: Effects of System Rotation on the Performance of Two-Dimensional Diffusers . *ASME J. Fluids Eng.*, **98**, 422–429 (1976).

[6]Wu, W. and Piomelli, U.: Effects of surface roughness on a separating turbulent boundary layer. *J. Fluid Mech*, **841**, 552–580 (2018).

[7]Wu, W., Piomelli, U. and Yuan, J. Turbulence statistics in rotating channel flows with rough walls. *Int. J. Heat Fluid Flow*, **80**, 108467 (2019).

Session: Industrial and environmental applications 1

Thursday, October 27, 2022

09:50 – 10:50

WORKSHOP
Direct and Large-Eddy Simulation 13
October 26th-29th 2022, Udine, Italy

DIRECT NUMERICAL SIMULATIONS OF NON-LINEAR TRANSITION IN THE MAGNETOHYDRODYNAMIC PIPE FLOW SUBJECT TO A TRANSVERSE MAGNETIC FIELD

Y. Velizhanina[1] **and B. Knaepen**[1]
[1] Université Libre de Bruxelles, Faculté des Sciences, Physique des Système Dynamiques,
Boulevard du Triomphe CP231, 1050 Ixelles, Belgium
bernard.knaepen@ulb.be

INTRODUCTION

Numerous studies dedicated to the linear stability of Poiseuille flow through a circular pipe suggest that it is linearly stable for all Reynolds numbers [1]. At the same time surprisingly little attention has been devoted to the linear stability analysis of the magnetohydrodynamics (MHD) pipe flow. The only relevant study in this context is that of Åkerstedt who analyzed the stability of Poiseuille pipe flow subject to a uniform axial magnetic field and observed that it damps three-dimensional disturbances [2].

Generally the effect of an applied magnetic field on a flow of an electrically conducting fluid is two-fold. Firstly, it may modify the mean velocity profile and give rise to inflexion points, shear layers and regions of velocity overspeed ("jets") [3]. As a consequence, the flow may become less stable with respect to small disturbances. Secondly, the magnetic field tends to stabilize the flow due to the Joule dissipation resulting from the occurrence of induced currents.

PROBLEM DESCRIPTION AND RESULTS

In this work we analyze the stability and transition of the MHD pipe flow in the presence of a transverse magnetic field. To model the flow we use the quasi-static approximation of the MHD equations as we focus on liquid-metal flows at low magnetic Reynolds numbers.

Contrary to the case considered by Åkerstedt, the effect of Joule damping is combined with the stretching of the mean velocity profile and the occurrence of "jets". In terms of base flow deformation, it bears some similarities with the flow through an elliptic pipe due to the elongation of the velocity profile along the magnetic field. In the elliptic pipe, this deformation results in the occurrence of unstable modes even in the case of small ellipticity [4]. We observe here that while the flow elongation in the presence of the magnetic field has a destabilizing effect on the flow, it is not large enough to trigger any instability. However, we find that the hydromagnetic pipe flow becomes linearly unstable when this effect is combined with the occurrence of overspeed regions in the Roberts layers. These "jets" are known to emerge at sufficiently high values of the conductivity of the pipe wall and Hartmann numbers [5, 6].

In the first part of our presentation, we discuss the results of an extensive parametric study that explores the counter-balance between the stabilizing and destabilizing effects of the transverse magnetic field. We also discuss the structure of the unstable modes occurring in the different flow regimes in terms of Reynolds numbers Re, Hartmann numbers Ha and conductivity χ of the pipe wall. For example, we present in Figure 1 the critical Reynolds number as a function of the Hartmann number for infinitely conductive pipe wall and observe the existence of a global minimum Reynolds number $Re \approx 43605$.

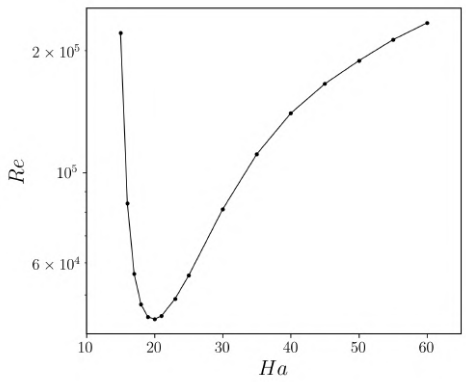

Figure 1: Critical Reynolds number as a function of the Hartmann number for infinitely conductive pipe wall.

In the second part of our presentation we discuss the non-linear evolution of the unstable modes obtained earlier. In figure 2 we illustrate the structure of such a mode by plotting isocontours of the streamwize velocity perturbation. We observe that in the presence of the magnetic field $\mathbf{B}$, the unstable modes are characterized by slow and rapid streamize streaks in the region of the flow where the pipe's wall is parallel to the magnetic field (regions also known as Roberts layers). Using high resolution direct numerical simulations we show how these streaks then become unstable through a secondary non-linear transition. Our simulations are performed using the YALES2 code [7] which discretizes the domain using a fourth order accurate unstructured finite volume method and the TRK4 fourth-order temporal scheme for time advancement. For the discretization of the MHD term, we use the method developed in [8] that allows to impose the divergence free condition on electrical currents up to machine precision.

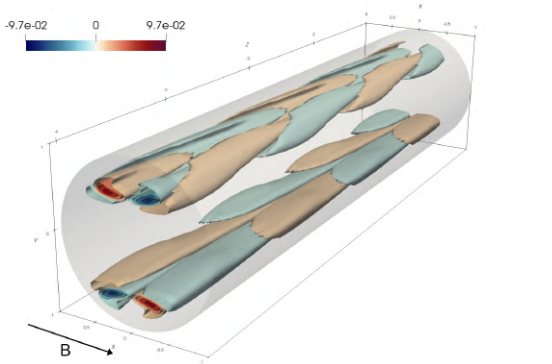

Figure 2: Isocontours of the streamwise velocity for the most unstable mode at $Re = 1.66 \cdot 10^5$, $Ha = 45$ and $\chi = \infty$.

REFERENCES

[1]Meseguer, À. and Trefethen, L. N. : Linearized pipe flow to Reynolds number 107," *J. Comput. Phys*, **186**(1), 178—197 (2003).

[2]Åkerstedt, H. O. : Damping of transient energy growth of three-dimensional perturbations in hydromagnetic pipe flow, *Fluid Dyn. Res.*, **15**(5), 295—312 (1995).

[3]Priede, J., Aleksandrova, S. and Molokov, S. : Linear stability of Hunt's flow, *J. Fluid Mech.*, **649**, 115-–134 (2010)

[4]Davey, A. and Salwen, H. : On the stability of flow in an elliptic pipe which is nearly circular, *J. Fluid Mech.*, **281**, 357–369 (1994).

[5]Samad, S. A. : The flow of conducting fluids through circular pipes having finite conductivity and finite thickness under uniform transverse magnetic fields, *Int. J. Eng. Sci.*, **19**(9), 1221–1232 (1981).

[6]Vantieghem, S., Albets-Chico, X. and Knaepen, B. : The velocity profile of laminar MHD flows in circular conducting pipes, *Theor. Comp. Fluid Dyn.*, **23**(6), 525–533 (2009)

[7]Moureau, V., Domingo, P. and Vervisch, L. : Design of a massively parallel CFD code for complex geometries, *C. R. Méc.*, **339**, 141–148 (2011)

[8]Ni, M., Munipalli, R., Huang, P., Morley, N. and Abdou M. : A current density conservative scheme for incompressible MHD flows at a low magnetic Reynolds number. Part II: On an arbitrary collocated mesh, *J. Comput. Phys.*, **227**(1), 205–228 (2007).

WORKSHOP
Direct and Large-Eddy Simulation 13
October 26th-29th 2022, Udine, Italy

A PRIORI ANALYSIS FOR LES OF A PLUME IN CROSSFLOW

Daniel Fenton[1], **Andrea Cimarelli**[2], **Jean-Paul Mollicone**[3], **Maarten van Reeuwijk**[4], **Elisabetta De Angelis**[1,5]
[1] School of Engineering, Cardiff University, UK, fentond@cardiff.ac.uk
[2] Dipartimento di Ingegneria "Enzo Ferrari", Università di Modena e Reggio Emilia, Italy
[3] Department of Mechanical Engineering, University of Malta, Malta
[4] Department of Civil & Environmental Engineering, Imperial College London, UK
[5] DIN, Università di Bologna, Forlí, Italy

INTRODUCTION

Buoyancy driven flows are very common in both industry and nature, with examples ranging from volcanic ash clouds to pollutant dispersion. Their prevalence and importance has led to great interest across many fields, from disaster management to the impact of industry on the climate. Despite decades of research, their often turbulent nature leaves their behaviour still difficult to understand and predict. In the present study, the behaviours of turbulent buoyant plumes subjected to uniform crossflow are investigated starting with a numerical data set obtained via direct numerical simulation (DNS).

SETUP AND PARAMETERS

In the absence of compressibility, the Navier-Stokes equations for velocity $\mathbf{u}$ and kinematic pressure perturbation p coupled with a buoyancy field b acting in the $\hat{\mathbf{k}}$ direction satisfy

$$\begin{aligned} \frac{\partial \mathbf{u}}{\partial t} + (\mathbf{u}\cdot\nabla)\mathbf{u} - \nu\nabla^2\mathbf{u} + \nabla p - b\hat{\mathbf{k}} &= \mathbf{0} \\ \frac{\partial b}{\partial t} + (\mathbf{u}\cdot\nabla)b - \kappa\nabla^2 b &= 0 \\ \nabla\cdot\mathbf{u} &= 0, \end{aligned} \tag{1}$$

where ν is the kinematic viscosity and κ the diffusivity constant. The buoyancy field is defined by $b = g(\rho_0 - \rho)/\rho_0$, where ρ_0 is a constant reference density and g the gravitational acceleration, and the pressure perturbation $p = \bar{p}/\rho_0 + gz$ with standard pressure $\bar{p}$. The case set up is the same as that of Jordan et al [1], however the plumes in the present study are not infinitely lazy at the source, meaning that a non-zero momentum and a non-zero buoyancy are responsible for the dynamics. For the current simulation the source Reynolds number, defined through the buoyancy velocity scale, and Richardson numbers are

$$Re_0 = \frac{2F_0^{1/3}r_0^{2/3}}{\nu} = 1000, \quad Ri_0 = \frac{F_0}{r_0 w_0^3} = 1, \tag{2}$$

where F_0 is the source integral buoyancy flux, r_0 is the radius of the source and w_0 is the velocity. The numerical scheme employed is that of Craske and van Reeuwijk [2], building on the work of Verstappen and Veldman [3], utilising a robust finite difference method with fourth-order spatial discretisation and a third-order Adams-Bashforth time integration scheme. A CFL target of 0.3 determines the variable timestep size, with a maximum Δt of 0.025. The large numbers of degrees of freedom ensure a highly accurate method which can resolve the multi-scale phenomena associated with turbulent flows, with staggered computational grids of $1350 \times 774 \times 774$ cells over a $28 \times 24 \times 24$ domain, in the streamwise, spanwise and vertical directions respectively.

DATA ANALYSIS

Owing to the multi-scale complexities of buoyancy driven turbulent flows, a highly refined simulation grid is required for DNS, see e.g. a cross section of enstrophy in the figure 1, hence the development of appropriate large eddy simulation tools would be advisable. In the present contribution, the ability of the large-scale resolved field to capture the main flow features will be firstly analyzed. The behavior of turbulence intensities of the resolved fluctuations as a function of the filter lengths will be also presented and the *a priori* assessment of the behaviour of turbulence models for large eddy simulation (LES) will be discussed.

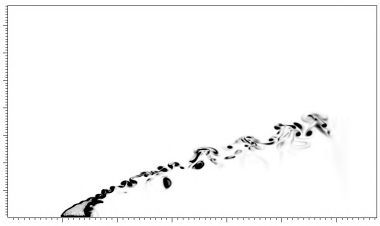

Figure 1: Instantaneous 2D snapshot of the plume enstrophy in the $x - z$ plane.

REFERENCES

[1] Jordan, O. H., Rooney, G. G., Devenish, B. J. and van Reeuwijk, M. : Under pressure: turbulent plumes in a uniform crossflow *J. Fluid Mech.*, **932**, A47 (2022).
[2] Craske, J. and van Reeuwijk, M. : Energy dispersion in turbulent jets. Part 1. Direct simulation of steady and unsteady jets *J. Fluid Mech.*, **763**, 500–537 (2015).
[3] Verstappen, R. W. C. P. and Veldman, A. E. P. : Symmetry-preserving discretization of turbulent flow *J. Comp. Phys.*, **187**, 343–368 (2003).

WORKSHOP
Direct and Large-Eddy Simulation 13
October 26th -29th 2022, Udine, Italy

LES STUDY OF THE URBAN BOUNDARY LAYER OVER A CITY

L. Yao[1], C.-H. Liu[1*]
[1] Department of Mechanical Engineering
The University of Hong Kong, Pokfulam Road, HKSAR
**Corresponding Author*, liuchunho@graduate.hku.hk

INTRODUCTION

With the accelerating urbanization and the persistent COVID-19 pandemics, air quality has been increasingly influential in people's lives [1]. Urban boundary layer (UBL) flow, which directly governs the air exchange between atmosphere and urban canopies, has received growing attention from the academic and engineering areas. Investigations into UBL dynamics are commonly conducted via field measurements (e. g. wind speed/pressure sensors mounted on towers) and scaled-down experiments (e. g. wind/water tunnels with 3D-printing models), as well as numerical methods (e. g. RANS, LES and DNS). Despite the good approximation of realistic wind field via situ measurements/experiments, there are inherent drawbacks that either the whole flow field could be barely obtained, or the space of the targeting-built area is rather limited. Therefore, LES is another feasible solution to sketch the whole picture of UBL flow over diversified urban built patches [2]. With the aid of LES and large-scale computers, the turbulence information at any point (based on the balance between accuracy required and affordable cost), especially, the higher-order moments of velocity fluctuations, as well as frequency information of eddies, would be obtained in details. Understanding UBL flow could benefit urban planning for air quality improvement.

METHODOLOGY

To study UBL flow, the full-scale building models from a representative densely built city, Hong Kong, are digitalized. The targeting area locates in Kowloon Peninsula, extending 10 km and 13 km in the East-West and South-North directions, respectively. LES is used to calculate the incompressible flows in neutral thermal conditions. The incoming wind (10 m sec^{-1}) is prescribed at the Western inlet (Figure 1). The governing equations consist of the continuity and momentum conservations that are solved by the finite volume (FV) method. OpenFOAM utilities *snappyHexMesh* are adopted for mesh discretization (110 million FV cells). The conservation of subgrid-scale (SGS) turbulence kinetic energy (TKE) and SGS momentum flux are modeled by one-equation SGS and Smagorinsky models, respectively. The gradient and divergence terms are calculated with the cell-limited gradient scheme and the limited linear divergence schemes, respectively. The implicit Euler scheme is used in the time integration. The PIMPLE (a combination of Pressure Implicit with Splitting of Operator and Semi-Implicit Method for Pressure-Linked Equations) algorithm is used to handle the velocity-pressure coupling. The Geometric Algebraic Multigrid (GAMG) preconditioner and the Conjugate Gradient (CG) method are used to solve the pressure while the Preconditioned Bi-Conjugate Gradient (PBiCG) method is used to solve other variables.

RESULTS

In the wind field, giant wakes are formed by the building clusters, extending several kilometers downstream (Figure 1). Urban buildings are highly 3D with a combination of height, ranging from 10 m to 500 m. This exceptional heterogeneity generates a flow field essentially different from that of the simplified roughness cases, such as cubes, riblets arranged in a regular layout (aligned/staggered) [3]. Besides, due to the blockage, the main flow deviates around 30^0 to 50^0 from the prescribed direction. To conduct the analysis of turbulence dynamics, the statistical terms are thusly computed after the rotation of velocity field to the streamwise-spanwise coordinate system.

To study the effects of the buildings, the inner layers of UBL are divided into roughness- and inertial-sublayers (i.e., RSL and ISL) via the identification of the law-of-the-wall (i.e., log-law) region. The depth of RSL is around 3 to 5 times of the average building height, falling into the typical UBL range. However, it is increased by upstream wakes. This RSL elevation would lead to the persistence of anisotropic turbulent structures. It would be interesting to examine the

flow dynamics affected by upstream wakes, for example, whether the upstream, large-structure meandering would increase the diversity of turbulence structures generation downstream or not, and how it affects the pedestrian-level ventilation. The related analysis is under preparation for the presentation.

Ejection (Q2) and sweep (Q4) are two main quadrant events dominating the momentum transport process [4]. It is confirmed that, for UBL flow, Q2 appears more frequently than does Q4 in RSL. However, Q4 dominates the contribution to the vertical momentum flux. An example is given in Figure 2. By filtering quadrant events with a range of bins, it is further found that a critical scale of momentum strength (around 4 times of the averaged value) determines the dominance of occurrence and flux fractions between the two events. In other words, there are larger portions of small-scale Q2 and large-scale Q4 in RSL, compared with their counterparts with the same strength, respectively. More interestingly, the two coherent structures switch their behaviors in ISL. The fundamental reasons behind need further study. Nevertheless, this critical value characterizes realistic UBL flow.

Unlike the turbulent flow over idealized roughness, other distinctive phenomenon for realistic UBL flow is observed: (1). Elevated peak and/or dual peaks of momentum flux profiles indicating the intensified turbulence generation; and (2). The highly skewed RSL flow with super Gaussian distribution, enhancing the intermittency and extremity of strong structures. Those details will be reported in the presentations. Despite the preliminary progress, the wind field of a dense urban area is complicated due to many uncertainties in nature. For example, the daily/seasonal change of wind incident angles not only affects the wake generation but also changes the spatial relative position. The contrast of different wind directions will be included in the next step. The findings could contribute to the theoretical framework of turbulent boundary layer flow over large-scale heterogenous roughness elements as well as help urban planners and policy makers to create a better air ambient in cities.

REFERENCES

[1] Li, Z., Guo, J., Ding, A., Liao, H., Liu, J., Sun, Y., Wang, T., Xue, H., Zhang, H. and Zhu, B. : Aerosol and boundary-layer interactions and impact on air quality. *National Science Review*, **4(6)**, 810-833 (2017).

[2] Argyropoulos, C.D. and Markatos, N.C. : Recent advances on the numerical modelling of turbulent flows. *Applied Mathematical Modelling*, **39(2)**, 693-732 (2015).

[3] Takimoto, H., Inagaki, A., Kanda, M., Sato, A. and Michioka, T. : Length-scale similarity of turbulent organized structures over surfaces with different roughness types. *Boundary-layer meteorology*, **147(2)**, 217-236 (2013).

[4] Wallace, J.M. : Quadrant analysis in turbulence research: history and evolution. *Annual Review of Fluid Mechanics*, **48**, 131-158 (2016).

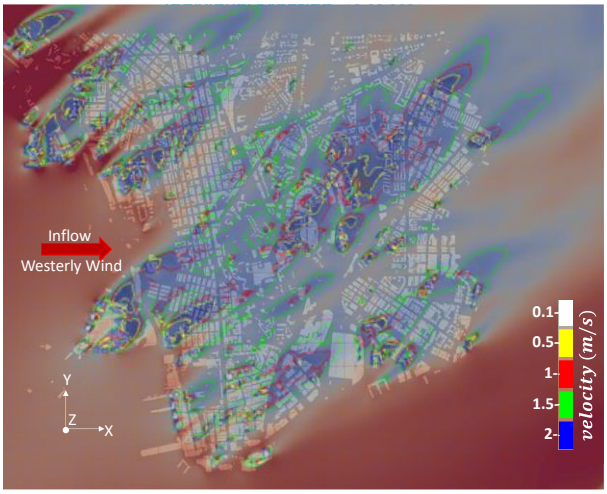

Figure 1: A planar view of the velocity field of UBL flow over Kowloon Peninsula (at z = 150m).

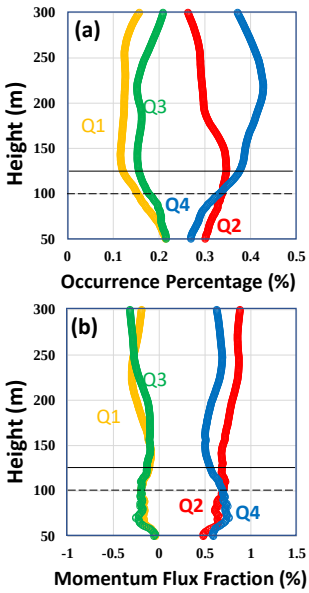

Figure 2: An example of UBL statistics of quadrant events: (a). the occurrence percentage of each quadrant; (b) the contribution to vertical momentum flux transport by each quadrant. Dashed and solid black lines indicate the upper limit of roughness- and inertial-sublayers (i.e., RSL and ISL).

WORKSHOP
Direct and Large-Eddy Simulation 13
October 26th-29th 2022, Udine, Italy

DEVELOPMENT AND APPLICATION OF AN ALGEBRAIC WALL-FUNCTION FOR CRYOGENIC SUPERCRITICAL FLOWS FROM A WALL-RESOLVED LES DATABASE

G. Indelicato[1] **P. E. Lapenna**[1] **A. Remiddi**[1] **F. Creta**[1]
[1] Department of Mechanical and Aerospace Engineering
Sapienza University of Rome, Italy
giuseppe.indelicato@uniroma1.it

INTRODUCTION

Nowadays a number of engineering and industrial applications envisages a cryogenic stream subjected to heat transfer within a pipe or a channel. Suffice it to think about nuclear reactors, power generation plants and rocket engines systems. Such wall-bounded, stratified (and generally reacting) flows represent a challenge both from the numerical modelling and the theoretical standpoint, given on one hand the interplay of different phenomena and on the other the resolution required by near-wall gradients. Specifically in the context of Liquid Rocket Engines (LRE), the mentioned configuration can be found in the propellant injection and in the regenerative cooling system of a LRE, where the fuel (hydrogen or methane) is in both case interested by some heat transfer mechanism due to the high temperature from the combustion chamber. Experimental campaigns could in this context provide a substantial help in sheding light on these heat transfer phenomena and on the near-wall behavior of such flows. However the extreme thermodynamic and operative conditions under which the aforementioned systems work, generally make these campaigns prohibitive and expensive, ultimately delegating the mentioned responsibility to Computational Fluid Dynamics (CFD). As a consequence, an increasing need of computationally affordable and reliable models is nowadays observed.

In view of reducing the stiffness of multi-dimensional wall-bounded simulations, specifically that associated to the resolution of turbulent boundary layers, one approach is to use wall-functions as approximate wall boundary conditions. Despite the large literature on the subject [2, 4] on both algebraic [3] and numerical [1] models, in the context of high pressure, cryogenic (trans- and/or supercritical) flows, a lack of dedicated models is observed to the best of the author's knowledge. Therefore this work aims at outlining and presenting the main steps behind the derivation of a newly developed algebraic wall-function for trans- and supercritical flows [5]. Concurrently it provides both *a-priori* and 2D/3D *a-posteriori* applications of the proposed model against a recently developed wall-resolved LES database of supercritical para-hydrogen in a cylindrical heated pipe [6]. The proposed model provides an Equation of State (EOS)-independent formulation, thus being specifically suited for real-gas flows.

WALL-RESOLVED LES DATABASE

The mentioned database, employed as a reference solution in the present work, includes a turbulent flow through a straight heated circular pipe of diameter $D = 0.16$ mm with a first $15D$ entrance length to let turbulence develop and a $35D$ heated segment. The flow is cryogenic para-hydrogen at a pressure $p_0 = 5$ MPa (LH2, critical pressure $p_{cr} = 1.28377$ MPa, pseudo-boiling temperature $T_{pb}(p_0) \approx 46$ K) and at an inlet temperature $T = 25$ K, corresponding to a density $\rho = 71.95$ kg/m3. The inlet mass flow is 1324 kg/m^2/s, leading to an inlet velocity $U = 18.4016$ m/s. Different wall heat fluxes q_w from 1 to 5 MW/m^2 are imposed on the pipe wall by keeping the inlet mass flux constant in order to gradually see the pseudo-boiling transition inside the pipe, as schematically displayed in the phase-diagram of H2 provided in Fig. 1. Main characteristics of each simulated case are summarized in Tab. 1.

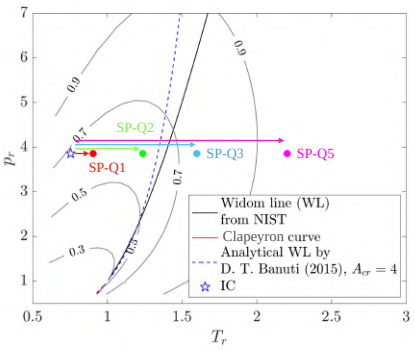

Figure 1: Phase diagram of para-hydrogen in reduced temperature ($T_r = T/T_{cr}$) and pressure ($p_r = p/p_{cr}$). Contour values of compressibility factor reported in grey. Colored markers denote outlet conditions of each case in terms of bulk pressure and temperature. Also displayed is the Widom line (WL) from the analytical expression proposed in [10] and obtained from NIST [9] as the locus of maximum specific heat c_p values. IC stands for Inlet Conditions.

All the simulations are obtained with an in-house unsteady and pressure-based solver based on OpenFOAM [7] and OpenSMOKE++ [8]. A modified version of the Pressure Implicit with Splitting of Operators (PISO) algorithm is used to handle the pressure-velocity coupling. The WALE sub-grid

Run label	ρU (kg/m^2/s)	q_w (MW/m^2)	$p_r = p_0/p_c$ (-)	$Re_{b,max}$ (-)
SP-Q1	1324	1	3.894	21000
SP-Q2	1324	2	3.894	33000
SP-Q3	1324	3	3.894	48000
SP-Q5	1324	5	3.894	52000

Table 1: Key quantities of the wall-resolved LES (WR-LES) database of cryogenic para-hydrogen in a heated pipe. The subscript b refers to bulk quantities. $Re_b = (\rho U)_b D/\mu_b$ is the bulk Reynolds number whose maximum is attained on the outlet section of the pipe.

model is chosen as turbulence closure [11].

THE NEWLY PROPOSED REAL GAS WALL-FUNCTION

The development of the proposed algebraic wall-function is based on:

1) an analytical law relating temperature T to velocity in the near-wall region:

$$\frac{T}{T_w} = D - B_q Pr_t U^+ \tag{1}$$

being D an integration constant depending on the Prandtl number of the fluid on the wall, $B_q = T_\tau/T_w$ the heat transfer coefficient and T_τ the friction temperature, Pr_t a turbulent Prandtl number and $U^+ = U/u_\tau$ with U velocity and u_τ the skin friction velocity.

2) the van Driest's compressible velocity transformation:

$$\int_0^{U^+} \left(\frac{\rho}{\rho_w}\right)^{1/2} dU^+ \approx \frac{1}{\kappa}\ln(y^+) + C \tag{2}$$

being ρ the density, κ the von Karman constant, $C = 5.5$ and $y^+ = y u_\tau/\nu_w$ the non-dimensional wall-distance with ν_w the kinematic viscosity on the wall.

3) substituting $\rho/\rho_w = \mathcal{Z}_w T_w/\mathcal{Z}T$ (with $\mathcal{Z}$ the compressibility factor obtained from an arbitrary EOS and assuming $R = R_w$ with R the gas constant and pressure imposed from the outer flow, $p = p_w$) inside Eq. (2) to get:

$$\frac{(\mathcal{Z}_w T_w)^{1/2}}{Pr_t T_\tau}\int_{T_a}^{T_b}\left(\frac{1}{\mathcal{Z}T}\right)^{1/2} dT \approx \frac{1}{\kappa}\ln(y^+) + C \tag{3}$$

where Eq. (1) is employed to change the integration variable from dU^+ to dT and obtain the integration bounds $T_a = T(U^+)$ and $T_b = T(U^+ = 0)$ accordingly.

4) proposing an analytical approximation of the function $G(T; p_0) = (1/\mathcal{Z}T)^{1/2}$ appearing in Eq. (3), where the parameter p_0 is the target thermodynamic pressure of the flow (5 MPa) in order to analytically solve the above integral.

5) solving the ensuing non-linear equation in u_τ from Eq. (3) which retains variation of properties (density) in the boundary layer due to the stratification of the flow.

RESULTS OF A-PRIORI APPLICATION

The real gas wall-function model (RG-WF) previously proposed is first tested a-priori on each case of Tab. 1 on different wall-modeled grids (although results from one grid only are shown here) obtained by radially coarsening the grid employed in the generation of the database. Results displayed in Fig. 2 show good performances in reproducing the reference solution in terms of skin friction velocity and promising results in view of future a-posteriori applications.

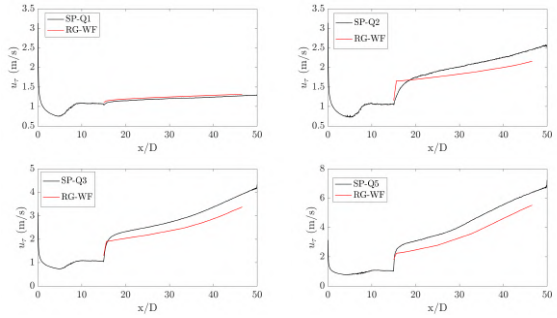

Figure 2: A-priori analysis of the newly developed algebraic wall-function on the WR-LES database of Tab. 1 in terms of skin friction velocity.

REFERENCES

[1]Craft, TJ and Gant, SE and Iacovides, Hector and Launder, BE : A new wall function strategy for complex turbulent flows *Numerical Heat Transfer, Part B: Fundamentals.*, **45**, 301–318, (2004)

[2]Larsson, Johan and Kawai, Soshi and Bodart, Julien and Bermejo-Moreno, Ivan : Large eddy simulation with modeled wall-stress: recent progress and future directions *Mechanical Engineering Reviews.*, **45**, 15–00418, (2016)

[3]Han, Zhiyu and Reitz, Rolf D : A temperature wall function formulation for variable-density turbulent flows with application to engine convective heat transfer modeling *International journal of heat and mass transfer.*, **40**, 613–625, (1997)

[4]Piomelli, Ugo and Balaras, Elias : Wall-layer models for large-eddy simulations *Annual review of fluid mechanics.*, **34**, 349–374, (2002)

[5]Indelicato, G. and Creta, F. : An algebraic equilibrium wall-function for trans- and supercritical flows *International Journal of Heat and Mass Transfer*(under review) (2022)

[6]Indelicato, G. and P. E. Lapenna and N. P. Longmire and A. Remiddi and D. T. Banuti and Creta, F. : Dataset of wall-resolved large eddy simulations turbulent pseudo-boiling in cryogenic hydrogen pipe flows *Journal of Thermophysics and Heat Transfer.*, under review, (2022)

[7]Weller, Henry G and Tabor, Gavin and Jasak, Hrvoje and Fureby, Christer : A tensorial approach to computational continuum mechanics using object-oriented techniques *Computers in physics.*, **12**, 620–631, (1998)

[8]Cuoci, Alberto and Frassoldati, Alessio and Faravelli, T and Ranzi, Eliseo : OpenSMOKE++: An object-oriented framework for the numerical modeling of reactive systems with detailed kinetic mechanisms *Computer Physics Communications.*, **192**, 237–264, (2015)

[9]Shen, Vincent K and Siderius, DW and Krekelberg, WP and Hatch, HW and others : NIST standard reference simulation website *NIST standard reference database.*, **173**, 20899, (2017)

[10]Daniel T. Banuti : Crossing the Widom-line–Supercritical pseudo-boiling *The Journal of Supercritical Fluids.*, **98**, 12–16, (2015)

[11]Nicoud, Franck and Ducros, Frédéric : Subgrid-scale stress modelling based on the square of the velocity gradient tensor *Flow, turbulence and Combustion.*, **62**, 183–200, (1999)

Session: LES fundamentals and modelling

Thursday, October 27, 2022

11:20 – 12:50

WORKSHOP
Direct and Large-Eddy Simulation 13
October 26th-29th 2022, Udine, Italy

DNS-BASED TURBULENT CLOSURES FOR SEDIMENT TRANSPORT USING SYMBOLIC REGRESSION

Y. Stöcker[1], C. Golla[1], R. Jain[1], J. Fröhlich[1], P. Cinnella[2]
[1] Institute of Fluid Mechanics, Technische Universität Dresden, Germany
[2] Institut Jean le Rond d'Alembert, Sorbonne Université, France
christian.golla@tu-dresden.de

INTRODUCTION

Particle-laden flows occur in many ways in natural and technological situations. Jain et al. [1] presented four DNS studies of sediment transport with different particle shapes. The one conducted with spherical particles was used in the present work to apply a machine learning (ML) algorithm to improve the turbulence modelling in RANS simulations.

Chauchat et al. [2] implemented a closure model in their two-phase CFD solver for sediment transport applications, SedFoam-2.0, but it shows inaccuracies especially in accounting for the impact of fluid-particle interaction on the turbulent kinetic energy. The aim of the present work is to improve the model. Based on the high-fidelity data from DNS, the error of the modelled turbulence transport equation was extracted. It served as the target data for the deterministic symbolic regression technique SpaRTA introduced by Schmelzer et al. [3]. The learnt models were implemented in the CFD solver for cross-validation to assess their predictive performance.

RANS MODEL

The phase-weighted average (the definition can be found in Burns et al. [4]) of a generic flow value ψ, is denoted by a tilde and the fluctuations can be obtained as $\psi^{\mathrm{p}\prime} = \psi - \widetilde{\psi}^{\mathrm{p}}$, where p indicates the phase, f or s. The volume fraction of the fluid, ϕ, and the sediment, α, are expressed as the spatially averaged respective phase indicator function χ^{p} [4].

The RANS equations employ the fluid Reynolds stress tensor $\tilde{R}_{ij}$, which in the present work is modelled based on the Boussinesq assumption, using the eddy viscosity ν_{t} and the deviatoric part of the mean fluid strain rate tensor $\tilde{S}_{ij}$ [2]. The eddy viscosity is determined using a k-ε-turbulence model employing $\nu_{\mathrm{t}} = C_\mu k^2/\varepsilon$, with $C_\mu = 0.09$. The transport equation for the turbulent kinetic energy of the fluid k reads

$$D_t k = \mathcal{P} - \varepsilon + \mathcal{T} + \mathcal{I}. \tag{1}$$

The turbulent production $\mathcal{P}$ and transportation $\mathcal{T}$ are modelled similar to the clear fluid closure and the dissipation ε is computed from its own transport equation, which is analogous to Eq. (1). The interfacial term $\mathcal{I}$ accounts for sediment-fluid interaction and is split in two parts. The first is modelled as a drag-induced turbulence damping effect and the second results from a density stratification which, for upwards decreasing sediment concentrations, also provides turbulence attenuation [2].

SETUP AND DNS DATA

The data basis is formed by high-fidelity simulations of particle laden flows, described in Jain et al. [1]. It is an incompressible turbulent open-channel flow with a rough sediment bed using various particle shapes. The domain is of size $108d \times 23d \times 36d$ in the stream-wise (x), wall-normal (y) and span-wise (z) direction, respectively, where d is the particle diameter. The present work is based on the case with spherical particles (Fig. 1).

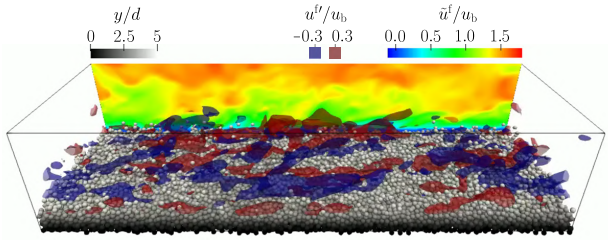

Figure 1: Instantaneous snapshot of the domain, flow from left to right.

The terms of Eq. (1), both exact and modelled, can be evaluated employing the high-fidelity data for u_i^{p}, k, $\tilde{R}_{ij}$, ε and χ^{p}. The term on the left-hand side is assumed to be negligible when averaging in time and periodic directions. Fig. 2 shows the resulting wall-normal profiles for all terms of the right-hand side (RHS) of Eq. (1). Compared to the exact terms, the modelled production is largely overestimating and the interfacial term is of the wrong sign. Hence, the model terms do not satisfy (1), a residual Δ is obtained, which is also displayed in Fig. 2.

SPARTA APPROACH

The basic idea of the approach is to add a corrective term $\mathcal{R}$ to the RHS of the modelled k-transport equation, which, ideally, would be equal to Δ for any situation. As this is impossible, an ansatz $\mathcal{R} \approx \Delta$ is made and optimized by ML. A counterpart of the corrective term for k is included in the ε-equation as in [3]. Two different modelling approaches were considered: The turbulent production analogy, expressing $\mathcal{R}$ as [3]

$$\mathcal{R} = 2k \left(b_{ij}^{\mathcal{R}} - 1/3\ \delta_{ij} \right) \partial_j \tilde{u}_i^{\mathrm{f}}, \tag{2}$$

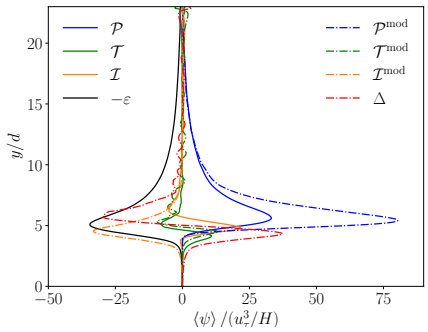

Figure 2: Wall-normal profiles for the exact and modelled terms of the RHS of the k-transport equation (1) using DNS data by Jain et al. [1].

and a newly introduced dissipation analogy, with

$$\mathcal{R} = c\,\varepsilon. \tag{3}$$

For the first one, a tensorial model for $b_{ij}^{\mathcal{R}}$ has to be found and for the second one, a functional expression for the scalar c is needed. It is assumed that both depend on the mean strain-rate tensor $\widetilde{S}_{ij}$ and the mean rotation-rate tensor $\widetilde{\Omega}_{ij}$.

For both approaches the polynomial model expressions for the target values were assembled from a predefined set of non-linear candidate functions. These candidates depend on the invariants that form the minimal integrity basis of the tensors. Additionally, for considering sediment-phase related quantities in the models, the sediment volume fraction α was included and an additive constant was also considered. These features were multiplied by themselves and each other so that they resulted in functions with a maximum degree of six. The scalar c was assembled directly from the resulting terms, and for building $b_{ij}^{\mathcal{R}}$, they were additionally multiplied with each base tensor of the minimal integrity basis.

The model selection and inference were employed following [3], using elastic net regularisation and ridge regression to promote sparsity and small model coefficients. This prevents overfitting and increases the likelihood of yielding models that are stable when implemented in a CFD solver. As a result, numerous symbolic model expressions $\mathcal{M}$ for $b_{ij}^{\mathcal{R}}$ or c were obtained that regress the target data.

CROSS-VALIDATION

These models were implemented in SedFoam-2.0 to evaluate their predictive quality. The main goal of the present study is to improve the modelling of the k-transport equation. However, other quantities should not be deteriorated, so that the cross-validation was performed not only on k, but also on the stream-wise velocity of the fluid $\tilde{u}^{\mathrm{f}}$ and sediment $\tilde{u}^{\mathrm{s}}$, the total shear stress τ_{tot} (as defined in [1]) and the fluid volume fraction ϕ. The performance on a single flow quantity ψ was evaluated using the mean-squared error ϵ via $P_\psi = 1 - \epsilon(\psi^{\mathcal{M}})/\epsilon(\psi^0)$, where the index $\mathcal{M}$ denotes that the value is obtained after running CFD simulations, where the machine-learnt model is implemented in the solver, and 0 indicates the result of the unmodified solver. The total performance P_{tot} of a model was assessed by the arithmetic mean of the single performances on all five quantities.

The performances P_k and P_{tot} are shown in Fig. 3. In general, the models of the dissipation-analogy performed better than the ones from the production-analogy, and the inclusion of α yielded an additional improvement, resulting in a total performance up to 35 %. No model was capable of improving all quantities at the same time, but particularly the turbulent fluctuations were better captured, thereby reducing the error on k and τ_{tot} up to 65 %.

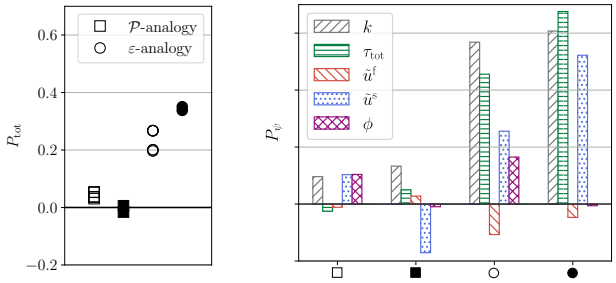

Figure 3: Performance of the models, split into models from the production analogy (2) and dissipation analogy (3). Filled symbols: same with α incorporated. Left: total performance P_{tot}, right: single performances of the best performing models.

CONCLUSIONS

In this work, the applicability of the SpaRTA algorithm of Schmelzer et al. [3] to multi-phase flows is demonstrated. The newly introduced dissipation analogy showed significantly better results than the production analogy, yielding an approximately twenty percent higher total performance. However, the improvements are not as good as in the separating single-phase flows evaluated in [3], where the objective was to improve predictions of separation and reattachment.

The dissipation analogy enables the possibility to easily include new values such as the gradient of the phase volume fraction in the models. One can also consider to incorporate the sediment velocity. In further studies, the other test cases could be considered, since they exhibit substantial differences with respect to spherical particles, e.g. different sediment bed behaviour, and most likely require different correction models.

REFERENCES

[1]Jain, R., Tschisgale, S. and Fröhlich, J. : Impact of shape: DNS of sediment transport with non-spherical particles, *J. Fluid Mech.*, **916**, A38 (2021).

[2]Chauchat, J., Cheng Z., Nagel, T., Bonamy, C. and Hsu, T.-J. : SedFoam-2.0: a 3-D two-phase flow numerical model for sediment transport, *Geosci. Model Dev.*, **10**, 4367-–4392 (2017).

[3]Schmelzer, M., Dwight R.P. and Cinnella, P. : Discovery of Algebraic Reynolds-Stress Models Using Sparse Symbolic Regression, *Flow Turbul. Combust.*, (2019).

[4]Burns, A.D., Frank, T., Hamill, I. and Shi, J.-M. : The Favre Averaged Drag Model for Turbulent Dispersion in Eulerian Multi-Phase Flows, *ICMF'04, May 30–June 4,Yokohama, Japan*, (2004).

WORKSHOP
Direct and Large-Eddy Simulation 13
October 26th-29th 2022, Udine, Italy

LES SUBGRID MODEL ASSESSMENT FOR WALLBOUNDED DECAYING TURBULENCE

L. Engelmann[1], D. Meller[1], P. Wollny[1], I. Wlokas[1], A. Kempf[1,2]
[1] Institute of Combustion and Gas Dynamics (IVG)
University of Duisburg-Essen, Germany
[2] Center of Computational Sciences and Simulation
University of Duisburg-Essen, Germany
linus.engelmann@uni-due.de

INTRODUCTION

Given the increasing accessibility of computational ressources and the effort spend into model development Large-Eddy Simulation (*LES*) is maturing as an engineering-tool for industrial and scientific applications. The ability to resolve the major energy-carrying turbulent structures makes LES an attractive tool for interdisciplinary studies like aerodynamics, reactive flows or magneto-hydrodynamics. LES is often recommended to resolve the largest part of the inertial range to operate reliably, as the subgrid model then only replaces the Kolmogorov scales, which are assumed to behave independent of the large scales. LES has been commonly applied in these cases at low and moderate Reynolds numbers. The DNS calculations of highest Reynolds numbers in research are typically performed for canonical flows and reach Reynolds numbers of up to $40,000$. This however is far below the common Reynolds numbers in technical or biological applications of CFD.

In the context of wall-dominated flows, increasing Reynolds-numbers become even more challenging. This is a major problem for modern LES, as nearly all technical flows involve walls to a certain extend. The quality of prediction of the flow with LES and DNS tools depends on the resolution of the boundary layer. The thickness of the boundary layer is determined by the Reynolds-number. Higher Reynolds-numbers lead to thinner boundary layers. In the case of developing boundary layers such as on airfoils or ships, or unstable boundary layers such as on pistons, moderate Reynolds-numbers already become challenging. It is sometimes argued, that the first wall-adjacent cell is required to lie within the first ten viscous wall-units to ensure a correct capturing of the near-wall velocity gradient in LES. However, placing a cell within the viscous sublayer or buffer layer is often considered expensive and hence, highly anisotropic cells are a popular choice trading wall-normal for span- and stream-wise resolution.

The present study aims for the study of Reynolds number effects and their role in the context of LES subgrid modeling.

CASE DESCRIPTION

Laminar-turbulent transition forms a highly challenging case for LES models. The understanding and prediction of the transition is crucial in numerous application-fields such as wing aerodynamics, reactor-design or marine-engineering. Most of the applications involving laminar-turbulent transition feature boundary layers due to the presence of walls. To increase the relevancy of the case in this context the idea of transition and decaying turbulence are combined with the idea of wall-driven turbulence. Thus, a temporally evolving vortex is chosen and bounded by two parallel walls.

The case-design is based on the well-known Taylor-Green Vortex configuration [1, 2]. The initial velocity field is given by the following expression

$$\begin{aligned} u\left(x,y,z,t=0\right) &= \cos\left(x\right)\sin\left(y\right)\sin\left(z\right) \\ v\left(x,y,z,t=0\right) &= -\sin\left(x\right)\cos\left(y\right)\sin\left(z\right) \\ w\left(x,y,z,t=0\right) &= 0 \end{aligned} \tag{1}$$

To make the setup suitable for the study of wall-driven turbulence, two parallel walls are added in the z-direction, as the initial values of w are set to zero.

The scalar ϕ is initialized with values of zero in the cell centers. As it is of interest to form a case, which can be used for the study of scalar wall-to-fluid transfer, the cell-faces at the wall are forced to hold constant values

$$\begin{aligned} \phi\left(x,y,z=0,t\right) &= 1 \\ \phi\left(x,y,z=2\pi,t\right) &= 1 \end{aligned} \tag{2}$$

This allows for the observation of diffusive wall-to-fluid scalar-transfer and convectively dominated transport in the fluid-phase. Because the walls are modeled as immersed boundaries, on the cubic Cartesian grid this can be achieved by manipulating the values within the immersed boundaries as follows:

$$\phi_{\text{wall}} = \text{IB}\cdot\phi_{\text{fluid}} + (1-\text{IB})\cdot(2-\phi_{\text{fluid}}) \tag{3}$$

The Schmidt-number Sc of the scalar ϕ is chosen to be 0.2. The transfer of the scalar from the wall to fluid is set to a be a diffusive flux between the scalar value of unity directly on the wall and the neighboring fluid value. The Schmidt-number to calculate the diffusivity is set to $\text{Sc}_{\text{wall}} = 0.2$ as well.

METHODS

All calculations are performed using the in-house solver *PsiPhi*, which has been developed at the Imperial College London and the University of Duisburg-Essen. The solver applies a Finite-Volume Method on a cubic equidistant grid. *PsiPhi* has been used in earlier application- and model-development

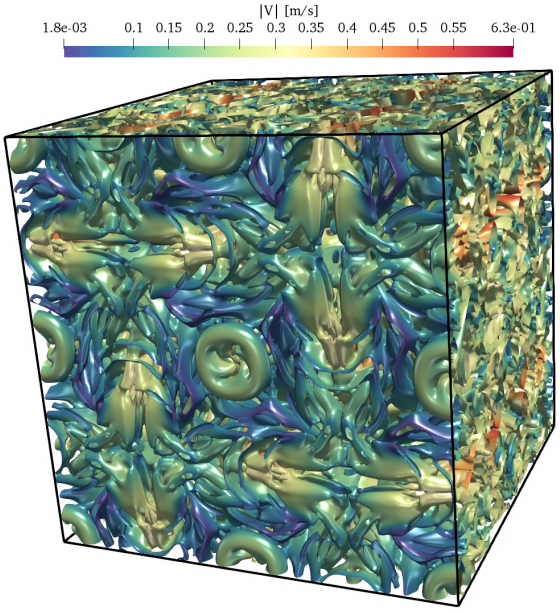

Figure 1: Q-criterion at value of zero colored using the velocity magnitude at $t = 25.0$s - the front face is the first wall-adjascent layer.

orientated studies [3, 4]. In this study the incompressible-formulated Navier-Stokes equations of momentum and a passive scalar are solved. The equations read

$$\begin{aligned} \frac{\partial \rho u_\mathrm{j}}{\partial x_\mathrm{j}} &= 0 \\ \frac{\partial \rho u_i}{\partial t} + \frac{\partial \rho u_\mathrm{i} u_\mathrm{j}}{\partial x_\mathrm{j}} &= -\frac{\partial p}{\partial x_\mathrm{i}} + \frac{\partial}{\partial x_\mathrm{j}} \left(\mu \left(\frac{\partial u_\mathrm{i}}{\partial x_\mathrm{j}} + \frac{\partial u_\mathrm{j}}{\partial x_\mathrm{i}} \right) \right) \\ \frac{\partial \rho \phi}{\partial t} + \frac{\partial \rho \phi u_\mathrm{j}}{\partial x_\mathrm{j}} &= \frac{\partial}{\partial x_\mathrm{j}} \left(D_\phi \left(\frac{\partial \rho \phi}{\partial x_\mathrm{j}} \right) \right) \end{aligned} \tag{4}$$

The momentum transport equations are spatially discretized using fourth-order central differencing (CDS - strictly speaking called linear interpolation in the context of FV) for the DNS calculations. The additional scalar transport equation is discretized using fourth-order central differencing in the DNS. The solution is advanced in time with an explicit low-storage third order Runge-Kutta scheme using a CFL number of 0.3. The Poisson-equation is solved using a Jacobi solver. The maximum allowed residual for that was chosen to 0.01 and approximately 20 iterations were used per Runge-Kutta step. *PsiPhi* uses a distributed memory, domain decomposition approach for parallelization, utilizing MPI (Message Passing Interface) communication.

RESULTS

Figure 1 shows the Q-criterion for Q = 0 as an iso-surface at the simulation time of 25.0s. The surface are colored by the local velocity magnitude. It visualizes coherent structures by means of the second invariant of the velocity gradient tensor, which is commonly used for subgrid modeling purposes. The domain is rotated to move the focus on the first wall adjascent layer. The front-face reveals periodical streak-like structures, with the most prominent one being the rotational structure in the center.

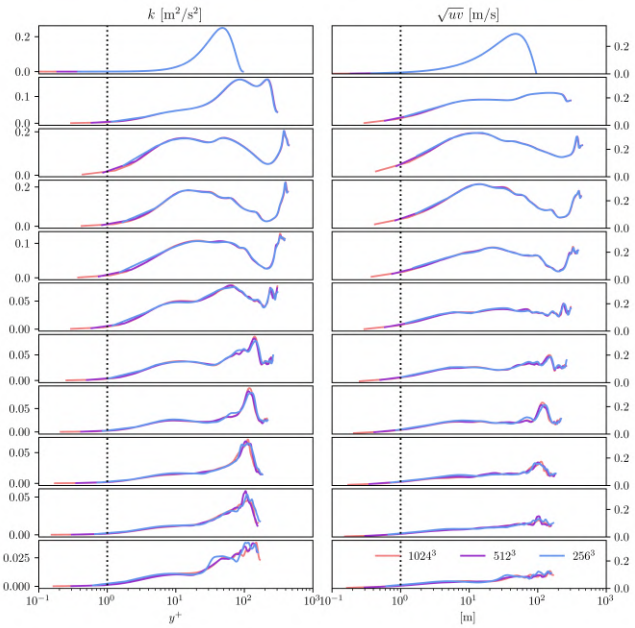

Figure 2: Wall-parallel averaged kinetic energy k and shear stress $\sqrt{uv}$ with wall distance in viscous wall unity y^+

In Fig. 2, the profiles of the kinetic energy k and the shear stresses $\sqrt{uv}$ can be seen versus the wall-distance in viscous wall units y^+. Three different resolutions are compared featuring 1024^3, 512^3 and 256^3 cells. To obtain the profiles, the samples from all wall-parallel slices were averaged for each timestep. The display of the profile in viscous wall units allows for better analysis of the near-wall resolution. The first viscous wall unit is visualized by the vertical-dashed line. The resolution during the simulation changes due to the interaction of decay of the initial vortex and the generation of additional turbulence at the walls. This can be seen by the change of the friction Reynolds number Re_τ, which is given by the maximum y^+ value of each profile.

The different resolutions begin to exhibit differences for the kinetic energy from 10s on-wards with the 256^3 gird starting to show deviations. The 512^3 grid begins to deviate from the 1024^3 simulation after about 17.5s. The shear stress profiles remain very consistent over the grids however for all timesteps. The overall energy level strongly decreases with time, while the overall stress values remain at similar magnitude. Despite the small deviations between the grids, the 1024^3 grid appears to be the best reference due to the most cells available below the first viscous wall unit.

REFERENCES

[1]Brachet, M.E., Meiron, D.I., Orszag, S.A., Nickel, B.G., Morf, R.H., Frisch, U. : Small-scale structure of the Taylor-Green vortex, *J. Fluid Mech.*, **130**, 411–452 (1983).

[2]Brachet, M.E. : Direct simulation of three-dimensional turbulence in the Taylor–Green vortex, *Fluid Dyn. Res.*, **8**, 1 (1991).

[3]Engelmann, L., Ihme, M., Wlokas, I., Kempf, A.M. : Towards the suitability of information entropy as an LES quality indicator, *Flow Turbul. Combust.*, **108**, 353–385, (2022).

[4]Nguyen, T.M., Proch, F., Wlokas, I., Kempf, A.M. : Large Eddy Simulation of an Internal Combustion Engine Using an Efficient Immersed Boundary Technique, *Flow Turbul. Combust.*, **97**, 195-230, (2016).

WORKSHOP
Direct and Large-Eddy Simulation 13
October 26th-29th 2022, Udine, Italy

COARSE-GRAINED MODELLING VIA CANONICAL SCALE SEPARATION IN 2D INCOMPRESSIBLE HYDRODYNAMICS

M. Viviani[3], K. Modin[5], P. Cifani[1,2], S. R. Ephrati[1], B.J. Geurts[1,4]
[1] Mathematics of Multiscale Modelling and Simulation, University of Twente, The Netherlands
[2] Gran Sasso Science Institute, Italy
[3] Scuola Normale Superiore di Pisa, Italy
[4] Multiscale Energy Physics, Eindhoven University of Technology, The Netherlands
[5] Chalmers University of Technology, Gothenburg, Sweden
milo.viviani@sns.it

INTRODUCTION

Two-dimensional incompressible ideal hydrodynamics is a fundamental model for studying various physical phenomena, such as atmospheric and oceanic dynamics. The equations of motion of such a fluid are the Euler equations. A primary feature of this model is that it possesses an infinite dimensional Hamiltonian structure, with an infinitely many conservation laws. Those are responsible for the characteristic formation of persistent large coherent structures, emerging after a transient, fine-scale turbulent stage. A quantitative description of this phenomenon was given by Kraichnan [1], in terms of the double cascade scaling: the energy concentrates at large scales, whereas the enstrophy (the L^2 norm of the vorticity) is dominated by small scales.

When the energy spectrum extends over several orders of magnitudes, as is the case for geophysical flows, resolving all scales of motion is not feasible and a suitable reduced-order model is required. The applicability of traditional eddy-viscosity models, developed for 3D turbulence, is questionable for two-dimensional dynamics since a significant part of the energy flows from unresolved scales toward larger scales. An intrinsically dissipative model would not account for such physical mechanisms. Furthermore, the choice of the cut-off filter width is, to some extent, arbitrary and often pragmatically related to a practical balance between modelling error and computational cost.

In this contribution we will show that there exists an intrinsic canonical splitting of Euler's equations by which one arrives at a novel set of equations for the resolved and the unresolved scales. The former can be simulated once a closure model is specified. The canonical splitting consists in dividing the vorticity field in two orthogonal components: one which commutes with the stream function and one which is its L^2 orthogonal complement. The splitting is remarkable in several ways:

- it is defined solely via the Poisson bracket and the Hamiltonian,
- without imposition it yields a separation of scales, enabling the dynamics behind Kraichnan's qualitative description,
- it accounts for the "broken line" in the power law for the energy spectrum (observed in both experiments and numerical simulations)[6].

The splitting originates from Zeitlin's truncated model of Euler's equations [4] in combination with the spectral decomposition of Hermitian matrices [3]. In addition to theoretical insight, we show how the scale separation dynamics can be used for stochastic model reduction, where small scales are modelled by a suitable multiplicative noise process.

CANONICAL SPLITTING

The Euler equations for a two-dimensional ideal fluid can be expressed in terms of the vorticity scalar field ω defined as the curl of the velocity field, projected onto the normal vector of the domain. To fix the ideas, let us take as domain the unitary 2-sphere embedded in $\mathbb{R}^3$. The equations of motion are

$$\dot{\omega} = \{\psi, \omega\}, \qquad \Delta\psi = \omega, \tag{1}$$

where ψ is the stream function, Δ is the Laplace-Beltrami operator and the bracket is defined as $\{\psi, \omega\}(x) = x \cdot (\nabla\psi \times \nabla\omega)$. For simplicity, we introduce the *canonical splitting* of the vorticity field only for the Euler-Zeitlin equations [4]. Let $W \in \mathfrak{su}(N)$[1] the vorticity matrix

$$\dot{W} = [P, W], \qquad \Delta_N P = W, \tag{2}$$

where $P \in \mathfrak{su}(N)$ is the stream matrix, Δ_N is a suitable discrete Laplacian and the bracket is the usual matrix commutator. The canonical splitting of the vorticity matrix

$$W = W_s + W_r \tag{3}$$

is obtained by defining W_s to be the part of W that commutes with the stream matrix P, i.e., $[W_s, P] = 0$. This can be formulated as the orthogonal projection of W onto

$$\mathrm{Stab}_P = \{A \in \mathfrak{su}(N) \mid [A, P] = 0\}. \tag{4}$$

If P is generic, so all its eigenvalues are distinct, W_s is obtained via the spectral decomposition: first find $E \in \mathrm{SU}(N)$[2] which

[1] We recall $\mathfrak{su}(N)$ is the space of $N \times N$ skew-Hermitian matrices with zero trace.

[2] We recall that $SU(N)$ is the space of $N \times N$ unitary matrices with determinant 1.

diagonalizes P, i.e., $E^\dagger P E = \Lambda$, then set $\Pi_P : \mathfrak{su}(N) \to \mathrm{Stab}_P$ as

$$W_s := \Pi_P(W) = E\mathrm{diag}(E^\dagger W E)E^\dagger.$$

Then W_s and W_r satisfy the following system of equations

$$\begin{aligned} \dot{W}_s &= [B, W_s] - \Pi_P[B, W_r] \\ \dot{W}_r &= -[B, W_s] + \Pi_P[B, W_r] + [P, W_r], \end{aligned} \tag{5}$$

where $P = \Delta_N^{-1}(W_s + W_r)$ and B is the unique solution in $\mathrm{Stab}_P^\perp$ to

$$[B, P] = \Pi_P^\perp \Delta_N^{-1}[P, W_r]. \tag{6}$$

We observe that the first of equations (5) can be interpreted as an evolution equation for the resolved scales, W_s, where a closure model is required to approximate the sub-scale dynamics of W_r.

EVIDENCES OF SCALE SEPARATION

Energy and enstrophy splitting

Let us now study how energy and enstrophy relate to the canonical splitting (3). Since $Tr(PW_r) = 0$, the energy, corresponding to the *energy norm*, fulfils

$$\begin{aligned} H(W) &= \frac{1}{2} Tr\big(W_s \Delta_N^{-1}(W_s + W_r)\big) \\ &= \frac{1}{2} Tr(W_s \Delta_N^{-1} W_s) - \frac{1}{2} Tr(W_r \Delta_N^{-1} W_r). \end{aligned}$$

Yet, the enstrophy, corresponding to the *enstrophy norm*, fulfils

$$E(W) = -Tr(W_s^2) - Tr(W_r^2).$$

This gives the interesting relations

$$\begin{aligned} H(W) &= H(W_s) - H(W_r) \\ E(W) &= E(W_s) + E(W_r). \end{aligned} \tag{7}$$

Notice that $H(W_s)$ is always larger than $H(W)$ and that the energy of W_s and W_r have to increase or decrease at the same rate, see Figure 1. On the other hand, if the enstrophy of W_s decreases with a rate then the enstrophy of W_r must increase with the same rate, see Figure 2. . The canonical splitting thus coheres with Kraichnan's [1] description of an inverse energy cascade and a forward enstrophy cascade, as shown in Figure 1 and 2.

Stochastic model reduction

Here we investigate to what extent equations (5) are suitable for a stochastic model reduction of the Euler equations. In particular, numerical evidence shows that for long times the field W_r can be approximately modelled as white noise. This is reflected in the l^{-1} scaling of the energy spectrum of W_r. On the other hand, we expect that the dynamics of W_s in this limit is approximately a SALT equation [5].

In the limit for long-times, the field B in equations (5) is well approximated by the orthogonal projection $\Pi_P^\perp(\Delta^{-1}W_s)$:

$$\dot{W}_s \approx [\Pi_P^\perp(\Delta^{-1}W_s), W_s] - \Pi_P[\Pi_P^\perp(\Delta^{-1}W_s), W_r]. \tag{8}$$

Furthermore, since $\Delta^{-1}W_r$ in the long-time limit becomes small, we have that $\Delta^{-1}W_s \approx P$, hence the second term in (8) $\Pi_P[\Delta^{-1}W_s, W_r] \approx 0$. Under this approximation, equations (8) can be modelled with a suitable transport noise such that W_s satisfies a SALT-type equation. The stochastic equation will then be of the form

$$\mathrm{d}W_s = [\Delta^{-1}W_s \mathrm{d}t + Z_i \circ \mathrm{d}B_t^i, W_s], \tag{9}$$

where Z_i are Proper-Orthogonal-Decomposition modes generated from the acquired data. In order to assess the quality of the proposed model, we will present flow statistics of the model compared to those obtained by the fully resolved flow dynamics.

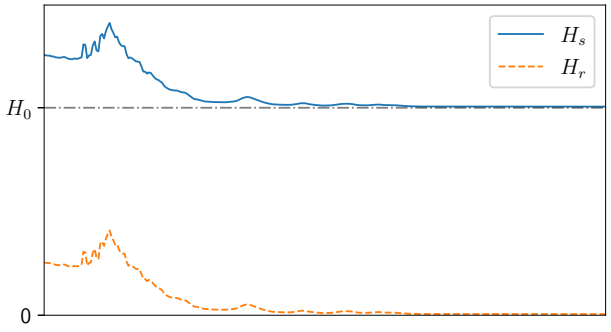

Figure 1: Time-series of energy for the three vorticity fields W, W_s, W_r for a long-time simulation of equations (2) for $N = 501$.

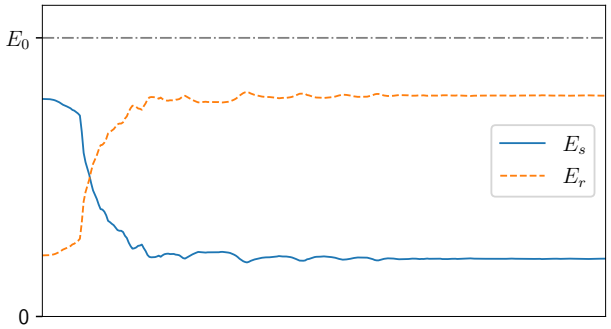

Figure 2: Time-series of enstrophy for the three vorticity fields W, W_s, W_r for a long-time simulation of equations (2) for $N = 501$.

REFERENCES

[1]Kraichnan, R.H., 1967. Inertial ranges in two-dimensional turbulence. The Physics of Fluids, 10(7), pp.1417-1423.

[2]Modin, K. and Viviani, M., 2020. A Casimir preserving scheme for long-time simulation of spherical ideal hydrodynamics. Journal of Fluid Mechanics, 884.

[3]Modin, K. and Viviani, M., 2021. Canonical scale separation in two-dimensional incompressible hydrodynamics, arXiv preprint arXiv:2102.01451.

[4]Zeitlin, V., 2004. Self-consistent finite-mode approximations for the hydrodynamics of an incompressible fluid on nonrotating and rotating spheres. Physical review letters, 93(26), p.264501.

[5]Holm, D. D. (2015). Variational principles for stochastic fluid dynamics. Proceedings of the Royal Society A: Mathematical, Physical and Engineering Sciences, 471(2176):20140963.

[6]Gage, K. S. and Nastrom, G. D. (1986). Theoretical Interpretation of Atmospheric Wavenumber Spectra of Wind and Temperature Observed by Commercial Aircraft During GASP. Journal of the Atmospheric Sciences, 43(7).

WORKSHOP
Direct and Large-Eddy Simulation 13
October 26th-29th 2022, Udine, Italy

SUBGRID-SCALE MODELLING FOR A SEMI-LAGRANGIAN METHOD

M. de Crouy-Chanel[1], C. Mimeau[1], I. Mortazavi[1], M. V. Salvetti[2]
[1] M2N Laboratory, Conservatoire des Arts et Métiers, Paris, France
[2]Università di Pisa - UNIPI, Department of Civil and Industrial Engineering, Pisa, Italia
marthe.de-crouy-chanel@lecnam.net

INTRODUCTION

Vortex methods [1, 2] are a type of particle methods in which the vorticity is discretized on numerical particles following the fluid dynamics. In this work, we use a semi-Lagrangian approach where particles are repositioned on a fixed mesh after being transported. This "hybridization" through remeshing allows for the use of Eulerian methods in an initially Lagrangian algorithm. This kind of approach has so positive features : they are less dispersive and less diffusive and do not require a CFL condition constraining the advection time step to the grid size.

This method has proved to be efficient for a number of laminar and highly transitional flows [2], illustrating the flexibility provided by the optimal coupling between Lagrangian and Eulerian schemes. However, this method has been mainly used for DNS technique until now. According to the features cited above (especially the low diffusivity property), the present approach represents a legitimate candidate to perform large eddy simulations with the introduction of a subgrid-scale viscosity.

Following the pioneer, but very few, works on turbulent models for vortex methods [3, 4] and semi-Lagrangian vortex methods [5] in the context of large eddy simulations (LES), the present study investigates and compares different closure models.

REMESHED VORTEX METHODS

Vortex methods are Lagrangian methods. They are based on the vorticity($\boldsymbol{\omega}$)-velocity($\mathbf{u}$) formulation of the incompressible Navier-Stokes equations:

$$\partial_t \boldsymbol{\omega} + (\mathbf{u}\cdot\nabla)\boldsymbol{\omega} - (\boldsymbol{\omega}\cdot\nabla)\mathbf{u} = \frac{1}{Re}\Delta\boldsymbol{\omega}\ ; \quad \Delta\mathbf{u} = -\nabla\times\boldsymbol{\omega}, \tag{1}$$

where $\boldsymbol{\omega} := \nabla\times\mathbf{u}$ and where $(\mathbf{u}\cdot\nabla)\boldsymbol{\omega}$ and $(\boldsymbol{\omega}\cdot\nabla)\mathbf{u}$ denote respectively the advection and stretching terms. The Poisson equation $\Delta\mathbf{u} = -\nabla\times\boldsymbol{\omega}$ allows to recover the velocity field $\mathbf{u}$ from the vorticity field $\boldsymbol{\omega}$. The vorticity field is discretized on a set of numerical particles with position $\mathbf{x}_p$ and the resolution of the governing equations is based on a fractional step algorithm. One time step of such algorithm is decomposed as follows: first the particles, carrying the vorticity field, are convected in a Lagrangian way :

$$\begin{cases} \partial_t \mathbf{x}_p = \mathbf{u}(\mathbf{x}_p(t), t) \\ \partial_t \boldsymbol{\omega}_p = 0 \end{cases} \tag{2}$$

Then, in order to avoid the vorticity field distortion, the vorticity $\boldsymbol{\omega}_p$ carried by each particle p is distributed on the neighboring points of an underlying Cartesian mesh. This step, called the "remeshing" is performed as follows:

$$\boldsymbol{\omega}_i(\mathbf{x}) = \sum_p \boldsymbol{\omega}_p(\mathbf{x})\Lambda\left(\frac{\mathbf{x}_p - \mathbf{x}_i}{\Delta\mathbf{x}}\right) \tag{3}$$

where the remeshing kernel Λ is a piecewise polynomial with compact support. At this stage, the whole vorticity field has been redistributed on the mesh and the stretching equation, the diffusion equation and the Poisson equation are finally solved on the grid using Eulerian schemes.

The present remeshed vortex method (RVM) is therefore based on a semi-Lagrangian approach which is characterized by the use of both Lagrangian vortex methods and Eulerian methods to solve the Navier-Stokes equations (1).

TURBULENCE MODELING

In order to perform large eddy simulations in the context of RVM, we write the filtered Navier-Stokes equations in their velocity-vorticity formulation:

$$\frac{\partial\overline{\boldsymbol{\omega}}}{\partial t} + \nabla\cdot(\overline{\boldsymbol{\omega}}\otimes\overline{\mathbf{u}} - \overline{\mathbf{u}}\otimes\overline{\boldsymbol{\omega}}) = \nu\Delta\overline{\mathbf{u}} - \nabla\cdot\mathbf{R} \tag{4}$$

where the subgrid scale vorticity stress to be modeled is expressed as:

$$\mathbf{R} = \overline{\boldsymbol{\omega}\otimes\mathbf{u}} - \overline{\boldsymbol{\omega}}\otimes\overline{\mathbf{u}} - \overline{\mathbf{u}\otimes\boldsymbol{\omega}} + \overline{\mathbf{u}}\otimes\overline{\boldsymbol{\omega}} \tag{5}$$

Subgrid scale models A first approach to model $\mathbf{R}$ in the vorticity-velocity formulation is to take the curl of $\nabla\cdot\tau_{SGS}$ where τ_{SGS} denotes the usual form of the subgrid scale stress tensor in velocity-pressure formulation. This finally gives:

$$\mathbf{R}_{SGS} = \nu_{SGS}(\nabla\overline{\boldsymbol{\omega}} - \nabla\overline{\boldsymbol{\omega}}^T) \tag{6}$$

We note that the tensor $\mathbf{R}_{SGS}$ is anti-symmetric, as is the tensor $\mathbf{R}$ to be modelled. Another model used in [5] is:

$$\mathbf{R}_{SGS} = \nu_{SGS}(\nabla\overline{\boldsymbol{\omega}} + \nabla\overline{\boldsymbol{\omega}}^T) \tag{7}$$

where $\mathbf{R}_{SGS}$ is here symmetric.

Finally, following [6] and [5], we explore a third model. Let $\overline{f}$ be some resolved field, we define, in Fourier space, the largest resolved scales of $\bar{f}$ by

$$\widehat{\overline{f}}(k) = \widehat{G}(k)\overline{f}(k) \tag{8}$$

where $\widehat{G}$ is some test filter, and the small resolved scales f_S by

$$\overline{f}_S = \overline{f} - \widehat{\overline{f}} \tag{9}$$

One therefore defines the third model by taking the smallest resolved scales of the vorticity field such that

$$\mathbf{R}_{SGS} = \nu_{SGS}(\nabla\overline{\boldsymbol{\omega}}_S + (\nabla\overline{\boldsymbol{\omega}}_S)^T) \tag{10}$$

We will refer to model (6) as the "anti-symmetric" model, model (7) as the "symmetric" model and model (10) as the "small" model.

Subgrid-scale viscosity We chose the classical Smagorinsky model for the subgrid-scale viscosity ν_{SGS}:

$$\nu_{SGS} = (C\Delta)^2|\overline{\mathbf{S}}| \tag{11}$$

where C is a coefficient to be chosen, Δ taken to be equal to the grid size, $\overline{\mathbf{S}} = \frac{1}{2}(\nabla\mathbf{u} + (\nabla\mathbf{u})^T)$ and $|\overline{\mathbf{S}}| = \sqrt{2\overline{\mathbf{S}}_{ij}\overline{\mathbf{S}}_{ij}}$ is the magnitude of $\mathbf{S}$.

NUMERICAL EXPERIMENTS

We tested the models presented above for the Taylor Green Vortex (TGV) test case at $Re = 5000$, which is a well suited benchmark to study transition to turbulence and the progressive formation of small scales. The simulations are performed in a periodic cubic box of side length $L = 2\pi$.

A posteriori tests In a first approach, we apply our LES models to the TGV simulation at a coarse resolution of 96^3 (the grid filtering is applied implicitly through the grid discretization). In figure 1, the time evolution of kinetic energy dissipation is represented. First of all, we note that all the proposed model improve greatly the performance of the simulation when compared to a no-model simulation, too coarse to represent accurately the energy in the smallest scales. We further note that the anti-symmetric model (6) is less dissipative than the symmetric one (7) although we obtain similar performance with the symmetric "small" model (10) by filtering the smallest scales of the resolved vorticity field. We also compare our results to the solution obtained in [7] through a Smagorinsky model and based on a high order finite-differences solver. We obtain similar trend and find our approach to be less dissipative for the three considered models.

A priori tests In the perspective of a model specifically derived for the present method, we are interested to know the relative importance played by the convection and the stretching respectively in the development of small scales in turbulence; to that end, we divide $\mathbf{R}$ in two parts:

$$\mathbf{R}_C = \overline{\boldsymbol{\omega}\otimes\mathbf{u}} - \overline{\boldsymbol{\omega}}\otimes\overline{\mathbf{u}} \qquad \mathbf{R}_S = \overline{\mathbf{u}\otimes\boldsymbol{\omega}} + \overline{\mathbf{u}}\otimes\overline{\boldsymbol{\omega}} \tag{12}$$

where $\mathbf{R}_C$ reflects the vorticity transport by subfilter scale (SFS) velocity fluctuations and $\mathbf{R}_S$ represents the SFS vortex stretching due to the unresolved motion. This work will therefore present *a priori tests* (realized by using a test filter to evaluate $\mathbf{R}$ (eq. 5)) in order to quantify the relative importance of $\mathbf{R}_C$ with respect to $\mathbf{R}_S$ when varying the Reynolds number.

In addition to the Taylor-Green test case, we will also present applications of the present approach to other test cases such as homogeneous isotropic turbulence (HIT). Computational issues will also be discussed.

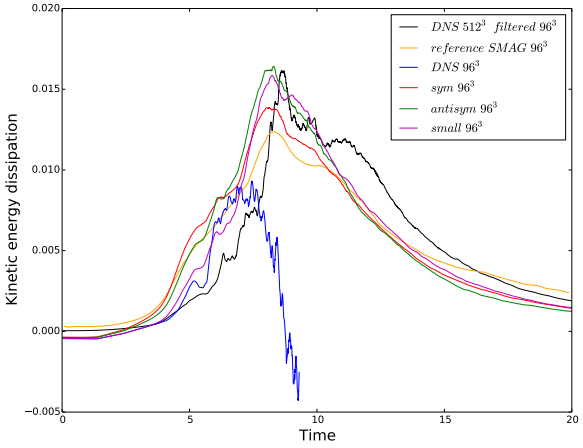

Figure 1: TGV at $Re = 5000$. Time history of kinetic energy dissipation; reference curve (yellow) refers to [7].

REFERENCES

[1] G.-H. Cottet and P. D. Koumoutsakos, *Vortex Methods: Theory and Practice*. Cambridge University Press, 2000.

[2] C. Mimeau and I. Mortazavi, "A review of vortex methods and their applications: From creation to recent advances," *Fluids*, vol. 6, p. 68, 2021.

[3] J. R. Mansfield, O. M. Knio, and C. Meneveau, "A Dynamic LES Scheme for the Vorticity Transport Equation: Formulation and a PrioriTests," *Journal of Computational Physics*, vol. 145, pp. 693–730, Sept. 1998.

[4] G.-H. Cottet, "Artificial viscosity models for vortex and particle methods," *Journal of Computational Physics*, vol. 127, no. 2, pp. 299–308, 1996.

[5] R. Cocle, L. Dufresne, and G. Winckelmans, "Investigation of multiscale subgrid models for les of instabilities and turbulence in wake vortex systems," in *Complex Effects in Large Eddy Simulations*, 2007.

[6] T. J. R. Hughes, L. Mazzei, A. A. Oberai, and A. A. Wray, "The multiscale formulation of large eddy simulation: Decay of homogeneous isotropic turbulence," *Physics of Fluids*, vol. 13, no. 2, pp. 505–512, 2001.

[7] V. C. B. Sousa and C. Scalo, "A unified quasi-spectral viscosity (qsv) approach to shock capturing and large-eddy simulation," *Journal of Computational Physics*, vol. 459, p. 111139, 2022.

WORKSHOP
Direct and Large-Eddy Simulation 13
October 26^{th}-29^{th} 2022, Udine, Italy

STRUCTURAL MODELS FOR PARTICLES IN LES: ASSESSMENT THROUGH THE SUBFILTER ENSTROPHY FIELD

M. Rajek, J. Pozorski
Institute of Fluid Flow Machinery, Polish Academy of Sciences
Fiszera 14, 80-231 Gdańsk, Poland
{mrajek, jp}@imp.gda.pl

INTRODUCTION

The large-eddy simulations (LES) are increasingly often applied to turbulent flows with particles or droplets. One of the general questions refers to the impact of LES smoothing on the dispersed phase. A considerable body of evidence has been gathered over the years concerning the droplet preferential concentration, the mean settling velocity in the gravity field, and the collision statistics [1, 2, 3]. In particular, for the statistical quantities that involve particle collective effects (another example is droplet evaporation or fuel particle devolatilisation at larger volume loadings of the dispersed phase), the *one-point* models of the functional type (such as stochastic Lagrangian closures for the fluid velocity seen by particles, see, e.g. [4]) are inadequate and some reconstruction of the subgrid scale (SGS) fluid velocity *field* is sought for (as an input to the particle equation of motion). One-point closures prove sufficient for the long term turbulent dispersion, but two-point models are necessary to correctly predict relative dispersion.

The structural-type models provide two- and multi-point statistics; the word "structural" simply means that the whole field (or a dynamically relevant part of it) is somehow reconstructed or mimicked in a simplified manner. Several proposals for such closures in the point-particle approximation have been put forward, including the kinematic simulations [5, 6], approximate deconvolution [7], fractal interpolation [8, 9], spectral enrichment [10], and hybrid variants of those. They are partly successful, depending on the droplet inertia quantified by the Stokes number St. In the following, modeling proposals to account of the SGS flow effects on particles is referred to as "the SGS particle models" for brevity.

A prospective candidate to be put forward should preferably be autonomous, i.e. based on the resolved LES quantities only (like the dynamic Germano model). Another non-trivial criterion for the assessment of the SGS particle models is computational complexity: any viable proposal has to be considerably less expensive than the full DNS.

In the present contribution, we attempt to tackle the issue of structural SGS particle closures, in particular through considering an interesting and physically-motivated model based on the multifractality (MF) concept of the enstrophy cascade in a turbulent flow [11]. The MF concepts used there serve to derive the closure for the SGS tensor in single-phase flow; however, so far, they have not been applied to conceive an SGS particle model (it would be cumbersome and computationally costly due to the Biot-Savart formulae present there).

ASSESSMENT OF STRUCTURAL MODELS: A PRIORI LES

The DNS, LES and *a priori* LES have already been well mastered for the pseudo-spectral code we use [3, 12]. As the departure point for analyses of general turbulent flows, we have simulated homogeneous isotropic turbulence (HIT) with a large-scale forcing. In a companion paper [12] results are reported from a particle-laden HIT where small droplets, otherwise treated as point-particles, were allowed to collide. There, *a priori* LES was studied with the spectral cutoff of the highest wavenumbers. The SGS field was taken from the high-pass filtered DNS data as frozen or evolving in time. This allowed us to estimate the role of time variability of this field. Then, we supplemented *a priori* LES with kinematic simulations (KS, either frozen or time-dependent). As an important statistic, we have computed the increase of the mean droplet settling velocity w.r.t. the droplet terminal velocity in DNS. The results clearly indicate that frozen SGS fields are inadequate. The use of evolving SGS velocity ("semi-frozen") improves the results, depending on St. We also determined the two-point statistics relevant for droplet collisions: the radial distribution function (RDF, a measure of particle concentration non-uniformity) and the radial relative velocity (RRV). Both are computed at contact (nearly touching droplets). Concerning the impact of the SGS time variability, the results are basically in line with those for the settling velocity.

The present work is meant to provide hints for conceiving new SGS particle models, beyond the KS reported in [12]. Detailed flow and dispersed phase data (DNS together with the Lagrangian particle tracking) are essential for the development of an SGS particle model, the parameter space including R_λ, St and Fr (for gravity-affected cases). Along with the DNS, *a priori* LES have been performed as well as *a posteriori* (true) LES with the spectral eddy diffusivity.

RESULTS: SGS ENSTROPHY

The experimental and DNS evidence has shown that the small-scale turbulence is dominated by vortical structures and the velocity gradients are strongly non-Gaussian. A relevant measure of this flow aspect is the enstrophy $\Omega = |\boldsymbol{\omega}|^2$ where $\boldsymbol{\omega} = \nabla \times \mathbf{u}$ is the vorticity. Given that the solid particles of low inertia (small St) are strongly sensitive to the small-scale eddy structures, we argue that the SGS enstrophy field is a useful quantity to assess structural models for LES. From among various proposals we have chosen the multifractal model and the kinematic simulations. The former is of particular interest

as it explictly reconstructs the cascades of vorticity magnitude and orientation out of locally available large-scale data.

In the DNS of HIT at $R_\lambda = 107$ on 256^3 grid we have computed the velocity field $\mathbf{u}_\Delta$ as the difference of two low-pass filtered fields at the scale Δ and 2Δ, respectively (Δ is the LES mesh size). The MF model input is an assumed PDF of a fractal multiplier needed to construct the vorticity magnitude values at each subsequent refinement level $\mathcal{N}$ [11]. In this work, we begin from the LES mesh of 64^3 down to the DNS mesh of 256^3 (here, $\mathcal{N} = 2$). This means that the vorticity data at each LES cell serve to construct the vorticity within $2^{3\mathcal{N}}$ fine-scale DNS cells. The SGS enstrophy $Q_{\rm sgs}$ that needs to be distributed over the fine-scale (DNS-size) cells is the control parameter of the MF model. It is determined as proportional to $Q_\Delta = |\nabla \times \mathbf{u}_\Delta|^2$.

Figure 1 shows snapshots of: (i) the SGS enstrophy (precisely: the vorticity magnitude $\omega_{\rm sgs}$) computed using the pseudospectral DNS code and high-pass velocity filtering and (ii) the SGS vorticity magnitude reconstructed from the MF cascade. The positive observation is that the MF model acts locally (through $\mathbf{u}_\Delta$) and this is confirmed by the maxima and minima approximately coinciding in both panels of Fig. 1. The negative message is that the spatial structures of the two fields are very much different. This fact from the naked-eye observation of the color maps is subsequently confirmed by results in Fig. 2 which can be more precisely interpreted.

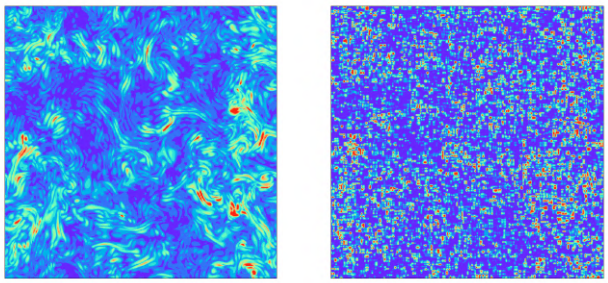

Figure 1: Subfilter vorticity magnitude in forced isotropic turbulence: a) computed in DNS, b) reconstructed from multifractal enstrophy cascade. Both quantities are normalised by the respective domain-averaged values of $|\boldsymbol{\omega}_{\rm sgs}|$.

Figure 2 shows sample profiles of vorticity magnitudes (normalised by their respective domain-averaged mean value), including those for KS as well. It is noticed that the spatial correlation of the MF-generated profile will be of much shorter range than the one resulting from the filtered DNS; also the variability of the enstrophy is way too strong; this may be further corroborated by the discrepancy in the PDFs of enstrophy in the computational domain (not shown).

CONCLUSION

In this paper, we have briefly recalled the issue of SGS particle models. Then, we focused on *a priori* LES to gain insights in the SGS enstrophy (or magnitude of vorticity) as this quantity plays a vital role in the subfilter dynamics of low inertia particles (the most problematic ones for all structural models proposed to date). We have extracted the SGS enstrophy from the DNS of forced isotropic turbulence using high-pass spectral filtering. To assess the viability of the multifractal

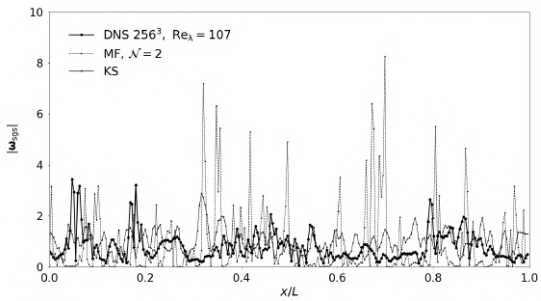

Figure 2: Subfilter vorticity magnitude in forced isotropic turbulence computed in DNS (solid line) on a 256^3 mesh, reconstructed from filtered DNS data on 64^3 mesh using a two-level ($\mathcal{N} = 2$) multifractal enstrophy cascade (dashed), and reconstructed from the kinematic simulation (thin line).

model [11] for dispersed flows, we reconstructed the SGS enstrophy using the multifractal cascade of vorticity magnitude. It reveals that the two SGS fields (high-pass DNS and the MF model) considerably differ, which is rather discouraging as far as the use of MF procedure to feed the SGS particle model is considered. The methodology is now being applied to assess other structural models in the same way, in particular the kinematic simulations and fractal interpolation.

Acknowledgement The work was supported by the National Science Centre (NCN), research projects 2017/27/B/ST8/00555 and 2018/30/Q/ST8/00341. The HPC resources were provided by ICM (University of Warsaw), grant G87-1145.

REFERENCES

[1]Fede, P. and Simonin, O.: Numerical study of the subgrid turbulence effects on the statistics of heavy colliding particles, *Phys. Fluids*, **17**, 045103 (2006).

[2]Marchioli, C.: Large-eddy simulation of turbulent dispersed flows: a review of modelling approaches, *Acta Mech.*, **228**, 741 (2017).

[3]Rosa, B. and Pozorski, J.: Impact of subgrid fluid turbulence on inertial particles subject to gravity, *J. Turb.*, **18**, 634–652 (2017).

[4]Knorps, M. and Pozorski, J.: Stochastic modeling for subgrid-scale particle dispersion in large-eddy simulation of inhomogeneous turbulence, *Phys. Fluids*, **33**, 043323 (2021).

[5]Ray, B. and Collins, L.R.: A subgrid model for clustering of high-inertia particles in LES of turbulence. *J. Turb.* **15**, 366 (2014).

[6]Pozorski, J. and Rosa, B.: The motion of settling particles in isotropic turbulence: Filtering impact and kinematic simulations as subfilter model, *Direct and Large-Eddy Simulation* **11** (Eds: M.V. Salvetti, V. Armenio, J. Fröhlich, B.J. Geurts and H. Kuerten), pp. 215–220 (2019).

[7]Kuerten, J.G.M.: Subgrid modeling in particle-laden channel flows, *Phys. Fluids* **18**, art. 025108 (2006).

[8]Marchioli, C., Salvetti, M.V. and Soldati, A.: Appraisal of energy recovering sub-grid scale models for large-eddy simulation of turbulent dispersed flows, *Acta Mech.*, **201**, 277–296 (2008).

[9]Akinlabi, E.O., Wacławczyk, M., Malinowski, S.P. and Mellado, J.P.: Fractal reconstruction of sub-grid scales for large eddy simulation. *Flow Turbul. Combust.* **103**, 293–322 (2019).

[10]Bassenne, M., Esmaily, M., Livescu, D., Moin, P. and Urzay, J.: A dynamic spectrally enriched subgrid-scale model for preferential concentration in particle-laden turbulence, *Int. J. Multiphase Flow*, **116**, 270–280 (2019).

[11]Burton, G.C. and Dahm, W.J.A.: Multifractal subgrid-scale modeling for large-eddy simulation. I. Model development and a priori testing, *Phys. Fluids*, **17**, art. 075111 (2005).

[12]Rajek, M. and Pozorski, J.: Kinematic simulations as a subgrid-scale model for particle motion: *a priori* LES of homogeneous isotropic turbulence, *J. Phys.: Conf. Ser.*, accepted (2022).

WORKSHOP
Direct and Large-Eddy Simulation 13
October 26th-29th 2022, Udine, Italy

POTENTIAL OF PERIODIC BOX HOMOGENEOUS ISOTROPIC TURBLENCE AS A SUB-GRID SCALE MODEL

Githin Tom Zachariah[1], **Harry E.A. Van den Akker**[1]
[1] Bernal Institute
University of Limerick, Ireland
githin.zachariah@ul.ie

INTRODUCTION

In Large Eddy Simulations (LES), the effects of the unresolved scales are modelled using Sub-Grid Scale (SGS) models. Many models have been proposed over the years with varying accuracy, but further work is necessary to develop a near-ideal SGS model[1]. The development of such advanced SGS models requires better understanding of the array of complex processes that occur at the smallest scales of motion. On the other hand, Direct Numerical Simulation (DNS) fully resolves all scales of motion and result in an exact solution. Due to its high computational requirement, a DNS is currently restricted to smaller and simpler problems. However, DNS has been used in the past to understand the behaviour of the smallest scales turbulence with the help of forced Homogeneous Isotropic Turbulence (HIT) simulations[2, 3, 4]. Here, the effects of the large scales are replicated by applying a specifically designed forcing function[4, 5, 6] to the largest scales of a periodic box, thereby inducing HIT. By the Kolmogorov isotropy hypothesis, HIT is a good representation of the smallest scales of turbulence.

In this study, we propose the use of Periodic Box (PB) HIT simulation to represent the unresolved small scales of a Large Eddy Simulation and thus assume the role of the SGS model. This would allow for fully resolved SGS turbulence with the accuracy only limited by that of the communication from the LES to the PB HIT. Such a method would be invaluable in testing and developing the next generation of SGS models. Additionally, the flexibility of this model would allow it to resolve the smallest scales selectively at regions of high turbulence. It can also be invaluable in understanding and modelling the effect of turbulence in complex small scale processes such as particle laden flows and crystallization.

As a proof of concept, a one-way coupling is used here to communicate the properties of the local flow from the LES to the PB HIT. The LES simulates a Homogeneous Isotropic Turbulence (HIT) scenario in order to avoid the effects of anisotropy near walls. A 128^3 domain was used, which corresponds to a minimum wavenumber of $k_{min}^{LES} = 0.5\,k_{min}^{DNS}$, leading to a nearly fully resolved simulation. The turbulent forcing scheme used and the simulation conditions are similar to those used by Siddhartha et al.[2]. In these ideal conditions, the local characteristic strain rate can be assumed to be representative of the effects of large scales of LES on the smallest. Additionally, this being the same assumption used in the static Smagorinsky model makes direct comparisons easier. Therefore, the characteristic strain rate at the smallest scales of the LES is matched with that at the largest usable scales of the PB HIT using a virtual controller that controls the power input to the periodic box. In order to avoid any direct effects of the SGS model on the PB HIT, the strain rate matching can also be performed at larger wavenumbers, in this study $k = 0.25\,k_{min}^{DNS}$ is tested. This requires the filtering of the smallest scale of the LES, which removes a large portion of the inaccuracies from the SGS model.

RESULTS AND DISCUSSION

The turbulence spectra for the LES and the PB HIT are plotted together in figure 1. The results were compared with an exact DNS solution obtained from the work by Siddhartha et. al.[2]. The LES covers the large scales and the PB HIT covers the smallest scales of the turbulence spectrum. It can be observed that the PB HIT spectrum forms a continuous extension to the LES spectrum and gives an overall result very close to the DNS solution. However, the PB HIT spectrum was found to be affected by the inaccuracies in the smallest scales of the static Smagorinsky LES simulation. This can be mitigated by filtering the LES to remove the erroneous scales. The resultant spectrum (black and purple lines in figure 1) were found to match exactly with the DNS solution. Additionally, varying the parameters from the forcing algorithm (variation in spreading factor C shown here) is seen to control the integral length scale and aid in tuning the PB HIT to the LES. This demonstrates the capability of a PB HIT to be tuned to reflect the particular conditions at the smallest scale of a well resolved LES simulation.

To evaluate the capability of PB HIT to assume the role of the SGS model, an a priori test was conducted using an exact DNS simulation of a standard HIT. The DNS is filtered (to the same wavenumber as the previous LES) and the filtered strain rate is measured and fed to both PB HIT and the Smagorinsky model. The effective Smagorinsky constant was calculated using the measured characteristic stress in the Smagorinsky model equation. This is then compared with that calculated from the exact DNS solution. The results obtained are shown in figure 2. The PB HIT was found to predict the effective Smagorinsky constant accurately and agrees well with the exact solution. At very high values of strain rate, the PB HIT diverges due to insufficient resolution to resolve the increasingly smaller eddies. Therefore, dynamically ensuring the resolution of the smallest scales in the PB HIT is essential

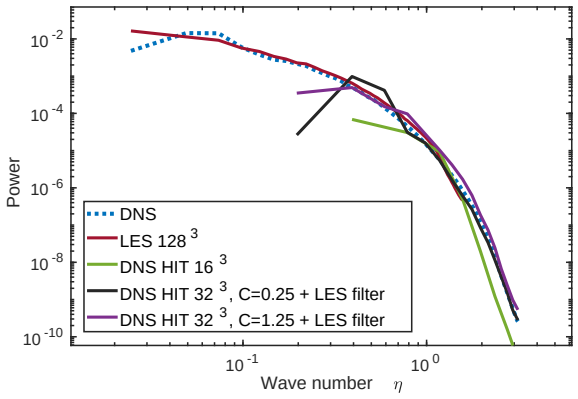

Figure 1: Turbulence spectra from the LES and the PB HIT with/without the filtering of the smallest scale of LES.

for a stable simulation.

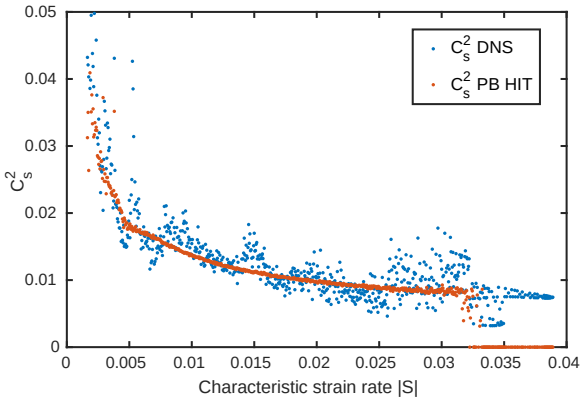

Figure 2: The effective (square of) Smagorinsky constant as observed from the PB HIT for varying values of the characteristic strain rate.

The results obtained are analysed from a different perspective by using a scatter plot to compare the modelled characteristic stress value to the exact solution from the DNS, as shown in figure 3. It can be clearly seen that the PB HIT exhibits better accuracy at all values of stress, and gives near exact solutions at smaller values. In contrast, the Smagorinsky model is seen to consistently overestimate the characteristic stress. Up to a |T| value of about 0.5, the PB HIT is seen to exactly match the full DNS solution. At higher stress values, the PB HIT results can be seen to increasingly deviate from the exact solution. This can be attributed towards the decreasing quality of the DNS as the Kolmogorov scale recedes to smaller and smaller scales. This further reinforces the need to dynamically ensure that the PB HIT is resolving the smallest scales of motion.

CONCLUSIONS

The above results demonstrate that a periodic box DNS simulation can be tuned to the local conditions of an LES and act as the SGS model. When compared with the constant Smagorinsky model, while working with the same assumptions and restrictions, the PB HIT is seen to be considerably more

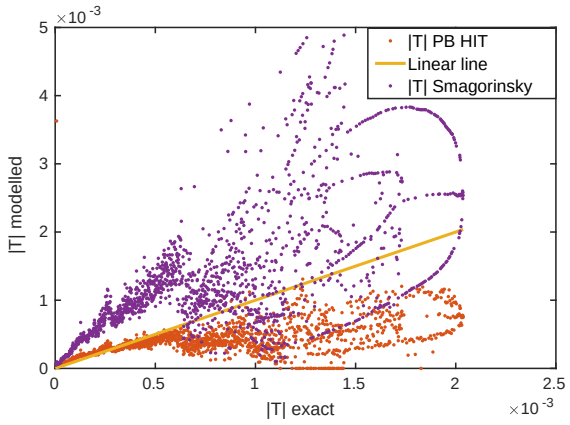

Figure 3: Scatter plot of the exact characteristic stress from DNS vs that modelled using PB HIT and smagorinsky model

accurate when compared with the exact solution. A priori tests also show that the PB HIT is able to model the variation in the effective Smagorinsky constant accurately, provided that it can resolve the smallest scales of turbulence. Therefore, this work demonstrates the potential of PB HIT to take the role of the SGS model. Future work includes the development of a fully coupled LES - PB HIT model to study this technique in practice. The model can also be extended to match the instantaneous anisotropies in small scale turbulence and extend the model beyond the ideal conditions used here.

REFERENCES

[1]Moser, Robert & Haering, Sigfried & Yalla, Gopal. (2021). Statistical Properties of Subgrid-Scale Turbulence Models. Annual Review of Fluid Mechanics. 53. 10.1146/annurev-fluid-060420-023735.

[2]Mukherjee, S., Safdari, A., Shardt, O., Kenjeres, S. & Van den Akker, Harry E.A.. Droplet–turbulence interactions and quasi-equilibrium dynamics in turbulent emulsions. *Journal Of Fluid Mechanics.* **878** pp. 221-276 (2019,11)

[3]Ten Cate, Andreas & van Vliet, Eelco & Derksen, J.J. & Van den Akker, Harry E.A.. (2006). Application of Spectral Forcing in Lattice-Boltzmann Simulations of Homogeneous Turbulence. Computers & Fluids. 35. 1239-1251. 10.1016/j.compfluid.2005.06.001.

[4]Bos, W., Laadhari, F. & Agoua, W. Linearly forced isotropic turbulence at low Reynolds numbers. *Phys. Rev. E.* **102**, 033105 (2020,9), https://link.aps.org/doi/10.1103/PhysRevE.102.033105

[5]Alvelius, K. Random forcing of three-dimensional homogeneous turbulence. *Physics Of Fluids.* **11**, 1880-1889 (1999), http://ojps.aip.org/phf/phfcpyrts.html

[6]Janin, J., Duval, F., Friess, C. & Sagaut, P. A new linear forcing method for isotropic turbulence with controlled integral length scale. *Cite As: Phys. Fluids.* **33** pp. 45127 (2021), https://doi.org/10.1063/5.0045818

Session: Compressible flow

Thursday, October 27, 2022

11:20 – 12:50

WORKSHOP
Direct and Large-Eddy Simulation 13
October 26th-29th 2022, Udine, Italy

COHERENT TURBULENT STRESSES IN TRANSONIC NOZZLE WITH SHOCK-WAVE/TURBULENT BOUNDARY LAYER INTERACTION

N. Goffart[1], B. Tartinville[1], C. Hirsch[1] and S. Pirozzoli[2]
[1] Cadence Design Systems
Brussels, Belgium
ngoffart@cadence.com
[2] Department of Mechanical and Aerospace Engineering
Sapienza University of Rome, Italy

INTRODUCTION

Shock-wave/boundary layer interactions (SWBLI) appear in many aeronautical applications such as aircraft wings, turbomachinery blades or air intakes for supersonic aircraft. The need for a better understanding and modeling of this performance limiting phenomenon is motivated by the desire of a more efficient aviation. High-fidelity simulations allow to reproduce the complex characteristics of SWBLI and are therefore suitable to generate data that can be exploited to derive reduced-order models for lower-fidelity tools.

In this context, this work presents the results of high-order Implicit Large-Eddy Simulations (ILES) of the transonic flow over a bump. The flow conditions are chosen such that a SWBLI occurs and leads to a large separated region on the lower wall. The data produced are used to study the oscillatory component of the turbulent stresses in this region and will serve as a basis for reduced-order modeling in a future work. In addition, the impact of a fluctuating outlet pressure, leading to a forced oscillation of the shock, will be investigated.

This extended abstract is composed of three sections. The first one describes the methods employed in the high-order solver used to perform the simulations. The second section introduces the case under investigation and finally, the method of analysis is described.

HIGH-ORDER SOLVER

The compressible Navier-Stokes equations are solved using a high-order solver based on the flux reconstruction approach, introduced by Huynh [1]. The temporal derivative is evaluated using the 5-stages 4th-order low-storage Runge-Kutta scheme of Carpenter and Kennedy [2].

A particular attention is given to the shock-capturing technique based on the Laplacian artificial viscosity of Persson and Peraire [3] in which a modal smoothness-based sensor is used to activate and compute the amount of artificial viscosity. To avoid the undesired application of the artificial viscosity in the boundary layer, which would damp the turbulence, the original shock-capturing technique is combined with the Ducros sensor [4].

The generation of turbulent inflow conditions is performed with the digital filtering technique. The initial 3D implementation of Klein et al. [5] has been modified according to Xie and Castro [6] and compressible fluctuations for density and temperature are introduced based on the Strong Reynolds Analogy and the hypothesis of negligible pressure fluctuations [7].

The solver capabilities have been assessed on transitional and turbulent turbomachinery flows [8] and the particular features described above have been validated by the authors in a previous work on an oblique shock-wave/boundary layer interaction [9].

TRANSONIC BUMP CASE

The configuration under investigation comes from an experiment led by Bron [10] in which a 2D bump is placed on the lower wall of a transonic wind tunnel. The experimental facility allows to generate downstream pressure perturbations with a frequency up to 500 Hz to study the effects of forced oscillation of the flow. This setup is particularly relevant since it reproduces the SWBLI that can occur on the suction side of turbomachinery blades. Moreover, the imposition of a fluctuating back pressure mimics the effects of the presence of a rotating downstream row.

While numerous operating points have been performed in the experiment, only two flow conditions will be considered here. Both are defined by $p_{t,in} = 160$ kPa, $T_{t,in} = 303$ K and $p_{s,out} = 106$ kPa such that the nozzle is completely choked as it can be seen in figure 1.

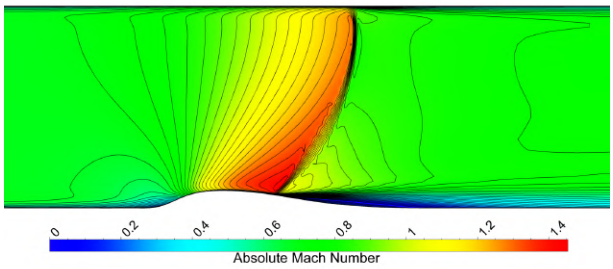

Figure 1: Mach number contours from a 2D RANS simulation.

The first case deals with the natural oscillation of the shock, whereas in the second case a fluctuating outlet pressure is imposed to highlight the effects of the forced motion.

To the authors' knowledge, this is the first analysis of an high-order ILES in this configuration including the forced oscillation of the shock-wave. Previous works are the LES of Wollblad et al. [11] and the DNS (at slightly different conditions) of Brouwer [12] for the case without fluctuating outlet pressure. Note that in all cases, the Reynolds number has been adapted to decrease the computational cost of the simulation.

ANALYSIS

The objective of this work is to study and model the oscillatory component of the turbulent stresses due to a shock-wave/boundary layer interaction. The simulation of the two different operating points will assess the influence of the natural and the forced oscillation of the shock-wave on the turbulence in the separated region.

The triple decomposition of Reynolds and Hussain [13] is adopted, stating that any flow quantity q can be expressed as the sum of a mean component $\bar{q}$, an oscillatory component (also called coherent motion) $\tilde{q}$ and a component corresponding to the turbulent motion (or incoherent motion) q''. This can be applied to the turbulent stresses, leading to

$$u_i'' u_j'' = \overline{u_i'' u_j''} + \widetilde{u_i'' u_j''} + \left(u_i'' u_j''\right)'', \tag{1}$$

and the attention is focused on the oscillatory component $\widetilde{u_i'' u_j''}$. Note that this decomposition is suitable for shock-wave/boundary layer interactions as there is a clear separation of time scales between the coherent and incoherent motions. Typically, the frequency associated to the natural motion of the shock-wave is two orders of magnitude lower than the characteristic frequency of the upstream boundary layer. Moreover, the frequency of the forced outlet disturbance is also low compared to the one of the upstream boundary layer.

Another point worth commenting is the way the coherent motion is extracted from the flow. Whereas it is typically obtained through phase-averaging, this cannot be applied in the context of SWBLI. Indeed, the low-frequency motion of the shock-wave is not harmonic but broadband in nature. To circumvent this problem, the conditional averaging is used instead. Conditional refers to the fact that the averaging process is performed according to a certain condition which will be here the position of the shock. This technique has been successfully applied to oblique shock-wave/boundary layer interactions, for example in Touber [7].

ACKNOWLEDGMENTS

This project has received funding from the European Union's Horizon 2020 research and innovation programme under the grant agreement MSCA-ITN-ETN TEAMAero No 860909.

REFERENCES

[1]Huynh, H. T. : A Flux Reconstruction Approach to High-Order Schemes Including Discontinuous Galerkin Methods, *18th AIAA Computational Fluid Dynamics Conference*, (2007).

[2]Carpenter, M. H. and Kennedy, C. A. : Fourth-Order 2N-Storage Runge-Kutta Schemes, (1994).

[3]Persson, P.-O. and Peraire, J. : Sub-Cell Shock Capturing for Discontinuous Galerkin Methods, *44th AIAA Aerospace Sciences Meeting and Exhibit*, (2006).

[4]Ducros, F., Ferrand, V., Nicoud, F., Weber, C., Darracq, D., Gacherieu, C. and Poinsot, T. : Large-Eddy Simulation of the Shock/Turbulence Interaction, *Journal of Computational Physics*, **152(2)**, 517–549 (1999).

[5]Klein, M. and Sadiki, A. and Janicka, J. : A Digital Filter Based Generation of Inflow Data for Spatially Developing Direct Numerical or Large Eddy Simulations, *Journal of Computational Physics*, **186(2)**, 652–665 (2003).

[6]Xie, Z.-T. and Castro, I. P. : Generation of Inflow Conditions for Large Eddy Simulation of Street-Scale Flows, *Flow, Turbulence and Combustion*, **81(3)**, 449–470 (2008).

[7]Touber, E. : Unsteadiness in Shock-Wave/Boundary Layer Interactions, Ph.D. Thesis, University of Southampton, (2010).

[8]Puri, K., Lorrain, E. and Hirsch, C. : Robustness, Accuracy and Reliability of High-Order Implicit-LES for Transitional and Turbulent Turbomachinery Flows, *HiFiLeD Symposium on Industrial LES & DNS, 14-16 November 2018, Brussels, Belgium*, (2018).

[9]Goffart, N., Tartinville, B., Hirsch, C. and Pirozzoli, S. : High-Order High-Fidelity Simulation of Unsteady Shock-Wave/Boundary Layer Interaction Using Flux Reconstruction, *In preparation for the ECCOMAS Congress 2022*, (2022).

[10]Bron, O. : Numerical and Experimental Study of the Shock-Boundary Layer Interaction in Transonic Unsteady Flow, Ph.D. Thesis, Royal Institute of Technology, Sweden, (2003).

[11]Wollblad, C., Davidson, L. and Eriksson, L. E. : Large Eddy Simulation of Transonic Flow with Shock Wave/Turbulent Boundary Layer Interaction, *AIAA Journal*, **44(10)**, 2340–2353 (2006).

[12]Brouwer, J. : A Study of Transonic Shock-Wave/Boundary-Layer Interactions using Conservative, Skew-Symmetric Finite-Differences, Ph.D. Thesis, Technischen Universität Berlin, (2016).

[13]Reynolds, W.C. and Hussain, A.K.M.F. : The Mechanics of an Organized Wave in Turbulent Shear Flow. Part 3. Theoretical Models and Comparisons with Experiments, *Journal of Fluid Mechanics*, **54(2)**, 263–288 (1972).

WORKSHOP
Direct and Large-Eddy Simulation 13
October 26th-29th 2022, Udine, Italy

HIGH-REYNOLDS COMPRESSIBLE FLOWS SIMULATION WITH WALL-MODELLED LES AND IMMERSED BOUNDARY METHOD

F. De Vanna[1,*], **F. Picano**[1], **E. Benini**[1]
[1] Dipartimento di Ingegneria Industriale
University of Padova, Italy
* francesco.devanna@unipd.it

INTRODUCTION

High-Reynolds compressible flows over complex geometries represent a real challenge for contemporary engineering. Fully resolved Direct Numerical Simulations (DNS) are still not feasible in realistic contexts and, therefore, accurate turbulence models are required. In this scenario, Large Eddy Simulation (LES) represents a superior approach compared to more standard Reynolds Averaged Navier-Stokes (RANS) strategies since the dynamics of the energy-dominant and flow-dependent large eddies are directly resolved on the computational mesh rather than being modelled [1]. However, even if Wall-Resolved LES (WRLES) can be highly accurate in predicting such flows when applied to high-Reynolds conditions, they are still too computational demanding due to the impressive resolution requirements imposed by the presence of the solid boundary. Thus, the technique does not fit the industrial needs and, for this reason, Wall-Modelled LES (WMLES) have taken charge during the last decades [2]. The approach aims to resolve the most significant flow portions with standard LES techniques, while a wall-stress model considers the near-wall regions. Compared to other hybrids/zonal numerical discretisation of the Navier-Stokes system of equations, the WMLES approach has proven to be more accurate in capturing near-wall dynamics, which is critical for enhanced predictions of unsteady problems at any applicative level in engineering.

In addition, treating complex geometries in a computationally efficient way is not trivial, and one of the most promising strategies in this path is the Immersed Boundary Method (IBM). The strategy allows the body surface to cut the computational cells so that a Cartesian mesh can be employed independently of the geometry complexity. Thus, highly efficient and massive parallel Cartesian solver can be used for aerodynamics applications. The problem with IBM lies in the difficulty of resolving the near-wall regions since the mesh does not fit the body locally. For this reason, the combination of a WMLES, that aims at placing the first off-the-wall point as far as possible, with an IB strategy looks promising, combining the possibility of dealing with high Reynolds number flows in a framework that is efficient from a computational point.

The present work proposes an innovative technique that unifies the IBM with a WMLES approach. The method has been validated in high-Reynolds canonical flows consisting of the turbulent channel and a turbulent pipe whose walls have been modelled using immersed bodies.

GOVERNING EQUATION AND NUMERICAL METHODS

The present study is carried out with URANOS (Unsteady Robust All-around Navier-Stokes Solver), a fully compressible Navier-Stokes solver developed at the Industrial Engineering Department of the University of Padova [3]. The solver deals with the filtered Navier-Stokes system of equations in a conservative formulation which, introducing both the Reynolds ($\phi = \bar{\phi} + \phi'$) and Favre ($\phi = \tilde{\phi} + \phi'', \tilde{\phi} = \overline{\rho\phi}/\bar{\rho}$) decompositions, reads as:

$$\frac{\partial \bar{\rho}}{\partial t} = -\frac{\partial \bar{\rho}\tilde{u}_j}{\partial x_j} \tag{1a}$$

$$\frac{\partial \bar{\rho}\tilde{u}_i}{\partial t} + \frac{\partial \bar{\rho}\tilde{u}_i\tilde{u}_j}{\partial x_j} = -\frac{\partial \bar{p}_i\delta_{ij}}{\partial x_j} + \frac{\partial \bar{\tau}_{ij}}{\partial x_j} - \frac{\partial T_{ij}^{SGS}}{\partial x_j} \tag{1b}$$

$$\frac{\partial \bar{\rho}\tilde{E}}{\partial t} + \frac{\partial \bar{\rho}\tilde{u}_j\tilde{E}}{\partial x_j} = -\frac{\partial \bar{p}\tilde{u}_j}{\partial x_j} + \frac{\partial \tilde{u}_j\bar{\tau}_{ij}}{\partial x_j} - \frac{\partial \bar{\mathcal{J}}_j}{\partial x_j} - \frac{\partial E_j^{SGS}}{\partial x_j} \tag{1c}$$

The SGS stress tensor, $T_{ij}^{SGS} = \overline{\rho u_i u_j} - \bar{\rho}\tilde{u}_i\tilde{u}_j$, is modelled via the canonical Boussinesq's hypothesis evaluating the turbulent viscosity, μ_{SGS} through the Wall-Adaptive Large-Eddy (WALE) viscosity model.

As far as the wall model, the one proposed by [2] is employed so that the wall shear-stress value, $\tau_{w,wm}$, and the wall heat flux, $q_{w,wm}$, are fed as boundary conditions for the external flow according to the procedure proposed by [4]. The latter locally augments the SGS viscosity and diffusivity in such a way that the resolved velocity and temperature gradients, $(du/dy)_{LES}$ and $(dT/dy)_{LES}$), are corrected by a factor that provides the proper $\tau_{w,wm}$ and $q_{w,wm}$ at the wall. Combined with a wall-turbulent consistent SGS model, such a strategy automatically recovers a classical WR setup if the near-wall resolution and dynamics allow it. The process fits the IB approach by locally modifying the turbulent parameters near the immersed surfaces. Concerning IBM, the one proposed by [3] is used.

RESULTS

IB turbulent channel flow

As a first test, a low-Mach channel flow simulation is carried out. In particular, the bulk Mach number, $M_b = u_b/c_w$, is set equal to 0.1 and the friction Reynolds number, $Re_\tau = \rho_w u_\tau h/\mu_w$, is enforce to 5200. Figure 1 shows some snapshots of the instantaneous velocity field inside the channel

from which it can be observed how the upper and lower portions of the domain are modelled by immersed blocks.

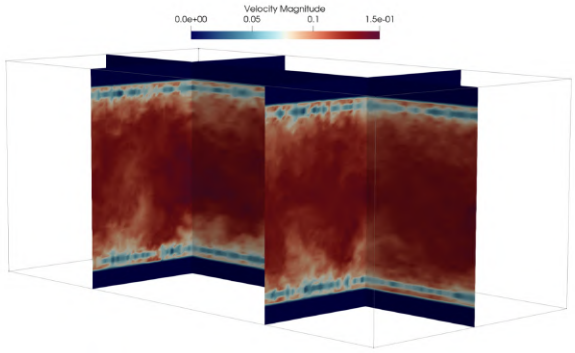

Figure 1: Representation of the domain of the turbulent channel flow, with the solid IBM entities clearly visible at the top and bottom.

The computation is carried out in a tridimensional box with size $L_x \times L_y \times L_z = 2\pi h \times 2h \times \pi h$ along the x, y and z coordinates, respectively, h being the channel half-height. A uniform mesh spacing is applied in all the three Cartesian directions. Two different near-wall resolutions are tested to address any mesh-related effect. Thus, Figure 2 reports the results of the computation. In particular, Figure 2a show the mean scaled velocity profiles, $u^+ = \tilde{u}/u_\tau$, while Figure 2b reports the density scaled Reynolds stress components, $\tau_{ij}^+ = \bar{\rho}\widetilde{u_i'' u_j''}/\tau_w$, as a function of the internal wall distance, $y^+ = yRe_\tau$. The first off-the-wall point is placed at $y_w^+ = \{40, 200\}^T$, respectively. Overall, the results well agree with DNS references by [5], showing minor discrepancies on the log-layer region of the mean velocity profiles. The issue is well known under the name of log-layer mismatch and is already the subject of several investigations in the literature (see, e.g., [2]).

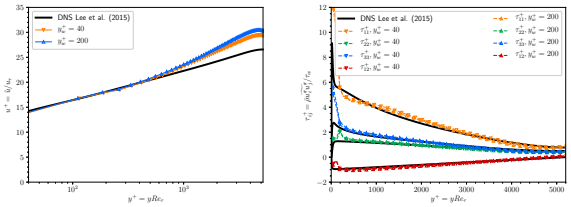

Velocity profile Reynolds stress components

Figure 2: Mean streamwise velocity profiles, $u^+ = \tilde{u}/u_\tau$, and density scaled Reynolds stress components $\tau_{ij}^+ = \bar{\rho}\widetilde{u_i'' u_j''}/\tau_w$ as a function of the inner scaled wall distance, $y^+ = yRe_\tau$, for channel flow cases at $M_b = 0.1$ and $Re_\tau = 5200$. Present results are compared with DNS data by [5].

IB turbulent pipe

In order to validate the current approach in a non-conformal geometrical arrangement, a fully developed turbulent flow through a circular pipe is here considered. The computational domain is made up of a rectangular box of dimensions $3R \times 3R \times 2\pi R$ being R the pipe radius and is discretized with a uniform grid in all directions. The grid spacing needed to account for the curvature of the wall; thus, the constantly changing wall-normal direction, which means that depending on the position in the domain radial grid resolution varied considerably. z-faces are made periodic, while no particular boundary conditions are required on the x and y-faces of the domain, as these are not adjacent to the flow. As in channel flow, IBM walls are modelled as no-slip and isothermal enforcing the wall-shear stress and heat flux according to the WMLES procedure. Figure 3 reports a snapshot of the axial instantaneous velocity field for a Pipe flow with a nominal Re_τ of 6000 and a bulk Mach number equal to 0.1, probing the effectiveness of the approach even in a non-conformal geometrical configuration

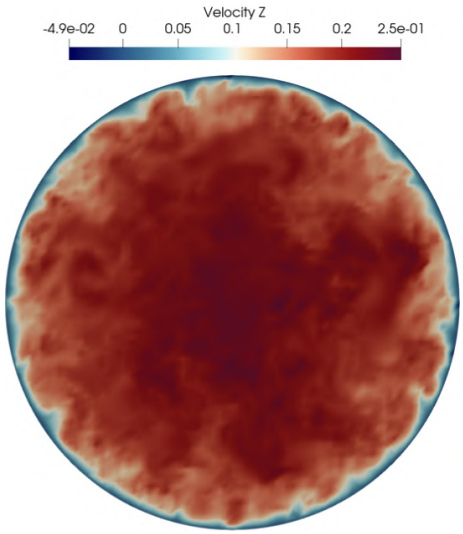

Figure 3: Instantaneous axial velocity field for the IBM+WMLES pipe flow.

REFERENCES

[1] S. T. Bose and G. I. Park, "Wall-Modeled Large-Eddy Simulation for Complex Turbulent Flows," *Annual Review of Fluid Mechanics*, vol. 50, no. 1, pp. 535–561, 2018.

[2] S. Kawai and J. Larsson, "Wall-modeling in large eddy simulation: Length scales, grid resolution, and accuracy," *Physics of Fluids*, vol. 24, no. 1, 2012.

[3] F. De Vanna, F. Picano, and E. Benini, "A sharp-interface immersed boundary method for moving objects in compressible viscous flows," *Computers and Fluids*, vol. 201, p. 104415, 2020.

[4] F. De Vanna, M. Cogo, M. Bernardini, F. Picano, and E. Benini, "Unified wall-resolved and wall-modeled method for large-eddy simulations of compressible wall-bounded flows," *Physical Review Fluids*, vol. 6, no. 3, pp. 1–24, 2021.

[5] M. Lee and R. D. Moser, "Direct numerical simulation of turbulent channel flow up to Reτ 5200," *Journal of Fluid Mechanics*, 2015.

WORKSHOP
Direct and Large-Eddy Simulation 13
October 26th-29th 2022, Udine, Italy

WAVELET-BASED ADAPTIVE LES FOR COMPRESSIBLE FLOWS

Giuliano De Stefano[1]
[1] Department of Engineering
University of Campania, Aversa, Italy
giuliano.destefano@unicampania.it

Oleg V. Vasilyev[2,3]
[2] Keldysh Institute of Applied Mathematics
Russian Academy of Sciences, Moscow, Russia
[3] Adaptive Wavelet Technologies
Louisville CO, USA
oleg.v.vasilyev@gmail.com

WAVELET-BASED ADAPTIVE LES

Fully-developed turbulent flows are characterized by the existence of intermittent coherent energetic eddies with a significant small scale component. Therefore, traditional lowpass filter-based large-eddy simulation (LES) methods are congenitally not able to investigate the multi-resolution features of coherent structures and intermittency of turbulence. Wavelet-based adaptive LES (WA-LES) is an extension of the LES methodology, where wavelet threshold filtering (WTF) is employed to separate resolved (more energetic) from residual (less energetic) turbulent flow structures, regardless of their size [1]. The effect of unresolved less energetic coherent structures on the resolved flow fields is approximated by means of subgrid-scale (SGS) modeling, with the turbulence resolution of the numerical solution being dictated by the wavelet threshold that is used for WTF.

The WA-LES governing equations are numerically solved by means of the anisotropic adaptive wavelet collocation (AWC) method [2], where the wavelet compression represents an integral part of the numerical algorithm such that the solution is obtained with an optimal number of grid points for a given level of accuracy. By separating the computational and the physical spaces, while introducing a suitable mapping between them, the structured rectilinear assembly of wavelet collocation points in the computational space can be retained, which allows the use of computationally efficient discrete adaptive wavelet transforms and derivative approximations, while the use of anisotropic curvilinear meshes for complex geometries is permitted.

COMPRESSIBLE FORMULATION

WA-LES has been recently extended for compressible flows, where the governing equations are expressed in terms of wavelet-based density-weighted Favre-filtered variables [3]. In this work, the compressible WA-LES approach is presented and discussed with a particular focus on wall-bounded turbulent flows, where different closure procedures are tested. The performance of the method is assessed by conducting adaptive numerical simulations of fully-developed compressible flow in a plane channel with isothermal walls, which represents a well-established benchmark case for wall-bounded compressible turbulent flows [4].

The governing equations for compressible WA-LES, which are not reported here for brevity, can be formally obtained from classical Favre-filtered LES equations by replacing the spatial low-pass filter with WTF. Here, the unclosed terms in the governing equations are approximated by using two different SGS models that were originally introduced for traditional LES, namely, the anisotropic minimum dissipation (AMD) model by Rozema et al. [5] and the dynamic k-equation model by Chai and Mahesh [6]. The AMD model, which has been further developed for compressible WA-LES by De Stefano et al. [3], seeks to approximate the least eddy-viscosity and eddy-diffusivity model coefficients necessary to prevent the formation of flow structures smaller than the mesh size, while imposing the balance of production and dissipation of SGS energy at the local grid scale.

Differently, the localized dynamic kinetic-energy model (LDKM), which extends the original formulation for incompressible WA-LES [7], is based on the explicit solution of the additional transport equation for the SGS turbulent kinetic-energy, which is formally derived. The various residual terms appearing in the wavelet-filtered governing equations are individually modeled by means of either Germano-like or Bardina-like dynamic procedures. This way, differently from other SGS modeling approaches involving the use of a priori prescribed model coefficients, the LDKM approach leads to a self-closed procedure. However, it is worth noting that LDKM has higher computational cost in both memory and complexity than the AMD model.

APPLICATION TO CHANNEL FLOW

To demonstrate the method, compressible WA-LES is applied for the simulation of isothermal-wall turbulent channel flow at various Mach and Reynolds numbers. For instance, the following results correspond to the flow case at Ma = 3

and Re = 4880, corresponding to the reference direct numerical simulation (DNS) study of Coleman et al. [4]. Figure 1 shows the adapted spatial grid at two different instants corresponding to a time distance of δ/U_{bulk}, where δ stands for the half channel height. The instantaneous grids, which are colored by the normalized temperature field, are depicted for five equispaced cross-sections of the channel. Apparently, the dynamic spatial-temporal adaptation of the numerical grid allows for the representation of dominant flow structures, with the finest grid that is occasionally used in the wall region practically corresponding to DNS-like resolution.

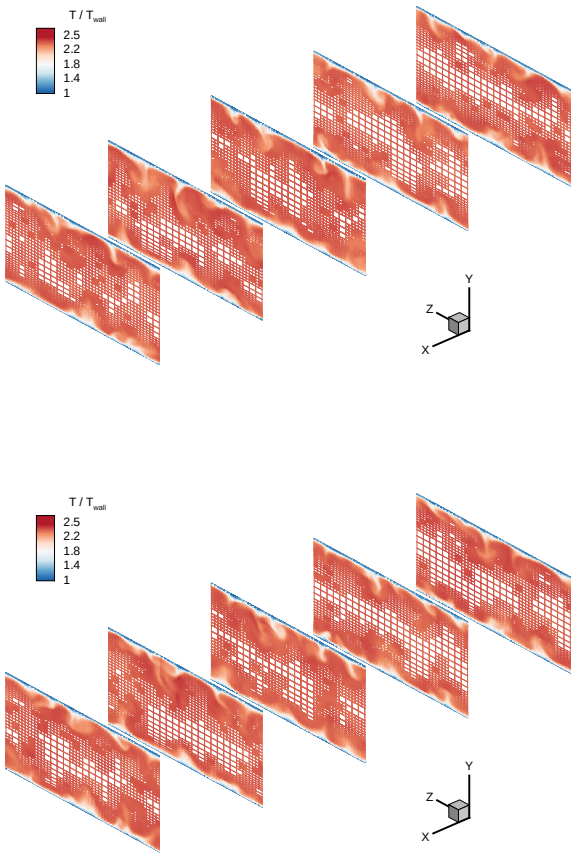

Figure 1: Adapted spatial mesh colored by the temperature field at two different time instants.

The average grid compression that is achieved in this case is reported in Table 1, along with some mean flow results, which are the friction Reynolds and Mach numbers, the heat flux coefficient and the normalized temperature at the center of the channel. Less than 6% of the potentially available grid points are actually employed by the various calculations, confirming the data obtained in the past for incompressible flows. The results of the statistical analysis, in terms of both mean flow variables and turbulent fluctuations, were found to be fully consistent with classical non-adaptive LES simulations [8].

While the good performances of the present solutions, supplied with either LDKM or AMD model, demonstrate that compressible WA-LES represents a viable alternative to the traditional LES approaches for wall-bounded attached turbulent flows, in the future, it would be beneficial to study the ability of the method for different scenarios involving, for instance, complex external flows.

Case	Compress.	Re_τ	Ma_τ	$-B_q$	T_c/T_{wall}
AMD	95%	458	0.107	0.13	2.69
LDKM	96%	435	0.113	0.13	2.37
LES [8]	0%	450	0.112	0.14	2.67
DNS [4]	0%	451	0.116	0.137	2.49

Table 1: Grid compression and some mean flow results for channel flow at Ma = 3 and Re = 4880.

REFERENCES

[1]De Stefano, G. and Vasilyev, O.V. : Hierarchical adaptive eddy-capturing approach for modeling and simulation of turbulent flows, *Fluids*, **6**, 83 (2021).

[2]Brown-Dymkoski, E. and Vasilyev, O.V. : Adaptive-anisotropic wavelet collocation method on general curvilinear coordinate systems, *J. Comput. Phys.*, **333**, 414–426 (2017).

[3]De Stefano, G., Brown-Dymkoski, E. and Vasilyev, O.V. : Wavelet-based adaptive large-eddy simulation of supersonic channel flow, *J. Fluid Mech.*, **901**, A13 (2020).

[4]Coleman, G.N., Kim, J. and Moser, R.D. : A numerical study of turbulent supersonic isothermal-wall channel flow, *J. Fluid Mech.*, **305**, 159–183 (1995).

[5]Rozema, W., Bae, H.J., Moin, P. and Verstappen, R. : Minimum-dissipation models for large-eddy simulation, *Phys. Fluids*, **27**, 085107 (2015).

[6]Chai, X. and Mahesh, K. : Dynamic k-equation model for large-eddy simulation of compressible flows, *J. Fluid Mech.*, **699**, 385–413 (2012).

[7]De Stefano, G., Vasilyev, O.V. and Goldstein, D.E. : Localized dynamic kinetic-energy-based models for stochastic coherent adaptive large eddy simulation, *Phys. Fluids*, **20**, 045102 (2008).

[8]Brun, C., Petrovan-Boiarciuc, M., Haberkorn, M. and Comte, P. : Large eddy simulation of compressible channel flow, *Theoret. Comput. Fluid Dyn.*, **22**, 189–212 (2008).

WORKSHOP
Direct and Large-Eddy Simulation 13
October 26th-29th 2022, Udine, Italy

A WALL-MODEL FOR COMPRESSIBLE FLOWS BASED ON A NEW SCALING OF THE LAW OF THE WALL

R. Debroeyer[1], M. Rasquin[2], T. Toulorge[2], Y. Bartosiewicz[1], G. Winckelmans[1]
[1] Institute of Mechanics, Materials and Civil engineering (iMMC)
Université catholique de Louvain (UCLouvain), 1348 Louvain-la-Neuve, Belgium
[2] Cenaero, 6041 Gosselies, Belgium
romain.debroeyer@uclouvain.be

INTRODUCTION

In order to perform scale-resolving simulations of problems at industrial scale, the only affordable way forward is wall-modeled Large-Eddy Simulation (wmLES). These simulations rely on the assumption that the flow in the near-wall region only loosely depends on the core flow and can thus be modeled using universal laws derived for simpler flows, hence drastically decreasing the grid-point requirements in the boundary layer. The law of the wall is fitted by Reichardt formula :

$$u^+_{\text{Reichardt}}\left(y^+\right) = \frac{1}{\kappa}\log\left(1+\kappa y^+\right) + \left(C - \frac{1}{\kappa}\log\kappa\right) \left(1 - \exp\left(-\frac{y^+}{11}\right) - \frac{y^+}{11}\exp\left(-\frac{y^+}{3}\right)\right),$$

where $u^+ = u\sqrt{\frac{\rho}{\tau_w}}$, $y^+ = y\frac{\sqrt{\rho\tau_w}}{\mu}$, $C \simeq 4.25$ and $1/\kappa \simeq 2.61$ according to latest measurements (see also Winckelmans and Duponcheel [1]). The law of the wall allows to model the velocity profile in the near-wall region (up to $y \simeq 0.12\,\delta$) by blending the viscous sublayer and the log law. It is often used to perform wmLES of incompressible or weakly compressible flows (see, e.g. Frère et al. [2]).

In order to maintain accuracy, the model must be rescaled when the flow Mach number and thus the compressibility effects become important. This work proposes a new scaling of this law to properly take the compressibility effects into account without significantly increasing the computational cost.

WALL-MODELING STRATEGY

In order to account for the variations of density and viscosity in the boundary layer, it is proposed to use scaled values of the wall-normal distance y and the velocity component tangent to the wall u at the wall-model injection location in Reichardt formula to evaluate the wall shear-stress. These scaled quantities, noted with uppercase letters are computed as:

$$Y_1 = \int_0^{y_1} \frac{\mu_w}{\mu}\sqrt{\frac{\rho}{\rho_w}}dy, \tag{1}$$

$$U_1 = \sqrt{\frac{\rho_1}{\rho_w}}\frac{\mu_1}{\mu_w}u_1, \tag{2}$$

where the subscript "1" is used for the quantities measured at the location where the wall-model is injected into the LES and the subscript "w" designates the wall quantities. The scaling of the wall-normal distance is similar to that proposed by Trettel and Larsson [3] for the representation of the universal velocity profiles for compressible flows and it mimics the non-dimensionalisation in wall-coordinates suggested by Huang et al. [4] and used in this paper. However, contrary to these previous works, the scaling here acts on dY/dy instead of Y/y. The velocity scaling is then obtained by imposing the same mass flow-rate below the wall-model injection point for the physical compressible flow and the transformed equivalent incompressible flow; as done in the Howarth-Stewartson transformation. The integral in Eq. (1) is evaluated using a trapezoidal rule.

The non-linear equation stemming from the injection of these transformed values, along with the wall density and viscosity in Reichardt formula is solved for the wall shear-stress τ_w, which is then imposed at the wall.

The proposed scaling relies on the wall density and dynamic viscosity, which can be obtained from the wall temperature, the assumption of constant pressure across the boundary layer, the (perfect) gas law and a suitable model for the dynamic viscosity. However, the wall temperature is unknown for flows with adiabatic walls; a Crocco-Busemann relation is used in that case, similarly to Catchirayer et al. [5].

SIMULATION RESULTS

Two cases of compressible turbulent channel flows at $Re_\tau \simeq 1000$ and with adiabatic walls were studied to validate this scaled wall-model, differing only by their centerline Mach number M_c : (1) a highly compressible, yet subsonic case ($M_c = 0.76$) and (2) a supersonic case ($M_c = 1.5$). Wall-modeled LES were performed for both cases using the scaled model, as well as using the unscaled incompressible model in order to measure the obtained improvement in accuracy. The results of these simulations are compared to reference wall-resolved LES (wrLES).

All simulations are performed using the Argo code [6], developed at Cenaero and which implements a high-order Discontinuous Galerkin method with Symmetric Interior Penalty (DG/SIP) method. Third-order interpolation polynomials ($p = 3$) are used for all simulations, except in the first off-wall element for the wmLES, where $p = 4$ is used, as recommended

by Frère et al. [2]. The flow statistics are accumulated over roughly 10 turbulent times $t^+ = \frac{h}{\sqrt{\tau_w/\rho_w}}$ and the Favre-averaged velocity, noted $\overline{u}$, is used.

The velocity profiles in wall-coordinates, i.e. $\overline{u}^+ = \overline{u}\sqrt{\frac{\rho}{\tau_w}}$ as a function of $y^+ = y\frac{\sqrt{\rho\tau_w}}{\mu}$ are presented in Fig. 1 for the wrLES and both wmLES.

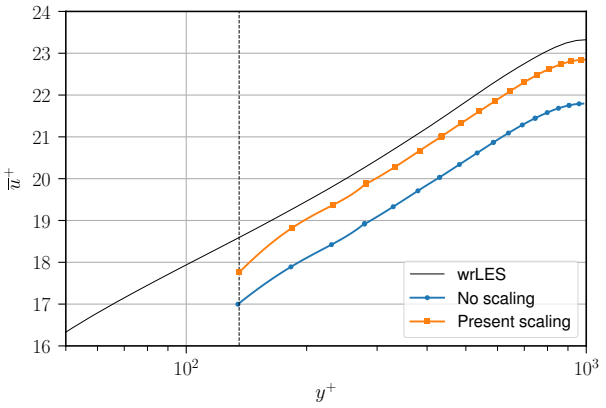

(a) $M_c = 0.76$

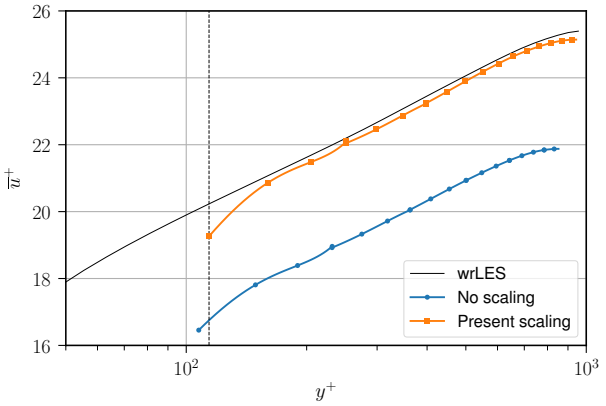

(b) $M_c = 1.5$

Figure 1: Velocity profiles in wall-coordinates for both cases. Reference wrLES (solid), incompressible wall-model (circles) and scaled wall-model (squares). Top: subsonic case; bottom: supersonic case. The vertical dashed line represents the upper boundary of the near-wall element for the wmLES mesh using the scaled model.

This figure clearly shows that the unscaled wall-model already fails to correctly capture the velocity profile in the subsonic case, and that its accuracy plummets when simulating the supersonic channel flow. On the other hand, the scaled wall-model shows a good accuracy for both cases.

	Error on Q_m [%]	
	$M_c = 0.76$	$M_c = 1.5$
No scaling	6.90	14.48
Present scaling	2.19	1.14

Table 1: Error on the mass flow-rate in the channel.

This can also be observed by computing the error on the mass flow-rate Q_m in the channel, as compared to the reference wrLES, see Table 1. The already higher error in the subsonic case is more than doubled in the supersonic case when no scaling of the wall-model is used; whereas the error remains around 2% with the proposed scaling.

CONCLUSIONS AND PERSPECTIVES

The use of an appropriate scaling of the flow before applying an algebraic wall-model formula developed for incompressible flows was shown to significantly increase the accuracy of wmLES of turbulent and adiabatic channel flows in subsonic and supersonic cases. With the proposed scaling, the error on the mass flow-rate remains very low (around 2%) when going from $M_c = 0.76$ to $M_c = 1.5$.

The proposed wall-model will be used to perform wmLES of flows at even higher Mach numbers to investigate the upper limitations of the scaling. It will then also be used to simulate more complex flows with non-equilibrium effects and mixing such as ejector flows.

ACKNOWLEDGEMENTS

The present research benefited from computational resources made available on the Tier-1 super- computer of the Fédération Wallonie-Bruxelles, infrastructure funded by the Walloon Region under the grant agreement n°1117545.

REFERENCES

[1]Winckelmans, G. and Duponcheel, M. : Modeling the law of the wake using an offset from the wall, *Phys. Rev. Fluids*, **6**, 064606 (2021)

[2]Frère, A., Carton de Wiart, C., Hillewaert , K., Chatelain, P. and Winckelmans, G. : Application of wall-models to discontinuous Galerkin LES, *Phys. Fluids*, **29**, 085111 (2017).

[3]Trettel, A. and Larsson, J. : Mean velocity scaling for compressible wall turbulence with heat transfer *Phys Fluids*, **28**, 026102 (2016).

[4]Huang, P. G., Coleman, G. N., and Bradshaw, P. : Compressible Turbulent Channel Flows: Dns Results and Modelling *J. Fluid Mech.*, **305**, 185–218, (1995).

[5]Catchirayer, M., Boussuge, J.-F., Sagaut, P., Montagnac, M., Papadogiannis, D., and Garnaud, X. : Extended integral wall-model for large-eddy simulations of compressible wall-bounded turbulent flows, *Phys. Fluids*, **30**, 065106 (2018).

[6]Hillewaert, K. : Development of the discontinuous Galerkin method for high-resolution, large scale CFD and acoustics in industrial geometries, *PhD Thesis, Ecole polytechnique de Louvain/iMMC*, (2013).

WORKSHOP
Direct and Large-Eddy Simulation 13
October 26th-29th 2022, Udine, Italy

SCALE-RESOLVING SIMULATION OF COMPRESSIBLE TURBULENT FLOWS WITH A DISCONTINUOUS GALERKIN METHOD

F. Bassi[1], **A. Colombo**[2], **F. Massa**[2]
[1] University of Bergamo (retired Professor)
francesco.bassi@unibg.it,
[2] University of Bergamo, Department of Engineering and Applied Sciences,
viale Marconi, 5 - 24044 Dalmine (BG), Italy
{alessandro.colombo, francescocarlo.massa}@unibg.it

In this work we present the results of two turbulent flow problems part of the Horizon 2020 HiFi-TURB project (GA 814837) suite. The first test case is characterized by a turbulent boundary layer featuring an incipient separation due to an adverse pressure gradient induced by a smooth backward facing step, see Figure 1. In this test case, denoted as Adverse Pressure Gradient (APG), the step height h based Reynolds number is $Re_h = 78490$ and the freestream Mach number is $Ma = 0.13455$. Since specifically designed within the HiFi-TURB project, see [1], no high-fidelity simulations are available for the APG test case in the literature. The second test case is the wing-body junction (WBJ) test case originally investigated by Devenport & Simpson in [2]. Here, the computational setup considers the experimental wing thickness based Reynolds number $Re_T = 115000$, the experimental Mach number $Ma = 0.078$ and half of the experimental incoming turbulent boundary layer thickness $\delta_{99.5} = 0.25\,T$, being T the wing thickness. Both test cases share the challenging numerical task of generating a turbulent boundary layer with specific conditions, *e.g.*, δ_{99}, Re_τ, Re_θ, etc., to be verified at particular domain locations. Accordingly, we adopt a synthetic turbulence injection approach based on the work of Schlatter & Örlü [3] and Hosseini et al. [4] This approach takes inspiration from the common practice of the experimental aerodynamics of forcing the turbulence transition through a roughness element, *e.g.*, a sandpaper band, disposed on the wall. In particular, it consists in introducing a space and time dependent volume forcing term within the momentum equation which acts in a small region of the laminar boundary layer above a smooth wall. In this work the compressible Navier-Stokes equations are discretized according to the high-order Discontinuous Galerkin solver MIGALE [5], using an exact Riemann solver for the evaluation of convective numerical fluxes and the Bassi-Rebay (BR2) method for the treatment of the diffusive terms. High-order linearly-implicit Rosenbrock schemes with optimal stability properties are adopted for time integration.

ACKNOWLEDGEMENTS

F. Bassi, A. Colombo and F. Massa acknowledge the European Project HiFi-TURB which has received funding from the European Union's Horizon 2020 research and innovation programme under the Grant Agreement No. 814837.

REFERENCES

[1]Alaya, E., Grabe, C., Knopp, T. : Design of a parametrized numerical experiment for a 2D turbulent boundary layer flow with varying adverse pressure gradient and separation behaviour, DLR-Interner Bericht, DLR-IB-AS-GO-2020-109, DLR Institute of Aerodynamics and Flow Technology (2021).

[2]Devenport, W.J., Simpson, R.L. : Time-dependent and time-averaged turbulent structure near the nose of a wing-body junction, *J. Fluid Mech.*, **210**, 23–55 (1990).

[3]Schlatter, P., Örlü, R. : Turbulent boundary layers at moderate Reynolds numbers: inflow length and tripping effects, *J Fluid Mech*, **710**, 5–34 (2012).

[4]Hosseini, S.M., Vinuesa, R., Schlatter, P., Hanifia, A., Henningson, D.S. : Direct numerical simulation of the flow around a wing section at moderate Reynolds number, *Int J Heat Fluid Fl*, **61**, 117–128 (2016).

[5]Bassi, F., Botti, L., Colombo, A., Ghidoni, A., Massa, F. : Linearly implicit Rosenbrock-type Runge-Kutta schemes applied to the Discontinuous Galerkin solution of compressible and incompressible unsteady flows, *Comp. Fluids*, **118**, 305–320 (2015).

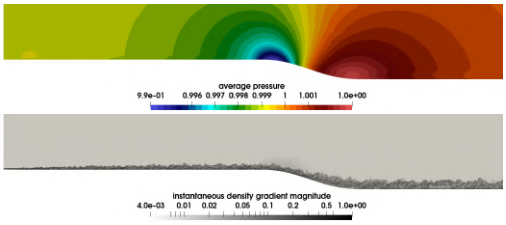

Figure 1: APG - Contours of the pressure average field (top) and the instantaneous density gradient magnitude (bottom) made dimensionless with respect to free-stream quantities.

Session: Turbulent flows 1

Thursday, October 27, 2022

15:20 – 16:20

WORKSHOP
Direct and Large-Eddy Simulation 13
October 26th-29th 2022, Udine, Italy

DIRECT NUMERICAL SIMULATION OF SCALAR TRANSPORT ACROSS THE INTERFACE BETWEEN A POROUS MEDIUM AND TURBULENT FLOW

S. v. Wenczowski[1], **M. Manhart**[1]
[1] Professorship of Hydromechanics
Technical University of Munich (TUM), Germany
simon.wenczowski@tum.de, michael.manhart@tum.de

INTRODUCTION

Exchange processes at the interface between a porous medium and a turbulent flow field are relevant in a wide range of natural and industrial systems: Prominent examples for technical applications range from food drying up to processes within modern fuel cells. In the environment, the exchange of mass within the hyporheic zone is vital for the health of aquatic ecosystems, whereas the evaporation from soils must be considered for sustainable land use. Despite the apparent heterogeneity of these fields, exchange processes at the interface are driven by a common set of mechanisms.

The objective of our research is to contribute to a more comprehensive mechanistic understanding of scalar transport in the interface region. Beyond (i) distinguishing different scalar transport processes, we (ii) identify the regions of influence of individual processes and shed a light on (iii) the interaction between processes. For this purpose, the porous medium is represented by a static random sphere pack. We consider shear Reynolds numbers in the range of $Re_\tau = 150 - 500$ and permeability Reynolds numbers of $Re_K = 0.4 - 2.5$. A Schmidt number of $Sc = 1$ ensures that Kolmogorov and Batchelor scales coincide. By means of a single-domain Direct Numerical Simulation (DNS), all temporal and spatial scales are resolved both in the free flow region as well as in the pore space of the porous medium. Thus, no a-priori assumption are made, that may distort the observations.

Whereas instantaneous flow fields allow us to identify typical structures in the flow, the obtained statistics of the results are analyzed by means of a double-averaging technique [4]. Observing that turbulent and dispersive scalar transport hardly co-exist in any regions, we evaluate budget equations for temporal and spatial fluctuations in the scalar concentration field to explain the interaction between these two processes.

METHODOLOGY

Discretisation and Solution

Our in-house code MGLET [1] uses a Finite-Volume discretization to solve the incompressible Navier-Stokes equations and has been optimized for computationally demanding simulations of turbulent flow in and along complex geometries. The computation of the flow field is coupled with a transport problem for the passive scalar, where the discretization of the advection-diffusion equation ensures precise mass conservation. The geometry of the porous medium is integrated by an Immersed Boundary Method (IBM) of second order [2]. Further, the code allows to embed grids for local refinement of the grid near the interface such that $\Delta x^+ = \Delta y^+ = \Delta z^+ < 1$ is achieved. MGLET is MPI-parallelized and has optimized I/O routines such that simulations with more than 10^9 grid cells can be run efficiently [3]. A newly developed visualization functionality provides the option to capture features of the simulated flow field in short intervals during runtime.

Boundary conditions

The porous medium is represented by a monodisperse random sphere pack. During the simulation, the spheres remain static and impose a no-slip boundary condition on the fluid-solid interface. The domain has periodic boundary conditions in directions parallel to the bed surface and a volume force drives the flow in x-direction. At the top boundary of the domain, a slip boundary condition is applied as a rigid lid approximation for the free water surface. A vertical concentration gradient of the scalar is built up by imposing different concentration values as Dirichlet boundary conditions at the bottom and top domain boundary. The sphere surfaces are defined to be impermeable to scalar fluxes (analogy to adiabatic behavior). Figure 1 shows the configuration together with a visualization of an instantaneous flow field.

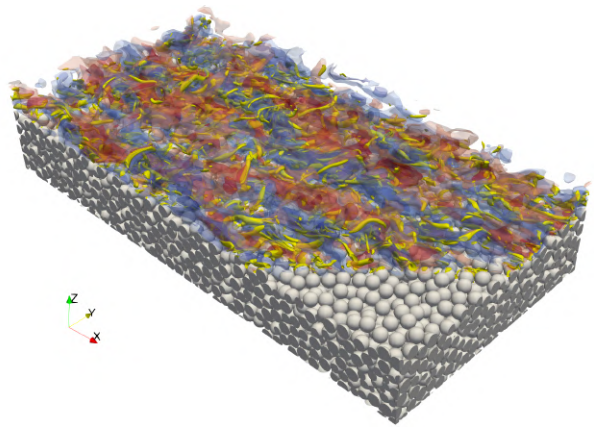

Figure 1: Instantaneous flow field with vortex structures in yellow, whereas red and blue indicate low- and high-velocity streaks, respectively.

Analysis framework

To discuss the complex and strongly three-dimensional flow situation, we resort to a double averaging technique [4]. An arbitrary quantity ϕ is first averaged in time

$$\phi_{(\boldsymbol{x},t)} = \overline{\phi}_{(\boldsymbol{x})} + \phi'_{(\boldsymbol{x},t)} \,, \qquad \overline{\phi}_{(\boldsymbol{x})} = \frac{1}{T}\int_0^T \phi_{(\boldsymbol{x},t)}\, dt \tag{1}$$

and, consecutively, the temporal mean is averaged within a horizontal plane parallel to the smoothed bed surface.

$$\overline{\phi}_{(\boldsymbol{x})} = \langle\overline{\phi}\rangle_{(z)} + \widetilde{\overline{\phi}}_{(\boldsymbol{x})} \,, \qquad \langle\overline{\phi}\rangle_{(z)} = \frac{1}{A_f}\iint_{A_f} \overline{\phi}_{(\boldsymbol{x})}\, dx\, dy \tag{2}$$

In the chosen notation, $\langle\overline{\phi}\rangle$ symbolizes the intrinsic average within a horizontal plane, while spatial deviations of the temporal mean from this in-plane average are indicated as $\widetilde{\overline{\phi}}$. Via the relation $\langle\phi\rangle^s_{(z)} = \theta_{(z)}\langle\phi\rangle_{(z)}$, a connection to the superficial horizontal average $\langle\phi\rangle^s_{(z)}$ is established, where $\theta_{(z)} = A_{f(z)}/A_0$ represents the in-plane porosity.

Validation

The simulation results are validated against experimental data from [5]. The plots on the left side of Figure 2 demonstrate reasonable agreement for the horizontally averaged streamwise velocity and the turbulent shear stress.

PRELIMINARY RESULTS

Within the horizontal averaging framework, an expression for the total vertical scalar flux J_c is given by Equation (3), where the symbol c represents the concentration of the passive scalar and Γ_c is the molecular diffusion coefficient.

$$\langle J_c\rangle^s_{(z)} = \underbrace{\theta\left\langle\overline{\Gamma_c\frac{\partial c}{\partial z}}\right\rangle}_{\text{molecular}} - \underbrace{\theta\left\langle\overline{w'c'}\right\rangle}_{\text{turbulent}} - \underbrace{\theta\left\langle\widetilde{\overline{w}}\widetilde{\overline{c}}\right\rangle}_{\text{dispersive}} = const \tag{3}$$

The terms on the right-hand side represent scalar fluxes due to molecular diffusion, turbulent transport and dispersive transport, respectively. Whereas the total superficially averaged scalar flux $\langle J_c\rangle^s$ is constant, the contributions of different transport processes vary depending on the vertical position z. The plot on the right in Figure 2 illustrates that for an exemplary case. Turbulent transport dominates in the free stream region. However, its influence declines rapidly within the topmost layers of the porous medium. In contrast to that, dispersive mass transport mainly affects deeper regions of the porous medium. We further distinguish between a background dispersion caused by the tortuosity of the flow in the pore space and an interface-induced part, the latter decaying with increasing depth. Even in the absence of macroscopic topographic features like dunes or riffles, large-scale spatial variability in the scalar concentration field is observed in regions dominated by dispersive transport. Only the region close to the impermeable bottom boundary of the simulation domain is dominated by scalar transport due to molecular diffusion and exhibits a comparatively high resistance for transfer in vertical direction.

The analysis of different simulation cases shows that turbulent transport and dispersive transport hardly co-exist, but rather appear to be mutually exclusive. As shown in the plot on the right of Figure 2, the contribution of turbulent transport declines at a high rate near the interface whereas the contribution of dispersive transport increases at a similar rate with increasing depth. To explain this observation, budget equations for the temporal and spatial variability in the scalar concentration field are evaluated using second-order statistics from MGLET. It becomes evident that a considerable part of the temporal fluctuations of the scalar field is produced at the expense of spatial fluctuations near the interface.

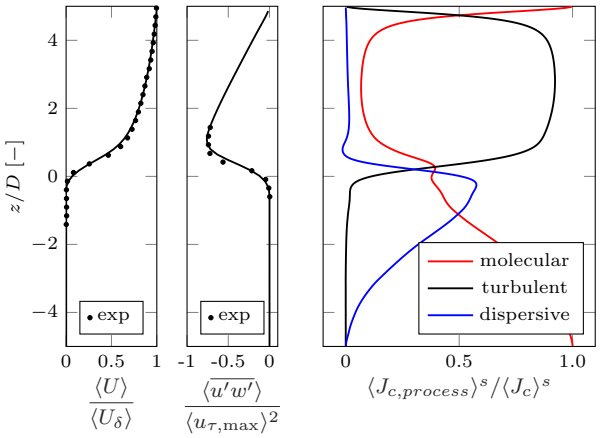

Figure 2: Validation of simulation results against experimental (exp) data of case S3 from [5] (left). Contribution of scalar transport processes to the total scalar flux (right). Position of geometrically defined interface at $z = 0$.

SUMMARY

We investigate scalar transport across the interface between a porous medium and a free turbulent flow by means of single-domain DNS. Analysis by horizontal averaging allows us to quantify the varying contribution of different transport processes to the total scalar flux over depth. Due to their inherent mechanisms, turbulent and dispersive transport are shown to be mutually exclusive, whereas the latter affects also deeper regions of the porous medium.

ACKNOWLEDGEMENTS

We gratefully acknowledge the financial support of the DFG in the scope of grant no. MA2062/15-1. Computing time for the project is granted by the Leibniz Supercomputing Centre on SuperMUC-NG under project `pn68vo`.

REFERENCES

[1]Manhart, M., Tremblay, F & Friedrich, R. : MGLET: A Parallel Code for Efficient DNS and LES of Complex Geometries. *Parallel Computational Fluid Dynamics 2000*. 449–456, (2001)

[2]Peller, N. Numerische Simulation Turbulenter Strömungen Mit Immersed Boundaries. (Technische Universität München, 2010)

[3]Y. Sakai, S. Mendez, H. Strandenes, M. Ohlerich, I. Pasichnyk, M. Allalen, and M. Manhart, "Performance optimisation of the parallel CFD code MGLET across different HPC platforms," in *Proceedings of the Platform for Advanced Scientific Computing Conference*, PASC '19, (New York, NY, USA), Association for Computing Machinery, 2019.

[4]Raupach M. R. and Shaw R. H., "Averaging procedures for flow within vegetation canopies," *Boundary-Layer Meteorology*, vol. 22, no. 1, p. 7990, 1982.

[5]J. J. Voermans, M. Ghisalberti, and G. N. Ivey, "The variation of flow and turbulence across the sedimentwater interface," *Journal of Fluid Mechanics*, vol. 824, p. 413437, 2017.

WORKSHOP
Direct and Large-Eddy Simulation 13
October 26th-29th 2022, Udine, Italy

TURBULENT POISEUILLE FLOW OF TWO IMMISCIBLE LIQUID LAYERS INSIDE A CHANNEL

George Giamagas[1,2], Francesco Zonta [1], Alessio Roccon[2] & Alfredo Soldati [1,2]
[1]Technical University of Vienna, Getreidemarkt 9, 1060 Wien, Austria
[2] University of Udine, Via delle Scienze 206, 33100 Udine, Italy
alfredo.soldati@tuwien.ac.at

We use pseudo-spectral Direct Numerical Simulation (DNS), coupled with a Phase Field Method (PFM), to investigate the turbulent Poiseuille flow of two immiscible liquid layers inside a channel. The two liquid layers, which have the same thickness ($h_1 = h_2 = h$), are characterized by the same density ($\rho_1 = \rho_2 = \rho$) but different viscosities ($\eta_1 \neq \eta_2$), so mimicking a stratified oil-water flow. This setting allows for the interplay between inertial, viscous and surface tension forces to be studied in the absence of gravity. The full problem is described in terms of the following flow parameters: the shear Reynolds number (Re_τ, which quantifies the importance of inertia compared to viscous effects), the Weber number (We, which quantifies surface tension effects compared to inertia) and the viscosity ratio, λ between the two fluids. In particular, we fix $Re_\tau = 300$, $We = 1$, and we consider viscosity ratios in the range $0.1 \leq \lambda = \eta_1/\eta_2 \leq 1$. We focus on the role of turbulence in initially deforming the interface and on the subsequent growth of capillary waves. Compared to a single phase flow at the same shear Reynolds number ($Re_\tau = 300$), in the two-layers case we observe a strong interaction between the turbulent flow and the deformable liquid-liquid interface. Capillary wave propagation and interaction is studied by means of a spatiotemporal spectral analysis and compared with previous theoretical and experimental results.

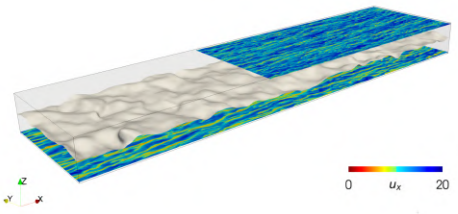

Figure 1: Channel geometry and flow topology of a two-layer turbulent flow simulation. Capillary wave formation can be seen at the interface between the two layers. The fluid in the upper half of the channel has a viscosity that is 50% lower than that of the fluid in the lower half of the channel. This fact is responsible for the difference between top and bottom near-wall turbulence structure, here made visible using the value of the streamwise component of the velocity vector (u_x).

WORKSHOP
Direct and Large-Eddy Simulation 13
October 26th-29th 2022, Udine, Italy

MODULATION OF TURBULENCE FLUX BUDGETS BY VARYING FLUID PROPERTIES IN HEATED HIGH PRANDTL NUMBER FLOW

C. Irrenfried[1] and **H. Steiner**[1]
[1]Institute of Fluid Mechanics and Heat Transfer
Graz University of Technology, Austria
helfried.steiner@tugraz.at

INTRODUCTION

High Prandtl number liquids are most commonly used for lubrication and cooling of various technical devices. The large disparity of the smallest turbulent thermal and dynamic scales strongly challenges the numerical modelling of the transport of heat and momentum. The inherently steeper temperature gradients due to the high thermal resistance generally lead to a marked variation of the fluid properties, whose often assumed neglect further adds to predictive uncertainty. The present Direct Numerical Simulation (DNS) study specially addresses this issue considering a typical heat transfer oil with a realistic variation in material properties in the heated near wall region. The effect of this variation on the turbulence budgets is highlighted by comparison against corresponding results with constant fluid properties, as it has been mostly assumed in existing DNS or LES studies on high Prandtl number flow in literature [1, 2].

GOVERNING EQUATIONS AND NUMERICAL SETUP

The present DNS solved the conservation equations of mass, momentum, and energy, generally written in non-dimensional representation as

$$\frac{\partial \varrho^*}{\partial t} + \nabla \cdot \left(\varrho^* \mathbf{U}^+\right) = 0 \tag{1}$$

$$\frac{\partial \varrho^* \mathbf{U}^+}{\partial t} + \nabla \cdot \left(\varrho^* \mathbf{U}^+ \, \mathbf{U}^+\right) = -\nabla P^+ + \nabla \cdot \left[\frac{\mu^*}{Re_\tau}\left(2\,\underline{S} - \frac{2}{3}\,tr(\underline{S})\,\underline{\mathbf{I}}\right)\right] + \mathbf{f}_w \tag{2}$$

$$\frac{\partial \chi^+}{\partial t} + \nabla \cdot \left(\mathbf{U}^+ \, \chi^+\right) - \chi^+ \nabla \cdot \mathbf{U}^+ = \frac{1}{\varrho^* Re_\tau Pr_w} \nabla \cdot \left(\frac{\lambda^*}{c_p^*} \nabla \chi^+\right) + f_\chi, \tag{3}$$

respectively, using the pipe diameter D, the wall friction velocity $w_\tau = (\tau_w/\varrho_w)^{1/2}$, and friction enthalpy $h_\tau = \langle q_w \rangle / \varrho_w w_\tau$ as reference scales. $\langle q_w \rangle$ represents the imposed constant average wall heat flux. $\mathbf{U}^+ = \mathbf{U}/w_\tau = (u^+, v^+, w^+)^T$ and $\chi^+ = (h_w - h)/h_\tau$ represent the non-dimensional velocity vector in cylindrical coordinates and enthalpy difference to the wall value, respectively. The asterisked material properties always refer to the corresponding wall values. $Re_\tau = \rho_w w_\tau D/\mu_w$ and $Pr_w = \mu_w c_{p,w}/\lambda_w$ denote the Reynolds and Prandtl number based on wall conditions, respectively. The terms $\mathbf{f}_w = 4\,\mathbf{e}_z$ and $f_\chi = w^+/\dot{m}^*$ with $\dot{m}^* = \dot{m}/D^2\pi\varrho_w w_\tau$ arise from axial periodicity.

Figure 1 shows the computational domain. No-slip boundary conditions are assumed for the velocity, $\mathbf{U}^+ = 0$, and isothermal boundary conditions are imposed for the instantaneous enthalpy difference, $\chi^+ = 0$, at the wall. The near wall resolution of the DNS grid is $\Delta r^+ = 0.05$, $R^+\Delta\varphi = 1.17$, and $\Delta z^+ = 0.90$ wall units in the radial, azimuthal, and axial direction, respectively.

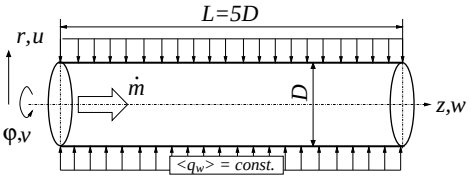

Figure 1: Computational domain

RESULTS

The investigated fully developed pipe flow is specified by the Reynolds number $Re_\tau = 380$ and the molecular Prandtl number $Pr_w = 56$, based on the average wall temperature $\langle T_w \rangle = 386.0K$. The uniform wall heat flux is assumed $\langle q_w \rangle = 1.6 \times 10^4 W/m^2$. The results for the variable and constant fluid properties are always referred to as "VFP" and "CFP", respectively.

The variation of the material properties of the considered oil relative to the wall values is shown in Figure 2(a). The dynamic viscosity quantitatively varies strongest, while the changes in density and thermal conductivity are negligibly small. The viscosity induced decrease of the local Reynolds number leads to a consistently strong dampening of the turbulent fluctuations of the radial and azimuthal velocity components, while the peak of the axial component is rather increased and shifted towards the center, as shown in Figure 3. The thermal fluctuations $\langle \chi'^{+2} \rangle^{1/2}$ are strongly enhanced due to the viscosity induced increase in the local molecular Prandtl number. This enhancement still do not compensate the reduction of the radial velocity fluctuations u'^+. The resulting lower turbulent flux component $\langle u'^+ \chi'^+ \rangle$ near the wall effectively leads to a significantly higher bulk-to-wall difference of the enthalpy for VFP, as seen from Figure 2(b), which indicates a markedly decreased global heat transfer coefficient. Accordingly, the Nusselt number drops from $Nu_{CFP} = 98.4$ to $Nu_{VFP} = 76.5$. The effect of the reduced turbulent flux con-

tribution due to the dampened radial velocity u'^+ is, however, not equivalently seen in the momentum transfer. Different from the almost uniform thermal conductivity, the strongly increasing molecular viscosity largely covers the increase in the laminar momentum flux component $\tau_{lam} = -\mu^* \frac{\partial \langle w^+ \rangle}{\partial r^*}$, as the turbulent component decreases in the budget of the total shear stress. This effectively keeps the average axial velocity for VFP very close to the profile for CFP near the wall, so that the finally obtained wall friction coefficient only marginally changes from $C_{f,CFP} = 0.0093$ to $C_{f,VFP} = 0.0091$.

The different trends observed for VFP in the velocity fluctuations are clearly reflected by the turbulence budgets in Figure 4. Starting out consistently lower near the wall, the production $P_{zz} = -\langle u'^+ w'^+ \rangle \frac{\partial \langle w^+ \rangle}{\partial r^*}$ for VFP notably exceeds the value for CFP in the inner region beyond $y^+ \approx 20$, which explains the occurrence of the peak of the axial fluctuation $\langle w'^{+2} \rangle^{1/2}$ at this position seen in Figure 3. At the same time the redistribution of turbulence energy from $\langle w'^+ w'^+ \rangle$ to $\langle u'^+ u'^+ \rangle$ is less pronounced for VFP, as indicated by the lower velocity-pressure gradient interaction term $\Pi_{rr} = -\langle 2u'^+ \frac{\partial p'^+}{\partial r^*} \rangle$ up to $y^+ \approx 60$, which effectively leads to more anisotropic fluctuating motion in this turbulent inner region. The shift and increase in the thermal fluctuations follows from the budgets of the variance $\langle \chi'^2 \rangle$ in Figure 5, where the peak production, $P_{\chi\chi} = -\langle u'^+ \chi'^+ \rangle \frac{\partial \langle \chi^+ \rangle}{\partial r^*}$ is moved radially further inside for VFP. On the other hand, the production term for the turbulent heat flux $P_{u\chi} = -\langle u'^+ u'^+ \rangle \frac{\partial \langle \chi^+ \rangle}{\partial r^*}$ consistently remains well below the values for CFP, reflecting again the different trends in $\langle u'^{+2} \rangle^{1/2}$ and $\langle \chi'^{+2} \rangle^{1/2}$ for VFP.

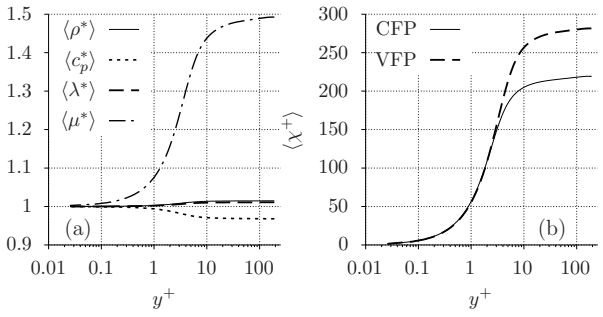

Figure 2: (a) average fluid properties, (b) average enthalpy difference (b) vs. wall distance y^+

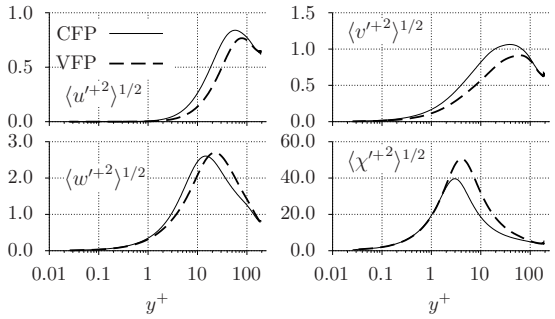

Figure 3: Fluctuations of velocity, and enthalpy vs. y^+

CONCLUSIONS

The different trends in the local Reynolds and Prandtl numbers distance to the heated wall give rise to different tendencies in the turbulent fluctuations. The strong dampening of the radial velocity essentially determines the significant reduction in heat transfer rate seen for the variable property case. The increase in thermal fluctuations appears as not sufficient to compensate for the deficit in turbulent convective mixing. The observed differences in the production and redistribution of the turbulence budgets counteract the general tendency towards a more isotropic fluctuating motion away from the wall.

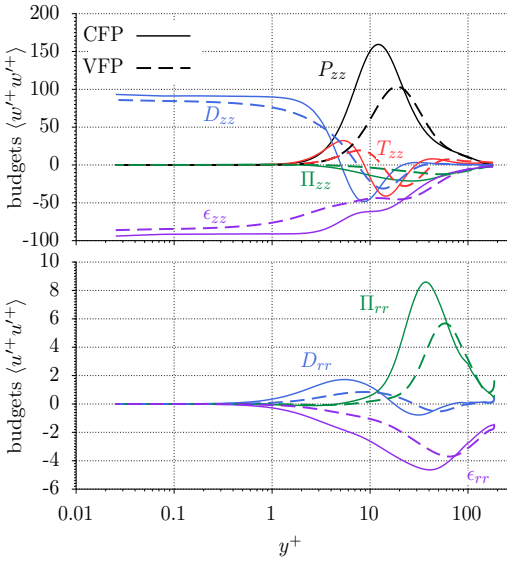

Figure 4: Budgets of $\langle w'^+ w'^+ \rangle$ and $\langle u'^+ u'^+ \rangle$

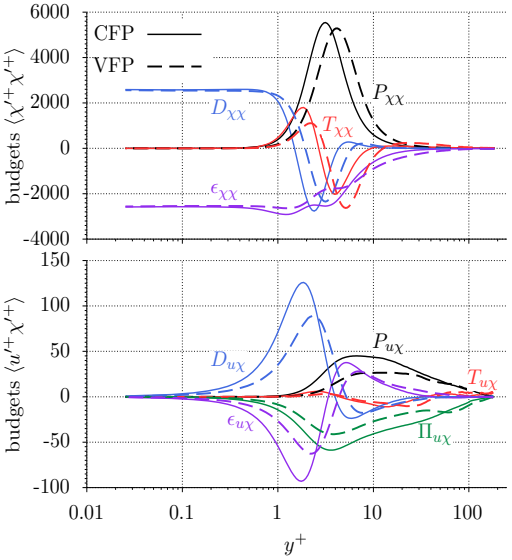

Figure 5: Budgets of $\langle \chi'^+ \chi'^+ \rangle$ and $\langle u'^+ \chi'^+ \rangle$

REFERENCES

[1]Kawamura, H., Ohsaka, K., Abe, H. and Yamamoto, K.: DNS of turbulent heat transfer in channel flow with low to medium-high Prandtl number fluid, *Int. J. Heat Mass Trans.*,**19**, 482–491 (1998).

[2]Schwertfirm, F. and Manhart, M.: DNS of passive scalar transport in turbulent channel flow at high Schmidt numbers, *Int. J. Heat Fluid Flow*,**28**, 1204–1214, (2007).

WORKSHOP
Direct and Large-Eddy Simulation 13
October 26$^{\text{th}}$-29$^{\text{th}}$ 2022, Udine, Italy

TURBULENCE CHARACTERISTICS OF HELICAL PIPE FLOWS

V. Lupi[1], **R. Örlü**[1], **P. Schlatter**[1]
[1] FLOW/SimEx, Engineering Mechanics
KTH Royal Institute of Technology, Sweden
lupi@mech.kth.se, ramis@mech.kth.se, pschlatt@mech.kth.se

INTRODUCTION

The flow in straight pipes has been studied since the 19^{th} century and it is regarded as one of the *canonical* flows. As soon as a non-zero curvature is introduced in the geometry, the flow is not axisymmetric anymore, whereas a planar symmetry still exists. This is the case of the flow in a toroidal pipe, symmetric with respect to the equatorial plane. Moreover, because of the curvature, a secondary motion of Prandtl's first kind is established. This secondary motion is present for any non-zero curvature [1] and it has the effect of increasing the cross-plane mixing and the heat transfer. Furthermore, if the pipe has non-zero torsion, *i.e.* its centerline is not a planar curve, then any kind of symmetry of the flow is lost, as in the case of the flow in a helical pipe.
Helical pipe flows are ubiquitous in a multitude of industrial applications, and they represent a more realistic counterpart of toroidal pipe flows, which, on the other hand, are relevant for studying the separate effect of curvature on the flow. The parameters governing the flow are the curvature δ, the torsion τ and the bulk Reynolds number Re_b, based on the bulk velocity, the diameter and the viscosity. The non-dimensional geometrical parameters are defined as follows

$$\delta = \frac{R_c\, R_p}{R_c^2 + p_s^2}, \quad \tau = \frac{p_s\, R_p}{R_c^2 + p_s^2}, \tag{1}$$

where R_p, R_c and p_s are the quantities shown in Figure 1.
To the best of the authors' knowledge, there are no studies on turbulent structures and spectra in helical pipe flows, and the only direct numerical simulations of turbulent helical pipe flows present in the literature are those performed by Hüttl & Friedrich [3], where only low-order turbulence statistics were investigated. The present work aims at studying the characteristics of turbulence in helical pipes from a modern perspective at sufficiently high Reynolds number.

NUMERICAL SETUP

Direct numerical simulations (DNS) of the incompressible flow of a Newtonian viscous fluid in a helical pipe are performed using the spectral element code `nek5000` [2]. The mesh resolution is the one typically used in DNS. The flow is assumed to be homogeneous in the streamwise direction and, therefore, cyclic boundary conditions are applied along this direction. No-slip boundary conditions are imposed at the pipe wall. In the work by Hüttl & Friedrich [3], the flow is driven by a mean streamwise pressure gradient, whereas in the present investigation a time-dependent volume force is imposed in the streamwise direction to keep the mass flux constant in time. The volume force varies across the cross-section because of the curved geometry. Since it has to reproduce the effect of the mean pressure gradient $\Delta P/\Delta s$, its integral along the streamwise direction needs to be of the form $C_s \Delta s$, where C_s is a constant. This can be accomplished by prescribing a volume force $\mathbf{f} = F/h_s\, \mathbf{e}_s$, where F is the constant forcing amplitude and h_s is the Lamé coefficient for the streamwise coordinate, accounting for the distribution of the volume force on the cross-section of the pipe.

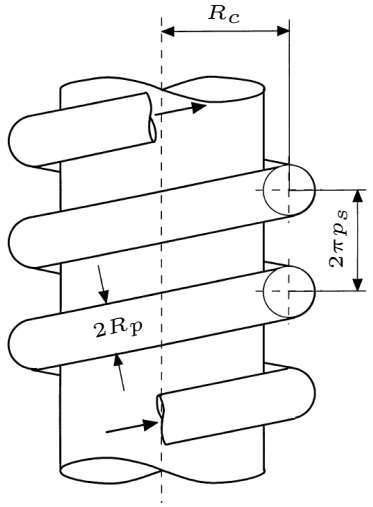

Figure 1: Sketch of the considered geometry, adapted from Hüttl & Friedrich [3].

VALIDATION

As a first validation step, a direct numerical simulation for $Re_b = 5613$, $\delta = 0.1$, $\tau = 0.11$ is performed, corresponding to $Re_\tau \approx 230$. The flow is barely turbulent, as it can be seen looking at the isosurfaces of the velocity vector magnitude, shown in Figure 2. The obtained flow statistics are validated against those by Hüttl & Friedrich [3]. Figure 3 shows the comparison for the mean streamwise velocity u_s and the turbulent kinetic energy, expressed in viscous units, along the line connecting the innermost and the outermost points. The former is in good agreement with the reference data, whereas, for the latter, a distinct pronounced peak is observed close to the outer wall ($r = 1$), which is not clearly evident in the data from Hüttl &

Friedrich [3]. The absence of the peak in the data from Hüttl & Friedrich [3] is thought to be attributed to either a lack of resolution close to the wall, or insufficient transient time that prevented the build-up of near-wall turbulence. Using these comparisons, we can conclude that our setup is indeed correct, and that there are some shortcomings of the literature data [3] that require re-analysis.

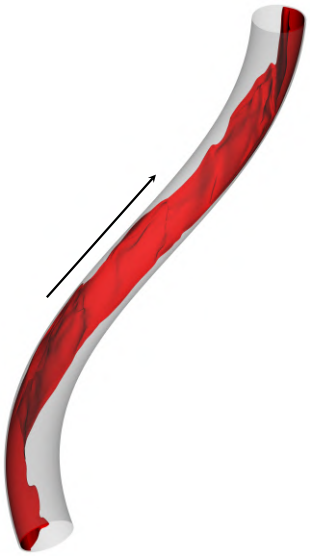

Figure 2: Isosurfaces of the velocity vector magnitude for $|\mathbf{U}| = 1.3$ at $Re_b = 5613$, $\delta = 0.1$, $\tau = 0.11$, corresponding to $Re_\tau \approx 230$. The flow is barely turbulent. The arrow indicates the flow direction.

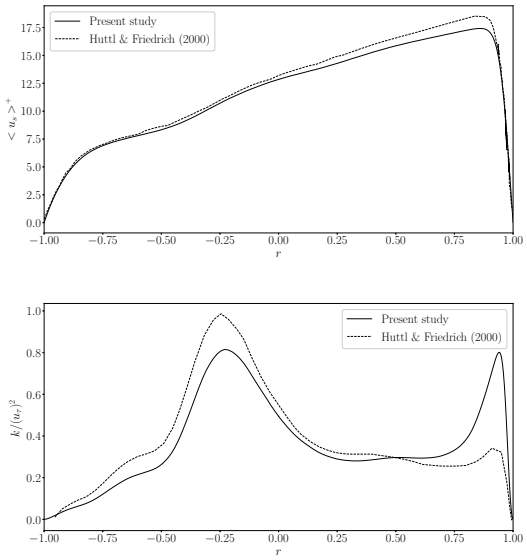

Figure 3: Comparison of the present results with data from Hüttl & Friedrich [3] along the line connecting the innermost and the outermost points: (top) mean streamwise velocity, (bottom) turbulent kinetic energy. The quantities are expressed in viscous units.

RESULTS

Direct numerical simulations for $Re_b = 11700$, $\delta = 0.1$ and various values of the torsion are performed to gain a better understanding of the effect of this parameter on this kind of flow. As it can be observed in Figure 4, the flow is fully turbulent in this case. To the best of the authors' knowledge, there are no studies in the literature involving DNS of helical pipe flows for such Reynolds number. Therefore, the present study will provide a reference database for future studies. Moreover, no previous work analyzes the coherent structures arising in a fully turbulent helical pipe flow. The comparison with the structures found by Noorani & Schlatter [4] for a toroidal pipe flow will provide a clearer picture of how turbulence is modified when non-zero torsion is introduced. Toroidal flows are susceptible to a phenomenon called "swirl switching" and it is unclear whether a similar process appears also in helical flows. To this end, spectral modal decomposition techniques will be employed. A more quantitative description of the size of these structures can be gained by computing spatial spectra of the velocity fields. This will provide information about the largest scales in the flow and their location in the pipe cross-section. Similarly, convection speed in the different parts of the flow provides relevant information regarding the spatial development of helical pipe flows.

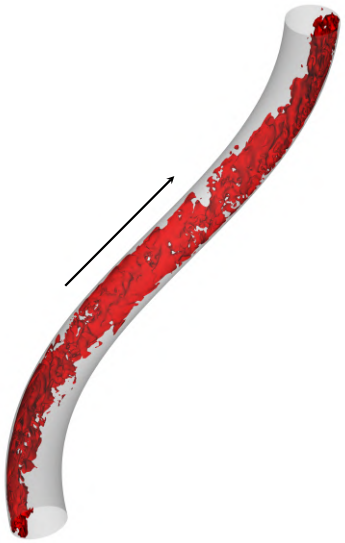

Figure 4: Isosurfaces of the velocity vector magnitude for $|\mathbf{U}| = 1.3$ at $Re_b = 11700$, $\delta = 0.1$, $\tau = 0.1$, corresponding to $Re_\tau \approx 410$. Small-scale turbulence is visible. The arrow indicates the flow direction.

REFERENCES

[1]Canton, J., Örlü R. and Schlatter, P. : Characterisation of the steady, laminar incompressible flow in toroidal pipes covering the entire curvature range, *Int. J. Heat Fluid Flow*, **66**, 95–107 (2017).

[2]Fischer, P. F., Lottes, J. W. and Kerkemeier, S. G. : Nek5000 web page, `https://nek5000.mcs.anl.gov` (accessed: 12 May 2022)

[3]Hüttl, T. J. and Friedrich, R. : Influence of curvature and torsion on turbulent flow in helically coiled pipes, *Int. J. Heat Fluid Flow*, **21** (3), 345–353 (2000).

[4]Noorani, A. and Schlatter, P. : Swirl-switching phenomenon in turbulent flow through toroidal pipes, *Int. J. Heat Fluid Flow*, **61**, 108–116 (2016).

Session: Multiphase flows

Thursday, October 27, 2022

15:20 – 16:20

WORKSHOP
Direct and Large-Eddy Simulation 13
October 26th-29th 2022, Udine, Italy

DRAG REDUCTION IN TURBULENT WALL-BOUNDED FLOWS OF REALISTIC POLYMER SOLUTIONS

F. Serafini[1], F. Battista[1], P. Gualtieri[1], C.M. Casciola[1]
[1] Department of Mechanical and Aerospace Engineering
Sapienza, University of Rome, Italy
francesco.serafini@uniroma1.it

Tom's effect, namely the drag-reducing capability of polymers in turbulence, is debated since its discovery in the 40s [1, 2]. Viscoelastic models (e.g FENE-P, finitely extensible nonlinear elastic model with Peterlin's approximation) achieve drag reduction in numerical simulations of prototypal flows [3, 4]. These models require unrealistically large concentrations to obtain drag reduction, well beyond the model limit of validity. Furthermore, many laboratory-scale experiments are performed at Weissenberg numbers unreachable by the viscoelastic models [5]. The adoption of a Lagrangian description of the polymer population, alongside a proper representation of its feedback effect on the turbulent flow field allows avoiding the use of the viscoelastic constitutive models with all their related shortcomings.

The system of dimensionless equations describing the polymer solution

$$\begin{aligned}
\boldsymbol{\nabla}\cdot\boldsymbol{u} &= 0 \\
\frac{\partial \boldsymbol{u}}{\partial t} + \boldsymbol{\nabla}\cdot(\boldsymbol{u}\otimes\boldsymbol{u}) &= -\boldsymbol{\nabla}p + \frac{1}{Re}\boldsymbol{\nabla}^2\boldsymbol{u} + \boldsymbol{F} \\
\frac{d\boldsymbol{x}_c^{(j)}}{dt} &= \frac{1}{2}\left(\check{\boldsymbol{u}}_1^{(j)} + \check{\boldsymbol{u}}_2^{(j)}\right) + \frac{1}{2}\sqrt{\frac{s^2}{3\mathrm{Wi}}}\left(\boldsymbol{\xi}_1^{(j)} + \boldsymbol{\xi}_2^{(j)}\right) \\
\frac{d\boldsymbol{r}^{(j)}}{dt} &= \check{\boldsymbol{u}}_2^{(j)} - \check{\boldsymbol{u}}_1^{(j)} - \frac{f^{(j)}}{\mathrm{Wi}}\boldsymbol{r}^{(j)} + \sqrt{\frac{s^2}{3\mathrm{Wi}}}\left(\boldsymbol{\xi}_2^{(j)} - \boldsymbol{\xi}_1^{(j)}\right)
\end{aligned} \tag{1}$$

is made dimensionless with the pipe radius ℓ_0^*, the kinematic viscosity ν^*, and the bulk velocity U_b^* of the reference Newtonian flow. In eq. 1, $\boldsymbol{u}(\boldsymbol{x})$ is the fluid velocity, $p(\boldsymbol{x})$ the hydrodynamic pressure, $\boldsymbol{F}(\boldsymbol{x})$ is the polymers feedback the Newtonian solvent, and Re is the Reynolds number of the reference Newtonian case. The evolution of the polymer dumbbells is written in term of the chain centre $\boldsymbol{x}_c^{(j)} = (\boldsymbol{x}_1^{(j)} + \boldsymbol{x}_2^{(j)})/2$ and the end-to-end vector $\boldsymbol{r}^{(j)} = \boldsymbol{x}_2^{(j)} - \boldsymbol{x}_1^{(j)}$ of the j-th dumbbell. $\boldsymbol{\xi}_{1/2}^{(j)}$ are white noise terms that set the equilibrium extension, s, of the chain, and Wi is the Weissenberg number, ratio of polymer relaxation time τ_p^* to fluid time scale ℓ_0^*/U_b^*.

The n-th bead ($n = 1, 2$) of the j-th dumbbell and the fluid exchange the friction force proportional to the relative velocity $\boldsymbol{D}_n^{(j)} = \gamma(\check{\boldsymbol{u}}_n^{(j)} - \boldsymbol{v}_n^{(j)})$, where γ is the friction coefficient, $\boldsymbol{v}_n^{(j)}$ the velocity of the bead, and $\check{\boldsymbol{u}}_n^{(j)}$ the fluid velocity at the position of the bead.

Given the disparity between polymer size and fluid scales, the polymer forcing appears to the flow as a sum of Dirac delta functions.

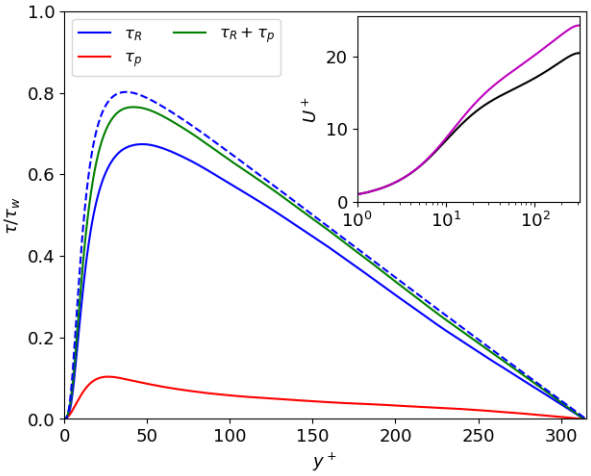

Figure 1: Radial profiles of Reynolds stress and polymer stress, compared to the Newtonian Reynolds stress (dashed line refers to the Newtonian Reynolds stress). Inset: mean velocity profile of the polymer solution (purple) compared to the Newtonian reference case (black).

$$\boldsymbol{F} = -\sum_{j=1}^{N_p}\left[\boldsymbol{D}_1^{(j)}\delta(\boldsymbol{x} - \boldsymbol{x}_1^{(j)}) + \boldsymbol{D}_2^{(j)}\delta(\boldsymbol{x} - \boldsymbol{x}_2^{(j)})\right] \tag{2}$$

The singular force field $\boldsymbol{F}$ displayed in eq. 2 is regularised on a physical base using the ERPP method [6, 7].

The addition of polymers reduces the Reynolds stress, although the drag-reducing effect is mitigated by the presence of a polymer extra-stress. However, the sum of Reynolds and polymer stress is lower than the Newtonian Reynolds stress both in the buffer and in the log-layer, thus drag reduction occurs. According to the previous observation the radial profile of mean axial velocity (displayed in fig. 1) departures from the Newtonian case since the buffer layer, and its slope is increased both in the buffer and in the logarithmic layer, where the drag-reducing effect takes place. Overall the increase in flow rate is 16 %, corresponding to a drag reduction of 26 %,

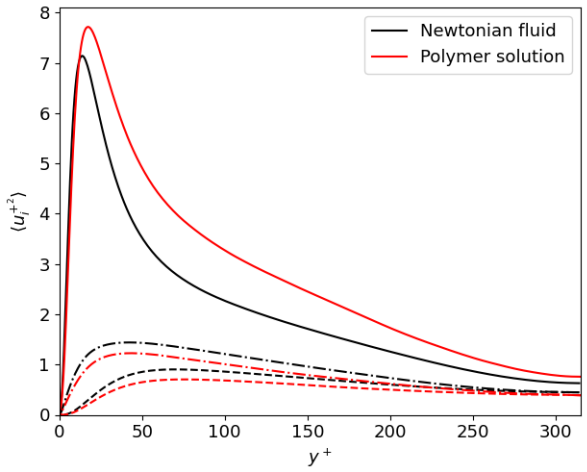

Figure 2: Radial profiles of root mean square velocity fluctuations: comparison between Newtonian and polymeric case. Solid line, $u_z^{'2}$; Dashed line, $u_r^{'2}$; Dot-dashed line, $u_\theta^{'2}$;

according to the definition of drag reduction,

$$DR = \frac{c_f^{(0)} - c_f^{(p)}}{c_f^{(0)}} = 1 - \left(\frac{Q_b^{(0)}}{Q_b^{(p)}} \right)^2 , \qquad (3)$$

where $c_f = 2\tau_w^*/(\rho^* U_b^{*2})$ is the friction coefficient and the superscripts $^{(0)}$ and $^{(p)}$ denote Newtonian and polymeric cases, respectively. Polymers induce an increase of velocity fluctuations in the streamwise direction, and a decrease in the radial and the tangential directions.

Figure 3 shows the coloured contour of the instantaneous axial velocity fluctuations to visualise low and high-speed streaks in a small portion of the pipe at $y^+ = 42$, where the maximum of the Reynolds stress occurs. Polymers, whose instantaneous configuration is reported in white lines, are prevalently aligned with the direction of the low-speed streaks since they come from the near-wall region where a large probability is associated with polymers aligned with the stream-wise direction. Polymer configuration is instead more isotropic far from the wall, thus the preferential orientation that occurs in the low-speed streaks is lost in the high-speed streaks.

During the oral presentation, Direct Numerical Simulations data of a realistic solution of DNA macromolecules fully coupled to the Newtonian fluid will be discussed, providing methodological details and a physical explanation of the drag reduction mechanism.

*

References

[1] P. S. Virk, "Drag reduction fundamentals," *AIChE Journal*, vol. 21, no. 4, pp. 625–656, 1975.

[2] B. Toms, "On the early experiments on drag reduction by polymers," *The Physics of Fluids*, vol. 20, no. 10, pp. S3–S5, 1977.

[3] E. De Angelis, C. Casciola, and R. Piva, "Dns of wall turbulence: dilute polymers and self-sustaining mechanisms," *Computers & fluids*, vol. 31, no. 4-7, pp. 495–507, 2002.

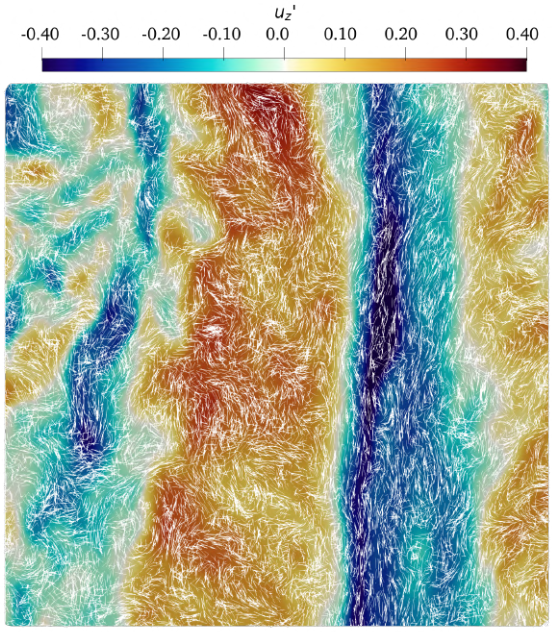

Figure 3: Instantaneous axial velocity fluctuations (coloured contour) and polymer configuration (while lines) in the buffer layer.

[4] R. Sureshkumar, A. N. Beris, and R. A. Handler, "Direct numerical simulation of the turbulent channel flow of a polymer solution," *Physics of Fluids*, vol. 9, no. 3, pp. 743–755, 1997.

[5] H. Choi, S. Lim, P.-Y. Lai, and C. Chan, "Turbulent drag reduction and degradation of dna," *Physical Review Letters*, vol. 89, no. 8, p. 088302, 2002.

[6] P. Gualtieri, F. Picano, G. Sardina, and C. M. Casciola, "Exact regularized point particle method for multiphase flows in the two-way coupling regime," *Journal of Fluid Mechanics*, vol. 773, pp. 520–561, 2015.

[7] F. Battista, J.-P. Mollicone, P. Gualtieri, R. Messina, and C. M. Casciola, "Exact regularised point particle (erpp) method for particle-laden wall-bounded flows in the two-way coupling regime," *Journal of Fluid Mechanics*, vol. 878, pp. 420–444, 2019.

WORKSHOP
Direct and Large-Eddy Simulation 13
October 26th-29th 2022, Udine, Italy

COLLISION STATISTICS OF CLOUD DROPLETS IN HOMOGENEOUS ISOTROPIC TURBULENCE CONSIDERING LUBRICATION FORCES AND NON-CONTINUUM MOLECULAR EFFECTS

A. Ababaei, **A. Michel**, and **B. Rosa**
Institute of Meteorology and Water Management – National Research Institute, Poland
ahmad.ababaei@imgw.pl

ABSTRACT

Using a new computational approach the dynamics of inertial particles in homogeneous isotropic turbulence is investigated under one-way momentum coupling. The implementation combines Hybrid Direct Numerical Simulations (HDNS) [1] with the analytical solutions of two rigid spheres moving in an unbounded fluid [2]. Merging these two approaches [3] allows us to jointly represent two important effects usually neglected in the previous studies: (i) HDNS accurately captures the effect of many-body interactions among widely separated droplets, while (ii) the analytical solution for two interacting rigid spheres in low-Reynolds-number flows enables representing the lubrication effects. In the case of droplets interacting from distances comparable to the mean free path of air molecules non-continuum effects are taken into account [4]. This resutls in corrections applied to the lubrication forces. Concerning the velocity field seen by the particles, the algorithm switches from the flow solution in terms of HDNS to analytical formulae when the separation distance between particles becomes comparable to their average radius. Switching to the analytical solutions is made knowing that the standard HDNS is unable to correctly represent the short-range interactions since this method is based on the superposition of the Stokes solutions for a single sphere.

RESULTS

In order to account for AI among the droplets, three approaches are adopted to represent drag forces and the results are compared with the basic case where AI is neglected. These three cases are demonstrated in Figure 1. HDNS (red: first method) is employed to represent AI among droplets interacting from large separation distances. However, the accuracy in the drag predicted by HDNS begins to decline when the gap between pairs is smaller than their average radius (normalized gap less than 1), as obtained from the analytical solutions to the Stokes flow around two spheres in a viscous flow (blue: second method). For pairs interacting from such short distances the algorithm switches to the analytical solutions (second or third method) to take lubrication effects into account. When the gap between the pair is of the order of the mean free path of air molecules, non-continuum effects are taken into account (brown: third method). This results in a reduction in lubrication drag predicted based on continuum solutions.

The kinematics and the dynamics of collisions for a system

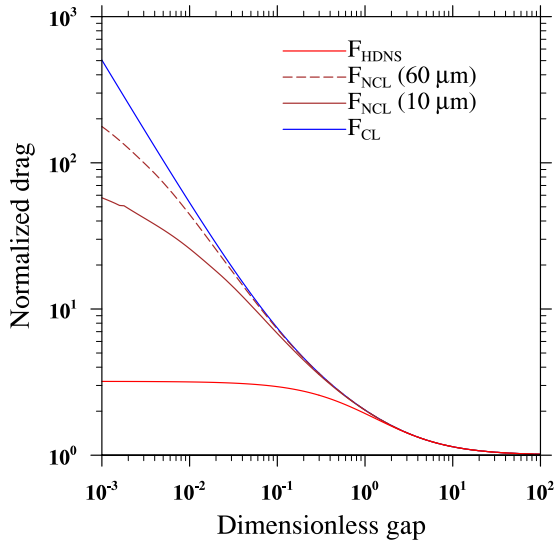

Figure 1: Changes in the normalized drag force with the size of the gap between two same-size droplets approaching along their line of centers described by different methods

of $N_p = 10^5$ non-settling (no gravity) particles interacting in a turbulent field with an average kinetic energy dissipation rate $\epsilon = 50$ cm^2/s^3 are presented in Figure 2. The changes are shown as a function of radii of the droplets with each curve representing a different approach to account for droplets AI. Figure 2(a) presents the average radial relative velocity (RRV) between all the pairs at contact, i.e. $r = R(= a_1 + a_2)$. In general, accounting for AI leads to a larger RRV. For small droplets (low inertia) lubrication effect notably enlarges RRV compared to the cases where there is no AI and the case where AI is handled purely by HDNS. When non-continuum lubrication (NCL) effects is additionally considered, this enhancement is not as large as that under continuum lubrication (CL). On the other hand, for larger droplets there is no significant difference between RRVs with continuum and non-continuum lubrication. Also, RRVs under HDNS show the highest values whereas the lowest RRVs are resulted from simulations performed with non-interacting droplets. The radial distribution function (RDF) values at contact are presented in Figure 2(b). In general, there is a substantial reduction in RDF once AI is

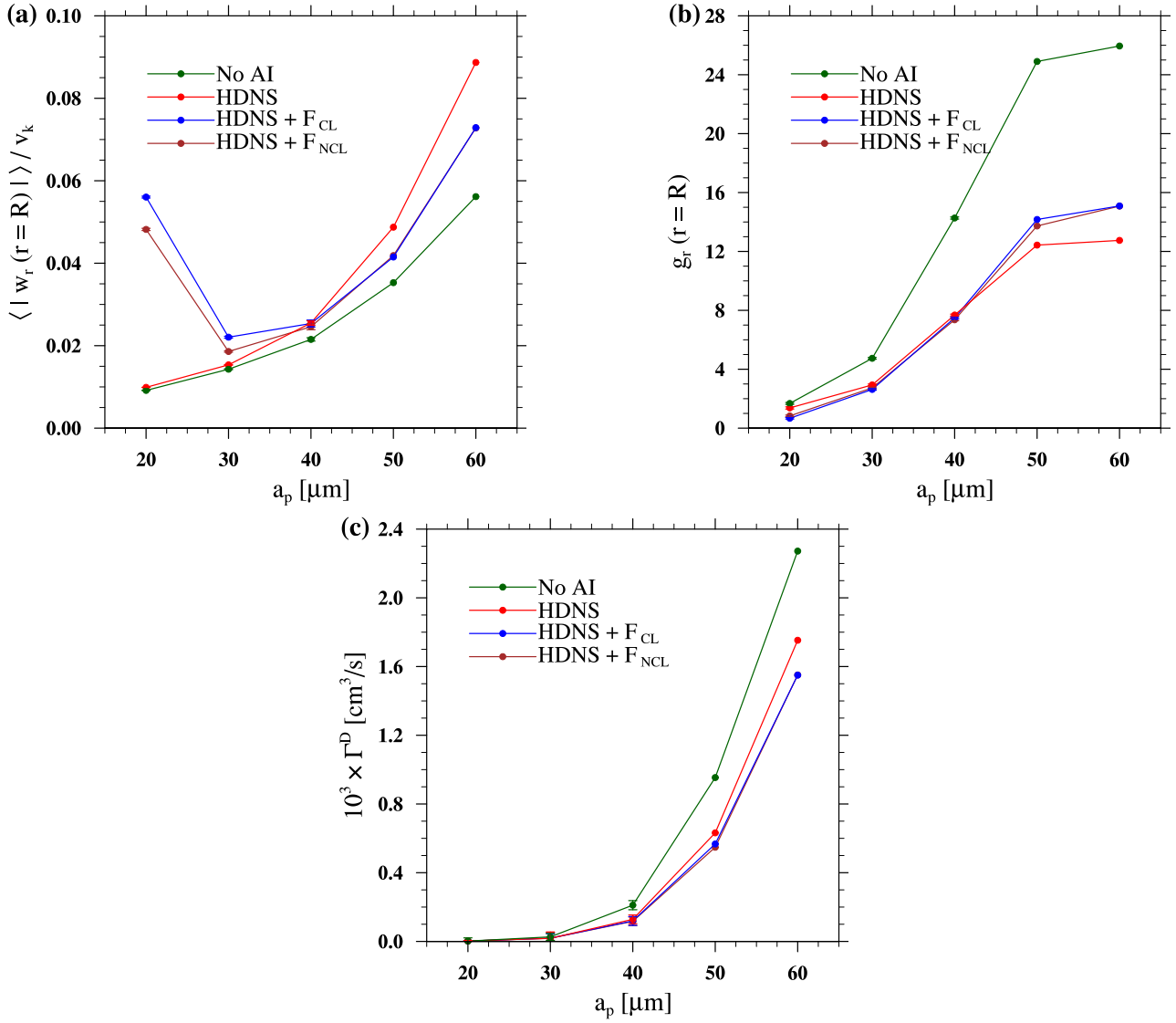

Figure 2: Variation in (a) at-contact radial relative velocity normalized by Kolmogorov velocity of the particle-free flow, (b) at-contact radial distribution function, and (c) dynamic collision kernel as a function of particle radius for $N_p = 10^5$ and $\epsilon = 50$ cm^2/s^3 using various approaches to handle AI: non-interacting, HDNS only (no lubrication effects), and HDNS with continuum and non-continuum lubrication effects

taken into account. Lubrication slightly augments RDFs for larger particles while no significant change is observed for low-inertia particles. Moreover, there is no noticeable difference between continuum and non-continuum lubrication representations. The dynamic collision kernel is shown in Figure 2(c). Generally, Γ^D decreases when AI is accounted for, mainly because of the large decline observed for RDFs (less clustering) especially at higher inertias. At lower inertias, there is almost no change in Γ^D, indicating that the enhanced RRV due to lubrication does not have a meaningful impact on collisions because RDF is small for such droplets. At high inertia, Γ^D is lowered when lubrication effects are additionally considered. This is caused by the decrease in RRVs as a results of large repulsive drags preventing pairs from appraching at large relative velocities, thereby hindering collisions.

ACKNOWLEDGMENT

We would like to thank the supports of NCN (grant no. 2018/30/Q/ST8/00341) as well as the ICM, University of Warsaw (grant no. G87-1145).

REFERENCES

[1]Ayala, O., Grabowski, W. W. and Wang, L.-P. : A hybrid approach for simulating turbulent collisions of hydrodynamically-interacting particles, *J. Comput. Phys.*, **225**, 51–73 (2007).

[2]Jeffrey, D. J. and Onishi, Y. : Calculation of the resistance and mobility functions for two unequal rigid spheres in low-Reynolds-number flow, *J. Fluid Mech.*, **139**, 261–290 (1984).

[3]Ababaei, A., Rosa, B., Pozorski, J. and Wang, L.-P. : On the effect of lubrication forces on the collision statistics of cloud droplets in homogeneous isotropic turbulence, *J. Fluid Mech.*, **918**, (2021).

[4]Sundararajakumar, R. R. and Koch, D. L. : Non-continuum lubrication flows between particles colliding in a gas, *J. Fluid Mech.*, **313**, 283–308 (1996).

WORKSHOP
Direct and Large-Eddy Simulation 13
October 26th-29th 2022, Udine, Italy

INFLUENCE OF MASS LOADING ON TURBULENT COLLISION COALESCENCE OF CLOUD DROPLETS

A. Michel[1], A. Ababaei[1] and B. Rosa[1]
[1] Institute of Meteorology and Water Management
Warsaw, Poland
antoine.michel@imgw.pl

INTRODUCTION

Droplet growth by collision-coalescence is a fundamental mechanism encountered in atmospheric processes and industrial applications. In recent years, numerical simulation has allowed to gather a significant amount of information about the influence of droplet inertia and turbulence on the collision statistics of mono and bidisperse suspensions of aerodynamically interacting droplets [1, 2, 3]. One drawback in these studies is that they do not account for coalescence. Thus the complex collective behaviour resulting from the temporally changing droplet size distribution is ignored. This topic was recently investigated by Chen *et al.* [4], who showed that higher turbulent intensity results in a broader droplet size distribution, therefore playing an important role to predict the onset of rainfall. To obtain more information about the influence of turbulence and aerodynamic interaction (AI) on the process of rain formation, we pursue these studies and analyse the influence of the liquid water content (mass loading) and the initial droplets diameter on the dynamics of the coalescence process and on the temporal evolution of the droplet size distribution.

GOVERNING EQUATIONS AND NUMERICAL SETUP

Carrier fluid

The turbulent flow in a periodic domain of dimension $(2\pi)^3$ is simulated by direct resolution of the continuity and momentum conservation equations using a pseudo-spectral method on a three dimensional uniform mesh. The fluid is treated as Newtonian, incompressible and isothermal. Statistical stationarity of the turbulent flow is ensured by supplying energy to the first two low wavenumbers modes. An extended description of the solver can be found in ref. [5]. For the simulations presented in the current document, the mesh is constituted of $N = 128$ cells in each direction and flow is characterized by the turbulent kinetic energy dissipation rate $\epsilon = 400$ cm^2/s^3 and kinematic viscosity $\nu = 0.17$ cm^2/s. These are typical values for moderate to strong convection in clouds. With these parameters, we obtained a Reynolds number based on Taylor microscale $Re_\lambda = 120$.

Dispersed phase

Small water droplets are represented in the model as rigid spheres. In the Lagrangian formalism, the position $\mathbf{x}_p$ and velocity, $\mathbf{u}_p$ of each particle are obtained by temporal integration of the particle equations of motion

$$\frac{\mathrm{d}\mathbf{x}_p}{\mathrm{d}t} = \mathbf{u}_p, \quad \frac{\mathrm{d}\mathbf{u}_p}{\mathrm{d}t} = -\frac{\mathbf{u}_p - \widetilde{\mathbf{u}} - \mathbf{u}_d}{\tau_p} + \mathbf{g}, \tag{1}$$

where $\widetilde{\mathbf{u}}$ is the turbulent background velocity at droplet location, $\mathbf{u}_d$ the disturbance velocity field due to the presence of neighbouring droplets, τ_p the particle relaxation time assuming Stokes drag and $\mathbf{g}$ is the gravity acceleration. The particles are characterized by $St = \tau_p/\tau_k$, the ratio of the particle relaxation time and Kolmogorov's time-scale, the smallest time-scale in the turbulent particle-free flow. To compute the disturbance velocity field, the improved superposition method (ISM) developed by Wang and Ayala is used [6]. This model assumes that the disturbance velocity felt by the kth droplet is the sum of Stokes disturbance velocity generated by all neighbouring droplets

$$\mathbf{u}_d^{(k)} = \sum_{m=1,\, m\neq k}^{N_p} \mathbf{u}_s(\mathbf{d}^{(mk)}; a^{(m)}, \mathbf{u}_p^{(m)} - \widetilde{\mathbf{u}}^{(m)} - \mathbf{u}_d^{(m)}), \tag{2}$$

$$\forall\, k = \{1, 2, ..., N_p\}\,. \tag{3}$$

This expression can be expanded into a linear system of dimension $3N_p$. It relates the disturbance velocity felt by each droplet to the distance between droplets pairs, $\mathbf{d}^{(mk)}$, and to the diameter and velocity of all other droplets. With ISM, lubrication or non continuum effects are not taken into account, but become important at short droplet separation distance. More information about the effect of lubrication forces on the collisions of cloud droplets was recently discussed by Ababaei *et al.* [3].

To investigate the influence of aerodynamic interactions on the dynamics of the coalescence process, simulations are conducted with two values of the liquid water content, 1 and 5 g/m^3. The droplets distribution is initially monodisperse, and characterized by their Stokes number. The properties of the dispersed phase are summarized in Table 1.

RESULTS

As a first step, we analyse the influence of aerodynamic interactions on the dynamics of the coalescence process. For this purpose, we introduce the percentage coalescence

$$P_c = 1 - N_p(t)/N_p(t=0), \tag{4}$$

Case	a (μm)	N_p (1 g/m^3)	N_p (5 g/m^3)
$St = 0.3$	21.8	92 172	460 860
$St = 0.5$	28.0	43 500	217 500
$St = 0.7$	33.0	26 572	132 860

Table 1: Initial value of Stokes number, radius, and number of droplets.

where $N_p(t)$ is the number of particles at current time. It is a measure of the fraction of droplets which have coalesced compared to the number of droplets initially present in the domain. Figure 1 shows the temporal evolution of the percentage coalescence as a function of time for initial Stokes number $St = 0.3$ and 0.7 and for two values of the liquid water content. There is a clear influence of these two factors on the dynamics of the coalescence process. First, coalescence is faster for high liquid water content, because the probability of collision increases with the droplet concentration. Second, the population initially composed of $St = 0.3$ droplets requires a longer time to achieve 50% coalescence than the one composed of $St = 0.7$ droplets. This can be explained by the influence of droplet inertia on their interaction with the turbulent background flow and on collisions. Droplets of small inertia ($St = 0.3$) closely follow the fluid motion and do not exhibit strong clustering and high radial relative velocities. As a consequence, they have smaller collision kernels compared to droplets of moderate inertia ($St = 0.7$). Figure 1 indicates that AI slow down the coalescence process for four considered cases.

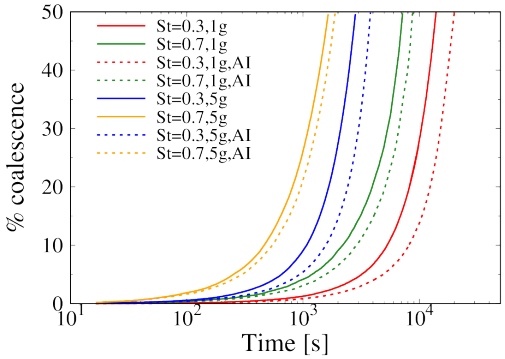

Figure 1: Evolution of the percentage coalescence as a function of time (in seconds) for different mass loadings and initial droplets Stokes numbers.

To gain more information about the influence of the dispersed phase on the coalescence process, we analyse the evolution of the droplet size distribution. For this purpose, we use different definitions of the average radius

$$a_{ij} = \left[\frac{\int a^i f(d) \mathrm{d}a}{\int a^j f(a) \mathrm{d}a} \right]^{\frac{1}{i-j}} \quad (5)$$

where $f(a)$ is the radius distribution function and i, j are positive integers. With this definition, a_{10} is the average radius representative of the largest number of droplets, a_{30} the volume average radius and a_{32} is Sauter equivalent radius, the radius of the equivalent sphere of same volume/surface ratio as the droplet distribution. High values of a_{32} are associated to a long tailed distribution. The value of these three radii as a function of the percentage coalescence is presented in figure 2. All definitions are initially equal to 1 because of the monodisperse distribution. In general, growth of a_{10} is slow, indicating that a large number of small size droplets remain in the domain even at 50% coalescence. The fast growth of a_{32}, however, indicates the broadening of the size distribution, similarly to what was reported by Chen *et al.*[4]. Interestingly, growth of a_{10} and a_{32} weakly depends on AI modelling for liquid water content 1 g/m^3. This suggests that long range collective interaction has a weak influence on the size of the particles created by coalescence. In contrast, for liquid water content 5 g/m^3, taking AI into account results in a slower growth of a_{10} and a faster of a_{32}. This trend indicates that aerodynamic interactions prevent the growth of the smallest droplets (hence a small d_{10}) but favour the formation of a small number of very large droplets.

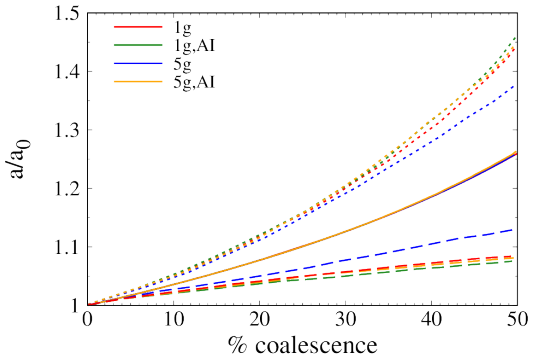

Figure 2: Evolution of the average radius a_{ij}, normalized by the initial radius, a_0 as a function of the percentage coalescence for initial $St = 0.3$. Dashed line, a_{30}; solid line, a_{10}; dotted line, a_{32}. The definition of a_ij is given by eq. 5.

REFERENCES

[1]Ayala O., Grabowski W.W. and Wang, L.P. : A hybrid approach for simulating turbulent collisions of hydrodynamically-interacting particles, *J. Comp. Phys.*, **225**, 51–73 (2007).

[2]Rosa, B., Parishani, H., Ayala, O. and Wang, L.P. : Bruno, L., Salvetti, M.V. and Ricciardelli, F. : Settling velocity of small inertial particles in homogeneous isotropic turbulence from high-resolution DNS *Int. J. Mult. Flow*, **83**,217–231 (2016).

[3]Ababaei, A. and B. Rosa, B. and Pozorski, J and Wang, L.P. : On the effect of lubrication forces on the collision statistics of cloud droplets in homogeneous isotropic turbulence, *J. Fluid. Mech.*, **918** (2021).

[4]Chen, S., Yau, M.K. and Bartello, P. : Turbulence Effects of Collision Efficiency and Broadening of Droplet Size Distribution in Cumulus Clouds, *J. Atmos. Sci.*, **75**, 203–217 (2018).

[5]Rosa, B., Parishani, H., Ayala, O. and Wang, L.P. : Effects of forcing time scale on the simulated turbulent flows and turbulent collision statistics of inertial particles, *Phys. Fluids*, **27**, 015105 (2015).

[6]Wang, L.P., Ayala, O. and Grabowski, W.W. : Improved Formulations of the Superposition Method, *J. Atmos. Sci.*, **62**, 1255–1266 (2005).

WORKSHOP
Direct and Large-Eddy Simulation 13
October 26th-29th 2022, Udine, Italy

TURBULENCE MODULATION BY SLENDER FLEXIBLE FIBERS IN CHANNEL FLOW

D. Di Giusto[1,2] and C. Marchioli[1,3]
[1] Department of Engineering and Architecture, University of Udine, Italy
[2] IUSTI, Aix-Marseille Université, France
[3] Department of Fluid Mechanics, CISM, Udine, Italy

Experimental evidence shows that even small loading of fibers dispersed in a turbulent flow produces drag reduction [1]. This phenomenon has been investigated in a number of previous numerical studies [2, 3], which were however focused on the effect produced by short fibers with length comparable to the smallest flow scale and aspect ratio up to $AR = 100$. In an effort to extend the range of aspect ratios investigated, in this work we examine numerically the modulation of turbulence produced by long flexible fibers in channel flow. The simulations are based on an Euler-Lagrangian approach, in which fibers are modelled as chains of constrained sub-Kolmogorov rods, as done in [4]. This approach is chosen as it allows to obtain a highly discretized description of the fibers even when their length spans several Kolmogorov scales. A novel algorithm is deployed in order to make the resolution of a dispersed system of constraint equations (representing the fibers) compatible with a state of the art, GPU-accelerated flow solver that is used for the direct numerical simulation of turbulence in the two-way coupling regime on HPC architectures. The bending stiffness of the fibers is also modelled, while collisions are neglected. Two-way coupling is accounted for using the ERPP method [5]. First, we validate experimentally the method for a single fiber in simple shear flow; then we implement the method by scaling it up to the full turbulent channel flow geometry, using a suitably-refined computational grid. We show how we are able to calculate the disturbance generated by the fibers on the surrounding flow, albeit at the price of a computational mesh (made of $1024 \times 512 \times 257$ grid-points in our simulations) that is over-refined as compared to the single-phase or one-way coupled counterpart at the same Reynolds number.

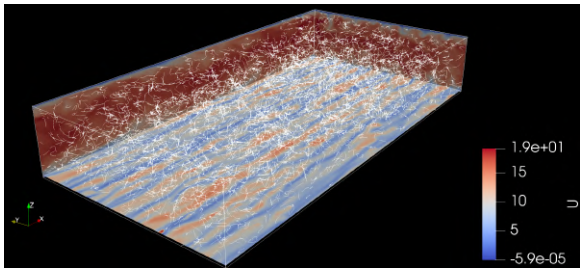

Figure 1: Visualization of the two-phase flow computational domain. Fibers are displayed in white color; flow sections are colored according to the streamwise fluid velocity magnitude.

In this way, reliable results are obtained for the stresses exerted by the particles on the flow, even in the dilute case. This would have not been possible had we applied the classical Particle In Cell method to complete the two-way coupling scheme. This method requires the presence of a large number of fibers all over the computational domain in order to obtain smooth Eulerian fields for the particle stresses, therefore making the dilute case, two-way coupled simulations hardly feasible [3, 6]. Results of fluid and fibers velocity statistics for friction Reynolds number of the flow Re=150 and fibers with Stokes number St=0.01 (nearly tracers) and 10 (inertial fibers) are presented, with special regard to the quantification of the turbulence modulation and its dependence on fiber inertia as well as aspect ratio. The volume fraction of the fibers is varied to simulate a suspension in both the dilute and semi-dilute regime, while considering fibers with length that spaces from the Kolmogorov scale to the inertial range of the turbulent flow.

REFERENCES

[1] R.C. Vaseleski and A.B. Metzner *Drag Reduction in the Turbulent Flow of Fiber Suspensions.* AlChE Journal, Vol. 20, 1974
[2] J. Paschkewitz, Y. Dubief, Y. Dimitropoulos, C. Shaqfeh, and P. Moin. *Numerical simulation of turbulent drag reduction using rigid fibres.* Journal of Fluid Mechanics, 518, 281-317, 2004
[3] Ze Wang and C. Xu and L. Zhao *Turbulence modulations and drag reduction by inertialess spheroids in turbulent channel flow.* Physics of Fluids, Vol. 33, 2021
[4] D. Dotto and C. Marchioli *Orientation, distribution, and deformation of inertial flexible fibers in turbulent channel flow.* Acta Mech., 230 597-621, 2019
[5] F. Battista, J. Mollicone, P. Gualtieri, R. Messina, and C. Casciola. *Exact regularised point particle (ERPP) method for particle-laden wall-bounded flows in the two-way coupling regime.* Journal of Fluid Mechanics, 878, 420-444, 2019
[6] J. J. J. Gillissen, and B. J. Boersma. *The stress generated by non-Brownian fibers in turbulent channel flow simulations.* Physics of Fluids, Vol. 19, 2007

Session: Aerodynamics/Aeroacoustics 1

Thursday, October 27, 2022

16:50 – 18:20

WORKSHOP
Direct and Large-Eddy Simulation 13
October 26th-29th 2022, Udine, Italy

AEROACOUSTIC SOURCE TERMS FROM TURBULENT FLOW THROUGH A 90° PIPE BEND PREDICTED BY LARGE-EDDY SIMULATION

J. Tieber[1], H. Steiner[1], P. Maurerlehner[2], S. Schoder[2], M.Kaltenbacher[2], G. Brenn[1]
[1] Institute of Fluid Mechanics and Heat Transfer
Graz University of Technology, Austria
helfried.steiner@tugraz.at
[2] Institute of Fundamentals and Theory in Electrical Engineering
Graz University of Technology, Austria
paul.maurerlehner@tugraz.at

INTRODUCTION

The large disparity of scales between the smallest relevant turbulent structures and the large acoustic wave lengths [1] makes a fully resolved Direct Numerical Simulation of both phenomena unfeasible for most technical applications, especially at low Mach numbers. In Computational Aeroacoustics (CAA) so-called hybrid methods allow for a separate computation of the incompressible turbulent flow field, providing acoustic source terms, and the Acoustic Simulation (AS) of the sound propagation.

The present study follows this approach using the Perturbed Convective Wave Equation (PCWE) [2] to predict the acoustic field inside a circular 90° pipe bend with relative curvature radius $R_m/D \approx 1$ at bulk Reynolds numbers $Re_B = Du_B/\nu = 5300$ and 12500. The incompressible flow field is computed using Large-Eddy Simulation (LES) to predict acoustic source terms as input into the AS. The unresolved subgrid scale fluxes are computed from a Boussinesq-type eddy viscosity model introduced as the Coherent Structure Model by [3].

The PCWE is based on a perturbation Ansatz, where the flow field variables are decomposed into a mean, a fluctuating incompressible, and an acoustic component, generally written as $\phi = \langle\phi\rangle + \phi^{\mathrm{ic}} + \phi^{\mathrm{a}}$. This finally yields a convective wave equation for the acoustic potential ψ^{a}, called PCWE and written as

$$\rho_0 \frac{D^2\psi^{\mathrm{a}}}{Dt^2} - \rho_0 c_0^2 \frac{\partial^2\psi^{\mathrm{a}}}{\partial x_j \partial x_j} = -\underbrace{\frac{Dp^{\mathrm{ic}}}{Dt}}_{\overline{Q}} = -\underbrace{\frac{\partial \overline{p}^{\mathrm{ic}}}{\partial t}}_{\overline{Q}_t} - \underbrace{\langle \overline{u}_i \rangle \frac{\partial \overline{p}^{\mathrm{ic}}}{\partial x_i}}_{\overline{Q}_c}, \quad (1)$$

providing the acoustic velocity $u_i^{\mathrm{a}} = -\partial\psi^{\mathrm{a}}/\partial x_i$ and pressure $p^{\mathrm{a}} = \rho_0 D\psi/Dt$. The source term on right-hand side of equation (1) is delivered by the LES.

SIMULATION SETUP

The investigated bend geometry with a relative curvature radius $R_m/D \approx 1$ is shown in figure 1. The operating fluid is air, assumed as a perfect gas.

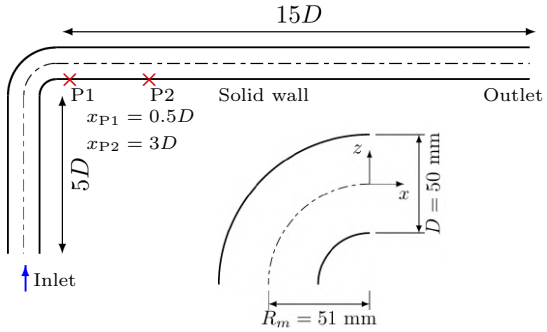

Figure 1: Upper subfigure: Computational domain with sensor positions P1 and P2. Bottom subfigure: Geometry of the pipe bend.

The LES equations were solved using a second order accurate finite volume method with an implicit first order accurate temporal discretization ($\Delta t = 10^{-5}$ s). At the inlet, an instantaneous inflow boundary condition (BC) was prescribed, obtained from a precursor-LES of fully developed pipe flow. An averaged pressure BC was applied at the outlet, and the no-slip BC was imposed at the solid walls. After statistical convergence was reached, acoustic source terms were exported on the AS mesh for a period of $t = 0.2$ s. The PCWE was solved using a finite element method, with a homogeneous von Neumann BC at the sound hard walls and adjacent Perfectly Matched Layer (PML) regions at the inlet and outlet to avoid reflections.

SIMULATION RESULTS

Flow field

Figure 2 shows LES results at $Re_B = 5300$ and 12500 compared against LES data and PIV measurements of Rütten et. al. [4] at $x = 1D$. Very good agreement is observed for the matching lower Reynolds number case.

As seen from the contours in figure 3, the flow detaches from the highly curved inner bend wall, producing a recirculation zone downstream of the bend exit, and a high-velocity region radially outside. A region of high turbulence kinetic energy extends near the reattachment point at $x_{\mathrm{RP}} = 0.7D$.

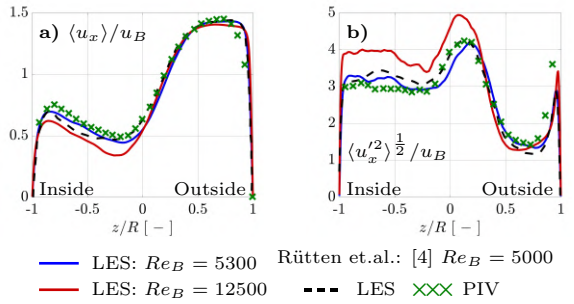

Figure 2: a) mean x-velocity and b) x-normal stresses.

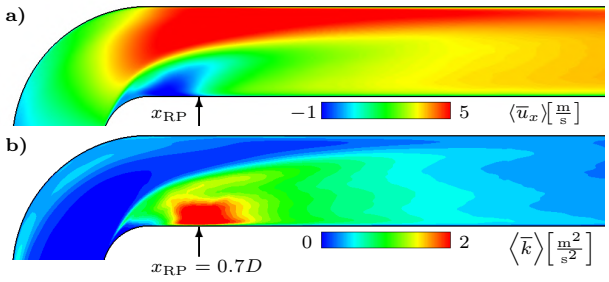

Figure 3: Contours of the a) mean $x-$velocity component $\overline{u}_x$ and b) the turbulent kinetic energy $\langle \overline{k} \rangle$ for $Re_B = 12500$.

Figure 4 shows contours of the instantaneous PCWE source term and its constitutive components as predicted from the LES. High values of both components are seen in the recirculation zone and in the highly sheared region. They are negatively correlated, especially on the high-velocity side of the shear layer, which effectively reduces the total term $\overline{Q}$. The highest total source terms are observed in the region near the reattachment point.

Figure 5 presents spectra of the PCWE source terms at two positions downstream of the bend near the radially outer and inner side, respectively. For the latter, located in the highly turbulent region inside the recirculation zone, the transient term is dominating, especially at higher frequencies. At the other position, located in the high axial velocity region, the amplitudes of the total PCWE source term is significantly smaller than its components, indicating mutual cancellation.

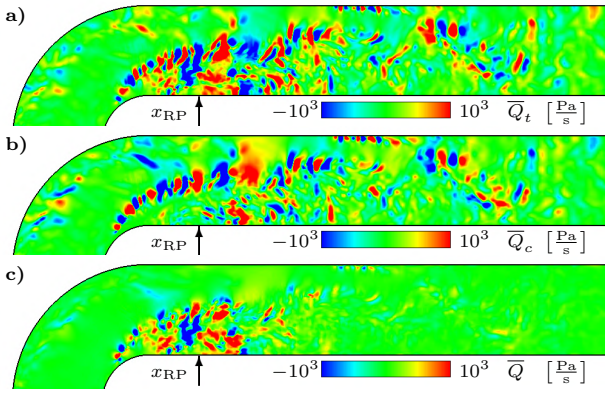

Figure 4: Contours of the a) transient, b) convective and c) total PCWE source term for $Re_B = 12500$.

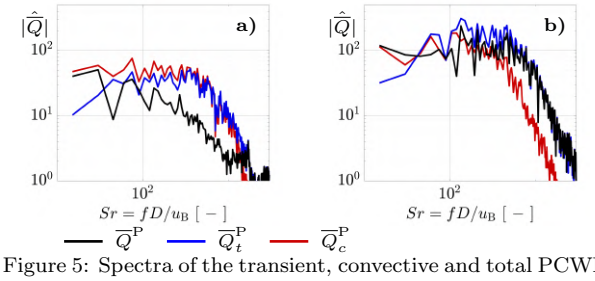

Figure 5: Spectra of the transient, convective and total PCWE source terms, at positions a) $z = 0.44D$ and b) $z = -0.44D$ at $x = 0.5D$ for $Re_B = 12500$.

Acoustic Simulation

Figure 6 shows spectral amplitudes of the AS predicted acoustic pressure together with LES predicted incompressible pressure amplitudes for $Re_B = 12500$. The collapse of the predictions with/without the convective component of the PCWE source term indicates the negligible effect of this component here. Overall the acoustic pressure p^a is significantly smaller than the incompressible pressure p^{ic}. At position P2 the amplitudes of the incompressible pressure are smaller in comparison to P1, while the acoustic pressure is fairly similar. The predicted sound pressure level is $SPL = 20 \log_{10}(p^a_{rms}/p_{ref}) \sim 25$ dB, where $p_{ref} = 2 \cdot 10^{-5}$ Pa.

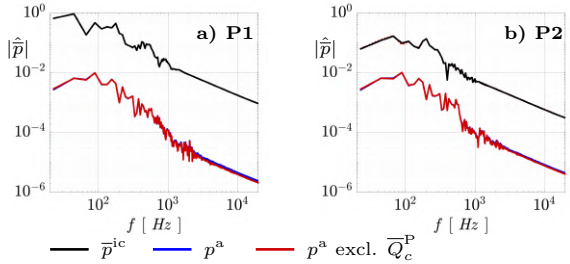

Figure 6: Pressure spectra from LES and AS at position a) P1 and b) P2, marked in figure 1 for $Re_B = 12500$.

CONCLUSIONS

A hybrid CAA approach with a PCWE based acoustic simulation was used to predict the internal flow-induced noise of the turbulent flow downstream of a 90° pipe bend. The applied LES method is proven as well-suited for supporting the acoustic PCWE simulation with instantaneous sources, such that the acoustic pressure field and the resulting sound pressure level are predicted reasonably well. The transient source term component was shown as clearly dominant, while the effect of the convective component appeared as negligible in the PCWE simulation.

REFERENCES

[1]Schoder, S. and Kaltenbacher, M.: Hybrid aeroacoustic computations: State of art and new achievements, Journal of Theoretical and Computational Acoustics, 27.04, 1950020, (2019).

[2]Schoder, S., Maurerlehner, P., Wurzinger, A., Hauser, A., Falk, S., Kniesburges, S., Döllinger, M. and Kaltenbacher M.: Aeroacoustic Sound Source Characterization of the Human Voice Production-Perturbed Convective Wave Equation, *Appl. Sci.*, 11, 2614, (2011).

[3]Kobayashi H. The subgrid-scale models based on coherent structures for rotating homogeneous turbulence and turbulent channel flow. *Phys. Fluids* 17, 045104, (2005).

[4]Rütten, F., Schröder, W. and Meinke, M.: Large-eddy simulation of low frequency oscillations of the Dean vortices in turbulent pipe bend flows. *Phys. Fluids* 17 (3) 035107, (2005).

WORKSHOP
Direct and Large-Eddy Simulation 13
October 26th-29th 2022, Udine, Italy

TRANSITION AND ACOUSTIC EXCITATION OF STENOTIC PIPE FLOWS AT DIFFERENT REYNOLDS NUMBERS

A. Abdelsamie[1,*], S.-R. Koh[2], G. Janiga[1], D. Thévenin[1]
[1] Lab. of Fluid Dynamics and Technical Flows (LSS/ISUT), University of Magdeburg "Otto von Guericke", Universitätsplatz 2, 39106 Magdeburg, Germany
[2] Forschungszentrum Jülich GmbH, Wilhelm-Johnen-Straße, 52425 Jülich, Germany
*abouelmagd.abdelsamie@ovgu.de

INTRODUCTION

A human respiratory system consists of phonation components that are coupled in a complex manner in order to ensure various vital functions, in particular voice generation. The interdisciplinary nature of the processes controlling sound generation complicates the analysis. Analytical studies are limited and can only be used to characterize the main acoustic sources in connection to various types of fluid motion. Numerical investigations of sound generation require an accurate simulation of the flow field with a proper representation of the respiratory pathways and process conditions in order to get the acoustic source terms. Furthermore, voice formation is closely related to the resonance of acoustic modes in and around the mouth cavity; in order to be able to model this properly, it is essential to identify first the sound sources excited within the vocal tract.

To better elucidate this complex process, the fundamental mechanisms in a biofluid flow mimicking such configurations have been first investigated based on a simplified stenotic pipe using high-resolution discretization methods [1, 2]. The variation in cross-section was regarded as critical to trigger flow transition. The geometry used in a previous experimental study [3] was applied to a numerical analysis in the Reynolds number range of Re=400–800 based on the pipe diameter [4]. Results from direct numerical simulation (DNS) reveal the development of flow instabilities as function of the selected Reynolds number. Later on, still based on DNS, a global linear stability analysis [5] showed that a symmetric flow becomes linearly unstable to an eigenmode when increasing Reynolds number. Over a critical value of Re, the instability triggers non-axisymmetric flow oscillations. Transition occurs in connection with the break-up of streamwise hairpin vortices generated by the jet downstream of the stenotic throat. Exchange processes are most intense at a turbulent spot where the sound generation is dominated by the dipole contribution on the surface [6]. On the other hand, the contribution of viscous shear stress is rapidly dissipated due to relaminarization further downstream [2]. Though already very interesting, these findings must be refined further to better understand the contribution of dipole and higher-order sources to acoustics in stenotic pipe flows.

NUMERICAL METHODS

The present work focuses on DNS using either a finite-difference or a lattice-Boltzmann formulation to solve for stenotic pipe flows at relevant Reynolds numbers in the range Re = 500–1800. The two in-house solvers are (1) DINO, providing a finite-difference solution of the incompressible Navier-Stokes equations (NSE), and (2) a lattice Boltzmann (LB) solver, providing a weakly-compressible solution. Proper Orthogonal Decomposition (POD) and spectral entropy S_d [7] are applied to analyze transition. A computational aeroacoustics (CAA) approach is then used to obtain the contribution of different noise sources by solving the Acoustic Perturbation Equations (APE) [8].

For the present study, the reference results are those obtained by the well-established DNS code DINO, first described in [9] and used since then for many DNS studies for a variety of configurations. DINO relies on a sixth-order central finite-difference scheme for spatial discretization and a fourth-order Runge-Kutta method for time integration. The code has been optimized for massively parallel High-Performance Computing (HPC) leading to an excellent scalability on various HPC systems [10]. Any complex geometry can be handled in DINO using a novel high-order directional ghost-cell immersed boundary method [11].

As an alternative, the LB method is used to solve the stenotic pipe flows in the weakly compressible regime. The single-relaxation-time (SRT) method has been selected. The Boltzmann equation with a Bhatnagar-Gross-Krook (BGK) approximation of the collision term is solved to get the fluid particle probability distribution functions (PPDFs) in a discretized form. The D3Q27 discretization scheme has been selected as set of lattice vector weights [12], with 27 direction in the three-dimensional flow field. The macroscopic variables are obtained from the moments of the PPDFs. The numerical approach has been validated in generic flow configurations [13] and later applied to bio-fluid mechanical problems such as the circulation of a brain fluid [14].

FLOW CONFIGURATION

Steady flows (i.e., non-pulsatile inflow) through both axisymmetric and eccentric stenosis models have been computed and analyzed. The baseline geometry is given in [2] and defined by a cosine function dependent on the axial coordinate x. The cross-section coordinates y and z are determined by using $S(x)$, specifying the shape of the stenosis by $S(x) = R[1 - s_0(1 + \cos(2\pi\, x/L))]$ where R is the radius of the

non-stenotic pipe, $s_0 = 0.25$ realizes the 75% area reduction, and $L = 4R$ is the length of the stenosis. When introducing now the eccentricity $E(x) = \varepsilon s_0[1 + \cos(2\pi\, x/L)]$, the y and z coordinates are defined by $y = S(x)\cos\theta + E(x)$ and $z = S(x)\sin\theta$ at the azimuthal angle θ along the yz-plane. The eccentric case offsets the stenosis axis by $0.1R$ ($\varepsilon = 0.2$) at $x/R = 0$. In Fig. 1 the cross-section profiles of the axisymmetric and the eccentric pipes are illustrated near the stenotic region. The inflow condition corresponds to a parabolic profile of the streamwise velocity component u. Based on the cross-sectional average velocity and the pipe diameter D=$2R$ at the inlet ($x = -8R$) the Reynolds number Re is 500, 1000, or 1800, for three different flow simulations. The computational domain extends up to the outflow boundary at $x = 40R$.

RESULTS

As preliminary results, two different cases obtained with DINO are first shown; the axisymmetric stenotic pipe at Re= 500 and at Re=1000. For both, the instantaneous vorticity magnitude is plotted in Fig. 2. This figure demonstrates that the critical Reynolds number is found between Re=500 and Re=1000 in this case. A more precise threshold can be quantified based on S_d [7], when results at intermediate Reynolds numbers are available. In Fig. 3 the flow fields at the three Reynolds numbers as obtained by LB are shown. Isocontours of $\lambda_2 = -0.001 c_S^2/R^2$ with the isothermal speed of sound c_S are plotted to identify vortical structures. When increasing the Reynolds number to 1800, flow transition occurs earlier in the streamwise direction. The instantaneous coherent structures reveal the development of velocity fluctuations and of vortices downstream of the stenotic throat.

At the conference, all simulation results and a detailed analysis will be presented.

REFERENCES

[1]Mallinger, F., Drikakis, D. : Instability in three-dimensional, unsteady, stenotic flows, *Int. J. Heat Fluid Fl.*, **23**(5):657–663 (2002).

[2]Varghese, S., Frankel, S., and Fischer, P. : Direct numerical simulation of stenotic flows. Part 1. steady flow, *J. Fluid Mech.*, **582**:253–280 (2007).

[3]Ahmed, S. A., Giddens, D. P. : Pulsatile poststenotic flow studies with Laser Doppler Anemometry, *J. Biomech.*, **17**(9):695–705 (1984).

[4]Sherwin, S. J., Blackburn, H. M. : Three-dimensional instabilities and transition of steady and pulsatile axisymmetric stenotic flows, *J. Fluid Mech.* **533**:297-–327 (2005).

[5]Samuelsson, J., Tammisola, O., and Juniper, M. P. : Breaking axisymmetry in stenotic flow lowers the critical transition Reynolds number, *Phys. Fluids*, **27**, 104103 (2015).

[6]Hu, Z., Morfey, C., and Sandham, N. : Sound radiation in turbulent channel flows, *J. Fluid Mech.*, **475**:269–302 (2003).

[7]Abdelsamie, A., Janiga, G., Thévenin, D.: Spectral entropy as a flow state indicator, *Int. J. Heat and Fluid Flow*, **68**:102–113 (2017).

[8]Ewert, R., and Schröder, W. : Acoustic Perturbation Equations based on flow decomposition via source filtering, *J. Comput. Phys.*, **188**:365–398 (2003).

[9]Abdelsamie, A., Fru, G., Dietzsch, F., Janiga, G., Thévenin, D.: Towards direct numerical simulations of low-Mach number turbulent reacting and two-phase flows using immersed boundaries, *Comput. Fluids*, **131**(5):123–141 (2016).

[10]Abdelsamie, A., Lartigue, G., Frouzakis, C.E., Thévenin D.: The Taylor-Green Vortex as a benchmark for high-fidelity combustion simulations using low-Mach solvers, *Comput. Fluids*, **223**:104935 (2021).

[11]Chi, C., Abdelsamie, A., Thévenin, D.: A directional ghost-cell immersed boundary method for incompressible flows, *J. Comput. Phys.*, **404**:109122–109142 (2020).

[12]Qian, Y. H., D'Humières, D., Lallemand, P. : Lattice BGK models for Navier-Stokes equation, *Europhys. Let.*, **17**(6):479–484 (1992).

[13]Freitas, R., Henze, A., Meinke, M., and Schröder, W. : Analysis of lattice-Boltzmann methods for internal flows, *Comput. Fluids*, **47**(1):115–121 (2011).

[14]Koh, S. R., Kim, J.-H., and Lintermann, A. : Numerical analysis of oscillatory flows in the human brain by a lattice-Boltzmann Method, *Proc. 14th WCCM-ECCOMAS*, (2021).

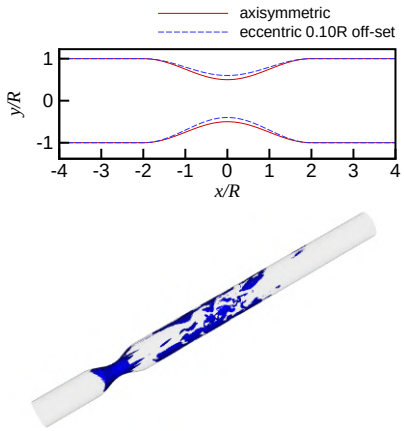

Figure 1: (Top): Profiles of the axisymmetric and eccentric pipes near the stenosis at axial position $x/R = 0$; the profiles are scaled by radius R. (Bottom): 3D-representation of the pipe with an iso-surface of vorticity magnitude at Re= 1000.

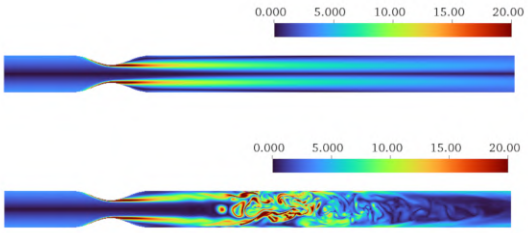

Figure 2: Shear layer computed by DINO, showing vorticity magnitude at Re = 500 (top) and 1000 (bottom), normalized by u_{avg}/D, where u_{avg} is the inlet cross-sectional average velocity.

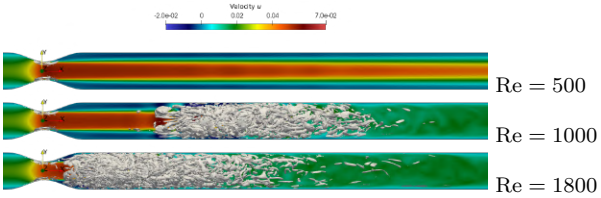

Figure 3: Axial velocity component u and isosurface of λ_2-criterion as determined by LB at Re = 500 (top), 1000 (middle), and 1800 (bottom).

WORKSHOP
Direct and Large-Eddy Simulation 13
October 26th-29th 2022, Udine, Italy

EXTENDED COMPARISON BETWEEN LATTICE BOLTZMANN AND NAVIER-STOKES SOLVERS FOR UNSTEADY AERODYNAMIC AND AEROACOUSTIC COMPUTATIONS

A. Suss[1], **I. Mary**[1], **T. Le Garrec**[1], **S. Marié**[2,3]
[1] DAAA, ONERA, Université Paris Saclay, F-92322 Châtillon - France
[2] Laboratoire DynFluid, F-75013 Paris - France
[3] Conservatoire National des Arts et Métiers, F-75003 Paris - France
alexandre.suss@onera.fr

INTRODUCTION

Within the past decades, Computational Fluid Dynamics (CFD) has dramatically risen in the aerospace industry enabling the simulation of configurations of growing complexity. The increasing computational power and the growing need of high-fidelity methods owing to new sustainable aviation objectives have lead to the development of Large Eddy Simulations (LES). As indicated by Löhner [1], structured finite-type Navier-Stokes (NS) methods and lattice Boltzmann methods (LBM) may be the first to achieve industrial-level LES.

While LES or hybrid RANS-LES applied to the Navier-Stokes equations are well established and studied approaches, the LBM, which relies on a mesoscopic description of collisions between fluid particles, has gradually emerged as an interesting alternative for the LES of weakly compressible flows [2]. Consequently, one question which naturally arises is: Which method is the most competitive, in terms of accuracy and computational cost, on canonical aerodynamic and aeroacoustic applications ?

Previous work on the comparison between the LBM and traditional NS methods focused on different topics such as convergence order [3], achievable error [4], and runtimes [5]. However, there still is a lack of fair one-to-one comparisons. Indeed, most runtime-based results were obtained with two different solver developed independently and having different levels of optimisation. In addition, the numerical properties of the lattice Boltzmann method are highly dependent on the selected collision operator [6, 7] such that the conclusions of [4], only considering the BGK model, have to be tempered.

SCOPE OF THIS CONTRIBUTION

This work aims at rigorously comparing a lattice Boltzmann solver with an LES-type finite-volume Navier-Stokes solver. The comparison is performed using ONERA's Cassiopée/Fast CFD environment implementing high-performance flow solvers which rely on the same code architecture and optimisation layers (see Figure 1).

MEANS AND METHOD OF COMPARISON

Firstly, the lattice Boltzmann method is compared to traditional finite-type Navier-Stokes schemes through von Neumann analyses. The latter consist in a linearisation of the corresponding algorithm about a mean flow and allow to investigate the behavior of linear waves in terms of propagation and dissipation. To do so, the von Neumann analysis introduced in [4] is extended by taking into account regularised LB collision models representative of those used for industrial-levels computations. Moreover, recent advances in LB linear stability analyses [6] set the path towards two-dimensionnal wavenumber plane studies. By applying this idea to NS schemes, isotopy defects are highlighted for both numerical methods as shown on Figure 2. These defects are attributed to the coupling between spatial and temporal discretisations.

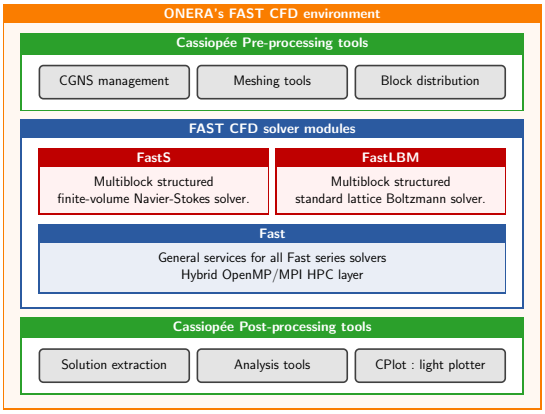

Figure 1: ONERA's Cassiopée/Fast CFD environment used for the comparison between the lattice Boltzmann and Navier-Stokes methods.

The results obtained by means of the von Neumann analyses are then validated through numerical test cases. The computation of monochromatic acoustic and shear plane waves gives an estimate of the number of points per wavelength required by each method to reach a certain error target. In addition, test cases representative of canonical aerodynamic problems such as a vortex convection (see Figure 3 for a qualitative comparison) and a 3D Taylor Green Vortex are considered. The influence of the LB collision model and NS spatial and time-stepping schemes are thoroughly discussed throughout the entire validation process.

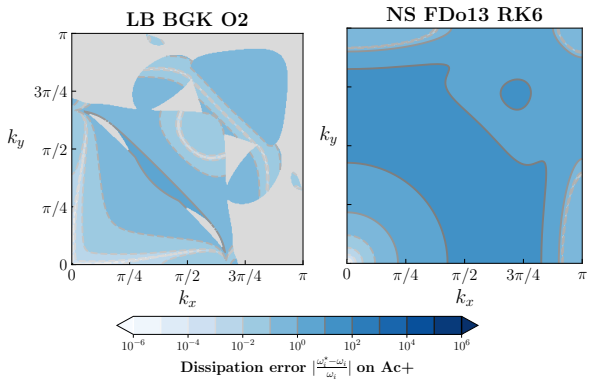

Figure 2: Dissipation error on the acoustic mode computed through the von Neumann analysis in a fluid medium at rest. Left : lattice Boltzmann BGK. Right: Navier-Stokes with 6th-order centered optimised spatial scheme.

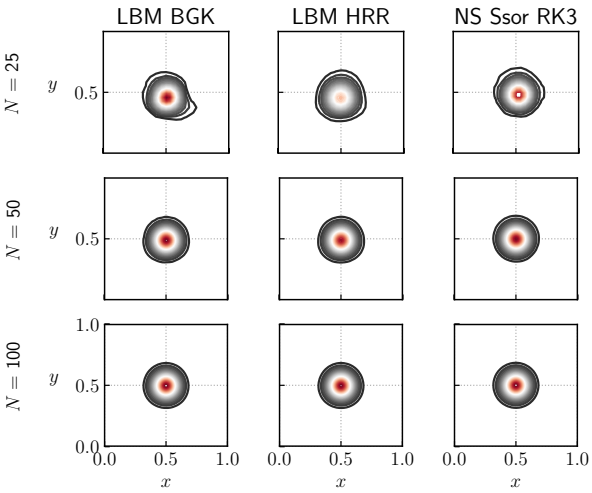

Figure 3: Comparison of the vortex shape obtained by two LBM and one NS computations after 5 advection cycles for three different resolutions where N is the number of mesh points per unit length.

Finally, the CPU performance of both solvers is studied. The Roofline model [8], reformulated in "cell update" units, is applied to the lattice Boltzmann and finite-volume Navier-Stokes algorithms. Estimates about the maximum attainable performance are obtained and the main bottlenecks of the core loop of both solvers are evidenced.

Single-node scaling is performed and the measured performances are confronted to the Roofline model estimates. A "time to solution" metric is also introduced in order to fairly compare the LB and NS methods. It is shown that, in contrast to LB solvers, the "time to solution" of NS schemes does not only depend on the number of points per wavelength but also on the CFL number.

The results of this extended comparison exhibit that a fluid cell update is about two to three times faster with the lattice Boltzmann method w.r.t the finite-volume Navier-Stokes solver (see Figure 4). Regardless of the collision operator, the LB solver is especially suited for acoustic applications, offering speedups up to 10 compared to an LES-type NS solver.

On more "realistic" test cases such as a vortex convection or a 3D Taylor Green vortex, it is demonstrated that good qualitative results can be obtained in competitive runtimes with lattice Boltzmann methods. The latter perform outstandingly well for very low resolutions. However, for highly accurate results measured through L^2 or L^∞ norms, the finite-volume Navier-Stokes method outperforms the lattice Boltzmann solver in terms of "time to solution".

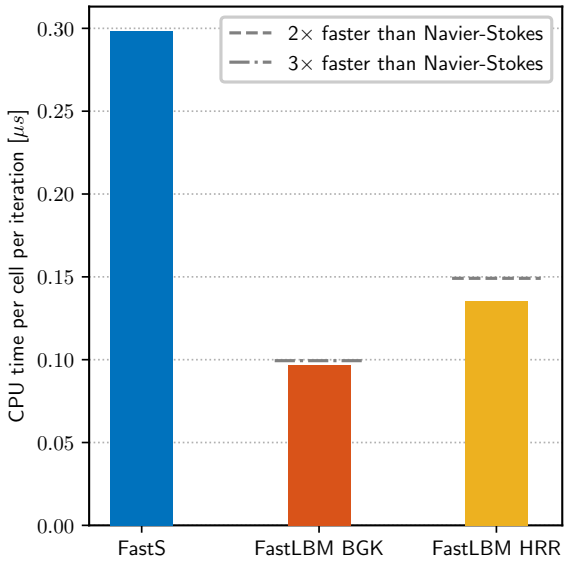

Figure 4: CPU time per cell per iteration for the FV-NS solver on structured cartesian grids and for the LBM with BGK and HRR [7] collision operators.

REFERENCES

[1]Löhner R. : Towards overcoming the LES crisis, *International Journal of Computational Fluid Dynamics*, **33**, 87–97 (2019).

[2]Touil H., Ricot D., and Lévêque E. : Direct and large-eddy simulation of turbulent flows on composite multi-resolution grids by the lattice Boltzmann method, *Journal of Computational Physics*, **256**, 220–233, (2014).

[3]Noble D. R., Georgiadis J. G., and Buckius R. O. : Comparison of accuracy and performance for lattice Boltzmann and finite difference simulations of steady viscous flows, *International Journal for Numerical Methods in Fluids*, **23**, 1–18 (1996).

[4]Marié S., Ricot D., and Sagaut P. : Comparison between lattice Boltzmann method and Navier-Stokes high order schemes for computational aeroacoustics, *Journal of Computational Physics*, **228**, 1056–1070 (2009).

[5]Wichmann K.-R., Kronbichler M., Löhner R., and Wall W. A. : A runtime based comparison of highly tuned lattice Boltzmann and finite difference solvers, *International Journal of High Performance Computing Applications*, 370-390, (2021).

[6]Wissocq G., Coreixas C., and Boussuge J.-F. : Linear stability and isotropy properties of athermal regularized lattice Boltzmann methods, *Physical Review E*, **102**, (2020).

[7]Jacob J., Malaspinas O., and Sagaut P., "A new hybrid recursive regularised Bhatnagar–Gross–Krook collision model for lattice Boltzmann method-based large eddy simulation," J. Turbul., **19**, 1051–1076, (2019).

[8]Williams S., Waterman A., and Patterson D. : Roofline: an insightful visual performance model for multicore architectures, *Commun. ACM*, **52**, 65–76, (2009).

WORKSHOP
Direct and Large-Eddy Simulation 13
October 26th-29th 2022, Udine, Italy

ADVANCED LES MODELING OF MULTIPERFORATED PLATES FOR AERONAUTICAL ENGINES

T. Duranton[1,2], L. Gicquel[1], F. Nicoud[3], A. Dauptain[1]
[1] CERFACS, France
[2] Safran Aircraft Engines, France
[3] CNRS I3M 5149, University Montpellier 2, France
duranton@cerfacs.fr

INTRODUCTION

To respect current and upcoming environmental regulations, aeronautical engine manufacturers are in constant need of improving gas turbine efficiency. By increasing the pressure ratio of the compressor, the overall efficiency is improved but the temperature of the burnt gases in the combustion chamber increases. Due to this increase, the walls of the combustion chamber need to be cooled to preverse the integrity of the machine. To do so, walls are nowadays perforated by thousands of submilimetric holes, allowing cooler air from the combustor casing to transpire on the combustor side, creating a shielding cold flow film along the wall [1]. The pressure drop between the cold casing and the hot flame tube is the primary driver of flow within each perforation. Due to the presence of the flame or of geometric accidents (spark plugs, primary or dilution holes), the flow around the multiperforated plates in combustion chambers is non-homogeneous.

Because of the high computational and engineer costs, the Large Eddy Simulation (LES) study of a system equiped with a resolved multiperforated plate is not suitable for real industrial applications. To reduce the costs associated with multiperforations, Mendez and Nicoud [2] designed a homogeneous model to take into account the effect of multiperforated plates in LES. The model consists in injecting the equivalent mass and momentum fluxes by imposing a homogeneous momentum field on the plate boundaries. As a consequence of the homogeneity, the geometry and the mesh lose their dependency on the perforation arrangement and on the cell size, leading to a reduction of both computational and engineer costs. To correct the lack of heterogeneity and direction of the injected flow, Lahbib [4] and then Bizzari et al. [3] proposed a model based on the same assumptions but imposing a heterogeneous momentum field on the plate boundaries. The introduced Thickened Hole Model allows different mesh sizes to be used, by locally increasing the projected hole diameter to respect a given minimum number of cells per diameter while conserving the mass and momentum fluxes.

In terms of method, the mass flow rate to be imposed on the boundary condition is estimated by group of perforations, by using ad hoc 1-D tools : each perforation of a given group injects the same mass flow rate. This simplification is acceptable until the flow around the multiperforated plate becomes heterogeneous due to geometric acceidents or the presence of the flame for example.

The first aim of the present study is to evaluate the behaviour of the flow near a multiperforated plate in the presence of an obstacle, and assess the impact of this obstacle on the mass flow rate distribution and the cooling efficiency. This specific question is here addressed by performing a wall resolved LES including all the perforations and the presence of an obstacle on the casing side. The second objective consists in designing a mass flow rate model which properly accounts for the flow disturbances induced by the obstacle.

LES SIMULATION OF A RESOLVED MULTIPERFORATED PLATE WITH AN OBSTACLE ON THE CASING SIDE

The mass flow rate distribution through a multiperforated plate is assumed to be dependent on the perforation geometry and the local flow properties. Obstacles found in casings of combustion chambers can therefore alter the flow and thus the mass flow distribution. To evaluate the behaviour of such a flow, a LES simulation of the flow around a multiperforated plate subject to an obstacle on the suction side is performed.

The geometry described in Fig.1 presents a flow going from left to right, separated by a multiperforated plate. An obstacle is placed in the casing vein to create flow heterogeneity. Flow and multiperforation charactaristics are set up to match standart helicopter conditions.

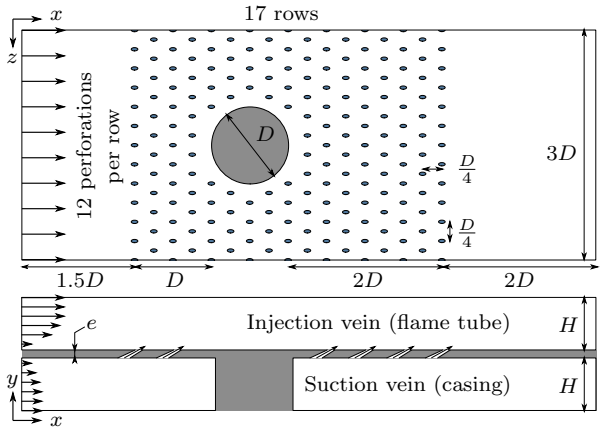

Figure 1: Domain geometry of multiperforated setup.

The mesh has been adapted with MMG3D using a LIKE

[10] criterion to make sure that the main flow features of the jetting flow downstream of each aperture are properly represented. The mesh obtained is made up of 110M tetrahedra.

The simulation is performed with the LES solver AVBP [5] developed by CERFACS and solves the compressible Navier-Stokes equations. The σ subgrid scale model of Nicoud et al. [6] is used, along with a 2nd order Lax-Wendroff [7] numerical convection scheme.

RESULTS AND DISCUSSION

As a result of the above mentionned simulation, different instantaneous and time-averaged quantities are made available in the entire domain, such as pressure, velocity or temperature. Figure 2 shows for example the time-averaged mass flow rate $\delta\dot{m}$ relative to the mean value, defined in Eq.(1), through the multiperforation. This mass flow rate distribution is observed to be no longer homogeneous since impacted by the obstacle, with around a maximum of $\pm 10\%$ deviation.

$$\delta\dot{m} = \frac{\dot{m} - \langle\dot{m}\rangle}{\langle\dot{m}\rangle} \tag{1}$$

with $\langle\dot{m}\rangle$ the average of mass flow rate over all perforations.

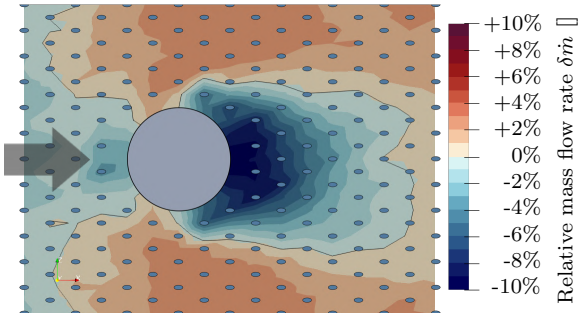

Figure 2: Map of the time-averaged mass flow rate deviation $\delta\dot{m}$ defined in Eq.(1) in the perforations.

Considering the flow inviscid, incompressible and steady, Bernoulli's equation is the standard starting point. The mass flow rate model expressed Eq.(2) is assumed to be mainly driven by the difference of the coolant total pressure and the crossflow static pressure. The pressure losses occuring in the perforation collapse into a discharge coefficient C_d, that apprehends the deviation from Bernoulli's equation. As discussed by Champion et al. [8] or Rowbury et al. [9], geometric parameters, flow conditions and in particular coolant Reynolds number influence the value taken by the discharge coefficient.

$$\dot{m}_{mod} = C_d \cdot S \cdot \sqrt{2 \cdot \rho \cdot \left(\Delta P_{stat} + P_{dyn,suc}\right)} \tag{2}$$

Thanks to the numerical databasis generated and discussed briefly previously, a mass flow rate model can be evaluated for the setup described in Fig.1. To do so and to improve the accuracy of this modeling process, different quantities can be considered from a time-averaged solution first. Results obtained through this modeling step to be detailed can then be compared with the time-averaged relative mass flow rate $\delta\dot{m}$ defined in Eq.(1) and captured for each perforation, as shown on Fig.3. As observed here, it is possible to obtain a model for which a 1% maximum erorr is obtained if adequate information is provided.

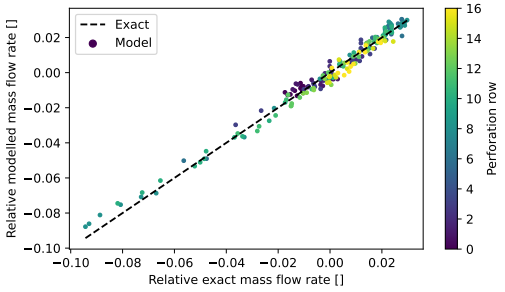

Figure 3: Relative modeled mass flow rate fitting with relative exact mass flow rate.

CONCLUSION

To understand the impact of an obstacle on the cooling properties of a multiperforated plate, a high fidelity LES simulation has been performed. Thanks to this specific databasis, an a priori mass flow rate model for such multiperforated plates is demonstrated to be feasible. Results extracted from the simulation will be discussed at the conference along with the details of the model.

ACKNOWLEDGMENTS

The authors acknowledge Julien Tillou from Safran Aircraft Engines for his help and support. The authors also acknowledge CCRT and Safran Aircraft Engines for providing computing resources that have contributed to the study presented in this abstract.

REFERENCES

[1]Lefebvre A. H. : Gas turbine combustion. *Taylor & Francis* (1999).

[2]Mendez S., Nicoud F. : Adiabatic Homogeneous Model for Flow Around a Multiperforated Plate, *AIAA Journal, American Institute of Aeronautics and Astronautics*, **46 (10)**, 2623–2633 (2008).

[3]Bizzari R., Lahbib D., Dauptain A., Duchaine F., Gicquel L., Nicoud F. : A Thickened-Hole Model for Large Eddy Simulations over Multiperforated Liners, *Flow, Turbulence and Combustion*, **101 (3)**, 705–717 (2018).

[4]Lahbib D. : Modeling of aerodynamics and thermal effects in multiperforations using LES, *PhD Thesis*, University Montpellier II (2015).

[5]Gicquel L., Gourdain N., Boussuge J.F., Deniau H., Staffelbach G., Wolf P., Poinsot T. : High performance parallel computing of flows in complex geometries, *Comptes Rendus Mécanique*, **339 (2-3)**, 104–124 (2011).

[6]Nicoud F., Toda H.B., Cabrit O., Bose S., Lee J. : Using singular values to build a subgrid-scale model for large eddy simulations, *Physics of Fluids*, **23 (8)**, 085106 (2011).

[7]Lax P.D., Wendroff B. : Systems of conservation laws, *Commun. Pure Appl. Math.*, **13**, 217–237 (1960).

[8]Champion J., Di Martino P., Coron X. : Influence of Flow Characteristics on the Discharge Coefficient of a Multiperforated Wall, *ASME Turbo Expo 2005: Power for Land, Sea, and Air*, 201–211 (2008).

[9]Rowbury D.A., Oldfield M.L.G., Lock G.D., Dancer S.N : Scaling of Film Cooling Discharge Coefficient Measurements to Engine Conditions, *ASME 1998 International Gas Turbine and Aeroengine Congress and Exhibition*, **4** (1998).

[10]Daviller G., Brebion M., Xavier P., Staffelbach G., Müller J., Poinsot T. : A Mesh Adaptation Strategy to Predict Pressure Losses in LES of Swirled Flows, *Flow, Turbulence and Combustion*, **99 (1)**, 93–118 (2017).

WORKSHOP
Direct and Large-Eddy Simulation 13
October 26th-29th 2022, Udine, Italy

TURBULENT BOUNDARY LAYER IN A 3-ELEMENT HIGH-LIFT WING: COHERENT STRUCTURES IDENTIFICATION

R. Montalà[1], B. Eiximeno[1,2], A. Miró [2], O. Lehmkuhl [2], I. Rodríguez[1]
[1] TUAREG - Turbulence and Aerodynamics Research Group, Universitat Politècnica de Catalunya
[2] Barcelona Supercomputing Center
ivette.rodriguez@upc.edu

INTRODUCTION

Aircraft design is a very complex and demanding field that requires taking into account a large number of disciplines. From an aerodynamic point of view, to cut down jet fuel burnt implies the reduction of the drag. Recently, flow analysis techniques have been used to disentangle the complexity of turbulence and in particular the intricacies of the near-wall turbulence. However, most of the works performed so far have been conducted on canonical cases such as plane turbulent boundary layer, channel, and pipe flows (see for instance [1, 2]).

In this work we propose to gain insight into the physics of the turbulent boundary layer and the interaction between coherent motions and drag by studying a more realistic configuration close to the ones used in aircrafts. Specifically, we will conduct simulations on the 30P30N three-element high-lift wing. The model has both slat and flap deployed in a landing configuration with a deflection of $-30°$ and $30°$, respectively. This high-lift wing has been used as a benchmark case for the AIAA Workshop on Benchmark Problems for Airframe Noise Computations (BANC), thus many contributions can be found in the literature (e.g., [3, 4, 5]). Most of the numerical works have been focused on the aeroacoustic noise from the wing but, as far as authors knowledge is concerned, there are no studies in the literature focusing on the interplay between coherent structures, Reynolds stresses and the drag. Thus, here we propose to identify key flow structures in the different zones of the wing, and connect them with its aerodynamic performance. By doing this we would like to answer the following questions: i) Which are the characteristic energy-containing structures and frequencies present in the different sections of the wing, and which is the interaction between them?; ii) Can we separate the structures so as to identify their contribution to the Reynolds stresses and the viscous drag?

In the present work, the Reynolds number based on the nested chord and the free-stream velocity is $Re_c = U_{ref}C/\nu = 7.5 \times 10^5$ and the angle of attack is $AoA = 9°$. Although most of the studies are conducted at higher Reynolds numbers, the study presented here is at a relatively lower Reynolds number, which makes current simulations more affordable from a computational point of view without losing generality.

MATHEMATICAL AND NUMERICAL MODEL

In this work, large eddy simulations (LES) of the flow are performed by means of a low-dissipation finite element (FE) scheme [6]. The basic idea behind this approach is to mimic the fundamental symmetry properties of the underlying differential operators, i.e., the convective operator is approximated by a skew-symmetric matrix and the diffusive operator by a symmetric, positive-definite matrix. The chosen low dissipation FE scheme presents good accuracy compared to other low dissipation finite volume and finite difference methods, with the advantage of being able to increase the order of accuracy at will without breaking the fundamental symmetry properties of the discrete operators. A non-incremental fractional-step method is used to stabilise the pressure. This allows for the use of finite element pairs that do not satisfy the inf-sup conditions, such as the equal order interpolation for the velocity and pressure used in this work. The set of equations are time integrated using an energy conserving fourth order Runge-Kutta explicit method combined with an eigenvalue based time-step estimator.

As for the LES, the Vreman [7] sub-grid scale (SGS) model is used. This methodology is implemented into Alya code, which is a multi-physics parallel code. For more details, the reader is referred to [8]. For the coherent structures identification, proper orthogonal decomposition (POD) is used. The POD procedure characterizes the relevant states of a model by a set of orthonormal basis functions, which correspond to the leading eigenvectors of a covariance matrix constructed from a set of computed solutions. The method of snapshots, introduced by [9] as a manner to efficiently identify the POD basis functions for large systems is here used.

RESULTS

The simulation have been conducted in a computational domain with a radius of $10C$ in the $x-y$ plane. Then, the two-dimensional plane is extruded in the z-direction, which has an extension of $L_z = 0.1C$, similar to the domains used in previous computations. An unstructured mesh is used with a $y^+ \sim 1$ along the whole wing. Computations have been carried out over 30 time-units ($TU = tU_{ref}/C$) and for computing statistics the last 16 time-units have been used. The POD analysis has been performed using a total of 1600 snapshots (i.e., about 15.5 time-units), with a sampling of $\Delta t U_{ref}/C = 9.67 \times 10^{-3}$. In figure 1, the comparison of the pressure coefficient distribution obtained with experimental results is presented. Notice that experimental results by Pascioni et al. [4] and by Murayama et al. [3] were obtained at $Re = 1.7 \times 10^6$, whereas those by Klausmeyer et al. [10]

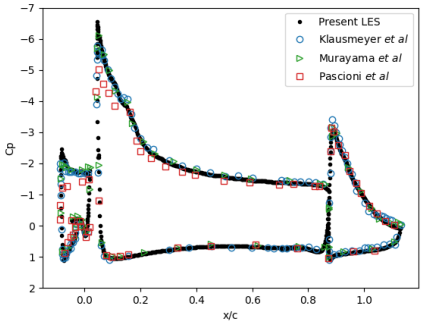

Figure 1: Pressure coefficient. Comparison with experimental results from the literature at $AoA = 9°$: Klausmeyer *et al*[10], Murayama *et al* [3] and Pascioni *et al*[4]

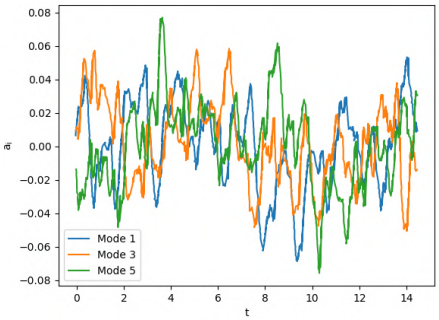

Figure 2: Evolution of the temporal coefficients a_i for modes 1, 3 and 5

were at $Re = 5 \times 10^6$. Nonetheless, a fair agreement with experimental measurements is observed. The temporal evolution of the POD coefficients for modes 1, 3 and 5 and the reconstructed streamwise and cross-streamwise velocity fields for these modes are presented in figures 2 and 3. The longitudinal structures arising from the shear layer in the slat can readily be seen in the figure. These structures dominate in the first modes of the cross-stream velocity fluctuations. In the final version of the manuscript the complex interaction between coherent structures in the slat cove with the main leading edge, and their impact on the main boundary layer development will be analysed and discussed in detail.

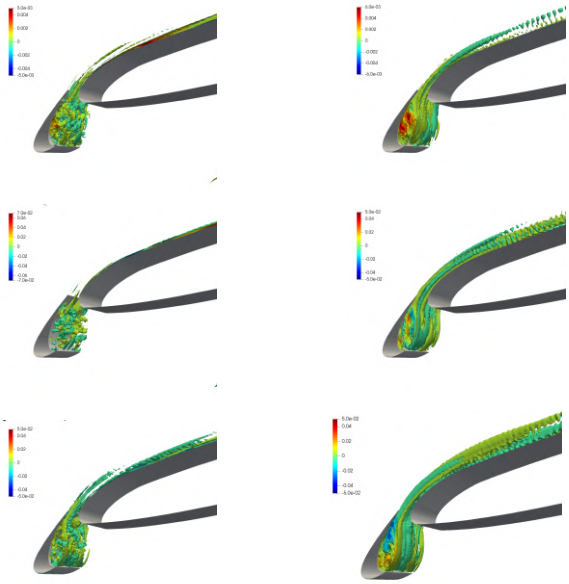

Figure 3: Contours of the reconstructed streamwise and cross-stream velocity fluctuation fields for modes 1, 3, and 5, coloured by the velocity magnitude in the region nearby the slat element

REFERENCES

[1] A. Lozano-Durán and J. Jiménez, "Time-resolved evolution of coherent structures in turbulent channels: characterization of eddies and cascades," *Journal of Fluid Mechanics*, vol. 759, pp. 432–471, 2014.

[2] L. Agostini and M. Leschziner, "The connection between the spectrum of turbulent scales and the skin-friction statistics in channel flow at Reτ =1000," *Journal of Fluid Mechanics*, vol. 871, pp. 22–51, 2019.

[3] M. Murayama, K. Nakakita, K. Yamamoto, H. Ura, Y. Ito, and M. M. Choudhari, "Experimental study of slat noise from 30P30N three-element high-lift airfoil in JAXA hard-wall low-speed wind tunnel," *20th AIAA/CEAS Aeroacoustics Conference*, no. June, 2014.

[4] "Aeroacoustic measurements of leading-edge slat noise," *22nd AIAA/CEAS Aeroacoustics Conference, 2016*, no. September, 2016.

[5] Y. Jin, F. Liao, and J. Cai, "Numerical simulation of 30p30n multi-element airfoil using delayed detached-eddy simulation," *Aiaa Aviation 2020 Forum*, pp. 1–24, 2020.

[6] O. Lehmkuhl, G. Houzeaux, H. Owen, G. Chrysokentis, and I. Rodriguez, "A low-dissipation finite element scheme for scale resolving simulations of turbulent flows," *Journal of Computational Physics*, vol. 390, pp. 51 – 65, 2019.

[7] A. W. Vreman, "The filtering analog of the variational multiscale method in large-eddy simulation," *Physics of Fluids*, vol. 15, no. 8, p. L61, 2003.

[8] M. Vázquez, G. Houzeaux, S. Koric, A. Artigues, J. Aguado-Sierra, R. Arís, D. Mira, H. Calmet, F. Cucchietti, H. Owen, A. Taha, E. D. Burness, J. M. Cela, and M. Valero, "Alya: Multiphysics engineering simulation toward exascale," *Journal of Computational Science*, vol. 14, pp. 15–27, 2016.

[9] L. Sirovich, "Turbulence and the Dynamics of Coherent Structure: I, II and III," *Quarterly Applied Mathematics*, vol. 45, no. May, p. 561, 1987.

[10] J. L. S.M. Klausmeyer, "An experimental investigation of skin friction on a multi-element airfoil," in *12th AIAA Applied Aerodynamics Conference*, (Colorado Springs), 20-22 June 1994.

WORKSHOP
Direct and Large-Eddy Simulation 13
October 26th-29th 2022, Udine, Italy

TRANSITION PREDICTION ON A WIND TURBINE BLADE AT RE = 10^6 UNDER VARYING INFLOW TURBULENCE BASED ON WALL-RESOLVED LES

M. Breuer[1], B.A. Lobo[2], A.P. Schaffarczyk[2]
[1] Professur für Strömungsmechanik, Helmut-Schmidt-Universität Hamburg, Hamburg, Germany
[2] Mechanical Engineering Department, Kiel University of Applied Sciences, Kiel, Germany
breuer@hsu-hh.de

INTRODUCTION

Wind energy plays a leading role as a renewable energy source, especially in countries where the annual solar yield is not very high. In 2019 more than half of the renewable energy supply in Germany was generated by wind turbines. The blades of the rotor are the most important components for optimizing the performance. To construct special aerodynamic profiles which possess large areas of low-resistance, requires the understanding of the laminar-to-turbulent transition process taking place at such profiles. That is a non-trivial task since the rotor blades operate under atmospheric inflow turbulence and partially in the wake of preceding wind turbines. Furthermore, the Reynolds numbers are very high. In a first step to predict these kinds of flows based on wall-resolved LES with modeled atmospheric turbulence, a precursor study [5] at a rather low Re number of 10^5 was carried out for a 20% thickness airfoil corresponding to the experiment by Reichstein et al. [6]. Five different turbulence intensities (TI) were studied. A laminar separation bubble roughly between 50 and 75% of the chord disappeared for higher turbulence intensities. Depending on the TI level different transition modes (inflectional instability vs. transition mechanism influenced by the presence of streaks within the boundary layer) were found. In summary, the results showed that the applied methodology of wall-resolved LES with injected inflow turbulence works reliably and provides physically meaningful results. In the present study the Reynolds number is increased to Re = 10^6 which is close to the real case. The objective is to understand the transition scenario under varying inflow conditions.

APPLIED METHODOLOGY

Three main ingredients are required to investigate the effect of the inflow turbulence on the transition process.

1. Simulation methodology

A wall-resolved LES relying on a dynamic Smagorinsky model is used. The filtered Navier-Stokes equations are solved based on a finite-volume method on block-structured grids, which is second-order accurate in space and time [1, 2]. This central scheme possesses low numerical dissipation, which is important for LES and especially the simulation of transitional flows. However, it is prone to numerical oscillations in case of high Re. In Lobo et al. [5] a blended scheme with a high percentage of the central difference scheme and a very low percentage of an upwind scheme was found to be a good compromise. Presently, the shares are 95 % and 5 %, respectively. The time marching within the predictor-corrector method uses a low-storage Runge-Kutta scheme. A C-type grid consisting of about 52 million control volumes is used. It is refined near the wall with a wall-normal distance of the first cell center of $y^+_{1st} < 0.5$. The streamwise resolution is $\Delta x^+ \leq 30$ on the suction side, $\Delta x^+ \leq 60$ on the pressure side and $\Delta z^+ \leq 25$ for the spanwise direction satisfying the requirements for a wall-resolved LES. The spanwise extension of the airfoil is only 6% of the chord length c and resolved by 105 control volumes.

2. Synthetic turbulence inflow generator (STIG)

The method proposed by Klein et al. [4] is applied. It relies on digital non-recursive filters which depend on statistical properties. These spatial and temporal correlations and the resulting length and time scales allow an adjustment to the particular flow case. Appropriate inflow data are generated by multiplying filter coefficients, which describe the two-point correlations and the autocorrelation of the inflow turbulence, with a series of random numbers. A required 3-D correlation between the filter coefficients is achieved by convolution of the three 1-D filter coefficients. Moreover, the cross-correlations between all velocity components are taken into account guaranteeing the representation of realistic inflow data.

The generated inflow turbulence is anisotropic in nature and follows the Kaimal spectrum. The input parameters of the STIG are based on those suggested by the IEC-61400-1 standard [8]. However, the corresponding length scales are far too large for the limited spanwise extension of the computational domain. Thus, they are scaled down to maintain the anisotropic nature such that the eddies have a similar form but not the same absolute size. The resulting maximal length scales in the three directions normalized by the chord length c are 0.211, 0.07 and 0.017, respectively. Note that the presently applied STIG only allows to define one length scale per direction. However, this disadvantage can be compensated by superimposing the solutions of different length scales given by the maximal length scale divided by the factor 2^n (n = 1-10).

Based on the turbulence intensity TI, the ratios of standard deviations of the fluctuations in the different directions, the normal Reynolds stress components can be determined for the anisotropic case. Furthermore, a non-zero Reynolds shear stress component $\overline{u'w'}$ can be included by an estimation based on the square of the friction velocity ($u_\tau/u_\infty \approx 0.05$).

3. Source term concept of the STIG

Instead of applying the inflow data at the inlet, where the grid resolution is coarse and thus leads to a strong damping of small flow structures, a recently developed source-term formulation [7] is applied as done in [3]. That allows to shift the artificial turbulence injection closer to the airfoil, where a higher resolution guarantees the correct development of the flow structures. The source terms are superimposed to the momentum equations in a predefined influence area upstream of the airfoil. Based on a Gaussian bell-shaped distribution the source terms are scaled within this influence area. The streamwise dimension of this region is defined by the integral length scale in main flow direction calculated with the help of the integral time scale and the Taylor hypothesis [3, 7]. Thus, all required parameters are directly coupled to the STIG.

SOME RESULTS

The profile considered corresponds to the section of the LM 43P blade of a Senvion MM92 wind turbine [6] at a radius of 35 m and a relative thickness of 20%. Figure 1 shows the distribution of the pressure coefficient c_p and the friction coefficient c_f for the averaged flow field, where the averaging is carried out in time over 8 dimensionless time units and additionally in spanwise direction. The results of three different turbulence intensities of the inflow ($TI = 0$, 0.6 and 4.5%) are depicted. Obviously, a laminar separation bubble is observed in the time-averaged flow field in case of no inflow turbulence. In this case the pressure distribution on the suction side exhibits a plateau indicating the presence of a separated flow region between 50 and 55% chord. Accordingly, c_f is negative in this range. Transition to turbulence is taking place between 52 and 59% chord as indicated by the sharp drop and then rise in c_f followed by a reduction indicating a fully turbulent flow. Analyzing the shape factor and the Reynolds shear stress close to the wall (not depicted here) the laminar, transitional and turbulent regimes can be clearly distinguished. For visualizing boundary layer streaks, snapshots of the instantaneous streamwise velocity disturbance are depicted in Fig. 2. At $TI = 0\%$ a spanwise roll of Kelvin-Helmholtz type is visible in Fig. 2(a) in the range $0.52 \leq x/c \leq 0.56$ discerning the laminar and turbulent regions.

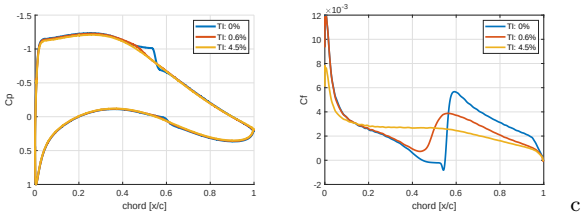

(a) c_p based on the mean flow. (b) c_f based on the mean flow.

Figure 1: Distribution of pressure coefficient c_p and friction coefficient c_f (suction side) at $\mathrm{Re} = 10^6$ and $\alpha = 4°$.

Increasing the inflow turbulence intensity to 0.6%, no separation of the mean flow is observed anymore. Nevertheless, in the instantaneous flow a temporary separation bubble is still found. Overall, it is visible that transition to turbulence moves upstream due to the added inflow turbulence. Boundary layer streaks are generated as a response of the boundary layer on account of the penetration of external disturbances. The formation of these boundary layer streaks is visible in Fig. 2(b) as elongated dark (slower than mean flow) and light (faster than mean flow) longitudinal regions of the flow.

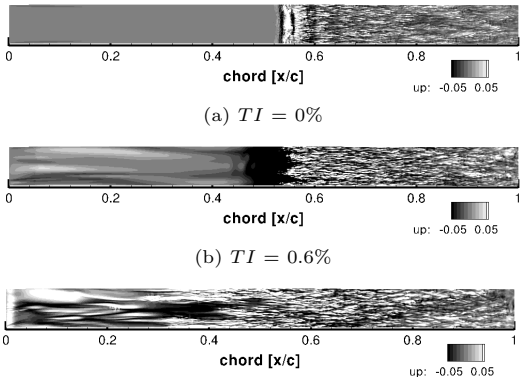

(a) $TI = 0\%$

(b) $TI = 0.6\%$

(c) $TI = 4.5\%$

Figure 2: Snapshots of the instantaneous streamwise velocity disturbance u' for the visualization of boundary layer streaks. Slices are taken at a wall-normal height corresponding to the displacement thickness at 0.5% chord.

A further increase of TI to 4.5% shows only marginally changes to the c_p distribution in the region between 40 and 50% chord. An increase in c_f indicating transitional flow is not apparent in Fig. 1(b) as in the two previous cases. Thus, a distinction between laminar, transitional and turbulent flow is not as easy as before. No evidence of instantaneous separation is found which is probably due to the increased frequency of streak formation within the boundary layer preventing the formation of a separation bubble as seen in Fig. 2(c).

For further investigations on the mode and process of transition and the influence of the inflow turbulence on the boundary layer receptivity, power spectral densities and profiles of the Reynolds shear stress should be analyzed at different locations along the chord. These and other evaluations will be included in the full paper.

REFERENCES

[1] Breuer, M.: Large–eddy simulation of the sub-critical flow past a circular cylinder: Numerical and modeling aspects. Int. J. Numer. Meth. Fluids **28**(9), 1281–1302 (1998).

[2] Breuer, M.: A challenging test case for large-eddy simulation: High Reynolds number circular cylinder flow. Int. J. Heat Fluid Flow **21**(5), 648–654 (2000).

[3] Breuer, M.: Effect of inflow turbulence on an airfoil flow with laminar separation bubble: An LES study. J. Flow, Turbulence and Combustion **101**, 433–456, (2018).

[4] Klein, M., Sadiki, A., Janicka, J.: A digital filter based generation of inflow data for spatially-developing direct numerical or large-eddy simulations. J. Comput. Phys. **186**, 652–665, (2003).

[5] Lobo, B.A., Schaffarczyk, A.P., Breuer, M.: Investigation into boundary layer transition using wall-resolved LES and modeled inflow turbulence. Wind Energy Science, DOI: 10.5194/wes-2021-30, (2022).

[6] Reichstein, T., Schaffarczyk, A. P., Dollinger, C., Balaresque, N., Schülein, E., Jauch, C., and Fischer, A.: Investigation of laminar-turbulent transition on a rotating wind-turbine blade of multi-megawatt class with thermography and microphone array, Energies **12**, 2102, DOI: 10.3390/en12112102, (2019).

[7] Schmidt, S. and Breuer, M.: Source term based synthetic turbulence inflow generator for eddy–resolving predictions of an airfoil flow including a laminar separation bubble. Computers & Fluids **146**, 1–22, (2017).

[8] DIN EN 61400-1, Wind turbines - Part 1: Design requirements. Technical report, IEC, (2006).

Session: Industrial and environmental applications 2

Thursday, October 27, 2022

16:50 – 18:20

WORKSHOP
Direct and Large-Eddy Simulation 13
October 26th -29th 2022, Udine, Italy

Modelling SGS-Turbulent Transport of Fine Particles with Application to Cyclone Separator Performance

M. Sommerfeld, M. Taborda and O. Sgrott
Multiphase Flow Systems, Institute for Process Engineering, Otto-von-Guericke-University Magdeburg;
Hoher Weg 7b, D-06120 Halle (Saale), Germany
Martin.sommerfeld@ovgu.de

INTRODUCTION

Dispersed particle-laden flows are very often numerically computed by using the point-mass Euler/Lagrange approach. With regard to turbulence modelling, RANS (Reynolds-Averaged Navier-Stokes) closure methods are mostly applied. These methods are well established also accounting for full two-way coupling including momentum transfer between the phases as well as turbulence modulation, for example using the k-ε turbulence model (Sommerfeld 2017; Lain et al. 2002; Lain and Sommerfeld 2003). However, in the case of inherently unsteady flows or if flow and particle transport are strongly governed by vortical structures LES is being increasingly applied to dispersed particle-laden flows (Kuerten 2016).

LES-LAGRANGE COUPLING

In the majority of LES applications, particle transport is only considered to be governed by the resolved flow field. However, when considering very small particles, relevant for example in cyclone separators, the transport by the SGS turbulence has to be modelled accordingly. This of course depends on the filter settings or the grid resolution of the LES and hence the energy contained in the SGS turbulence. For that purpose a number of models are used for generating the SGS fluctuating velocities acting eventually on the particle (Kuerten 2016). In the approach introduced by Lipowsky and Sommerfeld (2007) a dynamic Smagorinsky SGS model was used and a single-step Langevin model is applied for generating the fluid fluctuating velocities (Lipowsky and Sommerfeld 2005), which will be also considered here. The required turbulent kinetic energy and the dissipation rate were obtained according to the Lilly (1967) model, which also allowed an estimate of the relevant time and length scales of SGS turbulence. The influence of the particle phases onto the SGS turbulence was considered through a modification of the turbulent viscosity (Lipowsky and Sommerfeld 2007). Such an approach was also considered in the case of dispersed bubbly flows (Sommerfeld et al. 2018), where both SGS turbulence dissipation and enhancement through wake effects were accounted for. Such an enhancement is more pronounce in bubbly flows, since here the bubble Reynolds number is normally much larger, yielding unsteady wakes (Lain et al. 2002). The applicability of this novel source term formulation for the turbulent kinetic energy was also validated for particle-laden flows (Lain and Sommerfeld 2003).

In addition to an eddy viscosity approach for modelling SGS turbulence, also an additional transport equation for the SGS turbulence will be solved. Here the consideration of two-way coupling is more plausible compared to introducing a dispersed phase viscosity contribution. For bubbly flows the different approaches of “turbulence” two-way coupling were compared by Taborda and Sommerfeld (2019).

RESULTS CYCLONE SEPARATOR

In the present studies a small-scale reverse-flow cyclone separator is considered with a particle size spectrum being below about 20 μm (Sgrott and Sommerfeld 2019). The cyclone consists of the main body with a cylindrical (diameter 290 mm) and conical part connected to the dust collector bin. The tangential inlet is a rectangular vertical slit and the exit pipe in the roof of the cyclone has a diameter of 50% of the cylindrical part and is immersed into the cyclone body for the same distance, being equal to the inlet slit height (see Figure 1). Various grid dimensions were considered in order to vary the degree of resolving vortices and turbulence. In Figure 1 two meshes are shown with 830k and 1300k control volumes. Near the walls of

course mesh refinement is used. Besides the dynamic Smagorinsky SGS turbulence model, also simulations were conducted by solving for a k-transport equation. Normally, at least half a million parcels were tracked through the flow field for obtaining good statistical averaging. The forces acting on the particles were drag and gravity as well as transverse lift forces due to shear and particle rotation.

A number of simulations were conducted for quantifying the effect of modelling SGS turbulence transport in particle tracking. This was done by comparing the numerically obtained collection efficiency curves.

Finally, also the influence of different methods to account for two-way coupling on the cyclone collection efficiency was analysed.

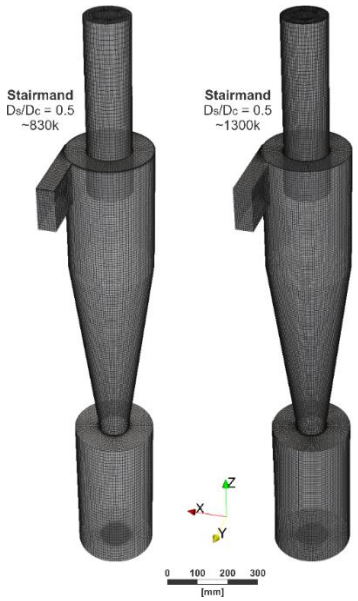

Figure 1: Structured grids used for a high efficiency Stairmand cyclone with body diameter Dc = 0.29 m and vortex-finder Ds = 0.145 m; left: coarser grid with around 830,000 elements; right) refined grid with around 1,300,000 elements.

REFERENCES

Hoekstra, A.J.: Gas flow field and collection efficiency of cyclone separators, The Netherlands: PhD Thesis - Delft University of Technology, 2000

Kuerten, J.G.M.: Point-particle DNS and LES of particle-laden turbulent flow - a state-of-the-art review. Flow Turbulence Combust, Vol. 97, 689–713 (2016)

Lain, S., Bröder, D., Sommerfeld, M. and Göz, M.F.: Modelling hydrodynamics and turbulence in a bubble column using the Euler-Lagrange procedure. International Journal of Multiphase Flows, Vol. 28, 1381-1407 (2002)

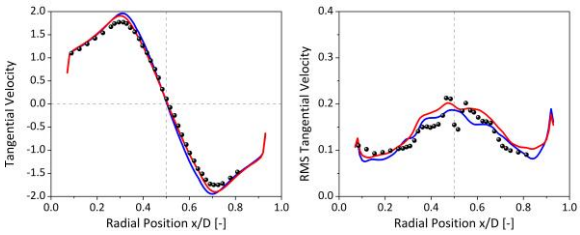

Figure 2: Normalized (by the inlet velocity of 16.1 m/s) mean and RMS tangential velocity profiles in the middle of the cyclone for single-phase flow in the middle of a high efficiency Stairmand cyclone with Rein = 280,000; the symbols represent the experimental data from Hoekstra (2000), the red and blue lines are the numerical results for the coarser and finer mesh, respectively.

Lain, S. and Sommerfeld, M.: Turbulence modulation in dispersed two-phase flow laden with solids from a Lagrangian perspective. Int. Journal of Heat and Fluid Flow, Vol. 24, 616-625 (2003)

Lilly, D.K.: The representation of small scale turbulence in numerical simulation experiments. In Proceedings of the IBM Scientific Computing Symposium on Environmental Sciences, 1967

Lipowsky, J. and Sommerfeld, M.: Time dependent simulation of a swirling two-phase flow using an anisotropic turbulent dispersion model. Proceedings of the ASME Fluids Engineering Summer Conference, Houston, Texas, Paper No. FEDSM2005-77210 (2005)

Lipowsky, J. and Sommerfeld, M.: LES-simulation of the formation of particle strands in swirling flows using an unsteady Euler-Lagrange approach. Proc. of the 6th Int. Conf. on Multiphase Flow, ICMF2007, Leipzig Germany, Paper No. S3_Thu_C_54 (2007)

Sgrott Junior, O.L. and Sommerfeld, M.: Influence of inter-particle collisions and agglomeration on cyclone performance and collection efficiency. Canadian Journal Chemical Engineering, Vol. 97, 511 – 522 (2019)

Sommerfeld, M.: Numerical methods for dispersed multiphase flows. In: Particles in Flows (Eds. T. Bodnár, G.P. Galdi, Š. Nečasová), Series Advances in Mathematical Fluid Mechanics, Springer Int. Publishing, 327 – 396 (2017)

Sommerfeld, M., Muniz, M. and Reichardt, Th.: On the importance of modelling bubble dynamics for point-mass numerical calculations of bubble columns. Journal of Chemical Engineering of Japan, Vol. 51, 301 – 317 (2018)

Taborda, M. and Sommerfeld, M.: Effect of bubble dynamics and bubble induced turbulence (BIT) on chemically reacting bubbly flows. *ECCE12, The 12th European Congress of Chemical Engineering, Florence, Italy 15-19 September 2019*

WORKSHOP
Direct and Large-Eddy Simulation 13
October 26th-29th 2022, Udine, Italy

EULER-LAGRANGE LES PREDICTIONS OF A POWDER DISPERSER INCLUDING A MULTISCALE WALL-IMPACT BREAKAGE MODEL

A. Khalifa and M. Breuer
Professur für Strömungsmechanik
Helmut-Schmidt-Universität Hamburg, Hamburg, Germany
khalifa/breuer@hsu-hh.de

INTRODUCTION

The evolution of the particle size in turbulent particle-laden flows is a complex phenomenon, which plays an important role in various environmental (e.g., air pollution) and industrial applications (e.g., dry powder inhalers). The main challenge for investigating such flows is the extensive range of length and time scales to be dealt with, especially in the case of turbulent flows. Thus, efficient and reliable methods for numerically simulating particle-laden flows are of interest. Namely, multiscale strategies, in which models derived at different scales are combined to efficiently describe the flow system, offer a practical alternative to expensive direct methods. The present study demonstrates the viability of a multiscale Euler–Lagrange technique for predicting the flow in a lab-scale powder disperser while effectively describing the development of the particle size. Of specific interest are breakup processes taking place in turbulent flows due to fluid forces and wall impact. For the latter models based on artificial neural networks were developed.

APPLIED METHODOLOGY

The continuous phase is predicted in the Eulerian frame of reference relying on the large-eddy simulation (LES) technique. The code applies the finite-volume method for block-structured grids [1]. Furthermore, an efficient Lagrangian tracking scheme is employed, which deterministically detects inter-particle collisions [1, 2]. The collisions are handled based on an extended hard-sphere model taking possible agglomeration processes into account [3]. Moreover, the effect of subgrid-scale motions on the particles is accounted for and the feedback effect of the particles on the carrier fluid is considered. Hence, the method is four-way coupled.

To maintain manageable computational costs, the detailed structure of agglomerates is substituted by a single sphere possessing an effective diameter. In this context, models describing the breakage of agglomerates due to fluid-induced stresses [4, 5] and wall impacts [6, 7, 8] have been developed and incorporated into the described simulation methodology.

ANN-BASED WALL-IMPACT BREAKAGE MODEL

In general, to fully describe a wall-impact breakage event a model needs to provide descriptions for (1) the number, (2) the size distribution, and (3) the post-impact velocity of the arising fragments. The proposed model is data-driven and is derived as follows. First, an extensive number of discrete element simulations (DEM) of single agglomerates impacting a wall in a vacuum environment are carried out (see Fig. 1). Wide ranges of different impact conditions are taken into account: Three silica powders distinguished by the size of the primary particle (0.97, 2.47 and 5.08 μm), eight agglomerate size classes ranging between 5 and 10^3, nine impact angles between a flat and a normal impact, and a range of velocities able to reproduce the full spectrum of breakage from a rebound of an intact agglomerate to a full disintegration.

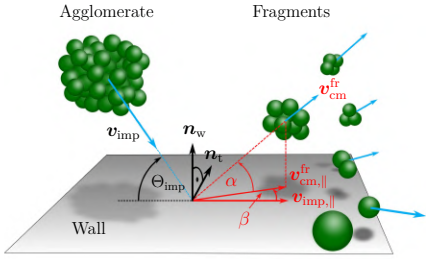

Figure 1: DEM wall-impact events used for generating a database [7, 8] for training artificial neural networks [8].

Second, the results of the DEM simulations are quantified based on useful parameters allowing a further modeling. Specifically, the number and the size distribution of the arising fragments are described in terms of the fragmentation ratio (FR) and the fragment size parameters (ζ_i). Furthermore, the collective post-breakage motion of the fragments is expressed relying on the Weibull probability density functions (PDFs) of the reflection angle α, the spreading angle β and the ratio of the velocity of the fragment with respect to the impact velocity of the agglomerate v_{ratio} (see Fig. 1). Additionally, the ratio of the kinetic energy $\mathrm{ER}_{\mathrm{kin}}$ of the fragments to the incident kinetic energy of the agglomerate is considered [6, 7].

Third, the relationships between the impact conditions and the breakage parameters are approximated using two feed-forward artificial neural networks (see Fig. 2). The first network is trained to predict the number of fragments and the particle size distribution, whereas the second network is devoted for learning the shape (k) and the scale (λ) parameters of the Weibull PDFs as well as the the energy ratio $\mathrm{ER}_{\mathrm{kin}}$. The training is performed in MATLAB applying the Bayesian regularization on the basis of the backpropagation algorithm [8]. After a reasonable training performance is achieved, the details of the trained networks are extracted and incorporated

into the Euler–Lagrange code to be used during the simulations.

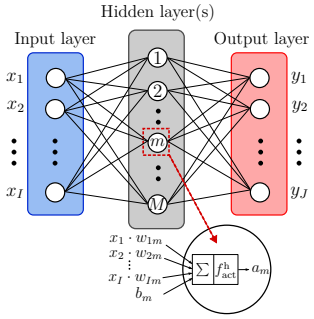

Figure 2: General setup of feed-forward artificial neural network [8].

SOME RESULTS FOR A DRY POWDER DISPERSER

The design of the dry powder disperser and the flow settings are inspired by the experimental study of Weiler [9]. The configuration consists of a duct with a square cross-section and a funnel protruding into the duct discretized by a block-structured grid. The resolution of the grid in the near-wall regions allows a wall-resolved LES. At the inlet of the main duct, inflow data generated by an auxiliary simulation of a single periodic duct are applied. Two different flow rates are investigated: 25 norm-liter/min [low-Re case: Re = 8700] and 200 norm-liter/min [high-Re case: Re = 69,600]. At the top of the funnel agglomerates each consisting of 100 silica particles are discharged at a mass flow rate of 10 mg/s. The diameter of a single primary particle is $d_{\text{pp}} = 0.97$ μm. In earlier studies [4, 5] the described Euler–Lagrange simulation methodology was applied to investigate the deagglomeration due to fluid-induced stresses in this disperser. However, breakage due to wall impact was not considered since a corresponding model was missing. Figure 3a depicts the typical flow field in the device for the high-Re case by contours of the instantaneous streamwise velocity at an arbitrarily chosen snapshot. As visible the funnel protrudes into the duct acting as an obstacle and thus leading to a strong contraction of the cross-section. Consequently, the flow is significantly accelerated below the funnel generating strong shear layers. Furthermore, a recirculation region is observed behind the obstacle. As a results, agglomerates reach the outlet of the funnel under the effect of gravity and emerge with negligible streamwise velocities into the main duct where they abruptly accelerate and pass through regions of high shearing. That gives rise to breakup by mechanisms such as the drag and the rotary stress as depicted in Fig. 3b and 3c, respectively.

In the present investigation, the computations are repeated while taking the wall-impact breakage into account. The motivation is to better explore the role of different breakage phenomena and to attempt enhancing the agreement between the numerically predicted and the experimentally measured dispersion efficiency. The latter is defined in the reference study [9] as the ratio of the median volumetric diameter $d_{50,3}^{\text{CD}}$ of the high-end commercial disperser (CD) to the median volumetric diameter $d_{50,3}^{\text{exp}}$ obtained in the considered lab-scale funnel-duct disperser. These and other evaluations to analyze the performance of the ANN-based breakage model will be included in the full paper.

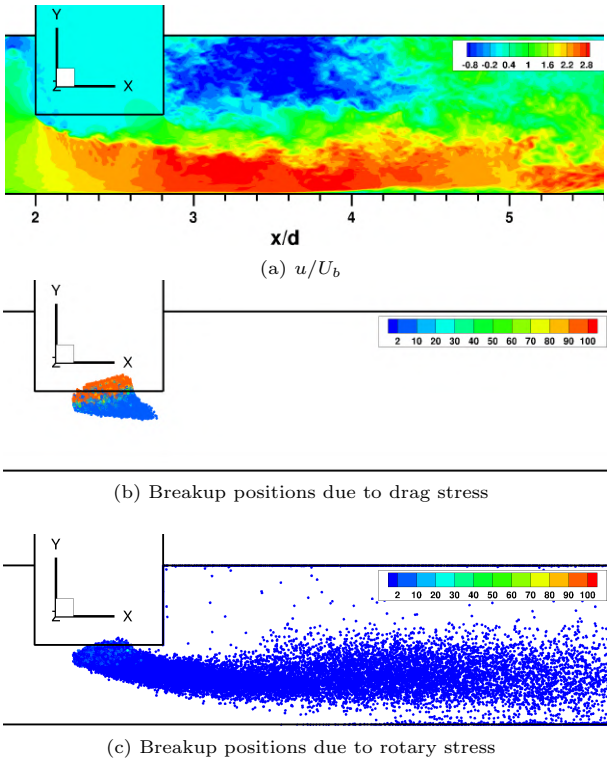

(a) u/U_b

(b) Breakup positions due to drag stress

(c) Breakup positions due to rotary stress

Figure 3: High-Re case: (a) Instantaneous streamwise velocity u/U_b, (b) Breakup positions by drag stress and (c) Breakup positions by rotary stress. The color levels describe the number of primary particles included in the agglomerate at the time of breakage [5].

REFERENCES

[1] Breuer, M. A challenging test case for large–eddy simulation: High Reynolds number circular cylinder flow. Int. J. Heat Fluid Flow **21**(5), 648–654 (2000).

[2] Breuer, M. & Alletto, M. Efficient simulation of particle–laden turbulent flows with high mass loadings using LES. Int. J. Heat Fluid Flow **35**, 2–12 (2012).

[3] Breuer, M. & Almohammed, N. Modeling and simulation of particle agglomeration in turbulent flows using a hard–sphere model with deterministic collision detection and enhanced structure models. Int. J. Multiphase Flow **73**,171–206 (2015).

[4] Breuer, M. & Khalifa, A. Revisiting and improving models for the breakup of compact dry powder agglomerates in turbulent flows within Eulerian–Lagrangian simulations. Powder Technology **348**, 105–125 (2019).

[5] Breuer, M. & Khalifa, A. Refinement of breakup models for compact powder agglomerates exposed to turbulent flows considering relevant time scales. Computers & Fluids **194**, 104315 (2019).

[6] Khalifa, A. & Breuer, M. Data-driven model for the breakage of dry monodisperse agglomerates by wall impact applicable for multiphase flow simulations, Powder Technology **376**, 241–253 (2020).

[7] Khalifa, A. & Breuer, M. An efficient model for the breakage of agglomerates by wall impact applied to Euler–Lagrange LES predictions, Int. J. Multiphase Flow **142**, 103625 (2021).

[8] Khalifa, A., Breuer, M. & Gollwitzer, J. Neural–network based approach for modeling wall–impact breakage of agglomerates in particle–laden flows applied in Euler–Lagrange LES, Int. J. Heat Fluid Flow **94**, 108897 (2022).

[9] Weiler, C. Generierung leicht dispergierbarer Inhalationspulver mittels Sprühtrocknung. Ph.D. thesis, Univ. Mainz, Germany (2008).

WORKSHOP
Direct and Large-Eddy Simulation 13
October 26th-29th 2022, Udine, Italy

HIGH-FIDELITY LARGE-EDDY SIMULATION OF A PULSED JET ACTUATOR

Özgür Yalçın[1], Xavier Gloerfelt[1], Georges Saliba[2], Ahmad Batikh[2], Lucien Baldas[2]
[1] Laboratoire DynFluid, Arts et Métiers Institute of Technology, Paris, France
ozgur.yalcin@ensam.eu
[2] Institut Clément Ader (ICA), Univ. Toulouse, CNRS, INSA, ISAE-SUPAERO, Mines Albi, UPS, Toulouse, France

INTRODUCTION

Pulsed jet actuators (PJAs) are a type of fluidic oscillators that can be served as an active flow control device on lifting bodies. PJAs are able to provide an unsteady periodic blowing in a wide frequency range, which adds momentum to the boundary layer to prevent separation, and thereby enhancing the aerodynamic performances [1]. This kind of fluidic oscillator has no moving parts and induces the oscillation using only its internal unsteady flow dynamics, which makes it attractive in the industry given its robust design and installation [2].

The geometry of the PJA examined in this study is given in Figure 1. In principle, a jet through a nozzle that is supplied by a pressurized flow attaches on the side wall of one of the branches due to the Coanda effect [3]. While the flow partially exits from the actuator outlet located on the same side, the bi-stable attached flow starts to fill the feedback loop with a compression wave. Then, this wave is reflected from the control nozzle, and creates an expansion wave travelling back to the branch exit. This back-and-forth traveling of the pressure wave inside the loop causes pressure differences between two branch exits as well as two control nozzles, which eventually results in a detachment of the main jet [4]. Consequently, the jet is switched quickly to the other side, and the same procedure is repeated. The switching of the pulsed jet provides an oscillatory blowing from the outlets.

The oscillation period, which is one of the critical design parameter, is simply a combination of the travel time of the pressure waves inside the feedback loops and the switching time of the main jet. As the supply pressure and/or the feedback loop length increase, the switching time becomes negligible. For this scenario, some simple algebraic formulas suggested in literature can provide reasonable prediction of the oscillation frequencies. However, the switching time is still being a mystery. There have been very few studies focused on understanding the switching period, which are mainly limited to subsonic nozzle jets [5]. Besides, most of the numerical studies on this topic are based on unsteady Reynolds-averaging Navier-Stokes (URANS) simulations. Although URANS approaches could predict the frequency of the oscillations having negligible switching time [4], they failed to predict the magnitude of the exit velocity [4, 6], which is also essential for the active flow control. In order to obtain internal and external flow fields accurately, and to understand the unsteady and highly compressible flow dynamics of the switching phenomenon, a high-fidelity numerical analysis is required [7]. For this purpose, a high-order Large-Eddy Simulation (LES) inside of the PJA used in [4], but having relatively short feedback loops is presented in this study. This abstract includes the solver description, the computational setup, and the preliminary results, respectively.

FLOW SOLVER AND COMPUTATIONAL SETUP

The numerical simulation is performed using a research code, called MUSICAA (MUltiscale Solver In Computational Aeroacoustics and Aerodynamics). The 3D filtered compressible Navier-Stokes equations are solved by a wall-resolved LES (WRLES) strategy that models the subgrid motions numerically with a Regularization Term approach, i.e. without using an explicit subgrid scale model. The inviscid fluxes are discretized by means of 10^{th}-order standard centred differences whereas 4^{th}-order is used for viscous fluxes. In order to introduce a minimal amount of numerical dissipation while ensuring computational robustness for compressible flow simulations, the centered scheme is supplemented by a high-order nonlinear artificial viscosity term, combining 2^{nd}- and 10^{th}-order derivatives approximated by standard central differences. The activation of the low-order term rests on a modified Jameson's pressure-based shock sensor. A four-stage Runge-Kutta algorithm is used for time integration and a 4^{th}-order implicit residual smoothing method is implemented to enlarge the stability and allow the use of larger timesteps. The curvilinear grid is taken into account by a coordinate transformation. More details can be found in [8].

The computational domain covers both the internal and external fields of the PJA, from the inlet reservoir to the farfield. Figure 1 shows the multiblock domain with structured grids. A subsonic inlet boundary condition based on Riemann invariants is enforced at the inlet by specifying the ratios of the inlet total pressure and temperature values to the freestream static ones as 2.5, and 1.0, respectively. At the farfield boundaries, non-reflective boundary conditions based on linearized Euler equations are applied. All walls are treated by no-slip conditions. The 2D domain given in Figure 1 is extruded uniformly along the 3^{rd}-direction where the faces are connected by periodicity. The depth is chosen as 4.5 times of the nozzle exit width, considering the jet size which is limited by the distance between the nozzle exit to the splitter edge as well as the branch inlet widths. The mesh generation of each block is started by taking the nondimensional wall distance as 1 wall unit. The maximum streamwise nondimensional grid spacing except the feedback loops is 30, whereas the spanwise one is 15. In the whole domain, the grid stretching ratios are no more than 1.05. In total, the grid consists of approximately 25 million nodes.

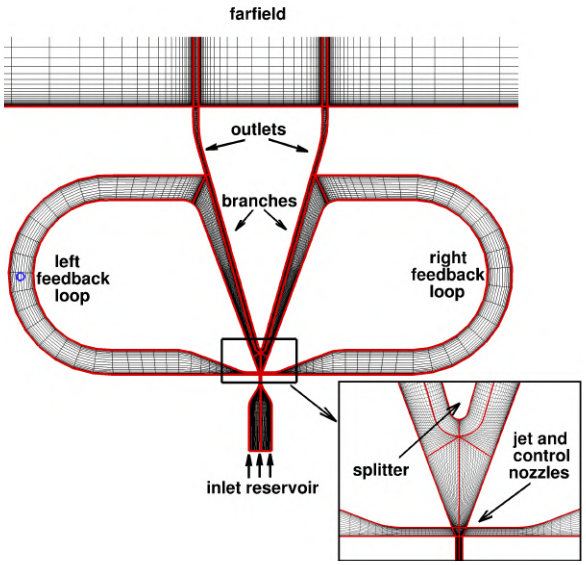

Figure 1: Multiblock structured grid of the PJA. Every four cells are shown. The subframe zooms the switching area.

RESULTS

The simulation is being performed using 508 processors, each of which has a single domain with $30 \times 30 \times 30$ grid nodes. The time step is around 6.0×10^{-10} s, which corresponds to the maximum CFL number of 0.4. So far, the simulation has been carried out only for two oscillation periods after the initial transients have left the computational domain. Presented in Figure 2 is the instantaneous Mach contours of the initial results representing the jet switching from left to right. The flow is choked at the nozzle throat at this inlet-to-outlet pressure ratio. The unsteadiness of the switching process which includes the evolution of the recirculation and separation bubbles can also be observed. Figure 3 shows the normalized pressure time history for one oscillation period at the location of left loop center (see the blue point in Figure 1). The results are compared with the experimental data measured in the National Institute of Applied Sciences of Toulouse. In general, the WRLES result is in fair agreement with the measurements although some discrepancies are observed which might be occurred due to the short simulation time and a relatively coarse grid inside the feedback loops. In addition, the oscillation frequency is computed as approximately 1.1 kHz from both the numerical and experimental data. In the final manuscript, a grid dependency study will be demonstrated. Moreover, the velocity field exiting from the outlets will be compared to hotwire measurements. Additionally, after obtaining the statistics for a sufficient time, the effects of the turbulent structures on the switching mechanism will be investigated in details.

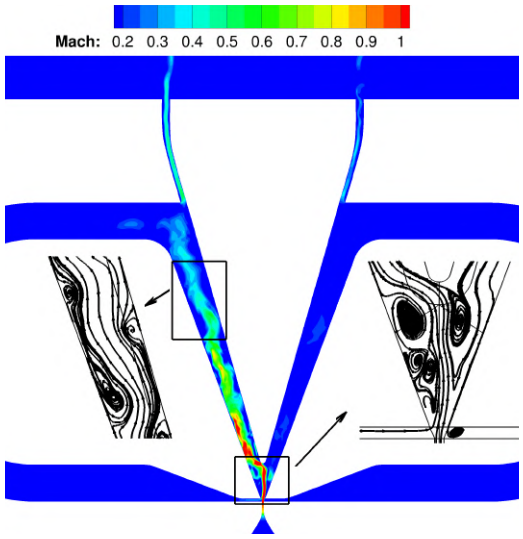

Figure 2: Instantaneous Mach contours during the jet switching from left to right.

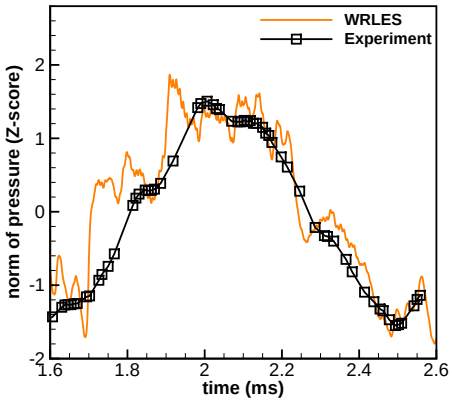

Figure 3: Comparison of pressure time history with measurements on the left loop center.

REFERENCES

[1] L. N. Cattafesta III and M. Sheplak, "Actuators for active flow control," *Annual Review of Fluid Mechanics*, vol. 43, pp. 247–272, 2011.

[2] P. Schlösser and M. Bauer, "Design of a pulsed jet actuator for separation control," *CEAS Aeronautical Journal*, vol. 11, no. 4, pp. 805–812, 2020.

[3] J. Gregory and M. N. Tomac, "A review of fluidic oscillator development and application for flow control," in *43rd AIAA fluid dynamics conference*, p. 2474, 2013.

[4] S. Wang, A. Batikh, L. Baldas, A. Kourta, N. Mazellier, S. Colin, and S. Orieux, "On the modelling of the switching mechanisms of a coanda fluidic oscillator," *Sensors and Actuators A: Physical*, vol. 299, p. 111618, 2019.

[5] H. R. Muller, "A Study of the Dynamic Features of a Wall-Reattachment Fluid Amplifier," *Journal of Basic Engineering*, vol. 86, pp. 819–826, 12 1964.

[6] S. Aram, Y.-T. Lee, H. Shan, and A. Vargas, "Computational fluid dynamic analysis of fluidic actuator for active flow control applications," *AIAA Journal*, vol. 56, no. 1, pp. 111–120, 2018.

[7] J. Kim, P. Moin, and A. Seifert, "Large-eddy simulation-based characterization of suction and oscillatory blowing fluidic actuator," *AIAA journal*, vol. 55, no. 8, pp. 2566–2579, 2017.

[8] X. Gloerfelt and P. Cinnella, "Large eddy simulation requirements for the flow over periodic hills," *Flow, Turbulence and Combustion*, vol. 103, no. 1, pp. 55–91, 2019.

WORKSHOP
Direct and Large-Eddy Simulation 13
October 26th-29th 2022, Udine, Italy

LARGE EDDY SIMULATION OF A LOW PRESSURE TURBINE CASCADE WITH TURBULENT ENDWALL BOUNDARY LAYERS

C. Morsbach[1], M. Bergmann[1], A. Tosun[1], E. Kügeler[1], M. Franke[2]
[1] Department of Numerical Methods, Institute of Propulsion Technology, German Aerospace Center (DLR)
[2] MTU Aero Engines AG, Munich, Germany
christian.morsbach@dlr.de

ABSTRACT

Many large eddy simulation (LES) studies of turbomachinery flows focus on the low-pressure turbine (LPT) due to its low Reynolds number regime of 10^5. To further reduce the simulation costs, the assumption of a statistically 2D flow at the midspan of a turbine blade is often made by applying periodic boundary conditions in the spanwise direction. However, a significant amount of the aerodynamic losses is generated in the secondary flow regions influenced by the interaction of endwall and blade boundary layers [1]. Hence, the next logical step to evaluate the performance of the cascade is to conduct 3D simulations, including the endwall boundary layers, e.g. [2].

The MTU T161, considered in this work, is representative of high lift low-pressure turbine airfoils used in modern jet engines [3]. Its geometry and boundary conditions are in the public domain and it has been the subject of both experimental [4] and numerical [5, 6, 7] investigations. The numerical investigations have focused on operating points with a Mach number of 0.6 and Reynolds numbers of 90,000 and 200,000 based on isentropic exit conditions. In contrast to the intensively studied T106 LPT, this case features diverging end walls at an angle of 12°, such that the flow cannot be studied using a simple spanwise periodic setup. The blades with a chord length of $c = 0.069935\,\mathrm{m}$ and an average aspect ratio of 2.65 are staggered at an angle of 61.72°. The cascade is arranged with pitch to chord ratio of 0.956. Müller-Schindewolffs et al. [5] performed a direct numerical simulation of a section of the profile in which the effect of the diverging end walls was modelled using inviscid walls (termed quasi 3D, Q3D). Various computations of the full 3D configuration were conducted using high-order codes during the EU project TILDA [6, 7]. However, due to the specification of laminar end wall boundary layers and no freestream turbulence at the inflow, no satisfactory results could be obtained. With a full 3D LES including turbulent endwall boundary layers and freestream turbulence, we aim to provide a high quality reference dataset for this configuration.

We use DLR's flow solver for turbomachinery applications, TRACE, to perform an implicit LES of the T161 LPT at a Mach number of 0.6, a Reynolds number of 90,000 and an inflow angle of $\alpha = 41°$. A kinetic-energy-preserving DG scheme is used for spatial discretisation of the implicitly filtered Navier-Stokes equations [8, 9]. The scheme is based on the collocated nodal Discontinuous Galerkin Spectral Element Method (DGSEM) on Legendre-Gauss-Lobatto nodes. The anti-aliasing is performed by the split-formulation of Kennedy and Gruber [10], cf. [11]. Due to the non-uniqueness of the solution at the element interfaces, Roe's approximate Riemann solver is applied for the advective part and the viscous terms are discretised by the Bassi-Rebay 1 scheme [12]. To advance in time, a third-order explicit Runge-Kutta scheme of [13] has been used. Resolved turbulent scales are injected at the inflow boundary using a synthetic turbulence generation (STG) method based on randomized Fourier modes [14].

Our approach to specifying appropriate inflow boundary conditions can be described as follows. We rescale a boundary layer profile from publicly available direct numerical simulation data (`https://www.mech.kth.se/~pschlatt/DATA/`, [15]) to the conditions in the wind tunnel and extract mean velocity, Reynolds stresses, and a turbulent length scale. This leads to a minimal adaptation length of the turbulent boundary layer. Subsequently, an LES of finite length channel flow is used to determine the position of the inflow plane with respect to the blade leading edge to match the momentum thickness of the boundary layer measured upstream of the blade. Once the distance of the inlet to the blade is known, we specify freestream Reynolds stresses and a turbulent length scale in a way to match the measured turbulent decay.

First results were obtained on a preliminary mesh of 312,424 hexahedral elements with a polynomial degree of 5, resulting in $67.5 \cdot 10^6$ degrees of freedom (DOF) per equation. Figure 1 gives an overall impression of the computational domain and the instantaneous vortex structures. Due the choice

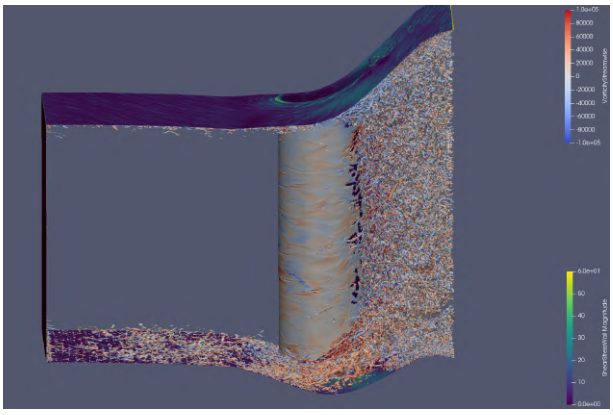

Figure 1: Computational domain and vortex structures.

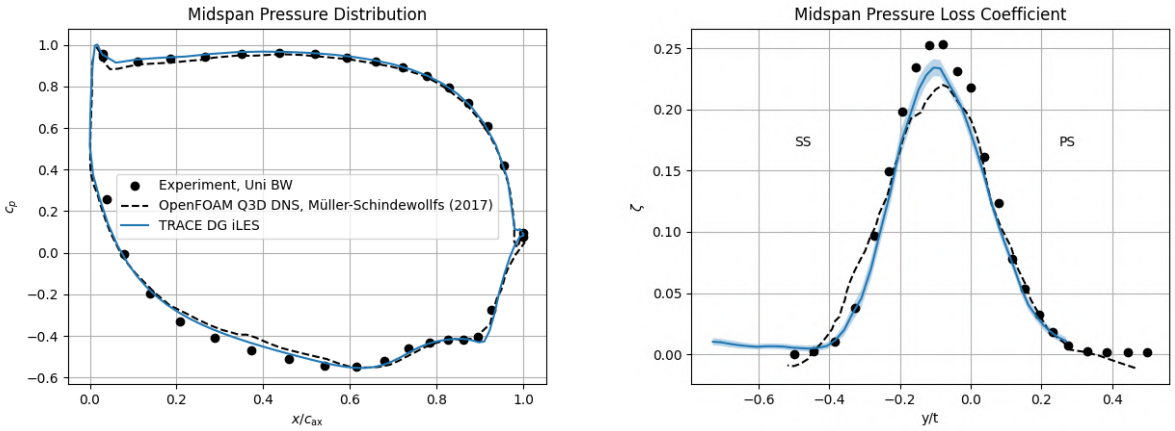

Figure 2: Midspan blade pressure distribution (left) and wake pressure loss coefficient at $x/c_{\mathrm{ax}} = 1.4$.

of λ_2-contour value, the free stream turbulence can only be seen as streamwise vorticity once it impacts the blade wall boundary layer. Figure 2 shows the blade pressure distribution (c_p) and wake pressure loss coefficient ζ at midspan averaged over 37 convective time units based on outflow velocity and chord length. In addition, the 95% confidence interval of the time-averaged quantities is displayed as a shaded area [16]. The Q3D DNS results [5] are plotted as a numerical reference. The results confirm that the operating point of the experiment is matched well and that the separation bubble and resulting wake shape are consistent with both experiments and numerical reference.

In the final paper, we will elaborate on the coupling of the STG with our DG solver and discuss the procedure to obtain appropriate inflow boundary conditions. The mesh will undergo further refinement and mesh sensitivity will be analysed. Finally, we will discuss the various 3D secondary flow structures resolved by this first fully 3D LES of the T161 with proper turbulent inflow boundary conditions.

Geometry and reference experimental results are graciously provided by MTU Aero Engines AG and the University of the Armed Forces in Munich.

REFERENCES

[1]J. D. Denton, "The 1993 igti scholar lecture: Loss mechanisms in turbomachines," *J. Turbomach.*, vol. 115, pp. 621–656, October 1993.

[2]R. Pichler, Y. Zhao, R. Sandberg, V. Michelassi, R. Pacciani, M. Marconcini, and A. Arnone, "Large-Eddy Simulation and RANS Analysis of the End-Wall Flow in a Linear Low-Pressure Turbine Cascade, Part I: Flow and Secondary Vorticity Fields Under Varying Inlet Condition," *Journal of Turbomachinery*, vol. 141, 11 2019. 121005.

[3]J. Gier, I. Raab, T. Schröder, N. Hübner, M. Franke, F. Kennepohl, F. Lippl, T. Germain, and L. Enghardt, "Preparation of aero technology for new generation aircraft engine lp turbines," in *1st CEAS European Air and Space Conference*, (Berlin, Germany), 2007.

[4]M. Martinstetter, R. Niehuis, and M. Franke, "Passive Boundary Layer Control on a Highly Loaded Low Pressure Turbine Cascade," in *Turbo Expo: Power for Land, Sea, and Air*, vol. Volume 7: Turbomachinery, Parts A, B, and C, pp. 1315–1326, 06 2010.

[5]C. Müller-Schindewolffs, R.-D. Baier, J. R. Seume, and F. Herbst, "Direct Numerical Simulation Based Analysis of RANS Predictions of a Low-Pressure Turbine Cascade," *Journal of Turbomachinery*, vol. 139, 03 2017. 081006.

[6]M. Rasquin, K. Hillewaert, A. Colombo, F. Bassi, F. Massa, K. Puri, A. S. Iyer, Y. Abe, F. D. Witherden, B. C. Vermeire, and P. E. Vincent, *Computational Campaign on the MTU T161 Cascade*, pp. 479–518. Cham: Springer International Publishing, 2021.

[7]A. Iyer, Y. Abe, B. Vermeire, P. Bechlars, R. Baier, A. Jameson, F. Witherden, and P. Vincent, "High-order accurate direct numerical simulation of flow over a mtu-t161 low pressure turbine blade," *Computers & Fluids*, vol. 226, p. 104989, 2021.

[8]M. Bergmann, R. Gölden, and C. Morsbach, "Numerical investigation of split form nodal discontinuous galerkin schemes for the implicit les of a turbulence channel flow," *7th European Conference on Computational Fluid Dynamics*, June 2018.

[9]M. Bergmann, C. Morsbach, and G. Ashcroft, "Assessment of split form nodal discontinuous galerkin schemes for the les of a low pressure turbine profile," in *Direct and Large Eddy Simulation XII* (M. García-Villalba, H. Kuerten, and M. V. Salvetti, eds.), (Cham), pp. 365–371, Springer International Publishing, 2020.

[10]C. A. Kennedy and A. Gruber, "Reduced aliasing formulations of the convective terms within the navier-stokes equations for a compressible fluid," *J. Comput. Phys.*, vol. 227, pp. 1676–1700, Jan. 2008.

[11]G. J. Gassner, A. R. Winters, and D. A. Kopriva, "Split form nodal discontinuous Galerkin schemes with summation-by-parts property for the compressible euler equations," *Journal of Computational Physics*, vol. 327, pp. 39–66, Dec. 2016.

[12]F. Bassi and S. Rebay, "A high order discontinuous finite element method for the numerical solution of the compressible navier–stokes equations," *Journal of Computational Physics*, vol. 00, pp. 267–279, July 1996.

[13]C.-W. Shu and S. Osher, "Efficient implementation of essentially non-oscillatory shock-capturing schemes," *Journal of Computational Physics*, vol. 77, pp. 439–471, aug 1988.

[14]M. L. Shur, P. R. Spalart, M. K. Strelets, and A. K. Travin, "Synthetic turbulence generators for RANS-LES interfaces in zonal simulations of aerodynamic and aeroacoustic problems," *Flow Turbul. Combus.*, vol. 93, no. 1, pp. 63–92, 2014.

[15]P. Schlatter and R. Örlü, "Assessment of direct numerical simulation data of turbulent boundary layers," *Journal of Fluid Mechanics*, vol. 659, p. 116–126, 2010.

[16]M. Bergmann, C. Morsbach, G. Ashcroft, and E. Kügeler, "Statistical Error Estimation Methods for Engineering-Relevant Quantities From Scale-Resolving Simulations," *Journal of Turbomachinery*, vol. 144, 10 2021. 031005.

WORKSHOP
Direct and Large-Eddy Simulation 13
October 26th-29th 2022, Udine, Italy

SPECTRAL ELEMENT BASED DIRECT NUMERICAL SIMULATION OF A FLETTNER ROTOR

M. Karp, D. Massaro, N. Jansson, S. Markidis, and P. Schlatter
KTH Royal Institute of Technology, Sweden
makarp@kth.se

INTRODUCTION

As global shipping emits more than 2% of all carbon dioxide in the world, ways to reduce the fuel consumption of ships have been gaining increased interest. One approach, that can reduce the fuel consumption by up to 20% for large ships, is the Flettner rotor, a rotating cylinder that uses the Magnus effect to generate lift and effectively work as a sail. We illustrate a so-called rotor ship that uses Flettner rotors in Figure 1.

While Flettner rotors have been considered in physical experiments [1] and in numerical simulations based on the Reynolds Averaged Navier-Stokes (RANS) [2], no direct numerical simulation (DNS) of a Flettner rotor in a turbulent boundary layer has been carried out. In the present work, we utilize our new solver Neko, based on the spectral element method, to carry out a large-scale, GPU-powered, DNS of the flow around a Flettner rotor at reduced but yet relevant Reynolds numbers.

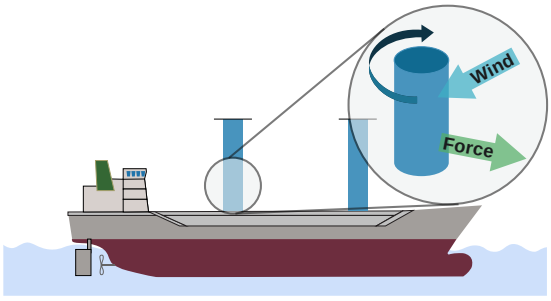

Figure 1: An illustration of a rotor ship which uses Flettner rotors (in blue) in addition to conventional propulsion. We highlight how the rotor and the wind coming from the side of the ship generates a force directed forward.

NEKO

Our simulation is carried out with our new CFD solver Neko, a solver that owes it homage to Nek5000, a spectral element code that has been largely acclaimed for its scalability and accuracy for high-fidelity computational fluid dynamics. Neko is based on similar numerical methods as Nek5000, but differs in that it also accommodates modern computer architectures such as GPUs and has an object-oriented codebase written in modern Fortran [3]. The equations under consideration are the incompressible, non-dimensional, Navier-Stokes (NS) equations:

$$\nabla \cdot \mathbf{v} = 0,$$
$$\frac{\partial \mathbf{v}}{\partial t} + \mathbf{v} \cdot \nabla \mathbf{v} = -\nabla p + \frac{1}{Re} \nabla^2 \mathbf{v} + \mathbf{F}$$

where Re is a Reynolds number, $\mathbf{v}$ is the instantaneous velocity field, p is the non-dimensional pressure, and $\mathbf{F}$ an external forcing/source term. We integrate the incompressible Navier Stokes in time using a spectral element method working on hexahedral elements. The combination of this discretization and a matrix-free approach to evaluate the linear system leads to high accuracy, scalability and can accommodate complex geometries. Neko uses the so-called $P_N - P_N$ splitting to split the pressure and velocity solve at each time step [4]. This approach is convenient in part because of the small splitting error and also because we do not need to introduce a staggered grid for the pressure and velocity solve respectively.

The linear system that arises from the temporal and spatial discretization is then solved using a Krylov subspace method such as the generalized minimal residual method (GMRES) or the conjugate gradient method (CG). An important aspect is that for the pressure solve, as it is the main source of stiffness in incompressible NS, we utilize an additive Schwarz multigrid method with a coarse grid solve as a preconditioner.

We illustrate the strong scaling efficiency of our approach in Figure 2 where we compare two state-of-the-art computer architectures, the Nvidia A100 GPU and the AMD EPYC 7742 CPU. We observe excellent parallel scaling, enabling us to perform large-scale DNS on modern heterogeneous computer systems. Neko is under active development new features are continually introduced.

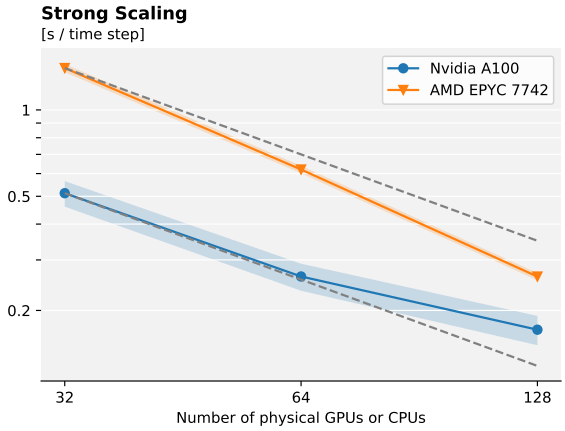

Figure 2: The strong scaling performance of Neko for our Flettner rotor case on two different computing units. The shaded areas correspond to one standard deviation.

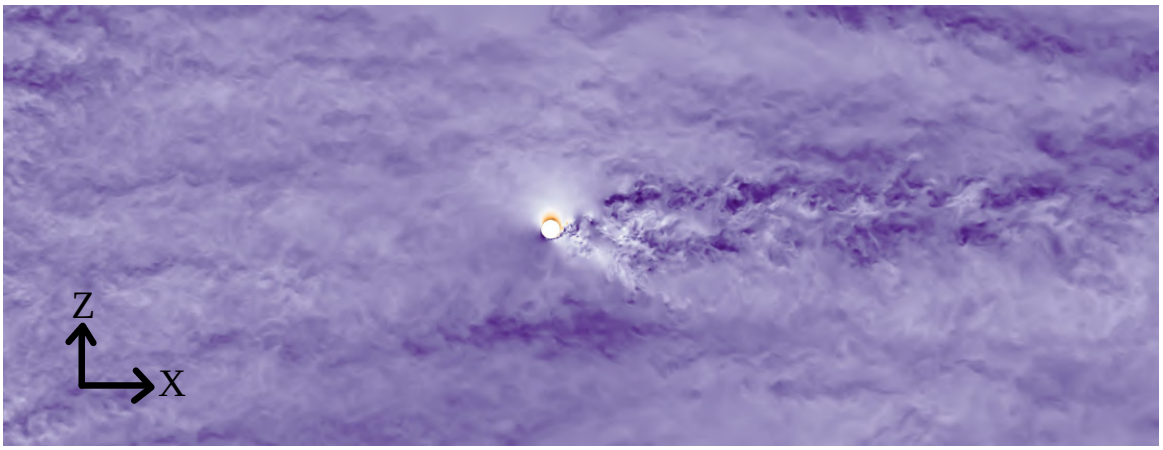

Figure 3: A zoomed-in visualization of the flow around our simulated Flettner rotor showing the $x-z$ plane at $y = 0.1h$ where h is the height of the open-channel. We show the velocity magnitude where a lower velocity is darker violet and a higher velocity becomes white then orange.

EXPERIMENTAL SETUP

The flow case under consideration is a Flettner rotor submerged in a turbulent boundary layer. Our simulation setup is an open channel with forced tripping upstream of the rotor. We apply this forcing in order to trip the boundary layer into becoming turbulent, reducing the size of the computational domain. The mesh is Cartesian with a block-structured configuration. The mesh takes into account the resolution requirements in the different regions and the flow physics. It counts 930070 spectral elements, which turns into $n \approx 0.48$ billion unique grid points as we use spectral elements of order is $N = 7$. The flow is characterized by three non-dimensional numbers

- the ratio between the half-channel height h and the cylinder diameter $\gamma = h/D$ as a proxy for the boundary-layer thickness
- the Reynolds number computed with the center-line velocity u_{cl} and the height h of the open channel: $Re_{cl} = u_{cl}h/\nu$, where ν is the kinematic fluid viscosity
- the ratio between the cylinder spinning velocity and the center-line velocity $\alpha = u_{sp}/u_{cl}$.

In our initial simulation we set $Re_{cl} = 30\ 000$, $\gamma = 10$, and $\alpha = 3$. This choice of parameters aims to be close to a real configuration when a Flettner rotor is used, but at a lower Re as we consider DNS. At the inflow ($x = -50D$) the Dirichlet boundary condition (BC) prescribes a turbulent channel velocity profile with the power-law $u_x/u_{cl} = (y/h)^{1/7}$. Unlike the parabolic laminar profile, it is flatter in the central part of the channel and drops rapidly at the walls. The rotor is resolved in the mesh, and a Dirichlet-like BC is used as well, prescribing the wall impermeability and setting a rotational velocity $u_\theta = u_{sp} = \alpha u_{cl}$ with $\alpha = 3$ and $u_\rho = 0$. We consider a cylinder of length equal to the boundary-layer thickness in the y direction, as a consequence symmetric mixex boundary conditions are prescribed at the top surface ($\mathbf{u} \cdot \mathbf{n} = 0$ with $(\nabla \mathbf{u} \cdot \mathbf{t}) \cdot \mathbf{n} = 0$). For the spanwise boundaries mixed conditions allowing transpiration are used, similar to the open boundary, but prescribing a Dirichlet condition for the velocity in the non-normal directions.

INITIAL RESULTS

The Flettner rotor flow case is under active investigation with each run taking a few days on 100 GPUs. We illustrate a snapshot of the velocity magnitude in Figure 3. Our initial findings are that our computed spanwise lift coefficient $C_l = 7.464$ is in excellent agreement with experimental data from [1] where this coefficient was measured to be between 7 and 8 for the same $\alpha = 3$. While our Re is smaller, the lift coefficient does not seem to exhibit a high dependence on the Reynolds number. For the drag, on the other hand, we have that the drag coefficient $C_d = 1.092$ is highly dependent on the Reynolds number. We observe that there is a strong interaction between the rotor and the turbulent boundary layer. We are currently actively analyzing our simulation data further. At the conference we will present standard turbulence statistics that can readily compare to field measurements. However, the main benefit of DNS comes from the availability of the full 3D flow fields, which allows to perform various modal analyses in order to identify the interaction between the boundary-layer shear and the vortex shedding downstream of the rotating cylinder. In particular, for future deployment of Flettner rotors the question of more efficient designs is relevant, which can be guided with simulation data as the current one. Therefore, we will present the various coherent modes in the flow case.

REFERENCES

[1]Bordogna, G., Muggiasca, S, Giappino, S., Belloli, M., Keuning, J., and Huijsmans, R. : Experiments on a Flettner rotor at critical and super-critical Reynolds numbers, *J. Wind Eng. Ind. Aerod.*, **188**, 193—204, (2019).

[2]De Marco, A., Mancini S., Pensa, C., Calise, G., and De Luca, F. : Flettner rotor concept for marine applications: A systematic study, *Int. J. of Rot. Mach.*, (2016).

[3]Jansson, N., Karp, M., Podobas, A., Markidis, S., and Schlatter, P. : Neko: A Modern, Portable, and Scalable Framework for High-Fidelity Computational Fluid Dynamics, `https://arxiv.org/abs/2107.01243`, (2021).

[4]Karniadakis, G. E., Israeli, M., and Orszag, S. A. : High-order splitting methods for the incompressible Navier-Stokes equations. *J. Comput. Phys.*, **97(2)**, 414-443, (1991).

WORKSHOP
Direct and Large-Eddy Simulation 13
October 26th-29th 2022, Udine, Italy

LES OF THE TRANSITIONAL FLOW INSIDE A CYLINDRICAL ROTOR CAVITY SUPPLIED BY A TURBULENT PIPE FLOW

T. Hultsch, J. Stiller, F. Rüdiger, J. Fröhlich
Institute of Fluid Mechanics
Technische Universität Dresden, Germany
thomas.hultsch@tu-dresden.de

INTRODUCTION

A new cooling concept of electric vehicle drives with high power density is the rotor internal cooling. A turbulent pipe flow enters a cylindrical cavity in the rotor with bigger radius forming a jet. The flow is deflected in the cavity and leaves it through an annular duct formed by the stationary pipe wall on the inside and the rotor wall on the outside. This creates a complex transitional flow. The basic effects of turbulence intensification and damping by flow rotation are known in simple configurations, such as a rotating pipe [2], [4], [5], but so far have not been investigated in the present much more complex flow situation. The general structure of the flow and the turbulence properties will be compared for two cases: with and without rotation. In specific areas the turbulence is enhanced or reduced, which has significant impact on the heat transfer in the cooling application.

SETUP

Fig. 1 shows the considered configuration. The flow enters the domain through a stationary pipe with diameter d and a length of $L_\mathrm{p} = 15d$. The turbulence is activated by a tripping force [6] near the inlet resulting in a developed turbulent pipe flow with $Re = 17640$ at the outlet of the pipe based on the bulk velocity U_b. The cylindrical cavity has a length of $L_\mathrm{c} = 5d$ and a diameter of $D = 2R = (7/3)d$. The annular duct leading to the outlet of the domain has a width of $s = (7/12)d$ and a length of $L_\mathrm{a} = 12s$. The outlet of the domain is located in the outer wall at the end of the annular duct. A blue coloring indicates walls rotating around the x-axis. The ratio of the circumferential velocity of the wall to the bulk velocity in the pipe is $Ro = \Omega R/U_\mathrm{b} = 2.0$ in the rotating case. When a statistically stationary flow was reached, the time averaging was started. The flow was averaged for about 18.5 revolutions of the rotor wall, which is 4100 viscous time units of the pipe flow.

NUMERICAL METHOD AND DISCRETISATION

The flow was simulated with the spectral element solver Semtex [1], which solves the incompressible Navier-Stokes equations in an axisymmetric domain using a cylindrical coordinate system. The domain was discretised by 5253 elements with a polynomial order of 10 in the meridional plane. With such a grid the wall boundary layers are fully resolved for the present physical parameters. In the circumferential direction a Fourier expansion with 240 modes was used. The time integration was carried out with a third-order semi-implicit scheme.

To stabilize the solver and account for the smallest turbulent eddies a spectral vanishing viscosity (SVV) approach was used. The radially shifted SVV kernel of Koal et al. [3] was adapted and applied in circumferential direction. Local maxima of the additional dissipation generated by the SVV remain in the same order of magnitude as the resolved dissipation. The volume averaged ratio of the additional dissipation to the resolved dissipation is about 12 %.

RESULTS

Fig. 2, top, shows the mean flow, averaged in time and circumferential direction. A snapshot of the instantaneous flow is presented below. When the jet reaches the back wall of the cavity the fluid starts to rotate with the wall. Centrifugal forces accelerate the flow in radial direction along the back wall. The rotating boundary layer along the outer wall remains very thin in the jet region ($x \geq 0.25\,L_\mathrm{c}$) since the incoming non rotating fluid of the jet inhibits the rotation. The turbulent shear layer of the jet causes high momentum exchange. This results in a steep velocity gradient and enhanced turbulence production near the rotating wall. Fig. 3 shows a radial profile of the turbulent kinetic energy (TKE) at $x = 0.25\,L_\mathrm{c}$. Near the outer wall ($r = R$) a clear peak of TKE is observed in the rotating case. On the other hand, the TKE of the jet shear layer between $r = 0.3\,R$ and $r = 0.9\,R$ is slightly reduced. Close to the pipe outlet (and annulus inlet) the influence of the jet decreases and the rotating boundary layer grows radpidly ($x \approx 0.2\,L_\mathrm{c}$). This causes an increase of pressure at the rotating wall due to the centrifugal force. The axial flow towards the annular duct is deflected radially inwards by the high pressure area. This can be seen from the streamlines in fig. 2, top.

In the annular duct the situation changes completely. The flow rotates within the entire cross-section and the axial bulk velocity is lower ($U_\mathrm{b,a} = 0.25\,U_\mathrm{b}$). The circumferential velocity component is dominating the flow causing a strong reduction of TKE as can be seen in fig. 4. Especially near the rotating wall the flow laminarises. But even in the inner half of the duct ($r \leq 0.75\,R$), where the rotation is low, the turbulence is significantly reduced.

The final contribution will show the turbulence properties of the rotor internal flow in more detail. A better understand-

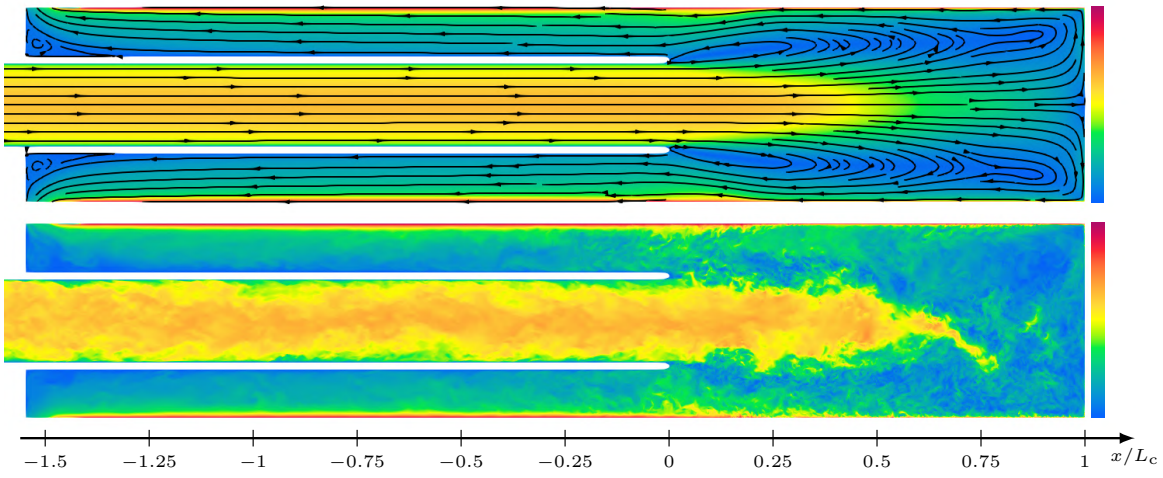

Figure 2: Flow in rotating cavity with $Ro = 2$. Top: Streamlines and velocity magnitude of mean flow. Bottom: Snapshot of the instantaneous velocity magnitude. Inflow pipe not shown.

ing of the mechanisms is crucial to develop optimized cooling concepts. The specific enhanced or reduced level of turbulence near the rotor wall is a key quantity in this respect. So far a similar LES of this type of flow is not known to the authors.

REFERENCES

[1]Blackburn, H.M., Lee, D., Albrecht, T. and Singh, J. : Semtex: A spectral element–Fourier solver for the incompressible Navier–Stokes equations in cylindrical or Cartesian coordinates, *Comput. Phys. Commun.*, **245**, 106804 (2019).

[2]Imao, S., Itoh, M. and Harada, T. : Turbulent characteristics of the flow in an axially rotating pipe, *Int. J. Heat Fluid Flow*, **17**, 444–451 (1996).

[3]Koal, K., Stiller, J. and Blackburn, H.M. : Adapting the spectral vanishing viscosity method for large-eddy simulations in cylindrical configurations, *J. Comput. Phys.*, **231**, 3389–3405 (2012).

[4]Nishibori, K., Kikuyama, K. and Murakami, M. : Laminarization of turbulent flow in the inlet region of an axially rotating pipe, *JSME*, **30**, 255–262 (1987).

[5]Orlandi, P. and Fatica, M. : Direct simulations of turbulent flow in a pipe rotating about its axis, *J. Fluid Mech.*, **343**, 43–72 (1997).

[6]Schlatter, P. and Örlü, R. : Turbulent boundary layers at moderate Reynolds numbers: inflow length and tripping effects, *J. Fluid Mech.*, **710**, 5–34 (2012).

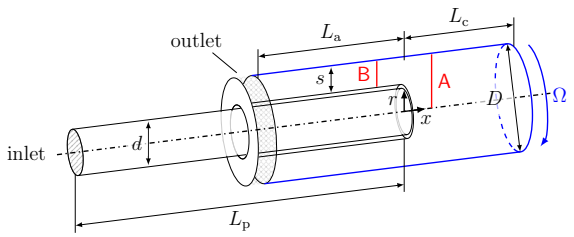

Figure 1: Simulation domain. Radial direction enlarged by a factor 2. Blue walls indicate possible rotation around the x-axis. The vertical red lines A and B mark the position of the profiles in figures 3 and 4, respectively.

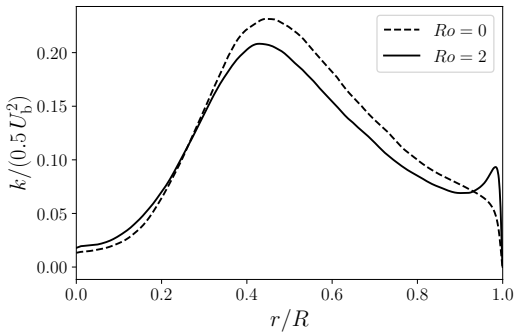

Figure 3: Profile of TKE in jet region at $x = 0.25\,L_c$ (line A in fig. 1). Comparison of rotating case (solid line) and non rotating case (dashed line).

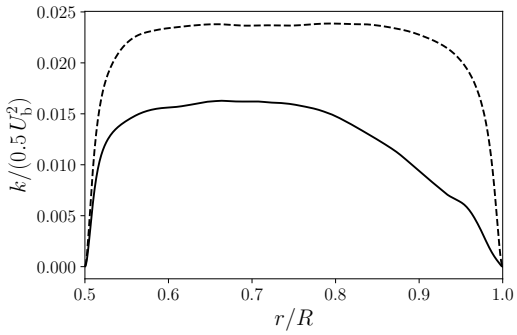

Figure 4: Profile of TKE in annular duct at $x = -0.25\,L_c$ (line B in fig. 1). Comparison of rotating case (solid line) and non rotating case (dashed line).

Session: Numerical techniques

Friday, October 28, 2022

09:50 – 10:50

WORKSHOP
Direct and Large-Eddy Simulation 13
October 26th-29th 2022, Udine, Italy

TOWARDS A NUMERICAL PROOF OF TURBULENCE CLOSURE

G. Ortali[1,2], A. Corbetta[1], G. Rozza[2] and F. Toschi[1]
[1] Eindhoven University of Technology, Eindhoven, The Netherlands
[2] Sissa (International School for Advanced Studies), Trieste, Italy

INTRODUCTION

In this work we tackle the issue of defining a subgrid closure model that, employed in a LES approach in the contect of homogeneous isotropic turbulence, exhibits correct scaling laws in high order structure functions, encompassing intermittent effects and energy cascade dynamics.

Due to the massive amount of data needed to reach converged statistics of high order statistical moments, we consider the simplified setting of Shell Models of Turbulence [2], reduced dynamical systems of Ordinary Differential Equations that describe the dynamics of homogeneous isotropic turbulence in Fourier space via a (small) number of complex-valued scalars u_n, $n = 0, 1, \ldots, \infty$, whose magnitude represents the energy of fluctuations at representative logarithmically equispaced spatial scales with wavelength $k_n = k_0\lambda^n$ (usually $\lambda = 2$).

Such models have been shown to reproduce, using a small number of DOFs, the main features of the turbulent energy cascade, including intermittency and anomalous scaling exponents practically indistinguishable from the real ones [2].

METHODOLOGY

The challenge of subgrid closure in the context of the shell model consists in resolving only a subset of the shell variables, $\{u_n, n = 0, \ldots, N_{cut}\}$, above an arbitrary *subgrid cutoff scale* $N_{cut} \ll N_\eta$, where N_η corresponds to the Kolmogorov scale (i.e. k_{N_η} is the wavelenght of the Kolmogorov scale). This entails modelling the effects of the small scales $\{u_n, n = N_{cut} + 1, \ldots, N_\eta\}$ on the large scales.

This problem has been recently adressed in [3], where it has been formalized in terms of reduced systems of probability distributions, allowing a precise definition of an optimal subgrid model, although practically intractable, and a series of systematic approximations, yet lacking relevant physical features (correct scaling, energy backscatter).

Our method employs a novel custom-made Deep Learning architecture comprising a classical 4^{th} order Runge-Kutta integration scheme for the large scales of turbulence, augmented with a Recurrent Artificial Neural Network to obtain the values of the fluxes to the small scales, modelling the subgrid closure.

RESULTS AND CONCLUSION

Using this approach, we are able to reproduce, within statistical error bars, the intermittent behavior of high Reynolds turbulent flows, obtaining the correct scaling laws for high order Eulerian (Figure 1) and Lagrangian structure functions, and outperforming classical physics based methods [3].

This work demonstrates the capability of Machine Learning to capture complex multiscale dynamics and reproduce complex multi-scale and multi-time non-gaussian behaviors. Generalizing our approach to 3d Navier-Stokes turbulence still requires overcoming several challenges. These include having to deal with many more subgrid variables to be modeled and by the computational cost of producing enough high-quality 3d training data.

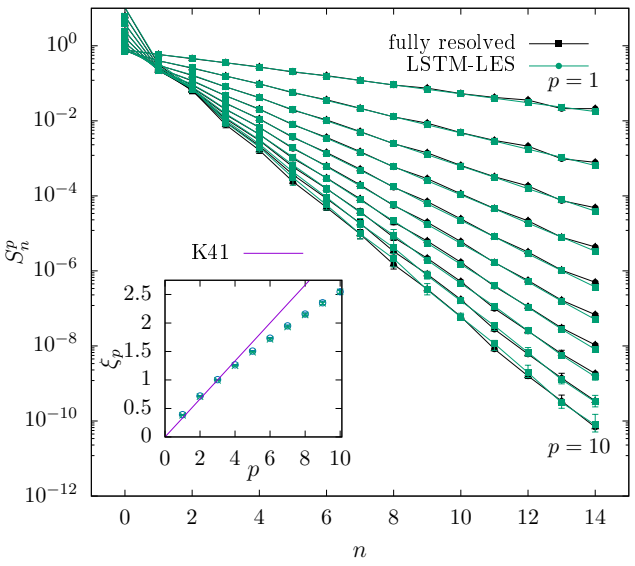

Figure 1: Eulerian structure functions S_n^p vs. shell index n, in lin-log scale, for orders $p = 1, \ldots, 10$ and with subgrid cutoff at shell $n = 14$, comparison between fully resolved model (FRM) and our LSTM-LES model. Inset plot: anomalous scaling exponents $/xi_p$ of Eulerian structure fuctions, $S_n^p \approx k_n^{\xi_p}$ for the fully resolved model (FRM), our LSTM-LES model and the K41 predictions

REFERENCES

[1]Ortali, G. and Corbetta, A. and Rozza, G. and Toschi, F., Towards a Numerical Proof of Turbulence Closure, *arXiv:2202.09289*
[2]Biferale, L., Shell models of energy cascade in turbulence,*Annual Review of Fluid Mechanics* **35**, 441–468 (2003).
[3]Biferale, L. and Mailybaev, A. A. and Parisi, G., Optimal subgrid scheme for shell models of turbulence,*Physical Review E* **95**, 2470–0053 (2017).

WORKSHOP
Direct and Large-Eddy Simulation 13
October 26th-29th 2022, Udine, Italy

ON A CONSERVATIVE SOLUTION TO CHECKERBOARDING: EXAMINING THE DISCRETE LAPLACIAN KERNEL USING MESH CONNECTIVITY

J.A. Hopman[1], **F.X. Trias**[1], **J. Rigola**[1]
[1] Heat and Mass Transfer Technological Center
Technical University of Catalonia, Carrer Colom 11, 08222 Terrassa (Barcelona), Spain.
jannes.hopman@upc.edu

INTRODUCTION

CFD codes that are used for industrial applications commonly use a collocated grid arrangement to calculate the physical flow variables. The main advantages of this arrangement, in comparison to the staggered one, are the possibility to extend the solution domain to more complex geometries and a more efficient data structure, which are both of great importance in industry. When using a central differencing scheme to discretise the continuous operators of the Navier-Stokes equations, a wide stencil is obtained for the Laplacian operator. This wide stencil, in turn, leads to a decoupling between odd and even grid points of the pressure field that results from the pressure Poisson equation. This decoupling can lead to nonphysical, spurious modes in the solution, a problem commonly known as the checkerboard problem [1].

Generally, this problem is avoided by using a compact stencil Laplacian. A method to do so was first developed by Rhie and Chow [2]. This method solves the problem of decoupled grid points and eliminates the possibility of spurious modes in the pressure field. However, this method introduces nonphysical, numerical dissipation of kinetic energy [2, 3]. This dissipation disrupts the delicate interaction between convective transport and physical dissipation, especially at the smallest scales of motion. By doing so, it becomes impossible to capture the essence of turbulence, which is of high importance in accurate LES and DNS simulations [4].

Many commercial codes favour the extra stability that this method offers at the price of a lower accuracy. Unconditional stability, however, can also be achieved by mimicking the underlying symmetry properties of the continuous operators of the Navier-Stokes equations, when discretising them. A method that does this was developed for staggered Cartesian grid arrangements by Verstappen and Veldman [4] and later extended to collocated unstructured grids by Trias *et al.* [5]. Since the kinetic energy is conserved and stability is unconditional, using the method of Rhie and Chow comes at a higher price and an alternative method should be sought after. One method mentioned here is the one described by Larsson and Iaccarino [6], in which the kernel of the discrete Laplacian operator matrix is determined and used to eliminate the spurious modes. However, on non-Cartesian grids, this method involves performing a singular value decomposition (SVD), for which the computational cost grows exponentially with the number of grid points, as $\mathcal{O}(N_{grid}^3)$, making this method nonviable for industrial applications [7].

In this work a conservative solution to the checkerboard problem will be examined by looking at the relation between the connectivity of the mesh and the kernel of the discrete Laplacian operator matrix. By understanding this relation better, a prediction can be made for a set of vectors that span the nullspace, and by projecting the pressure solution field onto this nullspace, the spurious modes can be eliminated. The relation between the mesh and the kernel will first be examined, after which a method is developed to predict and remove spurious modes, this method is then tested and compared to the conventional Rhie-Chow interpolation method. The new method could prove to be especially useful in the field of magnetohydrodynamics, where a second Poisson equation for the electric potential has to be solved and stability and conservative properties are important to accurately balance high opposing forces.

RELATION BETWEEN THE MESH AND THE KERNEL

Let the discrete wide stencil Laplacian operator be denoted by $L_c = M\Gamma_{cs}\Gamma_{sc}G$, which follows the discretisation of Trias *et al.* [5] and is a chain operations: (1) face gradient, (2) face-to-cell interpolation, (3) cell-to-face interpolation and (4) divergence. The first thing to note is that the gradient at cell i is given by:

$$\begin{aligned}\left[\Gamma_{sc}G\phi_c\right]_i &= \frac{1}{2\left[\Omega_c\right]_{i,i}}\sum_{f\in F_f(i)}\left[\Omega_s\right]_{f,f}\frac{\phi_n-\phi_i}{\delta_{nf}}\mathbf{n}_{if}\\ &= \frac{1}{2\left[\Omega_c\right]_{i,i}}\sum_{f\in F_f(i)}A_f\phi_n\mathbf{n}_{if}\end{aligned} \tag{1}$$

because the sum of outward pointing face area vectors always equals 0:

$$-\frac{1}{2\left[\Omega_c\right]_{i,i}}\phi_i\sum_{f\in F_f(i)}A_f\mathbf{n}_{if}=0 \tag{2}$$

Therefore, the value in the central cell i does not contribute to the gradient in the central cell itself. Similarly, the cell-centered divergence at cell i is given by:

$$\begin{aligned}\left[M\Gamma_{cs}\boldsymbol{\psi}_c\right]_i &= \frac{1}{2}\sum_{f\in F_f(i)}\left(\boldsymbol{\psi}_i+\boldsymbol{\psi}_n\right)\cdot\mathbf{n}_{if}A_f\\ &= \frac{1}{2}\sum_{f\in F_f(i)}\boldsymbol{\psi}_n\cdot\mathbf{n}_{if}A_f\end{aligned} \tag{3}$$

Again, the value in the central cell i does not contribute to the divergence in the central cell itself. L_c is a sequence of both operators and will therefore only potentially connect cell i to cell k, if they share a neighbour j:

$$[L_c]_{i,k} = \sum_j \frac{1}{4\,[\Omega_c]_j} \left(A_{i,j}\mathbf{n}_{i,j}\right) \cdot \left(A_{j,k}\mathbf{n}_{j,k}\right) \tag{4}$$

If we use $A_{j,i}\mathbf{n}_{j,i} = -\sum_{k\neq i} A_{j,k}\mathbf{n}_{j,k}$, then we can verify that L_c should be negative-definite symmetrical, with columns and rows summing to 0:

$$\begin{aligned}[L_c]_{i,i} &= \sum_j \frac{1}{4\,[\Omega_c]_j} \left(A_{i,j}\mathbf{n}_{i,j}\right) \cdot \left(A_{j,i}\mathbf{n}_{j,i}\right) \\ &= -\sum_{k\neq i}\sum_j \frac{1}{4\,[\Omega_c]_j} \left(A_{i,j}\mathbf{n}_{i,j}\right) \cdot \left(A_{j,k}\mathbf{n}_{j,k}\right)\end{aligned} \tag{5}$$

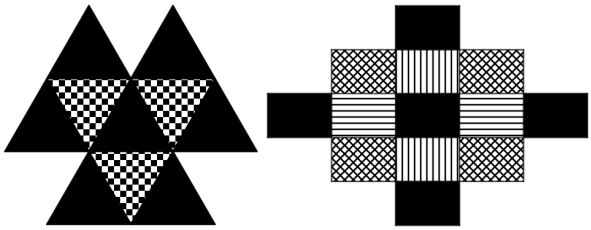

Figure 1: 2 disconnected cell groups in a regular triangular mesh (left) and $2^{dim} = 4$ in a Cartesian mesh (right)

Now we can predict from equation (4) that an extra vector, in addition to the constant vector, is needed to span the nullspace of L_c, if an odd-even parity can be established in the mesh, as seen in figure 1. In the special case that the dot product in (4) equals zero due to orthogonal faces, there will not be any connection. Therefore, in Cartesian meshes, no diagonal connections exist and the number of disconnected cell groups will equal 2^{dim}, as will the rank of the nullspace of L_c.

0	1	2	3	4	5
6	7	8	9	10	11
12	13	14	15	16	17
18	19	20	21	22	23
24	25	26	27	28	29
30	31	32	33	34	35

(a) Conventional

(b) L_c structure

0	9	1	10	2	11
18	27	19	28	20	29
3	12	4	13	5	14
21	30	22	31	23	32
6	15	7	16	8	17
24	33	25	34	26	35

(c) Deliberate

(d) Block diagonalised

Figure 2: Representation of Laplacian matrix entries for a Cartesian 6×6 mesh, with cyclic boundaries

The disconnected groups can also be visualised with a block diagonalisation of the Laplacian matrix. When using conventional cell numbering, as seen in figure 2a, the disconnection is not immediately apparent from the matrix in figure 2b. When renumbering the cells deliberately, as done in figure 2c, the separation is evident from the block diagonal matrix, figure 2d. This block diagonalisation is not possible for the compact Laplacian. One final way to express this relation, in terms of graph connectivity, is that the rank of the nullspace equals the number of connected components in the graph Laplacian, which is constructed using mesh connectivity. Since the connectivity can be derived from the mesh and is tied to the kernel of L_c, the spurious modes can be removed from the solution while avoiding the high cost of the SVD.

COMPUTATIONAL VERIFICATION

A solver is developed with symmetry-preserving discretisation of the continuous operators [5], with optionally compact or wide stencil Laplacian in the pressure Poisson equation. A priori a set of nullspace spanning vectors will be predicted from the mesh connectivity, so that spurious modes can be removed in calculating the pressure field. A Taylor-Green vortex and a turbulent channel flow, figure 3, will be used to verify the method, by monitoring evolution of kinetic energy and the presence of spurious modes. It is expected that the compact stencil Laplacian will show numerical dissipation and that the wide stencil Laplacian will show checkerboarding, whereas the new approach solves both problems.

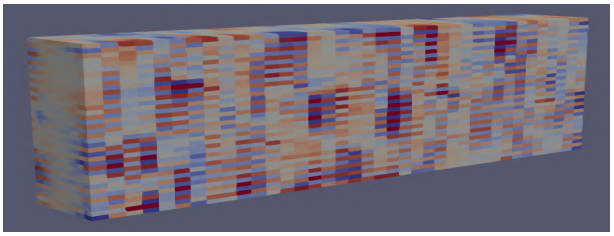

Figure 3: Channel flow with checkerboarding

REFERENCES

[1]Ferziger, J. H., Perić, M., & Street, R. L. (2002). Computational methods for fluid dynamics (Vol. 3, pp. 196-200). Berlin: springer.

[2]Rhie, C. M., & Chow, W. L. (1983). Numerical study of the turbulent flow past an airfoil with trailing edge separation. AIAA journal, 21(11), 1525-1532.

[3]Felten, F. N., & Lund, T. S. (2006). Kinetic energy conservation issues associated with the collocated mesh scheme for incompressible flow. Journal of Computational Physics, 215(2), 465-484.

[4]Verstappen, R. W. C. P., & Veldman, A. E. P. (2003). Symmetry-preserving discretization of turbulent flow. Journal of Computational Physics, 187(1), 343-368.

[5]Trias, F. X., Lehmkuhl, O., Oliva, A., Pérez-Segarra, C. D., & Verstappen, R. W. C. P. (2014). Symmetry-preserving discretization of Navier–Stokes equations on collocated unstructured grids. Journal of Computational Physics, 258, 246-267.

[6]Larsson, J., & Iaccarino, G. (2010). A co-located incompressible Navier-Stokes solver with exact mass, momentum and kinetic energy conservation in the inviscid limit. Journal of Computational Physics, 229(12), 4425-4430.

[7]Golub, G. H., & Van Loan, C. F. (1996). Matrix computations, johns hopkins u. Math. Sci., Johns Hopkins University Press, Baltimore, MD.

WORKSHOP
Direct and Large-Eddy Simulation 13
October 26th-29th 2022, Udine, Italy

AN ENERGY-PRESERVING UNCONDITIONALLY STABLE FRACTIONAL STEP METHOD FOR DNS/LES ON COLLOCATED UNSTRUCTURED GRIDS

D. Santos, F.X. Trias, G. Colomer, A. Oliva
[1] Heat and Mass Transfer Technological Center (CTTC)
Technical University of Catalonia, C/Colom 11, 08222 Terrassa (Barcelona), Spain
daniel.santos.serrano@upc.edu
francesc.xavier.trias@upc.edu
guillem.colomer@upc.edu
asensio.oliva@upc.edu

INTRODUCTION

A finite-volume discretization over unstructured meshes is the most used formulation to solve Navier-Stokes equations by many general purpose CFD packages codes as OpenFOAM or ANSYS-Fluent. These codes work with collocated stencil formulations, that is, once the equations are discretized, an algorithm goes cell by cell computing the required quantities.

On the other hand, algebraic formulations maintain the equations in matrix-vector form, and compute the required quantities by using these matrices and vectors. A collocated fully-conservative algebraic symmetry-preserving formulation of incompressible Navier-Stokes equations was proposed by Trias et. al. in [1], assuming n control volumes and m faces:

$$\Omega \frac{d\mathbf{u}_c}{dt} + \mathbf{C}(\mathbf{u}_s)\mathbf{u}_c = \mathbf{D}\mathbf{u}_c - \Omega \mathbf{G}_c p_c, \quad (1)$$

$$\mathbf{M}\mathbf{u}_s = \mathbf{0}_c, \quad (2)$$

where $\mathbf{u}_c \in \mathbb{R}^{3n}$ and $\mathbf{p}_c \in \mathbb{R}^n$ are the cell-centered velocity and the cell-centered pressure, respectively. The staggered quantities, such as $\mathbf{u}_s \in \mathbb{R}^m$ are related to the cell-centered quantities via an interpolation operator $\Gamma_{c\to s} \in \mathbb{R}^{m\times 3n}$:

$$\mathbf{u}_s = \Gamma_{c\to s}\mathbf{u}_c. \quad (3)$$

Finally, $\Omega \in \mathbb{R}^{3n\times 3n}$ is a diagonal matrix containing the cell volumes, $\mathbf{C}(\mathbf{u}_s) \in \mathbb{R}^{3n\times 3n}$ is the discrete convective operator, $\mathbf{D} \in \mathbb{R}^{3n\times 3n}$ is the discrete diffusive operator, $\mathbf{G}_c \in \mathbb{R}^{3n\times n}$ is the cell-to-cell discrete gradient operator and $\mathbf{M} \in \mathbb{R}^{n\times m}$ is the face-to-cell discrete divergence operator. The velocity correction after applying the Fractional Step Method (FSM) to the Navier-Stokes equations reads:

$$\mathbf{u}_c^{n+1} = \mathbf{u}_c^p - \Gamma_{s\to c}\mathbf{G}p^{n+1}, \quad (4)$$

where $\Gamma_{s\to c} \in \mathbb{R}^{3n\times m}$ is the face-to-cell interpolator, which is related to the cell-to-face interpolator via the volume matrices $\Gamma_{s\to c} = \Omega^{-1}\Gamma_{c\to s}\Omega_s$, and $\mathbf{G} \in \mathbb{R}^{m\times n}$ is the cell-to-face gradient operator.

All the operators needed to formulate the equations can be constructed using only five discrete ones: the cell-centered and staggered control volumes (diagonal matrices), Ω_c and Ω_s, the face normal vectors, N_s, the scalar cell-to-face interpolation, $\Pi_{c\to s}$ and the cell-to-face divergence operator, $\mathbf{M}$. For more details of these operators and its construction, the reader is referred to [1]. Due to its simplicity, these operators can be easily builded in existing codes, such as OpenFOAM [2].

The most popular open-source code used to solve Navier-Stokes equations with LES modelization is OpenFOAM due to its stability and robustness. However, as it was shown in [3], this code introduces a large amount of numerical dissipation. In our opinion, this is not an appropiate approach for DNS and LES simulations since this artificial dissipation interferes with the subtle balance between convective transport and physical dissipation. Hence, reliable numerical methods for DNS/LES must be free of numerical dissipation (or, at least, have an small amount), and, of course, unconditionally stable, i.e. simulations must be stable regardless of the mesh quality and resolution.

AN ENERGY-PRESERVING UNCONDITIONALLY STABLE FSM

From our point of view, respecting the symmetries of these differential operators is crutial in order to respect the physical structure of the equations. For example, constructing $\mathbf{G} = -\Omega_s\mathbf{M}^T$ is essential to preserve kinetic energy [1], but it is also mimicking the symmetries of the continuos level operators. So, we do not only have physical arguments to do so, but also mathematical ones.

The turbulence phenomenon arises from a balance between convective transport and diffusive dissipation. These two physical processes are described (in its discrete form) by $\mathbf{C}(\mathbf{u}_s)$ and $\mathbf{D}$, respectively. At continuous level, the convective operator is skew-symmetric, and the diffusive operator is symmetric and negative-definite. If we retain these properties at the discrete level (namely $\mathbf{C}(\mathbf{u}_s)$ being a skew-symmetric matrix, $\mathbf{D}$ being a symmetric negative-definite matrix and $\mathbf{G} = -\Omega_s\mathbf{M}^T$), the discrete convective operator is going to transport energy from resolved scales of motion to others without dissipating energy, as one should expect.

The utility of an algebraic formulation can be found, as an example, in [4]. In that work, the matrix-vector formulation is used in order to study the stability of the solution in terms of the pressure gradient interpolation. To do so, the eigenvalues

of $\mathbf{L} - \mathbf{L}_c$ were deeply studied ($\mathbf{L} = \mathbf{MG} \in \mathbb{R}^{n\times n}$ is the compact Laplacian operator whereas $\mathbf{L}_c = \mathbf{M}\Gamma_{c\to s}\Gamma_{s\to c}\mathbf{G} \in \mathbb{R}^{n\times n}$ is the collocated wide-stencil Laplacian operator), and the cell-to-face interpolation that leads to an unconditionally stable FSM turned out to be:

$$\Pi_{c\to s} = \Delta_s^{-1}\Delta_{sc}^T \in \mathbb{R}^{m\times n}, \tag{5}$$

where $\Delta_s \in \mathbb{R}^{m\times m}$ is a diagonal matrix containing the projected distances between two adjacent control volumes, and $\Delta_{sc} \in \mathbb{R}^{n\times m}$ is a matrix containing the projected distance between a cell node and its corresponding face. For details, the reader is referred to [4].

With the construction of a reduced set of (algebraic) kernels, these matrix operators can be constructed, along with basic operations like matrix-vector product, and we can solve the equations numerically using proper solvers.

PRELIMINARY RESULTS

In order to check the stability of the method, some tests have been carried out with very coarse and very bad quality meshes. Figures 1 and 2 show an example of an air-filled ($Pr = 0.71$) differentially heated cavity with aspect ratio 2 at Rayleigh number (based on the cavity height) of 10^6, respecting the symmetries of the operators and using (5) to interpolate the pressure gradient:

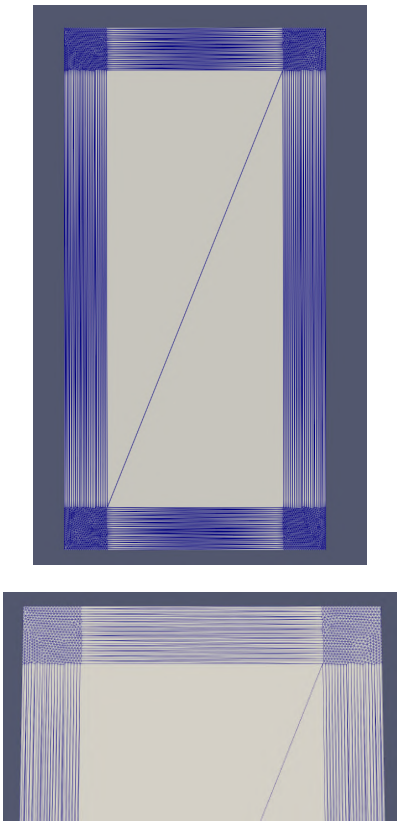

Figure 1: (Top) Test mesh used to check the stability of the method. (Bottom) Zoom at the top part of the mesh.

As you can see in Fig. 2, the method is stable, giving us results and not blowing up the simulation. As we can expect with such a bad quality mesh, the accuracy is not going to be very high. It is worth to mention that trying other interpolations for the pressure gradient, such as using $\frac{1}{2}$ weights will blow up the simulation from the very beginning.

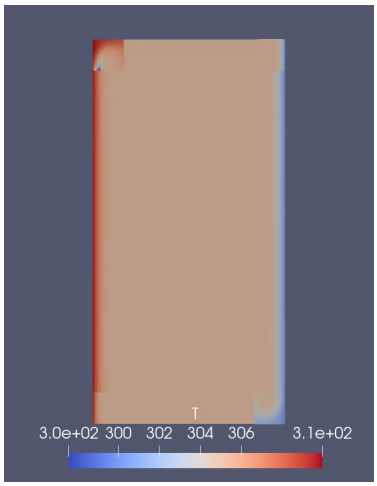

Figure 2: Temperature distribution obtained for $Ra = 10^6$.

CONCLUSIONS AND FUTURE WORK

Respecting the symmetries of the differential operators at the discrete level is essential to retain invariances from the continuos level and preserve kinetic energy. Furthermore, the interpolation of the pressure gradient from faces to cells should be done with the correct interpolator (5) to obtain stable solutions. The aim of this work is to solve Navier-Stokes equations (1,2), from an algebraic point of view, while preserving the symmetries of the differential operators [1] and interpolating in the proper way the pressure gradient [4]. To do so, we plan to study a set of DNS/LES cases (Rayleigh-Bénard convection, Channel Flow...). The accuracy and the preservation of energy due to the introduction of this new interpolation will be tested. All the simulations will be carried out on a new CFD code based on the fully-portable algebra-based HPC^2 framework [5].

REFERENCES

[1]Trias, F.X., Lehmkuhl, O., Oliva, A., Pérez-Segarra, C.D., and Verstappen,R.W.C.P.: Symmetry-preserving discretization of Navier-Stokes equations on collocated unstructured meshes. *Journal of Computational Physics, 258:246–267*, (2014).

[2]Komen, E., Hopman, J.A., Frederix, E.M.A., Trias, F.X., and Verstappen, R.W.C.P.: *A symmetry-preserving second-order time-accurate PISO-based method. Computers & Fluids, 225:104979*, (2021).

[3]Komen, E.M.J, Camilo, L.H., Shams, A., Geurts, B.J., Koren, B.: *A quantification method for numerical dissipation in quasi-DNS and under-resolved DNS, and effects of numerical dissipation in quasi-DNS and under-resolved DNS of turbulent channel flows. Journal of Computational Physics, 345:565-595*, (2017).

[4]Santos, D., Muela J., Valle, N., Trias, F.X.: On the Interpolation Problem for the Poisson Equation on Collocated Meshes. *14th WCCM-ECCOMAS Congress 2020, DOI: 10.23967/wccm-eccomas.2020.257*, July 2020 (postponed to January 2021 due to COVID19 pandemic)

[5]Álvarez, X., Gorobets, A., Trias, F.X.: *A hierarchical parallel implementation for heterogeneous computing. Application to algebra-based CFD simulations on hybrid supercomputers. Computers & Fluids, 214:104768*, (2021).

WORKSHOP
Direct and Large-Eddy Simulation 13
October 26th-29th 2022, Udine, Italy

DLES13: FEATURE-BASED MESH ADAPTATION APPLIED TO THE LARGE-EDDY SIMULATION OF A HIGH-REYNOLDS NUMBER ANISOTHERMAL IMPINGING JET ON A FLAT SURFACE

A. Grenouilloux[1,2], V. Moureau[1], G. Lartigue[1], P. Bénard[1], P. Ferrey[2]
[1] CORIA, CNRS UMR6614,
Normandie Universite, UNIROUEN, INSA of Rouen,France
[2] Safran Nacelles
Gonfreville-l'Orcher, 76700, France
adrien.grenouilloux@coria.fr

INTRODUCTION

Impinging jets are used in several industrial applications such as heat exchangers. The design of these devices is essential, as the high thermal loads they withstand can have an impact on the product life-cycle. For the past decades, Reynolds Averaged Navier-Stokes (RANS) simulations have been used to predict the aerothermal response in these configurations. Yet the presence of two main flow regions before and after impingement compromise the accuracy of the results [1]. Large-Eddy Simulation (LES) has become a valuable tool for the simulation of turbulent and unsteady flows. Within this framework, a scale separation is obtained by filtering the Navier-Stokes equations. Hence, large scales are solved explicitly while the smallest ones are modelled. This numerical method has particularly been used for the study of impinging jets [2, 3, 4], due to its high accuracy at a reasonable cost when compared to Direct Numerical Simulation (DNS), where all the scales are explicitly solved. Yet, the design of the optimal grid is often a long and repetitive process, especially for complex geometries. Recent developments regarding mesh adaptation [5, 6, 7] have shown that targeting specific features can improve results. In the present paper, a methodology for the feature-based mesh adaptation based on the dissipation of the mean kinetic energy (MKE) combined with specific near-wall refinement is used [8]. An anisothermal high-Reynolds number impiging jet of $Re = 60000$, $\Delta T = 130K$ and a nozzle-to-plate distance $H/D = 3$ is considered for validation [4, 9].

MESH ADAPTATION METHODOLOGY

In his work, Bénard et al. [6] proposed a methodology to adapt the grid based on two quantities called Q_{C1}, a Hessian-based error on the mean velocity field, and Q_{C2}, a quantity that targets the correct resolution of turbulent scales. This approach allowed to control the final grid size and thus, the computational resources used for the numerical simulation. In Daviller et. al [5], a method for the mesh adaptation of swirl flows based on the overall dissipation of the kinetic energy was presented. The quantity used was the so-called LIKE criterion, designed to adapt the mesh in complex geometries to match the correct pressure loss. Yet, in this latter formulation, no control of the final cell count was presented, and the grid was refined until a posteriori mean flow quantities were validated with experimental data.
This paper proposes to use the dissipation of the kinetic energy to perform feature-based mesh adaptation with the quantity Q_{C3}:

$$Q_{C3} = \Delta^2 \;\; 2(\nu + \nu_t)\overline{S}_{ij} \;\; \overline{S}_{ij} \,, \tag{1}$$

With Δ and $\overline{S}_{ij}$ accounting for the local cell size and the symmetric part of the strain tensor based on the filtered velocity, respectively. The iterative mesh convergence approach consists of a succession of simulations for statistical convergence and a series of mesh adaptation steps. To ensure the correct time average of Q_{C3} in key regions, a dedicated methodology based on a binary tree decomposition of the instantaneous $Q_{C3}(t)$ time signal is performed. Such a treatment is applied to a set of probes located in regions of interest, e.g. the shear layer, so that the statistical convergence of Q_{C3}, both average and RMS, is guaranteed. Once converged, a refinement ratio τ_{QC3} based on the time average of the dissipation of the kinetic energy $\langle Q_{C3} \rangle_t$ is computed [6]. A series of constraints are then applied to τ_{QC3} in order to respect a set of user-defined parameters, such as a minimal h_{min} and maximal h_{max} cell size, a metric gradient h_{grad} to ensure the correct transition from coarse to fine cells, and a targeted number of elements on the adapted grid $N_{elem,target}$. On top of that, a characteristic near wall refinement τ_{y+} based on the equivalent non-dimensional wall unit y^+_{WL} is applied on boundaries of interest such as the impinging plate to impose a maximal value of y^+ [10]. The process is repeated until the adapted grid respects all the user-defined constraints.

VALIDATION TEST CASE

The impinging jet studied by Grenson et al. [4, 9] is considered. The numerical domain consists of a cylindrical geometry whose dimensions are given in Figure 1. A velocity profile presented in [3] is imposed at the inlet:

$$\frac{U(r)}{U_c} = \alpha \left(1 - \frac{2r}{D}\right)^{1/7.23} , \tag{2}$$

with a centerline velocity U_c derived from the bulk velocity as $U_b/U_c = 0.811 + 0.038(\log(Re_b) - 4)$. A rescaling coefficient α is used to guarantee the correct velocity flowrate

across the inlet. A homogeneous isotropic turbulence (HIT) based on a Passot-Pouquet spectrum [11] is injected. The latter is parametrized by a characteristic length $Le = D/3$ and a turbulence intensity of $TI = 5\%$. All the simulations are performed with the unstructured low-Mach number code YALES2 [12] featuring parallel dynamic mesh adaptation [6] with the MMG3D library. Due to the high temperature difference between the jet and the ambient air, a variable density solver (VDS) is used for the present simulations [13]. Within this approach, temperature and density are computed as from a passive scalar $Z \in [0, 1]$, where 1 defines the hot air coming from the jet and 0 then ambient air.

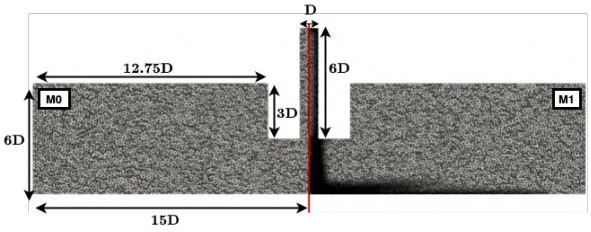

Figure 1: Domain dimensions - Left: Initial grid. Right: grid after first adaptation.

The methodology is applied to an initial an homogeneous grid of $7.7M$ elements. After a first adaptation, a first intermediate grid $M1$ of $168M$ is obtained (see Figure 1). On this latter grid, results are dramatically improved, as depicted by Figure 2 and Figure 3. The mesh is expected to be adapted until the cell counts are close the $N_{elem,target} \approx 500M$ elements.

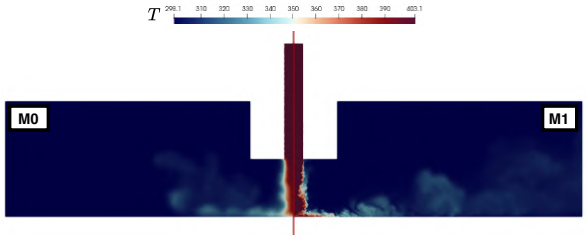

Figure 2: Left: Initial Temperature field. Right: Temperature on grid first adaptation.

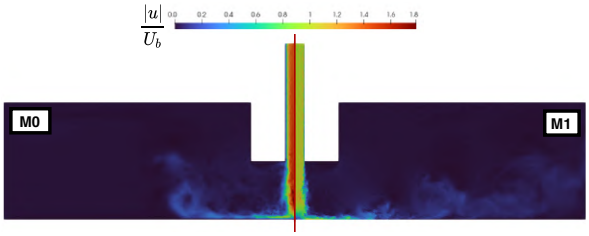

Figure 3: Left: Initial velocity field. Right: velocity field on grid first adaptation.

CONCLUSION AND PERPECTIVES

The proposed methodology is used to automatically refine or coarsen the mesh of a high-Reynolds number anisothermal impinging jet. To show the robustness of the methodology, the whole process will be applied to a second initial grid with a different initial discretisation. Velocity, temperature as well as Nusselt number distribution will be compared with the available numerical and experimental data of Grenson et al. [4, 9]. Such a case will later be used as a reference benchmark to perform anisotropic mesh adaptation with the MMG3D library and see the possible improvements.

ACKNOWLEDGEMENTS

This work is granted access to the HPC resources of CINES/TGCC under the projects 2B06880 and made by GENCI and of CRIANN under the allocation 2012006.

REFERENCES

[1]Zuckerman, N. and Lior, N.:Jet Impingement Heat Transfer: Physics, Correlations, and Numerical Modeling, *Advances in Heat Transfer*, **39**, 565-631 (2006).

[2]Neumann, O., Uddin, N. and Weigand, B.: Grid Sensitivity of LES Heat Transfer Results of a Turbulent Round Impinging Jet, *High Performance Computing in Science and Engineering*, 307-325, (2011).

[3]Aillaud,P. and Duchaine,F. and Gicquel,L. Y. M. and Didorally, S.: Secondary peak in the Nusselt number distribution of impinging jet flows: A phenomenological analysis, *Physics of Fluids*, (2016).

[4]Grenson, P., Hugues, D. and Aupoix, B : LES of an impinging heated jet for a small nozzle-to-plate distance and high Reynolds number, *International Journal of Heat and Fluid Flow*, (2017).

[5]Daviller, G., Brebion, M.,Xavier, P., Staffelbach, G., Müller, J.-D. and Poinsot, T.: A Mesh Adaptation Strategy to Predict Pressure Losses in LES of Swirled Flows, *Flow, Turbulence and Combustion*, **99**, 93-118 (2017).

[6]Benard, P., Balarac, G., Moureau, V., Dobrzynski, C., Lartigue, G. and D'Angelo, Y. : Mesh adaptation for large-eddy simulations in complex geometries, *International Journal for Numerical Methods in Fluids*, **81**, 719-740 (2016).

[7]Agostinelli,P. W. and Rochette,B. and Laera,D. and Dombard,J. and Cuenot,B. and Gicquel,L. : Static mesh adaptation for reliable large eddy simulation of turbulent reacting flows, *Physics of Fluids*, **33**, (2021).

[8]Grenouilloux, A., Moureau, V., Lartigue, G., Bénard, P.: Feature-based mesh adaptation applied to the Large-Eddy Simulation of Multiple Impinging Jets impinging on a surface , *UKHTC Conference Proceedings*, (2022).

[9]Grenson, P., Léon, O., Reulet, P., and Aupoix, B : Investigation of an impinging heated jet for a small nozzle-to-plate distance and high Reynolds number: An extensive experimental approach, *International Journal of Heat and Mass Transfer*, (2016).

[10]Grenouilloux, A., Balarac, G., Leparoux, J., Moureau, V., Lartigue, G., Benard, P., Mercier, R. and Ferrey, P. : On the use of kinetic-energy balance for the feature-based mesh adaptation applied to Large-Eddy Simulation in complex geometries, *ASME Proceedings*, (2022).

[11]Boughanem, H.: Validation du code de simulation directe ntmix3d pour le calcul des ecoulements turbulents reactif, *Technical report - IFP*, (1996).

[12]Moureau, V., Domingo, P., Vervisch, L.: Design of a massively parallel CFD code for complex geometries, *Comptes Rendus Mécanique*, (2011).

[13]Analyse et amelioration d'une chambre de combustion centimétrique par simulations aux grandes echelles, *PhD Thesis, INSA de Rouen*, (2015).

Session: Environmental and geophysical flows

Friday, October 28, 2022

09:50 – 10:50

WORKSHOP
Direct and Large-Eddy Simulation 13
October 26th-29th 2022, Udine, Italy

DIRECT AND LARGE–EDDY SIMULATION OF TURBULENT OSCILLATORY FLOW THROUGH A HEXAGONAL SPHERE PACK

L. Unglehrt[1], **M. Manhart**[1]
[1] Professorship of Hydromechanics
Technical University of Munich, Germany
lukas.unglehrt@tum.de, michael.manhart@tum.de

INTRODUCTION

In coastal engineering, the description of wave transmission and attenuation through rubble-mound breakwaters requires a model for the wave-induced flow inside the pore space of the breakwater [9, 14]. Extensive experimental investigations of oscillatory porous media flow were performed [3, 6, 13] in order to determine the coefficients of the unsteady Forchheimer equation [5] which relates the superficial velocity and the pressure gradient. These coefficients do not solely depend on the geometry, but they vary with time or frequency [2, 3, 13], raising doubts about the validity of this equation.

In order to gain insight into the flow physics and to obtain a high-fidelity data base for modelling, we simulated the flow through a hexagonal close-packed arrangement of spheres with uniform diameter d driven by a sinusoidal pressure gradient $f_x \sin(\Omega t)\,\vec{e}_x$. The flow problem is governed by two independent parameters: the Hagen number $Hg = f_x d^3/(\rho\nu^2)$ and the Womersley number $Wo = \sqrt{\Omega d^2/\nu}$. We define the Reynolds number as $Re = \max\langle u\rangle_\mathrm{s}\, d/\nu$ with the superficial velocity

$$\langle u\rangle_\mathrm{s} = \frac{1}{L_x L_y L_z}\int_{V_\mathrm{f}} u\,\mathrm{d}V \tag{1}$$

where L_x, L_y, L_z are the domain sizes and V_f is the fluid volume . We performed a direct numerical simulation (DNS) at $Hg = 10^8$ and $Wo = 100$ resulting in $Re = 1090$ and a large–eddy simulation (LES) at $Hg = 10^9$ and $Wo = 100$ resulting in $Re = 3500$. Both simulations lie within the range of the experiments of Hall et al. [3].

In this contribution, we investigate the temporal behaviour of the superficial velocity and relate it to characteristic events in the instantaneous flow fields. We present instantaneous velocity fields which, despite the strong confinement of the flow, exhibit features that are predominantly found in external bluff body flow. For instance, the flow has a boundary layer structure and shows massive flow separations. The high frequency of the forcing leads to a strongly varying turbulence intensity over the course of the cycle.

METHODOLOGY

Numerical method

Our in-house code MGLET [8] solves the incompressible Navier-Stokes equations on a staggered Cartesian grid using a finite volume discretisation with second-order central differencing. A third-order explicit Runge-Kutta scheme is employed for the time integration. The no-slip boundary condition on the spheres is enforced using an immersed boundary method [11]. For the LES the sub-grid stresses are formulated with the WALE viscosity model [10].

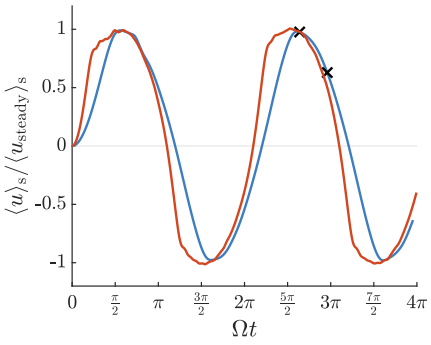

Figure 1: Time series of the superficial velocity at $Re = 1090$ (blue) and $Re = 3500$ (red). The crosses mark the time of the instantaneous fields presented in figure 2. The reference velocity was obtained from the steady state correlations of [7].

Domain and grid

The domain size was chosen as $L_x = 2\,d$, $L_y = \sqrt{3}\,d$ and $L_z = 2\sqrt{6}/3\,d$ with triple periodic boundary conditions. The domain contains two spheres in every lattice direction and every pore is repeated eight times. For their DNS of stationary turbulent flow, He et al. [4] found that a domain of equal volume "showed little variation in statistics compared to a larger domain.".

At $Wo = 100$, the flow belongs to the high frequency regime and features very thin boundary layers and high velocities near the contact points of the spheres. Thus, a higher resolution than in stationary flow is required. The flow was simulated with a resolution of 384 and 768 cells per diameter (cpd) for the DNS at $Re = 1090$ and 384 cpd for the LES at $Re = 3500$.

RESULTS

Superficial velocity

The time series of the superficial velocity is plotted in figure 1. For both Reynolds numbers, the amplitude of $\langle u\rangle_\mathrm{s}$

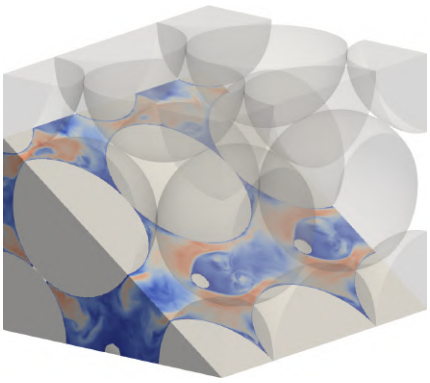

(a) at the maximum superficial velocity ($\Omega t = 8.3$)

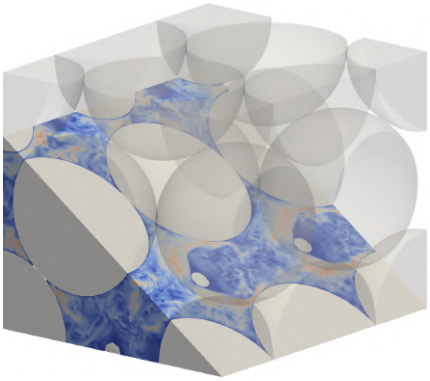

(b) during deceleration ($\Omega t = 9.3$)

Figure 2: Instantaneous velocity magnitude of the simulation at $Re = 1090$ and $Wo = 100$. The colours are chosen based on the maximum superficial velocity $\langle u \rangle_s$.

lies within 2% of the steady state value obtained from the correlations of Macdonald et al. [7]. This is in line with the observation of Hall et al. [3] that "the Forchheimer unsteady-stationary flow law described the oscillatory measurements well when velocities and energy losses were maximum". Based on the time of the zero crossings, the superficial velocity lags behind the sinusoidal forcing by a phase angle of 0.2π at $Re = 1090$ and of 0.1π at $Re = 3500$. At $Re = 3500$ the superficial velocity shows a strong acceleration followed by a low acceleration plateau. The instantaneous velocity fields indicate that this change is caused by flow separations at the contact points and an increase in turbulence intensity.

Instantaneous velocity fields

The spatial distribution of the velocity magnitude for $Re = 1090$ at the maximum superficial velocity and during the deceleration is displayed in figure 2. The most prominent feature of the flow is the separation at the contact points between the large pores. Due to the confined pore space, the flow around the separation bubble is concentrated into two jets that are diverted towards the wake by the spheres bounding the pore. The flow topology appears similar to the results of Sakai & Manhart [12] for stationary turbulent flow. Inside the separation bubble we can observe some complicated vortex structures which disintegrate into turbulence in the course of the cycle. Whereas the velocity field is quite smooth at the end of the acceleration phase, a lot of small vortical structures appear during the deceleration. This behaviour is common in oscillatory flow [1]. For $Re = 3500$ (not shown), the flow topology is similar, but a high turbulence intensity can be observed over most of the cycle.

CONCLUSION

We performed DNS and LES of a turbulent oscillatory flow through a hexagonal sphere pack at $Re = 1090$ and 3500, respectively, with $Wo = 100$. An investigation of the superficial velocity and of instantaneous velocity fields shows that a separation occurs at the contact points of the spheres that significantly alters the behaviour of the flow. At $Re = 1090$ turbulence can be observed mainly during the deceleration phase whereas at $Re = 3500$ turbulence can be observed over a longer part of the cycle.

ACKNOWLEDGEMENTS

We gratefully acknowledge the financial support of the DFG under grant no. MA2062/13-1. Computing time was granted by the Leibniz Supercomputing Centre on its Linux-Cluster.

REFERENCES

[1]Akhavan, R., Kamm, R. & Shapiro, A.: An Investigation of Transition to Turbulence in Bounded Oscillatory Stokes Flows Part 1. Experiments. *Journal Of Fluid Mechanics.* **225**, 395–422 (1991)

[2]Burcharth, H. & Andersen, O.: On the One-Dimensional Steady and Unsteady Porous Flow Equations. *Coastal Engineering.* **24**, 233–257 (1995)

[3]Hall, K., Smith, G. & Turcke, D. : Comparison of Oscillatory and Stationary Flow through Porous Media. *Coastal Engineering.* **24**, 217–232 (1995)

[4]He, X., Apte, S., Finn, J. & Wood, B.: Characteristics of Turbulence in a Face-Centred Cubic Porous Unit Cell. *Journal Of Fluid Mechanics.* **873** pp. 608–645 (2019)

[5]Polubarinova-Kochina, P. & De Wiest, R.: Theory of Ground Water Movement. (1962)

[6]Losada, I., Losada, M. & Martn, F. : Experimental Study of Wave-Induced Flow in a Porous Structure. *Coastal Engineering.* **26**, 77–98 (1995)

[7]Macdonald, I., El-Sayed, M., Mow, K. & Dullien, F. : Flow through Porous Media – the Ergun Equation Revisited. *Industrial And Engineering Chemistry Fundamentals.* **18**, 199-208 (1979)

[8]Manhart, M., Tremblay, F & Friedrich, R. : MGLET: A Parallel Code for Efficient DNS and LES of Complex Geometries. *Parallel Computational Fluid Dynamics 2000.* 449–456, (2001)

[9]Muttray, M.: Wellenbewegung an und in einem geschütteten Wellenbrecher – Laborexperimente im Großmaßstab und theoretische Untersuchungen. (Technische Universität Braunschweig, 2000)

[10]Nicoud, F. & Ducros, F.: Subgrid-Scale Stress Modelling Based on the Square of the Velocity Gradient Tensor. *Flow, Turbulence And Combustion.* **62**, 183–200 (1999)

[11]Peller, N. Numerische Simulation Turbulenter Strömungen Mit Immersed Boundaries. (Technische Universität München, 2010)

[12]Sakai, Y. & Manhart, M.: Consistent Flow Structure Evolution in Accelerating Flow Through Hexagonal Sphere Pack. *Flow, Turbulence And Combustion.* **105**, 581–606 (2020)

[13]van Gent, M. : Stationary and Oscillatory Flow through Coarse Porous Media. *Communications On Hydraulic And Geotechnical Engineering.* **9**, (1993)

[14]van Gent, M. : The Modelling of Wave Action on and in Coastal Structures. *Coastal Engineering.* **22**, 311–339 (1994)

WORKSHOP
Direct and Large-Eddy Simulation 13
October 26th-29th 2022, Udine, Italy

STRUCTURE-PRESERVING INTEGRATION FOR HIGH-PERFORMANCE DNS OF GEOPHYSICAL FLOWS

P. Cifani[1,2], M. Viviani[3], K. Modin[4], B.J. Geurts[1,5]
[1] Mathematics of Multiscale Modelling and Simulation, University of Twente, The Netherlands
[2] Gran Sasso Science Institute, Italy
[3] Scuola Normale Superiore di Pisa, Italy
[4] Department of Mathematical Sciences, Chalmers University Technology, Sweden.
[5] Multiscale Energy Physics, Eindhoven University of Technology, The Netherlands
p.cifani@utwente.nl

INTRODUCTION

Navier-Stokes equations in two dimensions constitutes a fundamental model for numerous physical phenomena. Most notable examples are large scales dynamics of oceanic and atmospheric flows. In the limit of vanishing viscosity, two-dimensional fluid dynamics is characterised by an infinite number of first integrals, i.e., the integrated powers of vorticity. This set of constraints has profound effects on the energy transfer mechanisms across scales of motion, e.g., the double energy cascade, absent in three dimensions, theorised by Kraichnan [1]. It is therefore natural to embed these fundamental properties of the continuum into the numerical algorithm used for the simulation for the corresponding discrete system.

In this work we will present recent developments in structure-preserving methods for fluid dynamics in two dimensions. In particular, we will illustrate a recently developed efficient and scalable Lie-Poisson integrator for flows on the sphere based on [2]. For extremely large discrete systems, however, the latter method becomes unfeasible. For such cases, we propose a constrained pseudo-spectral method enabling to capture important invariants of the motion while retaining more favourable computational complexity. Emphasis will be given to the construction of the numerical method, the description of the main algorithms and their parallelisation. Furthermore, an illustration of fundamental geophysical flows, such as two-dimensional turbulence on the sphere, will be provided.

LIE-POISSON INTEGRATOR

Geometric integration for fluid systems has been elusive, owing to the high computational complexity of established geometric integrators. Nevertheless, recent advances in structure-preserving integration [2] have laid down the basis for direct numerical simulation of realistic flow models. The geometric description of fluid dynamics arises when characterising the motion of inviscid fluid parcels on general manifolds. Here, we describe the approach for the incompressible Euler equations. Addition of viscous dissipation and forcing can be accounted for in the same manner proposed in [4], also described in our recent work [5] for homogeneous two-dimensional turbulence. In terms of vorticity ω, Euler's equations can be written as

$$\begin{cases} \dot{\omega} = \{\psi, \omega\}, \\ \Delta\psi = \omega, \end{cases} \tag{1}$$

where $\{\cdot,\cdot\}$ is the Poisson bracket, defined as

$$\{\psi, \omega\}(x) = x \cdot (\nabla\psi \times \nabla\omega), \tag{2}$$

for any x on the surface of the sphere $\mathbb{S}^2$, ψ the stream function and Δ the Laplace-Beltrami operator. System (1) admits an infinite number of first integrals, called Casimir functions, corresponding to integrated powers of vorticity

$$\mathcal{C}_k(\omega) = \int \omega^k, \quad k = 1, 2, \dots \tag{3}$$

In other words, functions (3) are invariants of motion. A discretisation that preserves these invariants can be constructed from a Lie algebra of $N \times N$ complex matrices which approximates the Poisson bracket (2) by the matrix commutator [6]. The resulting discrete system can be written analogously as:

$$\begin{cases} \dot{W} = [P, W] \\ \Delta_N P = W, \end{cases} \tag{4}$$

where Δ_N is the discrete Laplacian while W, the vorticity matrix, and P, the stream matrix, are skew-Hermitian traceless matrices. As noted in [6], traces of powers of W,

$$C_k(W) = \mathrm{Tr}(W^k) \quad \text{for } k = 1, \dots, N, \tag{5}$$

are conserved by system (4). This is the discrete analogue of conservation of Casimirs, i.e. integrated powers of vorticity in the continuum.

A key property of system (4) is that it evolves such that the eigenvalues of W are constant over time. This property is referred to as isospectrality [9]. Conservation of the spectrum of W is equivalent to conservation of the Casimir functions (5). In [2], a class of Lie-Poisson integrators for isospectral flows was derived. A particularly simple integrator in this class (adopted in this work), is characterised by a low count of matrix operations per time-step [7]. Here, we have reformulated the latter method to work efficiently on modern supercomputers. Fig. 1 shows a scaling test conducted on a problem of

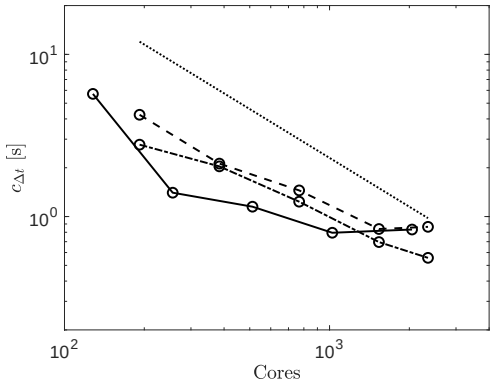

Figure 1: Computational time per time-step as a function of the number of cores for $N = 4096$, using MPI parallelisation (solid line), hybrid MPI parallelisation with 12 threads (dash-dotted line) and hybrid MPI parallelisation with 24 threads (dashed line). Linear scaling is shown as a reference by the dotted line.

matrix size $N = 4096$, demonstrating the feasibility of this geometric integrator.

APPLICATION

In this section we illustrate the capability of the developed numerical method by simulating the discrete Euler equations (4) for $N = 2048$. At the initial time, modes of spherical harmonics of degree $2 \leq l \leq 20$ are given a random value of approximately the same magnitude. The system then evolves for a total of 10^6 time-steps corresponding to 200 time units. For this simulation 512 cores were employed. A qualitative illustration of a typical vorticity field is shown in Fig. 2. From

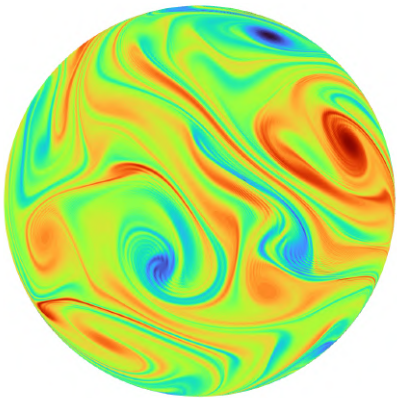

Figure 2: Illustration of vorticity field on a sphere. Colours range from blue corresponding to $\omega = -0.8$ to red corresponding to $\omega = 0.8$.

an initial random distribution of vorticity in spherical harmonics space, the flow evolves into well recognisable large-scale vortical structures. At the same time, owing to non-linear interactions, part of the energy injected at larger scales flows toward the high-wave number end of the spectrum. This is further illustrated in Fig. 3 where we present the evolution over time of the kinetic energy spectrum. We observe that energy is transferred to small scales where an approximate l^{-3} scaling is established. The -3 exponent is consistent with the theory of Kraichnan [1] on the direct cascade of enstrophy of

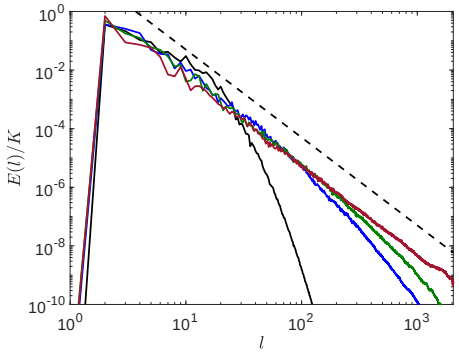

Figure 3: Kinetic energy spectrum scaled by the mean kinetic energy K as a function of the spherical harmonic index l at different times: $t = 10$ (black line), $t = 60$ (blue line), $t = 100$ (green line) and $t = 200$ (red line). The l^{-3} scaling is represented by the dashed black line.

two-dimensional turbulence, extensively investigated numerically [8] and recently also revisited in [5].

OUTLOOK

A computationally efficient and scalable geometric integrator for Lie-Poisson flows on the sphere has been proposed. This enables explicit conservation of the integrated powers of vorticity in the two-dimensional Navier-Stokes equations in the limit of vanishing viscosity. The structure-preserving core, in combination with computational efficiency make this tool valuable for numerical studies of long-time behaviour of complex geophysical flows. At much larger matrix sizes N than those investigated here, the geometric integrator becomes unfeasible owing to the $\mathcal{O}(N^3)$ complexity of the computation of the commutator. As a complementary study, we will consider reducing the computational complexity to $\mathcal{O}(N^2 \log(N)^2)$, by applying a pseudo spectral method, while still retaining conservation of important Casimir functions. This will be achieved by enforcing a suitable constraint on the Euler equations (1).

REFERENCES

[1]Kraichnan, R.H., 1967. Inertial ranges in two-dimensional turbulence. The Physics of Fluids, 10(7), pp.1417-1423.

[2]Modin, K. and Viviani, M., 2020. A Casimir preserving scheme for long-time simulation of spherical ideal hydrodynamics. Journal of Fluid Mechanics, 884.

[4]Verstappen, R.W.C.P. and Veldman, A.E.P., 2003. Symmetry-preserving discretization of turbulent flow. Journal of Computational Physics, 187(1), pp.343-368.

[5]Cifani, P., Viviani, M., Luesink, E., Modin, K. and Geurts, B.J., 2022. Casimir preserving spectrum of two-dimensional turbulence. arXiv preprint arXiv:2204.11794.

[6]Zeitlin, V., 2004. Self-consistent finite-mode approximations for the hydrodynamics of an incompressible fluid on nonrotating and rotating spheres. Physical review letters, 93(26), p.264501.

[7]Viviani, M., 2020. A minimal-variable symplectic method for isospectral flows. BIT Numerical Mathematics, 60(3), pp.741-758.

[8]Boffetta, G. and Musacchio, S., 2010. Evidence for the double cascade scenario in two-dimensional turbulence. Physical Review E, 82(1), p.016307.

[9]Hairer, E., Hochbruck, M., and Wanner, G., 2006. Geometric Numerical integration: structure-preserving algorithms for ordinary differential equations, Springer.

WORKSHOP
Direct and Large-Eddy Simulation 13
October 26th-29th 2022, Udine, Italy

DLES13: NEW INSIGHTS ON BUOYANCY-DRIVEN TURBULENT FLOWS WITH ACTIVE SCALAR TRANSPORT USING LES

Kiran Bhaganagar[1]
[1] Center for Advanced Measurements in Extreme Environments, Department of Mechanical Engineering
University of Texas, San Antonio, Texas
kiran.bhaganagar@utsa.edu

INTRODUCTION

For incompressible, turbulent flows at a low Mach number, when the buoyancy effects are dominant, the variations in density are substantial and, in fact, dominate the flow physics. In these flows, the scalar field (temperature, density, or concentration) cannot be considered a passive variable. In pure buoyancy-driven flows such as turbulent plumes, the scalar gradients are coupled to the momentum through the buoyancy term (density-gravity term) as a source term in the momentum equation.The focus of this work is to understand the dynamical interactions between the thermodynamics and the flow in the generation of turbulence and the transport processes in buoyant plumes.Buoyancy-generated turbulence processes with substantial density variations within the flow are critical in applications such as thermal convection in the atmosphere; wildland smoke plumes; mixing of different density fluids in an acceleration/gravitational field. In the present work, we analyze the transport processes of Reynolds stresses, the temperature variance and density variance in the axial and the horizontal direction, along with the spectral analysis of TKE, temperature and density fluctuations to understand the key mechanisms that contribute to turbulence production, transport and mixing processes.

A large-eddy simulation tool has been used to simulate heavier- and lighter- than air plumes released from a circular heated source for high Re. Figure 1 shows the buoyant plume released from a circular source at high Reynolds number. This is a representation of turbulent buoyant plume in which the Q-criterion is plotted. A buoyancy source at the bottom of the domain generates an upward buoyancy flux which induces entrainment of the ambient fluid as the plume rises. Turbulence velocity fluctuations and temperature fluctuations are generated by the plume. The budget equations are developed using a Favre-averaging approach. The study focuses on addressing key questions - Does the turbulence kinetic energy (TKE) spectra follow the classical inertial $-5/3$ spectra or is there a buoyancy regime with a different scaling law. Fundamental pathways for generation of turbulence through both velocity fluctuations, temperature and density fluctuations are discussed.

SECTION METHODOLOGY

Large eddy simulation (LES) within a weather research and forecasting (WRF) model was developed and validated to simulate thermal buoyant plumes. The governing equations are the compressible Euler equations with eddy viscosity and gravitational forces as follows:

$$
\begin{aligned}
&\frac{\partial \rho}{\partial t} + \frac{\partial \rho u_i}{\partial x_i} = 0, \\
&\frac{\partial \rho u_i}{\partial t} + \frac{\partial \rho u_j u_i}{\partial x_j} = -\frac{\partial p}{\partial x_i} + \frac{\partial \tau_{ij}}{\partial x_j} - \delta_{3i}\rho g, \\
&\frac{\partial \rho \theta}{\partial t} + \frac{\partial \rho u_j \theta}{\partial x_j} = \frac{\partial}{\partial x_j}\rho\mu_t\frac{\partial \theta}{\partial x_j} - \delta_{i3}\frac{h_0 g}{C_p}, \\
&\frac{\partial \rho q_m}{\partial t} + \frac{\partial \rho u_j q_m}{\partial x_j} = \frac{\partial}{\partial x_j}\rho\mu_t\frac{\partial q_m}{\partial x_j} + Q_p, \\
&\frac{\partial \rho K}{\partial t} + \frac{\partial \rho u_j K}{\partial x_j} = \mu_t\left(\frac{\partial u_i}{\partial x_j} + \frac{\partial u_j}{\partial x_i}\right)^2 - \mu_t N^2 - \rho\frac{CK^{3/2}}{l},
\end{aligned}
\tag{1}
$$

where ρ is the mixture density, u_i is the velocity component at i direction, θ is the potential temperature, q_m is the mass fraction of m-th species, and K is the modeled TKE. p is the pressure, τ_{ij} is the modeled stress tensor given by $\tau_{ij} = \mu_t(\partial_j u_i + \partial_i u_j - (2/3)\delta_{ij}\partial_k u_k$, δ is the Kronecker delta function, C_p is the specific heat capacity at constant pressure, and h_0 is the heat flux at the source. The gravitational term g is considered as a body force, which acts in the negative vertical direction. The eddy viscosity, μ_t, is defined as $\mu_t \equiv C_k l\sqrt{K}$ where $C_k = 0.1$ and l is a length scale given as $l = min[(\Delta x\Delta y\Delta z)^{1/3}, 0.76\sqrt{K}/N]$ if $N > 0$, otherwise $l = (\Delta x\Delta y\Delta z)^{1/3}$. Brunt–Väisälä frequency, N, is computed as $N^2 = (g/\theta)\partial_3\theta$. Ideal gas is assumed in the equation of state, and therefore, potential temperature can be related in the equation of state, $p = p_0(\rho R\theta/p_0)^\gamma$, where R is the specific gas constant and γ is the specific heat ratio. In the following discussion, horizontal and vertical velocities, u_1 and u_3, will be presented as u and w. For the spatial directions x_1 and x_3, they will be replaced by x and z.

CASES

The physical problem that is being investigated in this study is as follows: The physical domain is filled with ambient fluid that is at rest and maintained at a constant temperature. A circular region of the source at the bottom boundary with diameter $D(= 400m)$ is heated with a constant surface heat flux (h_o). The heating causes a temperature difference between the surface and the ambient fluid and convection is initiated (see Fig.1). In this work, three different gases are studied: heated air (thermal), heated methane (CH_4) and heated sulfur dioxide (So_2). In addition to the surface heat

Case	1	2	3	4	5	6	7
species	air	air	air	air	air	CH_4	SO_2
R	287	287	287	287	287	159	638
h_0 $(kg \cdot s^{-3})$	4.4E-4	8.8E-4	1.3E-3	1.8E-3	2.4E-3	2.4E-3	2.4E-3
$\Delta\rho$	0.988	0.977	0.972	0.967	0.961	0.979	0.971
g_0' $(m \cdot s^{-2})$	0.082	0.145	0.185	0.237	0.272	0.189	0.061
l^*	0.31	0.32	0.35	0.37	0.37	0.7	0.5
z^*	1.62	1.63	1.63	1.75	1.75	6.35	2.08
Re	$6.02E7$	$9.12E7$	$1.15E8$	$1.33E8$	$1.47E8$	7.00E7	5.38E7
Re_t	$9.9E5$	$1.7E6$	$2.0E6$	$2.1E6$	$2.2E6$	1.66E6	1.64E6
Fr	1.091	1.089	1.110	1.141	1.149	1.149	1.1629

Table 1: Scaled parameters of the source and the plume: R is the specific gas constant, h_0 is the heat flux of the source; $\Delta\rho = (\rho_0 - \rho_\infty)/\rho_\infty$ is the density difference betweeen the source (ρ_0) and the ambience (ρ_∞); g_0' is the initial reduced gravity at the source defined as $g_0' = (T_0 - T_\infty)g/T_0$ where T_0 is the temperature at the source and T_∞ is the ambient temperature; z^* is the streamwise location of maximum mean velocity normalized by D; l^* is the half width of the plume at z^* normalized by D; $Re = wl^*D/\nu$ at x_3^* with viscosity obtained from air temperature while Re_t is calculated based on the eddy viscosity at z^*; $Fr = w/\sqrt{g_0' D}$ at z^*.

flux, for CH_4 and SO_2 cases, the gases are released with a constant surface density flux at the source. Chemical reactions and phase change are not considered in the presented simulations.

The simulations have been performed for 7 different cases. The details of the cases are provided in Table 1.

SECTION ANALYSIS

The existence of buoyancy regime has been identified for both thermal and gas plumes[1]. Using the LES database, we will present the results for the scaling, budget and spectra of turbulent kinetic energy, thermodynamic variables and their cross-relations within turbulent buoyant plumes. To assess the generality of the fundamental investigations, the heat source with a range of thermal flux conditions will be presented. The different heat fluxes result in different values of Reynolds number, and effects of released heat are discussed through the dimensionless number. Besides thermal plumes, additional heated methane and heated sulfur dioxide released from the source were also included in the studies for a comprehensive discussion. Turbulent fluctuations exist in a wide range of scales. As the axial dilatation is identified of being the mechanism that contributes to thermodynamic fluctuations in the buoyant plumes, it is important to identity at what scales does the interaction occur. We have analyzed the spectra of mass and heat flux, turbulent kinetic energy and the scalar variances.

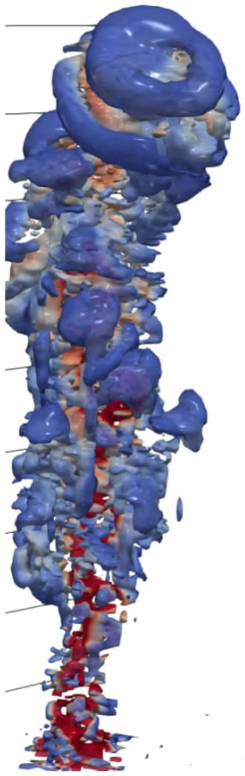

Figure 1: Buoyant plume released from a circular sources into a Neutral Environment.

REFERENCES

[1]Bhaganagar, K. and Bhimireddy, S. R.: Numerical investigation of starting turbulent buoyant plumes released in neutral atmosphere, J. Fluid Mech. (2020).

WORKSHOP
Direct and Large-Eddy Simulation 13
October 26th-29th 2022, Udine, Italy

WATER-LUBRICATED CHANNEL FLOW

A. Roccon[1,2], F. Zonta[1] and A. Soldati[1,2]
[1] Polytechnic Department, University of Udine, 33100 Udine, Italy
[2] Institute of Fluid Mechanics and Heat Transfer, TU-Wien, 1060 Vienna, Austria
alessio.roccon@uniud.it

ABSTRACT

We use direct numerical simulation (DNS) to study the problem of drag reduction in a lubricated channel, a flow instance in which two thin layers of a lubricating fluid (density ρ_1, viscosity η_1, thickness h_1) are injected in the near-wall region of a plane channel, so to favor the transportation of a primary fluid (density ρ_2, viscosity η_2, thickness h_2). All DNS are run within the constant power input (CPI) approach, which prescribes that the flow-rate is adjusted according to actual pressure gradient so to keep constant the power injected into the flow. The CPI approach has been purposely extended here for the first time to the case of multiphase flows. A phase-field method (PFM) is used to describe the dynamics of the liquid-liquid interface. We unambiguously show that a significant drag reduction (DR) can be achieved for all the four configurations considered. Upon a detailed analysis of the turbulence activity in the two lubricating layers and of the interfacial wave dynamics, we are able to characterize the effects of surface tension forces, surfactant concentration and viscosity contrast on the drag reduction performance.

REFERENCES

[]Roccon, A., Zonta, F. and Soldati, A. : Energy balance in lubricated drag-reduced turbulent channel flow, *J. Fluid Mech.*, **911**, A37 (2021).

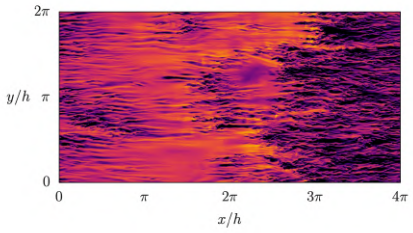

Figure 1: Visualization of the instantaneous streamwise velocity on a $x-y$ plane. The plane is located inside the top lubricating layer and is located at $\simeq 10$ $w.u.$ from the top wall.

Session: Aerodynamics/Aeroacoustics 2

Friday, October 28, 2022

11:10 – 12:40

WORKSHOP
Direct and Large-Eddy Simulation 13
October 26th-29th 2022, Udine, Italy

ANALYSIS OF A TRANSONIC CASCADE WITH WALL-MODELED LES BASED ON DGSEM

B. F. Klose[1], **E. J. Munoz Lopez**[2], **A. Hergt**[2], **J. Klinner**[2], **C. Morsbach**[2],
[1] Institute of Test and Simulation for Gas Turbines
German Aerospace Center (DLR), Am Technologiezentrum 5, 86159 Augsburg, Germany
[2] Institute of Propulsion Technology
German Aerospace Center (DLR), Linder Höhe, Cologne 51147, Germany
bjoern.klose@dlr.de

ABSTRACT

Scale-resolving simulations are an integral part in the validation of lower-cost computational fluid dynamics (CFD) methods and, with increasing computational resources, are also becoming an attractive tool for the design process in modern-day turbomachinery. Because such flows are typically at high Reynolds numbers, possibly transonic, and strongly affected by the incoming turbulence levels, agreement of experimental and numerical results can be challenging [1]. Small spatial and temporal scales of high-Reynolds number flows require sufficiently well resolved discretizations and advanced numerical methods to accurately capture such multi-scale flow problems. In compressible flows, numerical codes with explicit time-marching schemes are particularly affected by the small element sizes within the boundary layer near no-slip walls, as they restrict the time step size even further and hinder advancement of the solution in time.

A remedy to the strict resolution requirements of wall-resolved LES (wrLES) is the use of wall functions to model the inner part of the turbulent boundary layer based on analytic or empirical wall laws. In this so-called *wall-modeled* LES (wmLES) approach, the boundary layer is no longer explicitly resolved and the wall-shear stress entering the viscous fluxes is computed from the velocity some distance away from the wall [4, 5]. Because the grid sizing in wmLES is not governed by the $y^+ \leq 1$ condition, this family of schemes allows for significantly larger elements near the wall, resulting in a reduction of the number of degrees of freedom and larger time-step sizes for a given CFL number. The wmLES thereby enables the simulation of large-scale turbomachinery configurations or operating points that are otherwise computationally too expensive (see e.g. Pérez Arroyo et al. [6]).

For high-fidelity simulations such as LES or direct numerical simulations (DNS), CFD codes belonging to the family of high-order spectral methods are commonly used, as they feature reduced dispersion and dissipation errors over lower-order schemes [2]. In particular, the discontinuous Galerkin spectral element method (DGSEM) has become a popular choice as it is computationally efficient, geometrically flexible, and numerically robust [7]. While wmLES is already established in finite volume community [4], results based on spectral methods are sparse. Only recently, Frère et al. [8] presented results on the application of the wall-modeled LES approach to the discontinuous Galerkin method and elaborated on guidelines based on the canonical channel flow. Frère [9] also applied the wmLES to the flow over NACA4412 airfoil at $Re = 1.64 \cdot 10^6$, where deviations to highly resolved wrLES are attributed to the growing boundary layer over the profile and the associated change of the velocity probe location within the boundary layer.

Given that realistic operating points in turbomachinery are not only at high Reynolds number, but also at transonic flow conditions, shock capturing and prevention of spurious polynomial oscillations to avoid unphysical solutions are required. The development of shock capturing methods tailored for the DGSEM framework is an active area of research and Hennemann et al. [3] only recently developed a novel subcell shock capturing approach for the split-form DG method. In this method, the high-order element is divided into a set of subcells and the fluxes are computed using a first-order FV scheme, as well as the high-order DG ansatz. The high-order and low-order fluxes are then blended in proportion to a shock sensor based on the relative amount of energy in the highest modes of the polynomial, i.e. the scheme locally approaches a low-order method if the solution in the element exhibits strong oscillations, thereby diffusing the gradients.

In this work, we present results from wall-modeled and wall-resolved LES of the flow over a transonic compressor cascade based on the discontinuous Galerkin spectral element method. The wmLES strategy published by Frère et al. [8], where the velocity for the input of the wall function is sampled from the bottom of the second high-order element, is adopted and evaluated for transonic flows in turbomachinery. Both wrLES and wmLES are based on the implicit (no-model) LES approach, i.e. the dissipation is added implicitly via the numerical dissipation of the Riemann solver.

The implementation of the wall-modeled LES is validated on a periodic channel flow at $Re_\tau = 2003$, where we compare wmLES, under-resolved wrLES, and DNS results from literature. The flow is simulated in a box of dimensions [$2\pi\delta$, 2δ, $\pi\delta$] consisting of $20 \times 10 \times 10$ elements with periodic boundaries in x and z direction. Results of time- and space-averaged solutions are given in Figure 1, where we show that the flow conditions in the log-layer are more accurately captured by the wmLES than by under-resolved wrLES.

For the transonic cascade simulations, we employ the shock

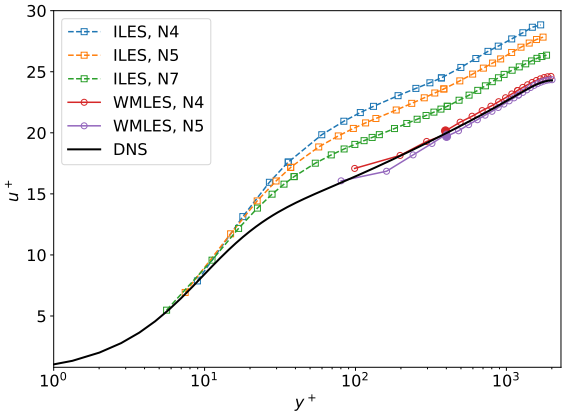

Figure 1: Velocity profile of the periodic channel flow at $Re_\tau = 2003$ in wall units. Solid points indicate velocity sampling location for wmLES.

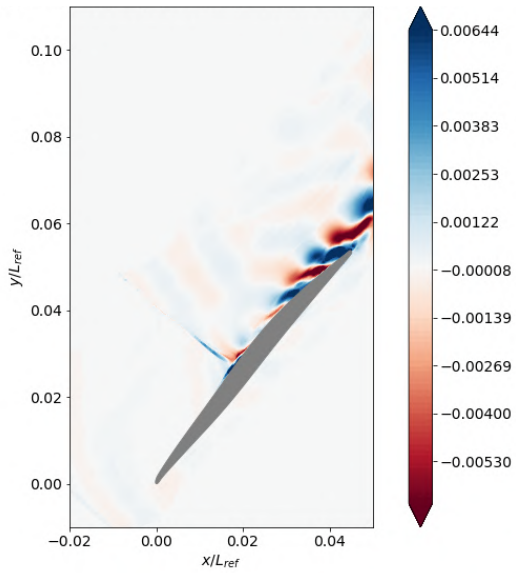

Figure 2: Contours of the first x-velocity mode of the SPOD at frequency of 7.8 kHz of the flow over a transonic compressor cascade. The SPOD is based on the kinetic energy norm.

capturing method by Hennemann et al. [3] to locate and reduce unphysical oscillations near the steep gradients. The shock-boundary layer interaction (SBLI) and the ensuing spatio-temporal oscillations of the shock over the blade are analyzed by performing a spectral proper orthogonal decomposition (SPOD) on the time-resolved data set and identifying the dominant modes in the flow. A plot of the first x-velocity mode at a frequency of 7.8 kHz is given in Figure 2 and highlights the vortex shedding that originates from the shock-induced separation bubble at mid-chord.

In the final paper, we plan to

- compare flow simulations of a transonic compressor cascade based on wall-resolved and wall-modeled LES with DGSEM
- analyze the shock-boundary layer interaction based on SPOD
- compare numerical and experimental results

REFERENCES

[1]D. Dupuy, L. Gicquel, N. Odier, F. Duchaine and T. Arts: Analysis of the effect of intermittency in a high-pressure turbine blade, *Physics of Fluids*, **32**, (2020).

[2]M. Kronbichler and P.-O. Persson: Efficient High-Order Discretizations for Computational Fluid Dynamics, *CISM International Centre for Mechanical Science*, **602**, (2021).

[3]S. Hennemann, A. M. Rueda-Ramírez, F. J. Hindenlang and G. J. Gassner: A provably entropy stable subcell shock capturing approach for high order split form DG for the compressible Euler equations, *Journal of Computational Physics*, **426**, (2021).

[4]Bose, S. T. and Park, G. I.: Wall-Modeled Large-Eddy Simulation for Complex Turbulent Flows, *Annual Review of Fluid Mechanics*, **50**, (2018).

[5]J. Larsson and S. Kawai and J. Bodart and I. Bermejo-Moreno: Large eddy simulation with modeled wall-stress: recent progress and future directions, *Mechanical Engineering Reviews*, **3**, (2016).

[6]Pérez Arroyo, C., Dombard, J., Duchaine, F., Gicquel, L., Martin, B., Odier, N., Staffelbach, G.: Towards the Large-Eddy Simulation of a full engine: Integration of a 360 azimuthal degrees fan, compressor and combustion chamber. Part I: Methodology and initialisation, *Journal of the Global Power and Propulsion Society*, (2021).

[7]A. R. Winters and R. C. Moura and G. Mengaldo and G. J. Gassner and S. Walch and J. Peiro and S. J. Sherwin: A comparative study on polynomial dealiasing and split form discontinuous Galerkin schemes for under-resolved turbulence computations, *Journal of Computational Physics*, **372**, ()2018

[8]Frère, A. and Carton de Wiart, C. and Hillewaert, K. and Chatelain, P. and Winckelmans, G.: Application of wall-models to discontinuous Galerkin LES, *Physics of Fluids*, **29**, (2017).

[9]Frère, A.: Towards wall-modeled Large-Eddy Simulations of high Reynolds number airfoils using a discontinuous Galerkin method, *Dissertation*, (2018).

WORKSHOP
Direct and Large-Eddy Simulation 13
October 26th-29th 2022, Udine, Italy

NUMERICAL INVESTIGATION OF THE TRANSONIC NON-IDEAL GAS FLOW AROUND A CIRCULAR CYLINDER AT HIGH REYNOLDS NUMBER.

C. Matar[1], P. Cinnella[1], X. Gloerfelt[2], S. Sundermeier[3], L. Hake[3], S. aus der Wiesche[3]
[1] Institute Jean le Rond d'Alembert, Sorbonne University, Paris
[2] DynFluid Laboratory, Arts et Métiers ParisTech, Paris
[3] FH Münster, Department of Mechanical Engineering, Steinfurt, Germany
camille.matar@dalembert.upmc.fr

INTRODUCTION

The high Reynolds number flow around a circular cylinder of an organic vapour at transonic inlet conditions is investigated by means of a Large Eddy Simulation (LES). This case is challenging on both the physical and computational point of view, due to the highly complex flow features requiring fine grids and long time integration [1]. The objective of this study is to provide high-fidelity data for an investigation of real-gas effects on turbomachinery flow measurement devices, presently ongoing in the frame of a joint Franco-German collaboration. The latter aims at getting insight on non-ideal gas effects in turbomachinery flows through combined experimental and numerical investigations. Experiments are being conducted in the closed-loop wind tunnel (CLOWT) at University of Muenster, using a dense organic vapor (Novec^{TM}649) as the working fluid [2]. Low Reynolds number dense gas flows, representative of a hot wire immersed in this organic vapor cross flow at $M \approx 0.65$, has been recently studied by the authors using LES and compared with companion experimental results [3]; furthermore, compressible flows of a dense vapor past a cylinder, representative of a rotating cylinder Pitot tube, has been simulated by solving the steady and the unsteady Reynolds-Averaged Navier Stokes (RANS) equations, and cross validated with pressure measurements obtained in CLOWT. Although a reasonable agreement between the experimental and numerical results was obtained for some operating conditions, the discrepancy between RANS, URANS and experiments became larger as the Mach number was increased and dense gas effects became stronger. This motivates the present LES of cylinder flows at Mach numbers in the and transonic regime, which will be compared with the preceding (U)RANS and experimental results, as well as recent Backward-Oriented Schlieren (BOS) visualizations obtained in the CLOWT facility.

FLOW CONFIGURATION AND NUMERICAL APPROACH

A smooth circular cylinder of diameter D is immersed in a cross-flow of an organic vapor Novec™649 at mildly non-ideal thermodynamic conditions, matching those used in the CLOWT experiments. The thermodynamic behaviour of the gas is modelled by the Peng-Robinson-Stryjek-Vera (PRSV) equation of state. The dynamic viscosity is obtained with the Chung-Lee-Starling model. The inlet Reynolds (based on the cylinder diameter) and Mach numbers are $Re_D = 3.4\times10^5$ and $M \in [0.6; 0.8]$, where the Mach number will be varied. The fundamental derivative of gas dynamics Γ is lower than unity at inlet, resulting in non-monotonic variations of the speed of sound through isentropic compressions and expansions. The flow being transonic, shock waves exist near the peak suction points of the cylinder and interact with the boundary layer, essentially controlling the separation mechanism, or behind the recirculation bubble for high Mach number cases. Complex shock-vortex interactions are also expected in the near wake due to the locally supersonic speeds reached in the vortices [5].

The compressible LES equations are solved with the in-house MUSICAA finite-difference solver. The inviscid fluxes are discretized by means of 10th-order standard centred differences whereas 4th-order is used for viscous fluxes. The scheme is supplemented with a 10th-order selective filtering to eliminate grid-to-grid unresolved oscillations. A four-stage Runge-Kutta algorithm is used for time integration and the IRS method [6] is implemented to enlarge the stability and allow the use of larger timesteps. The filter also acts as a regularization term draining energy at subgrid scales, so that no explicit subgrid-scale model is used (implicit LES). The numerical domain consists in a structured curvilinear grid combining H- and O-type topologies, split in any number of sub-domains to allow for parallel computation via the MPI library. The grid resolution has been set based on previous experience and literature [1, 7] and will ensure a wall non-dimensional flow unit $y^+ \leq 1.5$ to fully resolve the boundary layer. Adiabatic no-slip conditions are applied at the wall, and non-reflecting Tam & Dong's conditions are imposed at the inlet, top, bottom and outflow boundaries. Periodicity is enforced in the spanwise direction.

VALIDATION AND BACKGROUND

The case of the cylinder in cross flow has been established as a benchmark test for the LES. Prior to the dense gas flow LES campaign, the present solver has been validated against numerical and experimental data from the literature for the well known perfect gas flow at $Re_D = 3900$ and low inlet Mach number using a mesh with the same topology as the one we use for the high Reynolds number case. Figure 1 shows the time-averaged streamwise velocity and turbulent intensity at fixed streamwise stations. Our predictions compare well with those of [8] which is often referenced for this flow configuration.

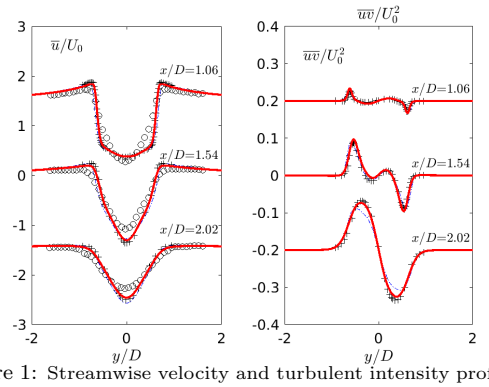

Figure 1: Streamwise velocity and turbulent intensity profiles for cylinder flow at $Re_D = 3900$. Present LES (red line), experiments (++) and LES (blue dash-dot line) from Parnaudeau *et al.*, experiments of Lourenco and Shih (○).

Moreover, we have already performed LES of an isothermal cylinder representative of a hot wire immersed in a dense gas flow in the range $700 \leq Re_D \leq 1500$ at transonic speeds [3]. We see in figure 2 the development of coherent structures in the wake at $Re_D = 717$ and $M_{in} = 0.67$ which remain laminar until they break down to turbulence.

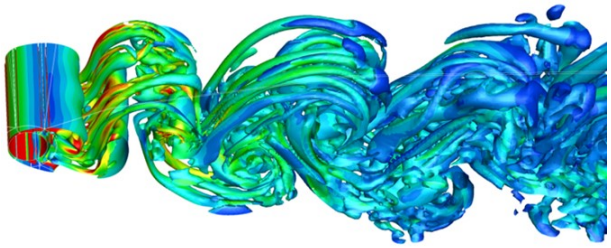

Figure 2: Low-Reynolds flow of a dense vapor past a cylinder. Q-criterion instantaneous iso-surfaces colored by local vorticity magnitude.

WORK IN PROGRESS

As mentioned in the above, a preliminary numerical campaign allowed to compare measurements of time-averaged cylinder wall pressure, in a high-subsonic dense gas high-Reynolds number $10^5 \leq Re_D \leq 10^6$ cross-flow, with (U)RANS simulations. Figure 3 shows the very large difference in recirculation length (shown by the null streamwise velocity component contour in white) prediction between the two methods at $Re = 6.1 \times 10^5$ and $M = 0.6$. Thus, the present LES will help investigating this phenomenon. Figure 4 shows the evolution of the cylinder drag coefficient with Mach number from the literature as well as from the measurements in Novec™649 [2] and the RANS and URANS computations for both air and Novec™649. Because the speed of sound does not vary monotonically through compressions, when the Mach number reaches values $M \geq 0.6$, shock waves may or may not be present on the cylinder apex depending on the thermodynamic conditions of the gas. Furthermore, the boundary layer separation location in this flow regime is driven by the presence of these shock waves. Therefore, the drag coefficient, mostly governed by the wake dynamics, strongly depends on the nature of the gas. The LES at $Re_D = 3.4 \times 10^5$ and the range $M \in [0.6; 0.8]$ will allow us to qualify the non-ideal gas effects, as these are exacerbated by the shock wave formation.

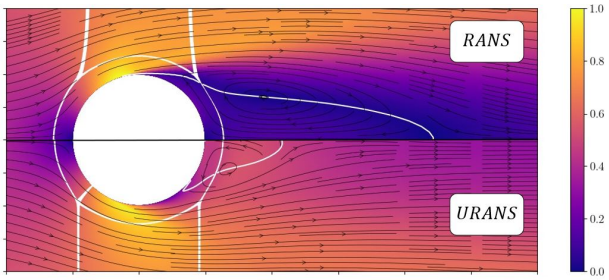

Figure 3: Mach number field, streamlines and null streamwise velocity component contour (white) of a dense gas flow around a cylinder obtained using the RANS (top) and URANS (bottom) methods.

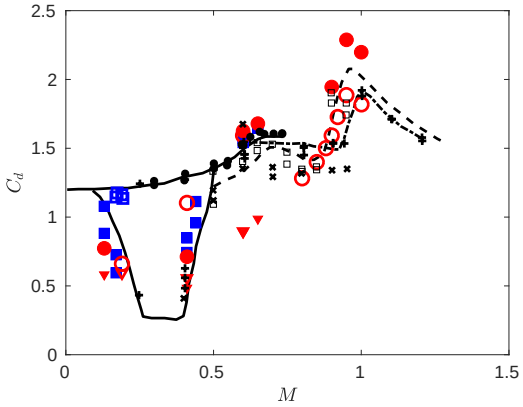

Figure 4: Evolution of the drag coefficient C_d vs. the Mach number. ● present URANS, Novec™649; ○ present URANS, air; present RANS, Novec™649; ▽ present RANS, air; experiments of Reinker *et al.* [2], Novec™649; experiments of Reinker *et al.* [2], Air; —— data from various experiments from Jorgensen; — — data from flight tests of Welsh; —· mean line through data of Macha; * experiments of Gowen & Perkins; + experiments of Murthy & Rose; × experiments of Ackerman; LES of Xia

REFERENCES

[1]Breuer, M. : A challenging test case for large eddy simulation: high Reynolds number circular cylinder flow, *International Journal of Heat and Fluid Flow*, vol. 21, 648—654, (2000).

[2]Reinker, F., Wagner, F., Hake, L. and aus der Wiesche, S. : High subsonic flow of an organic vapor past a circular cylinder, *Experiments in Fluids*, vol. 62, (2021).

[3]Hake, L., et al. : Hot-wire anemometry in high subsonic organic vapor flow, *ASME Turbo Expo 2022*, Paper GT2022-81686, (2022).

[4]Cinnella, P., Matar, C., Gloerfelt, X., Reinker, F., and aus der Wiesche, S. : High subsonic organic vapor flow past a circular cylinder, *6th International seminar on ORC power systems, Munich*, (2021)

[5]Chen, L. W. and Lu, X. Y. : Effect of Mach number on transonic flow past a circular cylinder, *Chinese Science Bulletin*, (2009).

[6]Cinnella, P. and Content, C. : High-order implicit residual smoothing time scheme for direct and large eddy simulations of compressible flows, *Journal of Computational Physics*, vol. 326, 1-–29, (2016).

[7]Cheng, W., Pullin, D. I., Samtaney, R., Zhang, W. and Gao, W. : Large-eddy simulation of flow over a cylinder with ReD from 3.9×10^3 to 8.5×10^5: a skin-friction perspective, *Journal of Fluid Mechanics*, vol. 820, 121-–158, (2017).

[8]Parnaudeau, P., Carlier, J., Heitz, D. and Lamballais, E. : Experimental and numerical studies of the flow over a circular cylinder at Reynolds number 3900, *Physics of Fluids*, vol. 20, (2008).

WORKSHOP
Direct and Large-Eddy Simulation 13
October 26th-29th 2022, Udine, Italy

LEADING-EDGE EFFECTS IN FREESTREAM TURBULENCE INDUCED TRANSITION IN A DENSE GAS FLOW

A. Bienner[1], X. Gloerfelt[1], P. Cinnella[2]
[1] DynFluid Laboratory, Arts et Metiers Institut of Technology, Paris (75013), France
[2] Jean Le Rond D'Alembert Institute, Sorbonne University., Paris (75005), France
aurelien.bienner@ensam.eu

INTRODUCTION

Organic Rankine Cycle (ORC) power systems offer a great potential for waste heat recovery and environmental-friendly power generation but relatively little is known regarding the impact of real-gas effects on loss mechanisms in ORC turbine expanders. A new experimental facility has been built at University of Muenster which consists in a continuously running pressurized closed-loop wind tunnel using Novec$^{\text{TM}}$649 in the high subsonic speed range. Due to the peculiar properties of the working fluid, notably its high density, detailed flow measurements are challenging and numerical simulation are carried out in parallel to characterize flow properties and guide experimental setup. The final aim of this Franco-German collaboration is to get insights in loss mechanisms in ORC expanders using an idealized turbine vane (see figure 2). In this configuration, the asymmetric contouring of the walls enables pressure gradients in the flow domain that corresponds to pressure distributions typical of turbine flows. As the laminar-turbulent transition on turbine blades are generally induced by free-stream-turbulence (FST), we first wish to study the FST transition mechanism for the organic vapor Novec$^{\text{TM}}$649, before simulating the complete blade vane configuration. In particular, the leading-edge and pressure gradient effects in the bypass transition will be analyzed.

LARGE-EDDY SIMULATION STRATEGY

The in-house finite-difference code MUSICAA is used for the large-eddy simulations (LES). The code solves the compressible Navier-Stokes equations for multiblock geometries, using a coordinate transform for curvilinear grids. The inviscid fluxes are discretized by means of 10th-order standard centred differences whereas 4th-order is used for viscous fluxes. The scheme is supplemented with a 10th-order selective filtering to eliminate grid-to-grid unresolved oscillations and provide a selective regularization of subgrid-scales. A four-stage Runge-Kutta algorithm is used for time integration. To relax the CFL stability criteria close to the solid walls and allow the use of larger timesteps, a fourth-order implicit residual smoothing (IRS4) method [1] is applied in the wall-normal direction. Non-reflecting Tam & Dong's conditions are imposed at the inlet and outflow boundaries. Adiabatic no-slip conditions are applied at the blade wall and slip conditions are applied at top and bottom boundaries. A sponge zone combining grid stretching and a Laplacian filter is added at the oulets. Periodicity is enforced in the spanwise direction. Concerning the fluid, the Novec$^{\text{TM}}$649 is modeled with the Peng-Robinson-Stryjek-Vera equation of state [2] and the Chung-Lee-Starling model [3] for the transport properties.

A first study of Novec$^{\text{TM}}$649 boundary layer (BL) transition by oblique modes was conducted [4] at the conditions given in Table 1, where the implicit LES strategy described above was validated against a DNS reference. The good agreement obtained between the DNS and the wall-resolved LES simulations gives good confidence in the regularization filtering strategy and a LES resolution target for following studies (Δx^+=29-27, Δz^+=11-10 and, at the wall, Δy_w^+=0.9-1.0). Concerning the time implicitation, the results of LES with and without it were almost superposed. A spectral analysis realized after even showed that the resolution of the LES with IRS, w.r.t its explicit counterpart, was better due to lower dissipation as the numerical dissipation for the LES-IRS is applied less frequently. The overcost of the method, due to the parallel solving of a pentadiagonal system with variable coefficients at each iteration, represented approximately 15% for our code. The resulting enlargement of the CFL permitted the timestep to be increased by a factor of 4 compared to the stability limit of the explicit integration scheme, which resulted in computational time reduction by of a factor 3.5.

U_∞ [m/s]	c_∞ [m/s]	p_∞ [bars]	T_∞ [°C]	ρ_∞ [kg/m^3]	μ_∞ [μPa.s]
76.2	84.7	4	100	48.5	12.84

Table 1: Thermodynamic and aerodynamic conditions.

FREE-STREAM TURBULENCE INDUCED TRANSITION

To characterize the disturbances ahead of the blade vane, preliminary experiments of the decay of grid-generated homogeneous isotropic turbulence (HIT) for Novec$^{\text{TM}}$649 are conducted in the CLOWT facility [5]. Hot-wire measurements at low speeds with a grid mesh size of 4 mm indicate a turbulence with an integral length scale $L_{11} \sim 3$ mm and a turbulence intensity $T_u \sim 2.8$ %. This corresponds to large disturbances and to a very high Reynolds number based on L_{11} ($Re_{L_{11}} \approx 9 \times 10^5$) at the chosen operating conditions, to be compared for instance in Brandt et al. [6] where $Re_{L_{11}}$ is varied between 750 and 2250.

Thus, a numerical study to investigate the role of large-scale disturbances on bypass transition for various T_u with the dense gas Novec$^{\text{TM}}$649 at M=0.9 has been conducted [8]. The study was realised over the zero-pressure gradient flat-plate BL canonical configuration, in the same conditions as given in

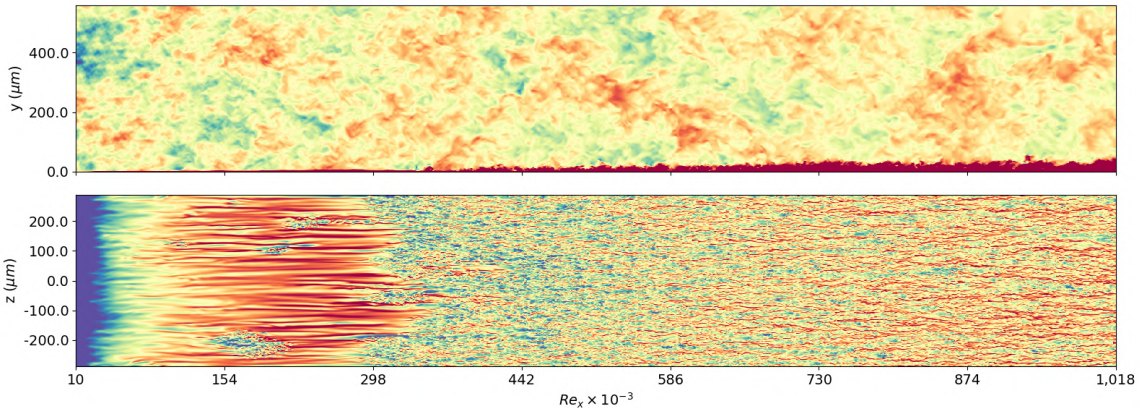

Figure 1: Instantaneous slice xy (top) at $z = 0$ and xz (bottom) at $y/\delta_{99,in} = 1.1$ for case D shown for the full domain.

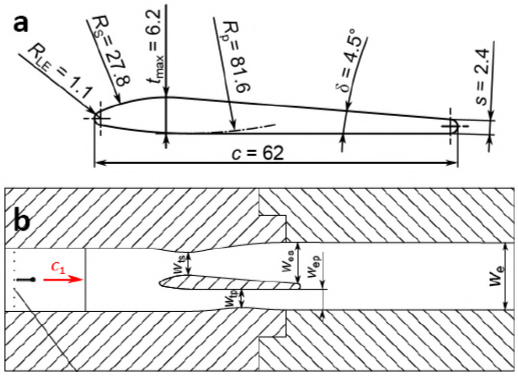

Figure 2: Sketch of the idealized vane configuration. a) blade profile (dimensions in mm). b) blade in contoured channels. Figures from Passmann et al. [7].

Table 1. The inlet Reynolds number was taken as $Re_x = 10^4$, which corresponds to a position close to the virtual flat plate leading edge. The numerical strategy described above was used and synthetic turbulence, generated by the method of random Fourier modes, was added at the inlet a certain height above the BL (in the same way as Pinto et al. [9]). Despite the high subsonic Mach number and due to the high specific heat of Novec^{TM}649 which reduces the friction heating at the wall, we found that the dense gas BL exhibits a behaviour a close to the incompressible regime and that there is no peculiar non-ideal real gas effects. Even for the lowest turbulence intensity case, the transition length on the flat plate is inferior to 2 mm, to be compared with the 62 mm of the blade vane. Moreover, the LES results show that the high increase of the integral length scale, $Re_{L_{11}} = 1728$ to 17280, tends to delay transition and increase the spanwise scales of the Klebanoff streaks. The decrease of the inlet turbulence intensity, in presence of large scale, moves the transition downstream.

As we observed that the injection height, which intends to mimick the shear sheltering effect, is a tunable parameter that influences the onset of transition, we want to get rid of that artefact by including the leading edge. To reproduce a configuration similar to the blade vane, the geometry of the blade is now taken. As we expect the transition location to be rather close to the leading edge, only the onset of the profile is simulated. A precursor RANS simulation is conducted over the entire test section and is used to impose the boundary conditions. The influence of integral length scale of incoming turbulence on the wrapping leading edge structures, the shear-sheltering effect and the breakdown mechanism will be investigated using wall-resolved LES, with specific focus on the role of the strong favorable pressure gradient

REFERENCES

[1]P. Cinnella and C. Content, "High-order implicit residual smoothing time scheme for direct and large eddy simulations of compressible flows," vol. 326, pp. 1–29, 2016.

[2]R. Stryjek and J. Vera, "PRSV: An improved Peng-Robinson equation of state for pure compounds and mixtures," *The Canadian Journal of Chemical Engineering*, vol. 64, no. 2, pp. 323–333, 1986.

[3]T. Chung, M. Ajlan, L. Lee, and K. Starling, "Generalized multiparameter correlation for nonpolar and polar fluid transport properties," *Industrial & Engineering Chemistry Research*, vol. 27, no. 4, pp. 671–679, 1988.

[4]A. Bienner, X. Gloerfelt, and P. Cinnella, "Numerical study of boundary-layer transition in a high-subsonic organic vapor flow," *56th 3AF Conference* 28-30 March, Toulouse, France, FP108-AERO2022, 2022.

[5]F. Reinker, K. Hasselmann, S. aus der Wiesche, and E. Kenig, "Thermodynamics and fluid mechanics of a closed blade cascade wind tunnel for organic vapors," *ASME Journal of Engineering for Gas Turbines and Power*, vol. 138, pp. 052601–1–052601–8, 2016.

[6]L. Brandt, P. Schlatter, and D. Henningson, "Transition in boundary layers subject to free-stream turbulence," *J. Fluid Mech.*, vol. 517, pp. 167–198, 2004.

[7]M. Passmann, S. aus der Wiesche, and F. Joos, "Focusing schlieren visualization of transonic turbine tip-leakage flows," *Int. J. Turbomach. Propuls. Power*, vol. 5, 2020.

[8]A. Bienner, X. Gloerfelt, P. Cinnella, H. Leander, S. aus der Wiesche, and S. Strehle, "Study of bypass transition in dense-gas boundary layers," *12th TSFP conference* 19-22 July, Osaka, Japan (Online), 2022.

[9]B. Pinto and G. Lodato, "Synthetic freestream disturbance for the numerical reproduction of experimental zero-pressure-gradient bypass transition test cases," *Flow, Turbulence and Combustion*, vol. 103, pp. 25–54, 2019.

WORKSHOP
Direct and Large-Eddy Simulation 13
October 26th-29th 2022, Udine, Italy

IMPLICIT LARGE EDDY SIMULATION OF A NEAR POST-STALL NACA0012 AEROFOIL

M. Lahooti[1], G. Vivarelli[1], F. Montomoli[1] and S.Sherwin [1]
[1] Aeronautical Engineering Deparment
Imperial College London, United Kingdom
m.lahooti@imperial.ac.uk

INTRODUCTION

In this study, a high-fidelity numerical simulation is reported to reveal the key flow dynamics near post-stall regime of *NACA*0012 aerofoil section at $Re = 1.5 \times 10^5$ with the focus on the separation bubble and laminar-to-turbulent transition. There are numerous works on the stall regime, but most of them concentrate on integral quantities such as aerodynamic coefficients [2, 4]. Further, the studies that reported the details of flow dynamics are majorly at low Reynolds numbers. For example, Zakaria et al. [1] investigated the flow over NACA0012 at high angles of attack (AoA) at $Re = 7.99 \times 10^4$ using both experimental and computational approach with the focus on the vortex shedding characteristics from the trailing edge. Eljack et al. [3] presented a detailed study of the flow and laminar separation bubble over AoAs enveloping the the onset of stall. However, they only considered two low Reynolds numbers of 5×10^4 and 9×10^4. Additionally, the flow conditions in their work is slightly compressible with $M = 0.4$ with variable temperature and viscosity. Similarly, Rosti [6] conducted a DNS study of NACA0012, where despite the detailed report on the flow field, the study only covers $Re \leq 5 \times 10^4$. Finally, more recently, Poels et al. [5] experimentally investigated and presented a detailed flow field for a range of Reynolds number $Re \leq 1.2 \times 10^5$, however, their study is limited to angles of attack less than $\alpha = 8°$.

In the present study, a higher Reynolds number of $Re = 1.5 \times 10^5$ is considered which is in a more practical range of high-altitude low-endurance (HALE) aero vehicles as well as vertical-axis wind turbines. Additionally, aiming at understating the transition mechanism near the post-stall, three angles of attack is considered that are corresponds to near pre-stall, near max-lift and near post-stall regimes respectively. Details of the flow dynamics, separation, laminar bubble and distribution of shear stress are studied over these AoAs and will be presented. Finally, numerical requirements of accurate prediction of aerodynamic coefficients using the high-order implicit LES method will be discussed to highlight the practical aspect of this work.

NUMERICAL METHOD AND PROBLEM DESCRIPTION

The flow simulation is conducted using high-order spectral/hp element implementation of incompressible Navier-Stokes equations in the *Nektar++* frame work. *Nektar++* [7] is an open-source *spectral/hp* finite element solver library written in *C++*. Simulations are performed using Quasi-3D assumptions where the flow is assumed to be homogeneous in the cross-flow direction, with the period length equal to the spanwise length [9]. The *Gradient Jump Penalisation* methodology [10] is used for stablisation of the solution. Finally the flow dynamics is evolved in time using second-order accurate implicit-explicit formulation.

Simulations are performed at Reynolds number $Re = 1.5 \times 10^5$ at three angles of attack: $\alpha = 9°$ $10°$ and $12°$. A rectangle computational domain is used for the computations where the airfoil of chord length $c = 1$m is located $10c$ from the inlet and the side boundaries and the domain spans $15c$ to the downstream. Geometry-conforming high-order mesh is used to tessellate the domain. The mesh consists of 2400 high-order elements (macro-elements) with the size ranging from maximum of $3c$ in the far fields to the minimum of $1 \times 10^{-3}c$ near the wall. Within each macro-element, the polynomial order $\mathcal{P} = 12$ in the xy plane is used that results in $y^+ < 1$, while for the spanwise direction, the airfoil is extruded to a chord length and is discretised with 128 Fourier planes (64 complex Fourier modes).

RESULTS

The flow-field at the three AoAs showed a significant degree of similarity, therefore AoA=12° results will be shown and any difference with the other cases will be described.
The time-averaged flow field at an angle of 12° is reported in figure 1. This shows the main flow features appearing: due to the large angle of attack, the stagnation point moves onto the pressure side with a very thin, laminar boundary layer forming thereafter. On the other hand, along the suction side of the aerofoil, the flow immediately experiences separation, with a re-circulation bubble forming. On top of this, an acceleration region appears with the fastest flow of the entire domain. Consequently, the boundary layer transitions to turbulent thickening in height. Large vortices are then shed from the wing trailing edge.

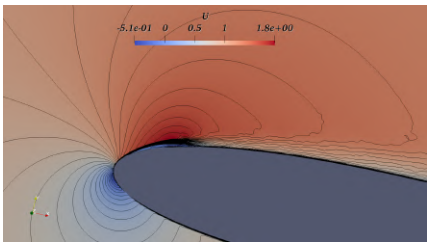

Figure 1: Leading edge t-averaged solution at AoA=12°.

One of the big differences concerning the separation region, is the length. In fact, it was seen that as the AoA is increased, the re-circulation bubble region shortens with the acceleration region above it increasing in both magnitude and size.
One the first quantities analysed was the pressure coefficient as reported in figure 2. Along the aerofoil upper surface (continuous line, dashed is for pressure side), the flow immediately experiences an adverse pressure gradient. It is clear from the three trends, that as the AoA is decreased, the plateau representing the re-circulation region moves upstream and shortens in length. Following, this there is an intermediate region of aggressive pressure loading increase, till it roughly flattens between 15% and 20% chord length depending on the AoA. The pressure coefficient jump at the end of the separation indicates the beginning of turbulent transition. This region then ends where the C_p slope abruptly changes.

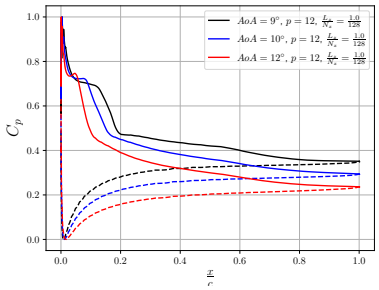

Figure 2: Pressure coefficient for different AoAs.

These findings were confirmed by the instantaneous span-wise wall-shear stress of the aerofoil surface (figure 3). At the aerofoil leading-edge, the flow presents limited three-dimensionality. Nevertheless, spots of higher shear-stress are visible, indicating the presence of $3D$ structures inside the reversed flow patch. Once the separation re-attaches we have a region of very high-intensity shear-stress fluctuations that dies out around the 15% chord length. This can be considered as the transition region, and in the case of the $9-10°$ angles, was found to be longer.

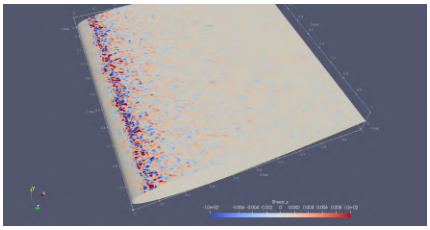

Figure 3: Span-wise instantaneous wall shear-stress AoA=12°.

To assess the validity of this assumption, the power-spectral density (PSD) of the fluctuating velocity (u') was computed at various chord lengths within the boundary layer. One of the sampling points is shown in figure 4. Clearly, there are dominant frequencies present in the lading-edge region: this is indicative of comment made earlier on concerning the $3D$ structures forming. All three AoA simulations highlighted relatively broadband peaks appearing in the frequency mid-range. Moving further downstream, i.e. points sampling the boundary layer around 20% chord, it was seen that turbulence transition has occurred given the decay rate matching the $-\frac{5}{3}$-law.

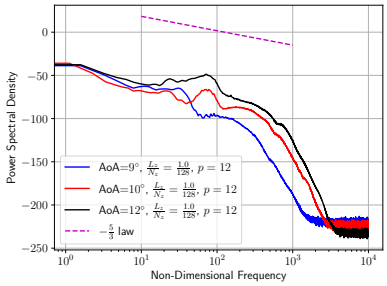

Figure 4: PSD Comparison in the separated region.

Finally, the spatial correlation of the three fluctuating velocity components was calculated to check whether all the flow structures are contained in the domain. These showed that there is still a large degree of correlation in the x-velocity component: this was seen throughout the simulations at various AoAs and may be attributed to a very large structure that could be captured by increasing the span-wise length.

ACKNOWLEDGEMENTS

The authors would like to thank EPSRC for the computational time made available on the UK supercomputing facility ARCHER2 via the UK Turbulence Consortium (EP/R029326/1). Financial support was provided by the *FANFARE* grant number 113286.

REFERENCES

[1]M. Y. Zakaria et al.: A computational study of vortex shedding from a NACA-0012 airfoil at high angles of attack, International Journal of Aerodynamics, **6**, **1**, 1–17 (2018), Inderscience Publishers (IEL).

[2]S. Eftekhari et al.: Investigation of a NACA0012 Finite Wing Aerodynamics at Low Reynold's Numbers and 0º to 90º Angle of Attack, *Journal of Aerospace Technology and Management*, **11**, SciELO Brasil.

[3]E. Eljack et al.: Simulation and characterization of the laminar separation bubble over a NACA-0012 airfoil as a function of angle of attack, Physical Review Fluids, **6**, **3**, 034701–034729 (2021), APS

[4]S. Martínez-Aranda et al.: Comparison of the aerodynamic characteristics of the NACA0012 airfoil at low-to-moderate Reynolds numbers for any aspect ratio, International Journal of Aerospace Sciences, **4**, **1**, 1–8 (2016), International Journal of Aerospace Sciences

[5]A. Poels et al.: Mode and regime identification for a static NACA0012 airfoil at transitional Reynolds numbers, Mechanics & Industry, **21**, **6**, 620 (2020), EDP Sciences

[6]M. Rosti et al.: Direct numerical simulation of the flow around an aerofoil in ramp-up motion, Physics of Fluids, **28**, **2**, 025106, AIP Publishing LLC (2016).

[7]D. Moxey et al. : Nektar++: Enhancing the capability and application of high-fidelity spectral/hp element methods, *Computer physics communications*, **249**, 107–110 (2020), Elsevier.

[8]E. Tadmor : Convergence of spectral methods for nonlinear conservation laws, *SIAM Journal on Numerical Analysis*, **26**, 30–44 (1989), SIAM.

[9]G. E. Karniadakis : Spectral element-Fourier methods for incompressible turbulent flows, *Computer Methods in Applied Mechanics and Engineering*, **80**, 367–380 (1990), Elsevier.

[10]R. C. Moura et al. : Gradient jump penalty stabilisation of spectral/hp element discretisation for under-resolved turbulence simulations, *Computer Methods in Applied Mechanics and Engineering*, **388**, 114–200 (2022), Elsevier.

WORKSHOP
Direct and Large-Eddy Simulation 13
October 26th-29th 2022, Udine, Italy

THE EFFECT OF WING-TIP VORTICES ON THE FLOW AROUND A NACA0012 WING

S. Toosi[1], A. Peplinski[1,2], P. Schlatter[1,2], R. Vinuesa[1,2] ,
[1] FLOW, Engineering Mechanics, KTH Royal Institute of Technology, Sweden
[2] Swedish e-Science Research Centre (SeRC), Stockholm, Sweden
siavasht@kth.se

INTRODUCTION

There are two basic contributions to the total drag of an airplane [1]: (i) parasite drag, which consists of friction drag, form drag, and interference drag, and (ii) induced drag (vortex drag, or drag due to lift), which is caused by lift generation in finite-span wings and the consequent presence of wing-tip vortices. The two types of drags have close to equal contributions to the total drag in cruise conditions, while the induced drag is the dominant source during the take-off, climb and landing phases of flight [1].

The goal of the present work is to perform a systematic study of the formation of wing-tip vortices and their interaction with and impact on the surrounding flow in more details. Of particular interest is the interaction of these vortices with wall turbulence and the turbulent wake. This is done by considering two wing geometries, i.e., infinite-span (periodic) and three-dimensional (wing-tip) wings, at three different angles of attack: $\alpha = 0^o$, 5^o, 10^o.

NUMERICAL METHOD

To ensure of the accuracy of the results, we perform high-resolution large-eddy simulations (LES), where only the smallest scales (e.g., $\leq 6\eta$ in the wake, where η is the Kolmogorov length scale) are accounted for by the subgrid scale (SGS) model. Simulations are performed by the high-order incompressible Navier−Stokes solver Nek5000 [2] with added adaptive mesh refinement (AMR) capabilities developed at KTH [3]. The AMR version adds the capability of handling non-conforming hexahedral elements with hanging nodes, and so, adds an h-refinement capability where each element can be refined individually. Solution continuity at non-conforming interfaces is ensured by interpolating from the "coarse" side onto the fine side.

The velocity field is expanded by a polynomial of order $p = 7$ on the Gauss−Lobatto−Legendre (GLL) points ($N = p + 1 = 8$ GLL points in each direction), while the pressure is represented on $p - 1$ Gauss−Legendre (GL) points following the $P_N - P_{N-2}$ formulation [2]. The nonlinear convective term is overintegrated to avoid (or reduce) aliasing errors. Time stepping is performed by an implicit third-order backward-differentiation scheme for the viscous terms and an explicit third-order extrapolation for the nonlinear terms. A high-pass-filter relaxation term [7] is added to the right-hand side of the equations, providing numerical stability and acting as a SGS dissipation.

Wings are located such that their mid-point along the chord line coincides with the origin of the coordinate system and have a no-slip no-penetration boundary condition. Here x, y and z denote the streamwise, wall-normal and spanwise directions, respectively. The computational domain has a rectangular cross-section in the xy-plane that extends $20c$ upstream, $30c$ downstream, and $20c$ in positive and negative y directions. Different angles of attack are achieved by rotating the wing along the z axis around its center. This specific design is to allow for the use of the "outflow-normal" boundary condition [2] on the y-normal boundaries; this allows for a non-zero y component of velocity. The three-dimensional (3D) wing domain extends $20c$ from the wing root (located at $z = 0$) in the spanwise direction and has an "outflow-normal" boundary condition at $z = 20c$. A symmetry boundary condition is used at the $z = 0$ plane. Boundary layers are tripped on both the suction and pressure sides of the airfoils for all six cases.

The production grids are generated by iterative refinement of the initial grids, where at each iteration the elements with the highest contribution to solution error [6], based on solution on that grid, are selected for refinement. The error indicator of Mavriplis [4] is used for this purpose. The convergence process is accelerated by some manual input from the user. The adaptation process is terminated based on the resolution criteria available in the literature [5]. Table 1 summarizes some information about the production grids used in this work, and Figure 1 shows the spectral elements of grid RWT-5 from Table 1.

RESULTS AND DISCUSSION

Some preliminary results are presented in this section. These results are from the production grids of Table 1 but have not been averaged for a sufficiently long period of time yet. Nevertheless, the observed phenomena are not expected to change for longer integration times.

Figure 2 shows the root-mean-square (rms) velocities in the streamwise and wall-normal directions near the trailing edge of the airfoil on a yz-plane. It can be observed that the two components are non-zero and very close in magnitude to one another. We also notice that the strong rotation and pressure gradient imposed by the vortex tends to relaminarize the turbulent boundary layer on the suction side, as seen for instance at spanwise locations $0.66 \leq z/c \leq 0.7$. This relaminarization can also be seen in the instantaneous vortical structures shown

Grid	N_{GLL}	N_{grid}	$(\Delta x^+_{\text{mean}}, y^+_1, \Delta z^+_{\text{mean}})$
P-0	376×10^6	249×10^6	(10.3,0.72,8.7)
P-5	381×10^6	252×10^6	(10.5,0.73,8.5)
P-10	435×10^6	288×10^6	(12,0.8,9)
RWT-0	950×10^6	630×10^6	(10.3,0.7,5.5)
RWT-5	1.58×10^9	1.05×10^9	(10.5,0.75,5.7)
RWT-10	2.16×10^9	1.43×10^9	(12,0.8,6)

Table 1: Summary of the production grids used in this study and their near-wall resolution. N_{GLL} shows the number of GLL points, while N_{grid} denotes the number of independent grid points. $\Delta_{\text{mean}} = \delta/p$ is the average resolution of the element, where δ and p are the element size and polynomial order. y_1 shows the distance of the second GLL point to the wall. Wall resolutions are normalized by the viscous length $\delta_\nu = \nu/\sqrt{\tau_w/\rho}$. The P-* grids denote periodic cases, whereas RWT-* stands for rounded wing-tip cases. The number next to each grid shows the angle of attack, α.

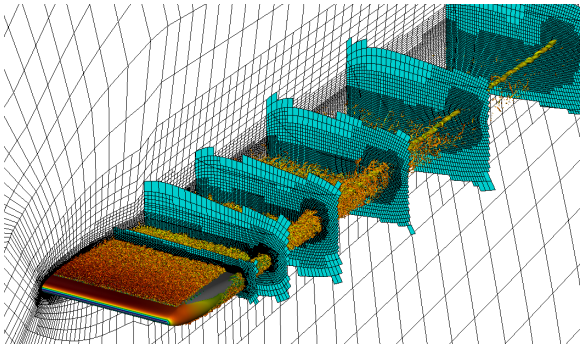

Figure 1: Spectral-element grid for case RWT-5 with 3.1 million spectral elements. The grid is generated using the h-adaptation capabilities of the AMR version of Nek5000. We show instantaneous vortical structures represented by $\lambda_2 = -100$ isosurface colored by streamwise velocity ranging from (blue) low to (red) high.

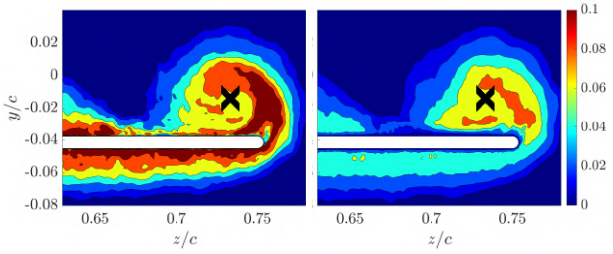

Figure 2: The rms velocities in the streamwise (left) and wall-normal (right) directions for the RWT-5 grid (Table 1) near the trailing edge. The black X shows the location of the core of the wing-tip vortex. The apparent noise is due to insufficient time averaging.

in Figure 1.

Another interesting observation from Figure 2 is the larger-magnitude of velocity fluctuations in the vortex region outside the core to the top of the wing-tip, as well as the lower fluctuations closer to the wing-tip surface. A very similar pattern to these fluctuations is observed in the turbulent kinetic energy (TKE) production and dissipation terms shown

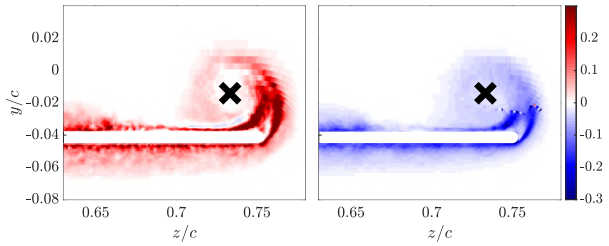

Figure 3: Turbulent kinetic energy (TKE) production (left) and dissipation (right) at the same location as Figure 2. The black X shows the location of the core of the wing-tip vortex. The apparent noise is due to insufficient time averaging.

in Figure 3, where we note a significant production region in the high-fluctuation area and very small production in the low-fluctuation regions. This can be most simply explained by the functional form of the production term, which has higher values where both the Reynolds stresses (i.e., velocity fluctuations) and velocity gradients (near the vortex core) are high. Also notice that the TKE dissipation rate does not completely match its production in shape or magnitude, suggesting a highly non-local turbulence with significant transport phenomena.

CONCLUSIONS AND OUTLOOK

This work leverages the AMR version of Nek5000 to perform several high-resolution large-eddy simulations of the flow around periodic and 3D NACA0012 wings to investigates the impact of wing-tip vortices on the flow.

Preliminary results suggest significant TKE production as a result of wing-tip formation, as well as a non-local turbulence characterized by the local imbalance between TKE production and dissipation.

The final work to be presented in the conference will be based on longer integration times with converged statistics, and will also include spectral analysis.

REFERENCES

[1]Federal Aviation Administration : Pilot's Handbook of Aeronautical Knowledge, *United States Department of Transportation, Federal Aviation Administration, Airman Testing Standards Branch, Oklahoma City, United States*, (2016).

[2]Fischer P.F., Lottes J.W., Kerkemeier S.G. : NEK5000: Open source spectral element CFD solver. *Available at:* `http://nek5000.mcs.anl.gov`, (2008).

[3]Offermans N., Peplinski A., Marin O., Schlatter P. : Adaptive mesh refinement for steady flows in Nek5000, *Computer & Fluids*, **197**, 104352 (2020).

[4]Mavriplis C. : A posteriori error estimators for adaptive spectral element techniques, *In: Wesseling, P. (ed.) Proceedings of the Eighth GAMM-Conference on Numerical Methods in Fluid Mechanics. Notes on Numerical Fluid Mechanics*, 333–342 (1990).

[5]Vinuesa R., Negi P.S., Atzori M., Hanifi A., Henningson D.S., Schlatter P. : Turbulent boundary layers around wing sections up to $Re_c = 1,000,000$. *International Journal of Heat and Fluid Flow*, **72**, 86–99 (2018).

[6]Fidkowski, K. J., Darmofal, D. L. : Review of Output-Based Error Estimation and Mesh Adaptation in Computational Fluid Dynamics, *AIAA Journal*, **49**, 673–694 (2011).

[7]Schlatter, P., Stolz, S., Kleiser, L. : LES of transitional flows using the approximate deconvolution model, *International Journal of Heat and Fluid Flow*, **25**, 549–558 (2004).

WORKSHOP
Direct and Large-Eddy Simulation 13
October 26th-29th 2022, Udine, Italy

LAMINAR-TURBULENT TRANSITION IN SUPERCRITICAL FORWARD-FACING STEPS IN CROSSFLOW

J. Casacuberta[1], S. Hickel[1], and M. Kotsonis[1]
[1] Faculty of Aerospace Engineering
Delft University of Technology, the Netherlands
J.CasacubertaPuig@tudelft.nl

INTRODUCTION

Achieving and maintaining laminar flow on large swept surfaces of subsonic transport aircraft is currently posing a considerable challenge for aerodynamic design. Surface roughness, for instance imperfect joints introducing sharp surface distortions, is a source of significant laminar flow deterioration, i.e., advancement of laminar-turbulent transition. The elucidation of roughness-induced transition has motivated a wealth of recent numerical and experimental studies, with particular attention to the effects of forward-facing steps.

The present work considers a laminar-turbulent transition route initiated by primary (stationary crossflow) eigenmode amplification, which is the prevalent scenario in low-disturbance environments as in free-flight [1]. This instability kind manifests in the developed flow field

$$\mathbf{q}(x,y,z,t) = \mathbf{q}_{\mathrm{B}}(x,y) + \mathbf{q}'(x,y,z) + \mathbf{q}''(x,y,z,t) \quad (1)$$

as co-rotating vortices whose axes of rotation are practically aligned with the direction of the streamlines in the outer-flow region. Under Decomposition (1), the developed flow $\mathbf{q} = [u\ v\ w\ p]^T$ is conceived as the superposition of the laminar unperturbed base flow, $\mathbf{q}_{\mathrm{B}}$, with steady, $\mathbf{q}'$, and unsteady, $\mathbf{q}''$, perturbation fields.

In stationary-crossflow-dominated flows, forward-facing steps significantly altering the laminar-turbulent transition path may be classified as critical or supercritical. Critical steps advance the transition front upstream, as compared to a reference clean (i.e., no step present) case. Conversely, supercritical steps have been found to drastically move the transition front to the vicinity of the step, essentially tripping the flow immediately downstream. The main goal of the present work is to identify and scrutinise the step-flow mechanisms responsible for inducing a supercritical transition scenario.

METHODOLOGY

The incompressible swept-wing flow is modeled as flat-plate flow with an externally imposed airfoil-like pressure gradient in the chordwise direction. The main coordinate system reads $\mathbf{x} = [x\ y\ z]^T$, where x, y, z indicate the chordwise (i.e., normal to the virtual leading edge), wall-normal, and spanwise directions, respectively. The free-stream velocity is decomposed into a chordwise component, u_∞, and a spanwise component, $w_\infty = -1.24u_\infty$, to model the effect of sweep angle. Pressure measurements from wind-tunnel experiments on a 45° swept wing [2] are used to guide the DNS setup. The inflow boundary layer thickness, $\delta_0 = 7.71\times10^{-4}$ m, and free-stream velocity, $u_\infty = 15.10$ m/s, are chosen as global characteristic quantities and used as non-dimensionalizing values.

A stationary crossflow mode, computed as solution to a local linear Orr-Sommerfeld analysis on the base flow profile, is prescribed at the inflow with an amplitude of $3.5\times10^{-3}u_\infty$. The step height, $h = 0.97\delta_0$, which is fixed, corresponds to approximately 50% of the undisturbed boundary layer thickness at the virtual step location. The spanwise domain length (i.e., fundamental spanwise wavelength) is set to $\lambda_z = 7.5$ mm.

The analysis of results discusses steady and unsteady perturbation effects. The steady perturbation field, $\mathbf{q}'$, is decomposed in spanwise Fourier modes, i.e.,

$$\mathbf{q}'(x,y,z) = \sum_{j=-N}^{N} \tilde{\mathbf{q}}_j(x,y)\mathrm{e}^{\mathrm{i}j\beta_0 z}, \quad (2)$$

where N is the number of modes considered, $\tilde{\mathbf{q}}_j$ is the Fourier coefficients of mode j, $\beta_0 = 2\pi/\lambda_z$, and $\mathrm{i}^2 = -1$.

Direct Numerical Simulations (DNS) of the incompressible Navier-Stokes equations are performed with INCA, a conservative finite-volume solver. The Navier-Stokes equations are marched in time with a third-order Runge-Kutta method. A fifth-order upwind scheme is used to discretize the convective terms. The Selective Frequency Damping (SFD) method is applied to numerically compute the stationary isolated form of $\mathbf{q}'$.

The computational domain encompasses $0 \le x/\delta_0 \le 517$ and $y/\delta_0 \le 26$ and the grid contains $N_x = 6760$, $N_y = 1008$, and $N_z = 144$ points in the chordwise, wall-normal, and spanwise directions, respectively. These values yield $\Delta x^+ = 1.8$, $\Delta y^+ = 0.9$, and $\Delta z^+ = 9$ in the developed flow near the step featuring explosive growth of secondary instabilities and laminar breakdown. Numerical computations of the base flow and the developed flow are performed independently for a similar numerical setup. In the former, the equations are converged in time up to a threshold value of 10^{-8} based on an L_2-norm evaluation of the temporal derivatives. In the developed flow runs, unsteady perturbation content is triggered via the Blowing-Suction (BS) technique at the wall near the inflow. Accordingly, the wall-normal velocity is modulated as follows:

$$v(x,0,z,t) = f_s(x)\sum_{k=1}^{M} A_k^{\mathrm{BS}}\cos(\beta_0 z + 2\pi k f_0 t + \phi_k), \quad (3)$$

with f_0 representing a fundamental temporal frequency, A_k^{BS} indicates the initial amplitude of a temporal component k, ϕ_k is a random phase, and f_s smoothly modulates the response in x. Unsteady forcing is applied ranging from 3 kHz to 14 kHz in intervals of 1 kHz. For the present setup, the DNS results reproduce the transitional-flow scenario observed in experiments in a low-disturbance wind tunnel [2].

RESULTS

The evolution of the stationary perturbation at the step is first discussed. Two major flow regimes are identified. *Far* from the wall, the pre-existing fundamental (i.e., primary Fourier mode) perturbation lifts off and passes over the step. *Close* to the wall, chordwise-velocity (u') perturbation streaks of alternating sign in z are induced at the step corner (Figure 1). This scenario develops analogously for each Fourier component, implying that a near-wall streak system contained in a particular Fourier mode *has adopted* the spanwise wavelength of the incoming crossflow component that induces it.

A Reynolds-Orr budget analysis applied to each Fourier component independently reveals that, for the primary mode, linear production is the dominant mechanism in both the near- and far-wall regimes. An algebraic instability associated to the lift-up effect is identified as the main mechanism responsible for altering the behaviour of the fundamental perturbation at the step. On the other hand, the significant amplification of the harmonic (i.e., smaller wavelength) perturbation field close downstream of the step is associated to a modal inflectional instability supported by the step-distorted base-flow profiles.

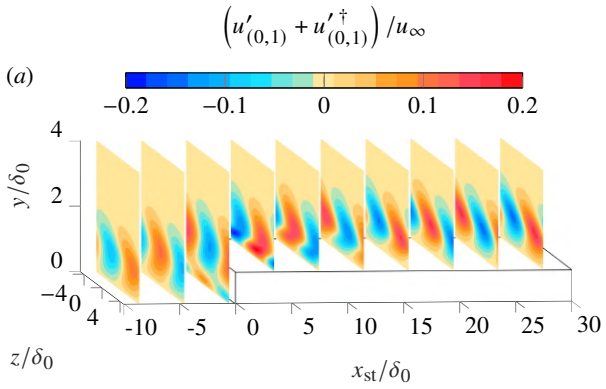

Figure 1: Organization of the primary perturbation Fourier mode at the step.

The rapid growth in x of perturbation streaks close to the step corner for all Fourier components introduces a strong distortion of the near-wall shear layer of the developed flow. This distorted shear layer is prone to unsteady perturbation amplification. The particular combination of step height and incoming crossflow amplitude tested in this work was shown to yield laminar breakdown close downstream of the step in the experiments of [2]. Their transition scenario is fully captured in the present DNS results.

Figure 2 portrays the instantaneous unsteady developed flow evolution by depicting an instantaneous isosurface of Q-criterion. Close downstream of the step, wedges of unsteady contamination are the precursor of turbulence activity. The unsteady activity initiating the breakdown process develops in the shears of the lower portion of the boundary layer distorted by the step-induced perturbation streak enhancement. In particular, the modulation in time of the wall-normal shear layer on top of the low-speed streak in the developed flow gives rise to large-scale hairpin-like vortices. This resembles the varicose secondary streak instability mechanism arising in scenarios of natural by-pass transition in a boundary layer subject to free-stream turbulence [3].

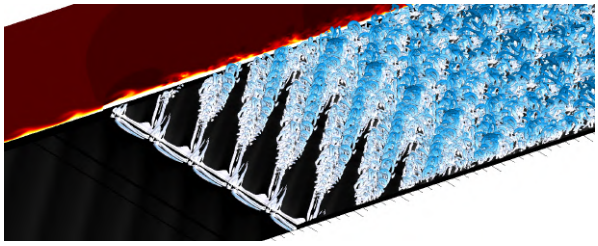

Figure 2: Instantaneous Q-criterion isosurface color-coded by wall distance (white indicates close to the wall) and x-y plane of instantaneous chordwise-velocity.

The present results suggest a possible universal role played by near-wall streaks in laminar-turbulent transition induced by two-dimensional surface elements, as previously identified in scenarios of isolated three-dimensional surface elements [4] and natural by-pass transition [3]. Furthermore, the results of this work would indicate that laminar-turbulent transition at the step is not promoted by an enhancement of the secondary crossflow instabilities naturally leading the transition route in a clean no-step configuration.

ADDITIONAL RESULTS

The results presented in this abstract will be complemented with statistical and Fourier-analyzed data of the evolution of the unsteady perturbation field at the step. The spatial development and frequency content of the unsteady flow structures leading the breakdown process will be characterised to scrutinise the nature of the secondary instability mechanisms at the step.

REFERENCES

[1]Saric, W.S., Reed, H.L. and White, E.B. : Stability and transition of three-dimensional boundary layer., *Annu. Rev. Fluid Mech.*, **35**, 413–40 (2003).

[2]Rius-Vidales, A.F., and Kotsonis, M.: Impact of a forward-facing step on the development of crossflow instability., *J. Fluid Mech.*, **924**, A34 (2003).

[3]Brandt, L., Schlatter, P. and Henningson, D.S.: ransition in boundary layers subject to free-stream turbulence., *J. Fluid Mech.*, **517**, 167–198 (2004).

[4]Casacuberta, J., Groot, K.J., Ye, Q. and Hickel, S.: Transitional flow dynamics behind a micro-ramp., *Flow Turbul. Combust.*, **104**, 533-552 (2004).

Session: Roughness

Friday, October 28, 2022

11:10 – 12:40

WORKSHOP
Direct and Large-Eddy Simulation 13
October 26th-29th 2022, Udine, Italy

DIRECT NUMERICAL SIMULATIONS OF TURBULENCE OVER TWO-DIMENSIONAL PERMEABLE RIBS

Y. Kuwata[1] **and K.Suga**[1]
[1] Department of Mechanical Engineering
Osaka Metropolitan University, Japan
kuwata@omu.ac.jp

INTRODUCTION

Turbulent flows over a rough surface are ubiquitous in engineering applications, and numerous studies have been undertaken to reveal the effects of roughness on turbulent flows. However, the roughness elements discussed so far have been impermeable despite the fact that roughness usually have a permeability. Examples include the river bed and vegetation canopy. This serves as a motivation to discuss the effects of permeable roughness.

Recently, the effects of the permeable roughness was experimentally studied by the author's group [1]. They showed that the roughness-induced drag force was decreased with increasing the permeability. The discussions on the log-law parameters including the zero-plane displacement and equivalent roughness suggested that the permeability increased the zero-plane displacement but decreased the equivalent roughness. However, owing to limited optical access, the flow physics around the permeable roughness remains not completely clear. The purpose of the present study is to shed light on the underlying physics on the effects of the permeable roughness by using the high-fidelity direct numerical simulation data.

METHODOLOGY

A schematic of a rough-walled channel flow is shown in Figure1. The top and bottoms walls were impermeable smooth walls, whereas the porous wall with two-dimensional transverse porous-ribs were considered in the bottom of the channel. The rib height was $k = 0.1H$ with H being the distance from the rib bottom to the top wall, and the separation between the neighboring ribs was varied: $w = k$ and $9k$. The flow was periodic in the streamwise (x) and spanwise (z) directions. The flow was driven by a streamwise pressure difference which was adjusted so as to yield the desired flow rate for the bulk mean Reynolds number of $Re_b \simeq 5500$. The size of the computational domain was $5H$ and $1.5H$ in the streamwise and spanwise directions, respectively. The porous medium under consideration consisted of the Kelvin cells (or tetrakaidecahedrons). The porosity of the porous medium was fixed at $\varphi = 0.8$, while we considered two permeability cases: one was the high permeable "HP" case, and the other was low permeable "LP" case. The size of a single Kelvin-cell unit for cases HP and LP were $D = 0.1H$ and $D = 0.05H$, respectively, and the resulting permeabilities were $K/k^2 = 6.4 \times 10^{-5}$ and 1.7×10^{-5}, respectively. The thicknesses of the porous wall were $h = 3D$ for case HP and $h = 2D$ for case LP. The transverse rib was comprised of $1(x) \times 1(y) \times 15(z)$ cells for case HP and $2(x) \times 2(y) \times 30(z)$ cells for case LP. The geometry of the porous-rib roughness was shown in Figure2.

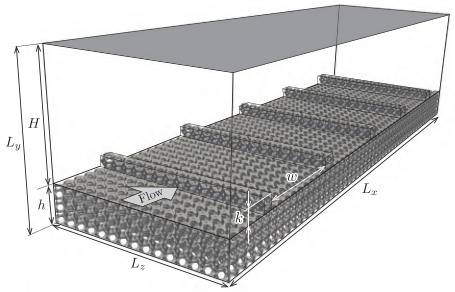

Figure 1: Flow geometry of a porous-rib channel flow.

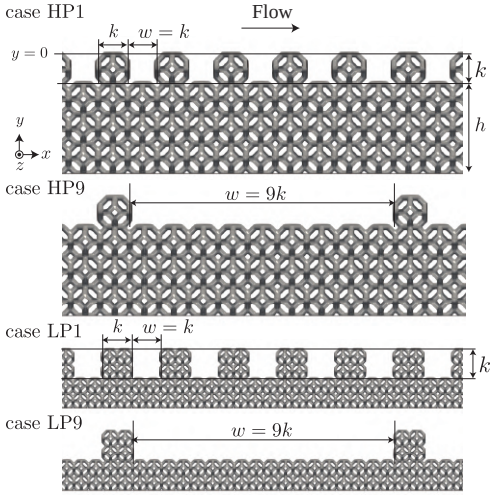

Figure 2: Geometry of the porous-rib roughness: the name of case consists of two letters follower by a number. The letters take "HP" or "LP", and the number stands for the value of w/k.

For the present DNSs, we used the three-dimensional 27 discrete velocities multiple relaxation time LBM [2]. This LBM model was originally developed by the author's group and has successfully been applied to turbulent flows over resolved porous and rough walls [3]. A single Kelvin-cell unit

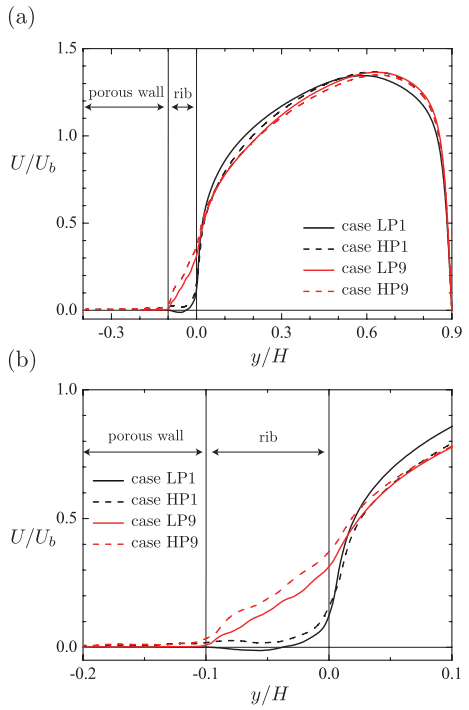

Figure 3: (a) streamwise mean velocity normalized by the bulk mean velocity U_b, (b) enlarged figure near the porous-rib.

was resolved by $40(x) \times 40(y) \times 40(z)$ grids, yielding to the grid spacings in wall units for cases HP and LP are $\Delta^+ \simeq 1.8$ and 0.7, respectively. The total number of grids were 0.4 and 1.30 billions, respectively.

RESULTS AND DISCUSSIONS

Figure 3 presents profiles of $x-z$ plane-averaged streamwise mean velocity U. In Fig.3(a), all the profiles are significantly skewed, that is, the maximum mean velocity location shifts toward the top wall, which is due to an increased frictional resistance by the porous-ribs. The inspection of the mean velocity near the porous-rib in Fig. 3(b) shows that a reduction in U by the porous-rib is larger for $w/k = 1$ as expected. For case LP1, we observe a negative mean flow in the porous-rib region ($-0.1 < y/H < 0$), whereas the negative flow region is washed out by the increased permeability (case HP1).

To better understand the effects of the permeability on the frictional resistance, Figure 4 compares the drag coefficient C_D, which is defined based on the total shear stress at the rib bottom ($y = -k$) [1]. The reference experimental data are for two-dimensional transverse metallic foam ribs [1] where the permeability for case #30 is 70% lower than that for case LP, and that for case #13 is 30% lower than that for case HP. The figure confirms that for the present DNS data, an increase in the rib separation w/k results in an increase in C_D, and the dependence of w/k is more significant for case LP. This suggests that the effects of the rib arrangement is weakened by the permeability, and this trend is qualitatively similar to the experimental data.

Finally, to obtain physical understanding on the effects of the permeability on C_D, we analyze the FIK identity [4] which decomposes the friction factor into the physically understandable contributors. Following [4], we derived the contributors

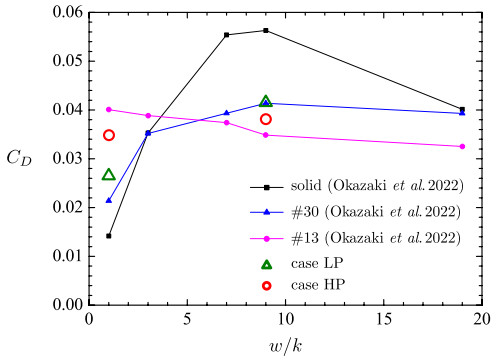

Figure 4: Comparison of the drag coefficient C_D with the experimental data [1].

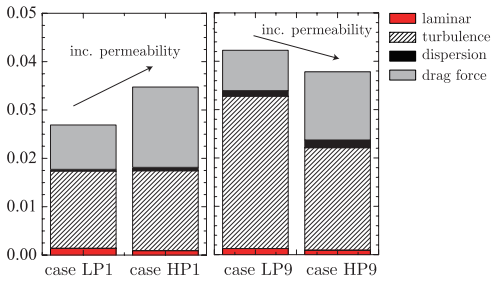

Figure 5: Contribution to the drag coefficient C_D.

to C_D based on the $x-z$ plane- and time-averaged momentum equation. For the present flows, the dispersion and drag-force contributions appear as well as the laminar and turbulence contributions. The dispersion contribution accounts for the dispersive covariance, which is generated by the streamwise and spanwise inhomogeneity of the mean velocity [3]. The drag force contribution accounts for the viscous and pressure drags offered by the porous-ribs. Those contributions are shown in Figure5. The first notable observation is that the turbulence and drag force contributions dominate C_D, whereas the laminar and dispersion contributions are negligibly small. For cases with $w/k = 1$, the drag force contribution is increased by the permeability, while the turbulence contribution is almost unchanged. The increased drag force contribution is considered to be due to the increased penetrating flow through the porous rib. The drag force contribution also increases with the permeability for cases with $w/k = 9$; however, the rib-induced turbulence generation is attenuated by the increased permeability, leading to a decrease in the turbulence contribution with the permeability. As a result, the C_D value for cases with $w/k = 9$ decreases with increasing the permeability.

REFERENCES

[1]Okazaki, Y. *et al.* : Turbulent channel flows over porous rib-roughed walls. *Exp. Fluids*, **63.4**, 1-20(2022).

[2]Suga, K. et al. *et al.* : A D3Q27 multiple-relaxation-time lattice Boltzmann method for turbulent flows. *Compt. Math. Appl.*, **69.6**, 518-529 (2015).

[3]Kuwata, Y., & Suga, K. : Lattice Boltzmann direct numerical simulation of interface turbulence over porous and rough walls. *Int. J. Heat Fluid Flow*, **61**, 145-157 (2016).

[4]Fukagata, K., Iwamoto, K., & Kasagi, N. : Contribution of Reynolds stress distribution to the skin friction in wall-bounded flows. *Phys. Fluids*, **14(11)**, L73-L76 (2002).

WORKSHOP
Direct and Large-Eddy Simulation 13
October 26th-29th 2022, Udine, Italy

LATTICE BOLTZMANN DNS OF TURBULENT TAYLOR-COUETTE FLOWS WITH A STATIONARY GROOVED OUTER CYLINDER

Y. Okada, Y. Kuwata, M. Kaneda & K. Suga[1]
Department of Mechanical Engineering
Osaka Metropolitan University, Japan
[1]suga@omu.ac.jp

INTRODUCTION

Taylor-Couette (TC) flows have been studied by many researchers since they are paradigmatic flow systems and occasionally appear in engineering applications as reviewed in Ref.[1]. Indeed, the flows between the rotor and stator coils of electric motors can be considered as turbulent TC flows. Although depending on the applications, the radius ratio of the inner to outer cylinders varies, its effect on torque can be scaled by the Taylor number at high Reynolds numbers [2]. When one considers drive motors of electric vehicles, the inside flows can be modelled as TC flows with axially grooved cylinders. Compared with the standard (groove-less) TC flows, there are not so many studies on the axially grooved TC (GTC) flows in the literature. While similar geometries with rib-roughed cylinder surfaces were extensively simulated in Ref.[4], to the best of the authors' knowledge, only a few experimental studies carried out for the axially grooved TC flows for electric motors. They were for heat transfer and torque experiments such as Ref.[3].

Therefore, to examine the similarity and difference between the rib-roughened and grooved TC flows, this study caries out DNSs of turbulent GTC flows by the D3Q27 MRT lattice Boltzmann method [5]. The considered outer stationary wall has 24 axial grooves while the inner wall surface is smooth. The groove-less standard TC flows of the corresponding geometry are also simulated for comparison.

NUMERICAL METHOD AND CONDITIONS

Since the present LBM is based on the regular lattice configuration, the linear interpolated bounce-back scheme with the second-order accuracy is applied to the curved shapes. In the D3Q27 MRT LBM, the time evolution equation of the distribution function f_α ($\alpha = 0 - 26$) can be written as

$$|f(\boldsymbol{x}+\boldsymbol{\xi}_\alpha\delta t, t+\delta t)\rangle - |f(\boldsymbol{x},t)\rangle = -\mathsf{M}^{-1}\hat{\mathsf{S}}(|m(\boldsymbol{x},t)\rangle - |m^{\mathrm{eq}}(\boldsymbol{x},t)\rangle), \quad (1)$$

where the notation such as $|f\rangle$ is $|f\rangle = {}^t(f_0, f_1, \ldots, f_{26})$, $\boldsymbol{x}$ is the position vector, $\boldsymbol{\xi}_\alpha$ is the discrete velocity and δt is the time step. The matrix M is a 27×27 matrix which linearly transforms the distribution functions to the moments as $|m\rangle = \mathsf{M}\,|f\rangle$. The collision matrix $\hat{\mathsf{S}}$ is diagonal and the equilibrium moment is $|m^{\mathrm{eq}}\rangle = \mathsf{M}\,|f^{\mathrm{eq}}\rangle$. The local equilibrium distribution function is

$$f_\alpha^{\mathrm{eq}} = w_\alpha \left\{ \rho + \rho_0 \left(\frac{\boldsymbol{\xi}_\alpha \cdot \boldsymbol{u}}{c_{\mathrm{s}}^2} + \frac{(\boldsymbol{\xi}_\alpha \cdot \boldsymbol{u})^2 - c_{\mathrm{s}}^2 |\boldsymbol{u}|^2}{2c_{\mathrm{s}}^4} \right) \right\}, \quad (2)$$

Table 1: Computational conditions and grid node numbers.

Case	η	Re	Ta ($\times 10^6$)	Nodes
TC	0.955	1050	1.16	11,888,200
		3500	12.85	90,782,800
GTC	0.932	1600	2.76	15,166,200
		5340	30.71	116,400,000

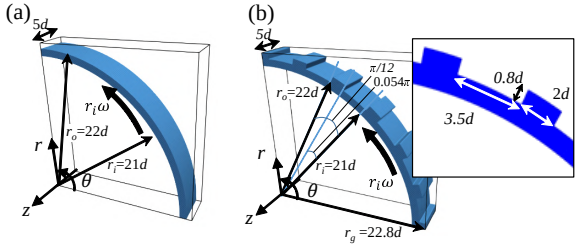

Figure 1: Geometries and computational domains: (a) case TC, (b) case GTC.

where w_α is the weighting coefficient, c_s is the sound speed in the LBM, $\boldsymbol{u}$ is the fluid velocity and ρ is the fluid density that is expressed as the summation of constant and fluctuation parts, $\rho = \rho_0 + \delta\rho$ .With the matrices and parameters proposed by Suga et al. [5], the macroscopic fluid variables such as the density, the momentum and the pressure are calculated by $\rho = \Sigma_\alpha f_\alpha$, $\rho_0 u_i = \Sigma_\alpha \boldsymbol{\xi}_{\alpha i} f_\alpha$ and $p = c_{\mathrm{s}}^2 \rho$, respectively.

Fig. 1 illustrates the computational domains and the flow geometries. Case TC is for the standard TC flows while case GTC is for the grooved TC flows. The angular rotation rate of the inner cylinder is ω while the outer cylinder is stationary. The inner and outer cylinder radii (r_i and r_o) are $21d$ and $22d$ for both cases with the gap $d = r_o - r_i$. For case GTC, since the radius of the groove bottom is $r_g = 22.8$, the radius ratio is modified as $\eta = r_i/(r_o + \delta r)$ with the averaged groove depth δr which is $0.53d$. Accordingly, $\eta = 0.955$ and 0.932 for cases TC and GTC, respectively. The Reynolds and Taylor numbers are $Re = r_i\omega(r_o + \delta r - r_i)/\nu$ and $Ta = (1+\eta)^6 Re^2/(64\eta^4)$ for the stationary outer cylinder cases, respectively. Note that without the modification, η, Re and Ta are the same as those for case TC. The computational domain covers a quarter of the system with the axial height $\ell = 5d$. The periodic boundary condition is applied to the azimuthal (θ) and axial (z) directions. The structured regular grid systems whose grid size is designed to be $\Delta^+ < 1.5$ are applied for the fluid regions. Note that since the flow variables are calculated with the Cartesian system, the results are converted to the cylindrical coordinate

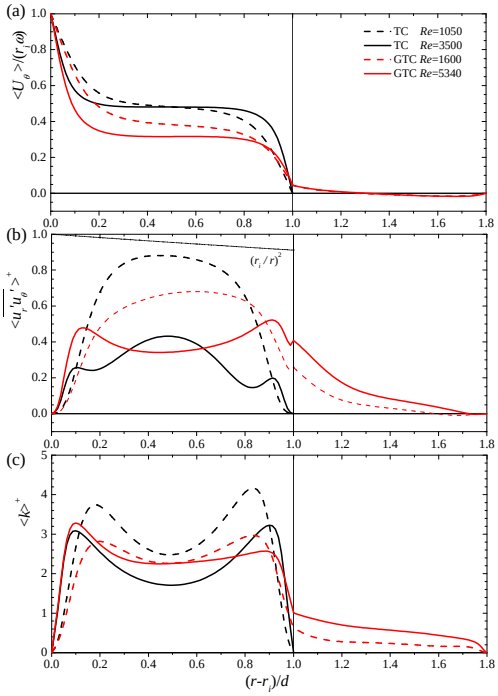

Figure 2: Azimuthally and axially averaged profiles: (a) mean azimuthal velocity, (b) Reynolds shear stress, (c) turbulent kinetic energy.

system for the discussion. The computational conditions and numerical grid numbers are summarized in Table 1.

RESULTS AND DISCUSSION

Fig. 2 compares the azimuthally and axially averaged time mean azimuthal velocity, Reynolds shear stress and turbulent kinetic energy profiles along the radial direction. The superscript "+" denotes a normalized value by the friction velocity on the inner cylinder. Fig. 2(a) shows that the velocity profiles are relatively constant in the bulk region $(0.2 < (r - r_i)/d < 0.8)$ for all cases and it becomes more obvious at the larger Re. For case GTC, the bulk velocity is dominated by the groove-side velocity. This trend is similar to that of the rib-roughened TC flows [4]. Also, as Re increases, the bulk velocity tends to be more dominated by the groove-side velocity. For the θ-z plane averaged Reynolds shear stress shown in Fig. 2(b), since the total shear stress profiles should be $\tau^+ = (r_i/r)^2$ in the TC flows, the shown profiles suggest that the existence of the Taylor vortices, which enhance dispersion stresses, becomes more evident at the higher Re cases. (Note that the predicted τ^+, which consists of the viscous, space averaged Reynolds and dispersion shear stresses, is confirmed to agree well with the theoretical line.) In case GTC, since the ratio of the groove width w to the groove depth k is $w/k = 2.5$, this geometry corresponds to the d-type roughness while the bulk region is very small compared with the groove depth as $d/k = 1.25$. At the higher Re case, the Reynolds shear stress has a high peak over the groove top at $(r - r_i)/d = 1$ and maintains a relatively high level inside the groove. This trend is similar to that seen in the corresponding d-type rib-roughened channel flow at $w/k = 3$ of Ref.[6]. Since the radius ratio is relatively large, the θ-z plane averaged turbulent kinetic energy of case TC shown in Fig. 2(c) have

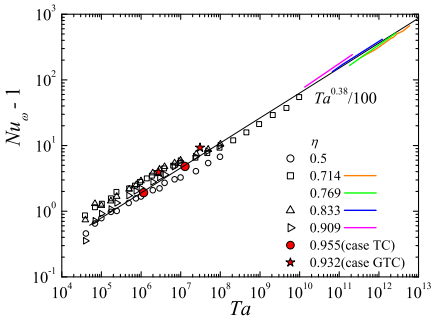

Figure 3: Dimensionless torque as a function of Taylor number. The reference data are from Ref.[2]

nearly symmetry profiles. In case GTC, although k maintains a certain level inside the groove, as the Re increases the peak value over the groove looks decreasing compared with the inner cylinder side. This is mainly because turbulence level near the inner cylinder tends to dominate in turbulent TC flows.

The key response parameter of the TC system is a Nusselt number Nu_ω which is the dimensionless torque τ normalized with the laminar angular velocity flux $J^\omega_{\rm lam}$ [1]. It is defined as $Nu_\omega = \tau/(2\pi\ell\rho J^\omega_{\rm lam})$ with $J^\omega_{\rm lam} = 2\nu r_i^2(r_o + \delta r)^2\omega/[(r_o + \delta r)^2 - r_i^2]$ for the stationary outer cylinder cases. Fig. 3 indicates plots of $Nu_\omega - 1$ versus Ta with several other reference data reported in Ref.[2]. The plots of the present TC case locate in the middle of the other plots. Although the Taylor numbers are not large enough in the present TC case, the present plots well accord with the thin black line of $Nu_\omega = Ta^{0.38}/100$ which indicates the scaling: $Nu_\omega \propto Ta^{0.38}$, for the ultimate regime [2]. For GTC case, the level of the Nusselt number becomes approximately 30% larger than the thin black line. Although the turbulence trends of case GTC are similar to those of the corresponding d-type rib roughness, this increasing ratio is relatively low compared to the rib roughness case. For the rough wall TC flows, Ref.[4] suggested $Nu_\omega \propto Ta^{0.5}$ for the ultimate regime. Although we have to investigate for much higher Ta flows, the present data indicate that the power index seems maintained at 0.38.

CONCLUSIONS

Although the turbulence trends of case GTC flows are generally similar to those of the corresponding d-type rib-roughness, the increasing ratio of the torque is considered to be relatively low compared to the rib roughness case. Although we have to investigate for much higher Ta flows, the present GTC data suggest that Nu_ω is still proportional to $Ta^{0.38}$.

REFERENCES

[1]S. Grossmann, D. Lohse, and C. Sun, *Annu. Rev. Fluid Mech.*, **48**, 53–80 (2016).

[2]R. Ostilla-Mónico, S. G. Huisman, T. J. G. Jannink, D. P. M. Van Gils, R. Verzicco, S. Grossmann, C. Sun, and D. Lohse, *J. Fluid Mech.*, **747**, 1–29 (2014).

[3]A. Nouri-Borujerdi and M. Nakhchi, *Int. J. Heat Mass Transfer*, **108**, 1449–1459 (2017).

[4]X. Zhu, R. A. Verschoof, D. Bakhuis, S. G. Huisman, R. Verzicco, C. Sun, and D. Lohse, *Nature Phys.*, **14**, 417–423 (2018).

[5]K. Suga, Y. Kuwata, K. Takashima, and R. Chikasue, *Comput. Math. App.*, **69**, 518–529 (2015).

[6]Y. Okazaki, Y. Takase, Y. Kuwata and K. Suga, *Exp. Fluids*, **63**, 66 (2022).

WORKSHOP
Direct and Large-Eddy Simulation 13
October 26th-29th 2022, Udine, Italy

INFLUENCE OF RIDGE ASPECT RATIO AND SPACING ON SECONDARY CURRENTS IN TURBULENT CHANNEL FLOW OVER TRIANGULAR RIDGES

O. Zhdanov[1], **A. Busse**[1]
[1] James Watt School of Engineering
University of Glasgow, UK
oleksandr.zhdanov@glasgow.ac.uk
angela.busse@glasgow.ac.uk

INTRODUCTION

Surfaces with spanwise variation of topology, such as ridge-type roughness, are known to generate secondary currents, which originate from turbulence anisotropy and spatial gradients of Reynolds stresses and represent Prandtl's secondary flows of the second kind [1]. The presence of secondary currents is reflected by spanwise heterogeneity of the time-averaged streamwise velocity field in the form of alternating high- and low-momentum pathways (HMPs and LMPs), which correspond to the downwash and upwash flow regions, respectively. In surfaces with ridge-type roughness, LMPs are typically observed above the ridges and HMPs occur in between them [2, 3]. However, a swap in their locations can be observed when ridge spacing exceeds channel half-height [4].

Spacing between adjacent ridges is one of the primary parameters that characterises spanwise heterogeneity of the ridge-type rough surface and consequently influences the size and strength of secondary currents [2, 4]. While the spacing dependency of secondary currents has been investigated for several different ridge shapes, the influence of other parameters has been studied only for rectangular ridges. Thus, due to lack of systematic studies, it is unclear whether results obtained for rectangular ridges, for example the appearance of tertiary flows for very wide ridges [3, 5], can be extrapolated to other ridge shapes. In the present ongoing study, flow over smooth triangular ridges, which are expected to produce strong secondary currents [5], is investigated using direct numerical simulations (DNS) in a closed channel configuration. In the first part of the project, the effects of ridge spacing on secondary currents and mean flow and turbulence statistics at two friction Reynolds numbers are investigated, and the results are compared to the data of Zampiron et al. [6], who conducted experiments with ridges with equilateral triangular cross-section, but placed on a rough bed in an open channel configuration. In the second stage, the triangular cross-section of the ridges is modified by varying the base width and side length at a fixed spacing to investigate the influence of these parameters, which have not been considered previously for triangular ridges.

METHODOLOGY

Direct numerical simulations of incompressible turbulent channel flow are conducted for each considered ridge spacing and configuration using code iIMB [7] at friction Reynolds number $Re_\tau = 550$. The channel size is $3\pi\delta \times \pi\delta \times 2\delta$ in streamwise, spanwise, and wall-normal directions, respectively. Periodic boundary conditions are applied in the streamwise and spanwise directions. In all considered cases, the ridges have a triangular cross-section of constant height, $h/\delta = 0.08$, and are placed on both walls of the channel, which are mirrored with respect to the channel centreline (Figure 1). The ridge geometry is resolved using an iterative version of the embedded boundary method by Yang and Balaras [8]. The computational grid is uniform in the streamwise and spanwise directions maintaining $\Delta x^+ < 5$ and $\Delta y^+ < 5$. The grid spacing in the spanwise direction is refined to resolve the ridge geometry with at least 16 points across the ridge width, b. In the wall-normal direction, uniform grid spacing is applied up to the ridge height ($\Delta z^+_{min} = 2/3$) and then is gradually increased up to the channel centre. The maximum wall-normal grid spacing is limited to $\Delta z^+_{max} < 5$ in all cases.

To study the influence of ridge spacing, s, this parameter is varied from $\pi\delta/8$ to $\pi\delta$ for ridges with an equilateral triangular cross-section. Investigation of the effects of the base width, b, on secondary currents is conducted at a fixed ridge spacing of $s/\delta = \pi/2$ and b is systematically increased from $2h\delta/\sqrt{3}$ (equilateral triangle) to $\pi\delta/2$ (ridges cover the whole channel).

In all simulations statistical data was acquired for a minimum of 140 flow through times and the double-averaging approach [9] was used for the computation of statistical quantities such as Reynolds and dispersive stresses.

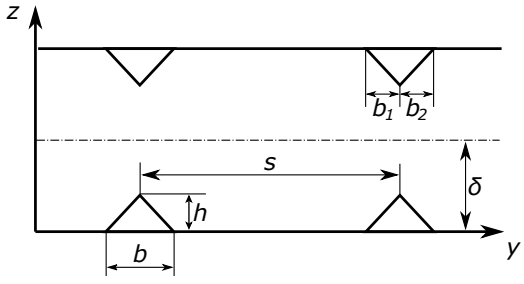

Figure 1: Schematic of a channel with triangular ridges. δ is the channel half-height, s is the spacing between ridges in spanwise direction, h is the height of the ridge, b is the base width of the ridge, b_1 and b_2 are the left and right segments of the ridge base.

RESULTS AND DISCUSSION

To date, DNS with varied ridge spacing and base width at $Re_\tau = 550$ have been completed. Spanwise heterogeneity of time and phase averaged streamwise velocity due to alternating low- and high-momentum pathways is observed in all cases (Figure 2). As expected from the experimental study by Zampiron et al. [6] on triangular ridges, the degree of flow heterogeneity increases as ridges are placed further apart. This is also reflected in the normal and shear dispersive stresses, which propagate further into the outer layer with an increase in s, and extend to the channel half-height for cases with the largest ridge spacings ($s/\delta = \pi/2$ and π). The dispersive shear stress $\langle\widetilde{u}\widetilde{w}\rangle^+$ levels in the outer layer increase with ridge spacing, reaching their highest values for $s/\delta = \pi/2$. With the further increase of s to π, dispersive shear stress levels reduce but still exceed the levels for the cases with $s/\delta \leq \pi/4$. The peak value of $\langle\widetilde{u}\widetilde{w}\rangle^+$ occurs close to the ridge crest and grows as s is decreased. The Reynolds shear stress follows exactly the opposite trends. Overall, secondary currents over triangular ridges are found to exhibit similar behaviour as secondary flows over rectangular ridges, where the size of the secondary currents increases with spanwise spacing and their strength is maximised when s reaches the outer length scale of the flow [2].

Increasing the width of the ridge base for fixed s has similar effects as reducing the spacing between ridges, i.e., a progressive reduction of the dispersive shear stress levels accompanied by a rise of turbulent shear stress is observed. However, variation of b does not influence the extent of turbulent and dispersive stresses in the wall-normal direction, which extend up to the channel half-height at the investigated ridge spacing $s/\delta = \pi/2$. These findings are consistent with the results reported for rectangular ridges, where with an increase in the ridge width the strength of secondary currents is reduced [3, 5].

The presence of tertiary flows is observed between ridges at the largest spacing $s/\delta = \pi$, which is in line with results of Zampiron et al. [6] for triangular ridges. For rectangular ridges with width comparable to the outer scale of the flow topological changes in secondary currents in the form of tertiary structures above the ridges have been found [3, 5]. In contrast, for the present triangular ridges no tertiary flows above the ridges are observed.

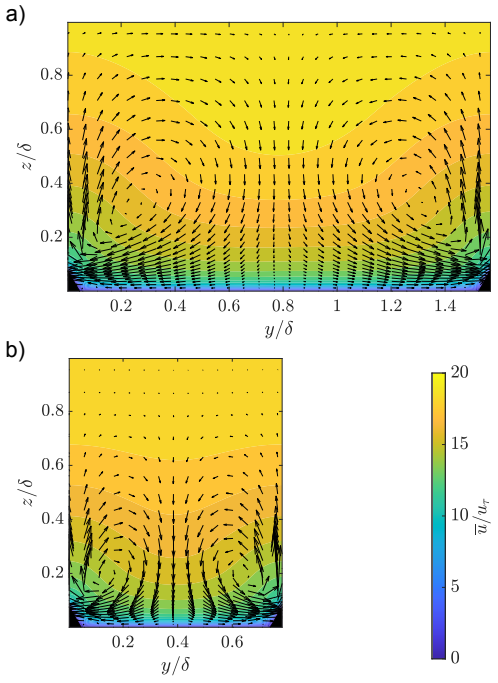

Figure 2: Contours of time and phase averaged streamwise velocity $\bar{u}/u_\tau$ with vectors of $\bar{v}/u_\tau$ and $\bar{w}/u_\tau$ for surfaces with varied ridge spacing: a) $s/\delta = \pi/2$, b) $s/\delta = \pi/4$.

CONCLUSIONS AND OUTLOOK

Variation of s, investigated in the first part of this project, has significant influence on both size and strength of secondary currents over triangular ridges. These results are in line with previous studies on triangular ridges but in different channel configuration [6] and other ridge shapes [2]. DNS at $Re_\tau = 1000$ are currently performed for all studied ridge spacings to check for Reynolds number dependence of the results.

In the second part of the project, which explores the influence of ridge configuration, currently only simulations with varied ridge width have been completed. The behaviour of secondary currents formed by triangular ridges partially corresponds to the one reported for rectangular ridges. In both cases, increasing b decreases the levels of dispersive stresses in the outer layer. However, no tertiary flows are observed above triangular ridges at any value of b in this study. In the next stage, the investigation of ridge shape dependency will be extended to ridges with scalene triangular cross-section to establish the influence of varied side length on secondary currents by varying the left and right segments of the ridge base b_1 and b_2 (Figure 1).

REFERENCES

[1] Anderson, W., Barros, J. M., Christensen, K.T. and Ankit, A.: Numerical and experimental study of mechanisms responsible for turbulent secondary flows in boundary layer flows over spanwise heterogeneous roughness, *J. Fluid Mech.*, **768**, 316–347 (2015).

[2] Vanderwel, C. and Ganapathisubramani, B.: Effects of spanwise spacing on large-scale secondary flows in rough-wall turbulent boundary layers, *J. Fluid Mech.*, **774**, R2 (2015).

[3] Hwang, G. H. and Lee, J. H.: Secondary flows in turbulent boundary layers over longitudinal surface roughness, *Phys. Rev. Fluids*, **3**, 014608 (2018).

[4] Yang, J. and Anderson, W.: Numerical study of turbulent channel flow over surfaces with variable spanwise heterogeneities: topographically-driven secondary flows affect outer-layer similarity of turbulent length scales, *Flow Turbul. Combust.*, **10**, 1–17 (2018).

[5] Medjnoun, T., Vanderwel, C. and Ganapathisubramani, B.: Effects of heterogeneous surface geometry on secondary flows in turbulent boundary layers, *J. Fluid Mech.*, **886**, A31 (2020).

[6] Zampiron, A., Cameron, S. and Nikora, V.: Secondary currents and very-large-scale motions in open-channel flow over streamwise ridges, *J. Fluid Mech.*, **887**, A17 (2020).

[7] Busse, A., Lützner, M. and Sandham, N.D.: Direct numerical simulation of turbulent flow over a rough surface based on a surface scan, *Comput. Fluids*, **116**, 1290147 (2015).

[8] Yang, J., Balaras, E.: An embedded-boundary formulation for large-eddy simulation of turbulent flows interacting with moving boundaries, *J. Comput. Phys.*, **215**, 12–40 (2006).

[9] Raupach, M.R., Shaw, R.H.: Averaging procedures for flow within vegetation canopies. *Bound.-Layer Meteorol.*, **22**, 79–90 (1982).

WORKSHOP
Direct and Large-Eddy Simulation 13
October 26th-29th 2022, Udine, Italy

REYNOLDS NUMBER-DEPENDENCY OF TURBULENT FLOW OVER A SURFACE FOULED BY BARNACLES

A. Busse[1] **and S. Sarakinos**[1]
[1] James Watt School of Engineering
University of Glasgow, United Kingdom
angela.busse@glasgow.ac.uk, sotirios.sarakinos@glasgow.ac.uk

INTRODUCTION

The shipping sector makes an increasing contribution to anthropogenic greenhouse gas emissions. The International Maritime Organisation reported that in 2018 total shipping contributed a 2.89% share (1,076 million tonnes) to global anthropogenic emission, a significant increase over the 2.76% share (977 million tonnes) in 2012 [1].

Friction drag makes the dominant contribution to the total resistance of typical merchant ships [2]. The drag of a ship hull significantly increases if the ship is affected by biofouling. Of the different forms of biofouling, calcareous macrofouling, i.e., fouling by organisms such as barnacles or tubeworms which have a calcareous outer shell, is considered one of the most severe form of biofouling. Schultz [3] predicted for a typical naval surface ship of the US Navy (Oliver Hazard Perry class frigate) an increase of the total resistance of approximately 36% for medium calcareous fouling and 55% for heavy calcareous fouling. Therefore, understanding the effects of different forms of biofouling on frictional drag is of importance for the assessment of resistance of biofouled ship hulls and the cost-effective scheduling of maintenance intervals [4].

In the present study, direct numerical simulations are used to investigate the Reynolds number dependency of turbulent flow over a surface affected by a common form of calcareous macrofouling, namely fouling by acorn barnacles (order *Sessilia*).

METHODOLOGY

A barnacle-fouled surface was generated using the BaRGE algorithm which mimics the settlement behaviour of barnacles [5]. Barnacles are represented in simplified form as conical frustra following the approach of Sadique [6]. 10% of the surface is covered by barnacle features, while the rest of the surface remains smooth. Key surface parameters are summarized in Table 1. This surface can also serve as an example for a heterogeneous roughness, a class of roughness that has received to date far less attention than homogeneous rough surfaces which are statistically uniformly covered by roughness features [7].

Direct numerical simulations of rough-wall turbulent channel flow were conducted using the in-house code iIMB [8] which employs an iterative version of the embedded boundary method of Yang & Balaras [9] to resolve the roughness features. The roughness was applied to both the lower and the upper wall of the channel (see Figure 1), and periodic boundary conditions were applied in the streamwise and spanwise direction. Key simulation parameters are summarised in Table 2. Uniform grid spacing was applied in the streamwise and spanwise direction of the flow; across the height of the roughness uniform grid spacing was also applied in the wall-normal direction. Above the roughness, the grid was gradually stretched reaching its maximum wall-normal spacing at the channel centre. The roughness Reynolds number $k^+ = k/\ell_d$, where k is set to the maximum barnacle height and ℓ_d is the viscous length scale of the flow, was varied using the method of Thakkar et al. [10]: For high k^+ the friction Reynolds number Re_τ of the channel flow was varied, while for low k^+ Re_τ was kept fixed and the size of the roughness features in outer units k/δ, where δ is the channel half-height, was decreased using a 'scaling and tiling' approach. In all cases, a domain length $L_x = 2\pi\delta$ and width $L_y = \pi\delta$ was used.

RESULTS

The Hama roughness function ΔU^+, i.e., the downwards shift in the mean streamwise velocity profile compared to smooth-wall conditions, is shown in Figure 2. Fully rough behaviour is approached at the highest Reynolds number and the equivalent sand grain roughness k_s corresponds to circa 45% of the maximum barnacle height. Compared to Nikuradse's [11] sand-grain roughness a more gradual increase in ΔU^+ can be observed over the transitionally rough region with the barnacle surface showing a trend that is close to the empirical formula of Colebrook [12]. Reynolds stress profiles (not shown) indicate a partial recovery of smooth-wall behaviour over the smooth sections of the rough surface. The streamwise Reynolds stresses display a 'roughness' peak which is associated with the crests of the barnacle features. In addition, for the higher Reynolds number cases, a smooth-wall like 'inner' peak, which falls into the buffer layer relative to the smooth surface, emerges.

CONCLUSIONS AND OUTLOOK

The fluid dynamic properties of a surface lightly fouled by barnacles have been investigated using direct numerical simulation. Further diagnostics, such as quadrant analysis and spectra of the turbulent velocity fluctuations, will be investigated in the next stage of the project. In addition, a series of DNS for a surface heavily fouled by barnacles are planned allowing direct comparison to a configuration where no smooth

surface sections remain.

ACKNOWLEDGEMENTS

This work was supported by the the Engineering and Physical Sciences Research Council [grant number EP/P009875/1]. A. B. gratefully acknowledges support via a Leverhulme Trust Research Fellowship.

REFERENCES

[1] International Maritime Organisation: Fourth IMO GHG Study 2020 - Full Report (2020)

[2] Ahmadzadehtalatapeh, M. and Mousavi, M. : A Review on the Drag Reduction Methods of the Ship Hulls for Improving the Hydrodynamic Performance, *Int. J. Maritime Tech.*, **4**, 51–64 (2015)

[3] Schultz, M. P. : Effects of coating roughness and biofouling on ship resistance and powering, *Biofouling*, **23**, 331–341 (2006)

[4] Schultz, M. P., Bendick, J. A., Holm, E. R. and Hertel, W. M : Economic impact of biofouling on a naval surface ship, *Biofouling*, **27**, 89–98 (2011)

[5] Sarakinos, S. and Busse, A. : An Algorithm for the Generation of Biofouled Surfaces for Applications in Marine Hydrodynamics, *Recent Advances in CFD for Wind and Tidal Offshore Turbines*, Springer International Publishing, 61–71 (2019)

[6] Sadique J. : *Turbulent flows over macro-scale roughness elements - from biofouling barnacles to urban canopies*, Doctoral dissertation, Johns Hopkins University, Baltimore (2016)

[7] Chung, D., Hutchins, N., Schultz, M. P. and Flack, K. A. : Predicting the Drag of Rough Surfaces, *Ann. Rev. Fluid Mech.* **53**, 438–471 (2021)

[8] Busse, A., Lützner, M. and Sandham, N. D. : Direct numerical simulation of turbulent flow over a rough surface based on a surface scan. *Computers & Fluids*, **116**, 1290147 (2015)

[9] Yang, J. and Balaras, E. : An embedded-boundary formulation for large-eddy simulation of turbulent flows interacting with moving boundaries, *J. Comput. Phys.* **215**, 12–40 (2006)

[10] Thakkar, M., Busse, A. and Sandham, N. D. : Direct numerical simulation of turbulent channel flow over a surrogate for Nikuradse-type roughness, *J. Fluid Mech.* **837**, R1 (2018)

[11] Nikuradse, J. : Strömungsgesetze in rauhen Rohren, *VDI Forschungsheft*, **361**, 1–22 (1933)

[12] Colebrook, C. F. : Turbulent flow in pipes with particular reference to the transition region between the smooth- and rough-pipe laws, *J. Inst. Civil Eng.* **11**, 133—156

Sq/δ	$S_z^{\max}/\delta$	Ssk	Sku	ES	L_{corr}^x/δ	L_{corr}^y/δ
0.0180	0.1267	4.06	19.5	0.067	0.26	0.19

Table 1: Overview of key surface topographical parameters: Sq - rms roughness height; $S_z^{\max}$: maximum peak-to-valley height; Ssk: skewness of height distribution Sku: kurtosis of height distribution; ES: effective slope, L_{corr}^x: streamwise correlation length, L_{corr}^y: spanwise correlation length. Note: height and length scales are given for the full-scale roughness pattern. For case 180hs these values need to be multiplied by a factor of 1/2.

case	Re_τ	k/δ	N_x	N_y	Δz_{min}^+	Δz_{max}^+
180hs	180	0.0634	1536	768	0.667	2.58
180fs	180	0.1267	768	384	0.667	2.58
270fs	270	0.1267	768	384	0.667	2.92
395fs	395	0.1267	768	384	0.667	3.03
540fs	540	0.1267	864	432	0.667	2.58
720fs	720	0.1267	960	480	0.667	2.54

Table 2: Overview simulation parameters: k maximum roughness height; N_x, N_y number of grid point grid spacing in streamwise and spanwise direction. Δz_{min}^+: minimum wall-normal grid spacing; Δz_{max}^+: maximum wall-normal grid spacing. All cases expect for 180hs use the full-scale roughness pattern. The case 180hs uses 2×2 tiles of the roughness pattern scaled by a factor of 1/2.

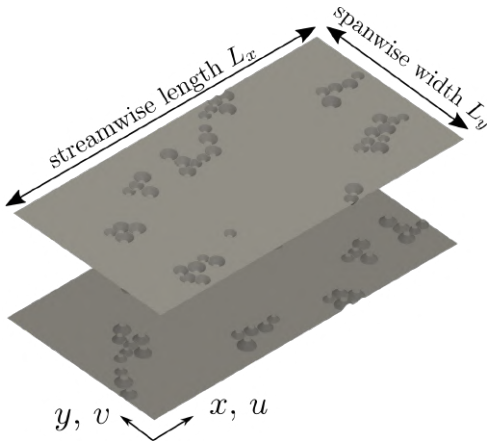

Figure 1: Schematic illustration of the channel flow domain. The rough surface is applied to both walls of the channel. On the upper wall, the rough surface pattern is shifted to minimize local blockage effects.

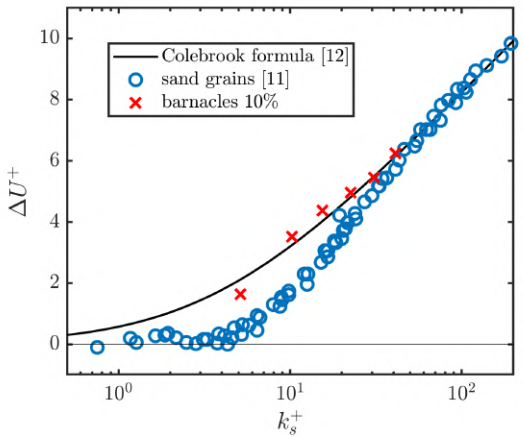

Figure 2: Roughness function ΔU^+ versus k_s^+ for the barnacle surface with 10% coverage. For comparison, sand grain roughness data by Nikuradse [11] and Colebrook's empirical formula [12] are shown.

WORKSHOP
Direct and Large-Eddy Simulation 13
October 26th-29th 2022, Udine, Italy

WALL-MODELLED LARGE-EDDY SIMULATIONS OF FLOWS WITH NON-UNIFORM ROUGHNESS

T. Salomone[1,2], U. Piomelli[1], G. De Stefano[2]
[1] Department of Mechanical and Materials Engineering
Queen's University, Canada
[2] Department of Engineering
University of Campania Luigi Vanvitelli, Italy
teresa.salomone@queensu.ca

INTRODUCTION

Sudden changes in surface roughness occur in a variety of applications in engineering and the natural sciences, such as atmospheric boundary layers, gas or water turbines, river or ocean flows. Understanding how the flow adjusts to new surface conditions is important, and still represents an open research field.

The effects of abrupt changes in surface conditions for wall-bounded flows have been extensively analyzed through theoretical, experimental and numerical simulation investigations. Several measurements of turbulent boundary layer following either a rough-to-smooth or a smooth-to-rough transition have been performed in the past decades [1, 2]. However, the accuracy of measurements close to the wall is not always good and the wall shear-stress could be significantly affected by measurement errors. This is especially true when the surface is rough, and knowing the effective position of the wall is non-trivial. Numerical simulations, on the other hand, are mainly limited by their high computational cost [3]. In fact, wall-resolved simulations of rough, wall-bounded flows are difficult and expensive to perform. Several modelling approaches have been designed to circumvent the resolution issues and conduct simulations at high Reynolds number. In particular, Wall-Modelled Large-Eddy Simulations (WMLES) and hybrid RANS/LES methods have been successful in a variety of flows.

In the present work, two modelling approaches were considered: the WMLES based on the logarithmic law of the wall, and a hybrid RANS-LES model that uses the Improved Delayed Detached-Eddy Simulation (IDDES) method [4]. Both models were originally designed for smooth-wall boundary layers, but roughness corrections can be introduced.

NUMERICAL METHODOLOGY

Both above mentioned approaches resolve the energy-carrying eddies away from the wall, but model the near-wall region. The filtered (or Reynolds-Averaged) Navier-Stokes equations for incompressible flow were solved:

$$\frac{\partial \overline{u}_i}{\partial x_i} = 0; \frac{\partial \overline{u}_i}{\partial t} + \frac{\partial}{\partial x_j}(\overline{u}_i \overline{u}_j) = -\frac{\partial \overline{p}}{\partial x_i} + \nu \nabla^2 \overline{u}_i - \frac{\partial \tau_{ij}}{\partial x_j}. \quad (1)$$

Here, filtered quantities are indicated with an overbar, $i = 1$, 2 or 3 denotes the streamwise, wall-normal and spanwise directions. The way the unresolved, sub-filter scale stresses, $\tau_{ij} = \overline{u_i u_j} - \overline{u}_i \overline{u}_j$, were modelled depended on the methodology: WMLES used the eddy-viscosity model proposed by Vreman [5]; IDDES used the Spalart-Allmaras eddy-viscosity model with modified length-scale, which produced a smooth blending of the RANS region close to wall with the LES region.

Wall roughness was introduced through modification of both the model for the unresolved stresses and the boundary conditions. In WMLES, approximate boundary conditions were applied: the wall shear stress was inferred from the logarithmic law-of-the-wall for smooth or rough surfaces:

$$U^+ = \frac{1}{\kappa} log\ y_{if}^+ + B; \quad U^+ = \frac{1}{\kappa} log(y_{if}/k_s) + 8.5. \quad (2)$$

In these equations, $B \simeq 5.0 - 5.2$ is the standard logarithmic-law intercept, $\kappa = 0.41$, k_s is the *equivalent sandgrain roughness*, y_{if} is the interface between inner and outer layers, which does not coincide with the first grid point to allow better development of the near-wall eddies [6]. In IDDES, the Spalart-Allmaras model was modified using the Boeing extension [7], which replaces the homogeneous Dirichlet boundary condition at the wall on the transported eddy viscosity, $\tilde{\nu} = 0$, with a non-homogeneous Neumann boundary condition that increases the transported eddy viscosity at the wall to account for surface roughness.

Simulations were performed in an open channel configuration as shown in Figure 1. The domain size is $56H \times H \times 14H$, where H is the open channel height, and the rough strip occupies 66% of the domain length. These dimensions match the experimental setup of [2] (where, however, a boundary

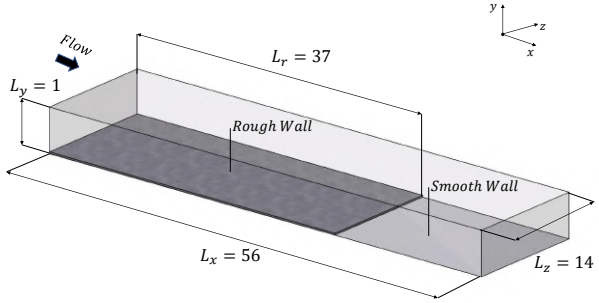

Figure 1: Computational domain (not to scale).

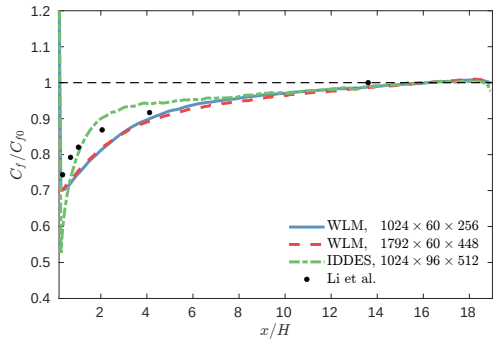

Figure 2: Recovery of the skin friction coefficient, C_f. Normalization is done by C_{f0}, which corresponds to value of C_f at the end of the smooth strip.

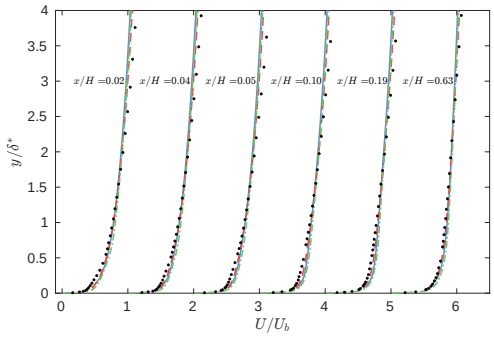

Figure 3: Mean velocity profiles at different x/H locations downstream the rough-to-smooth interface. Lines and symbols as in Figure 2.

layer flow rather than a periodic channel flow was reproduced). A grid convergence study was performed for the WMLES and the final grid had a spacing $\Delta x^+ = \Delta z^+ = 225$ ($\Delta x/H = \Delta z/H = 0.032$) and $N_x \times N_y \times N_z = 1792 \times 60 \times 448$ points. The resolution and the boundary conditions in the wall normal direction depended on the specific methodology considered. In the WMLES, the inner/outer layer interface was fixed at 5% of the channel height. Dirichlet boundary conditions at the wall were applied on the velocity field for the IDDES, which requires $\Delta y_1^+ < 1$ at the wall. Both approaches require a value of k_s as input, which was chosen to match the experimental value of the roughness function, ΔU^+, at the end of the rough strip. Namely, the equivalent roughness height in wall units was $k_s^+ \approx 130$ at the interface between rough and smooth strips. The Reynolds number based on the friction velocity at the same location was $Re_\tau \approx 7200$. Periodic boundary conditions were applied in the streamwise and spanwise directions, simulating an infinite domain of alternating rough-to-smooth strips.

RESULTS

The results from the simulations performed are compared to experimental data [2]. Here, a medium and a fine grid for the WMLES, and a medium grid for the IDDES, are considered (additional simulations with a finer grid will be presented at the conference). The recovery of the skin-friction coefficient downstream of the rough-to-smooth transition is shown in Figure 2. The IDDES gives a more accurate recovery compared to the WMLES, which does not predict the sharp increase of the skin friction at the beginning of the rough strip, but both models predict the recovery of the skin friction coefficient reasonably well. Note that the WMLES calculation requires significantly fewer computational resources than the IDDES, both because the number of grid points is much lower, and because the time-step can be larger. The mean-velocity profiles in outer units at different locations downstream of the rough-to-smooth transition are presented in Figure 3. Normalization is done by the bulk velocity, U_b, and the displacement thickness, δ^*. The simulations results match the experiment accurately.

A limitation of both models is the fact that they are designed to yield the smooth-wall logarithmic law when no roughness is present. Thus, the roughness function at the inner/outer layer interface (not shown) is zero by construction, while the experiments show a different behaviour. The implications of this issue will be discussed in the final version of the paper.

CONCLUSIONS AND FUTURE WORKS

Two modelling approaches, WMLES and IDDES, were tested on a non-uniform roughness configuration and compared with experimental results. Both methods predict accurately the velocity profiles in outer units downstream the rough-to-smooth transition. The recovery of the skin friction coefficient is better predicted by the IDDES, which however requires a higher computational effort. Future work will be focused on obtaining a grid-converged solution for the IDDES and identifying methods to relax the models to the smooth-wall solution in a more physically consistent manner.

ACKNOWLEDGEMENT

The authors are thankful for high performance computing resources provided by the CINECA award under the ISCRA initiative (Project HP10BSBCBZ).

REFERENCES

[1] R. A. Antonia and R. E. Luxton, "The response of a turbulent boundary layer to a step change in surface roughness. Part 2. Rough to smooth," *J. Fluid Mech.*, vol. 53, no. 4, pp. 737–757, 1972.

[2] M. Li, C. M. de Silva, A. Rouhi, R. Baidya, D. Chung, I. Marusic, and N. Hutchins, "Recovery of wall-shear stress to equilibrium flow conditions after a rough-to-smooth step change in turbulent boundary layers," *J. Fluid Mech.*, vol. 872, pp. 472–491, 2019.

[3] J. Jiménez, "Turbulent flows over rough walls," *Annu. Rev. Fluid Mech.*, vol. 36, pp. 173–196, 2004.

[4] M. L. Shur, P. R. Spalart, M. K. Strelets, and A. K. Travin, "A hybrid RANS/LES model with delayed DES and wall-modeled LES capabilities," *Int. J. Heat Fluid Flow*, vol. 29, pp. 1638–1649, 2008.

[5] A. W. Vreman, "An eddy-viscosity subgrid-scale model for turbulent shear flow: Algebraic theory and applications," *Phys. Fluids*, vol. 16, no. 10, pp. 3670–3681, 2004.

[6] S. Kawai and J. Larsson, "Wall-modeling in large eddy simulation: Length scales, grid resolution, and accuracy," *Phys. Fluids*, vol. 24, no. 1, p. 015105, 2012.

[7] B. Aupoix and P. R. Spalart, "Extensions of the Spalart–Allmaras turbulence model to account for wall roughness," *Int. J. Heat Fluid Flow*, vol. 24, pp. 454–462, 2003.

WORKSHOP
Direct and Large-Eddy Simulation 13
October 26th-29th 2022, Udine, Italy

EFFECT OF ROUGHNESS ON ELONGATED PARTICLES IN TURBULENT CHANNEL FLOW

M. De Marchis[1,*], D. Saccone[1], C. Marchioli[2]
[1] Department of Engineering and Architecture
University of Enna "Kore", Italy
[2] Department of Engineering and Architecture
University of Udine, Italy
[*] mauro.demarchis@unikore.it

INTRODUCTION

Elongated fibers dispersion and deposition is studied in turbulent channel flow through Direct Numerical Simulations (DNS), combined with Lagrangian Particle Tracking (LPT), under one-way coupling conditions. Simulations are carried out with relatively low friction Reynolds number equal to Re_τ = 180. The flow is bounded by two-dimensional irregular rough walls. The roughness effect is investigated increasing the mean roughness height of the asperities. Fibers are modelled as ellipsoidal particles having different aspect ratio (equal to 1, 3 and 10) and different Stokes number (equal to 1, 5, 50 and 100). The wall roughness and fiber elongation effects are investigated in term of particle dynamics, distribution, orientation, translation, and rotation. The achieved results over rough surfaces are compared with those over smooth walls, showing how roughness completely modifies the fibers behavior. In the near wall region, in fact, roughness dramatically reduces the deposit phenomenon while increasing the particle dispersion in the center of the channel, with a mean concentration equal to the specific one C_0. Table 1 shows the geometric features of the computational domain for all cases: the length along the streamwise (x_1), spanwise (x_2) and wall-normal (x_3) directions, the number of grid points used for discretization of the domain and the mesh resolution. As reported in Table 1, for the smooth channel (Case F1), the size of the computational domain is set to $2\pi\delta \times \pi\delta \times 2\delta$ in the streamwise, spanwise and wall-normal directions, respectively, with δ, as previously mentioned, the half channel width. The domain length in the streamwise direction was duplicated for the rough cases (R1, R2 and R3). Periodic boundary conditions are imposed in the streamwise and spanwise directions, while the no-slip condition is applied on the walls. Uniform cell distribution in used in the streamwise and spanwise direction, with dimension of grid cells equal to $\Delta x_1^+ \approx 8.8$ and $\Delta x_2^+ \approx 4.4$, respectively. The computational grid was designed as to achieve a distance from the solid wall well below one wall unit for the closest computational node. In particular, we adopted a non-uniform grid refinement strategy, with minimum grid spacing of about 0.05 wall units at the wall and maximum grid spacing, at the channel centerline, of about 7 wall units at the channel centerline. Such grid spacing was enforced both in the flat-wall case and in the different rough-wall cases, also considering that in rough conditions the mesh is boundary fitted. This technique ensures the possibility to impose the mesh resolution at the boundary.

Table 1: Details of all cases: Re_τ is the Friction Reynolds number , Lx_1, Lx_2 and Lx_3 are the domain sizes; Δx_1^+, Δx_2^+, $\Delta x_{3,min}^+$ and $\Delta x_{3,max}^+$ are the mesh resolution.

Case	Re_τ	Lx_1	Lx_2	Lx_3	Δx_1^+	Δx_2^+	$\Delta x_{3,min}^+$	$\Delta x_{3,max}^+$
F1	180	$2\pi\delta$	$\pi\delta$	2δ	8.8	4.4	0.12	7.1
R1	180	$4\pi\delta$	$\pi\delta$	2δ	8.8	4.4	0.06	7.7
R2	180	$4\pi\delta$	$\pi\delta$	2δ	8.8	4.4	0.06	7.7
R3	180	$4\pi\delta$	$\pi\delta$	2δ	8.8	4.4	0.06	7.7

Geometric and physics properties of solid phase, dispersed in computational domain, are reported in Table 2. Dimensionless values of ellipsoids are: semi-minor axis $a^+ = 0.36$, Stokes numbers $St^+ = 1, 5, 50$ and 100 and aspect ratios $\lambda = 1$ (spherical particles), 3 and 10. To ensure converged statistics, swarms of 200.000 ellipsoidal particles are tracked for each category, assuming dilute flow. Regarding initial conditions, at the start of the simulation, particles were distributed in the outer region of the computational domain, away from the rough walls; ellipsoid orientation were chosen randomly and their initial velocity was set similar to the fluid velocity in their position.

PARTICLE DISTRIBUTION

A visual comparison between the instantaneous distribution of particles with $St^+ = 1$ and $St^+ = 100$ for smooth and high rough walls cases is presented in Fig.1. Panels shows a channel slice along the directions $x_1 - x_3$ for the first case F1 and the last case R3. Particles are depicted according their streamwise velocity v_{x_1} using blue to red colour scale.

As stated in literature, in smooth domain, particles with small Stokes number are randomly distributed in the channel, whereas particles with $St^+ > 1$ accumulate at the wall.

Fig.1(a), relative to the lighter particles case, shows an almost uniform distribution of dispersed phase. Particles move faster in the central region of the channel and have slower velocity in the region close to the wall, coherently with fluid velocities. Due to their lower inertia, in fact, particles with $St^+ = 1$ are strongly influenced by the motion regime. Heavy particles, however, follow different behavior, Fig.1(b) shows particles with $St^+ = 100$.

Table 2: Particle parameters: St^+ is the Stokes number; λ is the aspect ratio; S is the density ratio; $2b^+$ is the ellipsoid major axis, expressed in wall units and ρ_p is the ellipsoid density.

Set	St^+	λ	S	$2b^+$	$\rho_p[kg/m^3]$
P1-1	1	1	34.70	0.72	45.11
P1-3	1	3	18.57	2.16	24.14
P1-10	1	10	11.54	7.20	15.00
P5-1	5	1	173.60	0.72	225.68
P5-3	5	3	92.90	2.16	120.77
P5-10	5	10	57.70	7.20	75.01
P50-1	50	1	1736.0	0.72	2256.8
P50-3	50	3	929.0	2.16	1207.7
P50-10	50	10	577.0	7.20	750.1
P100-1	100	1	3469.91	0.72	4510.88
P100-3	100	3	1857.13	2.16	2414.26
P100-10	100	10	1154.21	7.20	1500.48

As already amply demonstrated by the scientific community, ellipsoidal particle with greater inertia tend to accumulate near wall, making the distribution in the channel, uneven. From the Fig 1(b) it is also clear that particles moving with low velocities is much greater than fast particles.

Focusing our attention on rough walls cases, roughness tends to uniform the particles distribution. Fig.1(c) shows lighter particles ($St^+ = 1$) are distributed in a similar way to the flat case and are easily transported even inside the cavities of the rough wall.

Finally, Fig.1(d), related to particles with $St^+ = 100$, shows that heavy particles in rough domain assume a more uniform distribution than smooth case, thanks to increasing of rebounds and resuspension phenomena.

PARTICLE CONCENTRATION

Particle concentration profiles for the different aspect ratios considered in this study are shown in Fig. 2. The profiles refer to the steady state condition for particle concentration, namely to a stage of the simulation for which the wall-normal

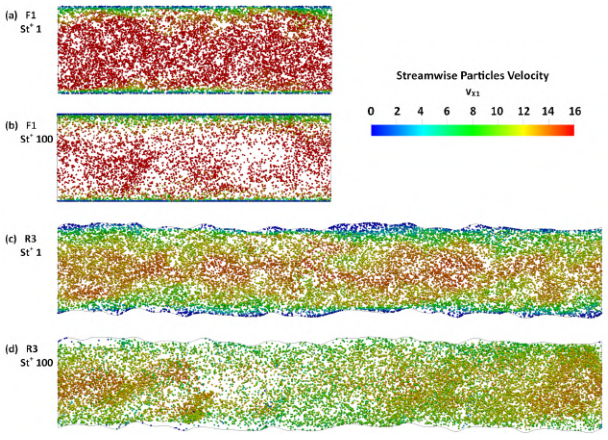

Figure 1: $x_1 - x_3$ slice of instantaneous particles distribution (at an arbitrary instant), Panels: (a) Case F1 and Set P1-1, (b) Case F1 and Set P100-1, (c) Case R3 and Set P1-1, (d) Case R3 and Set P100-1.

volumetric number density of the particles, labelled as C hereinafter, does not change in time anymore (due to a balance of transfer fluxes to and away from the wall). The concentration profiles show the behavior of the number density, C, normalized by its initial value C_0, given by the ratio of the total number of particles tracked and the total volume of the flow domain [2]. Plots are truncated at $x_3^+ = 80$ because the trend observed in the region $40 < x_3^+ < 80$ persists throughout the channel center. An inset has been added in each panel of Fig. 2 to highlight concentration profiles near the wall when plotted with respect to a *virtual* origin of the wall-normal axis. Specifically, this virtual origin is set equal to the maximum roughness peak k_{max}^+ where the coordinate $x_3^+ - k_{max}^+$ is equal to zero in all rough-wall cases [3]. By doing so, concentration profiles for a given particle set in the different flow configurations can be compared directly. As well know, inertial particles dispersed in a turbulent channel flow tend to accumulate in the near-wall region [1, 3]. Therefore, the peak of concentration developed by the particles inside the viscous sublayer in the smooth-wall case (solid line in each panel) is well expected.

Examination of the profiles for the rough-wall cases (R1, R2 and R3) shows that the near-wall peak of concentration decreases (ranging from $C/C_0 \approx 4.5$ in case R1 to $C/C_0 \approx 1.5$ in case R3) as the roughness is increased and its location shifts towards higher values of x_3^+, where the highest roughness peaks are found. Compared to the smooth-wall case, particles appear more uniformly distributed throughout the channel height.

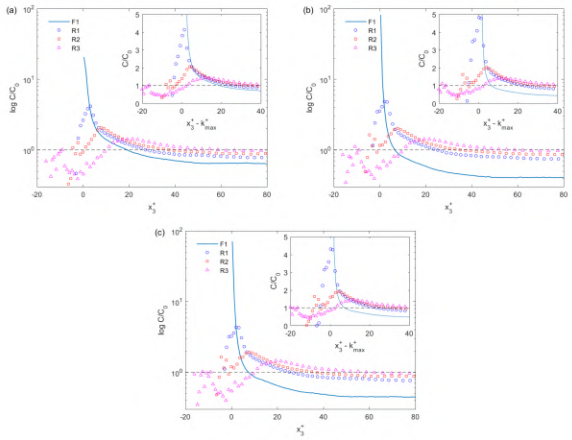

Figure 2: Wall-normal concentration profiles in the different flow configurations (the solid line refers to the smooth-wall case F1, symbols refer to the different rough-wall cases). Panels: (a) $\lambda = 1$, (b) $\lambda = 3$ and (c) $\lambda = 10$. Each inset provides a close-up view of the profiles in the near-wall fluid slab x_3^+ ¡ 40 of C/C_0 vs x_3^+ - k_{max}

REFERENCES

[1]Marchioli, C. and Soldati, A.: Mechanisms for particle transfer and segregation in a turbulent boundary laye, *Journal of Fluid Mechanics*, **468**, 283–315 (2002).

[2]Marchioli, C. and Fantoni, M. and Soldati, A.: Orientation, distribution, and deposition of elongated, inertial fibers in turbulent channel flow, *Physics of Fluids*, **22(3)**, 1–14 (2010).

[3]De Marchis, M. and Napoli, E. and Armenio, V.: Turbulence structures over irregular rough surfaces, *Journal of Turbulence*, **11(3)**, 1–32 (2010).

Session: Particle-laden flows

Friday, October 28, 2022

14:50 – 15:50

WORKSHOP
Direct and Large-Eddy Simulation 13
October 26th-29th 2022, Udine, Italy

TURBULENT TRANSPORT IN A LATERAL SQUARE CAVITY BASED ON LAGRANGIAN AND EULERIAN APPROACHES

Magdalena Barros[1] **and Cristián Escauriaza**[1]
[1] Departamento de Ingeniería Hidráulica y Ambiental, Pontificia Universidad Católica de Chile, Av. Vicuña Mackenna 4860, 7820436, Santiago, Chile
mmbarros1@uc.cl, cescauri@ing.puc.cl

INTRODUCTION

Lateral recirculating regions constitute surface storage zones in rivers, where large-scale coherent structures dominate the mass and momentum transport, playing a fundamental role in the dynamics of sediment transport, biogeochemical processes, and nutrient cycles. Mass transport in these systems can be studied from two different perspectives which consist of Eulerian and Lagrangian approaches. Most of the previous works have focused on estimating a mean residence time or a global mass exchange coefficient based on the transverse velocity and dye release methods from a Eulerian approach. To the best of the author's knowledge, only one previous investigation, which is based on laboratory experiments, has studied the mass exchange between the cavity and the main channel from Lagrangian perspective [1], and no work exists on local residence times and particle dispersion that can shed light about the Lagrangian transport patterns in a cavity flow. However, in conditions where pollutants, nutrients or sediments are present in a lateral cavity, Eulerian and Lagrangian data related to global and local mass transport can be highly different. To elucidate the differences in mass exchange and provide quantitative comparisons of the physical processes from both perspectives we performed large-eddy simulations (LES) of the flow in a straight rectangular channel with a lateral square cavity at $Re = 1.2 \times 10^4$ coupled with an advection-diffusion equation and a Lagrangian particle model. We also aim to characterize the Lagrangian transport patterns and timescales in the lateral cavity.

NUMERICAL MODEL

For the turbulent flow, we solved the three-dimensional, spatially-filtered unsteady, incompressible Navier-Stokes equations with the one-equation LES turbulence model (LDKM) of [2]. The system simulated correspond to the three dimensional cavity flow configuration of [3] by considering the entire experimental setup and the same Reynolds number. The domain consists of a long channel with a lateral square cavity and is presented in Figure 1. Also, a fine numerical grid consisting of approximately 27 millions grid points was used, and the distance from solid boundaries to the first row of grid points was set to values lower than $z^+ = 1$. Finally, to ensure a developed velocity profile at the entrance of the cavity, we implemented the stochastic turbulent inlet method of [4] in the upstream boundary.

For the mass transport, we solved an advection-diffusion equation for the concentration and a Lagrangian particle

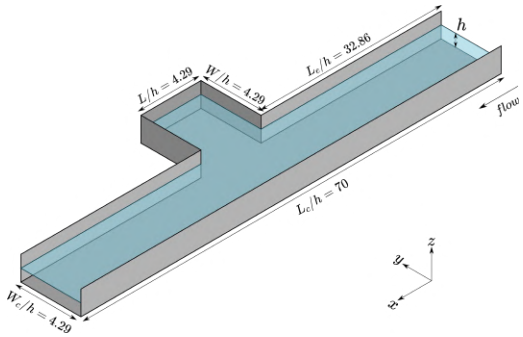

Figure 1: Computational Domain

model. For the later, particles were considered as tracers and the flow velocities were interpolated at the particle position. Also, the stochastic sub-grid scale model of [5] was used to account for the effect of the scales not directly resolved by the LES in Lagrangian dynamics. The initial condition correspond to a concentration equal to 1 and a total of 108,000 particles uniformly distributed inside the cavity, and a zero concentration and no particles at the main channel

GLOBAL MASS TRANSPORT

Based on the global mass conservation of a passive scalar in the entire system, equation (1) describes how the spatially averaged concentration changes over time, where C_0 and C_c are the initial and instantaneous concentration in the cavity respectively.

$$C_c/C_0 = e^{-t/\tau} \tag{1}$$

We compute the spatially averaged concentration and the fraction of the initial number of particles that remain inside the cavity over time, and we fitted the theoretical curve (1) to our data as is shown in Figure 2. The mean residence time obtained from Lagrangian and Eulerian data in dimensionless units (tU_b/h) are $\tau_L = 102$ and $\tau_E = 130$ respectively. The mean residence time is influenced by at least three different flow timescales which are: (i) the shear layer ($t_{sl} = 4$); (ii) the eddy turnover ($t_{ed} = 50$); and (iii) the vortex core timescale ($t_{vc} = 150$). Similarly, the mass exchange coefficients from Lagrangian and Eulerian data are $k_L = 0.042$ and $k_E = 0.033$ respectively. The larger mass exchange coefficient obtained from the Lagrangian data indicates a considerably more transport compared to the Eulerian approach. The values obtained are within the range of values found in the literature for cavity flows (0.01-0.05). Finally, both curves deviate from the

theoretical line in the semi-log plot at a concentration of 30% approximatively, but are still linear, indicating that two different timescales control the mass exchange with a decaying exponential trend.

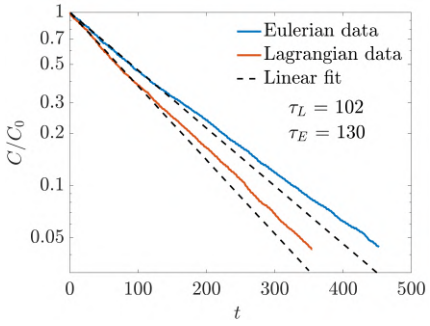

Figure 2: Exponential curve fitting of $C(t)$ in semi-log plot

LAGRANGIAN TRANSPORT

To characterize Lagrangian timescales inside the cavity, we plot particle residence times according to their initial position. Figure 3 shows instantaneous and space- and time-averaged particle residence times. The averaged was performed over one shear layer period in time, and vertically integrated in space. The strong spatial variability of particles residence times observed in many zones inside the cavity (Figure 3a), indicates that even particles starting close to each other can possess very different residence times, highlighting the complex Lagrangian dynamics of the cavity flow. This variability is mainly explained by the instantaneous dynamics of the shear layer, where particles approximating to the interface have some probability to leave the cavity or remain inside. Particles that do not leave, go around the cavity, adding an average time similar to the eddy turnover timescale to the residence time. Also, since the contours in Figure 3a depends on the flow initial condition, Figure 3b is a better indicator of the average time that takes a particle to leave the cavity from that time.

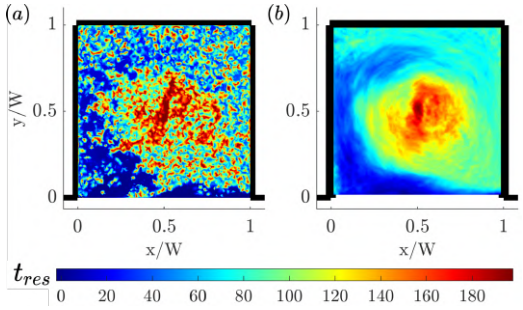

Figure 3: Spatial distribution of particle residence times according to their initial positions. (a) x-y plane of non-averaged values at $z/h = 0.6$. (b) space- and time-averaged values

SUMMARY AND CONCLUSIONS

Large differences were found on mean residence times from both perspectives, which implies that global transport of continuous and discrete substances can be highly different. With respect to Lagrangian patterns and timescales, the key points that can be deduced from particles trajectories and residence times and a schematic summary are presented below .

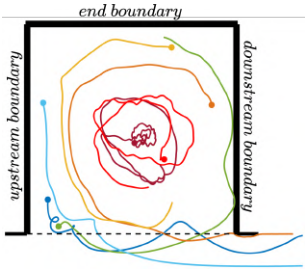

Figure 4: Lagrangian patterns in a lateral square cavity

(i) The cavity have two zones of more clear timescales which are the central region influenced mainly by the vortex core, and the interface and upstream boundary influenced mainly by the shear layer.

(ii) Particles starting at the central region remain inside the cavity on average for longer times than particles starting at any other positions, due to the small velocities that exist there (red in Figure 4).

(iii) Particles starting close to the interface and the upstream boundary have a higher probability of leaving the cavity immediately than remain inside (blue in Figure 4).

(iv) All other zones inside the cavity have a larger variability on residence time, which is almost entirely explain by the complex instantaneous dynamics of the shear layer.

(v) Particles starting close to the downstream and end boundaries are also influenced by the vortex developed inside the cavity, which scatter particles trajectories, moving them towards the central region and causing that they do not face the interface only in the zones of lower residence times (orange in Figure 4).

(vi) Particles that cross the interface but finally remain inside the cavity, enter very close to the downstream boundary, ejected at high velocity by the jet, and occupying more the perimeter than the central region of the cavity, unlike particles that never cross the interface, that occupy many times the central region along their trajectories (green in Figure 4).

REFERENCES

[1]Engelen, L., Perrot-Minot, C., Mignot, E., Rivière, N., and De Mulder, T. : Lagrangian study of the particle transport past a lateral, open-channel cavity, *Physics of Fluids*, **33.1**, 013303 (2021).

[2]Kim, W. W. and Menon, S. : An unsteady incompressible Navier–Stokes solver for large eddy simulation of turbulent flows, *International Journal for Numerical Methods in Fluids*, **31**, 983-1017 (1999).

[3]Mignot, E., Cai, W., Launay, G., Riviere, N., and Escauriaza, C. : Coherent turbulent structures at the mixing-interface of a square open-channel lateral cavity, *Physics of Fluids*, **28.4**, 045104 (2016).

[4]Smirnov, A., Shi, S., and Celik, I. : Random flow generation technique for large eddy simulations and particle-dynamics modeling, *J. Fluids Eng.*, **123.2**, 359-371 (2001).

[5]Vinkovic, I., Aguirre, C., Ayrault, M., and Simoëns, S. : Large-eddy simulation of the dispersion of solid particles in a turbulent boundary layer, *Boundary-layer meteorology*, **121.2**, 283-311 (2006).

WORKSHOP
Direct and Large-Eddy Simulation 13
October 26th-29th 2022, Udine, Italy

DIRECT NUMERICAL SIMULATION OF THE BREAKUP OF SOLID FIBERS IN HOMOGENEOUS ISOTROPIC TURBULENCE

F. Dalla Barba, F. Picano[1]
[1] Department of Industrial Engineering
University of Padova, Padova, Italy

The breakup of solid fibers transported in turbulent flows is a problem of crucial relevance in process and chemical engineering. The driving mechanism behind fiber breakup relies on the peaks of stress exerted by turbulent fluctuations on the solid fibers. These may cause such large deformations that the stress in the material overcomes the ultimate tensile strength resulting in fragmentations [1]. This peculiar problem can be generally enclosed within the macro category of Fluid-Structure Interaction (FSI), a strongly non-linear problem that involves the intricate coupling between the governing equations of fluid dynamics and solid mechanics. In FSI, the interaction between movable or deformable solid structures and internal or surrounding fluid flows occurs via the exchange of momentum through geometrically complex interfaces that evolve in time. The deformation of the immersed structures, and the consequent temporal modification of the solid-fluid interfaces, strongly couples the dynamics of the fluid with that of the solids involved in the process. The problem becomes even more complex if fracture mechanics is taken into account. Advancing our capability in the modeling of this class of problems, with a focus on fiber breakup, is of crucial relevance, but presents many challenges related to the complexity of the phenomena involved, their multi-physics nature and the high demand for computational resources. In this context, we aim to present a novel methodology for the three-dimensional, Direct Numerical Simulation (DNS) of generic fluid-structure interaction problems involving fracturing. Peridynamics [5] is used to describe the mechanical behavior of the solid phase, coupled via a multi-direct immersed boundary method [3, 4] with the incompressible formulation of the Navier-Stokes equations, which are used to resolve the dynamics of the fluid phase. The synchronization of the solution is achieved with a fully explicit, weak-coupling strategy that allows for fast and efficient computations. Peridynamics is a reformulation of continuum mechanics based on integral equations. The major advantage of using peridynamics relies on replacing partial differential equations with integral ones, such that derivatives are completely removed from the formulation, avoiding the occurrence of singularities in the presence of cracks, which are intrinsically considered within the theoretical framework. We tested our methodology against different benchmarking test cases whose results were compared to well-referenced and independent data available in the literature [2]. Finally, the proposed methodology was applied to the interface-resolved, direct numerical simulation of the breakup of brittle fibers in Homogeneous Isotropic Turbulence (HIT) The fibers, immersed in a triperiodic domain, are transported by turbulent fluctuations of the flow and undergo a breakup process due to the peaks of the stress exerted by the fluid. Some qualitative results of the simulation are presented to show the potential of the proposed approach.

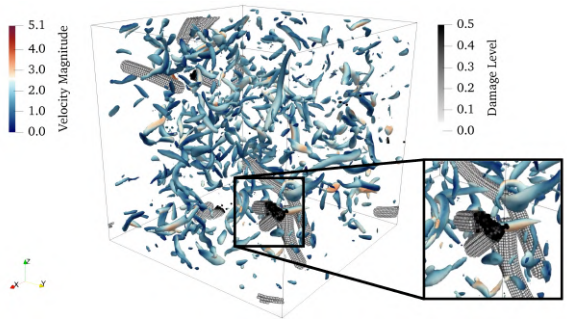

Figure 1: A snapshot of the break up of brittle fibers in HIT. Vortical structures are highlighted by Q-criterion and colored according to velocity magnitude.

REFERENCES

[1]Babler, M. U. et al. (2015). Numerical simulations of aggregate breakup in bounded and unbounded turbulent flows. Journal of Fluid Mechanics, 766, 104-128.

[2]Dalla Barba, F., & Picano, F. (2021). Direct numerical simulation of the scouring of a brittle streambed in a turbulent channel flow. Acta Mechanica, 232(12), 4705-4728.

[3]Breugem. W.P. A second-order accurate immersed boundary method for fully resolved simulations of particle-laden flows. Journal of Computational Physics, 231(13):4469–4498, 2012.

[4]Wang, S., Vanella, M., & Balaras, E. A hydrodynamic stress model for simulating turbulence/particle interactions with immersed boundary methods. Journal of Computational Physics, 382:240–263, 2019.

[5]Silling S.A. Reformulation of elasticity theory for discontinuities and long- range forces. Journal of the Mechanics and Physics of Solids, 48(1):175– 209, 2000.

[6]Dalla Barba, F., & Picano, F. (2021). Direct numerical simulation of the scouring of a brittle streambed in a turbulent channel flow. Acta Mechanica, 232(12), 4705-4728.

WORKSHOP
Direct and Large-Eddy Simulation 13
October 26th -29th 2022, Udine, Italy

ELONGATED NON-SPHERICAL PARTICLES IN TURBULENT CHANNEL FLOW USING EULER/LAGRANGE APPROACH

M. A. Taborda[1], M. Sommerfeld[1]
[1] Multiphase Flow Systems (MPS), Institute for Process Engineering
Otto-von-Guericke-University Magdeburg, Hoher Weg 7b, D-06120 Halle (Saale), Germany
manuel.taborda@ogvu.de

INTRODUCTION

In many industries such as paper making and pulp production involves particle transport in gas- or liquid-flow devices, such as mixing vessels, conveying in particle separators, pipes, and channel transport. These types of multiphase flows are wall bounded and typically highly turbulent. The particles found in these processes are rarely spherical but may have various shapes, from regular (e.g., fibers, rods, and plates) to irregular (i.e., agglomerates or sand grains). Though for many years, research is related to the behavior of regular non-spherical particles in turbulent flows, a conclusive description is, not yet available. For many design rules as well as in numerical computations of dispersed multiphase flows by computational fluid dynamics (CFD) methods the most common assumption is that the particles are spherical. This applies to the relevant fluid dynamic forces in a confined flow and to the interactions between particles as well as the particle-wall interactions (i.e., collisions and lubrication), which of course yields a non-realistic dealing of the problem. In this contribution, CFD computations in the Euler/Lagrange framework using the point-particle assumption of large-scale turbulent channel flows laden with elongated non-spherical particles was carried out.

NUMERICAL MODELING

A CFD model using an LES-Euler/Lagrange approach was developed and implemented in the open-source platform OpenFOAM®, elaborating a custom solver. The flow field and turbulence of the continuous phase are modelled by the Large Eddy Simulation (LES) approach, requiring a fully transient solution of the transport equations. In addition, the numerical calculation of particle-laden flows by point-particle Euler/Lagrange type of methods is based on tracking each non-spherical particle's translational and rotational motion, so that the center position and the orientation of the particles is known. For this purpose, three coordinate systems can be defined (Figure 1): **x** [x, y, z] the inertial or laboratory frame of reference, commonly referred to as world space, **x'** = [x', y', z'] the particle coordinate system centered at the particle mass center with the axis being parallel to the major axis of the particle, commonly referred to as body space, and **x"** = [x", y", z"] the co-moving particle coordinate system also centered at the particle mass center but with its axis being parallel to the laboratory coordinate system. For non-spherical particles the translational motion is calculated in world space, **x**, frame and the rotational motion in body space, **x'**, in the following way:

$$m_p \frac{d\boldsymbol{u}_p}{dt} = \boldsymbol{F_d} + \boldsymbol{F_{LS}} + \boldsymbol{F_{LR}} + m_p \boldsymbol{g}\left(1 - \frac{\rho_f}{\rho_g}\right) \quad (1)$$

$$I_{x'} \frac{dw_{x'}}{dt} - w_{y'} w_{z'}\left(I_{y'} - I_{z'}\right) = T_{H,x'} \quad (2)$$

$$I_{y'} \frac{dw_{y'}}{dt} - w_{z'} w_{x'}\left(I_{z'} - I_{x'}\right) = T_{H,y'} \quad (3)$$

$$I_{z'} \frac{dw_{z'}}{dt} - w_{x'} w_{y'}\left(I_{x'} - I_{y'}\right) = T_{H,z'} \quad (4)$$

Where m_p, F_d, F_{LS}, F_{LR} are the mass of the particle, the hydrodynamic drag, the profile or shape lift, and the slip-rotation lift, which includes the effect of angle of incidence on the respective coefficient [1, 2]. $I_{x'}$, $I_{y'}$, and $I_{z'}$ correspond to the moments of inertia about the particle principal axis [i.e., x'] and $T_{H,x'}$, $T_{H,y'}$ and $T_{H,z'}$ are the components of the hydrodynamic torques. As the calculation is conducted in different coordinate systems, a transformation between x' and x" is required through a transformation matrix [3]. This transformation matrix may be expressed in terms of the Euler angles or the Euler's four parameters or quaternions. Unfortunately, a singularity

exists when evaluating the temporal change of the Euler angles [4] wherefore, mostly the Euler parameters [5] or Quaternions [6] are applied instead. These can also be used to determine the particle orientation angles.

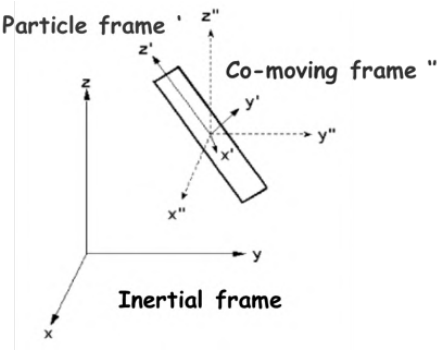

Figure 1: Definition of coordinate systems and characteristic angles; inertial coordinate system (**x**=[x, y, z]) and particle coordinate systems [**x′**=(x′, y′, z′)] and [**x′′**=(x′′, y′′, z′′)].

SIMULATION SETUP AND RESULTS

Model validation using the Euler/Lagrange point-particle framework for elongated, inertial fibers was accomplished comparing the obtained results with the numerical validation data obtained by Marchiolli's research group [6], in which a turbulent channel flow (considering DNS simulations), was studied. For the calculations, firstly a turbulent channel flow condition was obtained simulating it under periodic conditions in the streamwise and spanwise directions, while the no-slip condition was enforced at the walls. Figure 2 shows the obtained instantaneous velocity field for three perpendicular planes inside the turbulent channel flow, which is further used for the analysis of the particle's behavior. The comparison of the flow field was achieved evaluating the statistical moments of the turbulent flow such as mean streamwise velocity.

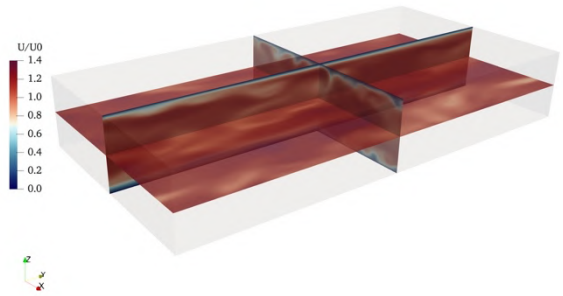

Figure 2: Instantaneous normalized flow velocity field obtained in the turbulent channel simulation.

The fiber behavior is characterized using the non-dimensional particle relaxation time based on the viscous time scale and the equivalent sphere volume diameter. Different particle sizes were considered and injected in the domain, differing in the particle size and aspect ratio. The simulations evolved with enough fibers ensuring statistically convergent results independent of particle number. Here, the shape and orientation angle were considered, especially in the treatment of the particle-wall interaction where the recent model proposed by Quintero et al. [6] was used.

A good agreement of the flow field with the results obtained by Marchiolli et al. was observed when the conditions were accurately established. Including the proper fiber dynamics in the simulations yield a different obtained behavior, such as particle concentration field near the wall, when considering only spherical particles. Particularly here, the hydrodynamic wall interaction (e.g., lubrication) was analyzed. In addition, deposition rates, accumulation, fiber orientation and alignment frequency were also compared against the results obtained by Marchiolli et al. [5].

REFERENCES

[1] Zastawny, M., Mallouppas, G., Zhao, F., van Wachem, B., Derivation of drag and lift force and torque coefficients for non-spherical particles in flows, International Journal of Multiphase Flows, 39, 227-239, 2012.

[2] Hölzer, A., Sommerfeld, M., New simple correlation formula for the drag coefficient of non-spherical particles, Powder Technology, 184, 361-365, 2008.alvetti, M.V. and Bruno, L.: Reliability of LES simulations.

[3] Goldstein, H., Classical Mechanics. 2nd Ed., Addison-Wesley, Reading 31, 1980.

[4] Fan, F., Ahmadi, G., A sublayer model for wall deposition of ellipsoidal particles in turbulent streams, Journal of Aerosol Science, 26, 813-840, 1995.

[5] Lain, S. and Sommerfeld, M., Kinematic simulations of non-spherical particle response behaviour. 8th International Conference on Multiphase Flow, ICMF 2013, Jeju, Korea, May 26–31, 2013.

[6] Zhao, F., and van Wachem, B: A Novel Quaternion Integration Approach for Describing the Behaviour of Non-Spherical Particles. Acta Mechanica 224, no. 12 3091–3109 (2013).

[5] Marchioli, C., Fantoni, M., Soldati, A., Orientation, distribution, and deposition of elongated, inertial fibers in turbulent channel flow, Physics of Fluids, 22, 033301, 2010.

[6] Quintero, B., Lain, S., Sommerfeld, M., Derivation and validation of a hard-body particle-wall collision model for non-spherical particles of arbitrary shape, Powder Technology, 380, 526-538, 2021.

WORKSHOP
Direct and Large-Eddy Simulation 13
October 26th-29th 2022, Udine, Italy

DNS OF MAGNETIC DENSITY SEPARATION IN THE WAKE OF A HONEYCOMB

L.C. Thijs[1], J.G.M. Kuerten[1], J.C.H. Zeegers[2], S. Tajfirooz[1]
[1] Department of Mechanical Engineering
[2] Department of Applied Physics
Eindhoven University of Technology, the Netherlands
j.g.m.kuerten@tue.nl

INTRODUCTION

Magnetic density separation (MDS) is an innovative technique that separates different types of plastic particles according to their different mass densities. To this end an effective vertical mass density gradient in a liquid is created by applying a strong magnetic field to a ferrofluid. Particles transported by this liquid settle at the height where their mass density equals the effective fluid mass density. To obtain a high separation efficiency, it is important that the level of turbulence in the liquid is kept as small as possible. The liquid is first guided through a honeycomb in which the flow is relaminarized. However, in the wake of the honeycomb cell walls disturbances are created [1], which together with the effect of the particle motion may lead to turbulent flow further downstream. In this paper, we investigate this and its effects on particle separation using temporal point-particle DNS of the system, taking into account the full interaction between particles and fluid and particle collisions.

GOVERNING EQUATIONS AND NUMERICAL METHODS

In figure 1 the schematic of the MDS apparatus is given. The ferrofluid enters the system from the left and is guided through a honeycomb, whereas the particles to be separated can only enter the separation chamber via the top and bottom channels. In the separation chamber, a strong magnetic field is applied by magnets on the bottom and top (not indicated in the figure). The top and bottom walls of the separation chamber move with the mean fluid velocity. At the downstream end of the separation chamber, the separated particles are sorted by means of the separator blades. In all simulations shown here the magnetic field corresponds to the one-dimensional magnetic field between two identical magnetic Halbach arrays with their stronger sides facing each other.

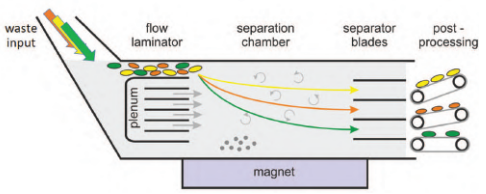

Figure 1: Schematic of magnetic density separation apparatus.

We use an Euler-Lagrange approach, in which the flow around the spherical particles is not resolved, but a point-particle approach is applied instead. The effect of the magnetic field on the flow can be incorporated in a reduced pressure [2]. Since the mass density of the particles is close to that of the fluid, the complete equation of motion is solved for each particle, including added mass force, force due to the undisturbed velocity field and history force, along with the equation for particle rotation. It has been shown that the history force has a significant effect on the particle motion [2]. This force has been implemented in an efficient way [3]. The reaction forces of the particles on the fluid are distributed over a volume equal to the particle volume. Particle collisions are taken into account by an efficient collision search method and taking into account conservation of linear and angular momentum and the coefficient of restitution for collisions of wet plastic particles.

The simulation domain is the region between the exit of the honeycomb and the separator blades, for which a temporal approach is applied with periodic conditions in streamwise and spanwise directions. The effect of the honeycomb is incorporated in the initial condition, which plays the role of the inflow condition in a temporal approach. A distinction is made between laminar and turbulent flow in the cells of the honeycomb, which are of rectangular shape. For laminar flow in the honeycomb cells the analytical solution is used as initial condition, on which perturbations are superposed with an amplitude that corresponds to experimental results at the same Reynolds number obtained by particle image velocimetry. The initial condition corresponding to turbulent flow in the honeycomb cells is obtained from a DNS of the flow in a rectangular duct at the same Reynolds number. For laminar flow symmetry between the honeycomb cells is broken by changing the perturbations and for turbulent flow behind each cell the DNS solution at a different time is taken. Directly behind the cell walls the initial velocity is set to zero.

A pseudo-spectral method is applied for the solution of the DNS with Fourier-Galerkin in the two periodic directions and Chebyshev-tau in the vertical direction. The equations are solved in a frame which moves with the mean fluid velocity where the top and bottom wall are stationary and the honeycomb moves in the negative streamwise direction. A combination of a three-stage Runge-Kutta method and the implicit Crank-Nicolson method is used for time integration of the fluid equations. Forward Euler is applied for integration of the particle equations of motion to enable deterministic

treatment of particle collisions [2].

In the results shown here we consider only one honeycomb consisting of 6×8 parallel rectangular ducts with height 15.2 mm, width 16.6 mm and wall thickness 3 mm. Above and below the honeycomb there are two channels in which the initial velocity has a Couette profile and where the particles are initially located. We consider three different Reynolds numbers in the honeycomb cells, 900, 1800 and 5600, all based on the hydraulic diameter of the cells and the mean velocity. Figure 2 shows the initial streamwise velocity in a plane perpendicular to the streamwise direction for the highest Reynolds number, where the flow in the honeycomb cells is turbulent. To fully resolve the honeycomb cells 576 Fourier and Chebyshev modes are applied in spanwise and vertical direction. The particle volume fraction is 2% and spherical particles with a diameter of 4 mm and ten different mass densities, both higher and lower than the fluid mass density, are used.

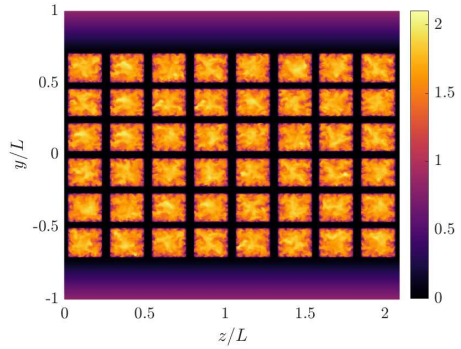

Figure 2: Initial condition for turbulent flow in the honeycomb cells. The colors indicate the streamwise velocity component

RESULTS AND CONCLUSIONS

In order to obtain good separation of particles of different mass density, particles should move towards the vertical position where the effective fluid mass density equals their own mass density as quickly as possible. To that end, disturbances in the fluid velocity should be kept as small as possible. Moreover, particle collisions generally result in a delay in the time at which they reach their equilibrium position. The purpose of the honeycomb is to eliminate velocity disturbances. However, the wakes of the walls between the honeycomb cells also generate disturbances, which may result in turbulent flow further downstream. Furthermore, the relative particle motion in vertical direction generates velocity disturbances as well. Comparison of results with and without two-way coupling shows the effect of the latter. The vertical motion of the particles with respect to the fluid moves the peak of the fluid velocity fluctuations that occurs downstream of the honeycomb in upstream direction.

Figure 3 shows the root-mean square of the streamwise fluid velocity component averaged over the vertical and spanwise direction as a function of the distance from the honeycomb exit, where the mean fluid velocity has been used to transform time to streamwise position. For the two laminar cases the peak position and maximum velocity fluctuation increase with increasing Reynolds number. The decay rate downstream of the peak is for both Reynolds numbers approximately the same. For the turbulent case, the peak in velocity fluctuations is located at the exit of the honeycomb and the fluctuations decay more slowly.

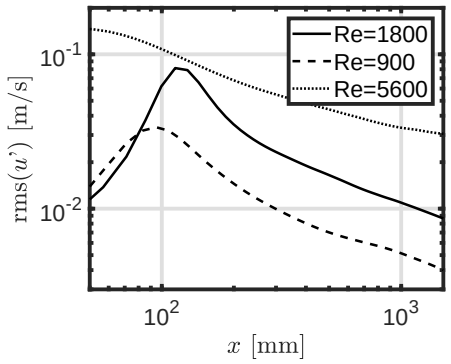

Figure 3: Root-mean square of the streamwise velocity fluctuations averaged over the vertical and spanwise direction for Re=900 (dashed), 1800 (solid) and 5600 (dotted).

Figure 4 shows the resulting separation error, which is quantified by the root-mean square of the deviation of the actual vertical position of the particles and their equilibrium position. This error is plotted as a function of the streamwise position and makes it possible to estimate the required length of the separation chamber to reach a certain separation error. The results correspond very well to the velocity fluctuations shown in figure 3. The higher the velocity fluctuations are, the larger the separation error is. This might lead one to conclude that a lower Reynolds number results in more efficient separation. However, a lower Reynolds number also implies a lower particle mass flow rate. The optimal choice is a trade-off between separation error and particle mass flow rate.

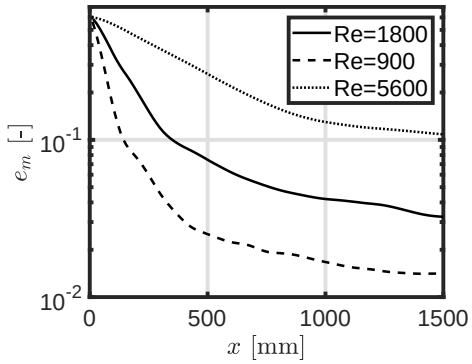

Figure 4: Separation error as a function of the streamwise coordinate for Re=900 (dashed), 1800 (solid) and 5600 (dotted).

REFERENCES

[1]Thijs., L.C., Dellaert, R.A., Tajfirooz, S., Zeegers, J.C.H. and Kuerten, J.G.M. : Honeycomb-generated Reynolds-number dependent wake turbulence, *J. Turbul.*, **22**, 535–561 (2021).

[2]Tajfirooz, S., Meijer, J.G., Dellaert, R.A., Zeegers, J.C.H. and Kuerten, J.G.M. : Direct numerical simulation of magneto-Archimedes separation of spherical particles, *J. Fluid Mech.*, **910**, A52 (2021).

[3]Van Hinsberg, M.A.T., ten Thije Boonkkamp, J.H.M. and Clercx, H.J. : An efficient, second order method for the approximation of the Basset history force, *J. Comp. Phys.*, **230**, 1465–1478 (2011).

Session: Turbulent flows 2

Friday, October 28, 2022

15:20 – 16:20

WORKSHOP
Direct and Large-Eddy Simulation 13
October 26th-29th 2022, Udine, Italy

MULTI-SCALE PHENOMENA IN TURBULENT FLOWS WITH WALLS AND INTERFACES

A. Cimarelli[1], **G. Boga**[1], **A. Pavan**[1], **E. Stalio**[1]
[1] Department of Engineering "Enzo Ferrari"
University of Modena and Reggio Emilia, Italy
andrea.cimarelli@unimore.it

INTRODUCTION

Due to its relevance, wall turbulence has been the subject of many studies over the years, see Smits et al. [1] for a partial review. Paradigmatic flows have been channels, pipes and turbulent boundary layers. Such flows represent the simplest kind of wall-bounded flows, thus allowing for a detailed analysis of the physical mechanisms underlying more complex real-world problems. With respect to channels and pipes, boundary layers are characterized by additional phenomena related with the presence of a turbulent/non-turbulent interface. Such phenomena make the study of boundary layers of a more general relevance for industrial and geophysical problems. However, the spatial inhomogeneity in the streamwise direction renders boundary layers more challenging for simulations in comparison with streamwise-homogeneous channels and pipes. Tied with this streamwise inhomogeneity is also the need for applying proper inflow and tripping conditions (leading to very long domains) or rescaling and recycling methods to circumvent the simulation of transition (leading to shorter domains), further complicating the computational approach [2]. A method to avoid all these issues is to consider a temporally rather than spatially evolving boundary layer. As recently shown in Kozul et al. [3], the temporal boundary layer presents similar statistical features but its ease of set-up and computational cost savings make it an attractive setting to study the physics of turbulent boundary layers.

THE SECOND-ORDER STRUCTURE FUNCTION EQUATION FOR VORTICITY

The aim of the present work is to investigate the role played by large and small scales in the entrainment processes and in the near-wall self-sustaining mechanisms of turbulence. Both processes are simultaneously present in the flow setting of a temporal boundary layer. In order to investigate their multi-scale character, the use of two-point statistics is demanding. In this respect, several works in the past have shown that the generalized Kolmogorov equation [4] represents a sufficiently general statistical formalism to address the multi-dimensional cascade processes of turbulence from its production to its dissipation. Examples of application of the generalized Kolmogorov equation in wall turbulence are Danaila et al. [5], Marati et al. [6], Cimarelli et al. [7, 8], in thermally driven turbulence are Rincon [9], Togni et al. [10], in separated and reattaching flows are Mollicone et al. [11], Gatti et al. [12] and in turbulent jets and wakes are Burattini et al. [13], Portela et al. [14], Cimarelli et al. [15]. The generalized Kolmogorov equation is based on the second-order structure function of the fluctuating velocity field

$$\langle \delta q^2 \rangle \equiv \langle \delta u_i \delta u_i \rangle \tag{1}$$

where $\delta u_i \equiv u_i(\boldsymbol{x'}, t) - u_i(\boldsymbol{x''}, t)$ is the fluctuating velocity increment and $\langle \cdot \rangle$ denotes ensemble average. Here, we aim at extending this formalism by addressing for the first time the exact evolution equation for the second-order structure function of the fluctuating vorticity field, hereafter called scale enstrophy

$$\langle \delta \zeta^2 \rangle \equiv \langle \delta \omega_i \delta \omega_i \rangle \tag{2}$$

where $\delta \omega_i \equiv \omega_i(\boldsymbol{x'}, t) - \omega_i(\boldsymbol{x''}, t)$ is the fluctuating vorticity increment. Indeed, enstrophy is widely recognized to be a suitable statistical observable for the study of the entrainment processes taking place at the turbulent/non-turbulent flow region [16]. In analogy with the generalized Kolmogorov equation, the equation for scale enstrophy is defined in a 6-dimensional space of scales $\boldsymbol{r}$ and positions $\boldsymbol{x_c}$, thus enabling a detailled scale-by-scale description of the multi-dimensional cascade processes of enstrophy from its production to its dissipation in the augmented-space regions of turbulence. The described multi-dimensional approach will shed light on the complex interactions between outer entrainment phenomena and near-wall self-sustaining mechanisms simultaneously occurring in turbulent boundary layers.

In closing this section, let us pointing out that the statistical homogeneity in both the streamwise and spanwise directions provided by the temporal boundary layer settings is a crucial aspect for the success of this approach because it allows us to reduce the second-order structure function problem from 6 to 4 dimensions.

DIRECT NUMERICAL SIMULATION OF THE TEMPORAL BOUNDARY LAYER

The temporal boundary layer consists in a moving wall at constant speed U_w at the bottom ($z = 0$) of an initially quiescent fluid [3]. To achieve transition to turbulence, an initial condition for the streamwise velocity field is assigned,

$$U_0(z, 0) = c' \frac{U_w}{2} \left\{ 1 + \tanh \left[\frac{D}{2\theta} \left(1 - \frac{z}{D} \right) \right] \right\} \tag{3}$$

The initial velocity profile is designed to mimic the wake of a wall-mounted trip wire with diameter D commonly

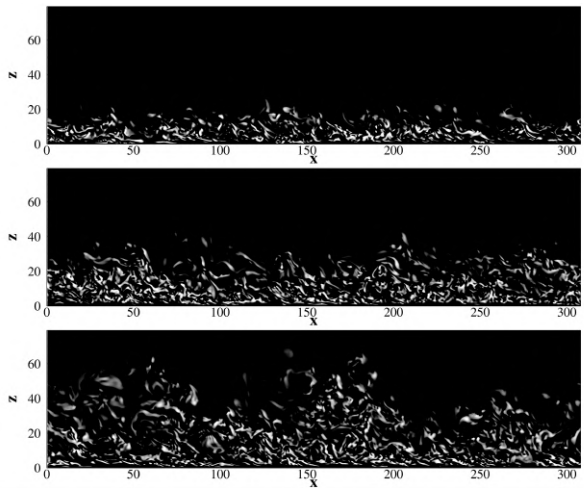

Figure 1: Direct Numerical Simulation of a temporal boundary layer. Instantaneous patterns taken by the spanwise vorticity at three different evolution times corresponding to $Re_\tau = 500$, $Re_\tau = 750$ and $Re_\tau = 1000$ from top to bottom, respectively.

used in wind tunnel experiments to trigger turbulence. Superimposed to this initial condition (3), a white noise $c'(x, y, z) \in [-0.05, 0.05]$ is also used to speed up transition. The adopted numerical domain has dimensions $(L_x, L_y, L_z) = (924D, 462D, 220D)$ and has been discretized using $(N_x, N_y, N_z) = (3072, 3072, 768)$ points. The size of the domain is determined by the planned largest boundary layer thickness $\delta(t)$ that, in turn, determines the largest friction Reynolds number of the simulation $Re_\tau = u_\tau \delta/\nu$ where u_τ is the friction velocity and ν the viscosity of the fluid. Indeed, when the flow is indefinitely evolved in time would reach the state of a fully developed open Couette flow thus requiring the definition of an end time such that $\delta/L_z \ll 1$. Following Kozul et al. [3], we consider $\delta/L_z = 1/3$ and the domain dimensions are defined in order to reach $Re_\tau = 1500$ at the end of the simulation. In contrast to the domain dimensions, the grid spacing is determined by the smallest value of the friction length that occurs at an early stage of the simulation when skin friction reaches its maximum. Even at this worst condition, the number of points used lead to a very good resolution that in friction units reads $(\Delta_x^+, \Delta_y^+, \Delta_z^+|_w) = (8.73, 4.37, 0.13)$. No-slip and impermeable boundary condition representing a moving wall is imposed at the bottom boundary, while a free-slip impermeable boundary condition is imposed at the top. Periodic boundary conditions are imposed in the streamwise and spanwise directions. The Direct Numerical Simulation has been performed by using the massively-parallel open-source code CaNS (https://github.com/p-costa/CaNS). The spatial discretization is based on a staggered second-order finite-difference scheme, while integration in time is performed using a third-order accurate Runge-Kutta method using a condition $CFL = 0.95$. A qualitative view of the flow solution at three different times is reported in figure 1 where the instantaneous pattern of spanwise vorticity is shown.

RESULTS

At the conference meeting, we will present the main statistical features of the temporal boundary layer with particular attention to their difference with respect to those of more classical spatially evolving boundary layers. Then, results from the second-order structure function equation of vorticity applied to the temporal boundary layer data will be presented with particular attention to the role played by reverse cascade processes in the outer entrainment and near-wall self-sustaining mechanisms of turbulence. The comparison of the main features of the reverse cascade with that occurring in turbulent channels [7, 8] where entrainment is absent, will be also presented in order to highlight the effects of the outer turbulent/non-turbulent phenomena on near-wall turbulence.

REFERENCES

[1]Smits, A.J., McKeon, B.J. and Marusic, I.: High–Reynolds number wall turbulence, *Ann. Rev. Fluid Mech.*, **43**, 353–375 (2011).

[2]Schlatter, P. and Örlü, R.: Assessment of direct numerical simulation data of turbulent boundary layers, *J. Fluid Mech.*, **659**, 116–126 (2010).

[3]Kozul, M., Chung, D. and Monty, J.P.: Direct numerical simulation of the incompressible temporally developing turbulent boundary layer, *J. Fluid Mech.*, **796**, 437–472 (2016).

[4]Hill, R.J.: Exact second-order structure-function relationship, *J. Fluid Mech.*, **468**, 317–326 (2002).

[5]Danaila, L., Anselmet, F., Zhou, T. and Antonia, R.A.: Turbulent energy scale budget equations in a fully developed channel flow, *J. Fluid Mech.*, **430**, 87–109 (2001).

[6]Marati, N., Casciola, C.M. and Piva, R.: Energy cascade and spatial fluxes in wall turbulence, *J. Fluid Mech.*, **521**, 191–215 (2004).

[7]Cimarelli, A., De Angelis, E. and Casciola, C.M.: Paths of energy in turbulent channel flows, *J. Fluid Mech.*, **715**, 436–451 (2013).

[8]Cimarelli, A., De Angelis, E., Jimenez, J. and Casciola, C.M.: Cascades and wall-normal fluxes in turbulent channel flows, *J. Fluid Mech.*, **796**, 417–436 (2016).

[9]Rincon, F.: Anisotropy, inhomogeneity and inertial-range scalings in turbulent convection, *J. Fluid Mech.*, **563**, 43–69 (2006).

[10]Togni, R., Cimarelli, A. and De Angelis, E.: Physical and scale-by-scale analysis of Rayleigh–Bénard convection, *J. Fluid Mech.*, **782**, 380–404 (2015).

[11]Mollicone, J.-P., Battista, F., Gualtieri, P. and Casciola, C.M.: Turbulence dynamics in separated flows: the generalised Kolmogorov equation for inhomogeneous anisotropic conditions, *J. Fluid Mech.*, **841**, 1012–1039 (2018).

[12]Gatti, D., Chiarini, A., Cimarelli, A. and Quadrio, M.: Structure function tensor equations in inhomogeneous turbulence, *J. Fluid Mech.*, **898** (2018).

[13]Burattini, P., Antonia, R.A. and Danaila, L.: Scale-by-scale energy budget on the axis of a turbulent round jet, *J. Turb.*, **6**, N19 (2005).

[14]Portela, F.A., Papadakis, G. and Vassilicos, J.C.: The turbulence cascade in the near wake of a square prism, *J. Fluid Mech.*, **825**, 315–352 (2017).

[15]Cimarelli, A., Mollicone, J.-P., Van Reeuwijk, M. and De Angelis, E.: Spatially evolving cascades in temporal planar jets, *J. Fluid Mech.*, **910** (2021).

[16]da Silva, C.B., Hunt, J.C.R., Eames, I. and Westerweel, J.: Interfacial Layers Between Regions of Different Turbulence Intensity, *Ann. Rev. Fluid Mech.*, **46**, 567–590 (2014).

WORKSHOP
Direct and Large-Eddy Simulation 13
October 26th-29th 2022, Udine, Italy

ASSESSMENT OF THE EFFECT OF THE SURFACE TENSION CONTRIBUTION ON THE EMULSIFICATION IN LINEARLY FORCED TURBULENCE

A. Begemann, T. Trummler, E. Trautner, J. Hasslberger, M. Klein
Department of Aerospace Engineering
University of the Bundeswehr Munich, Germany
elias.trautner@unibw.de

INTRODUCTION

Emulsions are suspensions of immiscible liquids, where the *dispersed* liquid is present in the form of poly-disperse droplets within the *carrier* liquid. In order to obtain and maintain an emulsion, a constant energy input in the form of kinetic energy is required to deform and breakup droplets. Both processes increase the total interface area, and thus the surface energy. Dodd & Ferrante [5] show that the power of the surface tension is either a source or a sink of turbulent kinetic energy (TKE), depending on the sign of the rate of change of the interface area. Consequently, the surface energy, or surface tension contribution, plays a central role for the emulsification process and the required energy input. In the present study, we focus on direct numerical simulations of emulsions in homogeneous isotropic turbulence (HIT), and especially on the temporal evolution of global and local surface tension contributions during emulsification.
For the forcing, we employ a physical space forcing method, introduced by Lundgren et al. [2]. We have extended this linear forcing with a PID controller to ensure a constant and pre-scribed TKE k in the context of two phase flows combined with fast convergence and to analyze the emulsifcation process [1].

GOVERNING EQUATIONS AND COMPUTATIONAL METHOD

The forced momentum equations for the two-phase flow under consideration read

$$\rho\left(\frac{\partial u_i}{\partial t}+\frac{\partial u_i u_j}{\partial x_j}\right)= \\ -\frac{\partial p}{\partial x_i}+\frac{\partial}{\partial x_j}\left[\mu\left(\frac{\partial u_i}{\partial x_j}+\frac{\partial u_j}{\partial x_i}\right)\right]+\sigma n_i \kappa \delta_s+\mathrm{F}^{\mathrm{PID}}u_i \tag{1}$$

with the density ρ, the dynamic viscosity μ, the i^{th} velocity component u_i and the pressure p. $\mathrm{F}^{\mathrm{PID}}=\beta^{\mathrm{PID}}\cdot\mathrm{F}$ denotes the pseudo shear term for the forcing, where β^{PID} denotes the controller output. The forcing parameter F is determined by k and the domain size [3].
Assuming incompressibility and homogeneity, the turbulent kinetic energy equation derived from the momentum equation reads [5]

$$\frac{dk}{dt}=-\varepsilon+\Psi_\sigma+2\,\mathrm{F}^{\mathrm{PID}}\,k. \tag{2}$$

Ψ_σ denotes the surface tension contribution defined as $\Psi_\sigma = \frac{-\sigma}{V_d\rho_d}\frac{\partial A}{\partial t}$ [5], with V_d, ρ_d, A denoting the volume and the density of the dispersed phase and A the interface area.
All simulations are conducted with the state-of-the-art open source code "PArallel Robust Interface Simulator" (PARIS) [4]. A red-black Gauss-Seidel solver with overrelaxation is employed to solve the Poisson equation for pressure in the framework of the projection method. The simulation is advanced in time using a second-order predictor-corrector method. For the spatial discretization, the finite-volume approach is realized using a cubic grid. The velocity components are stored on a staggered grid, while the pressure and the VOF marker function, as well as the local densities and the viscosities resulting from the latter, are computed at the cell centers. The third-order "Quadratic Upstream Interpolation for Convective Kinematics" (QUICK) scheme has been chosen to discretize the convective term of the momentum equation, while its viscous term is treated using central differences.

NUMERICAL SETUP AND CONFIGURATION

We consider a cubic box with length $L = 2\pi$ and periodic boundary conditions in each direction. The simulations are conducted as visualized in Fig. 1. First, we perform single phase simulations to obtain a fully developed single-phase HIT, subsequently we initialize the dispersed phase as spherical droplets. The last subfigure corresponds to an emulsion at stationary state.

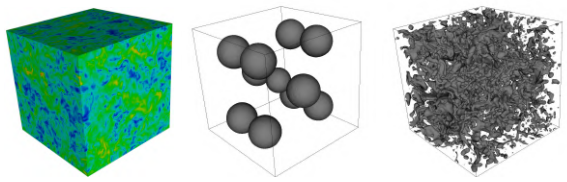

(a) (b) (c)

Figure 1: Simulation setup. (a) single phase forcing, flow field visualized by the velocity magnitude, (b) initialization droplets, (c) turbulent emulsion at stationary state.

RESULTS

To demonstrate the effect of Ψ_σ, we here compare and discuss the emulsification of two configurations with different surface tension coefficients adapted from Begemann et al. [1]. In both configurations, the density ratio of the *dispersed* and the *carrier* phase ρ_d/ρ is 0.9, resembling an oil-in-water emulsion, and the volume fraction of the dispersed fluid is 12.5%. Figure 2 visualizes the emulsion of the *Baseline* and *Low* σ case at statistically stationary state after 4τ. The time is normalized by the eddy turn-over time $\tau = k/\varepsilon$ evaluated with k_0 and ε_0 from statistically stationary state.

Figure 3 shows the temporal evolution of the normalized interface Area A/A_0 (a) and the surface tension contribution Ψ_σ (b). A_0 refers to the initial interface area, shown in Fig. 1 (b). Figure 3 (a) shows that the current forcing method reaches a statistically stationary state of the normalized interface area A/A_0 within an interval of about 4τ. Figure 3 (b) plots the temporal evolution of the surface tension contribution Ψ_σ, which is not directly considered by the linear forcing. During the emulsification process, droplet breakup is the prevailing mechanism. For configurations with a lower σ, the breakup of droplets requires less energy and thus occurs more frequently. Hence for decreasing σ, $|\Psi_\sigma|$ increases and therefore more TKE is drawn. This indicates a significantly higher $\partial A/\partial t$, respectively breakup rate, which even compensates the effect of the smaller σ on Ψ_σ. To compensate this effect, a higher energy input is required and leads to a different forcing input during the emulsification. At statistically stationary states, breakup and coalescence are more or less balanced and thus the net contribution of Ψ_σ vanishes.

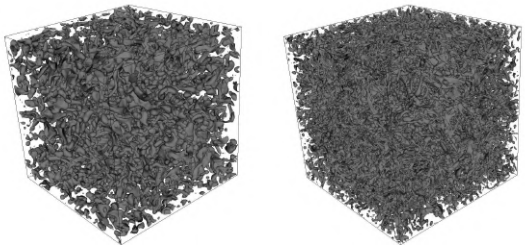

(a) (b)

Figure 2: Visualization of the emulsion at stationary state of the *Baseline* (a) and *Low* σ case (b)

PLANNED EVALUATIONS

In the current investigation we want to study the local effect of breakup and coalescence of single droplets to the net surface tension contribution. To this end, we plan to evaluate the Ψ_σ contribution of selected regions and compare the temporal evolution with that of the global Ψ_σ contribution. This analysis can allow for a deeper insight into local breakup processes. The plan is to consider a global volume fraction of about $\Phi \approx 1\%$ and to increase the resolution compared to our previous studies. Moreover, this enables detailed investigations of droplet size distributions.

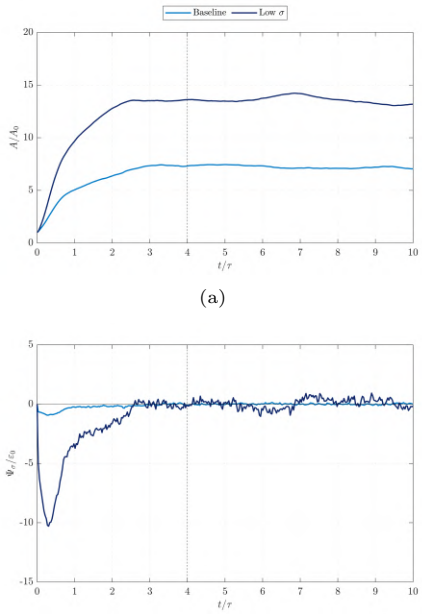

(a)

(b)

Figure 3: Temporal evolution of the normalized interface Area A/A_0 (a) and the surface tension contribution Ψ_σ normalized with the dissipation rate from stationary state ε_0 (b).

ACKNOWLEDGMENT

This project received funding by *dtec.bw* - Digitalization and Technology Research Center of the Bundeswehr - under the project *MORE*, which is gratefully acknowledged. Further, the authors thank the Gauss Centre for Supercomputing e.V. (www.gauss-centre.eu) for funding this project by providing computing time on the GCS Supercomputer SuperMUC-NG at Leibniz Supercomputing Centre (www.lrz.de).

REFERENCES

[1]Begemann, A., Trummler, T., Trautner, E., Hasslberger, J. and Klein, M. : Effect of turbulence intensity and surface tension on the emulsification process and its stationary state - A numerical study, *Canadian Journal of Chemical Engineering* (2022).

[2]Lundgren, T.S. : Linearly forced isotropic turbulence, *Annual Research Briefs Center for Turbulence Research, Stanford*, 461–473 (2003).

[3]Carroll, L., Blanquart, G. : A proposed modification to Lundgren's physical space velocity forcing method for isotropic turbulence, *Physics of Fluids*, **25**, 105–114 (2013).

[4]Aniszewski, W., Arrufat, T., Crialesi-Esposito, M., Dabiri, S., Fuster, D., Ling, Y., Lu, J., Malan, L., Pal, S., Scardovelli, R., Tryggvason, G., Yecko, P. and Zaleski, S. : PArallel, Robust, Interface Simulator (PARIS), *Computer Physics Communications* (2021).

[5]Dodd, M. S. and Ferrante, A. : On the interaction of Taylor length scale size droplets and isotropic turbulence, *Journal of Fluid Mechanics*, **806**, 356–412 (2016).

WORKSHOP
Direct and Large-Eddy Simulation 13
October 26th-29th 2022, Udine, Italy

A BAYESIAN HIERARCHICAL MULTIFIDELITY MODEL FOR TURBULENT FLOWS

S. Rezaeiravesh[1,2], T. Mukha[1,2] and P. Schlatter[1,2]
[1] SimEx/FLOW, Department of Engineering Mechanics,
KTH Royal Institute of Technology, Stockholm, Sweden
[2] Swedish e-Science Research Centre (SeRC), Stockholm, Sweden
{salehr, tmu, pschlatt}@mech.kth.se

INTRODUCTION

Despite the need for understanding the complex physics of turbulent flows, conducting high-fidelity experiments and scale-resolving numerical simulations such as large eddy simulation (LES) and direct numerical simulation (DNS) can be prohibitively expensive, particularly at high Reynolds numbers which are relevant to engineering applications. On the other hand, it is necessary to develop accurate yet cost-effective models for outer-loop problems involving turbulent flows which include uncertainty quantification (UQ), data fusion, prediction, and robust optimization. In these problems, exploration of the space of inputs and design parameters demands a relatively large number of flow realizations. A remedy can be using multifidelity models (MFMs) which aim at accurately predicting quantities of interest (QoIs) and their stochastic moments by combining the data obtained from different fidelities. When constructing MFMs, a given finite computational budget is optimally used through running only a few expensive (but accurate) simulations and many more inexpensive (but potentially less accurate) simulations.

In recent years, there has been a significant interest in developing and applying MFMs in various fields, see Ref. [1]. For turbulent flows, the main strategies for constructing effective MFMs can be summarized as: i) Co-Kriging models, see *e.g.* Ref. [2], ii) models based on non-intrusive polynomial chaos expansion and stochastic collocation methods, see *e.g.* [3], and iii) multi-level multifidelity Monte Carlo models [4, 5].

BAYESIAN HIERARCHICAL MFM WITH CALIBRATION

When constructing MFMs for turbulent flow simulations, two main characteristics have to be considered. Firstly, there is a distinguishable hierarchy in the fidelity of approaches such as Reynolds-averaged Navier-Stokes simulation (RANS), hybrid RANS-LES, wall-modeled and wall-resolved LES, and DNS, see *e.g.* Ref. [6]. Secondly, the outcome of any of these approaches can be potentially uncertain due to various modeling, numerical, and observational uncertainties. As the fidelity of approaches increases, the influence of modeling uncertainties decreases while the impact of numerical factors becomes more dominant.

The present study reports our recent progress on further development and application of a class of Bayesian hierarchical multifidelity models with calibration (HC-MFM) which rely on Gaussian processes. Following Goh et al. [7], at each fidelity level, which can be associated to any of the turbulence simulation approaches, the Kennedy-O'Hagan model [8] is used which allows for considering both model inadequacy and aleatoric uncertainties in the process of data fusion. As a main advantage of the present multifidelity modeling approach, the calibration parameters as well as the hyperparameters appearing in the Gaussian processes are simultaneously estimated within a Bayesian framework using a limited number of flow realizations (data). Furthermore, the use of Gaussian processes provides a natural way for incorporating observational uncertainty in the data (for instance due to finite time-averaging). The Bayesian inference of the posterior distribution of various parameters is done using a Markov Chain Monte Carlo (MCMC) approach. The constructed MFM can then be employed as a surrogate for uncertainty propagation and prediction over the space of input/design parameters.

RESULTS

The accuracy and efficiency of the described HC-MFM is evaluated for various problems involving turbulent flows. For instance, Figure 1 shows the prediction (mean and 95% confidence interval) of the lift coefficient, C_L, of a wing with a NACA0015 airfoil profile at Reynolds number 1.6×10^6. The flow angle of attack (AoA) is the design parameter and the data fed into the MFM comprises of: wind-tunnel experiments by Bertagnolio [9], detached-eddy simulations (DES) and two-dimensional RANS, both by Gilling *et al.* [10]. The study [10] showed a large sensitivity of the DES results with respect to the turbulence intensity (TI) of the flow at the domain inlet. Therefore, TI is considered as a calibration parameter for DES in the MFM. The stall angle of attack is another parameter which appears due to the construction of the kernel covariance function for the Gaussian processes representing the surrogate for the DES and experimental data. According to Figure 1, compared to the experimental data, the MFM is capable of accurately predicting C_L over the considered range of AoA. The sample posterior distribution of the TI and stall AOA obtained during the construction of the MFM are plotted in Figure 2

The described HC-MFM will also be applied to other problems including the flow over a periodic hill where both attached and separating turbulent boundary layers exist. Similar to Ref. [2], the design parameters are taken to be two

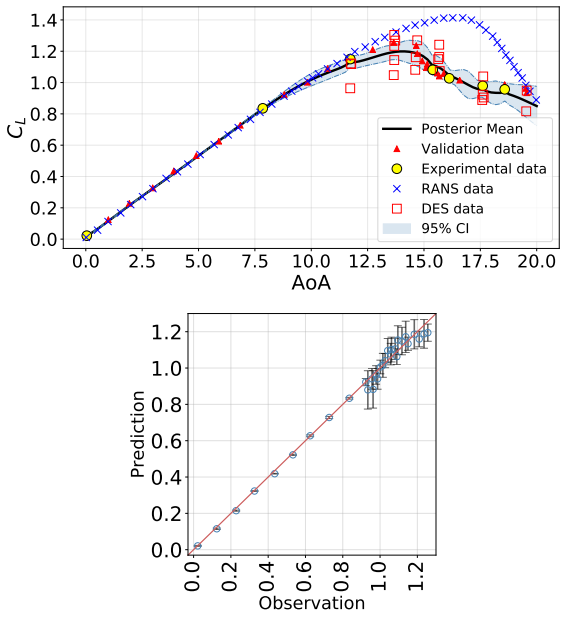

Figure 1: (Left) Lift coefficient C_L plotted against the angle of attack: the MFM is trained by the experimental data of Ref. [9] (yellow circles), as well as the DES (squares) and RANS (crosses) data by Gilling *et al.* [10]. The DES are performed in Ref. [10] with the resolved turbulence intensities $TI = 0\%, 0.1\%, 0.5\%, 1\%$, and 2% at the inlet. The validation data (red triangles) are also taken from the experiments of Ref. [9]. The mean prediction by the MFM is represented by the solid line along with associated 95% confidence interval. (Right) predictions by HC-MFM plotted against the validation data. The error bars represent the 95% CI.

geometrical parameters controlling the domain length in the streamwise direction. This example allows for a comparison between the performance of the HC-MFM with the MFM based on co-Kriging adopted in the recent study by Voet *et al.* [2]. The extra feature in HC-MFM is the ability of calibrating the RANS model parameters when constructing the MFM and hence actively incorporating their uncertainty in the predictions.

CONCLUSIONS

Based on applying the Bayesian hierarchical MFM with calibration to various problems involving turbulent flows, see Ref. [11], several conclusions can be drawn: i) the HC-MFM is accurate for outer-loop problems where the data from difference sources are combined. This MFM is consistent with the hierarchy of turbulence modeling approaches and can handle various forms of uncertainties. ii) For a fixed number of high-fidelity simulations the HC-MFM prioritizes the prediction of QoIs so that they become as close as possible to the high-fidelity data, while the posterior distributions of the calibrated parameters are found to be accurate only if sufficiently many low-fidelity data are provided.

REFERENCES

[1] B. Peherstorfer, K. Willcox, and M. Gunzburger, "Survey of multifidelity methods in uncertainty propagation, inference, and optimization," *SIAM Review*, vol. 60, no. 3, pp. 550–591, 2018.

[2] L. J. Voet, R. Ahlfeld, A. Gaymann, S. Laizet, and F. Montomoli, "A hybrid approach combining DNS and RANS simulations to quantify uncertainties in turbulence modelling," *Applied Mathematical Modelling*, vol. 89, pp. 885 – 906, 2021.

[3] P. S. Palar, T. Tsuchiya, and G. T. Parks, "Multi-fidelity non-intrusive polynomial chaos based on regression," *Computer Methods in Applied Mechanics and Engineering*, vol. 305, pp. 579 – 606, 2016.

[4] H. R. Fairbanks, A. Doostan, C. Ketelsen, and G. Iaccarino, "A low-rank control variate for multilevel Monte Carlo simulation of high-dimensional uncertain systems," *J. Comput. Phys*, vol. 341, pp. 121–139, 2017.

[5] L. Jofre, G. Geraci, H. R. Fairbanks, A. Doostan, and G. Iaccarino, "Exploiting multi-fidelity strategies to quantify uncertainty in irradiated particle-laden turbulent flow," *Proceedings of the 7th European Conference on Computational Fluid Dynamics*, pp. 1–12, 2018.

[6] P. Sagaut, S. Deck, and M. Terracol, *Multiscale and Multiresolution Approaches in Turbulence*. Imperial College Press, 2nd ed., 2013.

[7] J. Goh, D. Bingham, J. P. Holloway, M. J. Grosskopf, C. C. Kuranz, and E. Rutter, "Prediction and computer model calibration using outputs from multifidelity simulators," *Technometrics*, vol. 55, no. 4, pp. 501–512, 2013.

[8] M. C. Kennedy and A. O'Hagan, "Bayesian calibration of computer models," *Journal of the Royal Statistical Society: Series B (Statistical Methodology)*, vol. 63, no. 3, pp. 425–464.

[9] F. Bertagnolio, *NACA0015 Measurements in LM Wind Tunnel and Turbulence Generated Noise*. No. 1657(EN) in Denmark. Forskningscenter Risoe., Danmarks Tekniske Universitet, 2008.

[10] L. Gilling, N. Sørensen, and L. Davidson, "Detached eddy simulations of an airfoil in turbulent inflow," *47th AIAA Aerospace Sciences Meeting*, vol. 24, no. AIAA 2009-270, pp. 1–13, 2009.

[11] S. Rezaeiravesh, R. Vinuesa, and P. Schlatter, "Towards multifidelity models with calibration for turbulent flows," in *14th WCCM-ECCOMAS Congress*, CIMNE, 2021.

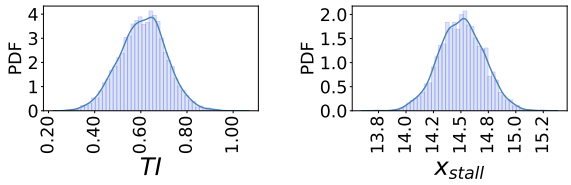

Figure 2: Posterior probability density function (PDF) of (left) DES turbulence intensity (TI) and stall AoA obtained during the construction of the MFM described in the caption of Figure 1.

WORKSHOP
Direct and Large-Eddy Simulation 13
October 26th -29th 2022, Udine, Italy

THE STRUCTURE BASED TURBULENT RESOLUTION APPROACH: EVOLUTION AND APPLICABILITY

E. Baglietto[1]
[1] Department of Nuclear Science and Engineering
Massachusetts Institute of Technology, USA
emiliob@mit.edu

INTRODUCTION

A large number of industrial applications of CFD requires the resolution of unsteady flow mixing in complex geometries at very large Reynolds numbers. This is particularly relevant for energy systems, where phenomena such as thermal striping and cycling often lead to accelerated failure from thermally or mechanically induced high cycle fatigue. While the cost of Large Eddy Simulation does not yet support effective design applications, attempts to adopt hybrid turbulence approaches have shown very limited success due to the excessive spurious hybridization of the models and their strong sensitivity to both spatial and temporal resolution, often interacting with specific approximation methods [1-3]. The STRUCT(ture) based turbulence resolution approach has been developed with the specific aim to robustly control its activation at all mesh finesses, where the increased scale resolution inside rapidly deformed turbulence regions can consistently reduce modeling error compared to the baseline URANS closure.

MODEL EVOLUTION

The STRUCT concept was first introduced by Lenci in 2015 [4], and relies on a baseline anisotropic $k-\varepsilon$ model [5] to provide improve modeling of complex strain flows. The hybridization approach compares the second invariant of the velocity gradient tensor, $\overline{II}$, representing the resolved time scales of the turbulent structures, with the averaged modeled time scales, k/ε . In regions where the timescales overlap, the turbulent eddy viscosity is reduced locally by a hybridization parameter to increase turbulence resolution. This concept is very general and has the potential of remaining largely insensitive to the selection of spatial and temporal resolutions. In order to assess the conceptual validity of the approach and its potential for robust applicability, a "controlled" approach was first adopted, where the activation closure coefficients are obtained from precursor URANS solutions. Simulation results obtained with the controlled approach provided understanding of the behavior of STRUCT activation and enabled assessment of the model coefficient and resolution sensitivities.

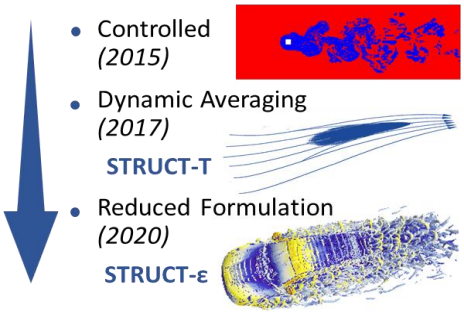

Figure 1: STRUCT model evolution.

In order to provide a closed formulation Lenci [6] introduced a Lagrangian averaging operator in the form of an additional transport equation, which extended the original proposal by Meneveau [7]. The proposed STRUTC-Transported formulation demonstrated robust applicability and consistent grid convergence, approaching the reference LES solutions on URANS type mesh configurations [6]. Demonstrations of the model capabilities have been presented for thermal mixing in T-junctions [8,9], triple-jet mixing [10] and cross flow in a helical-coiled tube bundle [11].

The Lagrangian averaging approach demonstrated undesirable sensitivity to the boundary conditions for external flow cases. Since the modeled scale on the inlet boundary is defined based on the ratio between the turbulent kinetic energy, k, and turbulent dissipation rate, ε, this can lead to unexpected hybrid activation based on users' definition. In addition, the solution of an additional transport equation increases the computational cost by approximately 10% when compared to the baseline URANS model. To overcome the limitations of the transported average STRUCT formulation, the STRUCT-ε model was recently proposed by Xu [12-13]. Rather than calculating

the reduction parameter based on explicit comparison between the resolved and modeled time scales, the new model introduces an additional source term in the ε equation to implicitly reduce the eddy viscosity, which directly compares the modeled and resolved time scales.

$$\frac{\partial k}{\partial t} + \bar{u}_j \frac{\partial k}{\partial x_j} = \frac{\partial}{\partial x_j}\left[\left(\nu + \frac{\nu_t}{\sigma_k}\right)\frac{\partial k}{\partial x_j}\right] + P_k - \varepsilon \qquad (1)$$

$$\frac{\partial \varepsilon}{\partial t} + \bar{u}_j \frac{\partial \varepsilon}{\partial x_j} = \frac{\partial}{\partial x_j}\left[\left(\nu + \frac{\nu_t}{\sigma_k}\right)\frac{\partial \varepsilon}{\partial x_j}\right] + C_{\varepsilon 1}\frac{\varepsilon}{k}P_k - C_{\varepsilon 2}\frac{\varepsilon^2}{k} + C_{\varepsilon 3} k|\bar{II}| \qquad (2)$$

Where $\bar{II}$ is the second invariant of velocity gradient and is defined as $1/2(||\Omega||^2 - ||S||^2)$. The value of the additional $C_{\varepsilon 3}$ coefficient was selected by Xu through a set of test cases, and has shown very low sensitivity on all performed validations. The hybridization in the new STRUCT-ε model no longer depends on the inlet and boundary conditions which eliminates the potential unexpected activation. In the meantime, the idea behind the original STRUCT-T and STRUCT-ε models are consistent: they both depend on the comparison of $|\bar{II}|^{\frac{1}{2}}$ and ε/k. In STRUCT-ε model, the modification of the ε equation would only become noticeable when $|\bar{II}|^{\frac{1}{2}}$ is larger than ε/k.

MODEL PERFORMANCE

The STRUCT concept has demonstrated the unique ability to consistently resolve activation regions across a large variation of test conditions, mesh resolutions, and solver implementations, resulting in very strong applicability for industrial cases. An example is shown here for the simulation of interacting flat jets [14], where STRUCT has shown the ability to consistently resolve the velocity and stresses up to very coarse URANS meshes, up to sizes of 1.7 times the average integral length scales (compared to an LES resolution requirement of 6 times).

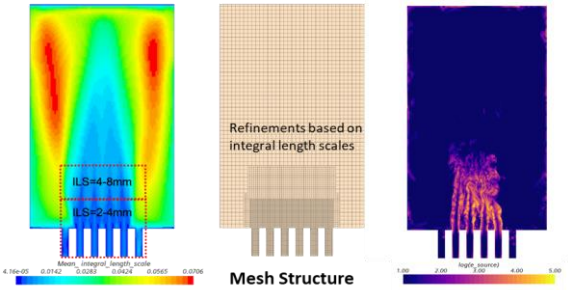

Figure 2: Interacting Jets Simulation [14].

Figure 2 provides a description of the test configuration, predicted integral length scales and model activation, while figure 3 demonstrates the model mesh sensitivity for the streamwise velocity and stress distributions.

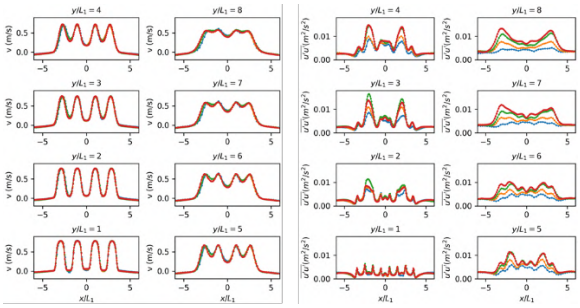

Figure 3: Streamwise velocities and stresses at all mesh resolutions [14].

Table 1: Summary of STRUCT model mesh sensitivity [14]

	Base Size	Local size / ILS	Number of Cells	Speedup from LES
Mesh 1	3.00 mm	1/3	4,300,000	16x
Mesh 2	4.00 mm	1/2.3	1,840,000	50x
Mesh 3	5.33 mm	1/1.7	795,000	156x
Mesh 4	6.93 mm	1/1.3	370,000	456x

REFERENCES

[1] L. Davidson. Evaluation of the SST-SAS model: channel flow, asymmetric diffuser and axi-symmetric hill, *Eur. Conf. Comput. Dyn. ECCOMAS CFD.* (2006).

[2] S.E. Gant, Reliability issues of LES-related approaches in an industrial context, *Flow, Turbul. Combust. 84* (2010).

[3] B.L. Smith, J.H. Mahaffy, K. Angele. A CFD benchmarking exercise based on flow mixing in a T-junction, *Nucl. Eng. Des. 264* (2013) 80–88.

[4] G. Lenci, E. Baglietto. A structure-based approach for topological resolution of coherent turbulence: overview and demonstration, *16th Int. Top. Meet. Nucl. React. Therm. Hydraul.* (2015) 1–14.

[5] E. Baglietto, H. Ninokata. Anisotropic eddy viscosity modeling for application to industrial engineering internal flows, *Int. J. Transp. Phenom. 8* (2006) 109.

[6] G. Lenci, J. Feng, E. Baglietto. A generally applicable hybrid unsteady Reynolds-averaged Navier–Stokes closure scaled by turbulent structures. *Phy. of Fluids 33* (10), (2021).

[7] C. Meneveau, T.S. Lund, W.H. Cabot, A Lagrangian dynamic subgrid-scale model of turbulence, *J. Fluid Mech. 319* (1996) 353–385

[8] Feng, J.; Baglietto, E.; Tanimoto, K.; Kondo, Y. Demonstration of the STRUCT turbulence model for mesh consistent resolution of unsteady thermal mixing in a T-junction. *Nucl. Eng. Des.,* 361, (2020).

[9] Feng, J.; Frahi, T.; Baglietto, E. STRUCTure-based URANS simulations of thermal mixing in T-junctions. *Nucl. Eng. Des., 340, 275–299* (2018).

[10] Acton, M.J.; Lenci, G.; Baglietto, E. Structure-Based Resolution of Turbulence for Sodium Fast Reactor Thermal Striping Applications. *In Proceedings of the 16th International Topical Meeting on Nuclear Reactor Thermal Hydraulics (NURETH-16);* (2015).

[11] Feng, J.; Acton, M.; Baglietto, E.; Kraus, A.R.; Merzari, E. On the relevance of turbulent structures resolution for

cross-flow in a helical-coil tube bundle. *Ann. Nucl. Energy, 140,* (2020) 107298.
[12] L. Xu, A second generation URANS approach for application to aerodynamic design and optimization in the automotive industry, *Ph.D. Thesis, Massachusetts Institute of Technology.* (2020).
[13] J. Feng, L. Xu, E. Baglietto. Assessing the Applicability of the Structure-Based Turbulence Resolution Approach to Nuclear Safety-Related Issues. *Fluids 6 (2),* (2021).
[14] M. Pham, E. Baglietto, V. Petrov, A. Manera. Assessing the Structure-Based Turbulence Model Performance with Symmetric Jet Experiments. *ATH22 Conference (2022).*

Session: Flow separation 2

Friday, October 28, 2022

16:20 – 17:20

WORKSHOP
Direct and Large-Eddy Simulation 13
October 26th-29th 2022, Udine, Italy

UNSTEADY SEPARATION IN A TURBULENT BOUNDARY LAYER

F. Ambrogi[1], U. Piomelli[1], and D. E. Rival[1]
[1] Department of Mechanical and Materials Engineering
Queen's University, Canada
f.ambrogi@queensu.ca

INTRODUCTION

Almost all turbulent boundary-layer flows of practical relevance are subject to pressure gradients, usually introduced by changes in geometry. The pressure gradient may be favorable (FPG) or adverse (APG) depending on whether the pressure decreases or increases along the flow direction. Both conditions are very common in engineering and physical systems such as airfoils or turbine blades, and in geophysical applications.

If the APG is strong enough, the boundary layer may separate from the wall. Flow separation can significantly affect the efficiency of fluidic devices. A comprehensive review on the physics of flow separation can be found in [1]. A strong FPG, on the other hand, may lead to a re-laminarization of the turbulent boundary layer (TBL) caused by the predominance of pressure forces over the turbulent Reynolds stresses [2].

Most studies of APG and FPG boundary layers consider pressure-gradients that vary only spatially. However, in many cases (e.g., helicopter blades, turbine blades, pitching airfoils etc.) the pressure gradient varies both spatially and temporally. In fish locomotion, for instance, unsteady pressure gradients are the norm: fish propel themselves by waving their tail, and (especially during maneuvers) the changing body curvature generates unsteadiness in the pressure distribution along the body, and pressure gradients that are space and time dependent [3].

While the steady flow in APG and FPG TBLs has been studied extensively, fewer investigations of the unsteady case can be found [4]. In the present paper we use large-eddy simulations to investigate a spatially developing turbulent boundary layer with a space- and time-dependent pressure gradient. By changing the freestream velocity periodically in time we generate a flow field that can either separate or tend towards re-laminarization, depending on the phase of the cycle. Several cases have been investigated for a range of reduced frequencies k, spanning between a very rapid flutter-like motions to a slower quasi-steady flapping. Time-averaged and phase-averaged fields are analyzed, and comparison is made with steady cases with fixed pressure gradients. In the following, we briefly describe the methodology and show some preliminary results. We will conclude by outlining the results that will be presented in the final paper.

NUMERICAL METHODOLOGY

In the present work, simulations are performed using the Large Eddy Simulation (LES) technique. In LES, the incompressible Navier Stokes equations are solved for filtered quantities (here indicated with a $\overline{\cdot}$):

$$\frac{\partial \overline{u}_i}{\partial x_i} = 0; \quad \frac{\partial \overline{u}_i}{\partial t} + \frac{\partial}{\partial x_j}\left(\overline{u}_i \overline{u}_j\right) = -\frac{\partial \overline{p}}{\partial x_i} + \nu \nabla^2 \overline{u}_i - \frac{\partial \tau_{ij}}{\partial x_j} \quad (1)$$

where, (x, y, z) are the streamwise, wall-normal, and spanwise directions, and $\tau_{ij} = \overline{u_i u_j} - \overline{u}_i \overline{u}_j$ is the sub-filter scale stress tensor. In the present study τ_{ij} is modelled using the Vreman eddy-viscosity model [5]. δ_o^* is the boundary layer displacement thickness at the inflow plane. We use a well-validated finite-difference code that has previously been applied to similar cases [6, 7, 8]. The dimensions of the computational domain are $L_x = 600\delta_o^*$, $L_y = 64\delta_o^*$, and $L_z = 55\delta_o^*$. The Reynolds number based on δ_o^* and the freestream velocity at the inflow (which is constant in time) is $Re_{\delta_o^*} = 1,000$. The grid uses $N_x \times N_y \times N_z = 1536 \times 192 \times 256$ points; a grid-convergence study was performed to verify that this resolution is adequate. In wall units (defined using the wall shear velocity u_τ at the inflow plane) we have $\Delta x^+ = 18.7$, $\Delta y^+_{\min} = 0.7$, and $\Delta z^+ = 10$. A periodic boundary condition is used in the spanwise direction, a convective boundary condition at the outflow plane, and a velocity obtained form a parallel auxiliary simulation is used at the inflow.

The pressure gradient is generated by imposing a vertical velocity $V_\infty(x,t)$ at the free-stream that changes both in space and time, $V_\infty(x,t) = V_o(x)\sin(2\pi t/T)$, where T is the oscillation period, and V_o a streamwise distribution of wall-normal velocity, which was chosen to match the case studied by [9]. The streamwise freestream velocity is obtained by imposing a zero vorticity condition [8, 9, 10].

The non dimensional parameter that characterizes the unsteadiness is the reduced frequency $k = \pi f L_{PG}/U_o$, where $f = 2\pi/T$ is the imposed frequency, L_{PG} is a characteristic length (we use the length over which the Pressure Gradient varies), and U_o is the free-stream velocity at the inflow plane. We performed numerical simulations for $k = 0.2,\ 1$ and 10. [11] found that a reduced frequency $k > 0.05$ was the threshold beyond which the boundary layer was clearly unsteady, and many experimental studies have been carried out for a wide range of reduced frequency $0.1 < k < 82$ [12, 13]. In our case the definition of the length-scale (L_{PG}) is not unique, and we chose the length of the region where the pressure-gradient is significant as the one that most closely resembles the chord length of an airfoil. Because of this arbitrariness, a one-to-one comparison with the studies in the literature is difficult; however, we obtained trends that are in agreement with the

results in the literature, as will be shown momentarily.

The oscillation period was divided into 20 equally spaced phases, and phase averaging (here indicated with $\langle\cdot\rangle$) has been carried out for every quantity. If ϕ is the phase angle, $\phi = 0^o$ and 180^o degrees correspond to a zero-pressure gradient (ZPG) case, whereas at 270^o an APG is followed by an FPG, and at 90^o the FPG precedes the APG. We also carried out numerical simulation with a steady pressure gradient corresponding to that imposed at $\phi = 0°$, $54°$, $90°$, $270°$, and $306°$.

RESULTS

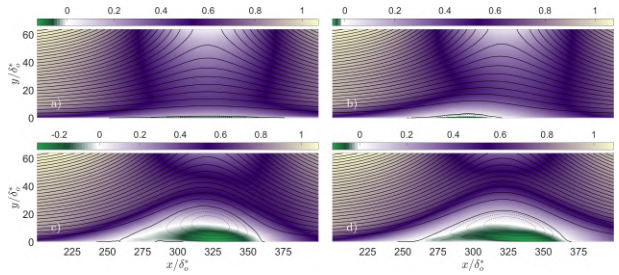

Figure 1: Contours of phase-averaged streamwise velocity $\langle u\rangle$ for the phase $\Phi = 270°$. (a) $k = 10$; (b) $k = 1$; (c) $k = 10$; (d) Steady calculation.

The first important result is the effect of the reduced frequency k on flow separation. Figure 1 shows contours of phase-averaged steamwise velocity $\langle u\rangle$ for the extreme phase $\Phi = 270°$. We can observe that flow separation (on average) occurs in each of the unsteady cases though the size of the separation region greatly changes as the frequency k decreases. For the high and medium frequency cases ($k = 10$ and $k = 1$) the separation region does not have the time to grow as thick as in the corresponding steady case (Figure 1 d), however it is very interesting to note that the length of the separation region for the $k = 10$ case is comparable with the corresponding steady case, but the length of the separation region for the $k = 1$ case is significantly lower. At this frequency, the region of slow-moving fluid generated by the flow reversal is advected downstream, causing a decorrelation between the forcing and the velocity and pressure in this region. As the frequency k is reduced to 0.2, a quasi-steady state is approached, and the dimensions of the separation bubble (both height and length) match very well the steady calculation.

Figure 2 shows the phase-averaged streamwise velocity $\langle u\rangle$ for 4 phases in the cycle at three stream-wise locations in the domain ($x/\delta_o^* = 270, 300, 450$). The dynamic simulations match reasonably well the steady cases when the FPG precedes the APG ($\phi = 54°$ and $\phi = 90°$), while significant differences can be observed when flow separation is present. In the $k = 1$ case there is a significant difference between $\phi = 0°$ and $\phi = 180°$ (the two ZPG phases), indicating the occurrence of hysteresis which is not seen if the frequency is either higher or lower. The $k = 0.2$ case, on the other hand, shows a clear trend towards a quasi-steady solution; the velocity profile at $\phi = 270°$, however, has a stronger backflow.

CONCLUSION AND FUTURE WORK

The simulations carried out so far show that (1) flow separation is significantly affected by the reduced frequency k,

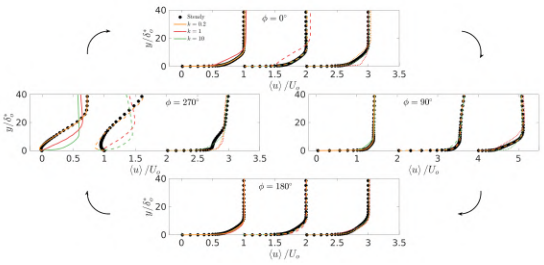

Figure 2: Stream-wise phase averaged $\langle u\rangle$ velocity profile for 4 phases in the cycle at different reduced frequencies k (colors) and stream-wise locations (line styles). Comparison is made with steady calculations (symbols) at the same stream-wise locations.

(2) hysteresis plays a significant role both in the near wall region (for the $k = 10$ case) and farther away from the wall (in the $k = 1$ case), (3) the $k = 1$ case not only shows that the separation region is significantly reduced, but also that a clear decorrelation between the forcing and other flow quantities is present downstream the separation bubble, and (4) although the $k = 0.2$ case shows a clear trend towards a quasi-steady state, a different behavior (compared with steady calculations) is observed in the backflow region. We are currently investigating the physical phenomena underlying the observed behaviors, and we are determining implications of our findings on real life and industrial applications.

REFERENCES

[1] R. L. Simpson, "Turbulent boundary-layer separation," *Ann. Rev. Fluid Mech.*, vol. 21, no. 1, pp. 205–232, 1989.

[2] R. Narasimha and K. R. Sreenivasan, "Relaminarization in highly accelerated turbulent boundary layers," *J. Fluid Mech.*, vol. 61, no. 3, pp. 417–447, 1973.

[3] P. Domenici, E. M. Standen, and R. P. Levine, "Escape manoeuvres in the spiny dogfish (squalus acanthias)," *J. Exp. Biol.*, vol. 207, no. 13, pp. 2339–2349, 2004.

[4] D. M. Schatzman and F. O. Thomas, "An experimental investigation of an unsteady adverse pressure gradient turbulent boundary layer: embedded shear layer scaling," *J. Fluid Mech.*, vol. 815, p. 592, 2017.

[5] A. W. Vreman, "An eddy-viscosity subgrid-scale model for turbulent shear flow: Algebraic theory and applications," *Phys. Fluids*, vol. 16, no. 10, pp. 3670–3681, 2004.

[6] A. Keating, U. Piomelli, K. Bremhorst, and S. Nešić, "Large-eddy simulation of heat transfer downstream of a backward-facing step," *J. Turb.*, vol. 5, no. 1, p. 020, 2004.

[7] J. Yuan and U. Piomelli, "Numerical simulation of a spatially developing accelerating boundary layer over roughness," *J. Fluid Mech.*, vol. 780, pp. 192–214, 2015.

[8] W. Wu and U. Piomelli, "Effects of surface roughness on a separating turbulent boundary layer," *J. Fluid Mech.*, vol. 841, pp. 552–580, 2018.

[9] Y. Na and P. Moin, "Direct numerical simulation of a separated turbulent boundary layer," *J. Fluid Mech.*, vol. 374, pp. 379–405, 1998.

[10] T. S. Lund, X. Wu, and K. D. Squires, "Generation of inflow data for spatially-developing boundary layer simulations," *J. Comput. Phys.*, vol. 140, pp. 233–258, 1998.

[11] G. J. Leishman, *Principles of helicopter aerodynamics*. Cambridge U. P., 2006.

[12] S. K. F. Karlsson, "An unsteady turbulent boundary layer," *J. Fluid Mech.*, vol. 5, no. 4, pp. 622–636, 1959.

[13] S. Brunton and C. Rowley, "Modeling the unsteady aerodynamic forces on small-scale wings." AIAA Paper 2009-1127, 2009.

WORKSHOP
Direct and Large-Eddy Simulation 13
October 26th-29th 2022, Udine, Italy

SIMULATION OF MASSIVELY SEPARATED FLOWS USING HYBRID TURBULENCE MODELS AND MESH ADAPTATION

F. Miralles[1], B. Sauvage[2], S. Wornom[1], F. Alauzet[3], B. Koobus[1] and A. Dervieux [2,4]
[1] IMAG, Univ. Montpellier, CNRS, France, florian.miralles@umontpellier.fr, bruno.koobus@umontpellier.fr, stephen.wornom@inria.fr
[2] Université Côte d'Azur, INRIA Sophia-Antipolis, France, bastien.sauvage@inria.fr, alain.dervieux@inria.fr
[3] INRIA Saclay, France, frederic.alauzet@inria.fr
[4] Lemma, Biot, France, alain.dervieux@inria.fr

INTRODUCTION

The simulation of unsteady flows characterized by large separations induced by adverse pressure gradient is still a challenge at high Reynolds numbers. For such simulations, hybrid models are those favored due to the cost/accuracy compromise they offer. In this study, we assess, next to the DDES approach, the performance of two hybrid models for the prediction of the flow around a circular cylinder at Reynolds numbers 10^6 and 2×10^6, and the flow over a NACA0021 airfoil in a deep stall at Reynolds number 270000. These hybrid models combine either a RANS model or the DDES approach with the dynamic variational multiscale (DVMS) model for the large eddy simulation. A mesh adaptation procedure is currently being applied for the NACA0021 benchmark, with the aim of improving the prediction of the aerodynamic and aeroacoustic characteristics of the flow, such as the airfoil self-noise generation and propagation.

TURBULENCE MODELING

We start by briefly specifying the base ingredients of our hybrid turbulence strategies, namely the RANS or DDES component, and the DVMS component.

• **RANS component**: two low Reynolds RANS models are used in our hybrid models, more specifically they are the $k-\varepsilon$ model proposed in Goldberg et al.[1] and the $k-R$ model recently introduced in [2] by Zhang et al. They have been chosen for their abilities to properly predict separated flows with adverse pressure gradients.

• **DDES component**: in this work, the classical DDES approach [3] is based either on the Spalart-Allmaras model or the $k-\varepsilon$ model of Goldberg [1].

• **LES-like component**: the DVMS approach proposed in [4] is used as the LES part of our hybrid models. In this approach, the variational multiscale (VMS) model, aiming to limit the effects of the subgrid-scale (SGS) model to the smallest resolved scales, is combined with the dynamic procedure which provides a tuning of the SGS dissipation in space and time, so that the resulting DVMS model enjoys synergistic effects. An important consequence is that the DVMS model introduces less dissipation than its LES counterpart (based on the same SGS model).

• **Hybrid models** Our hybrid strategies blend either a RANS or DDES model with the DVMS approach [5]. After semi-discretization, these hybrid models can be written as

$$\left(\frac{\partial W_h}{\partial t},\Phi_i\right)+(\nabla\cdot F(W_h),\Phi_i)= -\theta\left(\tau^{\mathrm{mod}}(W_h),\Phi_i\right)-(1-\theta)\left(\tau^{\mathrm{DVMS}}(W_h'),\Phi_i'\right) \quad (1)$$

where the stress tensor τ^{mod} holds for either the RANS stress tensor or the stress tensor used in the DDES approach based on a given RANS model, τ^{DVMS} is the SGS term that applies in DVMS on the small resolved scales component W_h' of the hybrid variable W_h, Φ_i denotes the basis and test functions, F denotes the convective and viscous fluxes, and θ is the blending function.

Two blending functions are applied in this work, which allow an automatic and progressive switch from RANS or DDES to DVMS where the grid resolution is fine enough to resolve a significant part of the local turbulence scales or fluctuations. Typically, it is desirable to have the DVMS component activated in the wake region instead of the RANS or DDES component due to the low dissipation introduced by the DVMS approach. Additionally, these blending functions prevent the activation of the DVMS mode in the boundary layer through the use of a shielding function. These blending functions can write as $\theta=1-f_d(1-\tanh(\xi^2))$ with $\xi=\frac{\Delta}{l_{RANS}}$ where l_{RANS} denotes the characteristic RANS scale, Δ is the filter width, and f_d is a shielding function which characterizes each of the two blending functions applied in this work:

∘ $f_d=f_{\mathrm{ddes}}$ the delaying function used in DDES (see [3])

∘ $f_d=f_{\mathrm{geo}}=\exp\left(-\frac{1}{\epsilon}\min^2(d-\delta_0,0)\right)$ with d the normal distance to the wall, $\epsilon>0$ small enough and $\delta_0>0$ (of the order of the boundary layer thickness).

NUMERICAL MODEL

The spatial discretization, detailed in [4, 5] is an upwing finite-volume/finite element of low dissipation (sixth-order space derivatives). A novelty is the combination with the Transient Fixed Point mesh adaptation loop of [6].

APPLICATIONS

• **Flow past a cylinder** Two Reynolds numbers, 10^6 and 2×10^6, based on the cylinder diameter and on the freestream velocity, are considered. From Table 1, it can be noted that

the prediction of these coefficients by the hybrid simulations at Reynolds number 10^6 are globally in good agreement with the experimental data. The distribution over the cylinder surface of the mean pressure coefficient, shown in Figure 1, confirms this trend. The same observations can be made at Reynolds number 2×10^6 (results not shown for the sake of brevity).

• **Flow over an airfoil in a deep stall** A NACA0021 airfoil at an angle of attack 60^o is considered at Reynolds number 270000 based on the chord length. A coarse mesh of 517 K vertices is used. Two bulk coefficients and the distribution of the mean pressure coefficient over the airfoil surface are respectively given in Table 2 and Figure 3 as an example. Ongoing results using an adapted mesh (Figure 2), as well as acoustic post-processing, will also be shown.

REFERENCES

[1]Goldberg, U., Peroomian, O. and Chakravarthy, S. : A wall-distance-free $k-\varepsilon$ model with Enhanced Near-Wall Treatment, *Journal of Fluids Engineering*, **120**, 457–462 (1998).

[2]Zhang, Y., Rahman, M.M. and Chen, G. : Development of k-R turbulence model for wall-bounded flows, *Aerospace Science and Technology*, **98** (2020).

[3]Spalart, P., Deck, S., Shur, M., Squires, S., Strelets, M., and Travin, A. A new version of detached-eddy simulation, resistant to ambiguous grid densities. *Theory and Computational Fluid Dynamics*, 20:181–195, 2006.

[4]Moussaed, C., Wornom, S., Salvetti, M.V., Koobus, B. and Dervieux, A. : Impact of dynamic subgrid-scale modeling in variational multiscale large-eddy simulation of bluff body flows, *Acta Mechanica*, **225**, 3309-3323 (2014).

[5]Moussaed, C., Salvetti, M.V., Wornom S., Koobus, B. and Dervieux, A. : Simulation of the flow past a circular cylinder in the supercritical regime by blending RANS and variational-multiscale LES models, *Journal of Fluids and Structures*, **47**, 114-123 (2014).

[6]Alauzet, F., Frey, P.J., George, P.-L., and Mohammadi, B.. 3D transient fixed point mesh adaptation for time-dependent problems: Application to CFD simulations. *J. Comp. Phys.*, 222:592–623, 2007.

	$\overline{C}_d$	C'_l	$-\overline{C}_{pb}$	$\overline{\theta}$
Present simulations				
DDES	0.20	0.04	0.22	138
DDES/DVMS (f_{ddes})	0.20	0.02	0.22	135
RANS/DVMS (f_{ddes})	0.25	0.09	0.25	132
Measurements				
Exp. Shih et al. (1993)	-	0.24	0.33	-
Exp. Szechenyi (1975)	0.25	0.32	-	-
Exp. Goelling (2006)	-	-	-	130

Table 1: Bulk coefficients of the flow around a circular cylinder at Reynolds number $\mathbf{10^6}$. $\overline{C}_d$ denotes the mean drag coefficient, C'_l the root mean square of lift time fluctuations, $\overline{C}_{p_b}$ the mean pressure coefficient at cylinder basis, and $\overline{\theta}$ the mean separation angle.

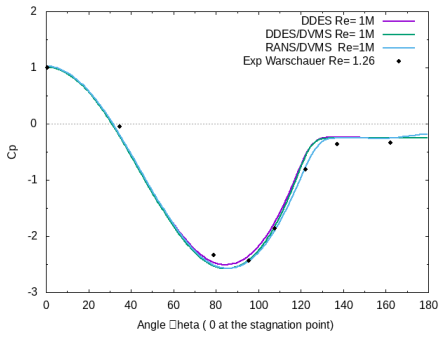

Figure 1: Distribution over the cylinder surface of the mean pressure coefficient at Reynods number $\mathbf{10^6}$.

	Mesh size	$\overline{C}_d$	$\overline{C}_l$
Present simulations			
RANS/DVMS (f_{dgeo})	0.5M	1.66	1.03
RANS/DVMS (f_{ddes})	0.5M	1.54	0.95
DDES/DVMS (f_{geo})	0.5M	1.77	1.06
DDES/DVMS (f_{ddes})	0.5M	1.64	1.01
DDES-SA/mesh adaptation	0.2M	1.53	0.97
Measurement			
Exp. Swalwell (2005)		1.517	0.931

Table 2: Mean drag and lift coefficients for the NACA0021.

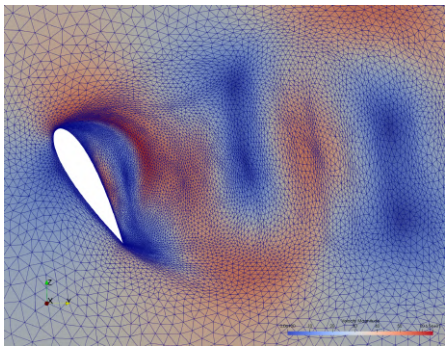

Figure 2: Partial view of a 0.9M adapted mesh and velocity $0 \leq ||U|| \leq 65$.

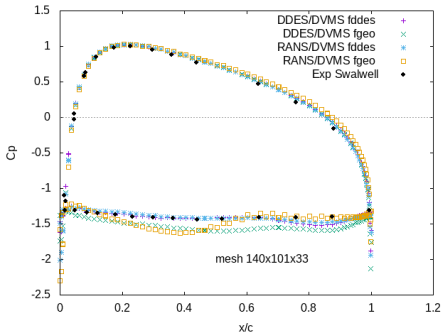

Figure 3: Mean pressure coefficient over the airfoil surface.

WORKSHOP
Direct and Large-Eddy Simulation 13
October 26th-29th 2022, Udine, Italy

ASSESSMENT OF A DISCONTINUOUS GALERKIN SOLVER FOR THE EFFICIENT SIMULATION OF TURBULENT SEPARATED FLOWS

F. Bassi[1], A. Colombo[2], A. Ghidoni[3], F. Massa[2], G. Noventa[3]
[1] University of Bergamo (retired Professor)
francesco.bassi@unibg.it,
[2] University of Bergamo, Department of Engineering and Applied Sciences,
viale Marconi, 5 - 24044 Dalmine (BG), Italy
{alessandro.colombo, francescocarlo.massa}@unibg.it,
[3] University of Brescia, Department of Mechanical and Industrial Engineering,
via Branze 38 - 25123 Brescia, Italy
{antonio.ghidoni, gianmaria.noventa}@unibs.it

In this work, to efficiently simulate separated turbulent flows at high Reynolds numbers, a high-order numerical tool for the solution of a composite RANS-LES model is investigated. In particular, the Extra-large Eddy Simulation (X-LES) of Kok et al. is considered [1], where the $k-\omega$ turbulence model is coupled with a k-equation-based subgrid-scale model. To mitigate the limitations of this DES-type approach, as shown in [2], the shielding function proposed in [3, 4] has been included within the original X-LES.

The numerical accuracy is guaranteed by a discontinuous Galerkin (DG) spatial discretization coupled with a high-order time integration based on linearly-implicit schemes of the Rosenbrock type [5]. To further increase the efficiency and robustness of time integration, especially during the initial transient, an automatic control strategy for the time step size is used. This adaptive algorithm aims at minimizing the computational effort to achieve a user-defined accuracy.

The performance of the solver will be assessed by computing the following test cases: *i*) the channel flow; *ii*) the flow over a backward facing step (BFS), Fig. 1 (*top*); *iii*) the flow over a smooth step (SMS) [6], Fig. 1 (*bottom*). The SMS shows a separation induced by an adverse pressure gradient caused by the wall geometry and is part of the test case suite of the Horizon 2020 HiFi-TURB project (GA 814837).

ACKNOWLEDGEMENTS

F. Bassi, A. Colombo and F. Massa acknowledge the European Project HiFi-TURB which has received funding from the European Union's Horizon 2020 research and innovation programme under the Grant Agreement No. 814837.

REFERENCES

[1] J. C. Kok, H. S. Dol, B. Oskam and H. van der Ven, Extra-large eddy simulation of massively separated flows, *AIAA paper*, 2004.

[2] A. Fracassi, R. De Donno, A. Ghidoni, G. Noventa, Assessment of an Improved Delayed X-LES Hybrid Model for the Study of Off-Design Conditions in Centrifugal Pumps, *ASME. J. Fluids Eng.*, 144(10): 101501, 2022.

[3] P. R. Spalart, S. Deck, M. L. Shur, K. D. Squires, M. K. Strelets, A. Travin A New Version of Detached-eddy Simulation, Resistant to Ambiguous Grid Densities. *Theoret. Comput. Fluid Dyn.*, 20, pp. 181-195, 2006.

[4] M. Gritskevich, A. Garbaruk, J. Schutze, F. Menter, Development of DDES and IDDES formulations for the k-ω shear stress transport model, *Flow, Turbulence and Combustion* 88, 2012.

[5] F. Bassi, L. Botti, A. Colombo, A. Ghidoni, F. Massa, Linearly implicit Rosenbrock-type Runge–Kutta schemes applied to the Discontinuous Galerkin solution of compressible and incompressible unsteady flows, *Computers & Fluids*, 118, 2015.

[6] E. Alaya, C. Grabe, T. Knopp, Design of a parametrized numerical experiment for a 2D turbulent boundary layer flow with varying adverse pressure gradient and separation behaviour. DLR-Interner Bericht. DLR-IB-AS-GO-2020-109. DLR Institute of Aerodynamics and Flow Technology, 2021.

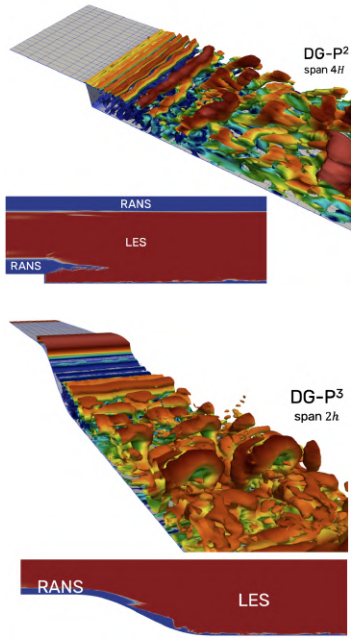

Figure 1: Isosurface of the Q-criterion colored with the velocity magnitude and RANS/LES distribution over the computational domain. BFS (width $4H$), DG $\mathbb{P}^2$ on 68 500 cells (*top*); SMS (width $2h$), DG $\mathbb{P}^3$ on 63 690 cells (*bottom*).

WORKSHOP
Direct and Large-Eddy Simulation 13
October 26th-29th 2022, Udine, Italy

CFD SIMULATION OF A THICK AIRFOIL PROFILE IN STALLED CONDITIONS ADOPTING SCALE-RESOLVING NUMERICAL METHODS

S. Passoni[1], **R. Mereu**[1], **F. Inzoli**[1]
[1] Department of Energy
Politecnico di Milano, Italy
riccardo.mereu@polimi.it;

INTRODUCTION

Flow separation is a classical problem encountered in rotating wind turbine blades, especially at the root section where thick airfoils are employed. Computational Fluid Dynamic (CFD) simulations have gained importance over the last decade to investigate in detail such phenomenon. Nowadays the core of industrial CFD simulations is based on Reynolds-Averaged Navier-Stokes (RANS). These methods could not provide a high level of accuracy for the simulation of stalled thick wind turbine profiles especially in the post-stall region. The purpose of this work is to show how the use of scale-resolving turbulence models can dramatically increase the accuracy in predicting the aerodynamic performance of a these airfoils in stalled conditions. The considered airfoil shape is the DU-97-W300 at a Reynolds number of $2 \cdot 10^6$ in fully turbulent flow regime. The airfoil will be considered both in clean configuration and with the presence of vortex generators (VGs).

GOVERNING EQUATIONS

The modeling procedure consists of an incompressible, scale-resolving approach through DES (Detached-Eddy Simulation) and SDES (Shielded Detached-Eddy Simulation) models. In this work, the scale-resolving modification is added to the k-ω SST model [3]. The transport equations of the turbulence quantities have the following structure:

$$\frac{\partial}{\partial t}(\rho k) + \frac{\partial}{\partial x_i}(\rho k \vec{U}_i) = \frac{\partial}{\partial x_j}\left(\Gamma_k \frac{\partial k}{\partial x_j}\right) + G_k - Y_k + S_k \qquad (1)$$

$$\frac{\partial}{\partial t}(\rho \omega) + \frac{\partial}{\partial x_i}(\rho \omega \vec{U}_i) = \frac{\partial}{\partial x_j}\left(\Gamma_\omega \frac{\partial \omega}{\partial x_j}\right) + G_\omega - Y_\omega + D_\omega + S_\omega \qquad (2)$$

The scale-resolving capabilities of DES model are introduced by modifying the dissipation term (Y_k) of the turbulent kinetic energy transport equation. In the original SST k-ω model this contribution is given by $Y_k = \rho\beta^* k\omega$ where β^* is a model calibration constant equal to 0.09. When DES option is turned on, the sink term becomes

$$Y_k = \rho\beta^* k\omega F_{DES} \quad \text{with} \quad F_{DES} = max\left(\frac{L_t}{C_{DES}\cdot\Delta_{max}}, 1\right) \qquad (3)$$

In equation 3, C_{DES} is a calibration constant equal to 0.61, Δ_{max} is the grid spacing and L_t represents the turbulence length scale defined as $L_t = \sqrt{k}/(\omega\beta^*)$. The mechanism behind the switch between RANS and DES model is straightforward: when $C_{DES}\Delta_{max} > L_t$ RANS mode is activated whereas, when $C_{DES}\Delta_{max} \leq L_t$, the F_{DES} is triggered and LES mode activated.

Differently from DES, the scale-resolving capabilities of SDES model are introduced by an extra sink term of k transport equation 1 and not by modifying directly Y_k:

$$Y_{k,SDES} = \rho\beta^* k\omega F_{SDES} \qquad (4)$$

with

$$F_{SDES} = \left[max\left(\frac{L_t}{C_{SDES}\cdot\Delta_{SDES}}(1 - f_{SDES}), 1\right) - 1\right] \qquad (5)$$

The shielding function, f_{SDES}, is designed to protect the boundary layer in order to make sure it is resolved with RANS models.

DOMAIN AND MESH

The mesh adopted for the clean profile is a hybrid, O-topology grid with a domain's radius of 20 chord lengths. Important for scale-resolving simulations is the domain's span-wise extension. A good compromise between a wide domain and cpu time is a width of one time the chord length, the value used in this work for the clean profile. The grid is discretized in span-wise direction with equal steps of 3%, 1% and 0.6% the chord length in order to perform a sensitivity analysis.

The same domain radius was adopted for the controlled profile simulations while the aspect radius was reduced to 0.16 and 0.49 times the chord length. VGs are modeled as zero-thickness triangular surfaces positioned at a distance of 20% the chord from leading edge and an inflow angle of 15°. A fully resolved approach is considered and the very fine mesh around the vanes is restricted to just a portion of the mesh with the aid of non-conformal mesh interfaces.

NUMERICAL SETTINGS

Simulations are performed on the finite volume solver ANSYS Fluent v19.1. Boundary conditions imposed at the inlet are velocity magnitude and flow direction, the atmospheric static pressure is imposed at the outlet, periodic boundary conditions are imposed on domain sides and no-slip wall condition on airfoil surface. Turbulence is initialized with a turbulence intensity of 0.07% and a turbulence length scale of 0.06 meters. A pressure-based solver is selected, P-V coupling algorithm is set to SIMPLEC algorithm and time integration is carried out using a bounded second order implicit formulation.

Gradient is discretized with least square cells method, pressure with second order scheme and momentum with bounded central differencing. Turbulence variables are discretized with a second order upwind scheme. The timestep chosen is $1.5{\cdot}10^{-4}$s for the simulation of clean profile and $1 \cdot 10^{-4}$s for the controlled one. In both cases this ensures a Courant Flow Number lower than 1 in the portion of the domain resolved with LES mode. Calculations are run for at least 5 turnover times and throughout the simulations, lift and drag coefficient are monitored to assess the statistical convergence of the unsteady flow. The angles of attack simulated ranges from 9° to about 24° in order to capture all the stall phases, from onset to massive flow detachment.

RESULTS AND DISCUSSION

The experimental benchmark by Baldacchino et Al. reported in [4] has been considered as the validation target. Sensitivity analyses on clean profile show that DES model should be used mild stall region ($\alpha \leq 14°$) while SDES for the deep stall zone ($\alpha \geq 16°$). This distinction is necessary because the shielding function of the latter method prevents the turbulence formation at low incidence angles with a negative impact on the accuracy. Also it showed that a unitary aspect ratio and a different mesh resolutions are needed for the various incidence angles. Mild stall regione is the one that benefits the most from a fine grid while the resolution can be relaxed at higher angles of attack. Attention should be paid at near-stall angles of attack when the combination of DES method and to fine grid may lead to grid-induced separation [2].

The profile with VGs is simulated with a base case aspect ratio of 0.16 and a resolution of 0.6% the chord to better adapt to the refinement near the vanes. Such a smaller domain width is justified by flow topology. Vortex generators create strongly confined turbulent structures reducing the presence of spanwise oscillations. DES model is no more used, SDES is able to render turbulence at any angle of attack because vortical structures have enough strength to not be shielded by this method. At angles of attack higher than 23° even the profile with VGs is completely stalled. Vortexes start to oscillate in the spanwise direction and therefore an aspect ratio of 0.49 is then needed to increase the accuracy of the simulation. For a complete sensitivity analyses on the different simulation parameters please refer to [1]. Table 1 and 2 report the results of the conducted analysis for the clean and controlled profile. Lift and drag curves for both cases are displayed in figure 1 and 2 where also RANS results are plotted for a visual comparison. Figure 3 shows and example of the resolved vortex structures at and angle of attack of 16°.

Concluding, scale-resolving simulations are a significant step ahead with respect to RANS approach when studying flow-detachment phenomena. The methodology proposed has shown a great potential in the simulation of thick wind turbine blades under stall conditions and the

REFERENCES

[1]Mereu, R., Passoni, S., Inzoli, F. (2019). Scale-resolving CFD modeling of a thick wind turbine airfoil with application of vortex generators: Validation and sensitivity analyses. Energy, 187, 115969.

Table 1: Numerical results and errors of the final lift and drag polar for clean profile

α [°]	Method	AR	ΔZ	C_L [-]	C_D [-]	δC_L [%]	δC_D [%]
9.218	DES	1	1%	1.1562	0.0327	3.84%	24.33%
11.643	DES	1	0.6%	1.0100	0.0706	14.03%	-11.64%
12.641	DES	1	0.6%	1.0535	0.0848	14.87%	-10.74%
14.154	DES	1	0.6%	1.0818	0.1099	15.94%	-0.81%
16.195	SDES	1	0.6%	1.1244	0.1299	15.83%	-3.28%
18.195	SDES	1	3%	1.1574	0.1525	13.17%	-2.68%
20.224	SDES	1	3%	1.1751	0.1856	7.65%	-1.07%
24.217	SDES	1	3%	1.2337	0.2646	3.49%	-5.03%

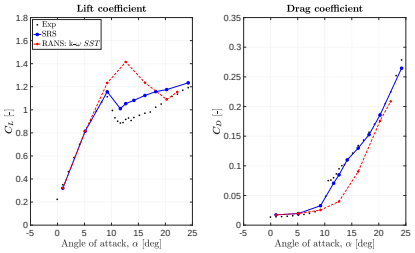

Figure 1: Resulting lift and drag polars for clean profile

Table 2: Numerical results for the final controlled profile polar

α [°]	Method	AR	C_L [-]	C_D [-]	δC_L [%]	δC_D [%]
9.238	SDES	0.16	1.2919	0.0273	0.76%	1.87%
12.239	SDES	0.16	1.5629	0.0346	-0.27%	9.15%
15.409	SDES	0.16	1.7633	0.0496	-0.76%	33.33%
16.429	SDES	0.16	1.8171	0.0608	1.58%	-2.72%
18.426	SDES	0.16	1.8791	0.0753	4.66%	-30.28%
20.413	SDES	0.16	1.8207	0.1080	5.30%	-35.29%
23.225	SDES	0.49	1.2425	0.2769	-1.76%	4.81%

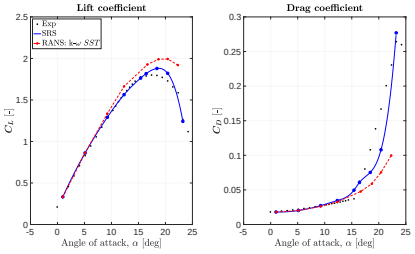

Figure 2: Resulting lift and drag polars for controlled profile

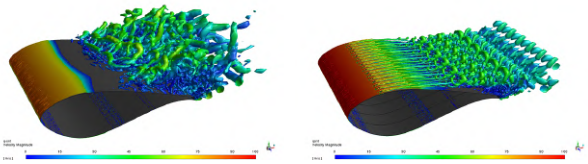

(a) Clean, $\alpha = 16°$, iso-surface value $= 1 \cdot 10^6$

(b) Controlled, $\alpha = 16°$, iso-surface value $= 4 \cdot 10^5$

Figure 3: Iso-surface of Q-criterion at an incidence of 16°, colored with instantaneous velocity magnitude

[2]P. Spalart, S. Deck, M. Shur, K. Squires, M. Strelets, A. Travin, A new version of detached-eddy simulation, resistant to ambiguous grid densities, Theoretical and Computational Fluid Dynamics 20 (2006) 181-195.

[3]F. R. Menter, Two-equation eddy-viscosity turbulence models for engineering applications, AIAA Journal 32 (1994) 1598-1605

[4]D. Baldacchino, C. Ferreira, D. De Tavernier, W. Timmer, G. van Bussel, Experimental parameter study for passive vortex generators on a 30% thick airfoil, Wind Energy (2018).

Session: Wall modelling

Friday, October 28, 2022

16:20 – 17:20

WORKSHOP
Direct and Large-Eddy Simulation 13
October 26th-29th 2022, Udine, Italy

WALL-MODELING OF TURBULENT FLOWS OVER A PERIODIC HILL USING MULTI-AGENT REINFORCEMENT LEARNING

D. Zhou[1] and **H. J. Bae**[1]
[1] Graduate Aerospace Laboratories
California Institute of Technology, USA
dizhou@caltech.edu

INTRODUCTION

Large-eddy simulation (LES) is an essential technology for the simulation of turbulent flows. The basic premise of LES is that energy-containing and dynamically important eddies must be resolved everywhere in the domain. This requirement is hard to meet in the near-wall region, as the stress-producing eddies become progressively smaller. Because of the cost involved in resolving the near-wall region, routine use of wall-resolved LES (WRLES) is far from being an industry standard, where short turnaround times are needed to explore high-dimensional design spaces. Consequently, most industrial computational fluid dynamics analyses still rely on cheaper but arguably lower-fidelity Reynolds-Averaged Navier-Stokes (RANS) tools. This has motivated the development of the wall-modeled LES (WMLES) approach, which uses LES to predict the turbulence in the outer region of the boundary layer but utilizes a reduced-order model in a relatively coarse grid to account for the effect of the energetic near-wall eddies, thus drastically reducing the grid resolution requirement and simultaneously increasing the maximum allowance time step size. Because of such characteristics, wall modeling has been accepted as the next step to enable the increased use of high-fidelity LES in realistic engineering and geophysical applications.

The most popular and well-known WMLES approach is the so-called RANS-based wall models [1, 2, 3, 4], which compute the wall shear stress using the RANS equations. However, these models assume explicitly or implicitly a particular flow state close to the wall (usually fully-developed turbulence in equilibrium over a flat plate) and rely on RANS parametrization which needs manually tuned for various pressure-gradient effects. The recent rise of machine learning has prompted supervised learning as an attractive tool for discovering robust wall models that automatically adjust for different conditions, such as variations in pressure gradient. [5] proposed a data-driven wall model that accounts for pressure-gradient effects based on the supervised learning approach. While the trained model performed well in *a priori* testing for a single time step, the model broke down in *a posteriori* testing due to integrated errors that could not be taken into account via supervised learning.

Recently, [6] demonstrated the efficacy of multi-agent reinforcement learning (MARL) as a model development tool for wall models in a canonical channel and zero-pressure-gradient boundary layer flow. Reinforcement learning (RL) is a semi-supervised learning framework with foundations on dynamic programming and has been used in the applications of flow control [7, 8] and subgrid-scale model development [9]. In [6], a series of RL agents are distributed along the computational grid points, with each agent receiving local states and rewards then providing local actions at each time step. The MARL wall model performs as well as the RANS-based equilibrium wall model, which has been tuned for this particular flow configuration. However, The MARL model is able to achieve these results by training on moderate Reynolds number flows with a reward function only based on the mean wall-shear stress.

In the present work, we extend the methodology of [6] to flow over a periodic hill, training on moderate Reynolds number cases and testing on higher Reynolds number cases. Our objective is to develop a wall model for LES based on MARL that is robust to pressure-gradient effects.

METHODOLOGY

We train the wall model on a flow configuration which (i) has widely available wall-shear stress profiles for several Reynolds numbers and (ii) does not require tuning of the inlet profile or other boundary conditions. The flow over periodically arranged hills in a channel (shown in Figure 1) as proposed by [10] has well-defined boundary conditions, can be computed at affordable costs, and nevertheless inherits all the features of a flow separating from a curved surface and reattaching on a flat plate. Furthermore, periodic hills do not require configurations of the inlet boundary condition for the different grid resolutions and wall models, which is necessary for non-periodic flows. This configuration has become a popular benchmark test case for validating computational fluid dynamics codes since numerous experimental and high-fidelity numerical references exist [11, 12, 13, 14] and provides extensive data on a wide range of Reynolds numbers covering $700 \leq Re_h \leq 37000$, where Re_h is the Reynolds number based on the hill height.

Based on the configuration of flow over periodic hills, we train the wall model using MARL, particularly on the lower Reynolds numbers, following the basic framework laid out in [6]. Additional states that inform the local pressure gradient are added to the model (e.g. velocity gradients in the streamwise direction, pressure measurements at the wall). The capability of the trained model is validated by comparing the WMLES results with the experimental and DNS data at the same Reynolds numbers. We test the model devel-

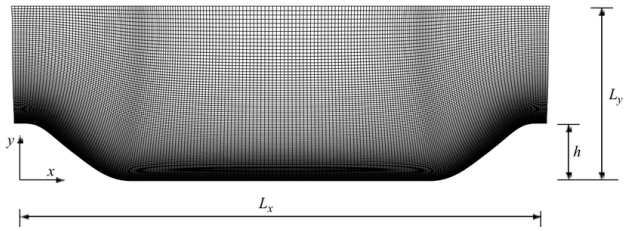

Figure 1: Geometry of the periodic hill.

oped through training on the higher-Reynolds-number cases of the periodic-hills configuration. In addition, we analyze state-action-reward maps of RL models with an additional dimension for the pressure gradient, which allows interpretability of the wall model trained via MARL.

The RL tool, smarties [15], is an open-source C++ library and is optimized for high CPU-level efficiency through fine-grained multi-threading, strict control of cache-locality, and computation-communication overlap. It implements many established deep RL algorithms [15] as well as methods that have been systematically tested for data-driven turbulence modeling [9]. On every step, it asynchronously obtains on-policy data by sampling the environment and computes the updates by sampling from the replay memory, which advances the gradient steps. Upon completion of all tasks, it applies the gradient update and proceeds to the next step. The RL tool is coupled with the flow solver, which is an unstructured collocated finite-volume discretization of low-Ma number variable-density Navier-Stokes equations.

REFERENCES

[1]E. Balaras, C. Benocci, and U. Piomelli, "Two-layer approximate boundary conditions for large-eddy simulations," *AIAA J.*, vol. 34, no. 6, pp. 1111–1119, 1996.

[2]M. Wang and P. Moin, "Dynamic wall modeling for large-eddy simulation of complex turbulent flows," *Phys. Fluids*, vol. 14, no. 7, pp. 2043–2051, 2002.

[3]D. Chung and D. I. Pullin, "Large-eddy simulation and wall modelling of turbulent channel flow," *J. Fluid Mech.*, vol. 631, pp. 281–309, 2009.

[4]G. I. Park and P. Moin, "An improved dynamic non-equilibrium wall-model for large eddy simulation," *Phys. Fluids*, vol. 26, no. 1, pp. 37–48, 2014.

[5]Z. Zhou, G. He, and X. Yang, "Wall model based on neural networks for LES of turbulent flows over periodic hills," *Phys. Rev. Fluids*, vol. 6, no. 5, p. 054610, 2021.

[6]H. J. Bae and P. Koumoutsakos, "Scientific multi-agent reinforcement learning for wall-models of turbulent flows," *Nat. Comm.*, vol. accepted, 2021.

[7]M. Gazzola, B. Hejazialhosseini, and P. Koumoutsakos, "Reinforcement learning and wavelet adapted vortex methods for simulations of self-propelled swimmers," *SIAM J. Sci. Comput.*, vol. 36, no. 3, pp. B622–B639, 2014.

[8]G. Novati, S. Verma, D. Alexeev, D. Rossinelli, W. M. Van Rees, and P. Koumoutsakos, "Synchronisation through learning for two self-propelled swimmers," *Bioinspir. Biomim.*, vol. 12, no. 3, p. 036001, 2017.

[9]G. Novati, H. L. de Laroussilhe, and P. Koumoutsakos, "Automating turbulence modelling by multi-agent reinforcement learning," *Nat. Mach. Intell.*, vol. 3, no. 1, pp. 87–96, 2021.

[10]C. P. Mellen, J. Fröhlich, and W. Rodi, "Large eddy simulation of the flow over periodic hills," in *16th IMACS world congress*, pp. 21–25, Lausanne, Switzerland, 2000.

[11]J. Fröhlich, C. P. Mellen, W. Rodi, L. Temmerman, and M. A. Leschziner, "Highly resolved large-eddy simulation of separated flow in a channel with streamwise periodic constrictions," *J. Fluid Mech.*, vol. 526, pp. 19–66, 2005.

[12]M. Breuer, N. Peller, C. Rapp, and M. Manhart, "Flow over periodic hills–numerical and experimental study in a wide range of Reynolds numbers," *Comput. Fluids*, vol. 38, no. 2, pp. 433–457, 2009.

[13]C. Rapp and M. Manhart, "Flow over periodic hills: an experimental study," *Exp. Fluids*, vol. 51, no. 1, pp. 247–269, 2011.

[14]P. Balakumar, G. Park, and B. Pierce, "DNS, LES, and wall-modeled LES of separating flow over periodic hills," in *Proceedings of the Summer Program*, pp. 407–415, 2014.

[15]G. Novati and P. Koumoutsakos, "Remember and forget for experience replay," in *Proceedings of the 36th International Conference on Machine Learning.*, 2019.

Development of wall-modelling capabilities for LES in Nek5000

T. Mukha[1], **G. Brethouwer**[1], **P. Schlatter**[1]
[1] Department of Engineering Mechanics
KTH Royal Institute of Technology, Sweden
tmu@mech.kth.se, geert@mech.kth.se, pschlatt@mech.kth.se

INTRODUCTION

To perform large-eddy simulation (LES) of wall-bounded flows at high Reynolds numbers it is necessary to introduce a model for the dynamics of the inner region of turbulent boundary layers (TBLs), otherwise the computational cost becomes prohibitive. In this contribution, we discuss the development of wall modelling capabilities in the spectral element solver Nek5000. We focus on the issues with the subgrid scale (SGS) modelling and wall model boundary conditions specific to this numerical framework. We then present results from wall-modelled LES (WMLES) of several flows: turbulent channel flow, flat-plate TBL, and the convective atmospheric boundary layer (ABL).

WALL MODELLING

The simplest wall model for LES uses a law-of-the-wall, such as Spalding's law [1] to obtain the magnitude of the wall shear stress $|\tau_w|$ based on the streamwise velocity sampled at some distance h from the wall node. Here, we employ this approach, which works well for attached TBLs. For a review of other methods, see [2].

Having obtained $|\tau_w|$, it is necessary to prescribe its two wall-parallel components (here, x and z):

$$\tau_{iy} = (\nu + \nu_t) S_{iy}, \quad i \in \{x, z\} \tag{1}$$

Here, ν is the kinematic viscosity, ν_t is the SGS viscosity at the wall, and S_{ij} is the rate-of-strain tensor.

Two main approaches for this can found in the WMLES literature. The most popular one is using a Neumann boundary condition for velocity instead of no-slip. Then, the direction of τ_w is chosen to be aligned with the velocity vector at the sampling location. The Neumann condition introduces a slip velocity that ensures that S_{ij} multiplied by the viscosity gives the correct stress. The main issue with this approach in the spectral element setting is the fact that the Neumann boundary condition is only enforced weakly. This means that on coarse meshes typical of WMLES there is no guarantee that the desired stress will be exactly prescribed.

An alternative, called the viscosity boundary condition here, is to retain the no-slip condition and model ν_t to obtain the desired stress, which amounts to setting

$$\nu_t = |\tau_w| / \sqrt{S_{xy}^2 + S_{zy}^2} - \nu \tag{2}$$

at the wall. In this case, however, one has no control over the direction of τ_w, since it is predetermined by the distribution of the components of S_{ij}. This has a negative consequence. If we consider a model that predicts the correct mean stress magnitude $\langle |\tau_w| \rangle$ at each time step, the boundary condition will somehow distribute it across the two wall-parallel directions. Consequently, the mean magnitude of the prescribed stress will be less than $\langle |\tau_w| \rangle$.

SUBGRID SCALE MODELLING

For SGS modelling, we experimented with the Vreman model [3] and the minimum dissipation model [4]. The latter is indeed significantly less diffusive, which generally affected the results negatively. Mean velocity profiles from channel flow at $Re_\tau \approx 8000$ are shown in Figure 1. Even after averaging, there are visible wiggles in the solution using the viscosity boundary condition, and these wiggles are even more pronounced in the profiles of the second-order statistics. The larger diffusivity of the Vreman model helps remove them. Overall, the accuracy of the solution is good for WMLES.

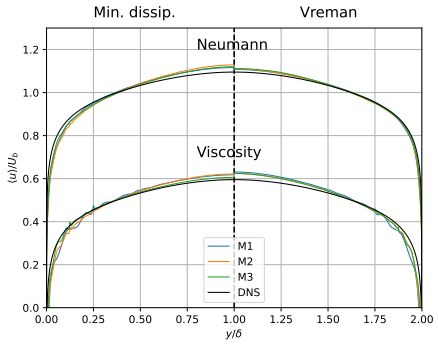

Figure 1: Mean velocity profiles from simulations of turbulent channel flow at $Re_\tau \approx 8000$. Simulations M1-M3 are performed on successively refined meshes. DNS results from [5].

The strongest effect of the SGS model manifested itself in combination with the Neumann boundary condition. For the minimum dissipation model, Re_τ was strongly underpredicted, up to 9.35% relative error, depending on the mesh. For the Vreman model, errors did not exceed 2.5%. Investigation showed that it is in fact the value of ν_t at the wall, which affects the Neumann boundary condition performance strongly. A larger value generally favoured the accuracy.

In fact, the distribution of ν_t on the wall as predicted by the SGS model plays a crucial role. This was revealed by simulations of flat-plate TBLs. Figure 2 shows the skin friction c_f obtained in a WMLES using the Vreman model and the Neumann boundary condition. The large spikes in the c_f followed exactly those that could be observed in the ν_t values at the wall. As an ad-hoc solution, we performed spatial averaging of ν_t at the wall within each element. This allowed to reduce the spikes significantly, as depicted by the orange curve in the

figure. However, it is necessary to look closely at the reason behind the spikes in ν_t in the first place. A suitable way of alleviating them can be spatial or modal filtering. This is a direction of current research.

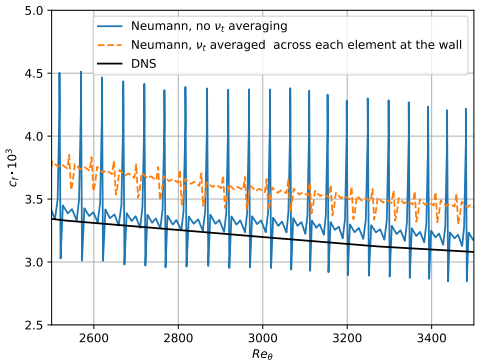

Figure 2: Skin friction coefficient in simulations of a flat-plate TBL, with and without spatial averaging of ν_t. DNS results from [6].

In spite of the presented issues, it is possible to conduct accurate WMLES with both boundary conditions. The Neumann condition is suitable for channel-like geometries where spatial averaging removes oscillations in τ_w. We have successfully applied it to simulations of thermally stratified ABLs. In Figure 3 we show the obtained mean velocity profile for the case of a convective ABL (together with results form [7]).

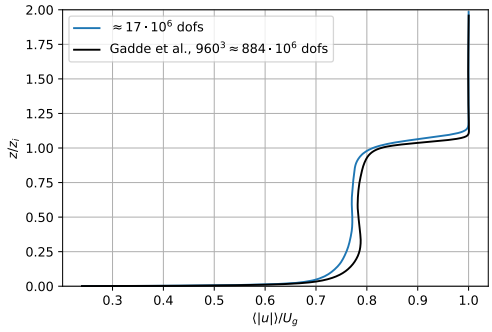

Figure 3: Mean velocity in a convective ABL. Here z_i is the thickness of the ABL, and U_g is the velocity of the geostrophic wind. The blue curve shows WMLES results on a relatively coarse grid. The black curve shows results from [7].

For evolving boundary layers, the viscosity boundary condition can be employed. Figure 4 demonstrates the skin friction obtained in a high Re-number simulation of a flat-plate TBL, which agrees well with reference data. Our future efforts will be dedicated to deriving a boundary condition that will be accurate, universally applicable and independent of the SGS model selection.

REFERENCES

[1] D. B. Spalding, "A single formula for the 'law of the wall'," *Journal of Applied Mechanics*, vol. 28, no. 3, pp. 455–458, 1961.

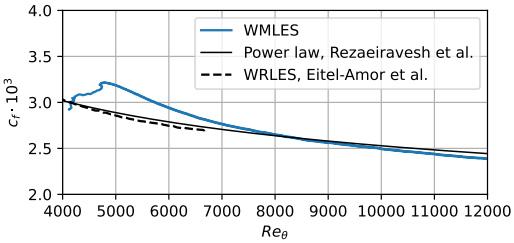

Figure 4: Skin friction coefficient in simulations of a flat-plate TBL, using the viscosity boundary condition. Reference wall-resolved LES (WRLES) from [8] and power law estimate from [9].

[2] J. Larsson, S. Kawai, J. Bodart, and I. Bermejo-Moreno, "Large eddy simulation with modeled wall-stress: Recent progress and future directions," *Mechanical Engineering Reviews*, vol. 3, no. 1, pp. 1–23, 2016.

[3] A. W. Vreman, "An eddy-viscosity subgrid-scale model for turbulent shear flow: Algebraic theory and applications," *Physics of Fluids*, vol. 16, no. 10, pp. 3670–3681, 2004.

[4] W. Rozema, H. J. Bae, P. Moin, and R. Verstappen, "Minimum-dissipation models for large-eddy simulation," *Physics of Fluids*, vol. 27, no. 8, 2015.

[5] Y. Yamamoto and Y. Tsuji, "Numerical evidence of logarithmic regions in channel flow at $Re_\tau = 8000$," *Physical Review Fluids*, vol. 3, no. 1, p. 012602, 2018.

[6] P. Schlatter and R. Örlü, "Assessment of direct numerical simulation data of turbulent boundary layers," *Journal of Fluid Mechanics*, vol. 659, pp. 116–126, 2010.

[7] S. N. Gadde, A. Stieren, and R. J. A. M. Stevens, "Large-eddy simulations of stratified atmospheric boundary layers: Comparison of different subgrid models," *Boundary-Layer Meteorology*, vol. 178, no. 3, pp. 363–382, 2021.

[8] G. Eitel-Amor, R. Örlü, and P. Schlatter, "Simulation and validation of a spatially evolving turbulent boundary layer up to $Re_\theta = 8300$," *International Journal of Heat and Fluid Flow*, vol. 47, pp. 57–69, 2014.

[9] S. Rezaeiravesh, M. Liefvendahl, and C. Fureby, "On grid resolution requirements for LES of wall-bounded flows," in *ECCOMAS Congress 2016*, (Crete, Greece), 2016.

WORKSHOP
Direct and Large-Eddy Simulation 13
October 26th-29th 2022, Udine, Italy

VISUALIZATION OF WALL-MODELED TURBULENT CHANNEL FLOW USING SPECTRAL PROPER ORTHOGONAL DECOMPOSITION

H. Hosseinzade and **D.J. Bergstrom**
Department of Mechanical Engineering
University of Saskatchewan, Canada
hadi.hosseinzade@usask.ca

INTRODUCTION

The visualization of flow structures originated with research explaining the shape of the two-point velocity correlations in the wake of a cylinder by Townsend [1]. He hypothesized the presence of organized turbulent flow structures that rarely repeat in detail but are energetically dominant. These flow structures, which are now known as coherent structures, can be identified using a modal decomposition analysis of flow data from either an experimental or numerical analysis. A post-processing technique was later developed that mathematically decomposed the unsteady dynamics of the coherent structures into a set of energy modes [2]. This analytical method is known as the proper orthogonal decomposition (POD). Recently, Sieber et al. [3] developed a complementary modal energy analysis that implements a low-pass temporal filter on the correlation matrix. They introduced the spectral proper orthogonal decomposition (SPOD) method to detect the coherent structures at low energies or multiple frequencies. It is believed that the SPOD fills the gap between the optimal decomposition of energy (POD) and clean spectral decomposition (discrete Fourier transform) analyses.

In this paper, a 3D turbulent channel flow at a moderate Reynolds number of $\mathrm{Re}_\tau = 395$ is initially studied through a wall-resolved large eddy simulation (WRLES). The SPOD analysis is performed on velocity fluctuations to capture the dominant energy modes. A wall-modeled large eddy simulation (WMLES) channel flow at the same Reynolds number is used to assess the effects of wall-modeling on the visualization of coherent structures. Next, the Reynolds number of the channel flow is increased to $\mathrm{Re}_\tau = 2000$ to compare the moderate and high-Reynolds number wall-modeled channel flows in the identification of coherent flow structures using the POD analysis. To the knowledge of the authors, only a few studies have implemented large eddy simulation (LES) to address space-time characteristics of turbulent channel flows. Finally, the energy spectrum analysis is conducted to determine the distribution of turbulence kinetic energy among eddies with different length scales in both WRLES and WMLES channel flows.

METHODOLOGY

The incompressible filtered Navier-Stokes equations are discretized using the finite volume method. A central differencing scheme is implemented to estimate the face velocities on a structured collocated grid. A second-order explicit Adam-Bashforth method is used to discretize the advection and diffusion terms in an explicit scheme. A two-step fractional step method solves the momentum equations for the velocity, and a discrete Poisson's equation is solved for the pressure field. A dynamic non-linear subgrid scale (SGS) model is implemented to solve turbulent flows in the context of wall-modeled large eddy simulation, while a dynamic non-equilibrium wall model is used to model the flow dynamics in the near-wall region.

The SPOD analysis is employed to identify the coherent structures using the velocity fluctuations in a 3D channel flow. The snapshot POD was implemented to calculate the correlation matrix ($\mathcal{S}$) between individual snapshots. A low-pass filter with a finite width of N_f along the diagonals of the correlation matrix is used to represent a specific range of frequencies. To find the temporal coefficients (b_i) and mode energies (μ_i), the eigenvalues and eigenvectors of the correlation matrix are determined by solving the following equation:

$$\mathcal{S}\ b_i = \mu_i\ b_i \quad , \quad i = 1, 2, 3, ..., N, \tag{1}$$

where subscript i refers to the individual eigenmodes. The spatial modes of the SPOD are obtained and the velocity components can be decomposed as follows:

$$u(X,t) = \overline{u}(X) + \sum_{i=1}^{N} b_i(t)\phi_i(X), \tag{2}$$

where $\overline{u}(X)$ is the mean velocity, and $\phi_i(X)$ is the spatial orthogonal mode. To identify and visualize vortex structures based on the invariants of the velocity gradient, the swirling strength method is implemented. The swirling strength method, which is independent of choosing a proper reference frame to detect the swirling motions, uses the imaginary part of the eigenvalue of the velocity gradient to extract the vortical flow structures.

NUMERICAL METHOD

Three distinct simulations were conducted at different Reynolds numbers and grid resolution. The same computational domain of size $2\pi\delta \times 2\delta \times \frac{4}{3}\pi\delta$ is used for all simulations, where δ is half of the channel height. In the WRLES channel flow at $\mathrm{Re}_\tau = 395$, a mesh with 96^3 grid points is used to resolve the flow field with a uniform grid in the wall-parallel planes and a non-uniform distribution in the wall-normal direction. The SPOD analysis is performed over 250 snapshots separated by time intervals of $\delta t^+ = 75$ ($\delta t^+ = \delta t/t_v$ where t_v is the viscous time scale). The WMLES channel flow at $\mathrm{Re}_\tau = 395$ is conducted using twelve times lower grid resolution with a uniform grid distribution in all directions and the matching point located at the 4^{th} node in the LES domain with $y^+ \approx 84$. In a high-Reynolds number channel flow at $\mathrm{Re}_\tau = 2000$, the matching point is moved to the 5^{th} node with $y^+ = 272$. Thirty grid points in the wall-normal direction are used for the wall layer.

RESULTS

The mean velocity profiles of the wall-modeled and wall-resolved simulations are shown in Fig. 1. The mean velocities are non-dimensionalized using the friction velocity estimated based on the flow data in the wall layer. The results of the wall-resolved channel flow match the direct numerical simulation (DNS) study of Moser and Moin [4]. Then, the wall-modeling is implemented for the simulation of turbulent channel flows at $\mathrm{Re}_\tau = 395$ and 2000. The mean velocity profiles of the wall-modeled channel flow closely follow the corresponding DNS profiles in the outer layer. In the near-wall region, some deviations are observed between the WMLES profiles and DNS data sets, which indicate an inconsistency between the grid spacing and the requirements of the SGS model. Note that the mean velocity profiles are shifted by five units for clarity.

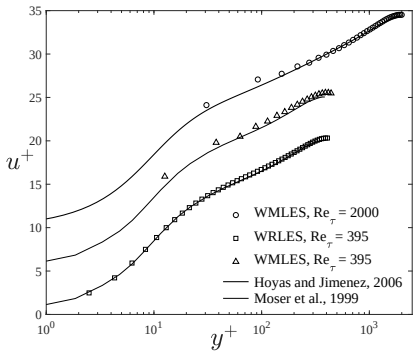

Figure 1: Mean velocity profiles in wall coordinates.

Fig. 2 shows the vortical structures in the WMLES channel flow for a Reynolds number of $\mathrm{Re}_\tau = 395$ for an instantaneous velocity field. For the SPOD analysis with a filtering width of $N_f = 15$, the second mode is used to identify the energetic structures. The structures are visualized using a specific value of swirling strength and colored with the magnitude of the streamwise velocity component. For illustration, a few select structures are highlighted in green. It is evident that only relatively large structures are resolved by the WMLES due to the coarse mesh used by the LES in the near-wall region. The grid resolution is unable to resolve the small-scale structures that would be present in a WRLES or a DNS. The large structures present in the WMLES appear to be inclined upwards and stretched in the streamwise direction.

The SPOD analysis for the WMLES channel flow indicates only relatively larger-scale structures in the near-wall region. The use of SPOD improves the visualization of the coherent

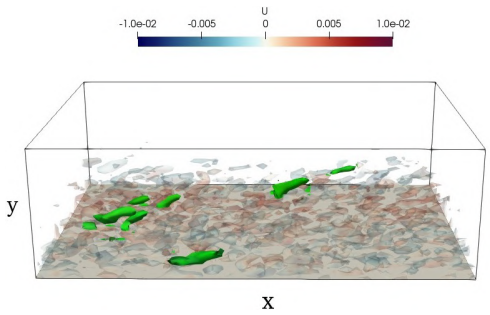

Figure 2: Iso-surface of coherent structures with swirling strength of $\lambda_{ci} = 0.2$ in WMLES channel flow at $\mathrm{Re}_\tau = 395$.

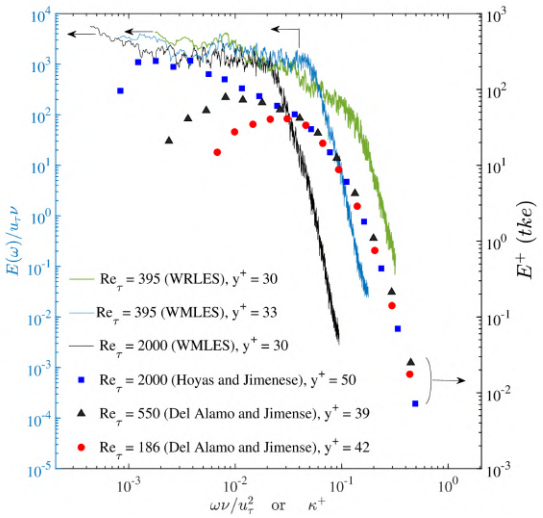

Figure 3: Energy spectra of wall-resolved and wall-modeled channel flow for moderate and high-Reynolds number channel flows.

structures by filtering the small-scale motions and noise. The one-dimensional energy spectra of the streamwise velocity fluctuations for the wall-resolved and wall-modeled channel flows are given in Fig. 3 for a wall-normal location of $y^+ \approx 30$. A low-pass filter was used to remove noise and improve the clarity of the spectral curves. For comparison, the turbulence kinetic energy spectra for DNS channel flows of similar Reynolds number are shown in the same plot (using the opposite axis). For the WRLES spectra, the green curve shows a narrow region with a slope of $-5/3$. The WMLES spectra at both Reynolds numbers show a flat low-frequency region, followed by a sharp drop off, which indicates the absence of higher frequency, small-scale structures. The frequency distribution is very different than that shown by the DNS curves.

CLOSURE

The final paper will use different SPOD modes to visualize the coherent motions in the near-wall region. It will also document the effect of changing the temporal filter used to condition the correlation matrix in SPOD. An overall conclusion of the study is that WMLES shows only large-scale structures in the region of the flow affected by the wall model, consistent with the coarse grid used in that region.

REFERENCES

[1] Townsend, A.A. : The turbulent boundary layer, *Boundary Layer Research Symposium Freiburg, August 26–29, Berlin, Germany*, 166–177 (1958).

[2] Lumley, J. : The structure of inhomogeneous flow turbulence, *Atmospheric Turb. and Radio Wave Propagation*, 685–703 (1967).

[3] Sieber, M., Paschereit, C.O., and Oberleithner, K. : Spectral proper orthogonal decomposition, *J. Fluid Mech.*, **792**, 798–828 (2016).

[4] Moser, R. D., and Moin, P. : Characteristic-eddy decomposition of turbulence in a channel, *J. Fluid Mech.*, **200**, 471–509 (1999).

[5] Hoyas, S., and Jimenez, J. : Scaling of the velocity fluctuations in turbulent channels up to $\mathrm{Re}_\tau = 2003$, *Physics Fluids*, **18**(011702), 1–4 (2006).

[6] Del Alamo, J. C., Jimenez, J., Zandonde, P., and Moser, R.D. : Scaling of the energy spectra of turbulent channels, *J. Fluid Mech.*, **800**, 135–144 (2004).